REVIEWS IN COMPUTATIONAL CHEMISTRY

Kenny B. Lipkowitz *Thomas R. Cundari*

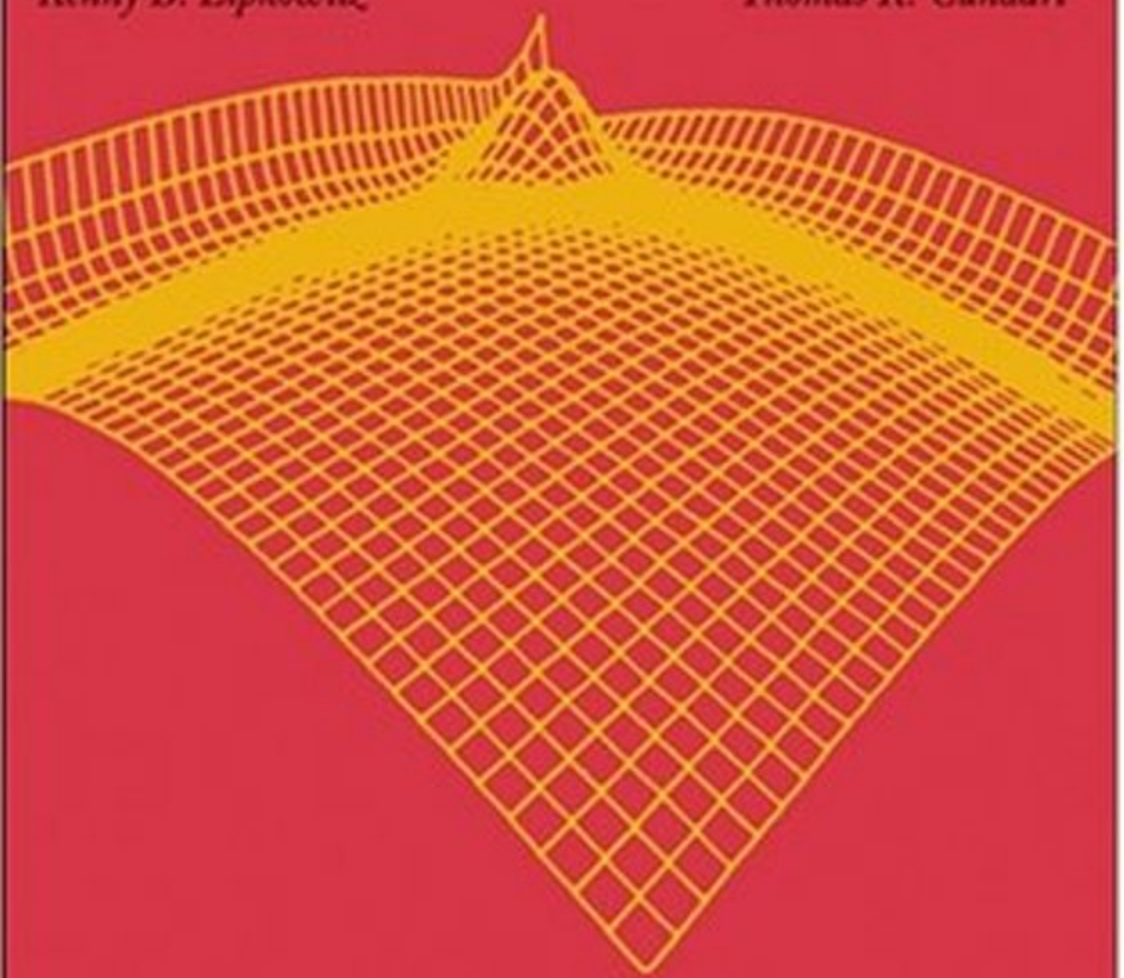

WILEY VOLUME 26

Reviews in Computational Chemistry Volume 26

Reviews in Computational Chemistry 26

Edited by

Kenny B. Lipkowitz
Thomas R. Cundari

Editor Emeritus

Donald B. Boyd

WILEY
A John Wiley & Sons, Inc., Publication

Kenny B. Lipkowitz
Office of Naval Research
875 North Randolph Street
Arlington, VA 22203-1995
kenny.lipkowitz@navy.mil

Thomas R. Cundari
Department of Chemistry
University of North Texas
Box 305070
Denton, Texas 76203-5070, U.S.A.
tomc@unt.edu

Donald B. Boyd
Department of Chemistry and Chemical Biology
Indiana University-Purdue University at Indianapolis
402 North Blackford Street
Indianapolis, Indiana 46202-3274, U.S.A.
boyd@chem.iupui.edu

Published by John Wiley & Sons, Inc., Hoboken, New Jersey
Published simultaneously in Canada

Library of Congress Cataloging-in-Publication Data:

ISBN 978-0470-38839-6
ISSN 1069-3599

Printed in the United States of America
10 9 8 7 6 5 4 3 2 1

Contents

Preface

Earning tenure at an academic institution and running a steeplechase race successfully have a lot in common. Both require extensive training before the event begins, both involve hurdles to overcome and pitfalls to avoid, and both are grueling events that inevitably lead to a few twisted ankles or broken marriages. Unlike the steeplechase race where there exists a single winner (second place is considered "first loser"), multiple winners can be found in the tenure race, however.

Tenure decisions are often based on some institutionally defined, linear combination of teaching, research, and service to the community. However, not all institutions share the same values, nor do they have the same goals. While some institutions focus mainly on teaching and others focus primarily on research, they all share the common theme of ensuring that competent and caring teachers are interfacing with their students.

For those colleges and universities that emphasize research in the tenure portfolio, another common theme is that they all *want* their new hires to be successful in their research endeavors. This usually means providing reduced teaching loads for those new faculty during the first academic year, assigning mentors to oversee new faculty teaching and/or research strategies so as to help them avoid pitfalls that might derail an otherwise successful career, and providing startup funding so that those new faculty members can obtain the requisite equipment, supplies, and personnel needed to jump-start their research careers.

One often hears, anecdotally, how much a particular institution paid in startup funding to attract a highly regarded candidate to accept its offer in lieu of one from a competing institution. Sometimes those funds include valuable but inflationary content such as laboratory renovation costs, machine time fees, repair shop costs, partial summer salaries, and so on, which, superficially, balloon the startup costs to the point of extravagance. So, what are the startup packages in academic laboratories nowadays, and, are those packages really as extravagant as some are saying? Moreover, with respect to the readership of this book series, how do computational chemists fare with respect to experimentalists in this regard?

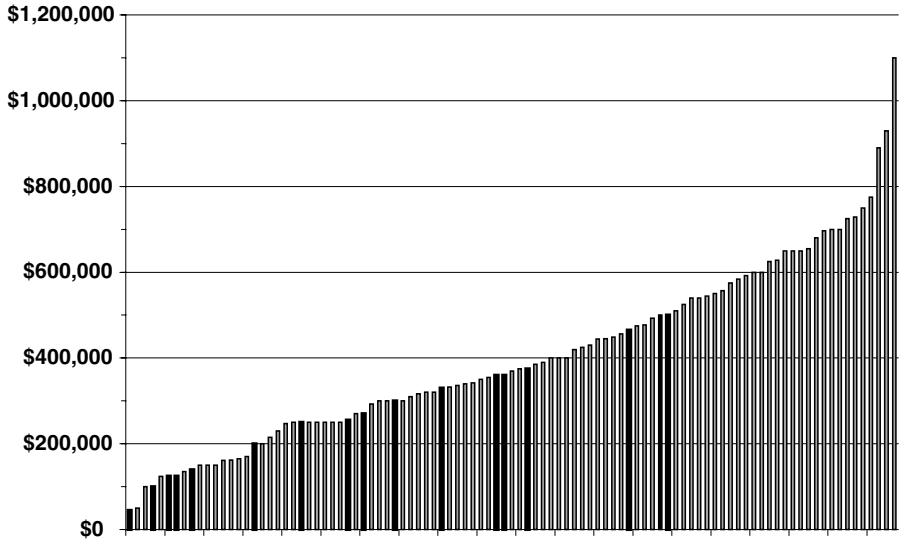

Figure 1 Representative set of startup packages provided by American chemistry departments in doctoral-granting institutions during the 2006–2007 academic year. Black lines are for computational chemists.

Some of these questions can be answered with data provided by the American Chemical Society's Petroleum Research Fund (PRF). The PRF asks new faculty members applying for a grant to delineate startup costs along with other information such as space allocations, teaching loads, etc. Figures 1 and 2 contain a random selection of startup packages during the 2006–2007 academic year. These plots show the data (sorted by increasing amount) for approximately 100 new investigators applying from universities with doctoral programs (Figure 1) and 45 new investigators from BS and MS granting institutions (Figure 2). Note that the scales are NOT the same in these figures, with doctoral institutions, providing significantly more research startup funds than do primarily undergraduate institutions, as expected.

The data in these plots are for Chemistry Departments only; excluded are data from engineering, geology, and physics departments (data for new investigators in the fields of chemical biology were not available). Parenthetically, chemists do significantly better in terms of their startup packages than do the people in these excluded groups, but this is a topic for another day. Also omitted are startup packages from non-American institutions because, frequently, one ends up comparing apples versus oranges in this regard.

The data depicted include real dollars made available for new investigators at American chemistry departments to use as they feel would be best for their research careers. Removed from these numbers are the costs of laboratory renovations and other such obligatory spending by an institution, as well as "in-kind" funds such as nuclear magnetic resonance (NMR) or

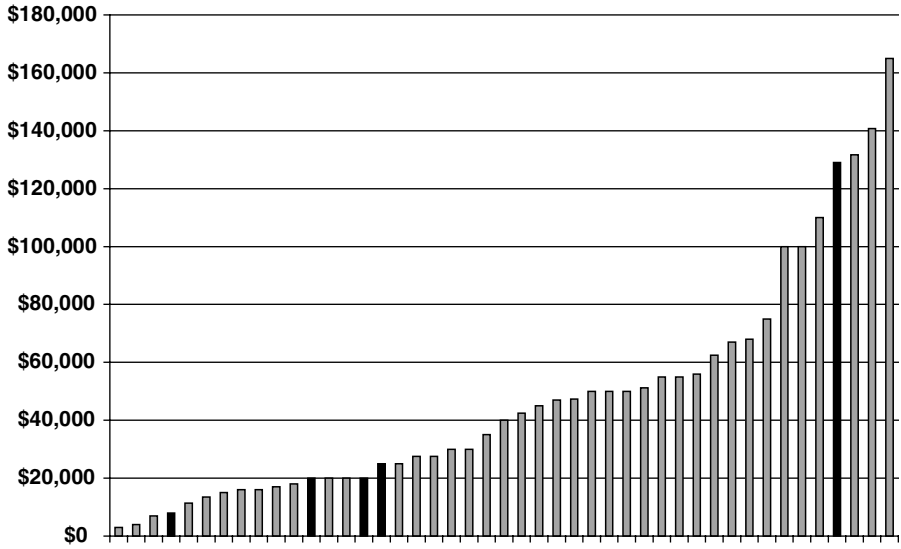

Figure 2 Representative set of startup packages provided by American chemistry departments in BS- and MS-granting institutions during the 2006–2007 academic year. Black lines are for computational chemists.

computer time, glass and machine shop time, and so on, each of which are desirable and meant to help the new faculty member but that were removed nonetheless because not all new faculty would think to put this kind of information into their PRF grant application. Also removed were summer salaries, travel monies, months of teaching assistant (TA) support, new journal costs, and other types of support that is already earmarked by a department for a particular use. What remains, then, is a noninflated, barebones, startup package that the new faculty member can use for what he or she thinks will best ensure success for the research component of his or her tenure portfolio. The data provided here, then, represents a lower bound on the level of support given by American institutions.

While some doctoral institutions are providing startup packages in excess of $800,000, most are giving $600,000 or less. Is this extravagant or is this necessary? The answer to that question clearly depends on the expectations each of those institutions have for their faculty, but also on their ability to provide those funds, especially when two or three new faculty are being hired in the same year (many institutions spread out their startup costs over 2–3 years). Given the cost of glassware, solvents/chemicals, spectrometers, chromatographs, and research assistantship line items, we will let you decide if these startup packages are reasonable or extravagant.

The undergraduate/MS-level schools can, in some cases, rival some of the doctoral program startup packages, but their packages are significantly less

than those provided by doctoral institutions in general. Some institutions provide more than $100,000, but the majority of them provide startup packages between $20,000 and $75,000 (it is not clear if these funds are to be used exclusively for research or if they are intended also for teaching/curriculum development). Nonetheless, a clear gradation in research support exists for both undergraduate and doctoral institutions alike.

What is surprising and somewhat disconcerting is that computational chemists are given far fewer startup dollars to jumpstart their careers than is given to experimentalists. A decade ago a Silicon Graphics workstation with dual processors cost about $25,000, a cost that was comparable to a liquid chromatograph. One can argue that chromatographic columns are costly (some columns were typically $1500 each and prone to easy degradation), as are the costs for high-purity solvents to justify more funding for the experimentalist, but, that chromatograph would likely last for 10–15 years with proper maintenance while the workstation would be outdated and in need of replacement every 3–5 years. One might also argue that the computational scientist could use departmental or school computing resources (if they exist) or perhaps receive a user's grant from a nationally funded supercomputing center, but, that does not obviate the fact that experimentalists usually have access to expensive department-provided resources such as NMR and mass spectrometers. What is not arguable, however, is that the costs of hiring a postdoctoral researcher to get any new faculty member's research going on a fast track is exactly the same for computational chemists as it is for experimentalists at a given institution, yet it appears, on the whole, that computational scientists are being short changed in their startup packages. This is an issue that senior computational chemists need to pay attention to and insist, when new hires are made, that theorists be treated on the same footing as experimentalists. The irony in all this is that a disproportionate number of computational chemists are cited heavily in the scientific literature compared to researchers in other disciplines. Indeed, in the preface of Volume 13 of this book series, we carried out a thorough assessment of citation trends and pointed out that 25% of the top-cited chemists are computational scientists, even though computational chemists constitute only about 5% of all chemists. Despite the shortcomings associated with less funding for computational chemistry than for experimental chemistry, we can say that computational chemists, as a group, are doing more than their fair share of having an impact on science.

Because computational chemistry is so important in today's laboratory setting, we know that many experimentalists want to use the theories and the associated software developed by computational scientists for their own needs. The theoretical underpinnings and philosophical approaches used by theorists and software developers are often buried in terse mathematics or hidden in other ways from the view of a traditional black-box-using bench chemist who has little time to become truly proficient as a theorist, or who

might stumble into some theoretical pitfall that would detract from the explanations of their scientific findings. Yet, those experimentalists want very much to use computational tools to rationalize their results or, in some instances, to make predictions about what next to do along their research trajectory. Because of this need we started the *Reviews in Computational Chemistry* book series that, in hindsight, could just as well have been called "Tutorials in Computational Chemistry."

Because the emphasis of the material covered in this book series is directed toward the novice bench chemist wanting to learn about a particular method to solve his or her problems (or for that matter, the seasoned veteran computational chemist needing to learn a new technique with a modicum of effort), we have again asked our authors to provide a tutorial on the topic to be covered in that chapter. As before, they have risen to the occasion and prepared pedagogically driven chapters with the novice in mind.

We begin this volume with a tutorial on quantum mechanical calculations of noncovalent π interactions because of their significance in directing crystal packing, supramolecular assembly, protein folding, drug binding, and the like. These interactions, especially π stacking of aromatic rings in the domain of organic and biological science, have a history of being perplexing to understand and difficult to assess numerically because they are generally weak interactions and they compete with other kinds of stabilizing interactions. In Chapter 1 C. David Sherrill outlines the challenges for computing π interactions by describing the problems associated with computing those interactions. He describes the application of robust electronic structure methods to compute π interactions reliably and reliable approximations one can make for speeding up the calculations. Covered are electron correlation and basis set requirements, counterpoise corrections, and additive basis/correlation approximations. The emphasis in this tutorial is on the prototype of aromatic π–π interactions, the benzene dimer. Many of the traps one could fall into with modern commercially available software are uncovered and revealed for the novice in the first part of the chapter. In the second part of the chapter the author explains how one can reduce computational costs while still maintaining a reasonable degree of accuracy. Described are truncated basis sets, Pauling points, and resolution of the identity, along with spin-component-scaled second-order Møller–Plesset (MP2) and explicitly correlated R12 and F12 methods to accelerate convergence to the complete basis set limit. Sherrill ends the tutorial by focusing on symmetry-adapted perturbation theory to compute the individual components of intermolecular interactions, e.g., electrostatic, induction, dispersion, and exchange repulsions, so that a rational framework can be constructed for describing the binding of even simple systems such as the benzene–toluene sandwich complex.

Gregory S. Tschumper expands on this topic in Chapter 2 where he describes ab initio and density functional calculations for weak, noncovalent interactions in clusters. Following an introduction that defines the scope of the

chapter and a historical perspective of the nature of weak interactions, the author provides a tutorial for the novice on fundamental concepts with a simple model system consisting of cyclic hydrogen fluoride molecules (trimer, tetramer, and pentamer). The rigid monomer approximation and supermolecular dissociation and interaction energies are described first, followed by a pedagogical section on counterpoise corrections for treating basis set superposition errors. Two-body approximations and cooperative/nonadditive effects are defined and described. Higher order cooperative effects are also described and a many-body decomposition scheme for weakly bound clusters is explained in detail with an application to hydrogen fluoride (HF) clusters. Because energy is an extensive property, a pedagogical section on size consistency and extensivity is provided for the reader. A section on high-accuracy computational strategies is then presented, beginning with a primer on electron correlation and a primer on atomic orbital (AO) basis sets that includes extrapolation methods and explicitly correlated methods. Linear scaling methods are described and a tutorial on estimating E_{int} in the CCSD(T) CBS (complete basis set) limit is given. The author balances this with a section on less demanding computational strategies using MP2 and density functional theory (DFT) techniques. Other computational issues are brought to light and illustrated with results from calculations on water clusters. Aspects of computing geometries and vibrational frequencies for noncovalent clusters are presented.

The theme of quantum mechanics is continued in Chapter 3 where Peter Elliott, Filipp Furche, and Kieron Burke describe how to compute excited-state properties using time-dependent density functional theory (TDDFT). Ground-state DFT has become the de facto standard, especially for chemists, biologists, and materials scientists for predicting ground-state properties of molecules, but it cannot in its typical implementation treat electronic excitations. TDDFT can be used to do this, and here the authors provide a state-of-the-art overview of the method. They begin with a review of the ground state covering the formalism, approximate functionals, and basis sets, and then introduce time-dependent theory. Here the Runge–Gross theorem is explained, Kohn–Sham equations described, and linear response to external fields is presented. While formally exact, a TDDFT calculation also requires an approximation for the exchange–correlation (XC) potential, and those approximations are then introduced. With that background the authors describe the implementation of TDDFT and the basis sets used commonly nowadays, using as an example the naphthalene molecule. That section is followed by one that assesses the performance of TDDFT, using naphthalene as an example. The authors examine the influence of the ground-state potential, the influence of the XC kernel, the errors in potential versus kernel, and then they describe how to understand linear response TDDFT. Also included in the chapter is a close look at how well TDDFT performs for noble-gas atoms. The authors then take a look beyond standard functionals by examining double excitations, polymers, solids, and charge-transfer systems. The chapter ends with

coverage of topics where TDDFT is being applied and where development goes beyond simple extractions from linear response theory.

The theme of quantum mechanics is again continued in Chapter 4 where Thomas Vojta provides a tutorial on quantum phase transitions. Understanding and describing phase transitions is important because of their ubiquitous nature and how they shape our world. The phase transitions that most of us are aware of take place at nonzero temperature where, for example, the ordered state of ice becomes less ordered water at the melting point or where iron loses its ferromagnetic character at its Curie point to become paramagnetic. Attention has now shifted to the study of another type of phase transition that occurs at zero temperature and is induced by nonthermal parameters such as pressure, magnetic field strength, or even chemical composition. Thus, at an applied magnetic field strength, of about 5 T, $LiHoF_4$ undergoes a phase transition from a ferromagnet to a paramagnet; one can envision the impact that such transitions have in defining magnetic, optical, and electrical properties of materials that technologists will soon employ to make advanced products for consumption. The purpose of this chapter is to introduce the theory of quantum phase transitions, showing similarities to and differences from typical thermal transitions that most of us are more familiar with and to point out the computational challenges presented by quantum phase transitions and successful approaches used to meet those challenges. Vojta begins by describing phase transitions and critical behavior. Landau theory, scaling, and renormalization group theory, finite-size scaling, and quenching disorder are then covered. Then, classical versus quantum phase transitions are described including quantum scaling and quantum-to-classical mapping, going beyond the Landau–Ginzburg–Wilson paradigm, and impurity quantum phase transitions. There exist formidable challenges to computing quantum transitions, which are explained clearly by the author. Also covered in this chapter are the classical Monte Carlo (MC) approaches, including the simplest models displaying quantum phase transitions—the quantum Ising model in a transverse field, the dissipative transverse-field Ising chain, and other such methods. This is followed by a discussion of quantum Monte Carlo approaches to the problem, including the world-line MC algorithm and the stochastic series expansion algorithm. The chapter ends with a brief overview of other computational approaches to quantum phase transitions.

We continue in the ensuing chapters with several tutorials tied together by the theme of how to exploit and/or treat multiple length scales and multiple time scales in simulations. In Chapter 5 Thomas Beck introduces us to real-space and multigrid methods used in computational chemistry. Real-space methods are iterative numerical techniques for solving partial differential equations on grids in coordinate space. They are used because the physical responses from many chemical systems are restricted to localized domains in space. This is a situation that real-space methods can exploit because the iterative updates of the desired functions need information in only a small area near the updated point.

A problem with this approach, however, is that the solver tends to stall due to the long wavelength components of the errors if the iterations are performed on only a single, fine grid. Multigrid methods overcome this problem by using information from a range of length scales. In this tutorial Beck gives us a few examples of where such computational methods can be used and then introduces us to the basics of representing partial differential equations in real space. Two of the most basic and useful equations used by computational chemists and engineers are considered: the Poisson equation and the Schrödinger equation. Finite-element representations, finite-difference representations, iterative updates of functions, and limitations of real-space methods for a single, fine grid are described. Multigrid methods are then introduced and explained in a pedagogical manner. Because eigenvalue problems are more difficult to solve than those encountered in solving the Poisson equation, a section is dedicated to this. Thereafter, treatments for nonlinear scaling for electronic structure calculations are described. Other nonlinear problems such as solving the Poisson–Boltzmann and Poisson–Nernst–Planck equations are then introduced and explained. The author provides some tips and advice about writing multigrid solvers and then provides a literature review of applications in chemistry, biophysics, and materials science. The chapter ends with a listing of real-space and multigrid codes for use in the areas of electronic structure, electrostatics, and transport, and speculation on research directions that may be pursued in the near future.

In Chapter 6 Francesca Tavazza, Lyle E. Levine, and Anne M. Chaka provide a tutorial on hybrid methods for atomic-level simulations that span multiple length scales in the solid state. To examine the mechanical behavior of materials, one needs to account for bond making/breaking, atom rearrangements, or defect properties using simulation techniques on the atomistic, nanoscale, but, one also needs to account for micro- or macroscale phenomena such as long-range stress fields that cover hundreds of nanometers and larger. Because one cannot yet simulate macroscopically large systems with atomic-level resolution, the use of hybrid technologies is commonly implemented where different length scales are simulated simultaneously in a coupled fashion. The main obstacle to overcome is the development of efficient and physically correct coupling schemes. The interface between different computational models is a region that is sometimes called the ''handshake'' region where nonphysical forces (ghost forces) can arise due to the intrinsically different interaction range associated with each of the computational models employed and where, for hybrid methods that deal with dynamical processes, wave reflections can occur at artificial boundaries. In this tutorial the authors divide the methodologies into two main classes: those dealing with coupling classical atomistic models to continuum models and those coupling classical atomistic models to quantum models. In the section on atomistic-continuum coupling the authors begin with zero temperature equilibrium methods including FEAt (finite-element coupled with atomistic modeling), the quasi-continuum (QC) method, the coupled atomistic and discrete dislocation method, the

atomic size finite-element method, and Green's function boundary condition methods. Finite-temperature equilibrium methods are then discussed including the QC-free energy functional method, the quasi-continuum Monte Carlo method, and others before turning to hybrid methods used to explore the dynamical evolution of systems composed of a continuum region. These systems are usually described with finite-element methods coupled to a discrete-described region that is usually modeled with molecular dynamics algorithms implementing classical potentials. Domain decomposition methods, adaptive model refinement techniques, coarse-grain molecular dynamics, and boundary conditions methods are introduced and then described in a straightforward manner. The second half of the tutorial involves the coupling of classically described domains to quantum mechanically described regions. Static and semistatic methods are described along with the first-principles Green's function boundary condition method and the quantum atomistic static interface method. Then the authors describe dynamics methodologies including the coupling of length scales method, the learn-on-the-fly method, and Ogata's method. The authors provide examples of applications of each method as they appear throughout the chapter. Also provided are easy to comprehend diagrams that illustrate what is being described.

The focus shifts in Chapter 7 from materials science to biology, but the theme remains multiscale modeling. In this chapter Alfredo E. Cárdenas and Eric Barth present a tutorial on extending the time scale in atomically detailed simulations. The authors begin by introducing the Verlet method and the potential functions used in molecular dynamics (MD) simulations. They then explain what multiple time step (MTS) methods are, and then they examine several such techniques. Cárdenas and Barth begin with the idea of splitting the forces that require different time steps for numerical resolution based on a simple distance parameter, and then they describe an alternative method of numerical integration with force splitting to deal with fast and slow components of the forces. An assessment of limitations on the size of the time steps allowed is presented before Langevin dynamics is introduced. Then a MATLAB-based tutorial is presented on impulse and extrapolation MTS methods. While MTS methodologies can extend simulation time scales somewhat, they are not useful for many applications such as examining large conformational changes in proteins. Accordingly, the authors introduce a different approach to extending the time scale that involves techniques that are generally referred to as "path methods." This includes transition path sampling, maximization of the diffusive flux (MaxFlux), discrete path sampling with the string method, and optimization of action. The latter path method described by the authors emphasizes the stochastic difference equation in length (SDEL). Here they use literature examples from the realm of biology such as protein folding, B-Z DNA transitions, and the like to make their point. An appendix containing MATLAB scripts for the tutorial is included.

The final chapter returns to the topic of materials science. In Chapter 8 Edward J. Maginn provides a historical account of atomistic simulations of

ionic liquids, especially room temperature ionic liquids (RTILs). After defining what RTILs are, he provides a short (pre)history of computational efforts in this field. Then, in a didactic fashion, Maginn reviews the history of early simulations by first introducing the potential functions used, then assessing the limitations of those functions, and, finally, examining sampling issues associated with simulations of this class of liquids, which differ (electrostatically) from most traditional liquids that have been studied to date. With that background Maginn delves into more refined models for RTILs focusing on how best to compute structures, energies, properties such as heat capacities, Henry's law constants, and other issues related to solubility in ionic liquids. Of particular note, especially for novices, are the implications of slow dynamics of RTILs when computing transport properties. Because of this potential "road block," the author presents a full section dedicated to this topic. That section is followed by one on computing macroscopic properties such as self-diffusivities, viscosities, electrical conductivities, and thermal conductivities of ionic liquids. Compared and contrasted are equilibrium and nonequilibrium methods used for calculating these properties. Coarse-graining techniques and ab initio MD methods are then described. Finally, Maginn takes the novice modeler through a tutorial on how to carry out an RTIL simulation. This tutorial contains an ample selection of "Do's and Don'ts" associated with the selection of codes one might use, the choice of force field to implement, how to analyze the data derived from the simulations, and the use of operating systems and parallel computing for large-scale atomistic simulation.

Reviews in Computational Chemistry is highly rated and well received by the scientific community at large; the reason for these accomplishments rests firmly on the shoulders of the authors we have contacted to provide the pedagogically driven reviews that have made this ongoing book series so popular. To those authors we are especially grateful.

We are also glad to note that our publisher now makes our most recent volumes available in an online form through Wiley InterScience. Please consult the Web (http://www.interscience.wiley.com/onlinebooks) or contact reference@wiley.com for the latest information. For readers who appreciate the permanence and convenience of bound books, these will, of course, continue.

We thank the authors of this and previous volumes for their excellent chapters.

Kenny B. Lipkowitz
Washington

Thomas R. Cundari
Denton

February, 2008

Contributors

Eric Barth, Department of Mathematics and Computer Science, Kalamazoo College, 1200 Academy Street, Kalamazoo, MI 49006 U.S.A.
(Electronic mail: eric.barth@kzoo.edu)

Thomas L. Beck, Department of Chemistry, Crosley Tower, University of Cincinnati, PO Box 210172, Cincinnati, OH 45221 U.S.A.
(Electronic mail: becktl@email.uc.edu)

Kieron Burke, Department of Chemistry, University of California-Irvine, 1102 Natural Sciences 2, Irvine, CA 92697 U.S.A. (Electronic mail: kieron@uci.edu)

Alfredo E. Cárdenas, Department of Chemistry, University of South Florida, 4202 E. Fowler Avenue, Tampa, FL 33620 U.S.A.
(Electronic mail: cardenas@cas.usf.edu)

Anne M. Chaka, National Institute of Standards and Technology, 100 Bureau Dr., STOP 8553, Gaithersburg, MD 20899 U.S.A.
(Electronic mail: anne.chaka@nist.gov)

Peter Elliott, Department of Physics and Astronomy, Frederick Reines Hall, University of California-Irvine, Irvine, CA 92697 U.S.A.
(Electronic mail: pelliott@uci.edu)

Filipp Furche, Institut für Physikalische Chemie, Universität Karlsruhe, Kaiserstrasse 12, D-76131 Karlsruhe, Germany
(Electronic mail: filipp.furche@chemie.uni-karlsruhe.de)

Lyle E. Levine, National Institute of Standards and Technology, 100 Bureau Dr., STOP 8553, Gaithersburg, MD 20899 U.S.A.
(Electronic mail: lyle.levine@nist.gov)

Edward J. Maginn, Department of Chemical and Biomolecular Engineering, Fitzpatrick Hall, University of Notre Dame, Notre Dame, IN 46556 U.S.A. (Electronic mail: ed@nd.edu)

C. David Sherrill, Department of Chemistry and Biochemistry, Georgia Institute of Technology, 770 State Street, Atlanta, GA 30332 U.S.A.
(Electronic mail: sherrill@gatech.edu)

Francesca Tavazza, National Institute of Standards and Technology, 100 Bureau Dr., STOP 8553, Gaithersburg, MD 20899 U.S.A.
(Electronic mail: ftavazza@nist.gov)

Gregory S. Tschumper, Department of Chemistry and Biochemistry, Coulter Hall, University of Mississippi, University, MS 38677 U.S.A.
(Electronic mail: tschumpr@olemiss.edu)

Thomas Vojta, Department of Physics, Missouri University of Science and Technology, Rolla, MO 65409 U.S.A. (Electronic mail: vojtat@mst.edu)

Contributors to Previous Volumes

Volume 1 (1990)

David Feller and **Ernest R. Davidson**, Basis Sets for Ab Initio Molecular Orbital Calculations and Intermolecular Interactions.

James J. P. Stewart, Semiempirical Molecular Orbital Methods.

Clifford E. Dykstra, **Joseph D. Augspurger**, **Bernard Kirtman**, and **David J. Malik**, Properties of Molecules by Direct Calculation.

Ernest L. Plummer, The Application of Quantitative Design Strategies in Pesticide Design.

Peter C. Jurs, Chemometrics and Multivariate Analysis in Analytical Chemistry.

Yvonne C. Martin, **Mark G. Bures**, and **Peter Willett**, Searching Databases of Three-Dimensional Structures.

Paul G. Mezey, Molecular Surfaces.

Terry P. Lybrand, Computer Simulation of Biomolecular Systems Using Molecular Dynamics and Free Energy Perturbation Methods.

Donald B. Boyd, Aspects of Molecular Modeling.

Donald B. Boyd, Successes of Computer-Assisted Molecular Design.

Ernest R. Davidson, Perspectives on Ab Initio Calculations.

Volume 2 (1991)

Andrew R. Leach, A Survey of Methods for Searching the Conformational Space of Small and Medium-Sized Molecules.

John M. Troyer and **Fred E. Cohen**, Simplified Models for Understanding and Predicting Protein Structure.

J. Phillip Bowen and **Norman L. Allinger**, Molecular Mechanics: The Art and Science of Parameterization.

Uri Dinur and **Arnold T. Hagler**, New Approaches to Empirical Force Fields.

Steve Scheiner, Calculating the Properties of Hydrogen Bonds by Ab Initio Methods.

Donald E. Williams, Net Atomic Charge and Multipole Models for the Ab Initio Molecular Electric Potential.

Peter Politzer and **Jane S. Murray**, Molecular Electrostatic Potentials and Chemical Reactivity.

Michael C. Zerner, Semiempirical Molecular Orbital Methods.

Lowell H. Hall and **Lemont B. Kier**, The Molecular Connectivity Chi Indexes and Kappa Shape Indexes in Structure-Property Modeling.

I. B. Bersuker and **A. S. Dimoglo**, The Electron-Topological Approach to the QSAR Problem.

Donald B. Boyd, The Computational Chemistry Literature.

Volume 3 (1992)

Tamar Schlick, Optimization Methods in Computational Chemistry.

Harold A. Scheraga, Predicting Three-Dimensional Structures of Oligopeptides.

Andrew E. Torda and **Wilfred F. van Gunsteren,** Molecular Modeling Using NMR Data.

David F. V. Lewis, Computer-Assisted Methods in the Evaluation of Chemical Toxicity.

Volume 4 (1993)

Jerzy Cioslowski, Ab Initio Calculations on Large Molecules: Methodology and Applications.

Michael L. McKee and **Michael Page,** Computing Reaction Pathways on Molecular Potential Energy Surfaces.

Robert M. Whitnell and **Kent R. Wilson,** Computational Molecular Dynamics of Chemical Reactions in Solution.

Roger L. DeKock, Jeffry D. Madura, Frank Rioux, and **Joseph Casanova,** Computational Chemistry in the Undergraduate Curriculum.

Volume 5 (1994)

John D. Bolcer and **Robert B. Hermann,** The Development of Computational Chemistry in the United States.

Rodney J. Bartlett and **John F. Stanton,** Applications of Post-Hartree–Fock Methods: A Tutorial.

Steven M. Bachrach, Population Analysis and Electron Densities from Quantum Mechanics.

Jeffry D. Madura, Malcolm E. Davis, Michael K. Gilson, Rebecca C. Wade, Brock A. Luty, and **J. Andrew McCammon,** Biological Applications of Electrostatic Calculations and Brownian Dynamics Simulations.

K. V. Damodaran and **Kenneth M. Merz Jr.,** Computer Simulation of Lipid Systems.

Jeffrey M. Blaney and **J. Scott Dixon,** Distance Geometry in Molecular Modeling.

Lisa M. Balbes, S. Wayne Mascarella, and **Donald B. Boyd,** A Perspective of Modern Methods in Computer-Aided Drug Design.

Volume 6 (1995)

Christopher J. Cramer and **Donald G. Truhlar,** Continuum Solvation Models: Classical and Quantum Mechanical Implementations.

Clark R. Landis, Daniel M. Root, and **Thomas Cleveland,** Molecular Mechanics Force Fields for Modeling Inorganic and Organometallic Compounds.

Vassilios Galiatsatos, Computational Methods for Modeling Polymers: An Introduction.

Rick A. Kendall, Robert J. Harrison, Rik J. Littlefield, and **Martyn F. Guest,** High Performance Computing in Computational Chemistry: Methods and Machines.

Donald B. Boyd, Molecular Modeling Software in Use: Publication Trends.

Eiji Ōsawa and **Kenny B. Lipkowitz,** Appendix: Published Force Field Parameters.

Volume 7 (1996)

Geoffrey M. Downs and **Peter Willett,** Similarity Searching in Databases of Chemical Structures.

Andrew C. Good and **Jonathan S. Mason,** Three-Dimensional Structure Database Searches.

Jiali Gao, Methods and Applications of Combined Quantum Mechanical and Molecular Mechanical Potentials.

Libero J. Bartolotti and **Ken Flurchick,** An Introduction to Density Functional Theory.

Alain St-Amant, Density Functional Methods in Biomolecular Modeling.

Danya Yang and **Arvi Rauk,** The A Priori Calculation of Vibrational Circular Dichroism Intensities.

Donald B. Boyd, Appendix: Compendium of Software for Molecular Modeling.

Volume 8 (1996)

Zdenek Slanina, Shyi-Long Lee, and **Chin-hui Yu,** Computations in Treating Fullerenes and Carbon Aggregates.

Gernot Frenking, Iris Antes, Marlis Böhme, Stefan Dapprich, Andreas W. Ehlers, Volker Jonas, Arndt Neuhaus, Michael Otto, Ralf Stegmann, Achim Veldkamp, and **Sergei F. Vyboishchikov,** Pseudopotential Calculations of Transition Metal Compounds: Scope and Limitations.

Thomas R. Cundari, Michael T. Benson, M. Leigh Lutz, and **Shaun O. Sommerer,** Effective Core Potential Approaches to the Chemistry of the Heavier Elements.

Jan Almlöf and **Odd Gropen,** Relativistic Effects in Chemistry.

Donald B. Chesnut, The Ab Initio Computation of Nuclear Magnetic Resonance Chemical Shielding.

Volume 9 (1996)

James R. Damewood, Jr., Peptide Mimetic Design with the Aid of Computational Chemistry.

T. P. Straatsma, Free Energy by Molecular Simulation.

Robert J. Woods, The Application of Molecular Modeling Techniques to the Determination of Oligosaccharide Solution Conformations.

Ingrid Pettersson and **Tommy Liljefors,** Molecular Mechanics Calculated Conformational Energies of Organic Molecules: A Comparison of Force Fields.

Gustavo A. Arteca, Molecular Shape Descriptors.

Volume 10 (1997)

Richard Judson, Genetic Algorithms and Their Use in Chemistry.

Eric C. Martin, David C. Spellmeyer, Roger E. Critchlow Jr., and **Jeffrey M. Blaney,** Does Combinatorial Chemistry Obviate Computer-Aided Drug Design?

Robert Q. Topper, Visualizing Molecular Phase Space: Nonstatistical Effects in Reaction Dynamics.

Raima Larter and **Kenneth Showalter,** Computational Studies in Nonlinear Dynamics.

Stephen J. Smith and **Brian T. Sutcliffe,** The Development of Computational Chemistry in the United Kingdom.

Volume 11 (1997)

Mark A. Murcko, Recent Advances in Ligand Design Methods.

David E. Clark, Christopher W. Murray, and **Jin Li,** Current Issues in De Novo Molecular Design.

Tudor I. Oprea and **Chris L. Waller,** Theoretical and Practical Aspects of Three-Dimensional Quantitative Structure–Activity Relationships.

Giovanni Greco, Ettore Novellino, and **Yvonne Connolly Martin,** Approaches to Three-Dimensional Quantitative Structure–Activity Relationships.

Pierre-Alain Carrupt, Bernard Testa, and **Patrick Gaillard,** Computational Approaches to Lipophilicity: Methods and Applications.

Ganesan Ravishanker, Pascal Auffinger, David R. Langley, Bhyravabhotla Jayaram, Matthew A. Young, and **David L. Beveridge,** Treatment of Counterions in Computer Simulations of DNA.

Donald B. Boyd, Appendix: Compendium of Software and Internet Tools for Computational Chemistry.

Volume 12 (1998)

Hagai Meirovitch, Calculation of the Free Energy and the Entropy of Macromolecular Systems by Computer Simulation.

Ramzi Kutteh and **T. P. Straatsma,** Molecular Dynamics with General Holonomic Constraints and Application to Internal Coordinate Constraints.

John C. Shelley and **Daniel R. Bérard,** Computer Simulation of Water Physisorption at Metal–Water Interfaces.

Donald W. Brenner, Olga A. Shenderova, and **Denis A. Areshkin**, Quantum-Based Analytic Interatomic Forces and Materials Simulation.

Henry A. Kurtz and **Douglas S. Dudis**, Quantum Mechanical Methods for Predicting Nonlinear Optical Properties.

Chung F. Wong, Tom Thacher, and **Herschel Rabitz**, Sensitivity Analysis in Biomolecular Simulation.

Paul Verwer and **Frank J. J. Leusen**, Computer Simulation to Predict Possible Crystal Polymorphs.

Jean-Louis Rivail and **Bernard Maigret**, Computational Chemistry in France: A Historical Survey.

Volume 13 (1999)

Thomas Bally and **Weston Thatcher Borden**, Calculations on Open-Shell Molecules: A Beginner's Guide.

Neil R. Kestner and **Jaime E. Combariza**, Basis Set Superposition Errors: Theory and Practice.

James B. Anderson, Quantum Monte Carlo: Atoms, Molecules, Clusters, Liquids, and Solids.

Anders Wallqvist and **Raymond D. Mountain**, Molecular Models of Water: Derivation and Description.

James M. Briggs and **Jan Antosiewicz**, Simulation of pH-dependent Properties of Proteins Using Mesoscopic Models.

Harold E. Helson, Structure Diagram Generation.

Volume 14 (2000)

Michelle Miller Francl and **Lisa Emily Chirlian**, The Pluses and Minuses of Mapping Atomic Charges to Electrostatic Potentials.

T. Daniel Crawford and **Henry F. Schaefer III**, An Introduction to Coupled Cluster Theory for Computational Chemists.

Bastiaan van de Graaf, Swie Lan Njo, and **Konstantin S. Smirnov,** Introduction to Zeolite Modeling.

Sarah L. Price, Toward More Accurate Model Intermolecular Potentials for Organic Molecules.

Christopher J. Mundy, Sundaram Balasubramanian, Ken Bagchi, Mark E. Tuckerman, Glenn J. Martyna, and **Michael L. Klein,** Nonequilibrium Molecular Dynamics.

Donald B. Boyd and **Kenny B. Lipkowitz,** History of the Gordon Research Conferences on Computational Chemistry.

Mehran Jalaie and **Kenny B. Lipkowitz,** Appendix: Published Force Field Parameters for Molecular Mechanics, Molecular Dynamics, and Monte Carlo Simulations.

Volume 15 (2000)

F. Matthias Bickelhaupt and **Evert Jan Baerends,** Kohn-Sham Density Functional Theory: Predicting and Understanding Chemistry.

Michael A. Robb, Marco Garavelli, Massimo Olivucci, and **Fernando Bernardi,** A Computational Strategy for Organic Photochemistry.

Larry A. Curtiss, Paul C. Redfern, and **David J. Frurip,** Theoretical Methods for Computing Enthalpies of Formation of Gaseous Compounds.

Russell J. Boyd, The Development of Computational Chemistry in Canada.

Volume 16 (2000)

Richard A. Lewis, Stephen D. Pickett, and **David E. Clark,** Computer-Aided Molecular Diversity Analysis and Combinatorial Library Design.

Keith L. Peterson, Artificial Neural Networks and Their Use in Chemistry.

Jörg-Rüdiger Hill, Clive M. Freeman, and **Lalitha Subramanian,** Use of Force Fields in Materials Modeling.

M. Rami Reddy, Mark D. Erion, and **Atul Agarwal,** Free Energy Calculations: Use and Limitations in Predicting Ligand Binding Affinities.

Volume 17 (2001)

Ingo Muegge and **Matthias Rarey**, Small Molecule Docking and Scoring.

Lutz P. Ehrlich and **Rebecca C. Wade**, Protein-Protein Docking.

Christel M. Marian, Spin-Orbit Coupling in Molecules.

Lemont B. Kier, **Chao-Kun Cheng**, and **Paul G. Seybold**, Cellular Automata Models of Aqueous Solution Systems.

Kenny B. Lipkowitz and **Donald B. Boyd**, Appendix: Books Published on the Topics of Computational Chemistry.

Volume 18 (2002)

Geoff M. Downs and **John M. Barnard**, Clustering Methods and Their Uses in Computational Chemistry.

Hans-Joachim Böhm and **Martin Stahl**, The Use of Scoring Functions in Drug Discovery Applications.

Steven W. Rick and **Steven J. Stuart**, Potentials and Algorithms for Incorporating Polarizability in Computer Simulations.

Dmitry V. Matyushov and **Gregory A. Voth**, New Developments in the Theoretical Description of Charge-Transfer Reactions in Condensed Phases.

George R. Famini and **Leland Y. Wilson**, Linear Free Energy Relationships Using Quantum Mechanical Descriptors.

Sigrid D. Peyerimhoff, The Development of Computational Chemistry in Germany.

Donald B. Boyd and **Kenny B. Lipkowitz**, Appendix: Examination of the Employment Environment for Computational Chemistry.

Volume 19 (2003)

Robert Q. Topper, **David, L. Freeman**, **Denise Bergin**, and **Keirnan R. LaMarche**, Computational Techniques and Strategies for Monte Carlo Thermodynamic Calculations, with Applications to Nanoclusters.

David E. Smith and **Anthony D. J. Haymet**, Computing Hydrophobicity.

Lipeng Sun and **William L. Hase**, Born-Oppenheimer Direct Dynamics Classical Trajectory Simulations.

Gene Lamm, The Poisson-Boltzmann Equation.

Volume 20 (2004)

Sason Shaik and **Philippe C. Hiberty**, Valence Bond Theory: Its History, Fundamentals and Applications. A Primer.

Nikita Matsunaga and **Shiro Koseki**, Modeling of Spin Forbidden Reactions.

Stefan Grimme, Calculation of the Electronic Spectra of Large Molecules.

Raymond Kapral, Simulating Chemical Waves and Patterns.

Costel Sârbu and **Horia Pop**, Fuzzy Soft-Computing Methods and Their Applications in Chemistry.

Sean Ekins and **Peter Swaan**, Development of Computational Models for Enzymes, Transporters, Channels and Receptors Relevant to ADME/Tox.

Volume 21 (2005)

Roberto Dovesi, **Bartolomeo Civalleri**, **Roberto Orlando**, **Carla Roetti**, and **Victor R. Saunders**, Ab Initio Quantum Simulation in Solid State Chemistry.

Patrick Bultinck, **Xavier Gironés**, and **Ramon Carbó-Dorca**, Molecular Quantum Similarity: Theory and Applications.

Jean-Loup Faulon, **Donald P. Visco, Jr.**, and **Diana Roe**, Enumerating Molecules.

David J. Livingstone and **David W. Salt**, Variable Selection- Spoilt for Choice.

Nathan A. Baker, Biomolecular Applications of Poisson-Boltzmann Methods.

Baltazar Aguda, **Georghe Craciun**, and **Rengul Cetin-Atalay**, Data Sources and Computational Approaches for Generating Models of Gene Regulatory Networks.

Volume 22 (2006)

Patrice Koehl, Protein Structure Classification.

Emilio Esposito, Dror Tobi, and **Jeffry Madura**, Comparative Protein Modeling.

Joan-Emma Shea, Miriam Friedel, and **Andrij Baumketner**, Simulations of Protein Folding.

Marco Saraniti, Shela Aboud, and **Robert Eisenberg**, The Simulation of Ionic Charge Transport in Biological Ion Channels: An Introduction to Numerical Methods.

C. Matthew Sundling, Nagamani Sukumar, Hongmei Zhang, Curt Breneman, and **Mark Embrechts**, Wavelets in Chemistry and Chemoinformatics.

Volume 23 (2007)

Christian Ochsenfeld, Jörg Kussmann, and **Daniel S. Lambrecht**, Linear Scaling Methods in Quantum Chemistry.

Spiridoula Matsika, Conical Intersections in Molecular Systems.

Antonio Fernandez-Ramos, Benjamin A. Ellingson, Bruce C. Garrett, and **Donald G. Truhlar**, Variational Transition State Theory with Multidimensional Tunneling.

Roland Faller, Coarse-Grain Modelling of Polymers.

Jeffrey W. Godden and **Jürgen Bajorath**, Analysis of Chemical Information Content Using Shannon Entropy.

Ovidiu Ivanciuc, Applications of Support Vector Machines in Chemistry.

Donald B. Boyd, How Computational Chemistry Became Important in the Pharmaceutical Industry.

Volume 24 (2007)

Martin Schoen and **Sabine H. L. Klapp**, Nanoconfined Fluids. Soft Matter Between Two and Three Dimensions.

Volume 25 (2007)

Wolfgang Paul, Determining the Glass Transition in Polymer Melts.

Nicholas J. Mosey and **Martin H. Müser**, Atomistic Modeling of Friction.

Jeetain Mittal, **William P. Krekelberg**, **Jeffrey R. Errington**, and **Thomas M. Truskett**, Computing Free Volume, Structured Order, and Entropy of Liquids and Glasses.

Laurence E. Fried, The Reactivity of Energetic Materials at Extreme Conditions.

Julio A. Alonso, Magnetic Properties of Atomic Clusters of the Transition Elements.

Laura Gagliardi, Transition Metal- and Actinide-Containing Systems Studied with Multiconfigurational Quantum Chemical Methods.

Hua Guo, Recursive Solutions to Large Eigenproblems in Molecular Spectroscopy and Reaction Dynamics.

Hugh Cartwright, Development and Uses of Artificial Intelligence in Chemistry.

CHAPTER 1

Computations of Noncovalent π Interactions

C. David Sherrill

Center for Computational Molecular Science and Technology, School of Chemistry and Biochemistry, and College of Computing, Georgia Institute of Technology, Atlanta, Georgia

INTRODUCTION

Noncovalent interactions govern such processes as protein folding, supramolecular assembly, crystal packing of organics, and drug binding. After hydrogen bonding and strong electrostatic interactions (e.g., charge–charge, charge–dipole, and dipole–dipole), the most significant noncovalent interactions in biological applications are probably those involving aromatic π systems.[1] For example, π–π interactions between aromatic rings help stabilize the double helix of DNA and RNA.[2] Protein structures are influenced by a variety of noncovalent interactions including π–π,[3,4] C–H/π,[5] and S/π interactions[6–8] between side chains. Drugs that intercalate between base pairs in DNA and RNA are bound largely due to π–π and cation–π interactions.[9] Proteins that bind DNA or RNA utilize such noncovalent interactions as cation–π,[10,11] π–π,[11] and C–H/π.[12] These π interactions can be equally critical in materials chemistry applications, including self-assembled supramolecular architectures.[13,14] For example, molecular wires can be formed from stacks of aromatic macrocycles.[15] The binding of small molecules to carbon nanotubes[16] and attraction between graphene sheets[17] are both determined by noncovalent π interactions. The crystal structure and charge-transport properties of π-conjugated organic materials are also largely determined by π–π interactions.[18]

Reviews in Computational Chemistry, Volume 26
edited by Kenny B. Lipkowitz and Thomas R. Cundari

Because of their widespread importance to so many areas of chemistry, biology, and materials science, noncovalent π interactions are a crucial topic of study. Moreover, a clear understanding of such interactions is indispensable for the rational design of new drugs and organic materials. Unfortunately, at present, many basic properties of noncovalent interactions—particularly those involving π systems—remain unknown.[19] Experiments aimed at elucidating the details of noncovalent interactions face a number of serious obstacles. Often the chemical systems of greatest interest are complex ones (e.g., a drug in the active site of a protein) where several different types of noncovalent interactions may contribute simultaneously. Indeed, even in model systems specifically designed to study a particular noncovalent interaction, it has often proven challenging to separate the interaction of interest from unexpected secondary interactions or solvent effects.[20–22]

Gas-phase studies of bimolecular complexes afford more control, but these can be quite challenging. Most noncovalent interactions between small molecules feature small binding energies (on the order of a few kilo calories per mole or less), often meaning that very low temperatures must be used to avoid thermal dissociation of the complex. Additionally, it is frequently necessary to use mass selection techniques to ensure that the sample contains only the complex of interest and not larger or smaller clusters. Furthermore, the potential energy surfaces for these systems tend to be fairly flat, meaning that the complexes may be fluxional without a well-defined structure. If the potential surface features two or more potential minima, conversion between them will be easy and rapid except at very low temperatures.

Due to these experimental difficulties, there are great opportunities for the computational chemist to answer important questions about the fundamental nature of noncovalent interactions and how they influence particular chemical systems. A significant advantage of computational studies is that one can directly study prototype systems featuring the noncovalent interaction of interest, in the absence of competing interactions or solvation effects. Computational studies of noncovalent interactions have therefore become increasingly popular over the past 5 years and have led to important insights. Until now, these studies have been rather difficult to carry out because the most commonly used computational chemistry techniques do not give reliable results for noncovalent interactions. It is the purpose of this review to explain how noncovalent interactions can be computed reliably using more robust electronic structure methods, and then to describe what approximations appear to be valid and helpful for speeding up the computations. Our focus is specifically on π interactions, but in terms of which techniques are appropriate to use, there are not large differences between these and other noncovalent interactions. Thus, the review on weakly interacting clusters in Tschumper[23] is directly relevant to the issues discussed here. For pedagogical reasons, we have retained some overlap in the topics discussed in the two reviews.

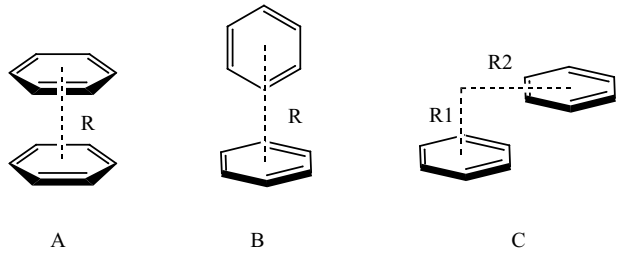

Figure 1 Three most commonly studied configurations of the benzene dimer: the sandwich (A), T-shaped (B), and parallel-displaced (C) configurations.

CHALLENGES FOR COMPUTING π INTERACTIONS

Many chemical problems can be addressed easily and reliably using Hartree–Fock molecular orbital theory or Kohn–Sham density functional theory with modest-sized basis sets. Unfortunately, π interactions, and noncovalent interactions in general, are not among them. In this section we consider the electron correlation and basis set requirements for computations of π interactions.

To illustrate the difficulties in finding a suitable theoretical method for the reliable computation of π interactions, let us consider the simplest possible prototype of aromatic π–π interactions, the benzene dimer. Despite a large number of theoretical[24–28] and experimental studies,[26,29–36] a clear picture of the the geometrical preferences and binding energy of the benzene dimer was not available until high-level theoretical studies were conducted by Tsuzuki's group[37] and our group[38] in 2002 using a combination of coupled-cluster theory and large-basis second-order Møller–Plesset (MP2) perturbation theory computations. Figure 1 shows the three most commonly studied geometrical configurations of the benzene dimer.

Electron Correlation Problem

One of the primary challenges for computing π interactions is that different theoretical methods can give quite different results. This is illustrated in Figure 2, which shows potential energy curves for the sandwich benzene dimer when the distance between the rings is systematically varied; the monomers are frozen at the recommended geometry of Gauss and Stanton.[39] Figure 2 compares the results from restricted Hartree–Fock (RHF), the very popular B3LYP hybrid density functional method,[40,41] MP2 perturbation theory [also referred to as many-body perturbation theory through second order, or MBPT(2)], coupled-cluster theory with single and double substitutions (CCSD),[42] and coupled-cluster through perturbative triple substitutions, CCSD(T),[43] all using

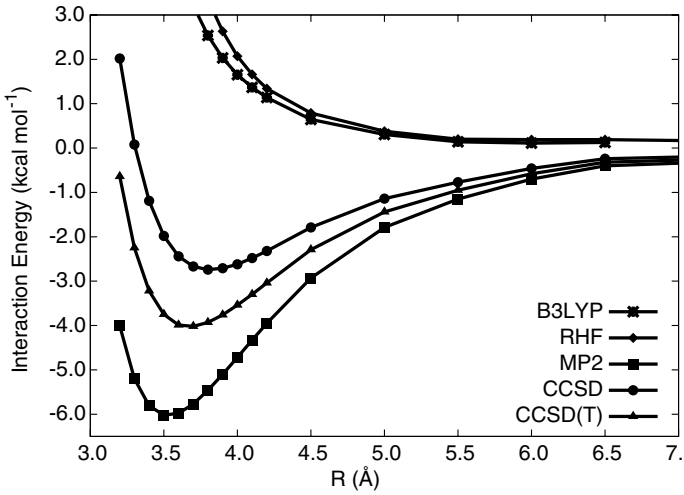

Figure 2 Interaction energy for the sandwich benzene dimer as a function of the intermolecular distance using various methods and the aug-cc-pVDZ basis, with the rigid monomer geometries of Ref. 39. Energies not counterpoise corrected.

Dunning's augmented correlation-consistent valence double-ζ basis set, aug-cc-pVDZ.[44] Of these approaches, CCSD(T) is considered the most sophisticated and reliable.

As one can see, none of the other methods provide a good approximation to the most complete treatment of electron correlation, CCSD(T). Particularly disappointing is the performance of Hartree–Fock and B3LYP, which are not even qualitatively correct for this problem. MP2 and even CCSD become good approximations only at large intermolecular separations. Clearly, the choice of theoretical method is of great importance in computational studies of π interactions, and to achieve good reliability, it would appear that of the methods considered, only CCSD(T) is adequate. This is unfortunate, given that CCSD(T) is very expensive computationally, scaling as $\mathcal{O}(N^7)$, where N is proportional to the size of the system. Fortunately, however, it is possible to use the CCSD(T) results as benchmarks in a search for less expensive yet still reliable computational approaches, as we discuss later.

Given the large discrepancies between the theoretical methods considered, one might ask whether CCSD(T) itself is adequate for highly accurate computations of π interactions. Although Figure 2 does not prove convergence with respect to the treatment of electron correlation, there are two good reasons to consider the CCSD(T) results to be very close to exact for a given basis set. First, a great deal of experience with large-basis-set CCSD(T) computations demonstrates their excellent agreement with experiment for properties such as geometries and vibrational frequencies.[45] Although diradicals,

transition metals, and unimolecular bond-breaking reactions can cause difficulties for CCSD(T) due to the presence of electronic near degeneracies,[46] such issues are not a concern for typical noncovalent interactions. Second, a study by Hopkins and Tschumper[47] indicates that quadruple substitutions make only small contributions to the interaction energies of small van der Waals complexes (perhaps about 5% or less).

Basis Set Problem

Compounding the difficulty of accounting for electron correlation effects properly, accurate computations of noncovalent interactions also require very large basis sets. This is not surprising because London dispersion interactions can be expressed in terms of the polarizabilities of the weakly interacting molecules, and polarizability computations are known to have large basis set requirements. In many weakly bound complexes, the dispersion terms can be the dominant ones.

Figure 3 again considers the potential energy curve for the sandwich benzene dimer, this time fixing the theoretical method to MP2 and varying the basis set. We consider Dunning's augmented, correlation-consistent basis sets[44] from double-ζ through quadruple-ζ (i.e., aug-cc-pVDZ, aug-cc-pVTZ, and aug-cc-pVQZ). These basis sets are the most commonly used for accurate computations of noncovalent interactions because they have been designed to converge smoothly to the complete (infinite) basis set limit. Note that these are

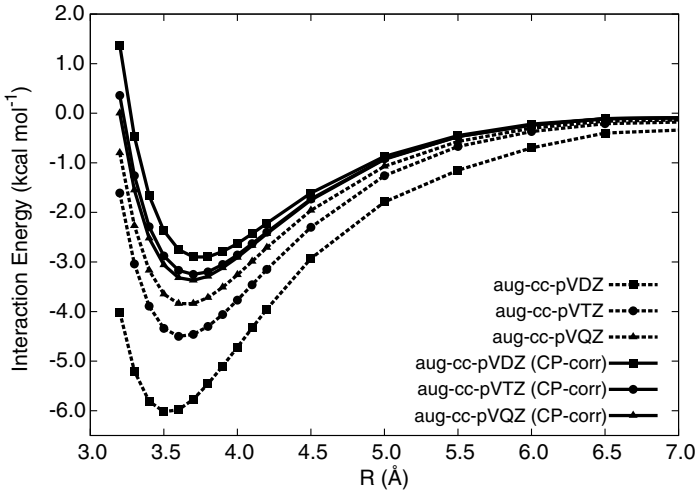

Figure 3 Interaction energy for the sandwich benzene dimer as a function of the intermolecular distance using the MP2 method and various basis sets, with and without counterpoise (CP) correction, using the rigid monomer geometries of Ref. 39.

the *augmented* correlation-consistent basis sets. The aug- prefix denotes that a set of diffuse functions has been added for every angular momentum present in the basis set. This makes the aug-cc-pVXZ basis sets truly enormous for large-basis-set cardinal numbers X. For example, the cc-pVQZ basis set for carbon contains 5 (contracted) *s* functions, 4 sets of *p* functions, 3 sets of *d* functions, 2 sets of *f* functions, and a set of *g* functions, for a total of 55 functions. The augmented version, aug-cc-pVQZ, adds a single set of diffuse *s*, *p*, *d*, *f*, and even *g* functions, or an additional 25 functions, to yield a total of 80 contracted basis functions for a single carbon atom! Note that our counting of basis functions assumed so-called pure angular momentum or spherical harmonic functions (somewhat misnamed because they are not actually complex functions), meaning that there are 5 *d* functions, 7 *f* functions, 9 *g* functions, etc. We note for the sake of pedagogy that some programs default to using these pure angular momentum functions, while others default to using Cartesian functions — e.g., 6 *d* functions, x^2, y^2, z^2, xy, xz, and yz. It is important to know whether Cartesian functions or pure angular momentum functions are being used and to be aware of this when attempting to compare your results to published results or to results from other programs that might have different defaults.

The aug-cc-pVDZ, aug-cc-pVTZ, and aug-cc-pVQZ basis sets thus contain 384, 828, and 1512 contracted Gaussian functions, respectively, for the benzene dimer. Straightforward application of the MP2 method with these basis sets to the sandwich benzene dimer yields the dotted curves in Figure 3. Compared to the largest and most complete basis set, aug-cc-pVQZ, the aug-cc-pVDZ basis greatly overestimates the binding energy near equilibrium (by more than 2 kcal mol^{-1}, or 50%). Improving the basis from aug-cc-pVDZ to aug-cc-pVTZ yields results much closer to the aug-cc-pVQZ values, but the binding energy remains overestimated by 0.7 kcal mol^{-1}. Given the huge differences between MP2 energies with these basis sets, Figure 3 gives us no confidence that even the enormous aug-cc-pVQZ basis has yet reached the complete basis set (CBS) limit.

Basis Set Superposition Errors and the Counterpoise Correction

The reason that the MP2/aug-cc-pVXZ results approach the MP2/CBS limit from below is that weakly bound complexes feature large basis set superposition errors (BSSEs). A tutorial on BSSEs, in theory and in practice, was presented earlier in this book series.[48] Qualitatively, each molecule in the complex desires more basis functions to describe electron correlation effects more accurately. Each molecule can gain access to more basis functions, and can thus be stabilized, by moving closer to another molecule. This creates an artificial stabilization that lowers the energy when the molecules come closer together—simply because the electrons around each molecule can be stabilized

by partially occupying the other molecule's basis functions. The counterpoise (CP) correction of Boys and Bernardi[49,50] is a technique to remove this kind of basis set superposition error, and it is widely employed in studies of weakly interacting complexes. In the absence of the CP correction, interaction energies such as those in Figure 3 can be computed by simply subtracting the sum of the monomer energies from the dimer energy. For a dimer, the CP correction is determined by evaluating the energy of each monomer in the *dimer* basis: that is, a monomer's energy is evaluated using all the basis functions of that monomer *and the basis functions of the other monomer of the dimer*. When one wishes to include basis functions at a particular point in space, but without the associated nuclear charge and electrons, this is called using a *ghost atom*. Most electronic structure programs have the ability to use ghost atoms to facilitate CP correction computations. The difference between a monomer's energy in isolation and the monomer's energy in the presence of the ghost functions of the other monomer constitutes the CP correction for that monomer. Of course, one must evaluate the CP correction for each monomer in a dimer (unless the monomers are symmetry equivalent, in which case only one computation is required because the other monomer would give the same results, and so the correction could be multiplied by 2).

It is helpful to look at some simple equations to see exactly how the CP correction is applied. We may write the interaction energy of a bimolecular complex consisting of molecules A and B as

$$E_{\text{int}} = E_{AB}^{AB} - E_A^A - E_B^B \quad [1]$$

where E_{AB}^{AB} represents the energy of the bimolecular complex (subscript AB) using its usual basis set (the union of the basis sets on A and B, denoted by superscript AB), and E_A^A and E_B^B represent the energies of the isolated molecules A and B using their own usual molecular basis sets. The degree of "artificial" stabilization, or CP error, that molecule A experiences due to the presence of the basis functions of molecule B present in the dimer computation is

$$E_A^{\text{CP err}} = E_A^{AB} - E_A^A \quad [2]$$

Of course, a similar equation holds for molecule B:

$$E_B^{\text{CP err}} = E_B^{AB} - E_B^B \quad [3]$$

If one then subtracts the total CP error, $E_A^{\text{CP err}} + E_B^{\text{CP err}}$, from the equation for the interaction energy, E_{int}, in Eq. [1], one obtains an equation for the CP-corrected interaction energy:

$$E_{\text{int}}^{\text{CP corr}} = E_{AB}^{AB} - E_A^{AB} - E_B^{AB} \quad [4]$$

Notice that the individual molecular energies, E_A^A and E_B^B, have canceled out. Thus the CP-corrected interaction energies do not require the energies of the isolated monomers, but only the energies of the monomers in the composite basis of the bimolecular complex (evaluated using ghost atoms). One downside of this CP correction scheme is that the ghost atom computations required to determine E_A^{AB} and E_B^{AB} must be performed at every bimolecular geometry of interest (because the positions of the ghost functions depend on the geometry of the complex). Another downside is that one may lose symmetry (and therefore increase computational cost) in dimer computations if one of the monomers is replaced by ghost atoms; a ghost atom is never symmetry equivalent with a real atom. For the benzene dimer, the symmetry of the sandwich configuration is D_{6h}, and most programs will use the highest nondegenerate subgroup of this, which is D_{2h}. In a CP computation, however, the symmetry is lowered to C_{6v} (with a highest nondegenerate computational subgroup of C_{2v}). Possibly offsetting this increase in computational cost due to loss of symmetry, however, is the fact that the ghost atom computations involve fewer electrons.

Situations exist where the CP correction "overcorrects," leading to answers that are even worse than the uncorrected values, particularly for smaller basis sets.[51,52] One can understand overcorrection by realizing that not all of the basis functions of molecule B are available to molecule A in the dimer—some of molecule B's basis functions are already occupied by electrons from molecule B itself. One situation where this overcorrection occurs is for hydrogen-bonded complexes.[53] On the other hand, our own experience for π complexes indicates that the CP correction gives greatly superior results. The solid curves in Figure 3 are the CP-corrected MP2/aug-cc-pVXZ curves. One immediately notices a great reduction in the gaps between the various (CP-corrected) curves as the basis is improved from double to triple to quadruple-ζ. Indeed, the difference between the aug-cc-pVTZ and aug-cc-pVQZ curves is small (a few tenths of 1 kcal mol^{-1}). The CBS curve will lie somewhere between the solid (CP-corrected) and dashed (uncorrected) aug-cc-pVQZ curves, but based on the convergence behavior seen in Figure 3 (and on even more elaborate computations performed by our group), it lies much closer to the CP-corrected curve. Our experience so far indicates that the CP correction is generally helpful for π interactions, although it is possible that in some situations it may lead to overcorrection as it does for H-bonded complexes.

Although we are concerned primarily with computations of bimolecular complexes in this review, it is worth mentioning how the CP correction scheme can be extended to trimers or larger clusters. For a trimeric system, the CP-corrected interaction energy may be written as

$$E_{\text{int},ABC}^{\text{CP corr}} = E_{ABC}^{ABC} - E_A^{ABC} - E_B^{ABC} - E_C^{ABC} \qquad [5]$$

where now the superscript ABC denotes computations using the trimer basis. It is convenient to decompose such interaction energies in terms of their

two-body components (the interaction due to pairs within the trimer) and the three-body component (the nonadditive part of the trimer energy not due to pairwise interactions). Hankins et al.[54] define many-body interactions in terms of lower order interaction energies. The two-body interactions would be defined as

$$\Delta^2 E_{\text{int},AB}^{\text{CP corr}} = E_{AB}^{ABC} - E_{A}^{ABC} - E_{B}^{ABC} \quad [6]$$

$$\Delta^2 E_{\text{int},AC}^{\text{CP corr}} = E_{AC}^{ABC} - E_{A}^{ABC} - E_{C}^{ABC} \quad [7]$$

$$\Delta^2 E_{\text{int},BC}^{\text{CP corr}} = E_{BC}^{ABC} - E_{B}^{ABC} - E_{C}^{ABC} \quad [8]$$

The total interaction energy is then written as a sum of these two-body interaction energies plus a three-body interaction energy:

$$E_{\text{int},ABC}^{\text{CP corr}} = \Delta^2 E_{\text{int},AB}^{\text{CP corr}} + \Delta^2 E_{\text{int},AC}^{\text{CP corr}} + \Delta^2 E_{\text{int},BC}^{\text{CP corr}} + \Delta^3 E_{\text{int},ABC}^{\text{CP corr}} \quad [9]$$

The total interaction energy can be computed according to Eq. [5] so that the three-body term can be obtained by subtraction:

$$\Delta^3 E_{\text{int},ABC}^{\text{CP corr}} = E_{\text{int},ABC}^{\text{CP corr}} - \Delta^2 E_{\text{int},AB}^{\text{CP corr}} - \Delta^2 E_{\text{int},AC}^{\text{CP corr}} - \Delta^2 E_{\text{int},BC}^{\text{CP corr}} \quad [10]$$

This scheme can be extended to tetramers and larger clusters.

We have ignored the possibility that the monomer geometries change when in the presence of other molecules in our discussion of the CP correction. In most studies of π interactions in our group to date, such geometry changes are very small, leading us to freeze the monomer geometries to simplify the computations. However, if the monomer geometries do change appreciably in the cluster, this rigid monomer approximation is no longer valid, and a full geometry optimization would be appropriate. Doing this can be problematic because most programs do not allow for full geometry optimization while using the CP correction. Moreover, there is some ambiguity in the appropriate generalization of the CP equations above to allow for relaxation of monomer geometries in the complex.[55]

Additive Basis/Correlation Approximations

At this stage, we face a dilemma because we have seen that both electron correlation and basis set effects are important for computing accurately π interactions. Unfortunately, at the time of this writing (2008), it is not possible to perform CCSD(T) computations using basis sets much larger than aug-cc-pVDZ for systems as large as the benzene dimer without resorting to massively parallel software running on large computer clusters. Fortunately, however, we can mimic large basis set CCSD(T) results using a relatively simple additive

scheme combining modest basis CCSD(T) with large basis MP2. This approach takes advantage of the fact that higher order correlation effects are more rapidly convergent with respect to basis set than are lower order correlation effects. This fact has been exploited in a number of composite computation schemes including the Gaussian-*n*[56,57] and Weizmann-*n*[58] thermochemical methods, and it underpins Allen's focal-point analysis.[59,60]

For our purposes, the approximation we need is

$$E_{\mathrm{CCSD(T)}}^{\text{large-basis}} \approx E_{\mathrm{MP2}}^{\text{large-basis}} + E_{\mathrm{CCSD(T)}}^{\text{small-basis}} - E_{\mathrm{MP2}}^{\text{small-basis}} \qquad [11]$$

This approximation can be viewed in two equivalent ways. First, $E_{\mathrm{CCSD(T)}}^{\text{small-basis}} - E_{\mathrm{MP2}}^{\text{small-basis}}$ can be considered a "coupled-cluster correction," ΔCCSD(T), which corrects the large basis MP2 results for higher order correlation effects. Second, one could consider $E_{\mathrm{MP2}}^{\text{large-basis}} - E_{\mathrm{MP2}}^{\text{small-basis}}$ as a basis set extension correction that can be added to correct the small-basis CCSD(T) results. We will adopt the first viewpoint here. As demonstrated by Table 1, the coupled-cluster correction ΔCCSD(T) is insensitive to the basis set used, so long as a basis of approximately aug-cc-pVDZ quality is used.[61] For example, the difference between the aug-cc-pVDZ and truncated aug-cc-pVTZ basis is no more than 0.03 kcal mol^{-1} for the three benzene dimer configurations considered. Neglect of diffuse functions can seriously degrade the effectiveness of the approximation, however, causing discrepancies in ΔCCSD(T) as large as 0.7 kcal mol^{-1} (parallel displaced configuration with the cc-pVDZ basis). Recent work by Janowski and Pulay[62] using parallel algorithms to perform explicit (and very costly) QCISD(T)/aug-cc-pVTZ computations for the benzene dimer suggests that the higher order correlation correction is not quite converged when computed with the aug-cc-pVDZ basis (errors around 0.1 kcal mol^{-1}). However, this level of error is probably acceptable in most applications. Moreover, it is possible that the ΔCCSD(T) correction may be somewhat less sensitive to basis set improvements than the ΔQCISD(T) correction evaluated by Janowski and Pulay.[62]

Table 1 Estimates of "Coupled-Cluster Correction," ΔCCSD(T) (in kcal mol^{-1}) for various Configurations of the Benzene Dimer[a]

Basis	S	T	PD
cc-pVDZ[b]	1.29	0.71	1.43
cc-pVTZ[b]	1.59	0.83	1.79
aug-cc-pVDZ*[c]	1.84	0.91	2.18
aug-cc-pVDZ	1.83	0.89	2.18
aug-cc-pVTZ(-f/-d)[d]	1.83	0.92	2.21

[a]At the MP2/aug-cc-pVTZ optimized intermonomer distances (Ref. 38) and using the best estimates of the monomer geometry (C–C = 1.3915, C–H = 1.0800Å, Ref. 39).
[b]Ref. 37.
[c]This is an aug-cc-pVDZ basis for carbon and a cc-pVDZ basis for hydrogen.
[d]This is an aug-cc-pVTZ basis minus *f* functions on carbon and *d* functions on hydrogen.

Table 2 Benzene Dimer Intermolecular Distances (in Å)[a]

				PD	
Method	Basis	S	T	R_1	R_2
MP2	aug-cc-pVDZ′	3.9	5.0	3.5	1.6
	aug-cc-pVDZ*[b]	3.8	5.0	3.4	1.6
	aug-cc-pVDZ	3.7	4.9	3.4	1.6
	aug-cc-pVTZ	3.7	4.9	3.4	1.6
	aug-cc-pVQZ*[c]	3.7	4.9	3.4	1.6
	aug-cc-pVQZ[d]	3.7	4.9	—	—
CCSD(T)	aug-cc-pVDZ*[b]	4.0	5.1	3.6	1.8
	aug-cc-pVDZ[d]	4.0	5.1	3.6	1.8
estd. CCSD(T)/aug-cc-pVQZ*		3.9	5.0	3.6	1.6
Expt[e]			4.96		

[a]All intermonomer parameters obtained using rigid monomers (C–C = 1.3915, C–H = 1.0800Å; Ref. 39). Data from Ref. 61 except as noted.
[b]This is aug-cc-pVDZ for carbon and cc-pVDZ for hydrogen.
[c]This is aug-cc-pVQZ less *g* functions for carbon and less *f* functions for hydrogen.
[d]Ref. 66.
[e]Ref. 35.

Using CCSD(T) with a basis of roughly aug-cc-pVDZ quality or better, in combination with MP2 computations using aug-cc-pVTZ or aug-cc-pVQZ basis sets, should thus yield interaction energies (intermolecular binding energies relative to separated molecules) accurate to a few tenths of 1 kcal mol^{-1} for noncovalent π interactions between two small molecules. As indicated by Figures 2 and 3 (see also Table 2), intermolecular distances are not very sensitive to improvements in the basis set (changes of around 0.1 Å or less) and are only mildly sensitive to improvements in electron correlation model (around 0.1–0.2 Å). This means that the additive MP2/CCSD(T) scheme discussed here can provide very reliable results for small prototype systems modeling various kinds of noncovalent π interactions, opening up a large number of possible applications. This procedure has been widely used in recent years by several groups to publish high-quality results for many interesting systems.

REDUCING COMPUTATIONAL COST

The additive scheme described above in which electron correlation effects beyond MP2 can be captured very accurately using a smaller basis set to yield a ΔCCSD(T) correction greatly reduces the computational cost relative to a large-basis CCSD(T) computation. Nevertheless, the computational costs remain high. Using an aug-cc-pVQZ basis, or even an aug-cc-pVTZ basis, for the MP2 computation can be computationally expensive except for the smallest molecules (recall that the augmented functions make these basis sets much larger than the unaugmented ones). Additionally, even

the aug-cc-pVDZ basis is large enough to make CCSD(T) computations very expensive for molecules the size of the benzene dimer or larger—particularly if they lack any symmetry. For example, in 2008, a CCSD(T)/aug-cc-pVDZ computation on benzene dimer with no symmetry takes approximately 2 weeks on a 3.2-GHz Intel EM64T Nocona workstation. For routine applications, then, computational studies require a less expensive procedure. In the following several sections, we will examine several possible approximations, all with the aim of maintaining a fairly high reliability in the computational results.

Truncated Basis Sets

One possible computational shortcut is to reduce the size of the basis sets used by throwing out certain functions. With respect to the correlation-consistent family of basis sets, this runs counter to the philosophy used in constructing the basis sets, where functions of similar energetic importance are added together in shells as the size of the basis is increased.[44,63] This may also degrade the smooth convergence toward the complete basis set limit and make it harder to perform basis set extrapolation. However, these concerns are more important for benchmark-quality studies than for routine chemical applications. We have examined the possible elimination of some groups of diffuse functions in studies of π interactions,[61,64] and a study by Wilson's group[65] indicates that some higher angular momentum functions can be removed from the (nonaugmented) cc-pVXZ basis sets without serious degradation of the total energies of several isolated small molecules.

In earlier studies of the potential energy curves of prototype configurations of the benzene dimer,[61] because we desired many points along the curve, we found it necessary to use basis set truncations to make the computations feasible (these computations were performed again later[66] without the basis set truncations). We originally used a truncated aug-cc-pVDZ basis, which we denoted aug-cc-pVDZ*, for the CCSD(T) computations, speeding them up significantly. This is the usual aug-cc-pVDZ basis, except that diffuse functions from hydrogen atoms were removed. For our symmetry-adapted perturbation theory (SAPT) computations,[67] an even smaller basis set was used that also deleted diffuse *d* functions from carbon; we denoted this basis set aug-cc-pVDZ′. The quadruple-ζ MP2 computations were sped up significantly by another basis set truncation. Instead of using the full aug-cc-pVQZ basis set (with an enormous 1512 basis functions for the benzene dimer), we removed *g* functions for carbon and *f* functions for hydrogen, yielding a basis we denoted aug-cc-pVQZ*.

Any time such approximations are used, it is important to evaluate the consequences of the basis set truncation on the quality of the results. Table 2 presents optimized intermolecular distances for the configurations of the benzene dimer depicted in Figure 1 using the monomer geometries of Gauss and

Table 3 Interaction Energies (kcal mol^{-1}) for the Benzene Dimer[a]

Method	Basis	S	T	PD
MP2	aug-cc-pVDZ′	−1.88	−2.35	−2.89
	aug-cc-pVDZ*[b]	−2.83	−3.00	−4.12
	aug-cc-pVDZ	−2.90	−3.07	−4.22
	aug-cc-pVTZ	−3.25	−3.44	−4.65
	aug-cc-pVQZ*[c]	−3.35	−3.48	−4.73
	aug-cc-pVQZ	−3.37	−3.53	—
CCSD(T)	aug-cc-pVDZ*[b]	−1.33	−2.24	−2.22
	aug-cc-pVDZ[d]	−1.39	−2.31	−2.30
estd. CCSD(T)/aug-cc-pVQZ*		−1.70	−2.61	−2.63

[a]Unless otherwise noted, all computations used intermonomer distances optimized at each level of theory with rigid monomers (C–C = 1.3915, C–H = 1.0800Å; Ref. 39). Data from Ref. 61 except as noted.
[b]This is aug-cc-pVDZ for carbon and cc-pVDZ for hydrogen.
[c]This is aug-cc-pVQZ less *g* functions for carbon and less *f* functions for hydrogen.
[d]Data from Ref. [66].

Stanton. Table 3 presents the corresponding interaction energies. Tables 2 and 3 contain some comparisons of these truncated basis sets against the corresponding full basis sets. Examining MP2 geometries using the aug-cc-pVDZ basis or its truncated versions, aug-cc-pVDZ* or aug-cc-pVDZ′, we see very little change in the optimum intermolecular distances for each of the configurations considered (we scanned the surface with a resolution of 0.1 Å around the minima). The distances generally agree within 0.1 Å. Similar results are observed when comparing CCSD(T) geometries using the aug-cc-pVDZ or aug-cc-pVDZ* basis sets. Again, when considering the aug-cc-pVQZ basis to its truncated version aug-cc-pVQZ*, the MP2 geometries are virtually identical. This suggests that, when necessary (and after careful benchmarking), some diffuse functions and/or higher angular momentum functions may be safely removed from the aug-cc-pVXZ basis sets for the prediction of intermolecular geometries. However, the main point of Table 2 is that the intermolecular distances for the benzene dimer are fairly insensitive to the basis set used. Electron correlation also has only a minor effect, typically increasing the intermolecular distances by about 0.2 Å upon improving the model from MP2 to CCSD(T).

When considering the interaction energies in Table 3, the truncated aug-cc-pVDZ basis sets can lead to significant differences. Although the aug-cc-pVDZ* basis (lacking only diffuse functions on hydrogens) remains within 0.1 kcal mol^{-1} for MP2 interaction energies, the smaller aug-cc-pVDZ′ basis (which excludes also diffuse *d* functions on carbon) is in error by as much as 1.3 kcal mol^{-1} compared to the MP2 values using the full basis. Thus, for comparison to results for a given electron correlation model, care should be exercised in any attempts to reduce the size of the basis by truncating certain functions. This is not to say, however, that the MP2/aug-cc-pVDZ′ results are not useful. Quite the contrary—they seem to exhibit a very favorable

cancellation of errors when compared to our most reliable results, as discussed in more detail below.

Pauling Points

As we have been discussing, it takes two components to specify a level of theory: the basis set and the electron correlation model. In computations of molecular structure, it has long been known that larger basis sets tend to yield shorter bond lengths, while more complete treatments of electron correlation tend to yield longer bond lengths. The best results tend to be those where a good balance exists between the basis set and the theoretical method; such a balance comes from favorable cancellation of errors between the incompleteness of the basis set and the incompleteness of the electron correlation model. The situation where a good result can arise even though an incomplete model is being used has been referred to as a *Pauling point*, after the famous chemist Linus Pauling.

Given the extreme expense of large-basis CCSD(T), we have sufficient motivation to seek theoretical Pauling points for π interactions. Returning to Tables 2 and 3, we observe that the MP2/aug-cc-pVDZ′ results are in remarkably good agreement with the best theoretical benchmark values. Although MP2/aug-cc-pVDZ′ slightly overestimates intermolecular distances compared to MP2 with the full aug-cc-pVDZ basis, this overestimation is just what is needed for good agreement (within 0.1 Å) with the benchmark values. The performance for interaction energies is even more impressive. Although MP2/aug-cc-pVDZ′ greatly underbinds compared to MP2/aug-cc-pVDZ, this underbinding is just what is needed for better agreement with the benchmark results. For the three prototype configurations of the benzene dimer, all of the interaction energies agree within 0.4 kcal mol^{-1} of the large-basis CCSD(T) results. Note that MP2 with the slightly larger aug-cc-pVDZ*, or the full aug-cc-pVDZ basis, yields much poorer agreement with the benchmark CCSD(T) results. Going to larger basis sets with MP2 gives even worse results due to dramatic overbinding. This suggests that, in the context of conventional quantum chemical computations, the MP2 method with a basis set such as aug-cc-pVDZ′ may be the most cost-effective approximation to large-basis CCSD(T). However, it should be noted that the good agreement between MP2/aug-cc-pVDZ′ and large-basis CCSD(T) may not hold for other weakly bound complexes. This is a topic our research group hopes to investigate in more detail. In the meantime, as discussed below, there may be some alternative approximations that may be even more effective at providing high-quality results at reduced computational cost.

Resolution of the Identity and Local Correlation Approximations

Even within the context of a given target level of theory, e.g., MP2/aug-cc-pVTZ, there exist various approximations that allow one to estimate the desired

value at a significantly reduced computational cost. One such approach is the resolution of the identity (RI) approximation,[68,69] also referred to as the density fitting (DF) approximation.[70] Applied with a well-chosen auxiliary basis, this approach introduces errors that are tiny compared to the error made by using a noninfinite basis set.[71,72]

In the RI/DF approximation, computing the necessary two-electron integrals is sped up by introducing an auxiliary basis set and representing products of orbitals as[71]

$$\nu(\mathbf{r})\mu(\mathbf{r}) \approx \sum_i c_{\nu\mu}^P P_i(\mathbf{r}) \qquad [12]$$

If one evaluates this product on a grid instead of using atom-centered Gaussian functions for the auxiliary functions $P_i(\mathbf{r})$, one then obtains the very similar pseudospectral approximation.[73,74] Minimizing the self-interaction error, the four-index electron repulsion integrals,

$$(\mu\nu|\rho\sigma) = \int \mu(\mathbf{r}_1)\nu(\mathbf{r}_1)\frac{1}{r_{12}}\rho(\mathbf{r}_2)\sigma(\mathbf{r}_2)\; d^3\mathbf{r}_1\; d^3\mathbf{r}_2 \qquad [13]$$

may be approximated as[71]

$$(\mu\nu|\rho\sigma) \approx \sum_{PQ}(\mu\nu|P)(P|Q)^{-1}(Q|\rho\sigma) \qquad [14]$$

where $(P|Q)$ is a two-index electron repulsion integral and $(\mu\nu|P)$ and $(Q|\rho\sigma)$ are three-index electron repulsion integrals:

$$(P|Q) = \int P(\mathbf{r}_1)\frac{1}{r_{12}}Q(\mathbf{r}_2)\; d^3\mathbf{r}_1\; d^3\mathbf{r}_2 \qquad [15]$$

and

$$(\mu\nu|P) = \int \mu(\mathbf{r}_1)\nu(\mathbf{r}_1)\frac{1}{r_{12}}P(\mathbf{r}_2)\; d^3\mathbf{r}_1\; d^3\mathbf{r}_2 \qquad [16]$$

This RI approximation can be applied to the four-index integrals needed during a Hartree–Fock computation,[68,71] and also to the integrals needed for post-Hartree–Fock procedures such as MP2.[69,70]

Although the above equations show that the RI approximation makes the formalism somewhat more complex, this speeds up the computation because it can be broken down into less costly steps. Formally, computing all of the possible four-index integrals would scale as $\mathcal{O}(N_{\text{bf}}^4)$ (with N_{bf} the

number of basis functions), but the most expensive step under the RI approximation scales as $\mathcal{O}(N_{\text{aux}}N_{bf}^2)$ (with N_{aux} the number of auxiliary functions).

Another way to reduce the cost of a given computation is to apply local approximations. Because the electron repulsion between the product $\mu(\mathbf{r}_1)\nu(\mathbf{r}_1)$ and $\rho(\mathbf{r}_2)\sigma(\mathbf{r}_2)$ in the integral $(\mu\nu|\rho\sigma)$ depends inversely on the distance r_{12} between electrons 1 and 2, at sufficiently large distances this interaction can be approximated by multipole expansions or even neglected entirely. Such local approximations have made Hartree–Fock and density functional theory computations feasible for systems with hundreds of atoms or more.[75,76] Similarly, one can employ local approximations to correlated electronic structure theories.[70,77–85] These approaches, pioneered by Pulay and Saebø,[77–79] localize the molecular orbitals and then exploit the fact that the motion of two electrons will only be correlated if those electrons are in nearby orbitals. Moreover, one may safely neglect virtual (unoccupied) orbitals that are not spatially close to the occupied orbitals in a given excitation. One advantage of local correlation methods is that they neglect some of the terms that lead to basis set superposition error.[86]

To date, very little work has been done to investigate either RI or local correlation approximations[87,88] for π interactions. However, it is likely that both will be very beneficial for speeding up computations significantly while introducing only small errors. The RI approximation will be particularly useful for computations involving large basis sets. Local approximations, on the other hand, only become helpful for computations of large molecules because they involve a certain "overhead" cost that can only be recovered once the molecule reaches a certain size (called the crossover point). It is possible to employ both approximations simultaneously, and in 2003 Werner, Manby, and Knowles reported a linear scaling resolution of the identity (RI) local MP2 method (RI-LMP2 or DF-LMP2).[70] This method has since been made available in the MOLPRO program.[89]

To demonstrate how these approximations may be helpful in computations of π interactions, Table 4 provides interaction energies for three prototype configurations of the benzene dimer using canonical MP2, the resolution of the

Table 4 MP2 Interaction Energies and Errors for Approximations to MP2 (kcal mol^{-1}) for Various Configurations of the Benzene Dimer[a]

	MP2		RI-MP2		LMP2		RI-LMP2	
Sandwich	−3.195	(14.2)	0.005	(3.3)	0.015	(29.4)	0.013	(3.9)
T-Shaped	−3.355	(13.7)	0.005	(3.8)	0.002	(28.3)	0.004	(4.3)
Parallel Displaced	−4.659	(17.1)	0.008	(2.7)	0.155	(35.4)	0.155	(4.5)

[a]Evaluated using the aug-cc-pVTZ basis set and the rigid monomer geometries of Gauss and Stanton (Ref. 39) with the counterpoise-corrected MP2/aug-cc-pVDZ optimized intermonomer distances (Ref. 38). RI energies and errors for sandwich and T-shaped configurations from Ref. 88. Computations performed on a 3.2-GHz Intel EM64T Nocona workstation. RI and local computations were performed without the use of point-group symmetry. Local methods not counterpoise corrected. CPU times in parentheses (h).

identity (RI-MP2), the local approximation (LMP2), and both approximations simultaneously (RI-LMP2). All comparisons are made using the reasonably large aug-cc-pVTZ basis, and results were obtained with the MOLPRO program.[89] Considering first the RI approximation, we see that it leads to errors smaller than 0.01 kcal mol^{-1} for binding energies, while decreasing computational times from 14–17 h per point to 3–4 h per point, a substantial savings. This reduced computational cost is even more impressive given that the canonical computation used point-group symmetry, whereas for technical reasons the RI and local approximations in MOLPRO do not.

Considering next the local approximation, the LMP2 errors are somewhat larger but are still modest (the largest error is 0.155 kcal mol^{-1} for the parallel-displaced configuration). Disappointingly, the computational cost for LMP2 is actually greater than that of conventional MP2 for this test case. This is probably because the conventional computation has the advantage of point-group symmetry while the LMP2 computation does not, and the benzene dimer is too small a system to have reached the crossover point where LMP2 becomes less computationally expensive. Adding the RI approximation to the LMP2 approximation (the RI-LMP2 column) decreases the computational time again, but the computational cost remains greater than that of RI-MP2. The errors for RI-LMP2 are essentially the same as for LMP2.

It should be noted that the RI and local approximations are not completely "black box." For the RI approximation, one must choose an auxiliary basis set. In Table 4 we have used the coulomb/exchange-fitting (JK-fitting) auxiliary basis[71] for the Hartree–Fock part of the computation, and the MP2-fitting auxiliary basis[72] for the computation of the correlation energy. It is possible that further investigation might yield even more efficient auxiliary basis sets.

In the local correlation methods, the program must determine the *orbital domains* that specify which pairs of orbitals should be correlated. This can be a little problematic for studies of weakly interacting molecules because as one scans the potential energy surface, two molecules might suddenly become close enough that the orbital domains change, leading to a discontinuity in the potential energy surface.[90] The simplest solution to this may be to define the orbital domains when the molecules are a large distance away, and fix the domains in this form for the entire study, as was done in the LMP2 study of Takatani and Sherrill.[88]

Additionally, we were surprised to discover that the local approximation in LMP2 can show significant errors when paired with the aug-cc-pVDZ basis for several example noncovalent interactions.[88] This error was reduced by using larger basis sets or if one removed diffuse functions on hydrogen. More systematic investigations may shed light on which basis sets are best to use for LMP2 computations.

Spin-Component-Scaled MP2

Grimme has argued that the MP2 method exhibits a bias toward same-spin excitations because Hartree–Fock-based methods already include some

degree of same-spin electron correlation due to the Pauli principle.[91] This led him to introduce separate scale factors for the same-spin and opposite-spin pair correlation energies, yielding the spin-component-scaled (SCS) MP2 method.[91] The scaling factors used by Grimme are $\frac{1}{3}$ for same-spin and $\frac{6}{5}$ for opposite-spin components of the correlation energy. The introduction of these two parameters does not increase the computational cost, but it leads to improved properties such as bond lengths and vibrational frequencies.[92] A related approach of Head-Gordon and co-workers[93] is the spin-opposite-scaled MP2 (SOS-MP2) method, which neglects the same-spin term and scales the opposite-spin term.

The SCS-MP2-type methods have generated significant interest from scientists, particularly for applications to noncovalent interactions. One investigation of SCS-MP2 for the benzene dimer[94] by Hill, Platts, and Werner demonstrated interaction energy errors of only 0.1–0.2 kcal mol^{-1} when compared to benchmark[61] CCSD(T) results. Hill and Platts later reoptimized the SCS-MP2 scaling parameters using nucleic acid base-pair interactions to obtain better results for a wider array of π interactions.[95] These workers dubbed the SCS-MP2 method with the new parameters (1.76 for same-spin terms, and neglecting the opposite-spin terms) as SCSN-MP2, where the N denotes the nucleic acids used in the parameterization. When applied to the S22 test set[96] of intermolecular interaction energies, the (density-fitted, local) MP2-based methods had mean absolute deviations of 0.81 (DF-LMP2), 0.27 (DF-SCSN-LMP2), 1.26 (DF-SCS-MP2), and 1.97 kcal mol^{-1} (DF-SOS-LMP2).[95] Another study by Antony and Grimme[97] of 165 biologically relevant, noncovalent complexes showed a clear improvement of SCS-MP2 over MP2 when comparing to CCSD(T) results in the complete-basis-set limit. Additionally, a good cancellation of errors was observed when using SCS-MP2 with polarized triple-ζ basis sets (without diffuse functions or counterpoise correction). However, in some saturated systems (e.g., methane dimer), the original MP2 method is accurate, and spin-component scaling degrades the quality of the results.

Apart from the first study of Hill et al.,[94] most of these studies considered only single-point energies. Our group investigated potential energy curves for a variety of prototype noncovalent complexes, with and without local correlation approximations.[88] In general, we found that both SCS-MP2 and SCSN-MP2 results are better than MP2 results for π interactions, but both lead to larger errors for the methane dimer. Except for that test case, the SCS-MP2 potential curves in the complete-basis-set limit tend to lie slightly above, and SCSN-MP2 curves slightly below, the benchmark CCSD(T) curves. SCSN-MP2 tends to overbind slightly at large intermolecular separations. On the other hand, more recent work[98] suggests that the original SCS-MP2 method may be more reliable than SCSN-MP2 for the potential energy curves of parallel-displaced configurations of π–π interactions.

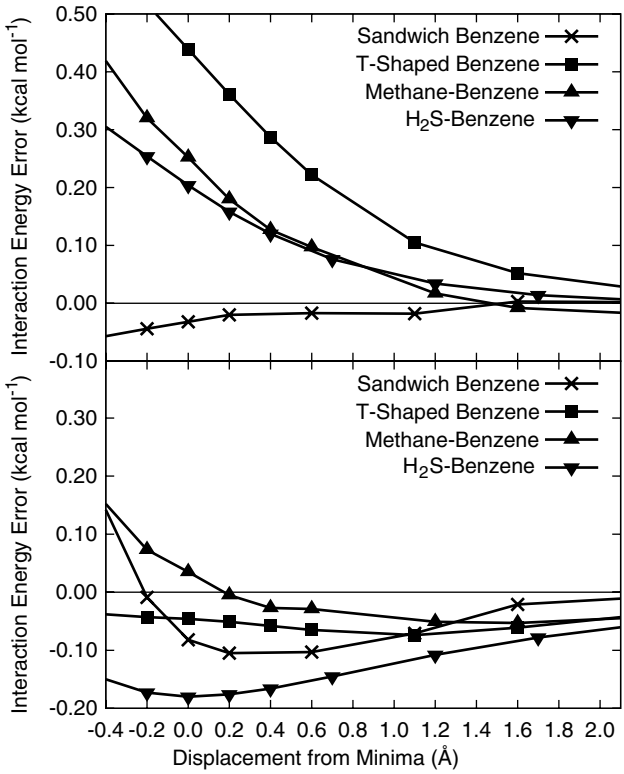

Figure 4 Errors in SCS-MP2/CBS (upper panel) and SCSN-MP2/CBS (lower panel) interaction energies vs. estimated CCSD(T)/CBS values for various bimolecular noncovalent complexes. Data from Ref. 88.

To illustrate the performance of SCS-MP2 and SCSN-MP2, Figure 4 presents errors in the potential energy curves for several π-interaction complexes when compared to estimated CCSD(T)/CBS benchmark curves. The MP2/CBS curves are significantly overbound and are not included in Figure 4. In all cases, the errors vs. the benchmark values are only a few tenths of 1 kcal mol^{-1}. The largest errors are observed for SCS-MP2 at shorter intermonomer separations, and SCS-MP2 tends to have positive errors (underbinds) while SCSN-MP2 tends to have negative errors (overbinds) in the CBS limit.

Table 5 presents benchmark, estimated CCSD(T) binding energies for several noncovalent complexes and the errors for the MP2, SCS-MP2, and SCSN-MP2 methods. Also included are local versions of the SCS-type methods (SCS-LMP2 and SCSN-LMP2). As already mentioned, in every case but the methane dimer, the MP2 method greatly overbinds in the CBS limit. The SCS-MP2 results are greatly improved over MP2 for all cases but the methane dimer, where the error increases from 0.04 to 0.27 kcal mol^{-1}. This remains a

Table 5 CCSD(T) Interaction Energies and Errors for MP2-Type Methods at the Extrapolated CBS Limit[a]

	CCSD(T)	MP2	SCS-MP2	SCS-LMP2[b]	SCSN-MP2	SCSN-LMP2[b]
Sandwich Benzene Dimer	−1.833	−1.337	−0.032	0.036	−0.082	−0.049
T-Shaped Benzene Dimer	−2.871	−0.728	0.439	0.496	−0.046	−0.033
Methane-Benzene	−1.466	−0.352	0.252	0.266	0.035	0.023
H_2S-Benzene	−2.843	−0.776	0.204	0.258	−0.180	−0.168
Methane Dimer	−0.541	0.043	0.266	0.265	0.277	0.216

[a]Intermolecular energies and errors are evaluated at estimated CCSD(T)/CBS optimized geometries. All energies and errors in kcal mol^{-1}. Density fitting approximations applied to all methods except for CCSD(T). Data from Ref. 88.
[b]Local methods not counterpoise corrected.

small error in an absolute sense, although it is somewhat large in a relative sense compared to the benchmark result of −0.54 kcal mol^{-1}. The local approximation hardly changes the SCS-MP2 results and increases errors by 0.06 kcal mol^{-1} or less. The SCSN-MP2 results are generally better than SCS-MP2 for these test cases, although the error for methane dimer is about the same as it was for SCS-MP2. Again, the local correlation approximation changes the error only by a small amount (and for these systems tends to decrease it).

Given the good performance of SCS-MP2 methods, one might ask how much results would be improved by scaling the spin components of the coupled-cluster singles and doubles (CCSD) method[42] to yield a SCS-CCSD method. Although SCS-CCSD would be more computationally expensive than SCS-MP2, scaling as $\mathcal{O}(N^6)$ instead of $\mathcal{O}(N^5)$, the increased accuracy might justify the expense in some applications. Moreover, SCS-CCSD would remain much less expensive than the CCSD(T) method, $\mathcal{O}(N^7)$, it would be meant to mimic. This is particularly true given that, to date, it has been easier to apply RI and local approximations to CCSD than to CCSD(T).[99–102] Even canonical CCSD computations have been performed[102] on systems as large as $(glycine)_{16}$, so suitable approximations will allow even larger computations.

Our group implemented an SCS-CCSD method and obtained scaling parameters by fitting to 48 reaction energies.[103] The scaling parameters are 1.13 and 1.27 for same- and opposite-spin components, respectively. These parameters are closer to one than those of the SCS-MP2 methods, reflecting the more robust electron correlation model of CCSD compared to MP2. Table 6 presents results for SCS-CCSD compared to MP2, SCS-MP2, SCSN-MP2, CCSD, and CCSD(T) for the optimal intermonomer distance and interaction energy for the methane dimer and the sandwich benzene dimer. The SCS-CCSD results provide the best comparison to CCSD(T). Additional study will examine the performance of SCS-CCSD for a wider range of systems.

Table 6 SCS-CCSD and Other Correlated Methods in Comparison to Estimated CCSD(T) Results[a]

	Sandwich Benzene Dimer[b]		Methane Dimer[c]	
	ΔE	R_e	ΔE	R_e
MP2	−3.25	3.7	−0.50	3.7
SCS-MP2	−1.76	3.9	−0.32	3.8
SCSN-MP2	−1.83	3.9	−0.36	3.8
CCSD	−0.89	4.1	−0.41	3.7
SCS-CCSD	−1.63	3.9	−0.57	3.6
CCSD(T)	−1.64	3.9	−0.54	3.6

[a]Energies in kcal mol^{-1} and distances in angstroms. Data from Ref. 103.
[b]Evaluated with the aug-cc-pVTZ basis set. Coupled-cluster methods estimated via an addition of the difference between MP2 and coupled-cluster correlation energies with the aug-cc-pVDZ basis set to the MP2/aug-cc-pVTZ energies.
[c]Extrapolated to the CBS limit.

Explicitly Correlated R12 and F12 Methods

One way to accelerate convergence to the complete-basis-set limit is to employ *explicitly correlated* methods, which make the electronic wave function depend explicitly on the distances between electrons. These methods have been motivated by the observation that the shape and size of the Coulomb hole around an electron (i.e., the effect that the electron has on decreasing the probability of finding another electron in the same vicinity) is slowly convergent with respect to the size of the basis set. However, convergence is improved greatly by introducing interelectronic distances into the expression of the wave function, as first noted by Hylleraas in 1929 in his work on the helium atom.[104] Interest in such methods has been limited because they are more mathematically complex than conventional approaches, and they can lead to a large number of integrals that are difficult to evaluate. However, a number of strategies have been developed to avoid these formal difficulties, one of the most successful of which is the "linear R12" approach of Kutzelnigg and Klopper,[105,106] which introduces terms linear in the interelectronic distance and prescribes *standard approximations* for the elimination of some integrals and the estimation of others using a resolution of the identity. Our group used such an approach in conjunction with the MP2 method, known as MP2-R12/A,[105,106] to estimate the CBS MP2 results with a custom basis set smaller than the explicit aug-cc-pVQZ basis.[38]

These linear R12 approaches, while helpful for very careful benchmarking studies, have had the drawback that they are rather expensive to use. One of the main reasons for this is that the particular resolution of the identity approximation they have typically employed is valid only when a large basis set is used. However, a number of recent developments indicate that in the

near future explicitly correlated methods may be the preferred electronic structure approach for problems with large basis set requirements. Theorists have improved the efficiency of integral evaluation,[107] allowed for the use of a different basis set for the resolution of the identity versus the other components of the computation,[108,109] and reformulated the resolution of the identity to make it more stable numerically,[110] among other achievements.

Perhaps more importantly, faster convergence to the complete basis set limit has been observed by replacing the linear R12 terms with alternative correlation factors that might be more complex functions of the interelectronic distance.[111,112] These new approaches are called F12 methods, and although they remain in a development and testing phase as this chapter is being written, it is anticipated that they are likely to move into mainstream use in only a few years. Already, MP2-R12 computations can be performed in a number of program packages, including MOLPRO,[89] MPQC,[113] TURBOMOLE,[114] and PSI.[115] As more experience is gained in benchmarking and using R12 and F12 methods, they will become more accessible to a wider array of users.

Density Functional Approaches

Despite its tremendous success in a wide variety of chemical applications, density functional theory (DFT)[116,117] has not yet had much impact on studies of weakly bound complexes. In principle, density functional theory with the exact functional would provide exact results for any chemical system, including van der Waals complexes. In practice, however, the Kohn–Sham formulation of DFT with mainstream functionals is not capable of capturing dispersion effects, even qualitatively.[28,118,119] This deficiency arises from the fact that these approaches lack the long-range, nonlocal terms required to model dispersion. This is true even of gradient-corrected functionals (which are sometimes confusingly referred to as "nonlocal" functionals) because including information about the gradient of the density does not extend the range of electron correlations very far. Hybrid functionals include some fraction of Hartree–Fock exchange,[40] which is nonlocal. However, dispersion is related to dynamical electron correlation, not exchange, and hence hybrid density functionals also fail to include the proper physics to model dispersion interactions.

Because DFT is so successful in other areas, and because it has become a familiar tool to many chemists, there is a great desire to use it for studies of noncovalent interactions, even though currently popular formulations are really not appropriate for such studies. The reader is urged to avoid giving in to this temptation, for the simple reason that there would be no reason to believe the results for properties such as interaction energies or intermolecular distances. In an eye-opening study, Johnson, Wolkow, and DiLabio[119] found that out of 25 different density functionals, *all* of them were in error

by 1 kcal mol^{-1} or more for the sandwich benzene dimer. Even worse, only 2 of the 25 functionals even bound the sandwich dimer at all; the rest gave the completely false picture that the potential curve is purely repulsive (see Figure 2 for the example of B3LYP). In light of such erroneous predictions, it is best to avoid standard DFT methods at all costs for studies of systems where dispersion is a dominant interaction. If the system is too large to use higher quality ab initio methods, then the reader is advised to use molecular mechanics instead, or perhaps one of the new DFT approaches being developed.

These deficiencies with DFT for noncovalent interactions have captured the interest of a large number of theorists, and as this review is being written, serious effort is being devoted to developing improved methods based upon DFT that can describe dispersion properly. Because the purpose of this chapter is more to give an introduction and tutorial in computing π interactions than it is to give an exhaustive technical review, I will not attempt to provide a complete summary of the voluminous work that has been done in this area in the past few years. However, the reader should be aware that initial results are very promising, and DFT methods adapted for dispersion may come into mainstream use in the near future.

One very simple but seemingly effective approach is to simply add an empirical dispersion correction to DFT energies. Because long-range dispersion interactions are reasonably well modeled in molecular mechanics approaches by pairwise $-C_6r^{-6}$ between atoms, it seems promising to add such terms to DFT. These contributions must be damped at small distances to avoid becoming too large (and to help avoid double counting by this empirical parameter and by the density functional). A number of researchers have tried this approach, which has been referred to as DFT plus dispersion (DFT-D).[120–132] A systematic study by Grimme[125] on 29 weakly bound complexes suggests that DFT-D with polarized triple-ζ basis sets can provide energies that are accurate to about 10–30% (better performance than large-basis MP2). DFT-D with double-ζ basis sets is not as good, however. Grimme recommends using tight convergence and large grids for these computations because of the flatness of the potential energy surfaces.[125] More recent systematic studies have arrived at similar conclusions.[127–132]

A less empirical approach has been to augment DFT with certain nonlocal terms. This strategy can be successful so long as the cost of computing the nonlocal terms is not allowed to become too large. Röthlisberger and co-workers have added effective atom-centered nonlocal potentials that have been fit to benchmark ab initio data.[133,134] Langreth, Lundqvist, and coworkers have introduced a van der Waals density functional (vdW-DF) that adds nonlocal terms to the correlation energy functional.[135] This approach has been tested for the benzene dimer[136] and substituted benzene dimers,[137] with reasonably good success (although the sandwich configuration is overbound). Energy changes due to substituents, which are somewhat easier to compute than binding energies, are reproduced well by this approach.

Becke has proposed a novel approach that formulates the dispersion interaction in terms of the dipole moment that would be created when considering an electron and its exchange hole.[138–140] Like DFT-D, these methods appear to be more reliable than MP2 for noncovalent interactions. Alternatively, other workers[141,142] have combined DFT with symmetry-adapted perturbation theory (SAPT)[67] (discussed below). These DFT-SAPT approaches evaluate the dispersion term via the frequency-dependent density susceptibility functions of time-dependent DFT, an approach that appears to be theoretically sound.

There have also been attempts to parameterize new functionals within the current standard framework, up to and including hybrid, meta-generalized gradient approximation functionals that depend on the local density, its gradient, and the kinetic energy density, and that mix in Hartree–Fock exchange (see, e.g., Refs. 143–145). Some of these functionals appear to be improved[129,146] over the most popular currently available functionals for noncovalent interactions between molecules that are close to each other (what Zhao and Truhlar have called *medium-range correlation*);[146] however, without truly nonlocal, nonexchange terms in the functional, such approaches are unlikely to work at larger distances and thus would not appear to be as promising in the long run as the more generally applicable approaches discussed above.

Semiempirical Methods and Molecular Mechanics

As discussed earlier, one of the simplest ways to correct the deficiencies of popular density functionals for noncovalent interactions is to add an empirical dispersion term proportional to r^{-6}, as is done in molecular mechanics methods. Given that this appears to work well, one may ask about the performance of purely empirical, molecular mechanics force-field methods. These approaches have the advantage that they are much simpler computationally and can be applied to systems with thousands of atoms. To date, there has been limited testing of force-field methods against high-quality quantum data for noncovalent interactions (in part because such benchmark data is only now becoming available for a reasonable number of systems). AMBER has been found to provide good results for intercalators in comparison to MP2 data with a modified 6-31G* basis set, but only after modification of some of the terms.[147] In tests of the benzene dimer, Macias and MacKerell[148] found binding energies within a few tenths of 1 kcal mol^{-1} using a refined CHARMM force field. Similarly good results have been reported using polarizable force fields.[149,150]

Using data from our recent work,[151] Figure 5 illustrates the performance of some popular force-field methods (namely, CHARMM,[152] AMBER,[153] MM3,[154] and OPLS[155]) compared to our estimated CCSD(T) complete basis set results[66] for the sandwich benzene dimer. Overall, CHARMM and OPLS

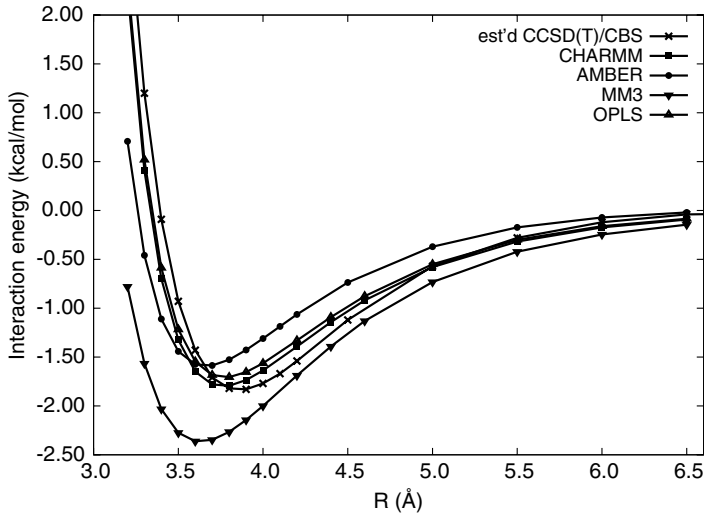

Figure 5 Interaction energy for the sandwich benzene dimer as a function of the intermolecular distance using various force field methods compared to benchmark quantum data. Data from Refs. 151 and 66.

perform well for this test case, while AMBER is somewhat underbound and MM3 is significantly overbound.

Finally, we should also briefly discuss the performance of semiempirical methods. These are methods that neglect some of the more expensive integrals in Hartree–Fock molecular orbital theory and replace others with empirical parameters. Because semiempirical methods are based on Hartree–Fock theory, and because Hartree–Fock theory does not capture dispersion effects, semiempirical methods are not suitable for computing dispersion-dominated noncovalent interactions. Semiempirical methods yield repulsive potentials for the sandwich benzene dimer, just as Hartree–Fock does. However, given that semiempirical methods already contain empirical parameters, there is no reason not to fix this deficiency by adding terms proportional to r^{-6}, as is done in force-field methods and the empirical DFT-D methods. Such an approach has been tested for some base pairs and sulfur-π model systems.[130]

ANALYSIS USING SYMMETRY-ADAPTED PERTURBATION THEORY

So far in this review, we have focused on various approaches to computing the strength and geometries of noncovalent π interactions. However, not only can computational chemistry provide such information, but it can also provide a means of analyzing that information. In studies of complex phenomena, data analysis can be the most important step if it yields a rational

framework for thinking about similar problems. To give just one example, the conventional wisdom about substituent effects in π–π interactions is that they are governed by electrostatic terms, as proposed by Hunter and Sanders[156] on the basis of a very simple mathematical model and experimental data. However, direct computations on substituted benzene dimers in our laboratory[157,158] show that this picture is oversimplified and cannot explain such phenomena as the greater binding of sandwich phenol–benzene and toluene–benzene complexes relative to the benzene dimer. Our explanation of this situation, which is summarized in a recent review,[159] relied heavily on analysis tools provided by SAPT.[67]

Symmetry-adapted perturbation theory is a well-motivated theoretical approach to compute the individual components of intermolecular interactions, namely, the electrostatic, induction, dispersion, and exchange-repulsion terms. The approach is a double-perturbation theory that uses a Hartree–Fock reference, with a Fock operator F written as the sum of Fock operators for the individual molecules. Both the intramolecular correlation potential (W) and the intermolecular interactions (V) are treated as perturbations, so that the Hamiltonian is expressed as

$$H = F + V + W \qquad [17]$$

These perturbations may be treated using second-order perturbation theory, resulting in an approach that is referred to as SAPT2.[67,160] One can also include certain higher order terms using coupled-cluster techniques, which yields the full SAPT. The approximate SAPT2 approach is less expensive computationally, but it appears to give good results for qualitative analysis of intermolecular interactions.

The SAPT energy may be written as

$$E_{\text{int}} = E_{\text{int}}^{\text{HF}} + E_{\text{int}}^{\text{corr}} \qquad [18]$$

where $E_{\text{int}}^{\text{HF}}$ is the Hartree–Fock component of the energy, which may be broken down as

$$E_{\text{int}}^{\text{HF}} = E_{\text{elst}}^{(10)} + E_{\text{exch}}^{(10)} + E_{\text{ind,resp}}^{(20)} + E_{\text{exch-ind,resp}}^{(20)} + \delta E_{\text{ind,resp}}^{\text{HF}} \qquad [19]$$

The superscripts in Eq. [19] refer to orders in the two perturbations, V and W, respectively. The terms denoted "resp" refer to the inclusion of higher order terms via the coupled-perturbed Hartree–Fock equations.[160] The term $E_{\text{exch}-\text{ind,resp}}^{(20)}$ is a cross term involving both exchange and induction. The term $\delta E_{\text{ind,resp}}^{\text{HF}}$ includes higher order Hartree–Fock induction as well as exchange-induction contributions.

Under the SAPT2 approximation, the correlation energy is comprised of the following individual contributions:[67]

$$E_{\text{int}}^{\text{corr}} = E_{\text{elst,resp}}^{(12)} + E_{\text{exch}}^{(11)} + E_{\text{exch}}^{(12)} + {}^{t}E_{\text{ind}}^{(22)} + {}^{t}E_{\text{exch-ind}}^{(22)} + E_{\text{disp}}^{(20)} + E_{\text{exch-disp}}^{(20)} \quad [20]$$

Again, cross terms involving two types of interactions appear—here, both exchange-induction and exchange-dispersion terms. Based on a subjective analysis of SAPT2 results for π–π interactions, we have decided somewhat arbitrarily to classify the exchange-induction and exchange-dispersion terms as induction and dispersion, respectively. This yields the following scheme:

$$E(\text{electrostatic}) = E_{\text{elst}}^{(10)} + E_{\text{elst,resp}}^{(12)} \quad [21]$$

$$E(\text{exchange}) = E_{\text{exch}}^{(10)} + E_{\text{exch}}^{(11)} + E_{\text{exch}}^{(12)} \quad [22]$$

$$E(\text{induction}) = E_{\text{ind,resp}}^{(20)} + E_{\text{exch-ind,resp}}^{(20)} + \delta E_{\text{int,resp}}^{\text{HF}} + {}^{t}E_{\text{ind}}^{(22)} + {}^{t}E_{\text{exch-ind}}^{(22)} \quad [23]$$

$$E(\text{dispersion}) = E_{\text{disp}}^{(20)} + E_{\text{exch-disp}}^{(20)} \quad [24]$$

Our group has obtained SAPT results using the programs of Szalewicz and co-workers, which are freely available.[161] The Appendix gives an example of the output from this program and how to extract the energetic components in Eq. [21]–[24].

In our experience, the SAPT computations can be time demanding even at second order (SAPT2), motivating the use of truncated basis sets. Fortunately, as discussed above, a fortuitous cancellation of error exists when using MP2 with the truncated aug-cc-pVDZ basis, aug-cc-pVDZ′, which removes diffuse functions from hydrogen and diffuse *d* functions from all heavier atoms. Because the SAPT2 results mimic MP2 for interaction energies, this means that SAPT2/aug-cc-pVDZ′ results should be fairly reliable.

As an example of the application of SAPT, consider the two C_{2v} configurations of the H_2S-benzene complex[162,163] shown in Figure 6. The hydrogens-down

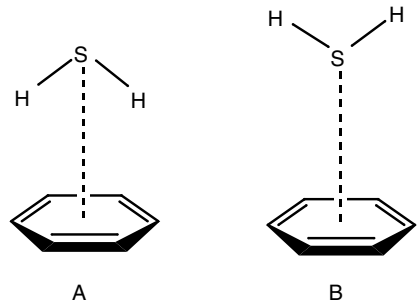

Figure 6 Two symmetric configurations of the H_2S–benzene complex.

Table 7 SAPT2/aug-cc-pVDZ Results for Contributions to the Interaction Energy (kcal mol^{-1}) at CCSD(T)/aug-cc-pVQZ Intermolecular Distances for Two Configurations of H_2S-Benzene[a]

Energy	A	B
E_{elst}	−2.37	0.01
E_{exch}	4.19	1.03
E_{ind}	−0.81	−0.17
E_{disp}	−4.16	−2.14
E_{int} (SAPT2)	−3.15	−1.27
E_{int} (MP2)	−3.06	−1.21

[a]Data from Ref. 162.

configuration, A, binds significantly more favorably (−3.15 kcal mol^{-1}, SAPT2/aug-cc-pVDZ) than the hydrogens-up configuration, B (−1.27 kcal mol^{-1}). SAPT analysis can help explain this difference.

As shown in Table 7, the individual components of the interaction energy change significantly between the hydrogens-down and hydrogens-up configurations. The exchange-repulsion and dispersion terms are the most sensitive to geometry. In fact, in our studies of substituent effects in π–π interactions, we have usually kept the distance between the π rings constant when comparing different substituted complexes, even when they might have slightly different optimal vertical separations, simply to make the comparison of the SAPT components more straightforward.[157] In the case of configurations A and B for H_2S–benzene, there is an unavoidable significant difference in the geometries. The hydrogens-down configuration has a much larger exchange energy (4.19 kcal mol^{-1}) because the hydrogens are much closer to the π cloud of the benzene, leading to greater steric repulsion. When the hydrogens are rotated away from the benzene, the steric repulsion is much less (1.03 kcal mol^{-1}). On the other hand, differences in exchange-repulsion energies usually lead to roughly opposite changes in dispersion interactions. Here, as one goes from A to B, the exchange energy becomes more favorable (less repulsive), but the dispersion energy becomes less favorable (less attractive). In such situations, it is often helpful to consider the sum of the exchange and dispersion terms. In this case, the change in the repulsion term is even larger than that in the dispersion term, so the sum of exchange and dispersion is attractive for configuration B (−1.11 kcal mol^{-1}) while it is almost zero for configuration A. This is consistent with the expectation that the (net) dispersion interaction should be larger for configuration B because the sulfur lone pairs will have a more favorable dispersion interaction with the benzene π cloud than will the hydrogens.

However, the change in the electrostatic term is even larger than this; configuration A is favored by 2.38 kcal mol^{-1} electrostatically compared to configuration B. This is consistent with the expectation that the partial positive charge on the hydrogens will interact much more favorably with a partial negative charge on the π cloud of benzene than would the sulfur lone pairs.

This change in the electrostatic term is larger than the change in the sum of exchange and dispersion, and it is also larger than the change in the induction term (which is probably describing mainly polarization of the π cloud due to the dipole of H_2S). For all these reasons, we would say that, loosely speaking, electrostatics appear to dominate the geometric preferences of the H_2S–benzene complex, and that the most important net interaction in this system is that between the partially positive hydrogens of H_2S and the negatively charged π cloud. Such an analysis, although ultimately losing much of the quantitative information present in the SAPT results, can be helpful in thinking (generally) about how noncovalent systems may interact.

CONCLUDING REMARKS

Noncovalent interactions, particularly those involving aromatic π systems, are of great significance to current research thrusts in supramolecular chemistry, nanostructured materials, crystal engineering, and drug design. We are at an exciting stage when many of the fundamental interactions governing these important areas are being revealed in unprecedented detail. Although computations of noncovalent π interactions remain challenging for current methods, a large number of promising possibilities are already on the horizon that may make reliable computations on such systems routine in the near future. This tutorial has provided some guidance in the selection of appropriate methods and in the avoidance of possible pitfalls in computational studies of noncovalent π interactions.

APPENDIX: EXTRACTING ENERGY COMPONENTS FROM THE SAPT2006 PROGRAM

It may be helpful for readers who have not yet used the SAPT programs of Szalewicz and co-workers[161] to provide an example of how to extract the energetic components of Eq. [21]–[24], although it is fairly straightforward to do so based on the available documentation. The following lines of the SAPT summary table are extracted to compute the components of the interaction energy of the benzene dimer as an example.

```
Correction      mHartree       Kcal/mol            1/cm
----------      --------       --------            ----

                                --- SCF (SAPT_super) ---
E^{HF}_{int}          15.431383270    9.68334732   3386.7971
E^{(10)}_{elst}       -7.301432558   -4.58172194  -1602.4792
E^{(10)}_{exch}       24.641729459   15.46293165   5408.2345
E^{(20)}_{ind,resp}  -10.363352572   -6.50310737  -2274.4930
E^{(20)}_{ex-ind,r}    9.863057594    6.18916727   2164.6909
\delta^{HF}_{int,r}   -1.408618652   -0.88392229   -309.1561
```

```
                                          --- CORRELATION ---
E^{(12)}_{elst,resp}   -0.435841575   -0.27349495    -95.6562
E^{(11)}_{exch}         0.941343304    0.59070234    206.6010
E^{(12)}_{exch}        -1.206428145   -0.75704573   -264.7804
^tE^{(22)}_{ind}        0.159009259    0.09977990     34.8985
^tE^{(22)}_{ex-ind}*   -0.151333024   -0.09496299    -33.2138
E^{(20)}_{disp}       -20.876202931  -13.10002610  -4581.7969
E^{(20)}_{exch-disp}    3.616236015    2.26922426    793.6721

                                       --- TOTAL (hybrid) ---
SCF+SAPT_{corr,resp}   -2.521833826   -1.58247594   -553.4785
```

Here $E_{\text{int}}^{\text{HF}}$ is the interaction energy of the complex calculated with the Hartree–Fock method. The $\texttt{SCF+SAPT}_{\text{corr,resp}}$ term is the sum of all of the other terms and represents the total interaction energy.

The program prints additional energy terms in the SAPT summary table for completeness, but these data provide redundant information for the purpose of computing the individual components of the interaction energy according to, e.g., Eq. [21]–[24]. For example, $E_{\text{exch}}^{(10)}S^2$ and $E_{\text{exch}}^{(10)} - S^2$ need not be included because their sum is already present in the table as $E_{\text{exch}}^{(10)}$. The term $E_{\text{ex}-\text{ind}}^{(20)}$ has a corresponding response term that is included. $\text{eps}_{\text{elst},r}^{(1)}(k)$, $\text{eps}_{exch}^{(1)}(k)$, and $E_{disp}^{(2)}(k)$ are the same as $E_{\text{elst,resp}}^{(12)}$, $E_{exch}^{(11)} + E_{exch}^{(12)}$, and $E_{disp}^{(20)}$, respectively. The terms $\texttt{SAPT SCF}_{\text{resp}}$, $\texttt{SAPT}_{\text{corr}}$, $\texttt{SAPT}_{\text{corr,resp}}$, and $\texttt{SCF + SAPT}_{\text{corr}}$ are the sums of other terms already included.

ACKNOWLEDGMENTS

The author wishes to thank Tait Takatani, Stephen Arnstein, and Ashley Ringer for assistance in preparing this review. This research was supported in part by the National Science Foundation (Grant No. CHE-0715268) and by the Donors of the American Chemical Society Petroleum Research Fund (Grant No. 44262-AC6). The Center for Computational Molecular Science and Technology is funded through an NSF CRIF award (CHE 04-43564) and by Georgia Tech.

REFERENCES

1. E. A. Meyer, R. K. Castellano, and F. Diederich, *Angew. Chem. Int. Ed. Engl.*, **42**, 1210 (2003). Interactions with Aromatic Rings in Chemical and Biological Recognition.
2. W. Saenger, *Principles of Nucleic Acid Structure*, Springer, New York, 1984.
3. S. K. Burley and G. A. Petsko, *Science*, **229**, 23 (1985). Aromatic-Aromatic Interaction: A Mechanism of Protein Structure Stabilization.
4. C. A. Hunter, J. Singh, and J. M. Thornton, *J. Mol. Biol.*, **218**, 837 (1991). π-π Interactions: The Geometry and Energetics of Phenylalanine-Phenylalanine Interactions in Proteins.
5. A. Gil, V. Branchadell, J. Bertran, and A. Oliva, *J. Phys. Chem. B*, **111**, 9372 (2007). CH/π Interactions in DNA and Proteins. A Theoretical Study.

6. R. S. Morgan, C. E. Tatsh, R. H. Gushard, J. M. Mcadon, and P. K. Warme, *Int. J. Pept. Prot. Res.*, **11**, 209 (1978). Chains of Alternating Sulfur and Pi-Bonded Atoms in 8 Small Proteins.
7. R. J. Zauhar, C. L. Colbert, R. S. Morgan, and W. J. Welsh, *Biopolymers*, **53**, 233 (2000). Evidence for a Strong Sulfur-Aromatic Interaction Derived from Crystallographic Data.
8. K. S. C. Reid, P. F. Lindley, and J. Thornton, *FEBS Lett.*, **190**, 209 (1985). Sulfur-Aromatic Interactions in Proteins.
9. M. F. Brana, M. Cacho, A. Gradillas, B. Pascual-Teresa, and A. Ramos, *Curr. Pharma. Design*, **7**, 1745 (2001). Intercalators as Anticancer Drugs.
10. R. Wintjens, J. Lievin, M. Rooman, and E. Buisine, *J. Mol. Biol.*, **302**, 395 (2000). Contribution of Cation-π Interactions to the Stability of Protein-DNA Complexes.
11. C. Biot, R. Wintjens, and M. Rooman, *J. Am. Chem. Soc.*, **126**, 6220 (2004). Stair Motifs at Protein-DNA Interfaces: Nonadditivity of H-Bond, Stacking, and Cation-π Interactions.
12. A. Anbarasu, S. Anand, M. M. Babu, and R. Sethumadhavan, *Int. J. Biol. Macromol.*, **41**, 251 (2007). Investigations of C–H $\cdots$ π Interactions in RNA Binding Proteins.
13. C. G. Claessens and J. F. Stoddart, *J. Phys. Org. Chem.*, **10**, 254 (1997). π-π Interactions in Self-Assembly.
14. M. C. T. Fyfe and J. F. Stoddart, *Acc. Chem. Res.*, **10**, 393 (1997). Synthetic Supramolecular Chemistry.
15. A. M. van de Craats, J. M. Warman, K. Müllen, Y. Geerts, and J. D. Brand, *Adv. Mater.*, **10**, 36 (1998). Rapid Charge Transport Along Self-Assembling Graphitic Nanowires.
16. T. C. Dinadayalane, L. Gorb, T. Simeon, and H. Dodziuk, *Int. J. Quantum Chem.*, **107**, 2204 (2007). Cumulative pi-pi Interaction Triggers Unusually High Stabilization of Linear Hydrocarbons Inside the Single-walled Carbon Nanotube.
17. S. Grimme, C. Muck-Kichtenfeld, and J. Antony, *J. Phys. Chem. C*, **111**, 11199 (2007). Noncovalent Interactions Between Graphene Sheets in Multishell (Hyper)Fullerenes.
18. M. D. Curtis, J. Cao, and J. W. Kampf, *J. Am. Chem. Soc.*, **126**, 4318 (2004). Solid-State Packing of Conjugated Oligomers: From π Stacks to the Herringbone Structure.
19. C. A. Hunter, *Angew. Chem. Int. Ed. Engl.*, **32**, 1584 (1993). Arene-Arene Interactions: Electrostatic or Charge Transfer?
20. K. Nakamura and K. N. Houk, *Org. Lett.*, **1**, 2049 (1999). Theoretical Studies of the Wilcox Molecular Torsion Balance. Is the Edge-to-Face Aromatic Interaction Important?
21. J. Ribas, E. Cubero, F. J. Luque, and M. Orozco, *J. Org. Chem.*, **67**, 7057 (2002). Theoretical Study of Alkyl-π and Aryl-π Interactions. Reconciling Theory and Experiment.
22. M. J. Rashkin and M. L. Waters, *J. Am. Chem. Soc.*, **124**, 1860 (2002). Unexpected Substituent Effects in Offset π-π Stacked Interactions in Water.
23. G. S. Tschumper, in *Reviews in Computational Chemistry*, K. B. Lipkowitz and T. R. Cundari, Eds., Wiley, Hoboken, NJ, 2008, Vol. 26, pp. 39–90. Accurate Ab Initio and Density Functional Computations for Weak Non-Covalent Interactions in Clusters.
24. S. Tsuzuki, T. Uchimaru, and K. Tanabe, *J. Mol. Struct. THEOCHEM*, **307**, 107 (1994). Basis Set Effects on the Intermolecular Interaction of Hydrocarbon Molecules Obtained by Ab Initio Molecular Orbital Method: Evaluation of Dispersion Energy.
25. P. Hobza, H. L. Selzle, and E. W. Schlag, *J. Am. Chem. Soc.*, **116**, 3500 (1994). Potential Energy Surface of the Benzene Dimer: Ab Initio Theoretical Study.
26. P. Hobza, H. L. Selzle, and E. W. Schlag, *J. Phys. Chem.*, **100**, 18790 (1996). Potential Energy Surface for the Benzene Dimer. Results of *Ab Initio* CCSD(T) Calculations Show Two Nearly Isoenergetic Structures: T-Shaped and Parallel-Displaced.
27. R. L. Jaffe and G. D. Smith, *J. Chem. Phys.*, **105**, 2780 (1996). A Quantum Chemistry Study of Benzene Dimer.

28. S. Tsuzuki and H. P. Lüthi, *J. Chem. Phys.*, **114**, 3949 (2001). Interaction Energies of van der Waals and Hydrogen Bonded Systems Calculated Using Density Functional Theory: Assessing the PW91 Model.

29. K. C. Janda, J. C. Hemminger, J. S. Winn, S. E. Novick, S. J. Harris, and W. Klemperer, *J. Chem. Phys.*, **63**, 1419 (1975). Benzene Dimer: A Polar Molecule.

30. J. M. Steed, T. A. Dixon, and W. Klemperer, *J. Chem. Phys.*, **70**, 4940 (1979). Molecular Beam Studies of Benzene Dimer, Hexafluorobenzene Dimer, and Benzene-Hexafluorobenzene.

31. K. S. Law, M. Schauer, and E. R. Bernstein, *J. Chem. Phys.*, **81**, 4871 (1984). Dimers of Aromatic Molecules: $(Benzene)_2$, $(Toluene)_2$, and Benzene-Toluene.

32. K. O. Börnsen, H. L. Selzle, and E. W. Schlag, *J. Chem. Phys.*, **85**, 1726 (1986). Spectra of Isotopically Mixed Benzene Dimers: Details on the Interaction in the vdW Bond.

33. J. R. Grover, E. A. Walters, and E. T. Hui, *J. Phys. Chem.*, **91**, 3233 (1987). Dissociation Energies of the Benzene Dimer and Dimer Cation.

34. H. Krause, B. Ernstberger, and H. J. Neusser, *Chem. Phys. Lett.*, **184**, 411 (1991). Binding Energies of Small Benzene Clusters.

35. E. Arunan and H. S. Gutowsky, *J. Chem. Phys.*, **98**, 4294 (1993). The Rotational Spectrum, Structure and Dynamics of a Benzene Dimer.

36. P. M. Felker, P. M. Maxton, and M. W. Schaeffer, *Chem. Rev.*, **94**, 1787 (1994). Nonlinear Raman Studies of Weakly Bound Complexes and Clusters in Molecular Beams.

37. S. Tsuzuki, K. Honda, T. Uchimaru, M. Mikami, and K. Tanabe, *J. Am. Chem. Soc.*, **124**, 104 (2002). Origin of Attraction and Directionality of the π-π Interaction: Model Chemistry Calculations of Benzene Dimer Interaction.

38. M. O. Sinnokrot, E. F. Valeev, and C. D. Sherrill, *J. Am. Chem. Soc.*, **124**, 10887 (2002). Estimates of the Ab Initio Limit for π-π Interactions: The Benzene Dimer.

39. J. Gauss and J. F. Stanton, *J. Phys. Chem. A*, **104**, 2865 (2000). The Equilibrium Structure of Benzene.

40. A. D. Becke, *J. Chem. Phys.*, **98**, 1372 (1993). A New Mixing of Hartree-Fock and Local Density-Functional Theories.

41. P. J. Stephens, F. J. Devlin, C. F. Chabalowski, and M. J. Frisch, *J. Phys. Chem.*, **98**, 11623 (1994). *Ab Initio* Calculation of Vibrational Absorption and Circular Dichroism Spectra Using Density Functional Force Fields.

42. G. D. Purvis and R. J. Bartlett, *J. Chem. Phys.*, **76**, 1910 (1982). A Full Coupled-Cluster Singles and Doubles Model: The Inclusion of Disconnected Triples.

43. K. Raghavachari, G. W. Trucks, J. A. Pople, and M. Head-Gordon, *Chem. Phys. Lett.*, **157**, 479 (1989). A 5th-Order Perturbation Comparison of Electron Correlation Theories.

44. R. A. Kendall, T. H. Dunning, and R. J. Harrison, *J. Chem. Phys.*, **96**, 6796 (1992). Electron Affinities of the First-Row Atoms Revisited. Systematic Basis Sets and Wave Functions.

45. T. J. Lee and G. E. Scuseria, in *Quantum Mechanical Electronic Structure Calculations with Chemical Accuracy*, S. R. Langhoff, Ed., Kluwer Academic, Dordrecht, 1995, pp. 47–108. Achieving Chemical Accuracy with Coupled-Cluster Theory.

46. C. D. Sherrill, in *Annual Reports in Computational Chemistry*, D. Spellmeyer, Ed., Elsevier, Amsterdam, 2005, Vol. 1, pp. 45–54. Bond Breaking in Quantum Chemistry.

47. B. W. Hopkins and G. S. Tschumper, *J. Phys. Chem. A*, **108**, 2941 (2004). Ab Initio Studies of $\pi \cdots \pi$ Interactions: The Effects of Quadruple Excitations.

48. N. R. Kestner and J. E. Combariza, in *Reviews in Computational Chemistry*, K. B. Lipkowitz and D. B. Boyd, Eds., Wiley, New York, 1999, Vol. 13, pp. 99–132. Basis Set Superposition Errors: Theory and Practice.

49. S. F. Boys and F. Bernardi, *Mol. Phys.*, **19**, 553 (1970). The Calculation of Small Molecular Interactions by the Differences of Separate Total Energies. Some Procedures with Reduced Errors.

50. F. B. van Duijneveldt, J. G. C. M. van Duijneveldt-van de Rijdt, and J. H. van Lenthe, *Chem. Rev.*, **94**, 1873 (1994). State of the Art in Counterpoise Theory.
51. T. H. Dunning, *J. Phys. Chem. A*, **104**, 9062 (2000). A Road Map for the Calculation of Molecular Binding Energies.
52. K. R. Liedl, *J. Chem. Phys.*, **108**, 3199 (1998). Dangers of Counterpoise Corrected Hypersurfaces. Advantages of Basis Set Superposition Improvement.
53. A. Halkier, W. Klopper, T. Helgaker, P. Jørgensen, and P. R. Taylor, *J. Chem. Phys.*, **111**, 9157 (1999). Basis Set Convergence of the Interaction Energy of Hydrogen-Bonded Complexes.
54. D. Hankins, J. W. Moskowitz, and F. H. Stillinger, *J. Chem. Phys.*, **53**, 4544 (1970). Water Molecule Interactions.
55. V. M. Rayón and J. A. Sordo, *Theor. Chem. Acc.*, **99**, 68 (1998). On the Validity of the Counterpoise Correction for the Basis Set Superposition Error Including the Fragment Relaxation Terms.
56. L. A. Curtiss, K. Raghavachari, G. W. Trucks, and J. A. Pople, *J. Chem. Phys.*, **94**, 7221 (1991). Gaussian-2 Theory for Molecular Energies of First- and Second-Row Compounds.
57. L. A. Curtiss, K. Raghavachari, P. C. Redfern, V. Rassolov, and J. A. Pople, *J. Chem. Phys.*, **109**, 7764 (1998). Gaussian-3 (G3) Theory for Molecules Containing First and Second-Row Atoms.
58. A. Karton, E. Rabinovich, J. M. L. Martin, and B. Ruscic, *J. Chem. Phys.*, **125**, 144108 (2006). W4 Theory for Computational Thermochemistry: In Pursuit of Confident Sub-kJ/mol Predictions.
59. A. L. L. East and W. D. Allen, *J. Chem. Phys.*, **99**, 4638 (1993). The Heat of Formation of NCO.
60. A. G. Császár, W. D. Allen, and H. F. Schaefer III, *J. Chem. Phys.*, **108**, 9751 (1998). In Pursuit of the *Ab Initio* Limit for Conformational Energy Prototypes.
61. M. O. Sinnokrot and C. D. Sherrill, *J. Phys. Chem. A*, **108**, 10200 (2004). Highly Accurate Coupled Cluster Potential Energy Curves for Benzene Dimer: The Sandwich, T-Shaped, and Parallel-Displaced Configurations.
62. T. Janowski and P. Pulay, *Chem. Phys. Lett.*, **447**, 27 (2007). High Accuracy Benchmark Calculations on the Benzene Dimer Potential Energy Surface.
63. T. H. Dunning, *J. Chem. Phys.*, **90**, 1007 (1989). Gaussian Basis Sets for Use in Correlated Molecular Calculations. I. The Atoms Boron Through Neon and Hydrogen.
64. T. P. Tauer and C. D. Sherrill, *J. Phys. Chem. A*, **109**, 10475 (2005). Beyond the Benzene Dimer: An Investigation of the Additivity of π-π Interactions.
65. B. Mintz, K. P. Lennox, and A. K. Wilson, *J. Chem. Phys.*, **121**, 5629 (2004). Truncation of the Correlation Consistent Basis Sets: An Effective Approach to the Reduction of Computational Cost?
66. C. D. Sherrill and T. Takatani, manuscript in preparation.
67. B. Jeziorski, R. Moszynski, and K. Szalewicz, *Chem. Rev.*, **94**, 1887 (1994). Perturbation Theory Approach to Intermolecular Potential Energy Surfaces of van der Waals Complexes.
68. O. Vahtras, J. Almlöf, and M. Feyereisen, *Chem. Phys. Lett.*, **213**, 514 (1993). Integral Approximations for LCAO-SCF Calculations.
69. M. Feyereisen, G. Fitzgerald, and A. Komornicki, *Chem. Phys. Lett.*, **208**, 359 (1993). Use of Approximate Integrals in Ab Initio Theory. An Application in MP2 Calculations.
70. H.-J. Werner, F. R. Manby, and P. J. Knowles, *J. Chem. Phys.*, **118**, 8149 (2003). Fast Linear Scaling Second-Order Møller-Plesset Perturbation Theory (MP2) Using Local and Density Fitting Approximations.
71. F. Weigend, *Phys. Chem. Chem. Phys.*, **4**, 4285 (2002). A Fully Direct RI-HF Algorithm: Implementation, Optimized Auxiliary Basis Sets, Demonstration of Accuracy and Efficiency.
72. F. Weigend, A. Köhn, and C. Hättig, *J. Chem. Phys.*, **116**, 3175 (2002). Efficient Use of the Correlation Consistent Basis Sets in Resolution of the Identity MP2 Calculations.

73. R. A. Friesner, R. B. Murphy, M. D. Beachy, M. N. Ringnalda, W. T. Pollard, B. D. Dunietz, and Y. Cao, *J. Phys. Chem. A*, **103**, 1913 (1999). Correlated Ab Initio Electronic Structure Calculations for Large Molecules.

74. T. J. Martinez and E. A. Carter, in *Modern Electronic Structure Theory*, No. 2 in *Advanced Series in Physical Chemistry*, D. R. Yarkony, Ed., World Scientific, Singapore, 1995, pp. 1132–1165. Pseudospectral Methods Applied to the Electron Correlation Problem.

75. C. White, B. G. Johnson, P. M. W. Gill, and M. Head-Gordon, *Chem. Phys. Lett.*, **253**, 268 (1996). Linear Scaling Density Functional Calculations via the Continuous Fast Multipole Method.

76. C. Ochsenfeld, J. Kussmann, and D. S. Lambrecht, in *Reviews in Computational Chemistry*, K. B. Lipkowitz and T. R. Cundari, Eds., Wiley-VCH, New York, 2006, Vol. 23, pp. 1–82. Linear Scaling Methods in Quantum Chemistry.

77. S. Saebø and P. Pulay, *Chem. Phys. Lett.*, **113**, 13 (1985). Local Configuration Interaction: An Efficient Approach for Larger Molecules.

78. P. Pulay and S. Saebø, *Theor. Chim. Acta*, **69**, 357 (1986). Orbital-Invariant Formulation and Second-Order Gradient Evaluation in Møller-Plesset Perturbation Theory.

79. S. Saebø and P. Pulay, *J. Chem. Phys.*, **88**, 1884 (1988). The Local Correlation Treatment. II. Implementation and Tests.

80. P. E. Maslen and M. Head-Gordon, *Chem. Phys. Lett.*, **283**, 102 (1998). Non-Iterative Local Second Order Møller-Plesset Theory.

81. G. Hetzer, P. Pulay, and H.-J. Werner, *Chem. Phys. Lett.*, **290**, 143 (1998). Multipole Approximation of Distant Pair Energies in Local MP2 Calculations.

82. G. E. Scuseria and P. Y. Ayala, *J. Chem. Phys.*, **111**, 8330 (1999). Linear Scaling Coupled Cluster and Perturbation Theories in the Atomic Orbital Basis.

83. M. S. Lee, P. E. Maslen, and M. Head-Gordon, *J. Chem. Phys.*, **112**, 3592 (2000). Closely Approximating Second-Order Møller-Plesset Perturbation Theory with a Local Triatomics in Molecules Model.

84. M. Schutz, *Phys. Chem. Chem. Phys.*, **4**, 3941 (2002). A New, Fast, Semi-Direct Implementation of Linear Scaling Local Coupled Cluster Theory.

85. A. Venkatnathan, A. B. Szilva, D. Walter, R. J. Gdanitz, and E. A. Carter, *J. Chem. Phys.*, **120**, 1693 (2004). Size Extensive Modification of Local Multireference Configuration Interaction.

86. S. Saebø, W. Tong, and P. Pulay, *J. Chem. Phys.*, **98**, 2170 (1993). Efficient Elimination of Basis Set Superposition Errors by the Local Correlation Method: Accurate *Ab Initio* Studies of the Water Dimer.

87. A. Reyes, M. A. Tlenkopatchev, L. Fomina, P. Guadarrama, and S. Fomine, *J. Phys. Chem. A*, **107**, 7027 (2003). Local MP2-Based Method for Estimation of Intermolecular Interactions in Aromatic Molecules. Benzene, Naphthalene, and Pyrimidine Dimers. A Comparison with Canonical MP2 Method.

88. T. Takatani and C. D. Sherrill, *Phys. Chem. Chem. Phys.*, **9**, 6106 (2007). Performance of Spin-Component-Scaled Møller-Plesset Theory (SCS-MP2) for Potential Energy Curves of Noncovalent Interactions.

89. H.-J. Werner, P. J. Knowles, R. Lindh, F. R. Manby, M. Schütz, P. Celani, T. Korona, G. Rauhut, R. D. Amos, A. Bernhardsson, A. Berning, D. L. Cooper, M. J. O. Deegan, A. J. Dobbyn, F. Eckert, C. Hampel, G. Hetzer, A. W. Lloyd, S. J. McNicholas, W. Meyer, M. E. Mura, A. Nicklass, P. Palmieri, R. Pitzer, U. Schumann, H. Stoll, A. J. Stone, R. Tarroni, and T. Thorsteinsson, MOLPRO, version 2006.1, a package of ab initio programs, 2006. Available: http://www.molpro.net.

90. N. J. Russ and T. D. Crawford, *J. Chem. Phys.*, **121**, 691 (2004). Potential Energy Surface Discontinuities in Local Correlation Methods.

91. S. Grimme, *J. Chem. Phys.*, **118**, 9095 (2003). Improved Second-Order Møller-Plesset Perturbation Theory by Separate Scaling of Parallel- and Antiparallel-Spin Pair Correlation Energies.

92. M. Gerenkamp and S. Grimme, *Chem. Phys. Lett.*, **392**, 229 (2004). Spin-Component Scaled Second-Order Møller-Plesset Perturbation Theory for the Calculation of Molecular Geometries and Harmonic Vibrational Frequencies.

93. Y. Jung, R. C. Lochan, A. D. Dutoi, and M. Head-Gordon, *J. Chem. Phys.*, **121**, 9793 (2004). Scaled Opposite-Spin Second Order Møller-Plesset Correlation Energy: An Economical Electronic Structure Method.

94. J. G. Hill, J. A. Platts, and H. Werner, *Phys. Chem. Chem. Phys.*, **8**, 4072 (2006). Calculation of Intermolecular Interactions in the Benzene Dimer Using Coupled-Cluster and Local Electron Correlation Methods.

95. J. G. Hill and J. A. Platts, *J. Chem. Theory Comput.*, **3**, 80 (2007). Spin-Component Scaling Methods for Weak and Stacking Interactions.

96. P. Jurečka, J. Šponer, J. Černý, and P. Hobza, *Phys. Chem. Chem. Phys.*, **8**, 1985 (2006). Benchmark Database of Accurate (MP2 and CCSD(T) Complete Basis Set Limit) Interaction Energies of Small Model Complexes, DNA Base Pairs, and Amino Acid Pairs.

97. J. Antony and S. Grimme, *J. Phys. Chem. A*, **111**, 4862 (2007). Is Spin-Component Scaled Second-Order Møller Plesset Perturbation Theory an Appropriate Method for the Study of Noncovalent Interactions in Molecules?

98. S. A. Arnstein and C. D. Sherrill, *Phys. Chem. Chem. Phys.*, **10**, 2646 (2008). Substituent Effects in Parallel-Displaced π-π Interactions.

99. M. Schütz, *Phys. Chem. Chem. Phys.*, **4**, 3944 (2002). A New, Fast, Semi-Direct Implementation of Linear Scaling Local Coupled Cluster Theory.

100. C. Hampel and H.-J. Werner, *J. Chem. Phys.*, **104**, 6286 (1996). Local Treatment of Electron Correlation in Coupled Cluster Theory.

101. M. Schütz and H.-J. Werner, *J. Chem. Phys.*, **114**, 661 (2001). Low-Order Scaling Local Electron Correlation Methods. IV. Linear Scaling Local Coupled-Cluster (LCCSD).

102. M. Schütz and F. R. Manby, *Phys. Chem. Chem. Phys.*, **5**, 3349 (2003). Linear Scaling Local Coupled Cluster Theory with Density Fitting. Part I: 4-external Integrals.

103. T. Takatani, E. G. Hohenstein, and C. D. Sherrill, *J. Chem. Phys.*, **128**, 124111 (2008). Improvement of the Coupled-Cluster Singles and Doubles Method via Scaling Same- and Opposite-Spin Components of the Double Excitation Correlation Energy.

104. E. A. Hylleraas, *Z. Phys.*, **54**, 347 (1929). A New Calculation of the Energy of Helium in the Ground State as Well as the Lowest Term of Ortho-Helium.

105. W. Kutzelnigg and W. Klopper, *J. Chem. Phys.*, **94**, 1985 (1991). Wave Functions with Terms Linear in the Interelectronic Coordinates to Take Care of the Correlation Cusp. I. General Theory.

106. W. Klopper, *Chem. Phys. Lett.*, **186**, 583 (1991). Orbital-Invariant Formulation of the MP2-R12 Method.

107. E. F. Valeev and H. F. Schaefer III, *J. Chem. Phys.*, **113**, 3990 (2000). Evaluation of Two-Electron Integrals for Explicit r_{12} Theories.

108. W. Klopper and C. C. M. Samson, *J. Chem. Phys.*, **116**, 6397 (2002). Explicitly Correlated Second-Order Møller-Plesset Methods with Auxiliary Basis Sets.

109. W. Klopper, *J. Chem. Phys.*, **120**, 10890 (2004). A Hybrid Scheme for the Resolution-of-the-Identity Approximation in Second-Order Møller-Plesset Linear-r_{12} Perturbation Theory.

110. E. F. Valeev, *Chem. Phys. Lett.*, **395**, 190 (2004). Improving on the Resolution of the Identity in Linear R12 Ab Initio Theories.

111. S. Ten-no, *Chem. Phys. Lett.*, **398**, 56 (2004). Initiation of Explicitly Correlated Slater-Type Geminal Theory.

112. W. Klopper, F. R. Manby, S. Ten-no, and E. F. Valeev, *Int. Rev. Phys. Chem.*, **25**, 427 (2006). R12 Methods in Explicitly Correlated Molecular Electronic Structure Theory.

113. C. L. Janssen, I. B. Nielsen, M. L. Leininger, E. F. Valeev, and E. T. Seidl, MPQC, the Massively Parallel Quantum Chemistry Program, Sandia National Laboratories, Livermore, CA, 2006. Available: http://www.mpqc.org/.

114. R. Ahlrichs, M. Bär, H.-P. Baron, R. Bauernschmitt, S. Böcker, N. Crawford, P. Deglmann, M. Ehrig, K. Eichkorn, S. Elliott, F. Furche, F. Haase, M. Häser, C. Hättig, A. Hellweg, H. Horn, C. Huber, U. Huniar, M. Kattannek, A. Köhn, C. Kölmel, M. Kollwitz, K. May, P. Nava, C. Ochsenfeld, H. Öhm, H. Patzelt, D. Rappoport, O. Rubner, A. Schäfer, U. Schneider, M. Sierka, O. Treutler, B. Unterreiner, M. von Arnim, F. Weigned, P. Weis, and H. Weiss TURBOMOLE, version *5.9*, Universität Karlsruhe, 2007. Available: http://www.turbomole.com.

115. T. D. Crawford, C. D. Sherrill, E. F. Valeev, J. T. Fermann, R. A. King, M. L. Leininger, S. T. Brown, C. L. Janssen, E. T. Seidl, J. P. Kenny, and W. D. Allen, *J. Comput. Chem.*, **28**, 1610 (2007). PSI3: An Open-Source *Ab Initio* Electronic Structure Package.

116. R. G. Parr and W. Yang, *Density-Functional Theory of Atoms and Molecules*, Vol. 16 of *International Series of Monographs on Chemistry*, Oxford, New York, 1989.

117. W. Koch and M. C. Holthausen, *A Chemist's Guide to Density Functional Theory*, Wiley-VCH, New York, 2000.

118. S. Kristyán and P. Pulay, *Chem. Phys. Lett.*, **229**, 175 (1994). Can (Semi)local Density Functional Theory Account for the London Dispersion Forces?

119. E. R. Johnson, R. A. Wolkow, and G. A. DiLabio, *Chem. Phys. Lett.*, **394**, 334 (2004). Application of 25 Density Functionals to Dispersion-Bound Homonuclear Dimers.

120. M. Elstner, P. Hobza, T. Frauenheim, S. Suhai, and E. Kaxiras, *J. Chem. Phys.*, **114**, 5149 (2001). Hydrogen Bonding and Stacking Interactions of Nucleic Acid Base Pairs: A Density-Functional-Theory Based Treatment.

121. X. Wu, M. C. Vargas, S. Nayak, V. Lotrich, and G. Scoles, *J. Chem. Phys.*, **115**, 8748 (2001). Towards Extending the Applicability of Density Functional Theory to Weakly Bound Systems.

122. Q. Wu and W. Yang, *J. Chem. Phys.*, **116**, 515 (2002). Empirical Correction to Density Functional Theory for van der Waals Interactions.

123. A. Kumar, M. Elstner, and S. Suhai, *Int. J. Quantum Chem.*, **95**, 44 (2003). SCC-DFTB-D Study of Intercalating Carcinogens: Benzo(a)Pyrene and Its Metabolites Complexed with the G-C Base Pair.

124. C. Gonzalez and E. C. Lim, *J. Phys. Chem. A*, **107**, 10105 (2003). Evaluation of the Hartree-Fock Dispersion (HFD) Model as a Practical Tool for Probing Intermolecular Potentials of Small Aromatic Clusters: Comparison of the HFD and MP2 Intermolecular Potentials.

125. S. Grimme, *J. Comput. Chem.*, **25**, 1463 (2004). Accurate Description of van der Waals Complexes by Density Functional Theory Including Empirical Corrections.

126. U. Zimmerli, M. Parrinello, and P. Koumoutsakos, *J. Chem. Phys.*, **120**, 2693 (2004). Dispersion Corrections to Density Functionals for Water Aromatic Interactions.

127. S. Grimme, *J. Comput. Chem.*, **27**, 1787 (2006). Semiempirical GGA-Type Density Functional Constructed with a Long-Range Dispersion Correction.

128. P. Jurečka, J. Černý, P. Hobza, and D. R. Salahub, *J. Comput. Chem.*, **28**, 555 (2007). Density Functional Theory Augmented with an Empirical Dispersion Term. Interaction Energies and Geometries of 80 Noncovalent Complexes Compared with *Ab Initio* Quantum Mechanics Calculations.

129. M. Kabeláč, H. Valdes, E. C. Sherer, C. J. Cramer, and P. Hobza, *Phys. Chem. Chem. Phys.*, **9**, 5000 (2007). Benchmark RI-MP2 Database of Nucleic Acid Base Trimers: Performance of Different Density Functional Models for Prediction of Structures and Binding Energies.

130. C. A. Morgado, J. P. McNamara, I. H. Hillier, N. A. Burton, and M. A. Vincent, *J. Chem. Theory Comput.*, **3**, 1656 (2007). Density Functional and Semiempirical Molecular Orbital Methods Including Dispersion Corrections for the Accurate Description of Noncovalent Interactions Involving Sulfur Containing Molecules.

131. E. Tapavicza, I.-C. Lin, A. von Lilienfeld, I. Tavernelli, M. D. Coutinho-Neto, and U. Rothlisberger, *J. Chem. Theory Comput.*, **3**, 1673 (2007). Weakly Bonded Complexes of Aliphatic and Aromatic Carbon Compounds Described with Dispersion Corrected Density Functional Theory.

132. K. E. Riley, J. Vondrasek, and P. Hobza, *Phys. Chem. Chem. Phys.*, **9**, 5555 (2007). Performance of the DFT-D Method, Paired with the PCM Implicit Solvation Model, for the Computation of Interaction Energies of Solvated Complexes of Biological Interest.

133. O. A. von Lilienfeld, I. Tavernelli, U. Rothlisberger, and D. Sebastiani, *Phys. Rev. Lett.*, **93**, 153004 (2004). Optimization of Effective Atom Centered Potentials for London Dispersion Forces in Density Functional Theory.

134. O. A. von Lilienfeld, I. Tavernelli, U. Rothlisberger, and D. Sebastiani, *Phys. Rev. B*, **71**, 195119 (2005). Performance of Optimized Atom-Centered Potentials for Weakly Bonded Systems Using Density Functional Theory.

135. M. Dion, H. Rydberg, E. Schröder, D. C. Langreth, and B. I. Lundqvist, *Phys. Rev. Lett.*, **92**, 246401 (2004). van der Waals Density Functional for General Geometries.

136. A. Puzder, M. Dion, and D. C. Langreth, *J. Chem. Phys.*, **124**, 164105 (2006). Binding Energies in Benzene Dimers: Nonlocal Density Functional Calculations.

137. T. Thonhauser, A. Puzder, and D. C. Langreth, *J. Chem. Phys.*, **124**, 164106 (2006). Interaction Energies of Monosubstituted Benzene Dimers via Nonlocal Density Functional Theory.

138. A. D. Becke and E. R. Johnson, *J. Chem. Phys.*, **123**, 154101 (2005). A Density-Functional Model of the Dispersion Interaction.

139. E. R. Johnson and A. D. Becke, *J. Chem. Phys.*, **123**, 024101 (2005). A Post-Hartree-Fock Model of Intermolecular Interactions.

140. A. D. Becke and E. R. Johnson, *J. Chem. Phys.*, **124**, 014104 (2006). Exchange-Hole Dipole Moment and the Dispersion Interaction: High-Order Dispersion Coefficients.

141. R. Podeszwa and K. Szalewicz, *Chem. Phys. Lett.*, **412**, 488 (2005). Accurate Interaction Energies for Argon, Krypton, and Benzene Dimers from Perturbation Theory Based on the Kohn-Sham Model.

142. A. Heßelmann, G. Jansen, and M. Schütz, *J. Chem. Phys.*, **122**, 014103 (2005). Density-Functional Theory-Symmetry-Adapted Intermolecular Perturbation Theory with Density Fitting: A New Efficient Method to Study Intermolecular Interaction Energies.

143. X. Xu and W. A. Goddard III, *Proc. Natl. Acad. Sci. USA*, **101**, 2673 (2003). The X3LYP Extended Density Functional for Accurate Descriptions of Nonbond Interactions, Spin States, and Thermochemical Properties.

144. Y. Zhao and D. G. Truhlar, *J. Phys. Chem. A*, **109**, 5656 (2005). Design of Density Functionals That Are Broadly Accurate for Thermochemistry, Thermochemical Kinetics, and Nonbonded Interactions.

145. Y. Zhao, N. E. Schultz, and D. G. Truhlar, *J. Chem. Theory Comput.*, **2**, 364 (2006). Design of Density Functionals by Combining the Method of Constraint Satisfaction with Parametrization for Thermochemistry, Thermochemical Kinetics, and Noncovalent Interactions.

146. Y. Zhao and D. G. Truhlar, *J. Chem. Theory Comput.*, **3**, 289 (2007). Density Functionals for Noncovalent Interaction Energies of Biological Importance.

147. D. Řeha, M. Kabeláč, F. Ryjáček, J. Šponer, J. E. Šponer, M. Elstner, S. Suhai, and P. Hobza, *J. Am. Chem. Soc.*, **124**, 3366 (2002). Intercalators. 1. Nature of Stacking Interactions Between Intercalators (Ethidium, Daunomycin, Ellipticine, and 4′,6-Diaminide-2-phenylindole) and DNA Base Pairs. *Ab Initio* Quantum Chemical, Density Functional Theory, and Empirical Potential Study.

148. A. T. Macias and A. D. MacKerell Jr., *J. Comput. Chem.*, **26**, 1452 (2005). CH/pi Interactions Involving Aromatic Amino Acids: Refinement of the CHARMM Tryptophan Force Field.

149. G. A. Kaminski, H. A. Stern, B. J. Berne, and R. A. Friesner, *J. Phys. Chem. A*, **108**, 621 (2004). Development of an Accurate and Robust Polarizable Molecular Mechanics Force Field from Ab Initio Quantum Chemistry.

150. A. G. Donchev, N. G. Galkin, L. B. Pereyaslavets, and V. I. Tarasov, *J. Chem. Phys.*, **125**, 244107 (2006). Quantum Mechanical Polarizable Force Field (QMPFF3): Refinement and Validation of the Dispersion Interaction for Aromatic Carbon.

151. C. D. Sherrill, B. G. Sumpter, M. O. Sinnokrot, M. S. Marshall, E. G. Hohenstein, R. Walker, and I. R. Gould, manuscript in preparation. Assessment of Standard Force-Field Models against High-Quality *ab initio* Potential Curves for Prototypes of π-π, CH/π, and SH/π Interactions.

152. B. R. Brooks, R. E. Bruccoleri, B. D. Olafson, D. J. States, S. Swaminathan, and M. Karplus, *J. Comput. Chem.*, **4**, 187 (1983). CHARMM: A Program for Macromolecular Energy, Minimization, and Dynamics Calculations.

153. D. A. Pearlman, D. A. Case, J. W. Caldwell, W. S. Ross, T. E. Cheatham, S. DeBolt, D. Ferguson, G. Seibel, and P. Kollman, *Comput. Phys. Commun.*, **91**, 1 (1995). AMBER, a Package of Computer Programs for Applying Molecular Mechanics, Normal Mode Analysis, Molecular Dynamics and Free Energy Calculations to Simulate the Structural and Energetic Properties of Molecules.

154. N. L. Allinger, Y. H. Yuh, and J.-H. Lii, *J. Am. Chem. Soc.*, **111**, 8551 (1989). Molecular Mechanics—The MM3 Force-Field for Hydrocarbons. 1.

155. W. L. Jorgensen and J. Tirado-Rives, *J. Am. Chem. Soc.*, **110**, 1657 (1988). The OPLS [Optimized Potentials for Liquid Simulations] Potential Functions for Proteins, Energy Minimizations for Crystals of Cyclic Peptides and Crambin.

156. C. A. Hunter and J. K. M. Sanders, *J. Am. Chem. Soc.*, **112**, 5525 (1990). The Nature of π-π Interactions.

157. M. O. Sinnokrot and C. D. Sherrill, *J. Am. Chem. Soc.*, **126**, 7690 (2004). Substituent Effects in π-π Interactions: Sandwich and T-Shaped Configurations.

158. A. L. Ringer, M. O. Sinnokrot, R. P. Lively, and C. D. Sherrill, *Chem. Eur. J.*, **12**, 3821 (2006). The Effect of Multiple Substituents on Sandwich and T-Shaped π-π Interactions.

159. M. O. Sinnokrot and C. D. Sherrill, *J. Phys. Chem. A*, **110**, 10656 (2006). High-Accuracy Quantum Mechanical Studies of π-π Interactions in Benzene Dimers.

160. H. L. Williams, K. Szalewicz, B. Jeziorski, R. Moszynski, and S. Rybak, *J. Chem. Phys.*, **98**, 1279 (1993). Symmetry-Adapted Perturbation Theory Calculation of the Ar-H_2 Intermolecular Potential Energy Surface.

161. R. Bukowski, W. Cencek, P. Jankowski, B. Jeziorski, M. Jeziorska, S. A. Kucharski, V. F. Lotrich, A. J. Misquitta, R. Moszynski, K. Patkowski, S. Rybak, K. Szalewicz, H. L. Williams, R. J. Wheatley, P. E. S. Wormer, and P. S. Zuchowski. SAPT2006: An Ab Initio Program for Many-Body Symmetry-Adapted Perturbation Theory Calculations of Intermolecular Interaction Energies. Available: http://www.physics.udel.edu/∼szalewic/SAPT.

162. T. P. Tauer, M. E. Derrick, and C. D. Sherrill, *J. Phys. Chem. A*, **109**, 191 (2005). Estimates of the Ab Initio Limit for Sulfur-π Interactions: The H_2S-Benzene Dimer.

163. A. L. Ringer, A. Senenko, and C. D. Sherrill, *Protein Sci.*, **16**, 2216 (2007). Models of S/π Interactions in Protein Structures: Comparison of the H_2S-Benzene Complex with PDB Data.

CHAPTER 2

Reliable Electronic Structure Computations for Weak Noncovalent Interactions in Clusters

Gregory S. Tschumper

Department of Chemistry and Biochemistry, University of Mississippi, University, Mississippi

INTRODUCTION AND SCOPE

If you are reading this chapter, you are most likely already aware of the importance of weak attractive interactions between molecules (and atoms), such has hydrogen bonding and London dispersion forces, in chemistry and related fields. The relatively weak interactions between uncharged molecules (and/or atoms) are also called nonbonded interactions and sometimes collectively referred to as van der Waals forces. These intermolecular forces are not only prevalent throughout chemistry, but they often provide the governing influence in a wide variety of chemical, physical, and biological processes.[1–7] Some general examples include, but are certainly not limited to, solvation, condensation, crystallization, asymmetric catalysis, bulk-phase properties, directed self-assembly of nanomaterials, chromatographic separation, micelle formation, molecular recognition, drug transport, as well as the structure and function of biomolecules. The initial step in HIV infection, for instance, involves the formation of a weakly bound (noncovalent) complex of the viral envelope and cellular receptor glycoproteins, HIV-gp120 and CD4, respectively.[8,9] The delivery and transport of pharmaceuticals in mammals frequently occurs through subcovalent complexation with blood-soluble proteins such as human serum

Reviews in Computational Chemistry, Volume 26
edited by Kenny B. Lipkowitz and Thomas R. Cundari

albumins.[10] The formation of weakly bound heterogeneous clusters plays a key role in the chemistry of the atmosphere on Earth and elsewhere.[11,12] Noncovalent interactions dictate not only the structure and function of biomolecules, from simple dipeptides to enzymes and DNA,[13–16] but also molecular recognition events.[17] In the closely related and rapidly growing field of nanotechnology, highly selective, directional supramolecular self-assembly can be achieved with the aid of intermolecular hydrogen bonding and π-type interactions.[18,19] Hydrogen bonding also affects the chemical shielding, and therefore the electronic properties, of metal atoms in metalloproteins.[20,21] These weak inter- and intramolecular forces are even used to control diastereoselectivity and mediate catalysis in important classes of organic reactions.[22,23] The very existence of the condensed phase (i.e., solids and liquids) is dependent on the noncovalent interactions between molecules (or atoms), as are phase transitions, liquid structure, diffusion, crystal structure, and solvation/solutions.[24,25] These ubiquitous interactions have even led to the development and refinement of many cardinal chemical concepts such as hydrophilicity and hydrophobicity as well as the very definition of the chemical bond.

Over the past decade, there have been numerous books[26–31] and articles[32–44] reviewing ab initio and density functional theory (DFT) computations of hydrogen bonding and other weak noncovalent interactions. In fact, the very first chapter of this entire review series examines basis sets for noncovalent interactions between atoms and/or molecules,[45] while a chapter in the second volume reviews ab initio methods for hydrogen bonding.[46] Three thematic issues of *Chemical Reviews* have been dedicated to van der Waals interactions (Vol. 88, No. 6, 1988; Vol. 94, No. 7, 1994; and Vol. 100, No. 11, 2000). Two articles in the centennial issue of the *Journal of Physical Chemistry* discuss weakly bound clusters and solvation.[47,48] It is also worth noting that π-type stacking interactions are very topical at the moment and are the subject not only of a separate chapter in this volume of *Reviews in Computational Chemistry*[49] but also of a special issue of *Physical Chemistry Chemical Physics* (Vol. 10, No. 19, 2008).

This chapter is intended to serve two very distinct purposes. Readers new to the subject matter will find a fairly thorough introduction to reliable electronic structure computations for weakly bound clusters (including a step-by-step tutorial). For more experienced readers, this chapter also reviews many of the significant advances made in the field since the turn of the twenty-first century, particularly current state-of-the-art benchmark studies. This work also offers some valuable perspective and will attempt to illustrate the importance of balancing what is possible with what is practical.

Clusters and Weak Noncovalent Interactions

Defining the scope of a chapter for *Reviews in Computational Chemistry* on clusters of molecules (and/or atoms) held together by hydrogen bonding,

London dispersion forces, and/or similar interactions is not a simple task. Chemical bonding, whether noncovalent, covalent, ionic, or metallic, covers a broad, continuous spectrum of electronic interactions and energies. Consequently, the classification of a bond or interaction (e.g., double versus triple[50] or covalent versus noncovalent[51]) is sometimes open to interpretation. As a result, there is no unique criterion or set of criteria that can be used to define *weak* interactions or *noncovalent* interactions. In the second volume of this review series, Scheiner already notes this issue and highlighted the difficulties associated with defining the hydrogen bond.[46] Here, matters are even more complicated because other weak interactions are also considered.

To limit the breadth of the present chapter, it focuses on the most common types of weakly bound clusters, namely those composed of neutral fragments. (The following discussion also assumes the weakly bound clusters are composed of closed-shell fragments that are in their ground electronic states and dominated by a single Hartree–Fock (HF) reference function. It is certainly feasible to perform reliable computations on systems composed of open-shell, excited state, or multireference fragments; however, by assuming the monomers have a "well-behaved" electronic structure, we can focus on computational methods that will accurately describe the weak noncovalent interactions within a cluster.) Clusters containing one or two charged species are mentioned (e.g., solvated ions or ion pairs). However, clusters with numerous charged species (e.g., room temperature ionic liquids[52]) fall outside the scope of this review. This emphasis still leaves a wide spectrum of weak chemical interactions that bind the clusters together (as depicted in Figure 1).

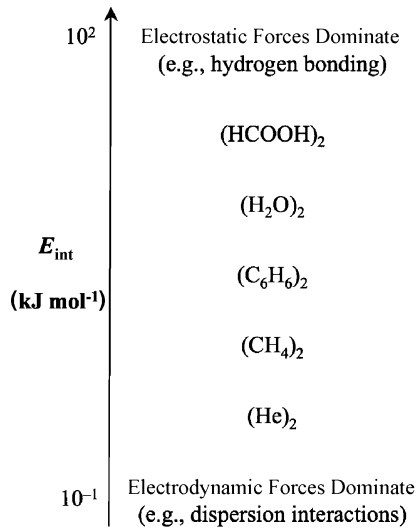

Figure 1 Weak noncovalent interactions between neutral fragments cover a wide spectrum of interactions and energies.

At one extreme (bottom of the figure), one finds complexes held together primarily by dispersion forces (rare gas dimers, He nanodroplets, etc.). On the opposite extreme (top of the figure) are clusters dominated by electrostatic interactions such as hydrogen bonding (formic acid dimer, water clusters, etc.). Of course, most interfragment interactions fall somewhere between these two extremes. [In this work, the term *interfragment* (or *intermonomer*) interaction is used because it is more general than and implicitly includes both *interatomic* and *intermolecular* interactions. Note that some researchers object to the latter adjective when describing weakly bound clusters because it is technically incorrect. For example, if $(HF)_3$ is considered an independent molecular species then, by definition, there can be only intramolecular interactions.] A more detailed analysis of this continuum of weak noncovalent interactions is presented below.

Given the current flurry of activity in the area of π-type interactions and halogen bonding (a specific case of sigma-hole interactions), special attention will be paid to these two types of weak interactions. In fact, an entire chapter in this volume of *Reviews in Computational Chemistry* is dedicated to noncovalent π interactions.[49] It should be noted that, although most examples are for relatively small (dimers, trimers, tetramers, and pentamers) homogeneous clusters, the principles discussed here can readily be extended to larger, heterogeneous systems.

Computational Methods

Although a wide variety of theoretical methods is available to study weak noncovalent interactions such as hydrogen bonding or dispersion forces between molecules (and/or atoms), this chapter focuses on size consistent electronic structure techniques likely to be employed by researchers new to the field of computational chemistry. Not surprisingly, the list of popular electronic structure techniques includes the self-consistent field (SCF) Hartree–Fock method as well as popular implementations of density functional theory (DFT). However, correlated wave function theory (WFT) methods are often required to obtain accurate structures and energetics for weakly bound clusters, and the most useful of these WFT techniques tend to be based on many-body perturbation theory (MBPT) (specifically, Møller–Plesset perturbation theory), quadratic configuration interaction (QCI) theory, and coupled-cluster (CC) theory.

This review concentrates on the fundamentals of supermolecule model chemistries for clusters of atoms/molecules held together by weak chemical forces. The principles behind the appropriate selection of theoretical method and basis set for a particular class of weak noncovalent interactions provide the foundation for understanding more complex computational schemes that might require the user to specify more than just a method and/or basis set, such as highly efficient fragmentation schemes [e.g., the effective fragment potential (EFP) method,[53,54] the fragment molecular orbital (FMO) method,[55,56] the

n-body decomposition (NBD) scheme,[57] and the multicentered integrated method (MC QM:QM or MC ONIOM) for clusters.[58–60]]

Some readers may have noticed that methods based on intermolecular perturbation theory such as symmetry-adapted perturbation theory (SAPT),[61–64] have not been mentioned. These methods are not discussed in this chapter because most versions of SAPT are actually 2-body methods. (See below for a description of 2-body, 3-body, and many-body interactions in clusters.) SAPT is not inherently limited to 2-body interactions; a 3-body implementation exists.[65–67] However, the author is not aware of higher order SAPT programs, let alone a general *n*-body program for clusters composed of *n* fragments. While SAPT can certainly be used to study trimers, tetramers, and larger clusters, such applications require a great deal of a priori knowledge about the nonadditivity (or cooperativity) in the system and are certainly not for novices.

Molecular mechanics methods are also omitted from the present discussion for similar reasons. Although very sophisticated force fields are available for water (including polarizable models), most force fields for weakly bound clusters are essentially 2-body (dimer) potentials that have been adjusted empirically to reproduce bulk-phase properties.[68–71] This procedure leads to very reliable descriptions of liquid water, but diminishes the quality of results for small clusters. Although force fields that include 3-body interactions are beginning to appear,[69,70] the effects of higher order interactions (4-body, 5-body, etc.) are still untested. Furthermore, the composition of a weakly bound cluster, not just its size, is a major concern with molecular mechanics force fields. The highly refined potentials that have been developed for water[68,71] are not necessarily transferable to other weak noncovalent systems (methanol, acetone, etc.).

WEAK NONCOVALENT INTERACTIONS

This section presents an overview of the nature of weak noncovalent interactions between molecules (and atoms). Readers interested in more detail are directed to classic references such as the 1954 text by Hirschfelder, Curtiss and Bird,[72] the 1971 book by Margenau and Kestener,[73] the 1996 monograph by Stone,[4] as well as some more recent sources.[7,27,31,74]

Historical Perspective

Theoretical treatments of attractive forces between molecules (and/or atoms) in the gas phase can be traced as far back as 1873 to the efforts by van der Waals to describe the deviation of real gases from ideal behavior at relatively high densities.[75] By the early 1930s, theoretical explanations of the origins of van der Waals' attractive forces began to emerge from the likes of Keesom,[76,77] Debye,[78,79] Falckenhagen,[80] and London.[81,82] This body of

work established that there are four rigorously defined fundamental components that contribute to interactions between a pair of uncharged molecules or atoms: electrostatic, induction (sometimes referred to as polarization), dispersion, and exchange-repulsion[83] (or simply exchange). The first two contributions to the interaction energy were readily explained in terms of classical electromagnetic theory. Interactions involving two permanent electrostatic multipole moments (dipole, quadrupole, etc.) are relatively easy to understand for anyone who has ever played with a pair of magnets; opposite poles (+/−) attract each other, and like poles (+/+ and −/−) repel each other. Similarly, adhering a balloon to a wall with static electricity provides a macroscopic analog for induction. However, quantum mechanics was required to rationalize the dispersion and exchange energies. The latter is a simple consequence of the Pauli exclusion principle, but an explanation of the dispersion energy is more involved.

London was the first to describe the dispersion interaction.[81,82] Through a quantum mechanical perturbation theory treatment of the interaction energy, he demonstrated that, at second, order attractive terms can arise due to the simultaneous electron correlation between two fragments even if they possess no permanent electrostatic moment (e.g., a pair of rare gas atoms). London dubbed the attraction *dispersion forces* because similar oscillator strengths appear in equations describing the dispersion of electromagnetic radiation (light). The attractive forces of these interactions are typically attributed to fluctuations (thermal or quantum mechanical) in the electron density that give rise to an instantaneous dipole in one fragment that induces a dipole in a neighbor. This semiclassical model was introduced after London's initial work, and its physical significance is not manifest since there are no expressions in the quantum mechanical derivation that can be interpreted as interactions between instantaneous dipoles. At the very least, this fluctuating charge or electrodynamic model provides a useful mnemonic.

As discussed in Paresegian's recent book,[7] the modern view of dispersion interactions has its roots in the the Casimir effect.[84] Rather than charge fluctuations, the phenomenon can be viewed in terms of zero-point electromagnetic-field fluctuations in the vacuum as allowed by the Heisenberg uncertainty principle ($\Delta E\,\Delta t \geq \hbar/2\pi$). Atoms and molecules can absorb some of these frequencies, namely those frequencies that are resonant with transitions between the quantum mechanical energy levels of the system as determined by its electronic structure. This absorption of the electromagnetic fluctuations gives rise to attractive forces between two bodies.

> We now recognize that "empty space" is a turmoil of electromagnetic waves of all frequencies and wavelengths. They wash through and past us in ways familiar from watching the two-dimensional version, a buoy or boat bobbing in rough water. We can turn the dancing charges idea around. From the vacuum point of view, imagine two bodies, such as two boats in rough water or a single boat near a dock, pushed

> by waves from all directions except their wave quelling neighbor. The net result is that the bodies are pushed together. You get close to a dock, you can stop rowing. The waves push you in. We can think of electromagnetic modes between the two bodies as the fluctuations that remain as tiny deviations from the outer turmoil. The extent of quelling is, obviously, in proportion to the material-absorption spectra. So we can think of absorption spectra in two ways: those at which the charges naturally dance; those at which charge polarization quells the vacuum fluctuations and stills the space between the [fragments].[7]

It will become evident in later sections that the nature of the weak noncovalent interactions in a cluster dictate which computational methods will produce accurate results. In particular, it is far more difficult to compute reliable properties for weakly bound clusters in which dispersion is the dominant attractive component of the interaction. For example, Hartree–Fock supermolecule computations are able to provide qualitatively correct data for hydrogen-bonded systems like $(H_2O)_2$[85] even with very small basis sets, but this approach does not even bind Ne_2.[86] What is the origin of this inconsistency? Dispersion is the dominant attractive force in rare gas clusters while the electrostatic component tends to be the most important attractive contribution near the equilibrium structure $(H_2O)_2$. As London's work demonstrated,[81,82,87,88] dispersion interactions are inherently an electron correlation problem and, consequently, cannot be described by Hartree–Fock computations.[89] To this day, dispersion interactions continue to pose a significant challenge in the field of computational chemistry, particularly those involving systems of delocalized π electrons.[49]

Some Notes about Terminology

Because the van der Waals equation of state preceeded "The General Theory of Molecular Forces,"[82] the interactions between molecules and/or atoms became known collectively as *van der Waals* forces. From a historical perspective, *van der Waals interactions* encompass the entire spectrum of weak interactions depicted in Figure 1, from the dispersion forces holding a He nanodroplet together to the hydrogen bonds in a cluster of water molecules. Although many researchers today associate van der Waals forces only with weak dispersion interactions, this review adopts the historical definition of van der Waals interactions and uses the term to collectively refer to all weak chemical interactions between uncharged molecules (and/or atoms).

Additional linguistic dilemmas are encountered in this area of research. For example, these weak chemical forces are sometimes referred to as *nonbonding interactions* despite meeting Pauling's utilitarian definition of a chemical bond introduced in 1939 (which is still one of the most useful and most widely used):[90]

> There is a chemical bond between two atoms or groups of atoms in the case that the forces acting between them are such as to lead to the formation of an

aggregate with sufficient stability to make it convenient for the chemist to consider it as an independent molecular species.

The term *noncovalent interaction* does not completely resolve the matter since ionic interactions (e.g., salt bridges) are frequently included in this category, particularly in the biochemistry community.[15] In this work, the moniker *weak noncovalent interaction* is used to denote the continuum of weak chemical forces between electrically uncharged molecules (and/or atoms).

FUNDAMENTAL CONCEPTS: A TUTORIAL

Model Systems and Theoretical Methods

Because of their relatively small size and high symmetry, the cyclic hydrogen fluoride clusters, $(HF)_n$ where $n = 3 - 5$, are very useful prototypes for studying hydrogen bonding. In this section, these model systems will be used to illustrate several aspects of computations on weakly bound clusters. These planar hydrogen-bonded complexes have C_{nh} symmetry and are shown in Figure 2. Their structures can be specified completely by three internal coordinates: R(HF), which is the length of the HF covalent bond; R(FF), which is the distance between neighboring F atoms; and θ(HFF), which is the small angle the H atoms make out of the ring formed by the F atoms.

The RHF method and aug-cc-pVDZ basis set have been adopted in this tutorial for two practical reasons. All calculations can be run in a few minutes on a reasonably modern desktop or laptop with a few hundred megabytes of memory, and all results should be reproduced readily regardless of the electronic structure software package you happen to be using. In contrast, electronic energies from DFT calculations will differ because the various electronic structure programs often employ different numerical integration grids. It is important to note that this particular model chemistry (RHF method and aug-cc-pVDZ basis set) is not expected to give reliable results. Correlated WFT methods such as second-order Møller–Plesset perturbation theory

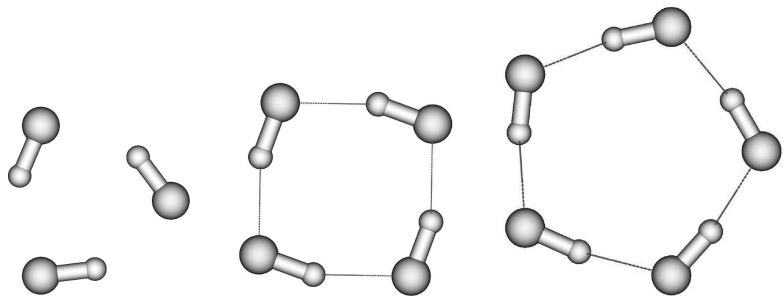

Figure 2 Cyclic hydrogen fluoride trimer, $(HF)_3$, tetramer, $(HF)_4$, and pentamer, $(HF)_5$, are planar structures with C_{3h}, C_{4h}, and C_{5h} symmetry, respectively.

(MP2) or coupled-cluster methods would certainly provide more reliable results, but they are not appropriate for a tutorial because the computations become rather time consuming. Furthermore, matching results from correlated WFT methods can be difficult for users not familiar with the frozen core or deleted virtual approximations because some software packages correlate all electrons by default while others exclude core electrons (i.e., adopt the frozen core approximation) by default. Computations in this work employed spherical harmonic (5*d*, 7*f*, etc.) rather than Cartesian (6*d*, 10*f*, etc.) functions, which gives 32 basis functions per HF monomer.

The geometrical parameters given in the top half of Table 1 for the HF clusters are from RHF/aug-cc-pVDZ optimizations and have been rounded off to three significant figures for bond lengths and two significant figures for bond angles. Although the values differ appreciably from the "best estimates" of Ref. 91, the bond lengths and angles are appropriate for the computational methods adopted for this tutorial. The electronic energies of these fixed structures (i.e., single-point energies) listed in Table 1 are from RHF computations with the aug-cc-pVDZ basis set. Step 1 in this tutorial is to reproduce the RHF/aug-cc-pVDZ electronic energies in Table 1. Sample input files for several popular software packages are available online.[92]

Rigid Monomer Approximation

Frequently, computational studies of weakly bound clusters employ the rigid monomer approximation (RMA). The RMA assumes that geometries of the monomers do not change as they coalesce to form the cluster. Because the interactions between the fragments of such clusters are, by their very definition, weak, the electronic structure, and hence the geometry, of the monomers does not change appreciably. This approach can simplify dramatically theoretical descriptions of the cluster because the intramolecular geometrical

Table 1 Geometrical Parameters and Electronic Energies of $(HF)_n$, $n = 1, 3-5$[a]

	Symmetry	R(FF)	R(HF)	θ(HFF)	*E*
HF	$C_{\infty v}$	n/a	0.900	n/a	−100.033816
		Fully Optimized Clusters			
$(HF)_3$	C_{3h}	2.71	0.910	25	−300.120482
$(HF)_4$	C_{4h}	2.64	0.915	13	−400.169746
$(HF)_5$	C_{5h}	2.61	0.916	6.6	−500.216512
		Rigid Monomer Approximation			
$(HF)_3$	C_{3h}	2.72	0.900	26	−300.120162
$(HF)_4$	C_{4h}	2.65	0.900	13	−400.168826
$(HF)_5$	C_{5h}	2.63	0.900	7.1	−500.215113

[a]Bond lengths (R) in Å, bond angles (θ) in degrees, and electronic energies (*E*) in E_h are from RHF/aug-cc-pVDZ calculations.

parameters are fixed. For example, by employing the RMA, geometry optimizations of weakly bound clusters need only consider the interfragment degrees of freedom. For a system as simple as $(H_2O)_2$, the RMA already reduces the full 12-dimensional problem to a more tractable 6-dimensional intermolecular potential energy hypersurface.

This approximation is typically valid for clusters held together by hydrogen bonds or van der Waals forces because the geometrical distortions tend to be modest and do not qualitatively change the structure of the monomers. As can be seen in bottom half of Table 1, fixing the intramolecular R(HF) distance at 0.900 Å for the HF trimer, tetramer, and pentamer has relatively little effect on the optimized interfragment parameters [R(FF) changes by no more than 0.02 Å and θ(HFF) by less than a degree]. This constraint also has relatively little effect on the electronic energies of $(HF)_3$, $(HF)_4$, and $(HF)_5$, which increase by only ≈ 1 mE_h on average.

These limited results demonstrate that the RMA can be accurate even for relatively strong hydrogen bonds, which can induce some of the largest geometrical distortions in weakly bound molecular clusters. The effect of the RMA on interaction energies will be discussed next. However, the RMA can break down if large qualitative geometrical changes occurs as the complex forms (e.g., conformational changes or isomerization).

Supermolecular Dissociation and Interaction Energies

Within the supermolecule approach, the dissociation energy (D_e) or interaction energy (E_{int}) of a cluster is obtained by calculating the energy difference between the cluster and the noninteracting fragments. This energy difference is depicted in Figure 3. Note that D_e and E_{int} are essentially the same quantity. The only significant difference is the sign ($D_e = -E_{\text{int}}$). A more subtle, technical distinction is that the term *dissociation energy* should be applied only to minima on the potential energy surface (PES) while *interaction energies* are more general and can describe any point on the surface.

When using a size-consistent method, the dissociation of homogeneous system such as $(HF)_n$ into n identical HF monomers [$(HF)_n \rightarrow n$HF] can be determined by computing the energy of the cluster and the energy of the monomer:

$$E_{\text{int}} = E[(HF)_n] - nE[HF] \qquad [1]$$

In the more general case of a heterogeneous cluster composed of N fragments ($f_1f_2f_3 \ldots f_N \rightarrow f_1 + f_2 + f_3 + \cdots + f_N$), up to $N + 1$ computations need to be performed to determine E_{int} or D_e:

$$\begin{aligned} E_{\text{int}} &= E[f_1f_2f_3 \ldots f_N] - E[f_1] - E[f_2] - E[f_3] - \cdots - E[f_N] \\ &= E[f_1f_2f_3 \ldots f_N] - \sum_{i=1}^{N} E[f_i] \end{aligned} \qquad [2]$$

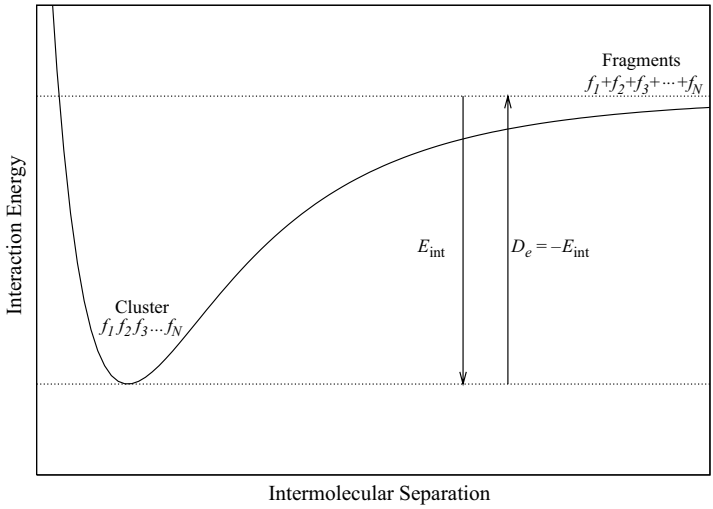

Figure 3 Interaction energies (E_{int}) and dissociation energies (D_e) are simply the energy difference between the cluster and the isolated fragments.

For example, to obtain E_{int} for the HF···H_2O···CH_3OH trimer requires four separate computations: E[HF], E[H_2O], E[CH_3OH], as well as the electronic energy of the cluster. The number of computations can be reduced if some of the fragments are identical (e.g., HF···H_2O···HF).

Interaction Energies: Rigid Monomers vs. Fully Optimized Clusters

The interaction energies reported toward the left side of Table 2 for the HF clusters were calculated with the electronic energies from Table 1 and Eq. [2] (which reduces to Eq. [1] for these homogeneous HF clusters). A simple conversion factor was used to convert E_{int} from E_{h} to kilojoule per mole ($1E_{\text{h}} \approx 2625.5\,\text{kJ mol}^{-1}$). Step 2 of this tutorial is to calculate the interaction energies on the left side of Table 2.

Because the RMA had relatively little effect on the electronic energies of the HF clusters (Table 1), it is not surprising that the approximation has only a modest effect on the interaction energies (Table 2). For all three clusters, the magnitude of E_{int} and $E_{\text{int}}^{\text{CP}}$ decreases slightly when the RMA is employed. Comparison of the values for E_{int} from the top of Table 2 to those at the bottom reveals that the change does not exceed 3% [−49.97 vs. −49.13 or 1.7% for $(HF)_3$, −90.53 vs. −88.12 or 2.7% for $(HF)_4$ and −124.53 vs. −120.86 or 2.9% for $(HF)_5$], which is tolerable for many applications. For systems with even smaller cluster-induced geometrical perturbations, such as π-type van der Waals interactions, the RMA has almost no discernable effect on the interaction energies.[93]

Note that the RMA must, by definition, decrease the magnitude of the interaction energy (for variational electronic structure methods). This result

Table 2 Interaction Energies of $(HF)_n$, $n = 3 - 5$ Computed at the RHF/aug-cc-pVDZ Level with (E_{int}^{CP}) and without (E_{int}) a Counterpoise Correction[a]

	E_{int}[b]	$E[HF]^{\text{cluster basis}}_{\text{cluster geom}}$	$E[HF]^{\text{monomer basis}}_{\text{cluster geom}}$	E_{int}^{CP}[c]
		Fully Optimized Clusters		
$(HF)_3$	−49.97	−100.034072	−100.033695	−47.00
$(HF)_4$	−90.53	−100.034030	−100.033543	−85.41
$(HF)_5$	−124.53	−100.034011	−100.033506	−117.90
		Rigid Monomer Approximation		
$(HF)_3$	−49.13	−100.034175	*d*	−46.30
$(HF)_4$	−88.12	−100.034287	*d*	−83.17
$(HF)_5$	−120.86	−100.034292	*d*	−114.61

[a]The monomer electronic energies for the counterpoise correction are also listed ($E[HF]$). Electronic energies are in E_h, and the interaction energies are in kJ mol^{-1}.
[b]Obtained via application of Eq. [1] or [2] to energies in Table 1.
[c]Obtained via application of Eq. [7] or [8] to energies in Tables 1 and 2.
[d]Equal to monomer energy from Table 1 which implies $E_{RLX} = 0$ in Eq. [7].

is readily illustrated with Figure 3. Although the RMA does not affect the asymptote associated with the noninteracting fragments, it does shift the bottom of the well up because the cluster is not allowed to reach its optimal geometry, which necessarily decreases the magnitude of E_{int} and D_e.

Counterpoise Corrections for Basis Set Superposition Error

The procedure outlined in Eq. [2] introduces an inconsistency when small, finite basis sets are used. Effectively, the monomers are using a larger basis set when the computation is performed on the cluster than when the computation is performed on the isolated monomer fragment. In the cluster calculation, monomer A can utilize the basis functions on monomers B, C, etc. When the computation is performed on the isolated monomer A, those basis functions are no longer available. This inconsistency was noted as early as 1968[94] and later termed basis set superposition error (BSSE).[95] A tutorial covering the theory and practice of basis set superposition errors has appeared earlier in this book series.[96] The most common procedure to correct for BSSE is the counterpoise (CP) procedure developed independently by Jansen and Ros in 1969[97] and Boys and Bernardi in 1970.[98] BSSE and CP corrections are discussed in greater detail below, and this portion of the tutorial merely demonstrates how to perform the necessary computations. Before proceeding, however, it is worth noting that BSSE is not limited to weakly interacting systems. It is a concern in any type of dissociation process (such as breaking a covalent bond) where the energies of fragments are compared to those of the whole system.

In this part of the tutorial, the standard Boys–Bernardi CP correction is applied to the interaction energies of the HF clusters in Figure 2 using the geometrical parameters in Table 1. Unfortunately, these corrections call for some rather hideous notation that denotes both the geometry and the basis set employed for computations on the monomers. The basic goal of the CP correction is to compute the energy of the monomer in the basis set of the cluster ($E[\mathrm{HF}]^{\text{cluster basis}}_{\text{monomer geom}}$). This is readily accomplished within the rigid monomer approximation because the geometry of the monomer is the same in the complex as in the isolated fragment ($E[\mathrm{HF}]^{\text{cluster basis}}_{\text{monomer geom}} = E[\mathrm{HF}]^{\text{cluster basis}}_{\text{cluster geom}}$), and the CP-corrected interaction energy within the RMA is simply

$$E_{\text{int}}^{\text{CP,RMA}} = E[(\mathrm{HF})_n] - nE[\mathrm{HF}]^{\text{cluster basis}}_{\text{cluster geom}} \qquad [3]$$

Again, this expression for the HF clusters can readily be generalized for the case of a heterogeneous cluster composed of N fragments:

$$E_{\text{int}}^{\text{CP,RMA}} = E[f_1 f_2 f_3 \ldots f_N] - \sum_{i=1}^{N} E[f_i]^{\text{cluster basis}}_{\text{cluster geom}} \qquad [4]$$

Let us use $(\mathrm{HF})_3$ in Figure 2 to illustrate the procedure. To perform a CP correction on the bottom HF unit in the trimer, the computations must place H and F basis functions, but not nuclei or electrons, at the appropriate coordinates of the other HF monomers at the top of the figure. In most computational chemistry programs this is accomplished with the use of ghost atoms or ghost orbitals. (Note, dummy atoms are also used to designate coordinates where nuclei are not present, but dummy atoms do not place basis functions at those locations.) Frequently, the input file for the CP-corrected monomer computation is created by modifying the input file from a cluster calculation such that the charges of all atoms are set to zero (i.e., the ghost atoms) except those in the monomer of interest. Because each computational chemistry software program has its own set of keywords for the specification of ghost atoms and nuclear charge, some sample input files for the CP corrections to the $(\mathrm{HF})_n$ interaction energies are available online.[92]

When the monomers are allowed to relax as the complex forms, the procedure becomes a bit more complicated because there is no straightforward, consistent manner by which a computation on the optimized monomer can be performed in the basis set of the cluster. Consequently, $E[\mathrm{HF}]^{\text{cluster basis}}_{\text{monomer geom}} \neq E[\mathrm{HF}]^{\text{cluster basis}}_{\text{cluster geom}}$ when the RMA is not employed. In other words, the energy of the monomer in the cluster basis set is too high (too positive) because the monomer is not at its optimal geometry. This overestimation of the monomer energy can be corrected easily by

calculating the energy liberated as the distorted monomers (complex geom) relax to their optimal structures in the (monomer geom) in the monomer basis set,

$$E_{\mathrm{RLX}}[\mathrm{HF}] = E[\mathrm{HF}]^{\text{monomer basis}}_{\text{monomer geom}} - E[\mathrm{HF}]^{\text{monomer basis}}_{\text{cluster geom}} \quad [5]$$

or more generally

$$E_{\mathrm{RLX}}[f_i] = E[f_i]^{\text{monomer basis}}_{\text{monomer geom}} - E[f_i]^{\text{monomer basis}}_{\text{cluster geom}} \quad [6]$$

Comparing the nearly optimal energy of the HF monomer in Table 1 to $E[\mathrm{HF}]^{\text{monomer basis}}_{\text{cluster geom}}$ in Table 2 reveals that the monomer energies at the distorted cluster geometries are too high by a range of roughly 0.1 $\mathrm{mE_h}$ for the trimer to 0.3 $\mathrm{mE_h}$ for the pentamer. This relaxation energy (E_{RLX}) can then be used to correct the monomer contributions to the CP-corrected interaction energy:

$$\begin{aligned} E^{\mathrm{CP}}_{\mathrm{int}} &= E[(\mathrm{HF})_n] - n(E[\mathrm{HF}]^{\text{cluster basis}}_{\text{cluster geom}} + E_{\mathrm{RLX}}[\mathrm{HF}]) \\ &= E[(\mathrm{HF})_n] - n(E[\mathrm{HF}]^{\text{cluster basis}}_{\text{cluster geom}} + E[\mathrm{HF}]^{\text{monomer basis}}_{\text{monomer geom}} - E[\mathrm{HF}]^{\text{monomer basis}}_{\text{cluster geom}}) \end{aligned} \quad [7]$$

Returning to the general case of a heterogeneous cluster composed of N fragments, an equivalent expression is obtained by summing over the fragments of the system:

$$\begin{aligned} E^{\mathrm{CP}}_{\mathrm{int}} &= E[f_1 f_2 f_3 \ldots f_N] - \sum_{i=1}^{N} (E[f_i]^{\text{cluster basis}}_{\text{cluster geom}} + E_{\mathrm{RLX}}[f_i]) \\ &= E[f_1 f_2 f_3 \ldots f_N] - \sum_{i=1}^{N} (E[f_i]^{\text{cluster basis}}_{\text{cluster geom}} + E[f_i]^{\text{monomer basis}}_{\text{monomer geom}} - E[f_i]^{\text{monomer basis}}_{\text{cluster geom}}) \end{aligned} \quad [8]$$

Note that when the RMA is applied, E_{RLX} vanishes since $E[f_i]^{\text{monomer basis}}_{\text{monomer geom}} = E[f_i]^{\text{monomer basis}}_{\text{cluster geom}}$ so that Eq. [8] reduces to Eq. [4] (and Eq. [7] reduces to Eq. [3]).

Step 3 in this tutorial is to reproduce the RHF/aug-cc-pVDZ electronic energies in Table 2. Sample input files for several popular software packages are available online.[92] To get the most out of this tutorial, it is recommended that you do not utilize features in some software packages that automatically perform the CP corrections for you. Step 4 of this tutorial is to calculate the interaction energies on the right side of Table 2 by applying Eq. [7] (or more generally Eq. [8]) to the electronic energies in Tables 1 and 2.

Interaction Energies: CP Corrected vs. CP Uncorrected

The rightmost column of Table 2 contains the CP-corrected interaction energies. The values of $E_{\text{int}}^{\text{CP}}$ were obtained by applying Eq. [8] to the electronic energies in Tables 1 and 2. With the relatively small aug-cc-pVDZ basis set, the BSSE at the RHF level is nearly $3\,\text{kJ mol}^{-1}$ (or 6%) for $(\text{HF})_3$, and it creeps up to more than $6\,\text{kJ mol}^{-1}$ (or 5%) for $(\text{HF})_5$. These values can change dramatically when different theoretical methods and/or basis sets are employed.

The magnitude of $E_{\text{int}}^{\text{CP}}$ is smaller than that of E_{int} for all three clusters. As with the RMA (discussed above), CP corrections for the BSSE also tend to decrease the magnitude of the interaction energy but for a different reason. With CP corrections, it is the monomer calculation that changes rather than the cluster calculation. Consequently, the bottom of the well in Figure 3 is unaffected by the procedure. The asymptote, however, is generally shifted downward because the larger basis set lowers the energies of the monomers. While this trend ($|E_{\text{int}}^{\text{CP}}| < |E_{\text{int}}|$) is generally true of most WFT conventional methods, CP corrections can actually increase the magnitude of the interaction energy when using resolution of the identity or techniques that employ auxiliary basis sets.[99]

A cautionary note concerning the deleted virtual approximation and CP corrections is offered. For appropriately constructed basis sets, high-lying unoccupied orbitals can be excluded from post-Hartree–Fock correlated computation in the same manner that low-lying core orbitals are omitted in the frozen core approximation. When performing monomer computations in the basis set of the cluster (particularly the heterogeneous variety), the ghost orbitals can sometimes have higher energies than the virtual orbitals centered on the monomer of interest. In such cases, most default procedures for the deleted virtual approximation will exclude the wrong virtual orbitals and special care must be taken to ensure the correct unoccupied orbitals are deleted (such as by reordering the orbitals).

Two-Body Approximation and Cooperative/Nonadditive Effects

Interactions in weakly bound clusters can frequently be dominated by 2-body interactions between pairs of fragments within the system. In other words, the sum of the interactions between each pair of fragments within the cluster can be used to approximate E_{int}. Conceptually, this 2-body approximation is straightforward when presented within the rigid monomer approximation because the geometries of the isolated monomers ($[f_1]$, $[f_2] \ldots [f_N]$) are identical to the monomer geometries in the cluster ($[f_1^*]$, $[f_2^*] \ldots [f_N^*]$). (In this section, an asterisk denotes that the fragment or group of fragments is at the cluster geometry.) For a trimer $f_1f_2f_3$, the pairwise or 2-body interaction

energy ($E_{\text{int}}^{2\text{-body}}$) is simply the sum of the interaction energies of each pair of fragments ($f_1f_2^*$, $f_1f_3^*$, and $f_2f_3^*$) within the cluster. This RMA prescription for a trimer can be extended readily to a cluster of arbitrary size, N, and composition in which there are $\binom{N}{2} = N!/(2!(N-2)!) = N(N-1)/2$ unique pairwise interactions:

$$E_{\text{int}}^{2\text{-body}}[f_1f_2\ldots f_N] = \sum_{i=1}^{N-1}\sum_{j>i}^{N} E[f_if_j^*] - E[f_i^*] - E[f_j^*] \qquad [9]$$

The pairwise approximation tends to be accurate in weakly coupled systems. For example, Tauer and Sherrill demonstrated that more than 98% of the interaction energy of various benzene tetramer structures can be recovered by simply adding together the pairwise interactions (or "dimers") in the system.[100] Despite ignoring higher order cooperative effects (3-body and 4-body in this case), $E_{\text{int}}^{2\text{-body}}$ differs from E_{int} by no more than 2% for the benzene tetramer configurations examined in the study. Because the higher order contributions account for deviations between the pairwise additive 2-body approximation and E_{int}, they are also frequently called nonadditive or cooperative effects (or just the nonadditivity or cooperativity). These many-body terms will be defined more precisely in the next section.

The nonadditivity tends to increase for more strongly coupled systems (sometimes dramatically), and, consequently, the quality of the 2-body approximation deteriorates.[101,102] In clusters of HF and/or H_2O, the nonadditivity can account for more than half of E_{int}, which necessarily implies that the error associated with the 2-body approximation can exceed 50%.[59] This section of the tutorial will use $(HF)_3$, $(HF)_4$, and $(HF)_5$ to demonstrate the procedure for calculating these 2-body interactions as well as higher order (3-body, ... N-body) contributions via a many-body decomposition of E_{int}.

Many-Body Decomposition

The most common rigorous many-body decomposition scheme for weakly bound clusters is based upon the approach introduced by Hankins, Moskowitz, and Stillinger in 1970.[103] Two lucid descriptions of the procedure can be found in Ref. 104 and 105. Technically, a many-body decomposition of E_{int} decomposes the energy of the cluster $E[f_1f_2\ldots f_N]$ into 1-body (E_1), 2-body (E_2), ..., N-body (E_N) contributions:

$$\begin{aligned} E_{\text{int}} &= E[f_1f_2f_3\ldots f_N] - \sum_{i=1}^{N} E[f_i] \\ &= \{E_1 + E_2 + E_3 + \cdots + E_N\} - \sum_{i=1}^{N} E[f_i] \end{aligned} \qquad [10]$$

Each n-body term is obtained by adding together the energies of each unique subset of n fragments within the cluster and subtracting from that the lower order (1-body, 2-body, ..., $(n-1)$-body) contributions. The first-order correction is merely a sum of "monomer" energies in the cluster:

$$E_1 = \sum_{i=1}^{N} E[f_i^*] \qquad [11]$$

Note that the monomer energies (at the cluster geometry) in this summation can be combined with monomer energies (at monomer geometry) from the summation in Eq. [10] to obtain the energy associated with the distortion of the monomers from their optimal structure to their geometry in the cluster (much like the relaxation energy for CP corrections in Eq. [6]). By definition, the contribution of E_{DIST} to the interaction energy is positive (net repulsive effect) when the clusters are fully optimized while $E_{\text{DIST}} = 0$ in the rigid monomer approximation:

$$E_{\text{DIST}} = \sum_{i=1}^{N} (E[f_i^*] - E[f_i]) \qquad [12]$$

$$E_{\text{int}} = E_{\text{DIST}} + E_2 + E_3 + \cdots + E_N \qquad [13]$$

The second-order term is obtained from the energies of each of the $\binom{N}{2} = N(N-1)/2$ unique pairs of fragments (or "dimers") from each of which $\binom{2}{1}$ 1-body contributions must be subtracted:

$$E_2 = \sum_{i=1}^{N-1} \sum_{j>i}^{N} \Delta_2 E[f_i f_j^*] \qquad [14]$$

$$\Delta_2 E[f_i f_j^*] = E[f_i f_j^*] - (E[f_i^*] + E[f_j^*]) \qquad [15]$$

One should recognize this expression for E_2 since it is identical to the 2-body interaction energy from Eq. [9] (i.e., $E_2 = E_{\text{int}}^{\text{2-body}}$). This relationship provides a rigorous definition of the nonadditivity or cooperativity:

$$\begin{aligned} E_{\text{int}} &= E_{\text{DIST}} + E_{\text{int}}^{\text{2-body}} + E_3 + \cdots + E_N \\ &= E_{\text{DIST}} + E_{\text{int}}^{\text{2-body}} + \delta E^{\text{nonadd}} \qquad [16] \\ &= E_{\text{DIST}} + E_{\text{int}}^{\text{many-body}} \qquad [17] \end{aligned}$$

Continuing to the third-order expression gives $\binom{N}{3} = N(N-1)(N-2)/6$ unique "trimers." There are $\binom{3}{2}$ 2-body and $\binom{3}{1}$ 1-body contributions that must be removed from each trimer energy:

$$E_3 = \sum_{i=1}^{N-2} \sum_{j>i}^{N-1} \sum_{k>j}^{N} \Delta_3 E[f_i f_j f_k^*] \quad [18]$$

$$\Delta_3 E[f_i f_j f_k^*] = E[f_i f_j f_k^*] - (\Delta_2 E[f_i f_j^*] + \Delta_2 E[f_i f_k^*] + \Delta_2 E[f_j f_k^*]) - (E[f_i^*] + E[f_j^*] + E[f_k^*]) \quad [19]$$

For the 4-body contribution, there are $\binom{N}{4}$ "tetramer" energies from each of which $\binom{4}{3}$ 3-body, $\binom{4}{2}$ 2-body, and $\binom{4}{1}$ 1-body terms are subtracted:

$$E_4 = \sum_{i=1}^{N-3} \sum_{j>i}^{N-2} \sum_{k>j}^{N-1} \sum_{l>k}^{N} \Delta_4 E[f_i f_j f_k f_l^*] \quad [20]$$

$$\Delta_4 E[f_i f_j f_k f_l^*] = E[f_i f_j f_k f_l^*] - (\Delta_3 E[f_i f_j f_k^*] + \Delta_3 E[f_i f_j f_l^*] + \Delta_3 E[f_i f_k f_l^*] + \Delta_3 E[f_j f_k f_l^*]) - (\Delta_2 E[f_i f_j^*] + \Delta_2 E[f_i f_k^*] + \Delta_2 E[f_i f_l^*] \Delta_2 E[f_j f_k^*] + \Delta_2 E[f_j f_l^*] + \Delta_2 E[f_k f_l^*]) - (E[f_i^*] + E[f_j^*] + E[f_k^*] + + E[f_l^*]) \quad [21]$$

A new indexing notation is introduced to help provide a generalized expression for the n-body contribution to the (interaction) energy of a cluster with N components. The indices $i, j, k, \ldots$ are replaced with $i_1, i_2, i_3, \ldots, i_{n-1}, i_n$ to emphasize that this n-body component, E_n, contains n nested summations giving rise to $\binom{N}{n} = N!/(n!(N-n)!$ terms:

$$E_n = \sum_{i_1=1}^{N-n+1} \sum_{i_2>i_1}^{N-n+2} \cdots \sum_{i_{n-1}>i_{n-2}}^{N-1} \sum_{i_n>i_{n-1}}^{N} \Delta_n E[f_{i_1} f_{i_2} f_{i_3} \ldots f_{i_{n-1}} f_{i_n}^*] \quad [22]$$

Again, each $\Delta_n E$ term is obtained by removing the lower order contributions from the electronic energy of the n-mers composed of fragments $f_{i_1} f_{i_2} f_{i_3} \ldots f_{i_{n-1}} f_{i_n}$. That is, one must subtract $\binom{n}{1}$ 1-body terms, $\binom{n}{2}$ 2-body terms, ..., $\binom{n}{n-1}(n-1)$-body terms from $E[f_{i_1} f_{i_2} f_{i_3} \ldots f_{i_{n-1}} f_{i_n}^*]$. To denote these terms; the indices $a_1, a_2, \ldots, a_{n-1}$ are used to run over the values of a particular set of fragment indices, $\mathbb{S} = \{i_1, i_2, i_3, \ldots, i_{n-1}, i_n\}$. Note that the index a_j corresponds to the jth element in $\mathbb{S}$ and, therefore, fragment f_{i_j}. It does not necessarily have anything to do with fragment f_j. This is a subtle but important distinction. For example, f_1 does not appear in $\Delta_3 E[f_3 f_5 f_7]$ even though a loops

over 1, 2, 3 to give $i_{a_1} = 3$, $i_{a_2} = 5$, and $i_{a_3} = 7$.

$$\begin{aligned}
&\Delta_n E[f_{i_1} f_{i_2} f_{i_3} \ldots f_{i_{n-1}} f_{i_n}^*] \\
&= E[f_{i_1} f_{i_2} f_{i_3} \ldots f_{i_{n-1}} f_{i_n}^*] \\
&\quad - \sum_{a=1}^{n} E[f_{i_a}^*] \\
&\quad - \sum_{a_1=1}^{n-1} \sum_{a_2>a_1}^{n} \Delta_2 E[f_{i_{a_1}} f_{i_{a_2}}^*] \\
&\quad - \sum_{a_1=1}^{n-2} \sum_{a_2>a_1}^{n-1} \sum_{a_3>a_2}^{n} \Delta_3 E[f_{i_{a_1}} f_{i_{a_2}} f_{i_{a_3}}^*] \\
&\quad - \cdots \\
&\quad - \sum_{1\le a_1<a_2\cdots<a_{n-2}} \sum^{n} \cdots \sum \Delta_{n-2} E[f_{i_{a_1}} f_{i_{a_2}} f_{i_{a_3}} \ldots f_{i_{a_{n-2}}}^*] \\
&\quad - \sum_{1\le a_1<a_2\cdots<a_{n-2}<a_{n-1}} \sum^{n} \cdots \sum \sum \Delta_{n-1} E[f_{i_{a_1}} f_{i_{a_2}} f_{i_{a_3}} \ldots f_{i_{a_{n-2}}} f_{i_{n-1}}^*]
\end{aligned} \quad [23]$$

By expanding $\Delta_2 E, \Delta_3 E, \ldots, \Delta_n E$, the expressions for the components of the cluster energy (and therefore interaction energy via Eq. [10] and [13]) can be simplified. In the following form, it is easier to see a connection between this many-body decomposition and the inclusion–exclusion principle (also known as the sieve principle) from combinatorial mathematics:

$$\begin{aligned}
E_2 &= \sum_{i=1}^{N-1} \sum_{j>i}^{N} E[f_i f_j^*] \\
&\quad - (E[i^*] + E[j^*])
\end{aligned} \quad [24]$$

$$\begin{aligned}
E_3 &= \sum_{i=1}^{N-2} \sum_{j>i}^{N-1} \sum_{k>j}^{N} E[f_i f_j f_k^*] \\
&\quad - (E[f_i f_j^*] + E[f_i f_k^*] + E[f_j f_k^*]) \\
&\quad + (E[f_i^*] + E[f_j^*] + E[f_k^*])
\end{aligned} \quad [25]$$

$$\begin{aligned}
E_4 &= \sum_{i=1}^{N-3} \sum_{j>i}^{N-2} \sum_{k>j}^{N-1} \sum_{l>k}^{N} E[f_i f_j f_k f_l^*] \\
&\quad - (E[f_i f_j f_k^*] + E[f_i f_j f_l^*] + E[f_i f_k f_l^*] + E[f_j f_k f_l^*]) \\
&\quad + (E[f_i f_j^*] + E[f_i f_k^*] + E[f_i f_l^*] + E[f_j f_k^*] + E[f_j f_l^*] + E[f_k f_l^*]) \\
&\quad - (E[f_i^*] + E[f_j^*] + E[f_k^*] + E[f_l^*])
\end{aligned} \quad [26]$$

Again, a general expression for E_n can be obtained in the same manner from Eq. [22]:

$$\begin{aligned}
E_n = & \sum_{1\le i_1<i_2\cdots<i_{n-2}<i_{n-1}<i_n}^{N}\cdots\sum\sum\sum E[f_{i_1}f_{i_2}f_{i_3}\ldots f_{i_{n-2}}f_{i_{n-1}}f_{i_n}^*] \\
& + (-1)^1 \sum_{1\le i_1<i_2\cdots<i_{n-2}<i_{n-1}}^{N}\cdots\sum\sum E[f_{i_1}f_{i_2}f_{i_3}\ldots f_{i_{n-2}}f_{i_{n-1}}^*] \\
& + (-1)^2 \sum_{1\le i_1<i_2\cdots<i_{n-2}}^{N}\cdots\sum E[f_{i_1}f_{i_2}f_{i_3}\ldots f_{i_{n-2}}^*] \\
& + \cdots \\
& + (-1)^{n-3} \sum_{i_1=1}^{N-2}\sum_{i_2>i_1}^{N-1}\sum_{i_3>i_2}^{N} E[f_{i_1}f_{i_2}f_{i_3}^*] \\
& + (-1)^{n-2} \sum_{i_1=1}^{N-1}\sum_{i_2>i_1}^{N} E[f_{i_1}f_{i_{n_2}}^*] \\
& + (-1)^{n-1} \sum_{i_1=1}^{N} E[f_{i_1}^*]
\end{aligned} \qquad [27]$$

Application to HF Trimer, Tetramer, and Pentamer

Because the cyclic $(HF)_n$ clusters ($n = 3 - 5$) used in this tutorial are symmetric, the number of computations required to perform a many-body decomposition of the interaction energy is reduced dramatically. In general, application of the decomposition procedure to a pentamer could require as many as 25 additional calculations: $\binom{5}{4} = 5$ for the tetramer subsets, $\binom{5}{3} = 10$ for the trimer subsets, and $\binom{5}{2} = 10$ for the dimer subsets. For $(HF)_5$, however, symmetry reduces this to 5 calculations (1 unique tetramer computation, 2 unique trimer computations, and 2 unique dimer computations).

For $(HF)_3$, there is only a single unique 2-body energy since $E[f_1f_2^*] = E[f_1f_3^*] = E[f_2f_3^*]$ while there are two such quantities for $(HF)_4$ and $(HF)_5$ ($E[f_1f_2^*] = E[f_1f_4^*] = E[f_2f_3^*] = E[f_3f_4^*] \equiv E[f_if_j^*]$ and $E[f_1f_3^*] = E[f_2f_4^*] \equiv E[f_if_k^*]$). These values are reported Table 3 for both relaxed and rigid monomers. One finds a single unique 3-body energy ($E[f_1f_2f_3^*] = E[f_1f_2f_4^*] = E[f_1f_3f_4^*] = E[f_2f_3f_4^*]$) for $(HF)_4$ but two for $(HF)_5$ ($E[f_1f_2f_3^*] = E[f_1f_2f_5^*] = E[f_1f_4f_5^*] = E[f_2f_3f_4^*] = E[f_3f_4f_5^*] \equiv E[f_if_jf_k^*]$ and $E[f_1f_2f_4^*] = E[f_1f_3f_4^*] = E[f_1f_3f_5^*] = E[f_2f_3f_5^*] = E[f_2f_4f_5^*] \equiv E[f_if_jf_l^*]$). Of course, $(HF)_5$ has only one unique 4-body energy, which is given in Table 3 along with all of the 2- and 3-body energies.

Step 5 in this tutorial is to reproduce the RHF/aug-cc-pVDZ electronic energies in Table 3. Sample input files for several popular software packages are available online.[92] It is worth noting that these computations could just as easily be performed in the entire basis set of the complex, thereby yielding a

Table 3 Unique Many-Body Electronic Energies (in E_h) for $(HF)_n$, $n = 3 - 5$ Computed at the RHF/aug-cc-pVDZ Level

	$E[f_i f_j^*]$	$E[f_i f_k^*]$	$E[f_i f_j f_k^*]$	$E[f_i f_j f_l^*]$	$E[f_i f_j f_k f_l^*]$
			Fully Optimized Clusters[a]		
$(HF)_3$[b]	−200.072923	—	—	—	—
$(HF)_4$[b]	−200.072748	−200.069328	−300.116161	—	—
$(HF)_5$[b]	−200.072425	−200.068570	−300.115003	−300.109494	−400.160289
			Rigid Monomer Approximation[c]		
$(HF)_3$[b]	−200.073038	—	—	—	—
$(HF)_4$[b]	−200.073100	−200.069755	−300.116246	—	—
$(HF)_5$[b]	−200.072990	−200.069093	−300.115406	−300.110113	−400.160256

[a]See Tables 1 and 2 for 1-body energies.
[b]See Table 1 for the full n-body energies for $(HF)_n$.
[c]See Table 1 for 1-body energy.

CP-corrected many-body decomposition. However, that would increase the time of the computations for this tutorial substantially.

The monomer energies from Tables 1 and 2 have been used to determine the E_{DIST} values (Eq. [12]) shown in Table 4. (Again, a conversion factor of $1E_h \approx 2625.5\,kJ\,mol^{-1}$ has been adopted.) For these symmetric cyclic $(HF)_n$ $(n = 3 - 5)$ clusters, E_{DIST} is simply $n \times (E[HF^*] - E[HF]) = n \times (-E_{RLX})$. The many-body interaction energy can then be calculated from E_{int} and E_{DIST} via Eq. [17]. Recall that within the RMA, $E_{DIST} = 0$ so that in the bottom half of Table 4 $E_{int}^{many\text{-}body}$ is the same as E_{int}.

The 2-body through 5-body contributions to the many-body interaction energy shown in Table 4 are relatively simple to compute because there are only a few symmetry-unique terms. As mentioned earlier, there exist at most two unique 2-body energies [in $(HF)_4$ and $(HF)_5$] and two unique 3-body energies [in $(HF)_5$]. Furthermore, all monomers in a given cluster are identical, and the corresponding energies can be obtained from Table 2 ($E[HF^*] = E[HF]^{\text{monomer basis}}_{\text{cluster geom}}$).

Table 4 Many-Body Decomposition of E_{int} for $(HF)_n$, $n = 3 - 5$[a]

	E_{dist}	$E_{int}^{many\text{-}body}$	E_2	E_3	E_4	E_5	δE^{nonadd}
				Fully Optimized Clusters			
$(HF)_3$	+0.96	−50.93	−43.58	−7.34	—	—	−7.34
$(HF)_4$	+2.87	−93.40	−71.23	−20.65	−1.51	—	−22.17
$(HF)_5$	+4.08	−128.61	−91.52	−33.43	−3.38	−0.27	−37.08
				Rigid Monomer Approximation			
$(HF)_3$	—	−49.13	−42.58	−6.55	—	—	−6.55
$(HF)_4$	—	−88.12	−68.56	−18.27	−1.28	—	−19.55
$(HF)_5$	—	−120.86	−89.51	−28.45	−2.66	−0.24	−31.35

[a]All values were computed at the RHF/aug-cc-pVDZ level and are reported in $kJ\,mol^{-1}$.

Consequently, Eq. [27] and the preceding equations end up with fairly simple forms for $(HF)_n$, $n = 3 - 5$:

$$E_{DIST}[HF_n] = -n \times E_{RLX}[HF] \quad [28]$$

$$E_2[HF_3] = 3E[f_i f_j^*] - 6E[HF^*] \quad [29]$$

$$E_2[HF_4] = 4E[f_i f_j^*] + 2E[f_i f_k^*] - 12E[HF^*] \quad [30]$$

$$E_2[HF_5] = 5E[f_i f_j^*] + 5E[f_i f_k^*] - 20E[HF^*] \quad [31]$$

$$E_3[HF_4] = 4(E[f_i f_j f_k^*] - \{2E[f_i f_j^*] + E[f_i f_k^*]\} + 3E[HF^*]) \quad [32]$$

$$E_3[HF_5] = 5(E[f_i f_j f_k^*] + E[f_i f_j f_l^*] - 3\{E[f_i f_j^*] + E[f_i f_k^*]\} + 6E[HF^*]) \quad [33]$$

$$E_4[HF_5] = 5(E[f_i f_j f_k f_l^*] - 2\{E[f_i f_j f_k^*] + E[f_i f_j f_k^*]\} + 3\{E[f_i f_j^*] + E[f_i f_k^*]\} - 4E[HF^*]) \quad [34]$$

The full n-body contribution to each $(HF)_n$ cluster can be obtained in different ways, the easiest of which is to subtract the lower order contributions $(E_2, E_3, \ldots, E_{n-1})$ from $E_{int}^{many\text{-}body}$. Alternatively, Eq. [27] can be simplified in the same manner as the lower order terms:

$$E_3[HF_3] = E[HF_3] - 3E[f_i f_j^*] + 3E[HF^*] \quad [35]$$

$$E_4[HF_4] = E[HF_4] - 4E[f_i f_j f_k^*] + 4E[f_i f_j^*] + 2[f_i f_k^*] - 4E[HF^*] \quad [36]$$

$$E_5[HF_5] = E[HF_5] - 5E[f_i f_j f_k f_l^*] + 5E[f_i f_j f_k^*] + 5[f_i f_j f_l^*] - 5E[f_i f_j^*] - 5[f_i f_k^*] + 5E[HF^*] \quad [37]$$

Although every contribution to the interaction energies of these HF clusters are attractive, this does not always hold. In certain cases, some of the many-body components may actually be repulsive.[100] In step 6, you should calculate components of E_{int} in Table 4 $(E_{DIST}, E_2, E_3, E_4, E_5)$ by applying Eqs. [12], [16], [17], [25]–[27] to the electronic energies in the Tables 1, 2, and 3.

Size Consistency and Extensivity of the Energy

Energy is an extensive property. This fundamental thermodynamic principle is introduced early in most general chemistry textbooks, and it provides the foundation for the supermolecule description of intermolecular interactions. Unfortunately, not all electronic structure techniques are size consistent[106] (or more generally size extensive[107]). That is, the energy computed by some methods does not scale properly with the number of noninteracting fragments. Readers interested in more detail may be interested in the sections discussing size consistency and extensivity in the review of coupled-cluster theory by Crawford and Schaefer.[108]

To illustrate the point, consider two noninteracting (i.e., well-separated) HF molecules. (This can effectively be achieved in a computation by placing the HF molecules on the z axis and separating them by ≈ 1000 Å so that the F atoms are at 0 and 1000 Å while the H atoms are at 0.900 and 1000.900 Å.) Using the data in Table 1, we know the electronic energy of a single HF molecule is $-100.033816\,E_h$ when computed with the SCF method and the aug-cc-pVDZ basis set. As you would expect, the corresponding energy of two noninteracting HF molecules (i.e., separated by 1000 Å) is exactly $2 \times -100.033816 = -200.067632\,E_h$ but only because the SCF method is size consistent. Truncated configuration interaction (CI) methods such as the one including only single and double configurations (CISD) are not. The CISD/aug-cc-pVDZ energy is $-100.253275\,E_h$ if all electrons are correlated while that of two monomers separated by 1000 Å is $-200.488703\,E_h$, which is significantly different than $2 \times -100.253275 = -200.506551\,E_h$. As mentioned in the Introduction, this review only focuses on size-consistent electronic structure techniques. In the final step (step 7) of this tutorial, you should compute the SCF and CISD (all electrons correlated) energies of two HF monomers separated by 1000 Å. Compare these energies to those of a single monomer.

Summary of Steps in Tutorial

1. Reproduce electronic energies in Table 1.
2. Calculate E_{int} values on the left side of Table 2 (Eq. [2]).
3. Reproduce electronic energies in Table 2.
4. Calculate E_{int}^{CP} values on the right side of Table 2 (Eq. [8]).
5. Reproduce electronic energies in Table 3.
6. Calculate components of E_{int} in Table 4 (Eqs. [12], [16], [17], [25]–[27]).
7. Reproduce the electronic energies discussed in the proceedings section and check the size consistency of the results obtained with the SCF and CISD methods.

Sample input files for various software packages are available online.[92] If the electronic energies that you compute do not agree with those presented here, make sure that the energy is converged to at least eight decimal places in the SCF procedure and that tolerances for integral screening are no larger than 10^{-10}. Additionally, discrepancies on the order of $1 \times 10^{-6}\,E_h$ have been observed in some cases that can be attributed to differences in the conversion factor used to change angstroms to bohrs. Finally, rounding errors may lead to discrepancies on the order of $0.01\,kJ\,mol^{-1}$ for the other data presented in Tables 2 and 4.

HIGH-ACCURACY COMPUTATIONAL STRATEGIES

Although quantum mechanical studies of weak interactions can be traced back to Slater's 1929 work on He,[109] the first supermolecule ab initio

investigations of hydrogen bonding (reminiscent of those outlined above) were conducted approximately four decades ago.[85,110,111] Accuracy has been and continues to be one of the major challenges facing theoreticians (as well as experimentalists) working with weakly bound clusters. Consider, for example, covalent versus noncovalent interactions. An error of a few kilojoules per mole (*chemical accuracy*) per covalent bond may be acceptable because it typically represents a relative error of just a few percent. However, for weak noncovalent bonding an absolute error of a few kilojoules per mole could easily amount to a relative error in excess of 100%. Fortunately, by carefully applying the arsenal of sophisticated electronic structure techniques available today, it is possible to reduce the major sources of error (basis sets and electron correlation) to acceptable levels.

One of the most important lessons learned over the years is that not all weak noncovalent interactions are created equal. A particular quantum model chemistry that provides quantitatively reliable results for hydrogen bonding may yield qualitatively incorrect results for something like π stacking. For example, second-order Møller–Plesset (MP2) perturbation theory and several popular density functional (DFT) techniques can characterize the water dimer and trimer with a reasonable degree of accuracy. However, the former method overestimates π-stacking interactions in benzene by a factor of 2, while the latter fail to yield any sort of attractive interaction between two stacked benzene molecules. Consequently, it is imperative that "the right answer" is obtained for "the right reason" rather than relying on (or hoping for) some sort of error cancellation. Fortunately, well-established procedures exist by which one can converge to "the right answer." The most common of these convergent approaches to high-accuracy computational chemistry systematically improve (i) the correlated electronic structure techniques and (ii) the atomic orbital (AO) basis sets. This dual extrapolation scheme is depicted in Figure 4.

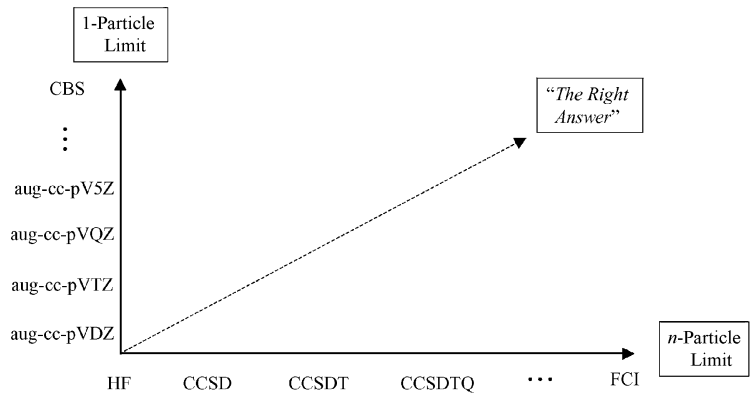

Figure 4 Example of convergent quantum chemistry scheme that employs AO basis sets that systematically approach the 1-particle or complete basis set (CBS) limit along with correlated electronic structure techniques that systematically approach the *n*-particle or full configuration interaction (FCI) limit.

Primer on Electron Correlation

The first component of convergent approaches to quantum chemistry is the computational procedure used to treat the electron correlation problem (depicted along the horizontal axis of Figure 4). A tutorial on treating electron correlation has been published earlier in this book series.[112] References 113 and 114 provide two additional excellent overviews of the subject. In any system with n interacting bodies (classical or quantum), the instantaneous motions of the bodies are correlated. Except for the simplest cases (e.g., certain one-electron systems), exact solutions to this n-particle (or many-body) problem cannot be obtained. Mean-field approximations (such as Hartree–Fock theory) neglect the instantaneous correlated motions of the bodies. The "missing" energy that corresponds to these simultaneous and instantaneous interactions is the correlation energy. In electronic structure theory, the correlation energy is typically (although not unambiguously) defined as the difference between the exact (nonrelativistic) electronic energy and the Hartree–Fock energy.[115]

Configuration interaction (CI) theory, coupled-cluster (CC) theory, and many-body perturbation theory (MBPT), of which Møller–Plesset (MP) perturbation theory is a specific case, are three of the most popular and relevant approaches that have been developed to systematically improve the computational description of electron correlation that is absent in Hartree–Fock theory. (Density functional methods are not mentioned here. Although DFT provides a very cost-effective means of recovering part of the electron correlation energy, the systematic improvement of individual functionals is problematic.) The missing correlation energy is recovered by constructing the wave function out of many different electron configurations (or Slater determinants) that are generated by "exciting" electrons from the occupied orbitals of the Hartree–Fock reference configuration to unoccupied (or virtual) orbitals. These additional (or excited) configurations are typically classified by excitation (or substitution) level: S for single excitations/substitutions, D for double, T for triple, etc.

Approximate many-electron wave functions are then constructed from the Hartree–Fock reference and the excited-state configurations via some sort of expansion (e.g., a linear expansion in CI theory, an exponential expansion in CC theory, or a perturbative power series expansion in MBPT). When all possible excitations have been incorporated (S, D, T, $\ldots, n$ for an n-electron system), one obtains the exact solution to the nonrelativistic electronic Schrödinger equation for a given AO basis set. This n-particle limit is typically referred to as the full CI (FCI) limit (which is equivalent to the full CC limit). As Figure 5 illustrates, several WFT methods can, at least in principle, converge to the FCI limit by systematically increasing the excitation level (or perturbation order) included in the expansion technique.

It is particularly important to note that while the linear CI expansion necessarily converges and all evidence suggests the exponential CC expansion always converges, the MBPT (or MP) series does diverge occasionally.[116,117]

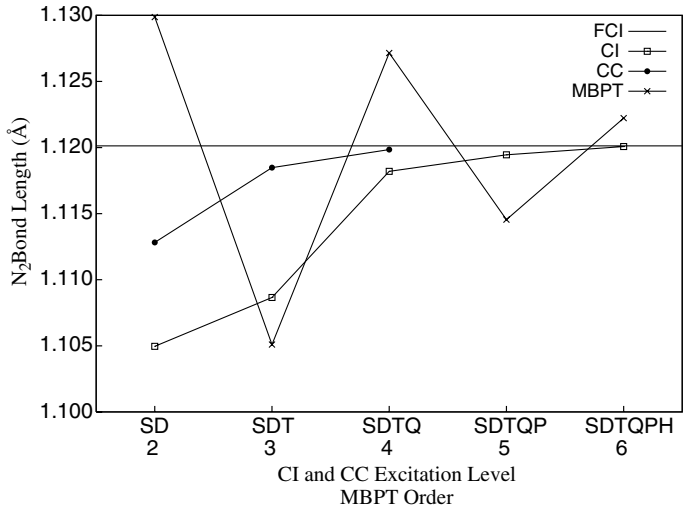

Figure 5 Convergence of correlated methods to the FCI bond length of N_2. All results were obtained with the cc-pVDZ basis set. The CCSDTQ bond length was computed for this work while all other data points were taken from Ref. 116.

Consequently, the most popular progression toward the FCI limit is MBPT2 (or MP2) → CCSD(T) rather than MBPT2 (or MP2) → MP3 → MP4. The CCSD(T) method, which includes a perturbative estimate of triple substitutions, is often referred to as the "gold standard" of quantum chemistry because (i) it generally provides results that are close to the FCI limit, especially for the systems that are the focus of this chapter, and (ii) it can be applied feasibly to moderately sized systems (a few dozen atoms). [Estimates of higher order correlation effects (e.g., quadruple substitutions) suggest that the CCSD(T) method provides converged results for the entire spectrum of noncovalent interactions.[118–120]] The CCSD → CCSD(T) sequence is also useful but is less commonly used because the CCSD method has more significant computational demands than MP2. These computational demands (or computational overhead) are the topic of the discussion below on the scaling problem.

Primer on Atomic Orbital Basis Sets

To introduce the concepts of a basis set and basis functions, we begin with a simple (unknown) function of a single variable, $f(x)$. A variety of procedures can be used to "fit" (or estimate) this function. For example, a simple power series could be used to approximate this simple function of the variable x:

$$f(x) \approx c_0 + c_1 x + c_2 x^2 + c_3 x^3 \qquad [38]$$

Here we are using a *basis set* to approximate the unknown function $f(x)$. The basis functions are $\{x^i : i = 0, 1, 2, 3\}$. The expansion coefficients, c_i, are determined by some sort of procedure that adjusts their values in order to obtain the best fit to the function $f(x)$. The approximation can generally be improved by using a larger basis set,

$$f(x) \approx c_0 + c_1x + c_2x^2 + c_3x^3 + c_4x^4 + c_5x^5 \qquad [39]$$

and it becomes exact in the limit of an infinitely large or complete basis set (CBS):

$$f(x) = c_0 + c_1x + c_2x^2 + c_3x^3 + \cdots = \sum_{i=0}^{\infty} c_ix^i \qquad [40]$$

In quantum chemistry we are concerned with approximating a molecular wave function, ψ, rather than a simple function of a single variable, $f(x)$. In the Hartree–Fock approximation, the many-electron wave function, ψ, is approximated with the antisymmetrized product of one-electron molecular orbitals (MOs). As you might expect, powers of x are not necessarily the best choice for a basis set in which to expand these one-electron functions. It does not require too much chemical intuition to recognize that the analytical wave functions for one-electron atoms (i.e., the s, p, and d orbitals shown in general chemistry textbooks) might provide a good set of basis functions in which to expand the molecular orbitals. After all, molecules are made of atoms. So, why not build molecular orbitals out of atomic orbitals? This is, of course, the familiar linear combination of atomic orbitals to form molecular orbitals (LCAO-MO) approximation. Both Slater and Gaussian atomic orbitals (AOs) provide fairly convenient basis functions for electronic structure computations. Of course, not all basis sets need to have a chemically motivated origin. For example, plane wave basis sets owe their success to computational efficiency.

Unfortunately, a bigger AO basis set does not necessarily give better results. Bigger is better only if the basis sets are properly constructed. In 1989, Dunning introduced the correlation-consistent family of basis sets,[121–123] which was a huge advance in the field of convergent quantum chemistry. They were designed to converge systematically to the complete basis set (CBS) or 1-particle limit. These basis sets are typically denoted cc-pV*X*Z where X denotes the maximum angular momentum of the Gaussian atomic orbitals in the basis set (2 for d functions, 3 for f functions, etc.) and is also referred to as the cardinal number of the basis (D for double-ζ basis set, T for triple-ζ, etc.). Because of the convergence properties of these basis sets, we can expect the larger basis sets to be more reliable. [$X = 4$ (or Q) is better than $X = 3$ (or T), which is better than $X = 2$ (or D).] The same is not true of other families of basis sets [e.g., 6-311G($2df, 2pd$) vs. 6-31G(d, p) or TZ2P vs. DZP].

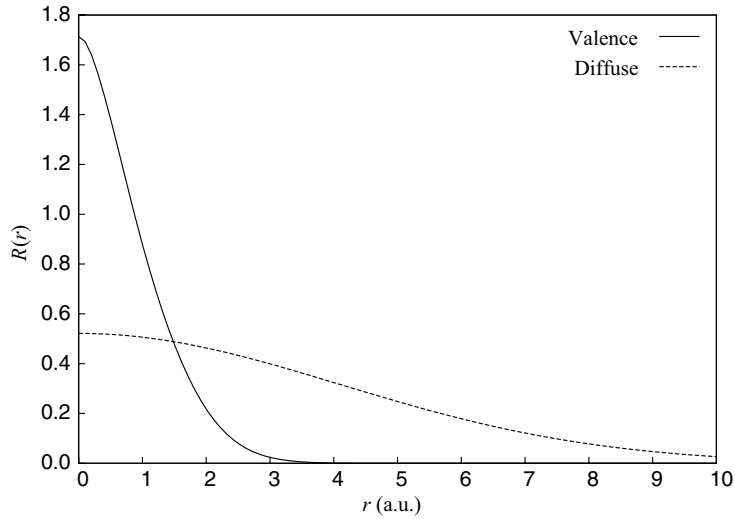

Figure 6 Diffuse basis functions are more spatially extended than their valence counterparts. The dashed curve represents the radial plot of the normalized diffuse 1*s* Gaussian basis function for H from the aug-cc-pVDZ basis set while the solid curve is for the corresponding contracted valence 1*s* basis function.

In the examples shown along the *y* axis in Figure 4, the "aug-" prefix indicates that the correlation-consistent basis sets have been augmented with diffuse basis functions.[122] These functions have small orbital exponents and are therefore spatially extended as can be seen in the radial plots shown in Figure 6. Diffuse functions are useful in computations for weakly bound clusters because they help describe the long-range interactions between fragments. (Basis sets augmented with diffuse functions are also commonly used to improve the description of negatively charged ions.) In fact, diffuse functions are practically essential for such applications. In some situations, diffuse functions need only be added to nonhydrogen atoms. However, results for weak noncovalent interactions obtained without diffuse functions must be analyzed carefully because CP corrections for basis set superposition error can still leave an unacceptably large basis set incompleteness error (see discussion below).

Extrapolation Techniques

Because of the systematic nature of the correlation-consistent family of basis sets, it is possible to use extrapolation techniques to estimate the CBS limit. For example, the three-parameter exponential function introduced by Feller nicely describes the convergence of SCF energy to the CBS limit with respect to the cardinal number of the basis set, X.[124,125] By fitting data from

three or more basis sets to this function, one can estimate the SCF CBS limit:

$$E_{\mathrm{SCF}} = E_{\mathrm{SCF}}^{\mathrm{CBS}} + a\exp(-bX) \qquad [41]$$

Various formulas have been proposed to describe the convergence behavior of the correlation energy (E_{corr}), which is distinctly different from and slower than that for the SCF energy. Here a few common examples are introduced. Note that the following extrapolation procedures are applied only to the correlation energy, not the total energy. In other words, $E_{\mathrm{corr}} = E_{\mathrm{total}} - E_{\mathrm{SCF}}$. The simple two-parameter formula suggested by Helgaker et al.[126] is popular:

$$E_{\mathrm{corr}} = E_{\mathrm{corr}}^{\mathrm{CBS}} + \frac{b}{X^3} \qquad [42]$$

because it can be manipulated into an expression that utilizes only the two most accurate data points. No fitting is required with the resulting equation. One simply inserts the correlation energies from the two largest basis sets with cardinal numbers $X_{\max}$ and $X_{\max} - 1$:

$$E_{\mathrm{corr}}^{\mathrm{CBS}} = \frac{E_{\mathrm{corr}}^{X_{\max}}(X_{\max})^3 - E_{\mathrm{corr}}^{X_{\max}-1}(X_{\max}-1)^3}{(X_{\max})^3 - (X_{\max}-1)^3} \qquad [43]$$

For the fitting of correlation energies obtained with extremely large hextuple- and heptuple-zeta (6Z and 7Z) basis sets, the following revision to Eq. [43] has been suggested based on MP2 pair energies:[127]

$$E_{\mathrm{corr}}^{\mathrm{CBS}} = \frac{E_{\mathrm{corr}}^{X_{\max}}(X_{\max}+0.5)^3 - E_{\mathrm{corr}}^{X_{\max}-1}(X_{\max}-0.5)^3}{(X_{\max}+0.5)^3 - (X_{\max}-0.5)^3} \qquad [44]$$

Also, Martin has proposed a two-parameter fit to a quartic polynomial (Schwartz4) and a three-parameter fit to a sixth-degree polynomial (Schwartz6):[128]

$$E_{\mathrm{corr}} = E_{\mathrm{corr}}^{\mathrm{CBS}} + \frac{a}{(X+\frac{1}{2})^4} + \frac{b}{(X+\frac{1}{2})^6} \quad \begin{cases} b = 0 \text{ Schwartz4} \\ b \neq 0 \text{ Schwartz6} \end{cases} \qquad [45]$$

Although many more incarnations describing the convergence of the correlation energy with respect to X can be found in the literature, they tend to adhere to the same philosophy as that adopted in Eqs. [42]–[45]. It is worth noting that better results are generally obtained when only the most accurate

data points are used in the extrapolation.[129,130] For example, if MP2 correlation energies are available for cc-pVDZ, cc-pVTZ, cc-pVQZ, cc-pV5Z, and cc-pV6Z basis sets, then the most reliable extrapolation schemes can be obtained by fitting the Q/5/6 data points or just the 5/6 data points. Some examples of these extrapolation procedures are presented in the tutorial below.

Explicitly Correlated Methods

A serious implication of the equations presented in the previous section is that the correlation energy converges to the CBS limit slowly with respect to the cardinal number (or angular momentum) of the basis set. In response, dramatic progress has been made in the development of explicitly correlated R12 methods that " bypass the slow convergence of conventional methods, by augmenting the traditional orbital expansions with a small number of terms that depend explicitly on the interelectronic distance $r12$."[131] Through various approximations (e.g., the resolution of the identity) and by changing the linear $r12$ dependence to a different functional form ($f12$), these R12 and F12 methods can provide correlation energies (typically at the MP2 level) that are converged to the CBS limit with only TZ or possibly even DZ quality basis sets. Readers interested in more details are strongly encouraged to consult the outstanding review by Klopper and co-workers.

Scaling Problem

Thanks to the concurrent development of more efficient computer algorithms and affordable high-performance computing hardware, the sophisticated electronic structure techniques described in the primer on electron correlation above can be brought to bear on weakly bound clusters of ever-increasing size (and with larger/better basis sets such as the correlation-consistent basis sets described in the preceding section). The drawback of these correlated electronic structure techniques is that their computational demands (memory, CPU time, disk space) increase sharply with the size of the system. For example, the "gold standard" of single-reference, ground-state quantum chemistry [i.e., the CCSD(T) method] scales as the 7th power of the size of the system, $\mathcal{O}(N^7)$. The practical consequences of this are devastating. Suppose you have the facilities to perform a CCSD(T) computation on the water hexamer with the aug-cc-pVTZ basis set (552 basis functions). By the time this chapter is printed, high-performance personal computers *might* be fast enough to perform a serial (nonparallel) computation of this magnitude in approximately 1 week. If one wishes to perform the same calculation on $(H_2O)_{18}$, the computational requirements will increase by $3^7 = 2187$ since the system has tripled in size. That means the time required to perform the computation would increase from 1 week to more than 42 years on the same computer. (A nice overview of the scaling requirements of some popular methods can be

found in Ref. 113, and a tutorial on linear scaling in quantum chemistry has appeared in this book series.[132]) Parallelization does not solve the issue. If a parallel CCSD(T) code executed on a high-performance cluster can reduce the time for the $(H_2O)_6$ computation to 1 day, the $(H_2O)_{18}$ calculation will still take 6 years to finish. Even if time was not a factor, these ludicrous computations would not be feasible because memory and disk requirements also increase by the same factor of 2187.

Estimating E_{int} at the CCSD(T) CBS Limit: Another Tutorial

High-accuracy model chemistries (for all types of chemical systems, not just weakly bound clusters) typically rely on additive schemes because of the hefty computational demands of highly correlated electronic structure techniques (see preceding section). In this section we demonstrate how to reliably estimate the CCSD(T) CBS limit even though it is generally not feasible to compute CCSD(T) energies for weakly bound clusters with basis sets large enough to yield a meaningful extrapolation to the CBS limit. This feat can be achieved because contributions from higher order (triple, quadruple, etc.) excitations tend to converge quickly with respect to the size of the AO basis set even though the total correlation energy converges slowly to the CBS limit (discussed above). As a result, the general strategy is to combine the CBS limit for a less demanding correlated method that includes only lower order excitations (e.g., MP2, CCSD, CISD) with a correction for higher order correlation effects obtained with small basis sets. The most popular combination is to use the MP2 CBS limit with a CCSD(T) correction.

Table 5 contains the MP2, CCSD, and CCSD(T) correlation energies for the HF monomer and trimer obtained with a series of correlation-consistent basis sets where diffuse functions are added only to the heavy (nonhydrogen) atoms, denoted ha*XZ*. The frozen core approximation was adopted for all of the calculations (i.e., electrons in the 1*s*-like orbitals on F were not included in the correlation procedure). The SCF energies converge very quickly. The ha5Z and ha6Z data points are within 1 mE_h of the SCF CBS limit that was obtained by fitting all five SCF energies (haDZ–ha6Z) to Eq. [41]. In contrast, the MP2 correlation energy converges more slowly. The ha5Z values are still more than 9 mE_h away from the MP2 CBS limit that was obtained by simply applying Eq. [43] to the ha5Z and ha6Z MP2 correlation energies (not the total MP2 electronic energies). The CCSD and CCSD(T) correlation energies are also provided for the haDZ, haTZ, and haQZ basis sets. No CCSD and CCSD(T) CBS limits are given, however, because extrapolations with smaller basis sets tend not to be as reliable as when larger correlation-consistent basis sets (e.g., pentuple- or sextuple-ζ) are used to obtain the correlation energies.[129,130,133] Unfortunately, such computations are often prohibitively demanding.

Table 5 SCF Electronic Energies and MP2, CCSD, and CCSD(T) Correlation Energies (in E_h) of HF and $(HF)_3$ Obtained with a Series of Correlation Consistent Basis Sets

Basis set[a]	E_{SCF}	E_{MP2}	E_{CCSD}	$E_{CCSD(T)}$
		HF Monomer		
haDZ (28)	−100.033348	−0.220691	−0.224524	−0.228425
haTZ (60)	−100.061354	−0.278496	−0.279840	−0.287214
haQZ (110)	−100.068993	−0.300097	−0.299628	−0.307789
ha5Z (182)	−100.071047	−0.309009	—	—
ha6Z (280)	−100.071251	−0.313005	—	—
CBS	−100.071625[b]	−0.318494[c]	—	—
		HF Trimer		
haDZ (84)	−300.119318	−0.665993	−0.676952	−0.689508
haTZ (180)	−300.202077	−0.840519	−0.844137	−0.867192
haQZ (330)	−300.224732	−0.905371	−0.903564	−0.929013
ha5Z (546)	−300.230791	−0.932136	—	—
ha6Z (840)	−300.231389	−0.944120	—	—
CBS	−300.232512[b]	−0.960582[c]	—	—

[a]haXZ denotes cc-pVXZ for H and aug-cc-pVXZ for F. Number of basis functions in parentheses.
[b]Obtained by fitting the haDZ–ha6Z data to Eq. [41].
[c]Obtained by applying Eq. [43] to the ha5Z and ha6Z MP2 correlation energies.

Step 1 in the tutorial associated with this section is to reproduce the SCF and correlation energies in Table 5. However, this step is optional because several of the computations require a good deal of time and resources. As such, it may not be worth the effort for most readers interested in the tutorial.

Step 2 in the tutorial, however, is more important and should not be considered optional. Readers should be able to reproduce the MP2 CBS limit by plugging the ha5Z and ha6Z data from Table 5 into Eq. [43]:

$$E_{MP2}^{CBS} = \frac{216(E_{MP2}^{ha6Z}) - 125(E_{MP2}^{ha5Z})}{91} \quad [46]$$

Similarly, you should be able to reproduce the SCF CBS limit by fitting all five SCF energies (haDZ–ha6Z) to Eq. [41]. This process is a bit more involved since it generally requires software capable of performing a nonlinear fit. Fortunately, a variety of freely available programs (including `gnuplot`[134]) can fit data to nonlinear equations.

The data in Table 5 have been used to compute the interaction energies (E_{int}) of $(HF)_3$ shown in Table 6. Here it is easier to achieve rapid convergence of higher order correlation effects. While the MP2 and CCSD(T) interaction energies continue to change appreciably as X increases, the *difference* between the two ($\delta_{MP2}^{CCSD(T)}$) converges very quickly to $\approx -1.5\,kJ\,mol^{-1}$. Thus the CCSD

Table 6 SCF, MP2, and CCSD(T) Interaction Energies (E_{int}) of $(HF)_3$ Obtained with a Series of Correlation-Consistent Basis Sets[a]

Basis set[b]	SCF	MP2	$\delta_{MP2}^{CCSD(T)}$	CCSD(T)
haDZ	−50.60	−60.89	−0.82	−61.71
haTZ	−47.30	−60.50	−1.37	−61.87
haQZ	−46.61	−59.94	−1.49	−61.44
ha5Z	−46.34	−59.75	—	—
ha6Z	−46.30	−59.71	—	—
CBS	−46.31[c]	−59.70[c]	[−1.49]	[−61.19]

[a]CCSD(T) corrections for higher order correlations effects are also reported relative to the MP2 values ($\delta_{MP2}^{CCSD(T)}$). All values are in kj mol^{-1}. Square brackets denote values obtained with the additive approximation described in the text.

[b]haXZ denotes cc-pVXZ for H and aug-cc-pVXZ for F.

[c]Obtained from data in Table 5.

(T) can be reasonably estimated by adding the $\delta_{MP2}^{CCSD(T)}$ correction obtained from smaller basis sets to the MP2 CBS limit of E_{int}:

$$E_{int}^{CCSD(T)/CBS} \approx E_{int}^{MP2/CBS} + \delta_{MP2}^{CCSD(T)} \quad [47]$$

For this example, the CCSD(T) correction of $-1.49\,kJ\,mol^{-1}$ obtained with the haQZ basis set is combined with the MP2 CBS limit to produce an estimate of $-61.19\,kJ\,mol^{-1}$ for the CCSD(T) CBS interaction energy of $(HF)_3$. Square brackets have been placed around these numbers in Table 6 to denote that they are based upon the additive approximation in Eq. [47] rather than an extrapolation of the correlation energy.

Step 3 in the tutorial associated with the section is to calculate the SCF and MP2 interaction energies (including the CBS values) in Table 6 from the energies given in Table 5.

Step 4 in the tutorial is to calculate the CCSD(T) E_{int} and $\delta_{MP2}^{CCSD(T)}$ values for the haDZ, haTZ, and haQZ basis sets.

Step 5 in the tutorial is to use Eq. [47] to estimate the CCSD(T) CBS limit of E_{int} for $(HF)_3$.

Accurate Potential Energy Surfaces

The systematic computational strategy outlined in this section of the review is necessary albeit demanding. The approach provides an accurate description of the entire spectrum of noncovalent interactions between fragments in a cluster. One can be confident in the calculated results regardless of cluster composition [i.e., whether examing the $(H_2O)_6$, $(C_6H_6)_2$, or a mixture of the two]. Less obviously but more importantly, one can also be confident in the calculated results across the entire (intermolecular) potential energy

surface (PES). The nature of the interactions not only depends on the identities of the fragments, but it is also highly sensitive to their separations and relative orientations in the cluster.[135]

The practical consequences of these dependencies can be severe. Consider, for example, the pairing of nucleic acid bases through both hydrogen bonding and stacking interactions.[136] If a particular quantum model chemistry does not properly describe both the dispersion interactions that play a major role in the latter configuration and the electrostatic interactions that dominate in the former orientation, qualitatively incorrect conclusions about the relative stability of stacked and hydrogen-bonded base pairs will be derived. The benzene dimer also illustrates this point nicely. The convergent approach outlined in this section has identified two isoenergetic, low-energy configurations on the PES, a T-shaped structure and a parallel displaced stacked structure.[137–139] Even at the CBS limit, the MP2 method overestimates the E_{int} for both structures. The more serious problem, however, is that the error is much larger for the stacked structure than for the parallel displaced structure because the nature of the interactions in the two configurations is different. By not considering high-order correlation effects, one arrives at the specious conclusion that the parallel displaced configuration is nearly 1.5 kcal mol^{-1} (6 kJ mol^{-1}) more stable than the T-shaped structure. Clearly, it is imperative that any computational strategy give consistent results across the entire PES, not just at one particular configuration (e.g., the global or a local minimum).

LESS DEMANDING COMPUTATIONAL STRATEGIES

The previous section outlined demanding computational procedures that provide the right answer for the right reason. Those convergent techniques[32,36] provide very accurate interaction energies across the entire PES for weakly bound clusters that can then be used as benchmarks[41,42,140–142] against which less demanding computational procedures may be measured. In this section, we review the performance of less demanding quantum model chemistries for different classes of weak noncovalent interactions, focusing on MP2 and DFT methods.

Second-Order Møller–Plesset Perturbation Theory

In general, second-order Møller–Plesset perturbation theory (a specific case of second-order many-body perturbation theory) is the workhorse of electronic structure techniques for weakly bound systems because the method tends to provide a reliable description of a wide range of weak interactions. For most hydrogen-bonding scenarios, MP2 energetics are extremely accurate and nearly identical to those from CCSD(T) computations with the same basis set. In fact, a recent study revealed that MP2 interaction energies obtained with an appropriate triple-ζ basis set agree favorably with CCSD(T) CBS

benchmark values.[143] Even for high-energy saddle points and structures with bifurcated hydrogen bonds, the deviations still tend to be less than a few tenths of a kilocalorie per mole per hydrogen bond.[118,119] Only for cyclic hydrogen-bonding motifs (like that found in the formic acid dimer), do MP2 interaction energies deviate substantially from CCSD(T) values.[143]

At the other end of the spectrum of weak interactions (Figure 1), the MP2 method can still provide a reasonable description of dispersion-bound clusters despite having a tendency to slightly overestimate the interaction energies between molecules relative to CCSD(T) results. For example, MP2 calculations yield interaction energies that are just a few tenths of a kilocalorie per mole larger than the CCSD(T) values for *n*-alkane dimers[142] and even some simple π-stacked dimers such as $(N_2)_2$ and $(C_2H_2)_2$.[120] If the π systems are delocalized, however, the MP2 errors can become massive (*vida infra*). Even the interactions between rare gas atoms are described reasonably well by the MP2 method.[144] However, MP2 tends to underbind the Ne_2 and He_2 by an amount that is small in an absolute sense but large in a relative sense, particularly in the case of He_2.

The MP2 method is not perfect, however, and the most notable (and fairly dramatic) failure of the MP2 method in the field of weak noncovalent interactions occurs for delocalized π stacking.[137–139] In fact, a separate chapter of this volume is dedicated to these π-type interactions.[49] The MP2 method overestimates dramatically the stability of "face-to-face" or "stacked"-type configurations relative to "edge-to-face" or "T-shaped" orientations that leads to a qualitatively incorrect description of delocalized π stacking as illustrated with the benzene dimer in described above. Consider the parallel-displaced stacked and T-shaped configurations of the diacetylene dimer $(H{-}C{\equiv}C{-}C{\equiv}C{-}H)_2$ (shown in Figure 7) along with the analogous configurations of the acetylene

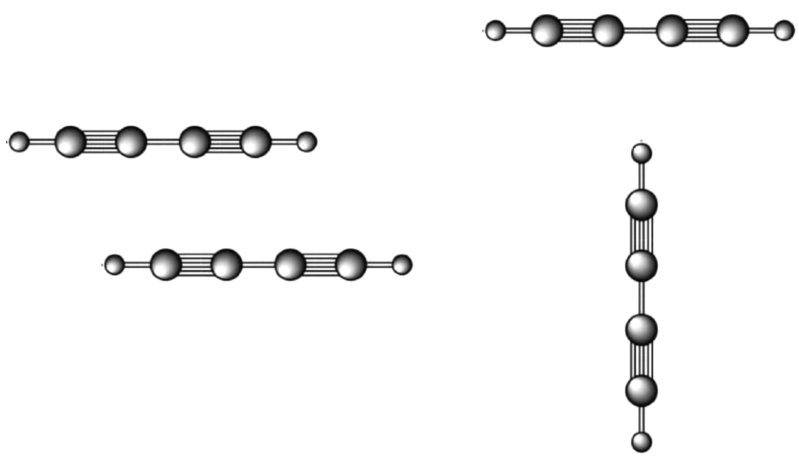

Figure 7 Parallel displaced and T-shaped configurations of the diacetylene dimer.

Table 7 MP2 and CCSD(T) Interaction Energies of the Stacked and T-shaped Dimers of Acetylene and Diacetylene[a]

Orientation	Dimer	CCSD(T)	MP2	$\delta_{MP2}^{CSD(T)}$
Stacked	$(H{-}C{\equiv}C{-}C{\equiv}C{-}H)_2$[b]	−1.31	−2.38	+1.07
T-shaped	$(H{-}C{\equiv}C{-}C{\equiv}C{-}H)_2$[b]	−1.63	−1.94	+0.31
Stacked	$(H{-}C{\equiv}C{-}H)_2$[c]	−1.72	−1.99	+0.17
T-shaped	$(H{-}C{\equiv}C{-}H)_2$[c]	−2.32	−2.45	+0.13

[a] All values are in kcal mol^{-1}.
[b] Reference 93
[c] Reference 120

dimer $(H{-}C{\equiv}C{-}H)_2$. In agreement with the "gold standard" of quantum chemistry [i.e., the CCSD(T) method], MP2 calculations correctly predict an attractive interactions in each case. (See data in Table 7.) However, for the dimers composed of fragments containing a delocalized π electron network, the MP2 method substantially overestimates the interaction energy (by more than 1 kcal mol^{-1}, which represents a relative error in excess of 80%) while the difference between the CCSD(T) and MP2 results ($\delta_{MP2}^{CCSD(T)}$) is modest for $(H{-}C{\equiv}C{-}H)_2$ (less than 0.17 kcal mol^{-1} or 10%). Matters are made even worse by the fact that the MP2 error is not uniform across the entire potential surface, which can lead to qualitatively incorrect conclusions about the nature of delocalized π-type interactions. With MP2 computations, one would conclude that the stacked configuration of $(H{-}C{\equiv}C{-}C{\equiv}C{-}H)_2$ is more stable than the T-shaped structure. However, the opposite (and correct) conclusion is reached when the effects of higher order excitations are included via CCSD (T) calculations.

Spin-Scaled MP2

Several approaches have been introduced that attempt to address this shortcoming of MP2 for delocalized π interactions. In 2003, Grimme introduced the spin-component-scaled second-order Møller–Plesset perturbation theory (SCS-MP2) method where the parallel spin (↑↑) and antiparallel spin (↑↓) pair correlation energies (which are related to the singlet and triplet components of the correlation energy) were assigned different weights.[145] The empirical scaling parameters ($p_{\uparrow\uparrow} = \frac{6}{5}$ and $p_{\uparrow\downarrow} = \frac{1}{3}$) improve MP2 results significantly not only for a variety of reaction energies and atomization energies but also for interaction energies between delocalized π systems (including the benzene dimer). The approach has no additional computational overhead relative to MP2, and it preserves the size consistency of the MP2 method. Other variations of these scaling parameters have since been introduced in an attempt to further improve the description of noncovalent interactions and/or reduce the computational demands.[146–149] Of particular interest is the SCSN-MP2 method of Platts and Hill in which the scaling parameters were optimized using

benchmark interaction energies for nucleic acid bases.[149] More recently, Takatani and Sherrill assessed the performance of several of these spin-scaled MP2 methods and found that the SCSN parameters reproduce nicely CCSD(T)/CBS interaction energies across the entire PES for a variety of dispersion-bound dimers.[150]

RI-MP2 and LMP2

Because the MP2 method has been so successful, there has also been a great deal of work done to reduce its computational demands, thereby further improving its price-to-performance ratio. These include schemes that employ localized orbitals (such as LMP2)[151–153] as well as the resolution of the identity approximation (RI), which is also known as density fitting (DF).[154–158] Werner, Manby, and Knowles have even introduced the DF-LMP2 method that incorporates both local approximations and density fitting.[159] (Those interested in more details about localization and RI techniques should consult their paper and the references contained therein.) Readers should be aware of a potential pitfall of some localization schemes. At certain points, the domain definitions can change, which leads to discontinuous PESs.[160] In large systems with many degrees of freedom, such discontinuities could lead to difficulties with geometry optimization procedures needed to locate minima or other stationary points on the PES. Fortunately, it is possible to construct local correlation models that are free of this problem.[161]

By reducing the overhead of MP2 computations substantially, these methods are helping to extend the domain of reliable electronic structure computations for noncovalent interactions to larger and larger systems (within the limits of the MP2 method). The RI-MP2 technique has been shown to yield structures and interaction energies that are virtually identical to canonical MP2 results when an extended basis set containing *f* functions is used while reducing the computational time by up to an order of magnitude.[44,162] The DF-LMP2 method has already been coupled with the aforementioned SCS approach of Grimme. The spin component scaled for nucleobases (SCSN) parameters were obtained from DF-LMP2 interaction energies.[149]

Density Functional Theory

As the previous millennium drew to a close, it became clear that density functional theory was not sufficiently reliable for the study of noncovalent interactions (including hydrogen bonding).[32,163–166] It was widely accepted at the time that the MP2 method and a high-quality triple-ζ (or larger) basis set were required to obtain chemically significant results for noncovalent interactions. Subsequently, a massive effort has been directed toward the development and calibration of new density functionals for noncovalent interactions.

Before proceeding, readers should be aware that caution must be exercised when drawing conclusions or making generalizations from a particular

systematic analysis (or calibration) of DFT methods, particularly in the case of weak interactions. Results depend heavily not only on the identity of the density functional[167] and the basis set[168,169] but also on the numerical integration grid, which differs from one quantum chemistry software package to the next (sometimes substantially).[170] Additionally, the criteria for a "reliable" DFT method are very different for someone trying to discern the energetic order of several low-lying minima than from someone merely trying to determine that a stable structure exists. While it is clear that some progress has been made, this section demonstrates that DFT methods are often reliable in the latter sense but rarely in the former sense.

For noncovalent interactions dominated by the electrostatic component of the interaction energy, it is likely that one of the well-established density functionals will produce reliable results. For example, it has been known for some time that DFT methods can provide an accurate description of charge–charge and charge–dipole interactions.[166,171,172] DFT methods can sometimes provide a reasonable description of hydrogen bonding when suitable basis sets are used,[39,166,173–177] especially for water.[178,179] Interestingly, despite the tendency of DFT interaction energy to converge rapidly to the 1-particle CBS limit (typically with aug-cc-pVTZ or aug-cc-pVQZ basis sets),[168] results are still sensitive to the type basis set used for the calculations.[169] The "best" functional tested with the correlation-consistent aug-cc-pVDZ and aug-cc-pVTZ basis sets will be far from the best when the split-valence Pople-style basis sets (e.g., 6-31++G*) are employed.

Some of the most disturbing news regarding the applicability of density functional methods to hydrogen bonding came in 2004 when Ireta, Neugebauer, and Scheffler noticed that, for the Perdew, Burke, Ernzerhof (PBE) functional, errors in E_{int} increase as hydrogen bonds deviate from linearity.[180] Shortly thereafter, Cybulski and Severson examined 12 popular functionals and reported a closely related observation that none can describe intermolecular PESs properly because they failed to reproduce the angular and distance dependencies of E_{int}.[181] A study from the author's lab noted that DFT methods can have problems characterizing the nature of transition states and higher order saddle points (i.e., the correct number of imaginary frequencies) for a system as simple as the water dimer.[182] Nevertheless, these studies suggest that the functionals can be used to identify minima in cases where electrostatic interactions dominate in that region of the PES.

Density functional theory methods should not be used when dispersion plays a significant role in the noncovalent interactions. Conventional DFT methods do not include dispersion, and the chemical consequences of this deficiency have been known for quite some time,[183,184] but the renewed interest in π-type interactions has fueled a great deal of work in this area.[141,185–188] A recent overview of these efforts can be found in Ref. 188. Of the three main ways to incorporate dispersion into DFT (empirical, nonempirical, and modification of existing functionals), the DFT method with an empirical

dispersion term (DFT-D) appears to be promising.[187–189] The DFT-D method, however, is still not nearly as reliable as high-accuracy WFT approaches such as those outlined above. While the nonempirical approaches (such as those of Becke[190–192]) are certainly appealing, they currently do not outperform DFT-D. The last approach, which attempts to include dispersion in DFT via modification of existing functionals, is by far the most popular of the three.[174,177,193–195] Unfortunately, it seems that modifications to the exchange functional leading to a successful description of dispersion interactions also happen to destroy any ability to reliably describe hydrogen bonding. When examining the performance of newly developed functionals, it is important to note that rare gas dimers are a poor model for dispersion-bound molecular clusters. Just because a functional gives reasonable results for rare gas dimers does not mean that similar performance can be expected for molecular dimers.

Guidelines

Although being an oversimplification, noncovalent interactions can be divided into three categories to help select less demanding computational procedures when studying a particular weakly bound cluster.

Category 1 (*Easy*) Strong noncovalent interactions that are dominated by the electrostatic component of the interaction energy tend to be fairly easy to compute. *MP2 will provide excellent results while most DFT methods will generally provide reliable results near minima on the PES.*

Category 2 (*Hard*) Interactions in which dispersion plays a non-negligible role tend to be more difficult to compute. *MP2 will provide reasonable results while conventional DFT methods will not even provide a qualitatively correct description of these interactions across the PES.*

Category 3 (*Problematic*) Dispersion interactions involving one or more delocalized π electron systems are exceptionally difficult to describe. *MP2 will overbind in a manner that is inconsistent across the PES, and conventional DFT methods still provide an unphysical description of the interactions.*

OTHER COMPUTATIONAL ISSUES

Basis Set Superposition Error and Counterpoise Corrections

As noted when introducing the Boys–Bernardi CP correction above, BSSE is a concern whenever the supermolecule method is used to compare the energies of fragments to the energy of the entire cluster [i.e., when computing the dissociation (D_e) or interaction (E_{int}) energy].

Although many arguments for and against CP corrections have been made over the years, this part of the chapter will briefly illustrate three important concepts related to this issue.

The CP procedure can lead to unphysical descriptions of PESs that are not easily corrected.

CP corrections often do not improve calculated interaction energies. In fact, the procedure can even make results worse.

BSSE is a poor diagnostic for the quality of a computed D_e or E_{int}. The crucial quantity is the basis set completeness error (BSCE).

While the CP procedure is useful when examining specific structures, it is sometimes desirable to examine a path across the PES or reaction profile that might include, for example, reactants, products, and a transition state (TS). Generating a CP-corrected potential energy curve or reaction profile can introduce a new set of problems in certain circumstances. As demonstrated by Lendvay and Mayer, the Boys–Bernardi CP procedure (and variations thereof) can actually produce discontinuities in the PES near the TS and even give different TS energies for the forward and reverse reactions.[196] Fortunately, this unphysical behavior is normally limited to regions near the TS.

To illustrate the last two points, consider the D_e of $(H_2O)_2$ and $(H_2O)_3$. The MP2 CBS limits have been determined from explicitly correlated MP2-R12 computations with the K2−− basis set to be 20.76 kJ mol^{-1} for the C_s global minimum of $(H_2O)_2$ and 66.12 kJ mol^{-1} for the cyclic C_1 global minimum of $(H_2O)_3$.[118,119,197] (The K2−− basis set is constructed by removing functions with the two highest angular momentum values from Klopper's K2 basis set,[198] which corresponds to *f* and *g* functions for H, and *g* and *h* functions for O.) Figures 8 and 9 show how CP-corrected and uncorrected MP2 calculations deviate from the corresponding CBS limit when using the aug-cc-pV*X*Z and haug-cc-pV*X*Z (diffuse functions only added to O atoms) families of basis sets. The height of a particular bar above the *x* axis indicates the basis set completeness error (BSCE) for that basis set while the combined height of a bar above and its CP-corrected counterpart below the *x* axis represents the magnitude of BSSE for that basis set. For both $(H_2O)_2$ and $(H_2O)_3$, the MP2 dissociation energies converge systematically to the CBS limit from below when the CP procedure is applied and from above when it is not.

Closer examination of the data presented in Figures 8 and 9 reveals that the errors associated with the CP-corrected dissociation energies are almost always larger than those that are not corrected for BSSE (i.e., the bars below the *x* axis are larger than those above it). Only for aug-cc-pVQZ, aug-cc-pV5Z, and aug-cc-pV6Z D_e values for $(H_2O)_2$ does the CP procedure offer any improvement (and merely on the order of 0.1 kJ mol^{-1}). In these particular cases, the CP corrections are clearly not worth the substantial additional effort.

Although these trends have been observed elsewhere,[133,199] they do not necessarily apply to all weakly bound complexes. Sinnokrot and Sherrill have

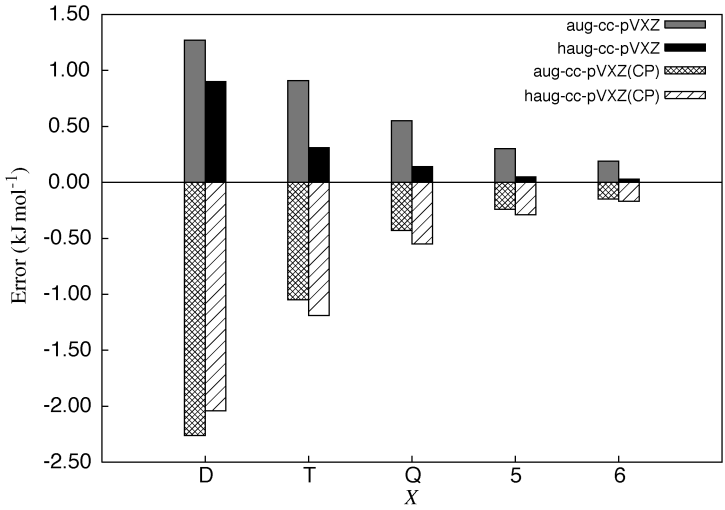

Figure 8 Errors relative to the MP2 CBS limit D_e for $(H_2O)_2$ using data from Ref. 118.

noted the opposite trend for benzene dimer interaction energies, and they report that the CP-corrected values converge to the CBS limit more rapidly than the uncorrected ones.[135]

The data in Figure 9 demonstrate nicely why BSSE should not be used to judge the quality of a particular D_e. The CP-corrected haug-cc-pVTZ D_e

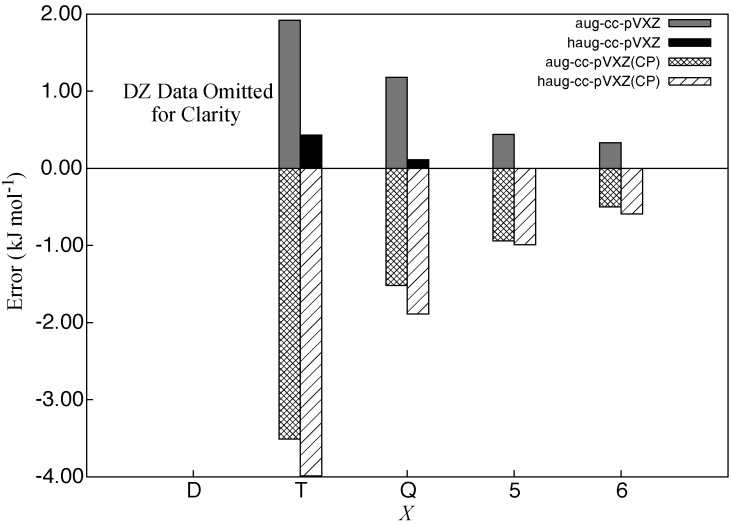

Figure 9 Errors relative to the MP2 CBS limit D_e for $(H_2O)_3$ using data from this work and Ref. 119. The errors with the double-ζ basis sets are so large that they have been omitted.

underestimates the MP2 CBS limit by 3.99 kJ mol^{-1} (striped bar) while the uncorrected value overestimates it by 0.43 kJ mol^{-1} (solid black bar). The difference between the two values, 4.42 kJ mol^{-1}, is the BSSE. If the MP2 CBS limit was not known, one would conclude that the haug-cc-pVTZ basis set is rather poor because of this large BSSE. However, the haug-cc-pVTZ is an excellent basis set for the D_e of the water trimer because the basis completeness error (BSCE) is only 0.43 kJ mol^{-1} (or $\approx$ 0.1 kcal mol^{-1}).

Beyond Interaction Energies: Geometries and Vibrational Frequencies

Care must be taken when interpreting computed equilibrium geometries and vibrational frequencies[44] when dealing with the extremely flat PESs of weakly bound clusters. For example, the vibrational frequencies associated with the large amplitude intermolecular motions are highly anharmonic. Consequently, estimates of the zero-point vibrational energy (ZPE or ZPVE) based on harmonic vibrational frequencies can be misleading. Furthermore, these harmonic frequencies for floppy vibrational modes can be sensitive to both the electronic structure method and basis set used, even for simple hydrogen bonding prototypes.[182,200]

In the case of equilibrium structures, the flat nature of the PESs can actually be an asset because it implies that the energy of a weakly bound cluster is fairly insensitive to changes in the intermolecular geometrical parameters. Consequently, MP2 optimizations with a sufficiently flexible triple-ζ basis set [e.g, TZ2P(f, d)+dif, aug-cc-pVTZ, TZVPP] usually provide sufficiently reliable structures for an accurate assessment of the interaction energy.[44,201] [Although "sufficiently flexible" is not a very precise description, it is generally agreed that the basis set needs to include two sets of polarization functions as well as at least one set of higher angular momentum functions (e.g., f functions for C, N, O, and F) and possibly diffuse functions.] However, the physical significance of these structures is not always clear since the ZPVE of the cluster may be larger than the barrier(s) separating minima on the PES.

Concluding Remarks

As with all areas of computational chemistry, the study of noncovalent interactions in weakly bound van der Waals clusters has benefited from the rapid improvements in hardware and software. As a result, high-accuracy benchmark databases that span the entire spectrum of weak interactions are now available.[42,177] Although relatively new, these collections of interaction energies have already been used to calibrate less demanding quantum model chemistries in the hopes of identifying methods that can be applied confidently to larger systems. However, a need exists for similar high-accuracy data for clusters (trimers, tetramers, etc.), not just dimers. Given the significant role

that cooperative effects can play in hydrogen-bonding networks, it is imperative that methods be able to describe the nonadditivity as well as the 2-body interactions. A consistent benchmark cluster database for the entire range of noncovalent interactions will play an essential role in the development of practical computational strategies for large clusters and explicit solvation models.

ACKNOWLEDGMENTS

I thank the current and former members of my research group at the University of Mississippi for their assistance and input during the preparation of this review, and I would also acknowledge the National Science Foundation for financial support (CHE-0517067, EPS-0132618).

REFERENCES

1. G. C. Pimentel and A. L. McClellan, *The Hydrogen Bond*, Freeman, San Francisco, 1960.
2. S. N. Vinogradov and R. H. Linnell, *Hydrogen Bonding*, Van Nostrand Reinhold, New York, 1971.
3. G. A. Jeffrey and W. Saenger, *Hydrogen Bonding in Biological Structures*, Springer, Berlin, 1991.
4. A. J. Stone, *The Theory of Intermolecular Forces*, Oxford University Press, Oxford, UK, 1996.
5. G. A. Jeffrey, *An Introduction to Hydrogen Bonding*, Oxford University Press, Oxford, UK, 1997.
6. C. Desfrançois, S. Carles, and J. Schermann, *Chem. Rev.*, **100**, 3943 (2000). Weakly Bound Clusters of Biological Interest.
7. V. A. Parsegian, *Van der Waals Forces*, Cambridge University Press, New York, 2006, page 10.
8. J. S. McDougal, M. S. Kennedy, J. M. Sligh, S. P. Cort, A. Mawle, and J. K. A. Nicholson, *Science*, **231**, 382 (1986). Binding of HLV-III/LAV to T4+ Cells by a Complex of the 110K Viral Protein and the T4 Molecule.
9. C. Borchers and K. B. Tomer, *Biochemistry*, **38**, 11734 (2000). Characterization of the Noncovalent Complex of Human Immunodeficiency Virus Glycoprotein 120 with Its Cellular Receptor CD4 by Matrix-Assisted Laser Desorption/Ionization Mass Spectrometry.
10. T. Peters, Ed., *All about Albumin: Biochemistry, Genetics and Medical Applications*, Academic, San Diego, 1996.
11. V. Vaida and J. Headrick, *J. Phys. Chem. A*, **104**, 5401 (2000). Physicochemical Properties of Hydrated Complexes in the Earth's Atmosphere.
12. W. Klemperer and V. Vaida, *Proc. Nat. Acad. Sci. U.S.A.*, **103**, 10584 (2006). Cluster Chemistry and Dynamics Special Feature: Molecular Complexes in Close and Far Away.
13. P. Schuster and P. Wolschann, *Monat. Chem.*, **130**, 947 (1999). Hydrogen Bonding: From Small Clusters to Biopolymers.
14. C.-D. Poon and E. T. Samulski, *J. Am. Chem. Soc.*, **122**, 5642 (2000). Do Bridging Water Molecules Dictate the Structure of a Model Dipeptide in Aqueous Solution?
15. A. Karshikoff, *Non-Covalent Interactions in Proteins*, Imperial College Press, London, 2006.
16. J. Černý and P. Hobza, *Phys. Chem. Chem. Phys.*, **9**, 5281 (2007). Non-Covalent Interactions in Biomacromolecules.
17. E. A. Meyer, R. K. Castellano, and F. Diederich, *Angew. Chem. Int. Ed. Engl.*, **42**, 1210 (2003). Interactions with Aromatic Rings in Chemical and Biological Recognition.

18. S. C. Zimmerman and P. S. Corbin, *Struct. Bonding*, **96**, 63 (2000). Heteroaromatic Modules for Self-Assembly Using Multiple Hydrogen Bonds.
19. S. H. M. Söontjens, R. P. Sijbesma, M. H. P. van Generen, and E. W. Meijer, *J. Am. Chem. Soc.*, **122**, 7487 (2000). Stability and Lifetime of Quadruply Hydrogen Bonded 2-Ureido-4 [1*H*]-pyrimidinone Dimers.
20. K. I. Hagen, C. M. Schwab, J. O. Edwards, J. G. Jones, R. G. Lawler, and D. A. Sweigart, *J. Am. Chem. Soc.*, **110**, 7024 (1988). Cobalt-59 NMR of Cobalt(III) Porphyrin Complexes. 2. Electric Field Gradients, d-Orbital Populations, and Hydrogen Bonding.
21. X. Xu and S. C. F. Au-Yeng, *J. Am. Chem. Soc.*, **122**, 6468 (2000). A DFT and ^{59}Co Solid-State NMR Study of the Chemical Shielding Property and Electronic Interaction in the Metalloporphyrin System.
22. W. Adam, K. Peters, E. Peters, and S. B. Schambony, *J. Am. Chem. Soc.*, **122**, 7610 (2000). Control through Hydrogen Bonding Mediated by the Urea Functionality of Chiral Auxilliaries.
23. K. N. Rankin, J. W. Gauld, and R. J. Boyd, *J. Am. Chem. Soc.*, **122**, 5384 (2000). Catalysis Mediated by Hydrogen Bonding: A Computational Study of the Aminolysis of 6-Chloropyrimidine.
24. D. Chandler, J. D. Weeks, and H. C. Andersen, *Science*, **220**, 787 (1983). Van der Waals Picture of Liquids, Solids, and Phase Transformations.
25. R. Ludwig, *Angew. Chem. Int. Ed. Engl.*, **40**, 1808 (2001). Water: From Clusters to the Bulk.
26. D. Hadži, Ed., *Theoretical Treatments of Hydrogen Bonding*, Wiley, Chichester, UK, 1997.
27. S. Scheiner, Ed., *Molecular Interactions: From van der Waals to Strongly Bound Complexes*, Wiley, Chichester, UK, 1997.
28. W. Gans and J. C. A. Boeyens, Eds., *Intermolecular Interactions*, Plenum, New York, 1998.
29. D. J. Wales, Ed., *Intermolecular Forces and Clusters I*, Vol. 115 of *Structure and Bonding*, Springer, Germany, 2005.
30. D. J. Wales, Ed., *Intermolecular Forces and Clusters II*, Vol. 116 of *Structure and Bonding*, Springer, Germany, 2005.
31. I. G. Kaplan, *Intermolecular Interactions: Physical Picture, Computational Methods and Model Potentials*, Wiley, Chichester, UK, 2006.
32. A. K. Rappe and E. R. Bernstein, *J. Phys. Chem. A*, **104**, 6117 (2000). Ab Initio Calculation of Nonbonded Interactions: Are We There Yet?
33. K. Müller-Dethlefs and P. Hobza, *Chem. Rev.*, **100**, 143 (2000). Noncovalent Interactions: A Challenge for Experiment and Theory.
34. O. Engkvist, P.-O. Åstrand, and G. Karlström, *Chem. Rev.*, **100**, 4087 (2000). Accurate Intermolecular Potentials Obtained from Molecular Wave Functions: Bridging the Gap between Quantum Chemistry and Molecular Simulations.
35. K. Kim, P. Tarakeshwar, and J. Lee, *Chem. Rev.*, **100**, 4145 (2000). Molecular Clusters of π-Systems: Theoretical Studies of Structures, Spectra, and Origin of Interaction Energies.
36. T. H. Dunning, *J. Phys. Chem. A*, **104**, 9062 (2000). A Road Map for the Calculation of Molecular Binding Energies.
37. C. E. Dykstra and J. M. Lisy, *J. Mol. Struct. (THEOCHEM)*, **500**, 375 (2000). Experimental and Theoretical Challenges in the Chemistry of Noncovalent Intermolecular Interaction and Clustering.
38. J. E. Del Bene and M. J. T. Jordan, *J. Mol. Struct. (THEOCHEM)*, **573**, 11 (2001). What a Difference a Decade Makes: Progress in Ab Initio Studies of the Hydrogen Bond.
39. P. Hobza, *Annu. Rep. Prog. Chem., Sect. C*, **100**, 3 (2004). Theoretical Studies of Hydrogen Bonding.
40. S. Tsuzuki, in *Intermolecular Forces and Clusters I*, Vol. 115 of *Structure and Bonding*, D. J. Wales, Ed., Springer, Berlin/Heidelberg Germany, 2005, pp. 149–193. Interactions with Aromatic Rings.

41. M. Sinnokrot and C. Sherrill, *J. Phys. Chem. A*, **110**, 10656 (2006). High-Accuracy Quantum Mechanical Studies of π–π Interactions in Benzene Dimers.

42. P. Jurečka, J. Šponer, J. Černý, and P. Hobza, *Phys. Chem. Chem. Phys.*, **8**, 1985 (2006). Benchmark Database of Accurate (MP2 and CCSD(T) Complete Basis Set Limit) Interaction Energies of Small Model Complexes, DNA Base Pairs, and Amino Acid Pairs.

43. S. Tsuzuki and T. Uchimaru, *Curr. Org. Chem.*, **10**, 745 (2006). Magnitude and Physical Origin of Intermolecular Interactions of Aromatic Molecules: Recent Progress of Computational Studies.

44. P. Hobza, R. Zahradnik, and K. Müller-Dethlefs, *Coll. Czech. Chem. Commun.*, **71**, 443 (2006). The World of Non-Covalent Interactions: 2006.

45. D. Feller and E. R. Davidson, in *Reviews in Computational Chemistry*, K. B. Lipkowitz and D. B. Boyd, Eds., VCH, New York, 1990, Vol. 1, pp. 1–44. Basis Sets for *Ab Initio* Molecular Orbital Calculations and Intermolecular Interactions.

46. S. Scheiner, in *Reviews in Computational Chemistry*, K. B. Lipkowitz and D. B. Boyd, Eds., VCH, New York, 1991, Vol. 2, pp. 165–218. Calculating the Properties of Hydrogen Bonds by *Ab Initio* Methods.

47. A. Castleman and K. Bowen, *J. Phys. Chem.*, **100**, 12911 (1996). Clusters: Structure, Energetics, and Dynamics of Intermediate States of Matter.

48. Z. Bačić and R. E. Miller, *J. Phys. Chem.*, **100**, 12945 (1996). Molecular Clusters: Structure and Dynamics of Weakly Bound Systems.

49. C. D. Sherrill, in *Reviews in Computational Chemistry*, K. B. Lipkowitz and T. R. Cundari, Eds., Wiley-VCH, Hoboken, NJ, 2008, Vol. 26, pp. 1–38. Computations of Noncovalent π Interactions.

50. Y. Xie, R. Grev, J. Gu, H. Schaefer, P. Schleyer, J. Su, X.-W. Li, and G. Robinson, *J. Am. Chem. Soc.*, **120**, 3773 (1998). The Nature of the Gallium-Gallium Triple Bond.

51. T. Ghanty, V. Staroverov, P. Koren, and E. Davidson, *J. Am. Chem. Soc.*, **122**, 1210 (2000). Is the Hydrogen Bond in Water Dimer and Ice Covalent?

52. M. G. Del Popolo, C. Pinilla, and P. Ballone, *J. Chem. Phys.*, **126**, 144705 (2007). Local and Semilocal Density Functional Computations for Crystals of 1-Alkyl-3-methyl-imidazolium Salts.

53. P. N. Day, J. H. Jensen, M. S. Gordon, S. P. Webb, W. J. Stevens, M. Krauss, D. Garmer, and D. Cohen, *J. Chem. Phys.*, **105**, 1968 (1996). An Effective Fragment Method for Modeling Solvent Effects in Quantum Mechanical Calculations.

54. I. Adamovic and M. S. Gordon, *J. Phys. Chem. A*, **110**, 10267 (2006). Methanol-Water Mixtures: A Microsolvation Study Using the Effective Fragment Potential Method.

55. K. Kitaura, E. Ikeo, T. Asada, T. Nakano, and M. Uebayasi, *Chem. Phys. Lett.*, **313**, 701 (1999). Fragment Molecular Orbital Method: An Approximate Computational Method for Large Molecules.

56. D. G. Fedorov and K. Kitaura, *J. Phys. Chem. A*, **111**, 6904 (2007). Extending the Power of Quantum Chemistry to Large Systems with the Fragment Molecular Orbital Method.

57. R. A. Christie and K. D. Jordan, in *Intermolecular Forces and Clusters II*, Vol. 116 of *Structure and Bonding*, D. J. Wales, Ed., Springer, Berlin/Heidelberg Germany, 2005, pp. 27–41. *n*-Body Decomposition Approach to the Calculation of Interaction Energies of Water Clusters.

58. B. W. Hopkins and G. S. Tschumper, *Chem. Phys. Lett.*, **407**, 362 (2005). Integrated Computational Methods for Extended π Systems: Multicentered QM/QM Studies of the Cyanogen and Diacetylene Trimers.

59. G. S. Tschumper, *Chem. Phys. Lett.*, **427**, 185 (2006). Multicentered Integrated QM:QM Methods for Weakly Bound Clusters: An Efficient and Accurate 2-Body:Many-Body Treatment of Hydrogen Bonding and van der Waals Interactions.

60. A. M. ElSohly, C. L. Shaw, M. E. Guice, B. D. Smith, and G. S. Tschumper, *Mol. Phys.*, **105**, 2777 (2007). Analytic Gradients for the Multicentered Integrated QM:QM Method for Weakly Bound Clusters: Efficient and Accurate 2-Body:Many-Body Geometry Optimizations.

61. B. Jeziorski, R. Moszynski, and K. Szalewicz, *Chem. Rev.*, **94**, 1887 (1994). Perturbation Theory Approach to Intermolecular Potential Energy Surfaces of van der Waals Complexes.

62. B. Jeziorski and K. Szalewicz, in *Encyclopedia of Computational Chemistry*, P. v. R. Schleyer, Ed., Wiley, Chichester, UK, 1998, pp. 1376–1398. Intermolecular Interactions by Perturbation Theory.

63. B. Jeziorski and K. Szalewicz, in *Handbook of Molecular Physics and Quantum Chemistry*, S. Wilson, Ed., Wiley, Chichester, UK, 2003, Vol. 3, pp. 232–279. Symmetry-Adapted Perturbation Theory.

64. K. Szalewicz, K. Patkowski, and B. Jeziorski, in *Intermolecular Forces and Clusters II*, Vol. 116 of *Structure and Bonding*, D. J. Wales, Ed., Springer, Berlin/Heidelberg Germany, 2005, pp. 44–117. Intermolecular Interactions via Perturbation Theory: From Diatoms to Biomolecules.

65. R. Moszynski, P. E. S. Wormer, B. Jeziorski, and A. van der Avoird, *J. Chem. Phys.*, **103**, 8058 (1995). Symmetry-Adapted Perturbation Theory of Nonadditive Three-Body Interactions in van der Waals Molecules. I. General Theory.

66. R. Moszynski, P. E. S. Wormer, T. G. A. Heijmen, and A. van der Avoird, *J. Chem. Phys.*, **108**, 579 (1998). Symmetry-Adapted Perturbation Theory of Nonadditive Three-Body Interactions in van der Waals Molecules. II. Application to the Ar_2–HF Interaction.

67. R. Moszynski, P. E. S. Wormer, B. Jeziorski, and A. van der Avoird, *J. Chem. Phys.*, **107**, 672 (1997). Erratum: Symmetry-Adapted Perturbation Theory of Nonadditive Three-Body Interactions in van der Waals Molecules. I. General Theory [J. Chem. Phys. **103**, 8058 (1995)].

68. T. J. Dick and J. D. Madura, in *Annual Reports in Computational Chemistry*, D. C. Spellmeyer, Ed., Elsevier, Amsterdam, 2005, Vol. 1, pp. 59–74. A Review of the TIP4P, TIP4P-Ew, TIP5P, and TIP5P-E Water Models.

69. A. J. Stone, *Science*, **315**, 1228 (2007). Water from First Principles.

70. R. Bukowski, K. Szalewicz, G. C. Groenenboom, and A. van der Avoird, *Science*, **315**, 1249 (2007). Predictions of the Properties of Water from First Principles.

71. A. DeFusco, D. Schofield, P. Daniel, and K. Jordan, *Mol. Phys.*, **105**, 2681 (2007). Comparison of Models with Distributed Polarizable Sites for Describing Water Clusters.

72. J. O. Hirschfelder, C. F. Curtiss, and R. B. Bird, *Molecular Theory of Gases and Liquids*, Wiley, New York, 1954.

73. H. Margenau and N. R. Kestner, *Theory of Intermolecular Forces*, Pergamon, Oxford, UK, 1971.

74. G. Chatasiński and M. M. Szczęśniak, *Chem. Rev.*, **94**, 1723 (1994). Origins of Structure and Energetics of van der Waals Clusters from Ab Initio Calculations.

75. J. D. van der Waals, 1873. Ph.D. Thesis, Leiden University, Leiden, Netherlands, 1873, *Over de Continuïteit van den Gas- en Vloeistoftoestand (On the Continuity of the Gas and Liquid State)*.

76. W. H. Keesom, *Physik. Z.*, **22**, 129 (1921). van der Waals Attractive Force.

77. W. H. Keesom, *Physik. Z.*, **23**, 225 (1922). Die Berechnung der Moleckularen Quadrupolmomente aus der Zustandgleichung.

78. P. Debye, *Physik. Z.*, **21**, 178 (1920). van der Waals' Cohesion Forces.

79. P. Debye, *Physik. Z.*, **22**, 302 (1921). Molecular Forces and Their Electrical Interpretation.

80. H. Falckenhagen, *Physik. Z.*, **23**, 87 (1922). Kohäsion and Zustandsgleichung bei Dipolgasen.

81. F. London, *Z. Phys. Chem. (B)*, **11**, 222 (1930). Über einige Eigenschaften und Anwendungen der Molekularkräfte.

82. F. London, *Trans. Faraday Soc.*, **33**, 8 (1937). The General Theory of Molecular Forces.

83. W. Heitler and F. London, *Z. Phys.*, **44**, 455 (1927). Interaction of Neutral Atoms and Homopolar Binding According to the Quantum Mechanics.

84. H. B. G. Casimir, *Proc. Nederl. Akad. Wetensch.*, **B51**, 793 (1948). On the Attraction between Two Perfectly Conducting Plates.

85. K. Morokuma and L. Pedersen, *J. Chem. Phys.*, **48**, 3275 (1968). Molecular-Orbital Studies of Hydrogen Bonds. An *Ab Initio* Calculation for Dimeric H_2O.

86. T. L. Gilbert and A. C. Wahl, *J. Chem. Phys.*, **47**, 3425 (1967). Single-Configuration Wavefunctions and Potential Curves for the Ground States of He_2, Ne_2, and Ar_2.

87. R. Eisenschitz and F. London, *Z. Physik*, **60**, 491 (1930). The Relation between the van der Waals Forces and the Homeopolar Valence Forces.

88. F. London, *Z. Physik*, **63**, 245 (1930). Theory and Systematics of Molecular Forces.

89. J. H. van Lenthe, J. G. C. M. van Duijneveldt-van de Rijdt, and F. B. van Duijneveldt, *Adv. Chem. Phys.*, **69**, 521 (1987). Weakly Bonded Systems.

90. L. Pauling, *The Nature of the Chemical Bond and The Structure of Molecules and Crystals: An Introduction to Modern Structural Chemistry*, 3 ed., Cornell University Press, Ithaca, NY, 1960 (first edition published in 1939), page 12.

91. C. Maerker, P. v. R. Schleyer, K. Liedl, T. -K. Ha, M. Quack, and M. A. Suhm, *J. Comput. Chem.*, **18**, 1695 (1997). A Critical Analysis of Electronic Density Functionals for Structural, Energetic, Dynamic and Magnetic Properties of Hydrogen Fluoride Clusters.

92. Example input files for NWChem, MPQC, PSI3, ACES2 and Gaussian03 are available at http://quantum.chem.olemiss/Tutorials.

93. B. W. Hopkins, A. M. ElSohly, and G. S. Tschumper, *Phys. Chem. Chem. Phys.*, **9**, 1550 (2007). Reliable Structures and Energetics for Two New Delocalized $\pi\cdots\pi$ Prototypes: Cyanogen Dimer and Diacetylene Dimer.

94. N. R. Kestner, *J. Chem. Phys.*, **48**, 252 (1968). He-He Interaction in the SCF-MO Approximation.

95. B. Liu and A. D. McLean, *J. Chem. Phys.*, **59**, 4557 (1973). Accurate Calculation of the Attractive Interaction of Two Ground State Helium Atoms.

96. N. R. Kestner and J. E. Combariza, in *Reviews in Computational Chemistry*, K. B. Lipkowitz and D. B. Boyd, Eds., Wiley-VCH, New York, 1999, Vol. 13, pp. 99–132. Basis Set Superposition Errors: Theory and Practice.

97. H. B. Jansen and P. Ros, *Chem. Phys. Lett.*, **3**, 140 (1969). Non-Empirical Molecular Orbital Calculations on the Protonation of Carbon Monoxide.

98. S. F. Boys and F. Bernardi, *Mol. Phys.*, **19**, 553 (1970). The Calculation of Small Molecular Interactions by the Differences of Separate Total Energies. Some Procedures with Reduced Errors.

99. G. S. Tschumper, unpublished work.

100. T. P. Tauer and C. D. Sherrill, *J. Phys. Chem. A*, **109**, 10475 (2005). Beyond the Benzene Dimer: An Investigation of the Additivity of π–π Interactions.

101. A. Karpfen, in *Molecular Interactions: From van der Waals to Strongly Bound Complexes*, S. Scheiner, Ed., Wiley, New York, 1997, pp. 265–296. Case Studies in Cooperativity in Hydrogen-Bonded Clusters and Polymers.

102. A. Karpfen, *Adv. Chem. Phys.*, **123**, 469 (2002). Cooperative Effects in Hydrogen Bonding.

103. D. Hankins, J. W. Moskowitz, and F. H. Stillinger, *J. Chem. Phys.*, **53**, 4544 (1970). Water Molecule Interactions.

104. S. S. Xantheas, *J. Chem. Phys.*, **100**, 7523 (1994). Ab Initio Studies of Cyclic Water Clusters $(H_2O)_n$, $n = 1 - 6$. II. Analysis of Many-Body Interactions.

105. M. Quack and M. A. Suhm, in *Conceptual Perspectives in Quantum Chemistry*, J. -L. Calais and E. S. Kryachko, Eds., Kluwer, Dordrecht, 1997, Vol. III, pp. 415–464. Potential Energy Hypersurfaces for Hydrogen Bonded Clusters $(HF)_N$.

106. J. A. Pople, in *Energy, Structure, and Reactivity*, D. W. Smith and W. B. McRae, Eds., Wiley, New York, 1973, pp. 51–61. Theoretical Models for Chemistry.

107. R. J. Bartlett, *Ann. Rev. Phys. Chem.*, **32**, 359 (1981). Many-Body Perturbation Theory and Coupled Cluster Theory for Electron Correlation in Molecules.

108. T. D. Crawford and H. F. Schaefer, in *Reviews in Computational Chemistry*, K. B. Lipkowitz and D. B. Boyd, Eds., Wiley-VCH, New York, 2000, Vol. 14, pp. 33–136. An Introduction to Coupled Cluster Theory for Computational Chemists.

109. J. C. Slater, *Phys. Rev.*, **32**, 349 (1928). The Normal State of Helium.

110. K. Morokuma and J. R. Winick, *J. Chem. Phys.*, **52**, 1301 (1970). Molecular-Orbital Studies of Hydrogen Bonds. Dimeric H_2O with the Slater Minimal Basis.

111. P. A. Kollman and L. C. Allen, *J. Chem. Phys.*, **52**, 5085 (1970). Theory of the Hydrogen Bond: *Ab Initio* Calculations on Hydrogen Fluoride Dimer and the Mixed Water-Hydrogen Fluoride Dimer.

112. R. J. Bartlett and J. F. Stanton, in *Reviews in Computational Chemistry*, K. B. Lipkowitz and D. B. Boyd, Eds., Wiley-VCH, New York, 1994, Vol. 5, pp. 65–169. Applications of Post-Hartree-Fock Methods: A Tutorial.

113. K. Raghavachari and J. B. Anderson, *J. Phys. Chem.*, **100**, 12960 (1996). Electron Correlation Effects in Molecules.

114. D. P. Tew, W. Klopper, and T. Helgaker, *J. Comput. Chem.*, **28**, 1307 (2007). Electron Correlation: The Many-Body Problem at the Heart of Chemistry.

115. P. O. Löwdin, *Adv. Chem. Phys.*, **2**, 207 (1959). Correlation Problem in Many-Electron Quantum Mechanics. I. Review of Different Approaches and Discussion of Some Current Ideas.

116. M. L. Leininger, W. D. Allen, H. F. Schaefer, and C. D. Sherrill, *J. Chem. Phys.*, **112**, 9213 (2000). Is Møller–Plesset Perturbation Theory a Convergent *Ab Initio* Method?

117. J. Olsen, O. Christiansen, H. Koch, and P. Jørgensen, *J. Chem. Phys.*, **105**, 5082 (1996). Surprising Cases of Divergent Behavior in Møller-Plesset Perturbation Theory.

118. G. S. Tschumper, M. L. Leininger, B. C. Hoffman, E. F. Valeev, H. F. Schaefer, and M. Quack, *J. Chem. Phys.*, **116**, 690 (2002). Anchoring the Water Dimer Potential Energy Surface with Explicitly Correlated Computations and Focal Point Analyses.

119. J. A. Anderson, K. Crager, L. Fedoroff, and G. S. Tschumper, *J. Chem. Phys.*, **121**, 11023 (2004). Anchoring the Potential Energy Surface of the Cyclic Water Trimer.

120. B. W. Hopkins and G. S. Tschumper, *J. Phys. Chem. A*, **108**, 2941 (2004). *Ab Initio* Studies of $\pi \cdots \pi$ Interactions: The Effects of Quadruple Excitations.

121. T. H. Dunning, *J. Chem. Phys.*, **90**, 1007 (1989). Gaussian Basis Sets for Use in Correlated Molecular Calculations. I. The Atoms Boron through Neon and Hydrogen.

122. R. A. Kendall, T. H. Dunning, and R. J. Harrison, *J. Chem. Phys.*, **96**, 6796 (1992). Electron Affinities of the First-Row Atoms Revisited. Systematic Basis Sets and Wave Functions.

123. D. E. Woon and T. H. Dunning, *J. Chem. Phys.*, **98**, 1358 (1993). Gaussian Basis Sets for Use in Correlated Molecular Calculations. III. The Atoms Aluminum through Argon.

124. D. Feller, *J. Chem. Phys.*, **96**, 6104 (1992). Application of Systematic Sequences of Wave Functions to the Water Dimer.

125. D. Feller, *J. Chem. Phys.*, **98**, 7059 (1993). The Use of Systematic Sequences of Wave Functions for Estimating the Complete Basis Set, Full Configuration Interaction Limit in Water.

126. T. Helgaker, W. Klopper, H. Koch, and J. Noga, *J. Chem. Phys.*, **106**, 9639 (1996). Basis-Set Convergence of Correlated Calculations on Water.

127. E. F. Valeev, W. D. Allen, R. Hernandez, C. D. Sherrill, and H. F. Schaefer, *J. Chem. Phys.*, **118**, 8594 (2003). On the Accuracy Limits of Orbital Expansion Methods: Explicit Effects of *k*-Functions on Atomic and Molecular Energies.

128. J. M. L. Martin, *Chem. Phys. Lett.*, **259**, 669 (1996). Ab Initio Total Atomization Energies of Small Molecules—Towards the Basis Set Limit.

129. A. Halkier, T. Helgaker, W. Klopper, P. Jørgensen, and A. G. Császár, *Chem. Phys. Lett.*, **310**, 385 (1999). Comment on "Geometry Optimization with an Infinite Basis Set" [*J. Phys. Chem. A*, **103**, 651 (1999)] and "Basis-Set Extrapolation" [*Chem. Phys. Lett.*, **294**, 45 (1998)].

130. D. Bakowies, *J. Chem. Phys.*, **127**, 084105 (2007). Extrapolation of Electron Correlation Energies to Finite and Complete Basis Set Targets.

131. W. Klopper, F. R. Manby, S. Ten-no, and E. F. Valeev, *Int. Rev. Phys. Chem.*, **25**, 427 (2006). R12 Methods in Explicitly Correlated Molecular Electronic Structure Theory, page 427.

132. C. Ochsenfeld, J. Kussmann, and D. S. Lambrecht, in *Reviews in Computational Chemistry*, K. B. Lipkowitz and T. R. Cundari, Eds., Wiley-VCH, Hoboken, NJ, 2007, Vol. 23, pp. 1–82. Linear-Scaling Methods in Quantum Chemistry.

133. A. Boese, J. Martin, and W. Klopper, *J. Phys. Chem. A*, **111**, 11122 (2007). Basis Set Limit Coupled Cluster Study of H-Bonded Systems and Assessment of More Approximate Methods.

134. http://www.134.info.

135. M. Sinnokrot and C. Sherrill, *J. Phys. Chem. A*, **108**, 10200 (2004). Highly Accurate Coupled Cluster Potential Energy Curves for the Benzene Dimer: Sandwich, T-Shaped, and Parallel-Displaced Configurations.

136. P. Jurecka and P. Hobza, *J. Am. Chem. Soc.*, **125**, 15608 (2003). True Stabilization Energies for the Optimal Planar Hydrogen-Bonded and Stacked Structures of Guanine···Cytosine, Adenine···Thymine, and Their 9- and 1-Methyl Derivatives: Complete Basis Set Calculations at the MP2 and CCSD(T) Levels and Comparison with Experiment.

137. W. Klopper, H. P. Luthi, T. Brupbacher, and A. Bauder, *J. Chem. Phys.*, **101**, 9747 (1994). Ab Initio Computations Close to the One-Particle Basis Set Limit on the Weakly Bound van der Waals Complexes Benzene–Neon and Benzene–Argon.

138. P. Hobza, H. Selzle, and E. Schlag, *J. Phys. Chem.*, **100**, 18790 (1996). Potential Energy Surface for the Benzene Dimer. Results of Ab Initio CCSD(T) Calculations Show Two Nearly Isoenergetic Structures: T-Shaped and Parallel-Displaced.

139. M. Sinnokrot, E. Valeev, and C. Sherrill, *J. Am. Chem. Soc.*, **124**, 10887 (2002). Estimates of the Ab Initio Limit for π–π Interactions: The Benzene Dimer.

140. W. Klopper, M. Quack, and M. A. Suhm, *Mol. Phys.*, **94**, 105 (1998). Explicitly Correlated Coupled Cluster Calculations of the Electronic Dissociation Energies and Barriers to Concerted Hydrogen Exchange of $(HF)_n$ Oligomers ($n = 2, \ldots, 5$).

141. Y. Zhao and D. Truhlar, *J. Chem. Theo. Comput.*, **1**, 415 (2005). Benchmark Databases for Nonbonded Interactions and Their Use to Test Density Functional Theory.

142. S. Tsuzuki, K. Honda, T. Uchimaru, and M. Mikami, *J. Chem. Phys.*, **124**, 114304 (2006). Estimated MP2 and CCSD(T) Interaction Energies of n-Alkane Dimers at the Basis Set Limit: Comparison of the Methods of Helgaker et al. and Feller.

143. K. Riley and P. Hobza, *J. Phys. Chem. A*, **111**, 8257 (2007). Assessment of the MP2 Method, along with Several Basis Sets, for the Computation of Interaction Energies of Biologically Relevant Hydrogen Bonded and Dispersion Bound Complexes.

144. T. Van Mourik, A. K. Wilson, and T. H. Dunning, *Mol. Phys.*, **96**, 529 (1999). Benchmark Calculations with Correlated Molecular Wavefunctions. XIII. Potential Energy Curves for He_2, Ne_2 and Ar_2 Using Correlation Consistent Basis Sets through Augmented Sextuple Zeta.

145. S. Grimme, *J. Chem. Phys.*, **118**, 9095 (2003). Improved Second-Order Møller–Plesset Perturbation Theory by Separate Scaling of Parallel- and Antiparallel-Spin Pair Correlation Energies.

146. Y. Jung, R. C. Lochan, A. D. Dutoi, and M. Head-Gordon, *J. Chem. Phys.*, **121**, 9793 (2004). Scaled Opposite-Spin Second Order Møller-Plesset Correlation Energy: An Economical Electronic Structure Method.

147. R. Lochan, Y. Jung, and M. Head-Gordon, *J. Phys. Chem. A*, **109**, 7598 (2005). Scaled Opposite Spin Second Order Møller-Plesset Theory with Improved Physical Description of Long-Range Dispersion Interactions.

148. J. G. Hill, J. A. Platts, and H.-J. Werner, *Phys. Chem. Chem. Phys.*, **8**, 4072 (2006). Calculation of Intermolecular Interactions in the Benzene Dimer Using Coupled-Cluster and Local Electron Correlation Methods.

149. J. Hill and J. Platts, *J. Chem. Theo. Comput.*, **3**, 80 (2007). Spin-Component Scaling Methods for Weak and Stacking Interactions.

150. T. Takatani and C. D. Sherrill, *Phys. Chem. Chem. Phys.*, **9**, 6106 (2007). Performance of Spin-Component-Scaled Møller–Plesset Theory (SCS-MP2) for Potential Energy Curves of Noncovalent Interactions.

151. S. Saebø and P. Pulay, *Ann. Rev. Phys. Chem.*, **44**, 213 (1993). Local Treatment of Electron Correlation.

152. M. Schütz, G. Hetzer, and H.-J. Werner, *J. Chem. Phys.*, **111**, 5691 (1999). Low-Order Scaling Local Electron Correlation Methods. I. Linear Scaling Local MP2.

153. S. Saebø, in *Computational Chemistry. Review of Current Trends*, J. Lecszsynski, Ed., World Scientific, NJ, 2002, Vol. 7, pp. 63–87. Low-Scaling Methods for Electron Correlation.

154. M. Feyereisen, G. Fitzgerald, and A. Komornicki, *Chem. Phys. Lett.*, **208**, 359 (1993). Use of Approximate Integrals in Ab Initio Theory. An Application in MP2 Energy Calculations.

155. O. Vahtras, J. Almlöf, and M. Feyereisen, *Chem. Phys. Lett.*, **213**, 514 (1993). Integral Approximations for LCAO-SCF Calculations.

156. D. E. Bernholdt and R. J. Harrison, *Chem. Phys. Lett.*, **294**, 477 (1996). Large-Scale Correlated Electronic Structure Calculations: The RI-MP2 Method on Parallel Computers.

157. F. Weigend and M. Häser, *Theor. Chim. Acta*, **97**, 331 (1996). RI-MP2: First Derivatives and Global Consistency.

158. F. Weigend, M. Häser, H. Patzelt, and R. Ahlrichs, *Chem. Phys. Lett.*, **294**, 143 (1998). RI-MP2: Optimized Auxiliary Basis Sets and Demonstration of Efficiency.

159. H.-J. Werner, F. R. Manby, and P. J. Knowles, *J. Chem. Phys.*, **118**, 8149 (2003). Fast Linear Scaling Second-Order Møller-Plesset Perturbation Theory (MP2) Using Local and Density Fitting Approximations.

160. N. J. Russ and T. D. Crawford, *J. Chem. Phys.*, **121**, 691 (2004). Potential Energy Surface Discontinuities in Local Correlation Methods.

161. J. E. Subotnik and M. Head-Gordon, *J. Chem. Phys.*, **123**, 064108 (2005). A Local Correlation Model That Yields Intrinsically Smooth Potential-Energy Surfaces.

162. P. Jurečka, P. Nachtigall, and P. Hobza, *Phys. Chem. Chem. Phys.*, **3**, 4578 (2001). RI-MP2 Calculations with Extended Basis Set: A Promising Tool for Study of H-Bonded and Stacked DNA Base Pairs.

163. J. Del Bene and I. Shavitt, in *Molecular Interactions: From van der Waals to Strongly Bound Complexes*, S. Scheiner, Ed., Wiley, Chichester, UK, 1997, pp. 157–180. The Quest for Reliability in Calculated Properties of Hydrogen-Bonded Systems.

164. H. Guo, S. Sirois, E. I. Proynov, and D. R. Salahub, in *Theoretical Treatments of Hydrogen Bonding*, D. Hadži, Ed., Wiley, Chichester, UK, 1997, pp. 49–74. Density Functional Theory and Its Applications to Hydrogen-Bonded Systems.

165. J. Del Bene, in *Encyclopedia of Computational Chemistry*, P. v. R. Schleyer, Ed., Wiley, Chichester, UK, 1998, pp. 1263–1271. Hydrogen Bonding: 1.

166. A. D. Rabuck and G. E. Scuseria, *Theor. Chim. Acta*, **104**, 439 (2000). Performance of Reccently Developed Kinetic Energy Density Functionals for the Calculation of Hydrogen Binding Strengths and Hydrogen Bonded Structures.

167. J. Van de Vondele, F. Mohamed, M. Krack, J. Hutter, M. Sprik, and M. Parrinello, *J. Chem. Phys.*, **122**, 014515 (2005). The Influence of Temperature and Density Functional Models in Ab Initio Molecular Dynamics Simulation of Liquid Water.

168. G. Csonka, A. Ruzsinszky, and J. Perdew, *J. Phys. Chem. B*, **109**, 21471 (2005). Proper Gaussian Basis Sets for Density Functional Studies of Water Dimers and Trimers.

169. K. Riley, B. Op'tHolt, and K. Merz, *J. Chem. Theo. Comput.*, **3**, 407 (2007). Critical Assessment of the Performance of Density Functional Methods for Several Atomic and Molecular Properties.

170. B. N. Papas and H. F. Schaefer, *J. Mol. Struct. (THEOCHEM)*, **768**, 175 (2006). Concerning the Precision of Standard Density Functional Programs: Gaussian, Molpro, NWChem, Q-Chem, and Gamess.

171. A. Pudzianowski, *J. Phys. Chem.*, **100**, 4781 (1996). A Systematic Appraisal of Density Functional Methodologies for Hydrogen Bonding in Binary Ionic Complexes.

172. M. Meot-Ner(Mautner), *Chem. Rev.*, **105**, 213 (2005). The Ionic Hydrogen Bond.

173. S. Sirois, E. I. Proynov, D. T. Nguyen, and D. R. Salahub, *J. Chem. Phys.*, **107**, 6770 (1997). Hydrogen-Bonding in Glycine and Malonaldehyde: Performance of the Lap1 Correlation Functional.

174. Y. Zhao and D. Truhlar, *J. Phys. Chem. A*, **108**, 6908 (2004). Hybrid Meta Density Functional Theory Methods for Thermochemistry, Thermochemical Kinetics, and Noncovalent Interactions: The MPW1B95 and MPWB1K Models and Comparative Assessments for Hydrogen Bonding and van der Waals Interactions.

175. J. Sponer, P. Jurecka, and P. Hobza, *J. Am. Chem. Soc.*, **126**, 10142 (2004). Accurate Interaction Energies of Hydrogen-Bonded Nucleic Acid Base Pairs.

176. J. Černý and P. Hobza, *Phys. Chem. Chem. Phys.*, **7**, 1624 (2005). The X3LYP Extended Density Functional Accurately Describes H-Bonding But Fails Completely for Stacking.

177. Y. Zhao, N. Schultz, and D. Truhlar, *J. Chem. Theo. Comput.*, **2**, 364 (2006). Design of Density Functionals by Combining the Method of Constraint Satisfaction with Parametrization for Thermochemistry, Thermochemical Kinetics, and Noncovalent Interactions.

178. J. Su, X. Xu, and W. Goddard, *J. Phys. Chem. A*, **108**, 10518 (2004). Accurate Energies and Structures for Large Water Clusters Using the X3LYP Hybrid Density Functional.

179. E. Dahlke and D. Truhlar, *J. Phys. Chem. B*, **109**, 15677 (2005). Improved Density Functionals for Water.

180. J. Ireta, J. Neugebauer, and M. Scheffler, *J. Phys. Chem. A*, **108**, 5692 (2004). On the Accuracy of DFT for Describing Hydrogen Bonds: Dependence on the Bond Directionality.

181. S. M. Cybulski and C. E. Seversen, *J. Chem. Phys.*, **122**, 014117 (2005). Critical Examination of the Supermolecule Density Functional Theory Calculations of Intermolecular Interactions.

182. J. A. Anderson and G. S. Tschumper, *J. Phys. Chem. A*, **110**, 7268 (2006). Characterizing the Potential Energy Surface of the Water Dimer with DFT: Failures of Some Popular Functionals for Hydrogen Bonding.

183. S. Kristyán and P. Pulay, *Chem. Phys. Lett.*, **229**, 175 (1994). Can (Semi)local Density Functional Theory Account for the London Dispersion Forces?

184. P. Hobza, J. Šponer, and T. Reschel, *J. Comput. Chem.*, **16**, 1315 (1995). Density-Functional Theory and Molecular Clusters.

185. E. R. Johnson, R. A. Wolkow, and G. A. DiLabio, *Chem. Phys. Lett.*, **394**, 334 (2004). Application of 25 Density Functionals to Dispersion-Bound Homomolecular Dimers.

186. Y. Zhao and D. Truhlar, *J. Phys. Chem. A*, **110**, 5121 (2006). Comparative DFT Study of van der Waals Complexes: Rare-Gas Dimers, Alkaline-Earth Dimers, Zinc Dimer, and Zinc-Rare-Gas Dimers.

187. C. Morgado, M. A. Vincent, I. H. Hillier, and X. Shan, *Phys. Chem. Chem. Phys.*, **9**, 448 (2007). Can the DFT-D Method Describe the Full Range of Noncovalent Interactions Found in Large Biomolecules?

188. P. Jurečka, J. Černý, P. Hobza, and D. R. Salahub, *J. Comput. Chem.*, **28**, 555 (2007). Density Functional Theory Augmented with an Empirical Dispersion Term. Interaction Energies and Geometries of 80 Noncovalent Complexes Compared with Ab Initio Quantum Mechanics Calculations.

189. S. Grimme, *J. Comput. Chem.*, **25**, 1463 (2004). Accurate Description of van der Waals Complexes by Density Functional Theory Including Empirical Corrections.

190. E. R. Johnson and A. D. Becke, *J. Chem. Phys.*, **123**, 024101 (2005). A Post-Hartree-Fock Model of Intermolecular Interactions.

191. E. R. Johnson and A. D. Becke, *J. Chem. Phys.*, **124**, 174104 (2006). A Post-Hartree-Fock Model of Intermolecular Interactions: Inclusion of Higher-Order Corrections.

192. A. D. Becke and E. R. Johnson, *J. Chem. Phys.*, **127**, 124108 (2007). A Unified Density-Functional Treatment of Dynamical, Nondynamical, and Dispersion Correlations.

193. A. D. Boese and N. C. Handy, *J. Chem. Phys.*, **114**, 5497 (2001). A New Parametrization of Exchange-Correlation Generalized Gradient Approximation Functionals.

194. A. D. Boese, A. Chandra, J. M. L. Martin, and D. Marx, *J. Chem. Phys.*, **119**, 5965 (2003). From Ab Initio Quantum Chemistry to Molecular Dynamics: The Delicate Case of Hydrogen Bonding in Ammonia.

195. X. Xu and W. A. Goddard, *Proc. Natl. Acad. Sci. USA*, **101**, 2673 (2004). The X3LYP Extended Density Functional for Accurate Descriptions of Nonbond Interactions, Spin States, and Thermochemical Properties.

196. F. Weigend, M. Häser, H. Patzelt, and R. Ahlrichs, *Chem. Phys. Lett.*, **297**, 365 (1998). RI-MP2: Optimized Auxiliary Basis Sets and Demonstration of Efficiency.

197. Additional computations performed for this work.

198. W. Klopper, *J. Chem. Phys.*, **102**, 6168 (1995). Limiting Values for Møller-Plesset Second-Order Correlation Energies of Polyatomic Systems: A Benchmark Study on Ne, HF, H_2O, N_2, and He$\cdots$He.

199. M. Masamura, *Theor. Chem. Acc.*, **106**, 301 (2001). The Effect of Basis Set Superposition Error on the Convergence of Interaction Energies.

200. G. S. Tschumper, M. D. Kelty, and H. F. Schaefer, *Mol. Phys.*, **96**, 493 (1999). Subtle Basis Set Effects on Hydrogen Bonded Systems.

201. S. S. Xantheas, C. J. Burnham, and R. J. Harrison, *J. Chem. Phys.*, **116**, 1493 (2002). Development of Transferable Interaction Models for Water. II. Accurate Energetics of the First Few Water Clusters from First Principles.

CHAPTER 3

Excited States from Time-Dependent Density Functional Theory

Peter Elliott,[a] Filipp Furche,[b,c] and Kieron Burke[c]

[a]*Department of Physics and Astronomy, University of California, Irvine, California*
[b]*Institut für Physikalische Chemie, Universität Karlsruhe, Karlsruhe, Germany*
[c]*Department of Chemistry, University of California, Irvine, California*

INTRODUCTION

Ground-state density functional theory[1–3] has become the method of choice for calculating ground-state properties of large molecules because it replaces the interacting many-electron problem with an effective single-particle problem that can be solved much more quickly. It is based on rigorous theorems[1,2,4] and a hierarchy of increasingly accurate approximations, such as the local density approximation (LDA), generalized gradient approximations (GGAs),[5–7] and hybrids of exact exchange with GGA.[8] For example, a recent ground-state calculation[9] for crambin ($C_{203}H_{317}N_{55}O_{64}S_6$), a small protein, using TURBOMOLE[10] on a 1.5-GHz HP Itanium workstation took less than 7 h, which is extraordinarily fast for 2528 electrons, with 5587 contracted Cartesian Gaussian basis functions. Formally, however, ground-state

Reviews in Computational Chemistry, Volume 26
edited by Kenny B. Lipkowitz and Thomas R. Cundari

density functional theory predicts only ground-state properties, not electronic excitations.

Time-dependent density functional theory (TDDFT),[11–15] in contrast, applies the same philosophy as ground-state DFT to time-dependent problems. Here, the complicated many-body time-dependent Schrödinger equation is replaced by a set of time-dependent single-particle equations whose orbitals yield the same time-dependent density. We can do this because the Runge–Gross theorem[16] proves that, for a given initial wave function, particle statistics and interaction, a given time-dependent density can arise from, at most, one time-dependent external potential. This means that the time-dependent potential (and all other properties) is a functional of the time-dependent density.

Armed with a formal theorem, we can then define time-dependent Kohn–Sham (TDKS) equations that describe noninteracting electrons that evolve in a time-dependent Kohn–Sham potential but produce the same density as that of the interacting system of interest. Thus, just as in the ground-state case, the demanding interacting time-dependent Schrödinger equation (TDSE) is replaced by a much simpler set of equations. The price of this enormous simplification is that the exchange–correlation piece of the Kohn–Sham potential has to be approximated.

The most common time-dependent perturbation is a long-wavelength electric field, oscillating with frequency ω. In the usual situation, this field is a weak perturbation to the molecule, and one can therefore perform a linear response analysis. From the linear response, we can extract the optical absorption spectrum of the molecule due to electronic excitations. Thus, linear response TDDFT can be used to predict the transition frequencies to electronic excited states (along with many other properties), and this has been the primary use of TDDFT so far, with many applications to large molecules.

Figure 1 compares TDDFT and experiment for the electronic Circular Dichroism (CD) spectrum of the chiral fullerene C_{76}. A total of 240 optically allowed transitions were required to simulate the spectrum. The accuracy is clearly good enough to assign the absolute configuration of C_{76}. TDDFT calculations of this size typically take less than a day on low-end personal computers.

A random walk through some recent studies using TDDFT gives some feeling for the breadth of applications. Most are in the linear response regime. In inorganic chemistry, the optical response of many transition metal complexes[20–35] has been calculated, as have some X-ray absorption spectra.[36,37] In organic chemistry, heterocycles[38–43] have been examined among others,[44–46] including the response of thiouracil,[47] *s*-tetrazine,[48] and annulated porphyrins.[49] We also see TDDFT's use in studying various fullerenes.[50–55] TDDFT is also finding many uses in biochemistry[56–66] where,

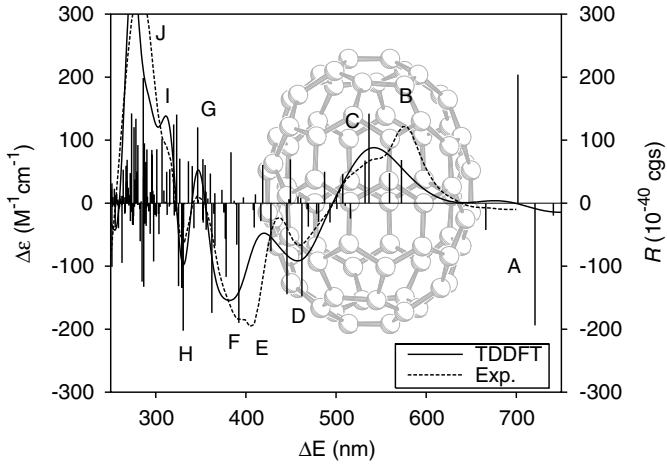

Figure 1 TDDFT calculation and experiment for the electronic CD spectrum of fullerene (^{f}A)-C_{76}. Calculations were performed with the BP86 functional and an augmented SVP basis set.[17] The RI-J approximation together with TZVP auxiliary basis sets[18] were used. Experimental data (in CH_2Cl_2) are from Ref. 19.

for example, DNA bases are under examination (an overview of this area may be found in Ref. 67). In photobiology, potential energy curves for the trans–cis photoisomerization of the protonated Schiff base of retinal[68] have been calculated, and calculations for green and blue fluorescent proteins have also been performed.[69,70] In the realm of photochemistry,[71] properties of chromophores[72–76] and dyes[77–83] have been computed. For these and other systems, there is great interest in charge-transfer excitations,[84–92] but, as we later discuss, intermolecular charge transfer is a demanding problem for TDDFT.

Another major area of application of TDDFT involves clusters, large and small, covalent and metallic, and everything in between,[93–112] as, for example, Met-Cars.[113] Several studies include solvent effects,[114–122] one example being the behavior of metal ions in explicit water.[123] TDDFT in the realm of linear response can also be used to examine chirality,[124–127] including calculating both electric and magnetic circular dichroism,[26,128–132] and it has been applied to both helical aromatics[133] and to artemisinin complexes in solution.[134] There exist applications in materials[135,136] and quantum dots,[137] but, as discussed below, the optical response of bulk solids requires some nonlocal approximations.[138]

Beyond the linear regime, there is also growing interest in second- and third-order response[139–142] in all these fields. In particular the field of nonlinear optics has been investigated heavily,[143–145] especially the phenomenon of two-photon absorption.[146–153]

In fact, TDDFT yields predictions for a huge variety of phenomena that can largely be classified into three groups: (1) the nonperturbative regime, with systems in laser fields so intense that perturbation theory fails, (2) the linear (and higher order) regime, which yields the usual optical response and electronic transitions, and (3) back to the ground state, where the fluctuation–dissipation theorem produces *ground-state* approximations from TDDFT treatments of excitations.

Overview

This chapter focuses primarily on the linear response regime. Throughout, we emphasize the difference between small molecules (atoms, diatomics, etc.) and the larger molecules that are of greater practical interest, where TDDFT is often the only practical first-principles method that can be used. We use naphthalene ($C_{10}H_8$) as an example to show how the selection of both the basis set and the exchange–correlation (XC) functional affects computed excitation energies and oscillator strengths. Small molecules are somewhat exceptional because they usually exhibit high symmetry that prevents strong mixing of the Kohn–Sham (KS) states due to configuration interaction, and also because basis set requirements are often exacerbated for small systems. Naphthalene is large enough to avoid these effects; reasonably accurate gas-phase experiments exist and correlated wave function calculations are still possible for such a molecule.

We will use atomic units ($e^2 = \hbar = m_e = 1$) throughout this tutorial, so that all energies are in hartrees ($1\mathrm{E_h} \simeq 27.2\,\mathrm{eV} \simeq 627.5\,\mathrm{kcal/mol}$) and distances in bohr ($\simeq 0.529$ Å) unless otherwise noted. For brevity, we drop comma's between arguments wherever the meaning is clear. In DFT and TDDFT, there is a confusing wealth of acronyms and abbreviations. Table 1 is designed to aid the readers' navigation through this maze.

The content of this review is organized as follows. The second and third main sections cover the basic formalism of the theory that is needed to understand where it comes from, why it works, and where it can be expected to fail. The fourth section focuses on details of implementation, especially basis-set selection, while the fifth section is devoted to performance and analyzing the sources of error in the basis-set limit. In the sixth section, we examine a few atoms in microscopic detail: Because we know the *exact* ground-state Kohn–Sham potential in such cases, we can assess the performance of TDDFT. The seventh section covers the many attempts that go beyond standard functionals approximations and highlights where such nonstandard functionals are needed. The eighth section covers topics outside the usual linear response approach to excitations, including ground-state functional derived from TDDFT, challenges for strong fields, and transport through single molecules. The last section summarizes this tutorial/review.

Table 1 Table of Acronyms and Abbreviations

A	Adiabatic
AC	Asymptotically corrected
ALDA	Adiabatic LDA
B88	Becke GGA of 1988
B3LYP	Hybrid functional using Becke exchange and LYP correlation
CASPT2	Complete active space second-order perturbation theory
CC	Coupled cluster
CIS	Configuration-interaction singlets
ee	electron–electron
ext	external
EXX	Exact exchange
GGA	Generalized gradient approximation
H	Hartree
HF	Hartree–Fock
HK	Hohenberg–Kohn
HXC	Hartree plus exchange–correlation
KLI	Krieger-Li-Iafrate approximation for exact exchange
KS	Kohn–Sham
LB94	van Leeuwen–Baerends asymptotically corrected functional
LDA	Local density approximation
LHF	Localized Hartree–Fock (accurate approximation to EXX)
LSDA	Local spin density approximation
LYP	Lee–Yang–Parr correlation
MAE	Mean absolute error
OEP	Optimized effective potential
PBE	Perdew–Burke–Ernzerhof GGA
PBE0	Hybrid based on PBE
QD	Quantum defect
QMC	Quantum Monte Carlo
RG	Runge–Gross
RPA	Random-phase approximation
SPA	Single-pole approximation
TDCDFT	Time-dependent current density functional theory
TDKS	Time-dependent Kohn–Sham
TDSE	Time-dependent Schrödinger equation
XC	Exchange–correlation

GROUND-STATE REVIEW

We review ground-state DFT rather quickly in this section and recommend reading Ref. 154 for a more comprehensive review. Many of the results discussed here are also referred to in later sections.

Formalism

Ground-state DFT is a completely different approach to solving the many-electron problem than is done in the traditional solution of the Schrödinger

equation. The Hohenberg–Kohn (HK) theorem[1] of 1964 states that for a given nondegenerate ground-state density $n(\mathbf{r})$ of fermions with a given interaction, the external potential $v_{\text{ext}}(\mathbf{r})$ that produced that density is unique (up to an additive constant). Hence if the density is known, $v_{\text{ext}}(\mathbf{r})$ is then known and so $\hat{H}$, the Hamiltonian, is known. From this and the number of particles (determined by the integral of the density), all properties of the system may be determined. In particular, the ground-state energy of the system E would be known. This is what we mean when we say these properties are functionals of the density, e.g., $E[n]$. It was later shown that the HK theorem holds even for degenerate ground states,[4] and modern DFT calculations use an analogous theorem applied to the spin densities, $n_\alpha(\mathbf{r}), n_\beta(\mathbf{r})$, where $\alpha, \beta = \pm\frac{1}{2}$, respectively.

The total energy for N electrons consists of three parts: the kinetic energy $T[\Psi]$, the electron–electron interaction $V_{\text{ee}}[\Psi]$, and the external potential energy $V_{\text{ext}}[\Psi]$, each of which is defined in Eqs. [1], [2], and [3], respectively:

$$T[\Psi] = \left\langle \Psi \middle| -\frac{1}{2}\sum_i^N \nabla_i^2 \middle| \Psi \right\rangle \quad [1]$$

$$V_{\text{ee}}[\Psi] = \left\langle \Psi \middle| \frac{1}{2}\sum_i^N \sum_{j\neq i}^N \frac{1}{|\mathbf{r}_i - \mathbf{r}_j|} \middle| \Psi \right\rangle \quad [2]$$

$$V_{\text{ext}}[\Psi] = \left\langle \Psi \middle| \sum_i^N v_{\text{ext}}(\mathbf{r}_i) \middle| \Psi \right\rangle \quad [3]$$

By the Rayleigh–Ritz principle, we find

$$\begin{aligned} E &= \min_\Psi \langle \Psi | \hat{H} | \Psi \rangle \\ &= \min_\Psi (T[\Psi] + V_{\text{ee}}[\Psi] + V_{\text{ext}}[\Psi]) \end{aligned} \quad [4]$$

If we rewrite the minimization as a two-step process,[155] we find

$$E = \min_{n_\alpha, n_\beta} \left\{ \min_{\Psi \to (n_\alpha, n_\beta)} (T[\Psi] + V_{\text{ee}}[\Psi] + V_{\text{ext}}[\Psi]) \right\}$$

where the inner search is over all interacting wave functions yielding spin densities n_α, n_β. We may pull the last term out of the inner minimization to give

$$\begin{aligned} E &= \min_{n_\alpha, n_\beta} \left(F[n_\alpha, n_\beta] + \sum_\sigma \int d^3 r \, v_{\text{ext}\sigma}(\mathbf{r}) n_\sigma(\mathbf{r}) \right) \\ &= \min_{n_\alpha, n_\beta} (E[n_\alpha, n_\beta]) \end{aligned} \quad [5]$$

where

$$F[n_\alpha, n_\beta] = \min_{\Psi \to (n_\alpha, n_\beta)} (T[\Psi] + V_{ee}[\Psi]) \quad [6]$$

$$= T[n_\alpha, n_\beta] + V_{ee}[n_\alpha, n_\beta] \quad [7]$$

is a universal functional independent of $v_{ext\sigma}(\mathbf{r})$.

Minimizing the total energy density functional, Eq. [5], for both spin densities by taking the functional derivative $\delta/\delta n_\sigma$, and using the Euler–Lagrange multiplier technique leads to

$$\frac{\delta F[n_\alpha, n_\beta]}{\delta n_\sigma} + v_{ext\sigma}(\mathbf{r}) = \mu \quad [8]$$

where μ is the chemical potential of the system.

Next we imagine a system of noninteracting electrons with the same spin densities. Applying the HK theorem to this noninteracting system, the potentials, $v_{S\sigma}$, that give densities $n_\sigma(\mathbf{r})$ as the ground-state spin densities for this system are unique. This is the fictitious Kohn–Sham (KS) system,[2] and the fully interacting problem is mapped to a noninteracting one that gives the exact same density. Solving the KS equations, which is computationally simple (at least compared to the fully interacting problem, which becomes intractable for large particle numbers), yields the ground-state density. The KS equations are

$$\left(-\tfrac{1}{2}\nabla^2 + v_{S\sigma}(\mathbf{r}) \right) \phi_{j\sigma}(\mathbf{r}) = \epsilon_{j\sigma} \phi_{j\sigma}(\mathbf{r}) \quad [9]$$

with spin densities

$$n_\sigma(\mathbf{r}) = \sum_{j=1}^{N_\sigma} |\phi_{j\sigma}(\mathbf{r})|^2 \quad [10]$$

where $v_{S\alpha}$, $v_{S\beta}$ are the KS potentials and N_σ is the number of spin σ electrons, $(N_\alpha + N_\beta = N)$.

In the top panel of Figure 2, we plot the exact density for the He atom from a highly accurate wave function calculation, and below that we plot the *exact* KS potential for this system. One can see that the KS potential is very different from the external potential. This is due to the fact that the KS single effective potential for the noninteracting system must give the correct interacting electron density. Because the Coulomb repulsion between the electrons shields the nucleus, and makes the charge density decay less rapidly than $e^{-4\mathbf{r}}$, the KS potential is more shallow than $v_{ext}(\mathbf{r})$.

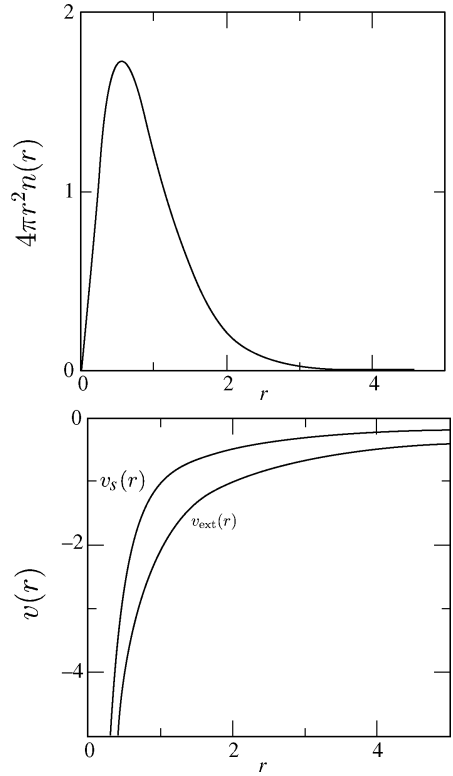

Figure 2 (*Top panel*) Exact radial density for the He atom found via the quantum Monte Carlo method.[156] (*Bottom panel*) The external and KS potentials for the He atom. The KS potential is found by inverting the KS equations using the exact KS orbitals (easily found for He if the exact density is known).

To derive an expression for $v_{S\sigma}(\mathbf{r})$, note that the Euler equation yielding the KS equations is

$$\frac{\delta T_S[n_\alpha, n_\beta]}{\delta n_\sigma} + v_{S\sigma}(\mathbf{r}) = \mu \qquad [11]$$

Here T_S is the kinetic energy of the KS electrons,

$$T_S = \sum_\sigma \sum_{j=1}^{N_\sigma} \int d^3r \frac{1}{2} |\nabla \phi_{j\sigma}(\mathbf{r})|^2$$

Rewriting $F[n_\alpha, n_\beta]$ in terms of the KS system gives

$$F[n_\alpha, n_\beta] = T_S[n_\alpha, n_\beta] + U[n] + E_{\text{XC}}[n_\alpha, n_\beta] \qquad [12]$$

where $U[n]$ is the Hartree energy, given by

$$U[n] = \frac{1}{2}\sum_{\sigma\sigma'}\int d^3r\, d^3r' \frac{n_\sigma(\mathbf{r})n_{\sigma'}(\mathbf{r}')}{|\mathbf{r}-\mathbf{r}'|} \quad [13]$$

and the exchange–correlation (XC) energy is defined by Eqs. [7] and [12]:

$$E_{\mathrm{XC}}[n_\alpha, n_\beta] = T[n_\alpha, n_\beta] - T_S[n_\alpha, n_\beta] + V_{\mathrm{ee}}[n_\alpha, n_\beta] - U[n] \quad [14]$$

Inserting Eq. [14] into Eq. [8] and comparing that to Eq. [11] gives a definition of the KS potential:

$$v_{S\sigma}(\mathbf{r}) = v_{\mathrm{ext}}(\mathbf{r}) + v_H(\mathbf{r}) + v_{\mathrm{XC}\sigma}(\mathbf{r}) \quad [15]$$

where the Hartree potential is the functional derivative of $U[n]$:

$$v_H(\mathbf{r}) = \frac{\delta U[n]}{\delta n(\mathbf{r})} = \sum_{\sigma'}\int d^3r' \frac{n_{\sigma'}(\mathbf{r}')}{|\mathbf{r}-\mathbf{r}'|} \quad [16]$$

while the XC potential is given by the functional derivative of the XC energy:

$$v_{\mathrm{XC}\sigma}(\mathbf{r}) = \frac{\delta E_{\mathrm{XC}}[n_\alpha, n_\beta]}{\delta n_\sigma(\mathbf{r})} \quad [17]$$

This derivation then closes the relationship between the KS system and the original physical problem. Once $E_{\mathrm{XC}}[n_\alpha, n_\beta]$ is known exactly or is approximated, $v_{\mathrm{XC}\sigma}(\mathbf{r})$ is determined by differentiation. The KS equations can be solved self-consistently for the spin densities and orbitals, and the total energy found by inserting those densities and orbitals into the total energy functional $E = T_S + U + E_{\mathrm{XC}} + V_{\mathrm{ext}}$. Unfortunately $E_{\mathrm{XC}}[n_\alpha, n_\beta]$ is not known exactly and must be approximated. There exists in the scientific community a *functional soup* of many different approximations of varying accuracy and computational cost, many of which are discussed in the following section.

For the He atom, when the KS equation is solved with the exact potential as shown in Figure 2, the highest occupied molecular orbital (HOMO) level is at -24.592 eV, the negative of the ionization energy of helium. In exact DFT, Koopmans theorem, which states $I = -\epsilon_{\mathrm{HOMO}}$, is exactly true.[157] In ground-state DFT, this is the only energy level of the fictitious KS system that has an immediate physical interpretation.

Before leaving our tutorial on ground-state formalism, we mention the optimized effective potential (OEP) method[158,159] in which the XC functional is written as a functional of the KS orbitals (which in turn are functionals of

the density). The exchange energy is then given by the familiar Hartree–Fock (HF) definition:

$$E_{\mathrm{X}} = -\frac{1}{2}\sum_{i,j=1}^{N}\sum_{\sigma}\int d\mathbf{r}\, d\mathbf{r}' \frac{\phi^*_{i\sigma}(\mathbf{r})\phi^*_{j\sigma}(\mathbf{r}')\phi_{j\sigma}(\mathbf{r})\phi_{i\sigma}(\mathbf{r}')}{|\mathbf{r}-\mathbf{r}'|} \qquad [18]$$

In contrast to HF, however, a single effective potential $v_{\mathrm{S}}^{\mathrm{XX}}(\mathbf{r})$ is found via the chain rule. Accurate orbital-dependent functionals for the correlation energy are extremely difficult to find, so only exchange is often used. In DFT, this is called exact exchange (EXX), because exchange is usually treated only approximately. EXX gives useful features such as derivative discontinuities and the correct asymptotic decay of the KS potential,[160] which, as we will see later, are important for TDDFT linear response.

Approximate Functionals

In any ground-state DFT calculation, we must use approximations for the functional dependence of the XC energy on the spin densities, and there now exists a hierarchy of such approximations. The simplest of these is the local density approximation (LDA), where the XC energy at a point $\mathbf{r}'$ is calculated as if it were a uniform electron gas with the spin densities $n_\sigma = n_\sigma(\mathbf{r}')$ in a constant positive background. The exchange energy for the uniform gas can be deduced analytically, but the correlation contribution is found using a combination of many-body theory and highly accurate quantum Monte Carlo (QMC) simulations for the electron gas of different densities.[161–164] The local spin density approximation (LSDA) is the simple generalization of LDA for different spins.

The local density approximation works remarkably well given the vast differences between homogeneous electron gases and atoms or molecules. Total energies are generally underestimated, however. Typically, the XC energy is underestimated by about 7%. When the performance of LDA is examined carefully, this small underestimation is due to a nice (but not completely accidental) cancellation of errors between the exchange part (underestimated by about 10%) and correlation (overestimated by 200–300%), which is typically four times smaller than exchange.

An obvious improvement to LDA would be to include information about how rapidly the density is changing via its gradient. This leads to the generalized gradient approximation (GGA). In the original Kohn–Sham study of 1965,[2] the simplest of these approximations was suggested. The gradient expansion approximation (GEA) was found by examining the slowly varying limit of the electron gas.[165] However it was soon found that GEA failed to improve the accuracy of LDA, and it sometimes made things worse. It was not until the late 1980s that accurate GGAs were constructed, the most

popular of which are BLYP [B88[5] (Becke) for exchange and LYP[6] (Lee, Yang, and Parr) for correlation] and PBE[7] (Perdew, Burke, Ernzerhof). These GGAs generally reduce atomization errors of LDA by a factor of 2–5.

The PBE functional is designed to improve upon the performance of LDA without losing the features of LDA that are correct. As such, it reduces to LDA for the uniform electron gas. A GGA should also satisfy as many exact conditions as possible, such as the Lieb–Oxford bound[166] or the form of the exchange energy in the slowly varying limit of the electron gas. In this regard, PBE is a nonempirical functional where all parameters are determined by exact conditions; and, because of its ability to treat bulk metals, it is the functional of choice in solid-state calculations and increasingly so in molecular quantum chemistry. When choosing a GGA, whether to use PBE or not should no longer be a question (although the crambin calculation of the introduction of this chapter used BP86,[5,316] for reasons explained in Ref. 9).

Finally, hybrid functionals mix in some fraction of exact exchange with a GGA. This is the Hartree–Fock exchange integral, Eq. [18], evaluated with the KS orbitals (which are functionals of the density). Only a small fraction of exact exchange (20–25%) is mixed in, so as to preserve the cancellation of errors that GGAs make use of.[167] The most widely used functional in chemistry is the hybrid functional B3LYP, which contains three experimentally fitted parameters[6,8,168] (although the parameter in B88 has recently been derived[169]). Other hybrid functionals include PBE0, where 25% of exact exchange is mixed in with the PBE functional.[170]

A less well-known feature to users of ground-state DFT is that while their favorite approximations may yield very good energies (and therefore structures, vibrations, thermochemistry, etc.) and rather good densities, they have poorly behaved potentials, at least far from nuclei. Figure 3 illustrates this for the He atom, showing the LDA potential compared to the exact KS potential. While the potential is generally good in the region $r < 2$, it decays much too fast far from the nucleus. The true KS potential falls off as $-1/r$,

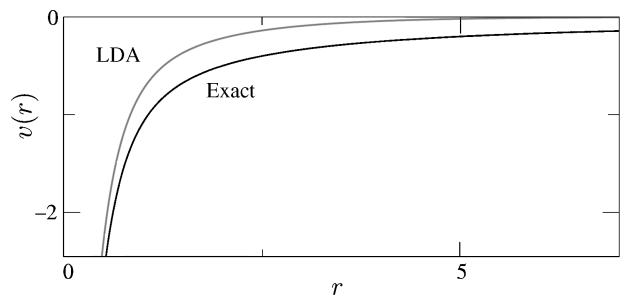

Figure 3 Exact and LDA KS potentials for the He atom. While the exact potential falls off as $-1/r$, the LDA decays much too quickly. This fast decay is common for nearly all existing functional and has major consequences for TDDFT.

whereas LDA decays exponentially. Accordingly, the KS eigenvalues and eigenvectors will be poor for the higher energy levels. To understand why poor potentials do not imply poor energies (and why these potentials are not as bad as they look), we recommend you read Ref. 171. But, as we shall see when we discuss performance, this has major consequences for TDDFT.

The technology for treating orbital-dependent functionals has developed over the past decade, and such functionals have helped cure this problem.[158] This technology is called the optimized effective potential (OEP)[172–174] described above. The first useful orbital functional was LDA-SIC, the self-interaction-corrected LDA of Perdew and Zunger.[162] More generally, the OEP method can handle any orbital-dependent functional, including treating exchange exactly. Orbital-dependent functionals naturally avoid the self-interaction error that is common in explicit density functionals. An (almost) exact implementation of the OEP equations is the localized Hartree–Fock (LHF) algorithm,[175,176] available in TURBOMOLE.[10]

Basis Sets

To actually solve the KS equations, the KS orbitals $\phi_{p\sigma}(\mathbf{r})$ are expanded in a *finite* set of basis functions $\chi_\nu(\mathbf{r})$:

$$\phi_{p\sigma}(\mathbf{r}) = \sum_\nu C_{p\nu\sigma}\chi_\nu(\mathbf{r}) \qquad [19]$$

The most common choice, by far, for the basis functions in quantum chemistry are atom-centered contracted Cartesian Gaussians[177]

$$\chi_\nu(\mathbf{r}) = \sum_i c_{i\nu} x^{l_x(\nu)} y^{l_y(\nu)} z^{l_z(\nu)} e^{-\zeta_{i\nu}(\mathbf{r}-\mathbf{R}_\nu)^2} \qquad [20]$$

where $l_x(\nu)$, $l_y(\nu)$, and $l_z(\nu)$ are positive integers or zero, and $l(\nu) = l_x(\nu) + l_y(\nu) + l_z(\nu)$ is somewhat loosely called l-quantum number of χ_ν. [$l = 0, 1, 2, 3, \ldots$ corresponds to $s, p, d, f, \ldots$ type Cartesian Gaussians.] The exponents $\zeta_{i\mu}$ and the contraction coefficients $c_{i\nu}$ are optimized in atomic calculations. Other common basis functions in use include Slater-type orbitals, plane waves, and piecewise defined functions on a numerical grid.

The approximation of the orbitals $\phi_{p\sigma}(\mathbf{r})$ by a finite linear combination of basis functions (also called LCAO, linear combination of atomic orbitals), Eq. [19], leads to a finite number of molecular orbitals (MOs). Thus, the KS equations and all derived equations are approximated by *finite*-dimensional matrix equations, which can be treated by established numerical linear and nonlinear algebra methods. When the basis set size is increased systematically, the computed properties converge to their basis set limit.

In a finite basis set, all operators become finite matrices; the matrix elements are integrals, as illustrated, for example, by Eq. [21]:

$$H_{\mu\nu\sigma}[n] = \int d^3r\, \chi_\mu(\mathbf{r}) H_\sigma[n] \chi_\nu(\mathbf{r}) \qquad [21]$$

The calculation and processing of such integrals is the main effort in almost all DFT numerical calculations. Gaussian basis functions have the distinct advantage that (1) most integrals can be evaluated analytically, and (2) they are spatially local. The latter advantage implies that many integrals vanish and need not be calculated. Whether a certain integral vanishes or not can be decided in advance by prescreening techniques.[178]

To illustrate the effect of basis set selection, we show in Table 2 the reaction energy for naphthalene combustion in the gas phase:

$$C_{10}H_8 + 12O_2 \rightarrow 10CO_2 + 4H_2O \qquad [22]$$

The basis sets are listed in order of increasing size and are well known in quantum chemistry (and are described in detail later in the chapter). We see that hydrogen polarization functions (basis sets ending in P) are important because C–H bonds are broken and O–H bonds are formed. Augmentation (aug-) with diffuse functions (small exponent) improves somewhat the smaller basis set results but is not economical in this case. Using the resolution of the identity (RI) for the Coulomb operator saves computational time, with no loss of

Table 2 Single-Point Calculations (with the PBE/TZVP/RI Geometry) Using PBE Functional for Reaction Energy for Naphthalene Combustion

Basis Set	Negative Reaction Energy (kcal/mol)	CPU[a] (s)
SV	916.8	9
SV(P)	1060.0	9
6-31G*	1047.1	25
SVP	1108.6	9
aug-SV(P)	1115.5	35
TZVP	1124.5	295
TZVPP	1131.2	420
cc-pVTZ	1129.0	375
aug-TZVP	1130.2	2525
aug-TZVP/RI	1130.2	155
QZVP	1140.3	5734
Reference Value[b]	1216.3	

[a]CPU denotes the CPU time is seconds.
[b]Computed using standard enthalpies of formation (from NIST[179]) using thermal and ZVPE corrections at the PBE/TZVP/RI level.

accuracy. Reasonable results are found with SVP, but convergence improves all the way to TZVP. We can see that after the TZVPP result, the basis set error is well below the functional error and the reaction energy is effectively converged. That is to say, we have reached the stage where adding more orbitals, which increases the computational cost, will no longer improve the result drastically. [This should be compared to the crambin calculation mentioned in the introduction, which is very large, and where only an SV(P) basis set could be used.]

Compared to the reference value we find quite a large error, $\Delta E = 76$ kcal/mol. However, given that 48 electron pair bonds are broken and formed, the error per carbon atom is only 7.6 kcal/mol, a value that is typical for this functional.

TIME-DEPENDENT THEORY

In this section we introduce all of the basic elements of TDDFT and how it differs from the ground-state case.

Runge–Gross Theorem

The analog of the Hohenberg–Kohn theorem for time-dependent problems is the Runge–Gross (RG) theorem.[16] Consider N nonrelativistic electrons, mutually interacting via the Coulomb repulsion, in a time-dependent external potential. The Runge–Gross theorem states that the densities $n(\mathbf{r}t)$ and $n'(\mathbf{r}t)$ evolving from a common initial state $\Psi_0 = \Psi(t = 0)$ under the influence of two external potentials $v_{\text{ext}}(\mathbf{r}t)$ and $v'_{\text{ext}}(\mathbf{r}t)$ (both Taylor-expandable about the initial time 0) are always different provided that the potentials differ by more than a purely time-dependent ($\mathbf{r}$-independent) function:

$$\Delta v_{\text{ext}}(\mathbf{r}t) \neq c(t) \qquad [23]$$

where

$$\Delta v_{\text{ext}}(\mathbf{r}t) = v_{\text{ext}}(\mathbf{r}t) - v'_{\text{ext}}(\mathbf{r}t) \qquad [24]$$

Thus, there is a one-to-one mapping between densities and potentials, and we say that the time-dependent potential is a functional of the time-dependent density (and the initial state).

The RG theorem was proven in two distinct parts. In the first part (RGI), one shows that the corresponding current densities differ. The current density is given by

$$\mathbf{j}(\mathbf{r}t) = \langle \Psi(t) | \hat{\mathbf{j}}(\mathbf{r}) | \Psi(t) \rangle \qquad [25]$$

where

$$\hat{\mathbf{j}}(\mathbf{r}) = \frac{1}{2i}\sum_{j=1}^{N}[\nabla_j \delta(\mathbf{r}-\mathbf{r}_j) + \delta(\mathbf{r}-\mathbf{r}_j)\nabla_j] \qquad [26]$$

is the current density operator. The equation of motion for the difference of the two current densities gives[16]

$$\left.\frac{\partial \Delta j(\mathbf{r}t)}{\partial t}\right|_{t=0} = -n_0(\mathbf{r})\nabla \Delta v_{\text{ext}}(\mathbf{r},0) \qquad [27]$$

If the Taylor expansion of the difference of the two potentials about $t = 0$ is not spatially uniform for some order, the Taylor expansion of the current density difference will then be nonzero at a finite order. Thus, RGI establishes the fact that the external potential is a functional of the current density, $v_{\text{ext}}[\mathbf{j}, \Psi_0](\mathbf{r}, t)$.

In the second part of the theorem (RGII), continuity is used:

$$\frac{\partial n(\mathbf{r}t)}{\partial t} = -\nabla \cdot \mathbf{j}(\mathbf{r}t) \qquad [28]$$

which leads to

$$\left.\frac{\partial^2 \Delta n(\mathbf{r}t)}{\partial t^2}\right|_{t=0} = \nabla \cdot [n_0(\mathbf{r})\nabla \Delta v_{\text{ext}}(\mathbf{r},0)] \qquad [29]$$

Suppose now that $\Delta v_{\text{ext}}(\mathbf{r}, 0)$ is not uniform everywhere. Might not the left-hand side of Eq. [29] still vanish? Apparently not, for real systems, because it is easy to show:[180]

$$\begin{aligned}\int d^3r\, \Delta v_{\text{ext}}(\mathbf{r},0)\nabla \cdot [n_0(\mathbf{r})\nabla \Delta v_{\text{ext}}(\mathbf{r},0)] \\ = \int d^3r [\nabla \cdot (\Delta v_{\text{ext}}(\mathbf{r},0) n_0(\mathbf{r})\nabla \Delta v_{\text{ext}}(\mathbf{r},0)) \\ - n_0 |\nabla \Delta v_{\text{ext}}(\mathbf{r},0)|^2]\end{aligned} \qquad [30]$$

Using Green's theorem, the first term on the right vanishes for physically realistic potentials (i.e., potentials arising from normalizable external charge densities) because for such potentials, $\Delta v_{\text{ext}}(\mathbf{r})$ falls off at least as $1/r$. But, the second term is definitely negative, so, if $\Delta v_{\text{ext}}(\mathbf{r}, 0)$ is nonuniform, the integral must be finite, causing the densities to differ in second order in t. This argument applies to each order and the densities $n(\mathbf{r}, t)$ and $n'(\mathbf{r}, t)$ will become

different infinitesimally later than t. Thus, by imposing these boundary conditions, we have shown that the external potential, $v_{\text{ext}}[n, \Psi_0](\mathbf{r}t)$, is a functional of the time-dependent density $n(\mathbf{r}t)$ and the initial wave function Ψ_0.

In this regard please note that:

1. The difference between $n(\mathbf{r}t)$ and $n'(\mathbf{r}t)$ is nonvanishing already in first order of $\Delta v_{\text{ext}}(\mathbf{r}t)$, ensuring the invertibility of the linear response operators described later.
2. Because the density determines the potential up to a time-dependent constant, the wave function is in turn determined up to a time-dependent phase, which cancels out of the expectation value of any operator.
3. We write $v_{\text{ext}}[n; \Psi_0](\mathbf{r}t)$ because the potential depends on both the history of the density and the initial wave function. The functional $v_{\text{ext}}[n; \Psi_0](\mathbf{r}t)$ is a very complex one, much more so than the ground-state case; knowledge of it implies solution of all time-dependent Coulomb interacting problems.
4. If we always begin in a nondegenerate ground state,[181,182] the initial-state dependence can be subsumed by the Hohenberg–Kohn theorem,[1] then $v_{\text{ext}}(\mathbf{r}t)$ is a functional of $n(\mathbf{r}t)$ alone: $v_{\text{ext}}[n](\mathbf{r}t)$.
5. A spin-dependent generalization exists,[183] so that $v_{\text{ext}}(\mathbf{r}t)$ will be a functional of the spin densities n_α, n_β. This is usually used in practical calculations.
6. Since RGI establishes that the external potential is a functional of the current density, one could choose to use the current density as the basic variable instead of the density. This is known as time-dependent current density functional theory (TDCDFT) (See discussion below on solids.)

Kohn–Sham Equations

Once we have a proof that the potential is a functional of the time-dependent density, it is simple to write the time-dependent Kohn–Sham (TDKS) equations as

$$i\frac{\partial \phi_{j\sigma}(\mathbf{r}t)}{\partial t} = \left(-\frac{\nabla^2}{2} + v_{S\sigma}[n](\mathbf{r}t)\right)\phi_{j\sigma}(\mathbf{r}t) \qquad [31]$$

whose potential is uniquely chosen (via the RG theorem) to reproduce the exact spin densities of the interacting system. For simplicity, the initial-state dependence of the KS potential is not written explicitly. As noted, if we start in a nondegenerate ground state, this dependence is subsumed into the density.

$$n_\sigma(\mathbf{r}t) = \sum_{j=1}^{N_\sigma} |\phi_{j\sigma}(\mathbf{r}t)|^2 \qquad [32]$$

We *define* the exchange–correlation potential via

$$v_{S\sigma}(\mathbf{r}t) = v_{\text{ext}\sigma}(\mathbf{r}t) + \int d^3r' \frac{n(\mathbf{r}'t)}{|\mathbf{r} - \mathbf{r}'|} + v_{\text{XC}\sigma}(\mathbf{r}t) \quad [33]$$

where the second term is the familiar Hartree potential.

Here the following should be noted:

1. The exchange–correlation potential, $v_{XC\sigma}(\mathbf{r}t)$ is in general a functional of the entire history of the densities, $n_\sigma(\mathbf{r}t)$, the initial interacting wave function $\Psi(0)$, and the initial Kohn–Sham wave function, $\Phi(0)$.[182] But if both the KS and interacting initial wave functions are nondegenerate ground states, it becomes a simple functional of $n_\sigma(\mathbf{r}t)$ alone.
2. By inverting the single doubly occupied KS equation for a spin-unpolarized two-electron system, it is straightforward (but technically demanding) to find the TDKS potential from an exact time-dependent density, a task that has been done several times[184–186] for simple model systems.
3. Some approximation is used for $v_{XC}(\mathbf{r}t)$ as a functional of the density in practical calculations, so that modifications of traditional TDSE schemes are needed for the propagation.[187]
4. Unlike the ground-state case, there is no self-consistency, merely forward propagation in time, of a density-dependent Hamiltonian.
5. Again, unlike in the ground state, there is no central role played by a single-number functional, such as the ground-state energy. In fact, while an action was provided in the original RG study, extremizing it was later shown to not yield the TDKS equations.[188]

Linear Response

The most common application of TDDFT is the response of a system to a weak, long-wavelength, optical field:

$$\delta v_{\text{ext}}(\mathbf{r}t) = -\xi \exp(i\omega t)\mathbf{z} \quad [34]$$

In the general case of the response of the ground state to an arbitrary weak external field, the system's first-order response is characterized by the nonlocal susceptibility:

$$\delta n_\sigma(\mathbf{r}t) = \sum_{\sigma'} \int dt' \int d^3r' \, \chi_{\sigma\sigma'}[n_0](\mathbf{r}, \mathbf{r}'; t - t')\delta v_{\text{ext}\sigma'}(\mathbf{r}'t') \quad [35]$$

This susceptibility χ is a functional of the *ground-state* density, $n_0(\mathbf{r})$. A similar equation describes the density response in the KS system:

$$\delta n_\sigma(\mathbf{r}t) = \sum_{\sigma'} \int dt' \int d^3r' \, \chi_{S\sigma\sigma'}[n_0](\mathbf{r}, \mathbf{r}'; t - t')\delta v_{S\sigma'}(\mathbf{r}'t') \quad [36]$$

Here χ_S is the *Kohn–Sham* response function, constructed from KS energies and orbitals:

$$\chi_{S\sigma\sigma'}(\mathbf{r}\mathbf{r}'\omega) = \delta_{\sigma\sigma'} \sum_q \left\{ \frac{\Phi_{q\sigma}(\mathbf{r})\Phi^*_{q\sigma'}(\mathbf{r}')}{\omega - \omega_q + i0_+} - \frac{\Phi^*_{q\sigma}(\mathbf{r})\Phi_{q\sigma'}(\mathbf{r}')}{\omega + \omega_q - i0_+} \right\} \quad [37]$$

where q is a double index, representing a transition from occupied KS orbital i to unoccupied KS orbital a, $\omega_{q\sigma} = \epsilon_{a\sigma} - \epsilon_{i\sigma}$, and $\Phi_{q\sigma}(\mathbf{r}) = \phi^*_{i\sigma}(\mathbf{r})\phi_{a\sigma}(\mathbf{r})$. 0_+ means the limit as 0_+ goes to zero from above (i.e., along the positive real axis). Thus, χ_S is determined completely by the ground-state KS potential. It is the susceptibility of the noninteracting electrons sitting in the KS ground-state potential.

To relate the KS response to the true response, we examine in Eq. [38] how the KS potential in Eq. [33] changes:

$$\delta v_{S\sigma}(\mathbf{r}t) = \delta v_{\text{ext}\sigma}(\mathbf{r}t) + \delta v_{\text{HXC}\sigma}(\mathbf{r}t) \quad [38]$$

Because $\delta v_{\text{HXC}\sigma}(\mathbf{r}t)$ is due to an infinitesimal change in the density, it may be written in terms of its functional derivative, i.e., as in Eq. [39]:

$$\delta v_{\text{HXC}\sigma}(\mathbf{r}t) = \sum_{\sigma'} \int d^3r' \int dt' \, f_{\text{HXC}\sigma\sigma'}(\mathbf{r}\mathbf{r}', t - t')\delta n_{\sigma'}(\mathbf{r}'t') \quad [39]$$

where

$$f_{\text{HXC}\sigma\sigma'}[n_0](\mathbf{r}\mathbf{r}', t - t') = \left. \frac{\delta v_{\text{HXC}\sigma}(\mathbf{r}t)}{\delta n_{\sigma'}(\mathbf{r}'t')} \right|_{n_0} \quad [40]$$

The Hartree contribution is found by differentiating Eq. [16]:

$$\begin{aligned} f_H[n_0](\mathbf{r}\mathbf{r}', t - t') &= \frac{\delta v_H(\mathbf{r}t)}{\delta n_{\sigma'}(\mathbf{r}'t')} \\ &= \frac{\delta(t - t')}{|\mathbf{r} - \mathbf{r}'|} \end{aligned} \quad [41]$$

while the remainder, $f_{\text{XC}\sigma\sigma'}[n_0](\mathbf{r}\mathbf{r}', t - t')$, is known as the XC kernel.

By the definition of the KS potential, $\delta n_\sigma(\mathbf{r}t)$ is the same in both Eqs. [35] and [36]. We can then insert Eq. [39] into Eq. [36], equate that result with Eq. [35], and solve for a general relation for any $\delta n_\sigma(\mathbf{r}t)$. After Fourier

transforming in time, the central equation of TDDFT linear response[189] is a Dyson-like equation for the true χ of the system:

$$\chi_{\sigma\sigma'}(\mathbf{r}\mathbf{r}'\omega) = \chi_{S\sigma\sigma'}(\mathbf{r}\mathbf{r}'\omega) + \sum_{\sigma_1\sigma_2}\int d^3r_1 \int d^3r_2 \chi_{S\sigma\sigma_1}(\mathbf{r}\mathbf{r}_1\omega) \times \left(\frac{1}{|\mathbf{r}_1 - \mathbf{r}_2|} + f_{\mathrm{XC}\sigma_1\sigma_2}(\mathbf{r}_1\mathbf{r}_2\omega)\right)\chi_{\sigma_2\sigma'}(\mathbf{r}_2\mathbf{r}'\omega) \quad [42]$$

It is to be noted here that:

1. The XC kernel is a much simpler quantity than $v_{\mathrm{XC}\sigma}[n](\mathbf{r}t)$ because the kernel is a functional of only the ground-state density.
2. The kernel is nonlocal in both space and time. The nonlocality in time manifests itself as a frequency dependence in the Fourier transform, $f_{\mathrm{XC}\sigma\sigma'}(\mathbf{r}\mathbf{r}'\omega)$.
3. When f_{XC} is set to zero in Eq. [42], physicists call it the random-phase approximation (RPA). The inclusion of f_{XC} is an exactification of RPA, in the same way that the inclusion of $v_{\mathrm{XC}}(\mathbf{r})$ in ground-state DFT was an exactification of Hartree theory.
4. The Hartree kernel is instantaneous; it is local in time, i.e., it has no memory and will have no frequency dependence when Fourier transformed to the frequency domain. Thus, it is given exactly by an adiabatic approximation.
5. The frequency-dependent kernel is a very sophisticated object since its frequency dependence makes the solution of an RPA-type equation yield the exact χ (including all vertex corrections at every higher order term). The kernel defies physical intuition; thus arguments based on the structure of the TDDFT equations are at best misleading. If any argument cannot be given in terms of many-body quantum mechanics, Eq. [42] cannot help.
6. The kernel is, in general, complex, with real and imaginary parts related via a Kramers–Kronig relation.[190]

The poles of the linear susceptibility, $\chi(rr'\omega)$, are the excitation frequencies of the true system. In order to extract these frequencies Casida[191] used ancient RPA technology to produce equations in which these poles of χ are found as the solution to an eigenvalue problem. In order to see this, first do an expansion of the density change in the basis of KS transitions. We write $\delta n_\sigma(\mathbf{r}t)$ as

$$\delta n_\sigma(\mathbf{r}\omega) = \sum_q [P_{q\sigma}(\omega)\Phi^*_{q\sigma}(\mathbf{r}) + P_{\bar{q}\sigma}(\omega)\Phi_{q\sigma}(\mathbf{r})] \quad [43]$$

where $\bar{q} = (a, i)$ if $q = (i, a)$. This representation is used to solve Eq. [36] self-consistently using Eq. [39], and yields two coupled matrix equations:[192]

$$\left[\begin{pmatrix} \mathbf{A} & \mathbf{B} \\ \mathbf{B}^* & \mathbf{A}^* \end{pmatrix} - \omega\begin{pmatrix} -\mathbb{1} & 0 \\ 0 & \mathbb{1} \end{pmatrix}\right]\begin{pmatrix} \mathbf{X} \\ \mathbf{Y} \end{pmatrix} = -\begin{pmatrix} \delta\mathbf{v} \\ \delta\mathbf{v}^* \end{pmatrix} \quad [44]$$

where $A_{q\sigma q'\sigma'} = \delta_{qq'}\delta_{\sigma\sigma'}\omega_{q\sigma} + K_{q\sigma q'\sigma'}$, $B_{q\sigma q'\sigma'} = K_{q\sigma q'\sigma'}$, $X_{q\sigma} = P_{q\sigma}$, $Y_{q\sigma} = P_{\bar{q}\sigma}$, and

$$K_{q\sigma q'\sigma'}(\omega) = \int d\mathbf{r} \int d\mathbf{r}'\, \Phi_{q\sigma}(\mathbf{r}) f_{\mathrm{HXC}\sigma\sigma'}(\mathbf{r}\mathbf{r}'\omega)\Phi^*_{q'\sigma'}(\mathbf{r}') \quad [45]$$

with

$$\delta v_{q\sigma}(\omega) = \int d\mathbf{r}\, \Phi_{q\sigma}(\mathbf{r})\delta v_{\mathrm{ext}}(\mathbf{r}\omega) \quad [46]$$

When $\delta v = 0$, then ω will be an excitation frequency of the true system. If the KS orbital are chosen as real and using the fact that $(\mathbf{A} - \mathbf{B})$ will be positive definite, then we can simplify Eq. [44] as the eigenvalue problem in Eq. [47]:

$$\sum_{q'\sigma'} \tilde{\Omega}_{q\sigma q'\sigma'}(\omega)\vec{a}_{q'\sigma'} = \omega^2 \vec{a}_{q\sigma} \quad [47]$$

where

$$\tilde{\Omega} = (\mathbf{A} - \mathbf{B})^{1/2}(\mathbf{A} + \mathbf{B})(\mathbf{A} - \mathbf{B})^{1/2} \quad [48]$$

or

$$\tilde{\Omega}_{q\sigma q'\sigma'}(\omega) = \omega^2_{q\sigma}\delta_{qq'}\delta_{\sigma\sigma'} + 2\sqrt{\omega_{q\sigma}\omega_{q'\sigma'}}\; K_{q\sigma q'\sigma'} \quad [49]$$

Oscillator strengths f_q may be calculated[191] from the normalized eigenvectors using

$$f_{q\sigma} = \tfrac{2}{3}(|\vec{x}^T\mathbf{S}^{-1/2}\vec{a}_{q\sigma}|^2 + |\vec{y}^T\mathbf{S}^{-1/2}\vec{a}_{q\sigma}|^2 + |\vec{z}^T\mathbf{S}^{-1/2}\vec{a}_{q\sigma}|^2) \quad [50]$$

where

$$S_{qq'} = \frac{\delta_{qq'}\delta_{\sigma\sigma'}}{w_{q'\sigma'}} \quad [51]$$

Figure 4 shows the results of *exact* DFT calculations for the He atom. On the left side of the diagram, we consider just transitions from the exact ground-state KS occupied orbital (1*s*) to unoccupied orbitals. These are *not* the true excitations of the system, nor are they supposed to be. However, applying TDDFT linear response theory, using the exact kernel with the exact orbitals, yields the exact excitation frequencies of the He atom. Spin decomposing produces both singlet and triplet excitations.

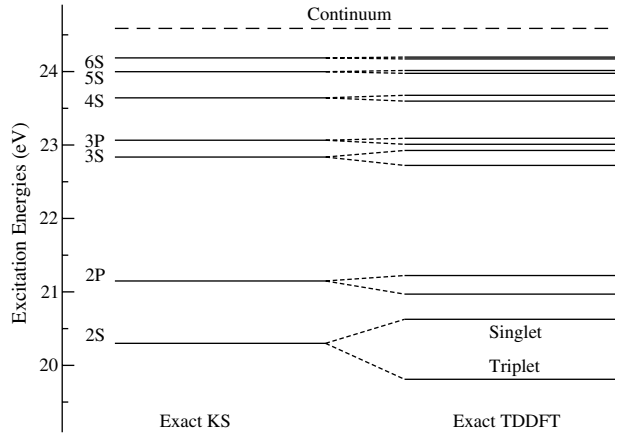

Figure 4 Transitions for the helium atom using only ground-state DFT on the left and TDDFT on the right. In both cases, the exact functionals have been used. The results for employing the exact XC kernel in TDDFT linear response were deduced from calculations using Ref. 193. In each pair of lines on the right, the triplet is below the singlet.

Approximations

While all the equations above are formally exact, as in the ground-state case, a TDDFT calculation requires an approximation for the unknown XC potential. The most common approximation in TDDFT is the *adiabatic* approximation[194,195] in which

$$v_{\mathrm{XC}\sigma}^{\mathrm{adia}}[n](\mathbf{r}t) = v_{\mathrm{XC}\sigma}^{\mathrm{gs}}[n_0](\mathbf{r})|_{n_{0\sigma}(\mathbf{r})=n_\sigma(\mathbf{r}t)} \qquad [52]$$

This means the XC potential at any time is simply the ground-state XC potential at that instant. This obviously becomes exact for sufficiently slow perturbations in time, in which the system always stays in its instantaneous ground state. Although most applications are not in this slowly varying regime, results obtained within the adiabatic approximation are, nevertheless, remarkably accurate in many cases.

Any ground-state approximation (LDA, GGA, hybrid) provides an adiabatic approximation for use in TDDFT automatically. The most famous is the adiabatic local density approximation (ALDA).[194,195] It employs the functional form of the static LDA with a time-dependent density:

$$v_{\mathrm{XC}\sigma}^{\mathrm{ALDA}}[n](\mathbf{r}t) = v_{\mathrm{XC}}^{\mathrm{unif}}(n_\alpha(\mathbf{r}t), n_\beta(\mathbf{r}t)) = \left.\frac{de_{\mathrm{XC}}^{\mathrm{unif}}}{dn_\sigma}\right|_{n_\sigma=n_\sigma(\mathbf{r}t)} \qquad [53]$$

Here $e_{\mathrm{XC}}^{\mathrm{unif}}(n_\alpha, n_\beta)$ is the accurately known exchange–correlation energy density of the uniform electron gas of spin densities n_α, n_β. For the time-dependent exchange–correlation kernel of Eq. [40], Eq. [53] leads to

$$f_{\mathrm{XC}\sigma\sigma'}^{\mathrm{ALDA}}[n_0](\mathbf{r}t, \mathbf{r}t') = \delta^{(3)}(\mathbf{r} - \mathbf{r}')\delta(t - t')\frac{d^2 e_{\mathrm{XC}}^{\mathrm{unif}}}{dn_\sigma dn_{\sigma'}}\bigg|_{n_\sigma = n_{0\sigma}(\mathbf{r})} \quad [54]$$

The time Fourier transform of the kernel has no frequency dependence at all in any adiabatic approximation. Via a Kramers–Kronig relation, this implies that it is purely real.[190]

Thus, any TDDFT linear response calculation is carried out in two steps:

1. An approximate ground-state DFT calculation is done, finding a self-consistent KS potential. Transitions from occupied to unoccupied KS orbitals provide zero-order approximations to the optical excitations.
2. An approximate TDDFT linear response calculation is done on the orbitals of the ground-state calculation. This corrects the KS transitions into the true optical transitions.

In practice both of these steps contain inherent errors. We shall dissect the relative importance of both of these errors later in the chapter.

IMPLEMENTATION AND BASIS SETS

Time-dependent DFT has the ability to calculate various physical and quantum quantities, and different techniques are sometimes favored for each type. For some purposes as, for example, if strong fields are present, it can be better to propagate forward in time the KS orbitals using either a real space grid[196,197] or plane waves.[198] For finite-order response, Fourier transforming to frequency space with localized basis functions may be preferable.[199] We discuss in detail below how the latter approach works, emphasizing the importance of basis set convergence.

Density Matrix Approach

We can write the dynamics of the TDKS systems in terms of the one-particle density matrix $\gamma_\sigma(\mathbf{r}\mathbf{r}'t)$ of the TDKS determinant, rather than the orbitals. $\gamma_\sigma(\mathbf{r}\mathbf{r}'t)$ has the spectral representation

$$\gamma_\sigma(\mathbf{r}\mathbf{r}'t) = \sum_{j=1}^{N} \phi_{j\sigma}(\mathbf{r}t)\phi_{j\sigma}^*(\mathbf{r}'t) \quad [55]$$

which means the N_σ TDKS orbitals are the eigenfunctions of γ_σ. The eigenvalue of all TDKS orbitals, which is their *occupation number*, is always 1,

reflecting the fact that the TDKS system is noninteracting. Equivalently, γ_σ satisfies the idempotency constraint

$$\gamma_\sigma(\mathbf{r}\mathbf{r}'t) = \int d\mathbf{r}_1\, \gamma_\sigma(\mathbf{r}\mathbf{r}_1 t)\gamma_\sigma(\mathbf{r}_1\mathbf{r}'t) \qquad [56]$$

The normalization of the TDKS orbitals implies that the trace of γ_σ be N_σ.

Using the TDKS equations [31], one finds that the time evolution of γ_σ is governed by the von Neumann equation:

$$i\frac{\partial}{\partial t}\gamma_\sigma(t) = [H_\sigma[n](t), \gamma_\sigma(t)] \qquad [57]$$

where $H_\sigma[n](\mathbf{r}t) = -\nabla^2/2 + v_{s\sigma}[n](\mathbf{r}t)$ is the TDKS one-particle Hamiltonian. Although γ_σ has no direct physical meaning, it provides the interacting density and current density. The density is simply

$$n_\sigma(\mathbf{r}t) = \gamma_\sigma(\mathbf{r}\mathbf{r}t) \qquad [58]$$

and the KS current density can be obtained from

$$\mathbf{j}_{S\sigma}(\mathbf{r}t) = \frac{1}{2i}(\nabla_\mathbf{r} - \nabla_{\mathbf{r}'})\gamma_\sigma(\mathbf{r}\mathbf{r}'t)\Big|_{\mathbf{r}'=\mathbf{r}} \qquad [59]$$

Thus, one can either propagate the TDKS orbitals using the TDKS equations [31] or equivalently one can propagate the TDKS one-particle density matrix γ_σ using the von Neumann equation [57], subject to the idempotency contstraint [56], and normalized to N_σ.

It is often preferable to use γ_σ instead of the TDKS orbitals in practice. γ_σ is unique (up to a gauge transformation), while the orbitals can be mixed arbitrarily by unitary transformations. Both n_σ and $\mathbf{j}_\sigma$ are linear in γ_σ, while they are quadratic in the orbitals; also, the TDKS response equations are inhomogeneous in the orbitals (i.e., the response of each orbital is coupled to the response of all other orbitals) due to the density dependence of H_σ, while they are homogeneous in γ_σ. A response theory based on the TDKS density matrix is therefore considerably simpler than one based on orbitals. Finally, the use of γ_σ is computationally more efficient than using orbitals.[199]

Basis Sets

In response theory, the basis functions $\chi_\nu(\mathbf{r})$ are usually chosen to be time independent; for strong fields or coupled electron-nuclear dynamics, time-dependent basis functions can sometimes be more appropriate.

Convergence for Naphthalene

Table 3 shows the basis set convergence of the first six singlet excitation energies of naphthalene computed using the PBE XC functional for both the ground-state and TDDFT calculations; the corresponding oscillator strengths for some of the transitions are also given. In this table N_{bf} denotes the number of Cartesian basis functions, and CPU denotes the CPU time (seconds). Similar basis set convergence studies on small model systems should precede applications to large systems. However, the systems and the states of interest, the target accuracy, the methods used, and the computational resources available will determine which basis set is appropriate in practice. With a model small molecule such as naphthalene, we can find the basis set convergence limit of a given method. For this hydrocarbon both excitation energies and oscillator strengths are essentially converged within the aug-QZVP basis set in Table 3. QZVP stands for a quadruple-zeta valence basis set with polarization functions,[202] and the prefix aug- denotes additional diffuse functions on nonhydrogen atoms, which were taken from Dunning's aug-cc-pVQZ basis set.[203] For C and H, this corresponds to [8*s*5*p*4*d*3*f*2*g*] and [4*s*3*p*2*d*1*f*], respectively, where the numbers in brackets denote shells of contracted Gaussian-type orbitals (CGTOs), as usual. We will take the aug-QZVP results as a reference to assess the effect of smaller basis sets.

Double-Zeta Basis Sets

The smallest basis in Table 3 is of split valence (SV) or double-zeta valence quality,[204] without polarization functions. This basis set consists of two CGTOs per valence orbital and one per core orbital, i.e., [3*s*2*p*] for C and [2*s*] for H. Another popular double-zeta valence basis set is 6-31G.[205] The SV basis set can be used to obtain a very rough qualitative description of the lowest valence excited states only, e.g., in this example 1^1B_{3u} and 1^1B_{2u}. Higher and diffuse excitations, such as 1^1A_u, are much too high in energy or can be missed completely in the spectrum. Because unpolarized basis sets also give poor results for other properties such as bond lengths and energies, their use is generally discouraged nowadays.

Polarization Functions

The SV results for valence excitations can be improved considerably at moderate computational cost by adding a single set of polarization functions to nonhydrogen atoms. The resulting basis set is termed SV(P) and consists of [3*s*2*p*1*d*] for C and [2s] for H.[204] The basis set errors in the first two valence excitation energies are reduced by about 50%. There is also a dramatic improvement in the oscillator strength of the dipole-allowed transitions. This improvement is expected from the limiting case of a single atom, where

Table 3 Basis Set Convergence of First Six Singlet Excitation Energies (in eV) and Oscillator Strengths (Length Gauge) of Naphthalene[a]

Basis Set[b]	1^1B_{3u}	1^1B_{2u} (Osc. Str.)	2^1A_g	1^1B_{1g}	2^1B_{3u} (Osc. Str.)	1^1A_u	N_{bf}	CPU (s)
SV	4.352	4.246 (0.0517)	6.084	5.254	5.985 (1.1933)	6.566	106	24
SV(P)	4.272	4.132 (0.0461)	5.974	5.149	5.869 (1.1415)	6.494	166	40
6-31G*	4.293	4.154 (0.0453)	6.021	5.185	5.902 (1.1029)	7.013	166	40
SVP	4.262	4.125 (0.0466)	5.960	5.136	5.852 (1.1402)	6.505	190	48
aug-SV(P)	4.213	4.056 (0.0417)	5.793	4.993	5.666 (1.1628)	5.338	266	168
TZVP	4.209	4.051 (0.0424)	5.834	5.030	5.715 (1.1455)	6.215	408	408
TZVPP	4.208	4.050 (0.0425)	5.830	5.027	5.711 (1.1464)	6.231	480	568
cc-pVTZ	4.222	4.064 (0.0427)	5.870	5.061	5.747 (1.1355)	6.062	470	528
aug-TZVP	4.193	4.031 (0.0407)	5.753	4.957	5.622 (1.1402)	5.141	608	2000
aug-TZVP/RI	4.193	4.031 (0.0407)	5.752	4.957	5.621 (1.1401)	5.142	608	400
QZVP	4.197	4.036 (0.0416)	5.788	4.989	5.667 (1.1569)	5.672	1000	6104
aug-QZVP	4.192	4.029 (0.0406)	5.748	4.954	5.616 (1.1330)	5.071	1350	28216
Expt.[c]	3.97, 4.0	4.45, 4.7 (0.102, 0.109)	5.50, 5.52	5.28, 5.22	5.63, 5.55, 5.89 (1.2, 1.3)	5.6		

[a]Calculations were performed on a single processor of a 2.4-GHz Opteron Linux workstation with the PBE functional (the ground-state structure was optimized at the PBE/TZVP/RI-level).

[b]The basis set acronyms are defined in the text.

[c]Experimental results were taken from Ref. 200.

the first dipole-allowed transition from a valence shell of l quantum number l_v generally involves orbitals with l-quantum number $l_v + 1$. Basis sets of SV(P) or similar quality are often the first choice for TDDFT applications to large systems, especially if only the lowest states are of interest and/or if diffuse excitations are quenched due, e.g., to a polar environment. The popular 6-31G* basis set[205,206] has essentially the same size as SV(P) but performed slightly worse in our example above.

Adding a single set of p-type polarization functions to hydrogen atoms produces the SVP basis set.[204] These functions describe mainly C-H σ^*-type excitation in molecules, which usually occur in the far ultraviolet (UV) and are rarely studied by most scientists. Going from SV(P) to SVP has no significant effect in our example. Such an observation may be different for molecules containing strongly polarized hydrogen element or hydrogen bridge bonds, however.

The aug-SV(P) is an SV(P) basis set augmented by a $[1s1p1d]$ set of primitive Gaussians with small exponents, often called "diffuse functions" (from Dunning's aug-cc-pVDZ[203]). The effect of diffuse augmentation is a moderate downshift of less than 0.1 eV for the first two singlet excitation energies, as shown in Table 3. This behavior is typical of lower valence excited states having a similar extent as the ground state. The naphthalene example also shows that diffuse functions can have a significant effect on higher excitations. An extreme case is the 1^1A_u state, which is an excitation into the $10a_u$ orbital having the character of a $3s$ Rydberg state (any state with principal quantum number higher than HOMOs) of the entire molecule. The excitation energy of this state is lowered by more than 1 eV upon diffuse augmentation.

While polarization functions are necessary for a qualitatively correct description of transition dipole moments, additional diffuse polarization functions can account for radial nodes in the first-order KS orbitals, which further improves computed transition moments and oscillator strengths. These benefits are counterbalanced with a significant increase of the computational cost involved: In our example, the aug-SV(P) basis increased the computation time by about a factor of 4. For molecules with more than 30–40 atoms, most excitations of interest are valence excitations, and the use of diffuse augmentation may become prohibitively expensive because the large spatial extent of these functions confounds integral prescreening.

Triple-Zeta Basis Sets

For large molecules where the use of diffuse augmentation is prohibitive, an alternative is to use triple-zeta valence (TZV) basis sets. The TZVP (def-2-TZVP[207]) basis set corresponds to $[5s3p2d1f]$ on C and $[3s1p]$ on H. It also includes a second set of polarization functions on nonhydrogen atoms and provides a description of the valence electrons that is

accurate for many purposes when density functionals are used. The excitation energies of valence states are essentially converged in this basis set (see Table 3). However, the diffuse states are too high in energy. Little change takes place when going to the TZVPP basis, which differs from TZVP only by an additional set of polarization functions on H. The performance of Dunning's cc-pVTZ basis set[208] is similar to TZVP and TZVPP. We point out that Dunning basis sets are based on a generalized contraction scheme for valence orbitals, as opposed to the segmented contracted SV, TZV, and QZV basis sets, the latter of which are more efficient for larger systems because more integrals vanish.

Diffuse Functions

By adding a $[1s1p1d1f]$ set of diffuse functions to TZVP, we obtain the aug-TZVP basis set. The aug-TZVP excitation energies of all states of naphthalene, except the 1^1A_u Rydberg state, are within 0.01 eV of the reference aug-QZVP results and can be considered essentially converged. A similar observation can be made for the oscillator strengths in Table 3.

When going to the larger quadruple-zeta valence (QZV) basis sets, the results change only marginally, but the computation times increase substantially. In density functional theory, these basis sets are mainly used for benchmarks and calibration.

Resolution of the Identity

We have included in Table 3 a result for the aug-TZVP basis set that was obtained using the resolution of the identity approximation for the Coulomb energy (RI-J).[209,210] It is obvious that the error introduced by the RI-J approximation is much smaller than the basis set error, while the computation time is reduced by a factor of 5. The RI-J approximation is so effective because the computation of the Coulomb (Hartree) energy and its response is the bottleneck in conventional (TD)DFT calculations. RI-J replaces the four-index Coulomb integrals by three-index and two-index integrals, considerably lowering the algorithmic prefactor.[211] It is generally safe to use with the appropriate auxiliary basis sets. As soon as hybrid functionals are used, however, the computation of the exact exchange becomes rate determining.

Summary

For larger molecules than naphthalene, SV(P) or similar basis sets are often appropriate due to their good cost-to-performance ratio. We recommend checking the SV(P) results by a TZVP calculation whenever possible. Diffuse functions should be used sparingly for molecules with more than about 20 atoms.

PERFORMANCE

This section of the tutorial is devoted to analyzing the performance of TDDFT, assuming basis set convergence. Here we dissect many of the sources of error in typical TDDFT calculations.

To get an overall impression of how well TDDFT does, we recommend reading a small survey by Furche and Ahlrichs.[212] Most chemistry calculations are done with the B3LYP[168] functional, and the results of those calculations are transition frequencies within 0.4 eV of experiment. Moreover, structural properties of excited states are almost as good as those of ground-state calculations (bond lengths to within 1%, dipole moments to within 5%, vibrational frequencies to within 5%). Most importantly, the level of accuracy of most TDDFT calculations appears sufficient to qualitatively identify the nature of the most intense transitions, often debunking cruder models that have been used for interpretation for decades. This is proving especially useful for the photochemistry of biologically relevant molecules.[69]

Example: Naphthalene Results

As an illustration of the performance of TDDFT, we compare various density functionals and wave function methods for the first singlet excited states of naphthalene in Tables 4, 5, and 6. All calculations were performed using the aug-TZVP basis set, while the complete active space self-consistent field (SCF) with second-order perturbation theory (CASPT2) results from Ref. 200 were obtained in a smaller double-zeta valence basis set with some diffuse augmentation. The experimental results correspond to band maxima from gas-phase experiments; however, the position of the band maximum does not necessarily coincide with the vertical excitation energy, especially if

Table 4 Performance of Density Functionals for First Six Singlet Excitation Energies (in eV) of Naphthalene

Method[a]	1^1B_{3u}	1^1B_{2u}	2^1A_g	1^1B_{1g}	2^1B_{3u}	1^1A_u
			Pure Density Functionals			
LSDA	4.191	4.026	5.751	4.940	5.623	5.332
BP86	4.193	4.027	5.770	4.974	5.627	5.337
PBE	4.193	4.031	5.753	4.957	5.622	5.141
			Hybrids			
B3LYP	4.393	4.282	6.062	5.422	5.794	5.311
PBE0	4.474	4.379	6.205	5.611	5.889	5.603
"best"[b]	4.0	4.5	5.5	5.5	5.5	5.7

[a] An aug-TZVP basis set and the PBE/TZVP/RI ground-state structure was used.

[b] The "best" estimates of the true excitations were from experiment and calculations, as described in text.

Table 5 Performance of Wave Function Methods for Excitations of Table 4

Method	1^1B_{3u}	1^1B_{2u}	2^1A_g	1^1B_{1g}	2^1B_{3u}	1^1A_u
CIS[a]	5.139	4.984	7.038	6.251	6.770	5.862
CC2[a]	4.376	4.758	6.068	5.838	6.018	5.736
CASPT2[b]	4.03	4.56	5.39	5.53	5.54	5.54
Expt.	3.97, 4.0	4.45, 4.7	5.50, 5.52	5.28, 5.22	5.63, 5.55	5.89
"best"[b]	4.0	4.5	5.5	5.5	5.5	5.7

[a]The aug-TZVP basis set and the PBE/TZVP/RI ground-state structure was used.
[b]CASPT2 results and experimental results are from Ref. 200.

the excited-state structure differs significantly from the ground-state structure. For the lower valence states, the CASPT2 results can therefore be expected to be at least as accurate as the experimental data. For higher excited states, the basis set used in the CASPT2 calculations appears rather small, and the approximate second-order coupled-cluster values denoted RICC2[213–215] might be a better reference with which to make comparisons. Thus, our best guess (denoted "best" in the tables) is from experiment for the first four transitions, CASPT2 for the fifth transition, and RICC2 for the sixth transition.

We begin with some general observations:

1. The excitation energies predicted by the GGA functionals BP86 and PBE differ marginally from the LSDA results (an exception being the 1^1A_u Rydberg state, whose PBE excitation energy is substantially lower than those of all other methods). Note, however, that GGA functionals generally improve the results compared to LSDA results for other excited-state properties such as structures or vibrational frequencies.

Table 6 Performance of Density Functional and Correlated Wave Function Methods for Oscillator Strengths of First Three Dipole-Allowed Transitions of Naphthalene

Method[a]	1^1B_{3u}	1^1B_{2u}	2^1B_{3u}
LSDA	0.0000	0.0405	1.1517
BP86	0.0000	0.0411	1.1552
PBE	0.0000	0.0407	1.1402
B3LYP	0.0000	0.0539	1.2413
PBE0	0.0000	0.0574	1.2719
LHF/LSDA	0.0000	0.0406	1.2089
LHF/PBE	0.0000	0.0403	1.2008
CIS	0.0002	0.0743	1.8908
CC2	0.0000	0.0773	1.4262
CASPT2	0.0004	0.0496	1.3365
expt.	0.002	0.102, 0.109	1.2, 1.3

[a]An aug-TZVP basis set and the PBE/TZVP/RI ground-state structure was used for all except the CASPT2 results, which were taken from Ref. 200.

2. The use of hybrid functionals leads to systematically higher excitation energies. On average, this is an improvement over the GGA results, which are systematically too low. However, while diffuse excitations benefit from mixing in some exact exchange due to a reduction of the self-interaction error, valence excitation energies are not always improved, as is obvious for the 1^1B_{3u} and 2^1B_{3u} valence states.
3. The 1^1B_{2u} state is erroneously predicted below the 1^1B_{3u} state by all density functionals in Table 4, which is a potentially serious problem for applications in photochemistry. This is not corrected by hybrid mixing.
4. The configuration–interaction singles (CIS) method, which uses a Hartree–Fock reference that is computationally as expensive as hybrid TDDFT, produces errors that are substantially larger than the hybrid TDDFT results, especially for valence states. The coupled-cluster (CC) and CASPT2 methods are usually more accurate but are far more CPU expensive, and they scale prohibitively as the system size grows. The cost of CASPT2 scales exponentially with the number of correlated electrons, while the cost of CC2 grows with the fifth power of the system size. This severely limits the application of these methods to larger molecules.

The 1^1B_{2u} excitation is polarized along the short axis of the naphthalene molecule. In Platt's nomenclature of excited states of polycyclic aromatic hydrocarbons (PAHs), 1^1B_{2u} corresponds to the ^1L_a state, which has more ionic character than the 1^1B_{3u} (or ^1L_b) state. Parac and Grimme have pointed out[216] that GGA functionals underestimate the excitation energy of the ^1L_a state in PAHs considerably. Our example of naphthalene agrees with this observation. The 1^1B_{2u} excitation is computed to be 0.4–0.5 eV too low in energy by LSDA and GGA functionals, leading to an incorrect ordering of the first two singlet excited states.

Influence of the Ground-State Potential

From the very earliest calculations of transition frequencies,[189,191] it was recognized that the inaccuracy of standard density functional approximations (LDA, GGA, hybrids) for the ground-state XC potential leads to inaccurate KS eigenvalues. Because the approximate KS potentials have incorrect asymptotic behavior (they decay exponentially, rather than as $-1/r$, as seen in Figure 3 and its discussion), the KS orbital eigenvalues are insufficiently negative, the ionization threshold is far too low, and the Rydberg states are often unbound.

Many methods have since been developed to asymptotically correct potentials[217,218] to correct this unfortunate behavior. Any corrections to the ground-state potential are dissatisfying, however, as the resulting potential is *not* a functional derivative of an energy functional. Even mixing one approximation for $v_{\mathrm{XC}}(\mathbf{r})$ and another for f_{XC} has become popular in an attempt to rectify the problem. A more satisfying route to asymptotically correct

potentials is to use the optimized effective potential (OEP) method[159,174] and include exact exchange or other self-interaction-free functionals.[219] OEP produces a far more accurate KS potential, with the correct asymptotic behavior. The major remaining error is simply the correlation contribution to the position of the HOMO, i.e., a small shift. Unfortunately, we do not yet have an accurate correlation energy functional to match with exact exchange for energetics.

N_2, a Very Small Molecule

To illustrate the influence of different ground-state potentials consider the N_2 molecule. In all the cases discussed below, a SCF step was carried out using the ground-state potential to find the KS levels, which are then used as input to Eq. [47] with the ALDA XC kernel.

The KS energy levels and KS orbitals for the LDA functional are shown in Table 7. The orbitals are calculated with two different numerical methods, the first is fully numerical basis set free (i.e., solved on a real space grid) while the other uses the Sadlej (52 orbitals) basis set[220] [the OEP results for the EXX (KLI) approximation shown in Table 7 are also calculated basis set free]. Note that the eigenvalues for the higher unoccupied states are positive. This is due to the LDA potential being too shallow and not having the correct asymptotic

Table 7 Orbital Energies of the KS Energy Levels for N_2 at Separation $R = 2.0744$ a.u.

	Energies in (eV)		
Orbital	LDA Basis Set Free[a]	LDA Sadlej[b]	OEP Basis Set Free[a]
Occupied Orbitals			
$1\sigma_g$	−380.05	−380.82	−391.11
$1\sigma_u$	−380.02	−380.78	−391.07
$2\sigma_g$	−28.24	−28.52	−35.54
$2\sigma_u$	−13.44	−13.40	−20.29
$1\pi_u$	−11.89	−11.86	−18.53
$3\sigma_g$	−10.41	−10.38	−17.15
Unoccupied Orbitals			
$1\pi_g$	−2.21	−2.23	−8.44
$4\sigma_g$	−0.04	0.66	−5.05
$2\pi_u$	>0	1.93	−4.04
$3\sigma_u$	>0	1.35	−3.54
$1\delta_g$	>0	—	−2.76
$5\sigma_g$	>0	3.20	−2.49
$6\sigma_g$	>0	—	−2.33
$2\pi_g$	>0	3.89	−2.17
$3\pi_u$	>0	—	−2.04

[a]From Ref. 221.
[b]From Ref. 222.

Table 8 Comparison of Vertical Excitation Energies for First 12 Excited States of N_2 Calculated Using Different Methods for SCF Step

State	Excitation	Excitation Energy (eV)					
		BARE KS[a]	ALDA[a]	ALDA[b]	LB94[c]	OEP[d]	Expt[e]
		Singlet → Singlet Transitions					
$w^1\Delta_u$	$1\pi_u \rightarrow 1\pi_g$	9.63	10.20	10.27	9.82	10.66	10.27
$a'^1\sum_u^-$	$1\pi_u \rightarrow 1\pi_g$	9.63	9.63	9.68	9.18	10.09	9.92
$a^1\Pi_g$	$3\sigma_g \rightarrow 1\pi_g$	8.16	9.04	9.23	8.68	9.76	9.31
$a''^1\sum_g^+$	$3\sigma_g \rightarrow 4\sigma_g$	—	—	10.48	—	12.47	12.20
$o^1\Pi_u$	$2\sigma_u \rightarrow 1\pi_g$	—	—	13.87	—	14.32	13.63
$c^1\Pi_u$	$1\pi_u \rightarrow 4\sigma_g$	—	—	11.85	—	13.07	12.90
		Singlet → Triplet Transitions					
$C^3\Pi_u$	$2\sigma_u \rightarrow 1\pi_g$	11.21	10.36	10.44	10.06	11.05	11.19
$B'^3\sum_u^-$	$1\pi_u \rightarrow 1\pi_g$	9.63	9.63	9.68	9.18	10.09	9.67
$W^3\Delta_u$	$1\pi_u \rightarrow 1\pi_g$	9.63	8.80	8.91	8.32	9.34	8.88
$B^3\Pi_g$	$3\sigma_g \rightarrow 1\pi_g$	8.16	7.50	7.62	7.14	8.12	8.04
$A^3\sum_u^+$	$1\pi_u \rightarrow 1\pi_g$	9.63	7.84	8.07	7.29	8.51	7.74
$E^3\sum_g^+$	$3\sigma_g \rightarrow 4\sigma_g$	—	—	10.33	12.32	11.96	12.00
Mean Absolute Error		(0.61)	(0.27)	0.54	(0.63)	0.34	

[a]Using the Sadlej basis set. From Ref. 222.

[b]Basis set free. From Ref. 221.

[c]From Ref. 223.

[d]Using KLI approximation. From Ref. 221.

[e]Computed in Ref. 224 from the spectroscopic constants of Huber and Herzberg.[225]

behavior as mentioned eariler. When comparing the basis set calculation with the basis set free calculation, the occupied orbitals are found to be in good agreement. However, for the unoccupied states that are unbounded in LDA, basis sets cannot describe these states correctly, giving a positive energy value that can vary greatly from one basis set to another.

For the LDA results calculated with the Sadlej basis set, the bare KS transition frequencies between these levels are shown in Table 8. Note that they are in rough agreement with the experimental values and that they lie in between the singlet–singlet and singlet–triplet transitions.[226] The ALDA XC kernel $f_{\mathrm{XC}}^{\mathrm{ACDA}}$ then shifts the KS transitions toward their correct values. Also given in Table 8 are the mean absolute errors for each method; errors in parentheses are calculated for the lowest eight transitions only. For the eight lowest transitions LDA does remarkably well, the mean absolute error (MAE) being 0.27 eV for the Sadlej basis set. For higher transitions LDA fails drastically, the MAE increasing to 0.54 eV when the next four transitions are included. This increase in the MAE is attributed to a cancellation of errors that lead to good frequencies for the lower transitions.[221] Because LDA binds

only two unoccupied orbitals, it cannot describe transitions to higher orbitals accurately. In basis set calculations, the energies of the unbound orbitals that have *converged* will vary wildly and give unreliable transition frequencies.

One class of XC functionals that should not have this problem are the asymptotically corrected (AC) functionals.[217,218,227–229] LB94[230] is one of these functionals, and its performance is shown in Table 8. AC XC potentials tend to be too shallow in the core region, so the lower KS energy levels will be too low while the AC piece forces the higher KS states to be bound and their energies will cluster below zero. Thus, it can be expected that when using AC functionals, the computed transition frequencies will be consistently underestimated.

The KS orbitals found using the OEP method are self-interaction free, and they are usually better approximations to the true KS orbitals. OEP also has the correct asymptotic behavior, and as we can see in Table 7, all orbital energies are negative. In Table 8, the MAE for OEP is 0.34 eV , which is much lower than that for LDA. Because OEP binds all orbitals, it allows many more transitions to be calculated. A common OEP functional is exact exchange (or an approximation[231] to it called KLI), which neglects correlation effects, which are generally small contributions to the KS orbital energies. Using exact exchange with the ALDA for f_{XC} (which does contain correlation) leads to good transition frequencies as shown in Table 8. Although LDA is sometimes closer to the experimental values for the lower transitions, the value of OEP lies in its ability to describe both the higher as well as the lower transitions.

Napthalene, a Small Molecule

Returning to our benchmark case of naphthalene: in Table 4 the LHF (an OEP exact exchange method described above) method is used to find the orbitals, which are then used with an LSDA or PBE kernel to find the transition frequencies. Also given are the results if the LSDA/PBE functional had been used for both steps. We find that excitation energies from combining LHF with a LDA/PBE kernel are in between the GGA and the hybrid results (given in Table 4), except for the 1^1A_u Rydberg state, whose excitation energy is significantly improved. The results do not change significantly whether the LSDA kernel or the PBE GGA kernel is used together with an LHF potential.

The 1^1B_{1g} and especially the 1^1A_u states of naphthalene are diffuse, so it is not surprising that their excitation energies are considerably underestimated in the LSDA and GGA treatment. Using the asymptotically correct LHF potential corrects the excitation energy of the 1^1A_u state, which is a pure one-particle excitation out of the $1a_u$ valence orbital into the $10a_g$ Rydberg orbital, the latter of which may be viewed as a $3s$ orbital of the $C_{10}H_8^+$ ion. In contrast, a strong mixture of valence and Rydberg excitations occurs in the 1^1B_{1g} state. The LHF potential improves the GGA results only

marginally here, suggesting that more accurate XC kernels are required to account properly for valence–Rydberg mixing.

Analyzing the Influence of the XC Kernel

As mentioned earlier, the TDDFT kernels used in practice are local or semilocal in both space and time. Even hybrids are largely semi-local, as they only mix in 20–25% exact exchange.

In these practical calculations, both the ground-state XC potential and TDDFT XC kernel are approximated. A simple way to separate the error in the XC kernel is to examine a test case where the exact KS potential is known. Figure 5 shows the spectrum of He using the exact KS potential, but with the ALDA XC kernel. The ALDA XC kernel does rather well[232] (very well, as we shall see later when we examine atoms in more detail), and very similar results are obtained with standard GGAs.

The errors in such approximate kernels originate from the locality in space and time. We can test the error of locality separately from the local time error for the He atom, by studying the exchange limit for the XC kernel. For two spin-unpolarized electrons, $f_x = -1/2|\mathbf{r} - \mathbf{r}'|$, i.e., it exactly cancels half the Hartree term. Most importantly, it is frequency-independent so that there is no memory, meaning that the adiabatic approximation is exact. In Figure 6, we compare ALDAx, which is the ALDA for just exchange, to the exact exchange result for He. ALDA makes noticeable errors relative to exact exchange, showing that nonlocality in space is important in this example.

Thus, the hybrid functionals, by virtue of mixing some fraction of exact exchange with GGA, will have slightly different potentials (mostly in the asymptotic region), but noticeably different kernels.

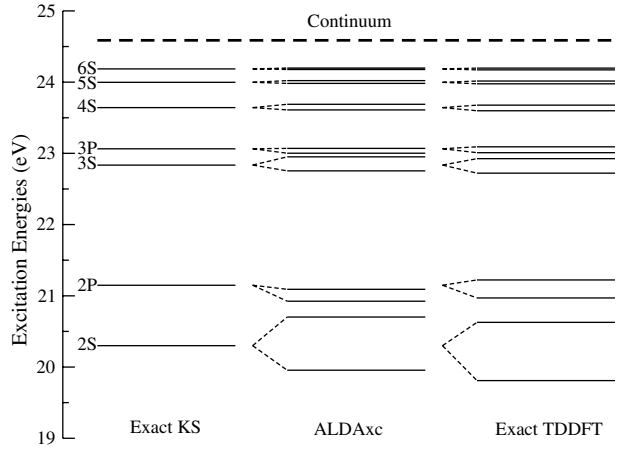

Figure 5 Spectrum of helium calculated using the ALDA XC kernel[232] with the exact KS orbitals.

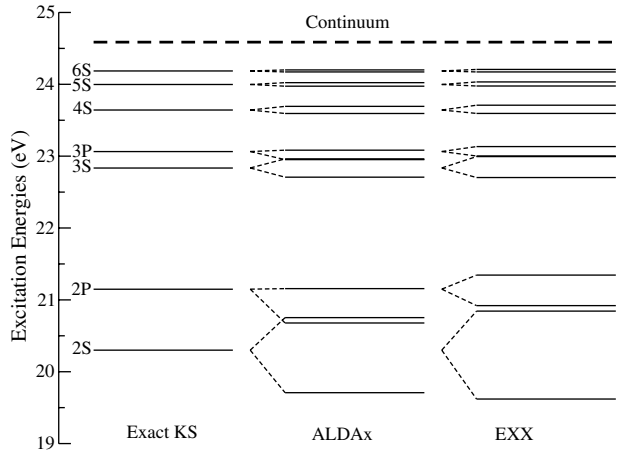

Figure 6 Spectrum of helium calculated using the ALDAx kernel and the exact exchange kernel[232] with the exact KS orbitals. The importance of nonlocality for the XC kernel can be seen, as the exchange part of ALDA gives a noticeable error compared to the exchange part of the true functional (the AEXX kernel for He).

Errors in Potential vs. Kernel

It has long been asserted that fixing the defects in the potential, especially its asymptotic behavior, is the major challenge to improving TDDFT results.[227–229] We argue here that this assertion is overly simplistic, and base this upon tests carried out on atoms and small molecules. In large molecules, where the scientific interest is in the many low-lying transitions, the potential can be sufficiently accurate, while the kernel may play a larger role.

The analysis done for naphthalene above can shed some light of the general failure of TDDFT in underestimation of the ^1L_a transitions in PAHs. Using the self-interaction free LHF potential does not obviate this problem, as is illustrated in Table 9. To the best of our knowledge, the cause of this shortcoming of TDDFT is not well understood. We note, however, that the same incorrect ordering of ^1L_a and ^1L_b occurs in the CIS approximation, which is also self-interaction free. The analysis here shows that this is a failure of approximations for the XC kernel rather than to the ground-state potential.

Table 9 Naphthalene: Effect of Ground-State Potential on the Excitations of Table 4

Method	1^1B_{3u}	1^1B_{2u}	2^1A_g	1^1B_{1g}	2^1B_{3u}	1^1A_u
LSDA	4.191	4.026	5.751	4.940	5.623	5.332
LHF/LSDA	4.317	4.143	5.898	5.097	5.752	5.686
PBE	4.193	4.031	5.753	4.957	5.622	5.141
LHF/PBE	4.295	4.121	5.876	5.091	5.741	5.693
"best"	4.0	4.5	5.5	5.5	5.5	5.7

Understanding Linear Response TDDFT

Several simple methods have evolved for understanding TDDFT results qualitatively. The most basic of these methods is the single-pole approximation (SPA),[189] which includes only one pole of the response function. The easiest way to see the SPA is to truncate Eq. [47] to a 1×1 matrix, yielding an (often excellent) approximation to the change in transition frequency away from its KS value:[196,233]

$$\omega^2 \approx w_{q\sigma}^2 + 2\omega_{q\sigma} K_{q\sigma q\sigma} \quad \text{(SPA)} \qquad [60]$$

(The original SPA was on an unsymmetric system yielding $\omega \approx w_{q\sigma} + K_{q\sigma q\sigma}$, which for a spin-saturated system, becomes $\omega \approx \omega_q + 2K_{qq}$.[232]) The SPA can also provide a quick and dirty estimate for the transition frequencies since only KS transitions and one integral over f_{XC} are needed to calculate each transition frequency. While SPA allows an estimate of the shift of transitions from their KS energy eigenvalue differences, it says nothing about oscillator strengths, which are unchanged from their KS values. A careful analysis[234] of the TDDFT equation shows that oscillator strengths are particularly sensitive to even small off-diagonal matrix elements, whereas transition frequencies are less sensitive to these elements.

A more advanced method for understanding TDDFT results qualitatively is the double-pole approximation[235] (DPA), which is applicable when two transitions are strongly coupled to one another, but not strongly coupled to the rest of the transitions. Under these conditions one can show explicitly the very strong influence off-diagonal elements have on oscillator strengths, where, sometimes, an entire KS peak can have almost no contribution to the absorption spectra. One also sees pole repulsion in the positions of the transitions, a phenomenon again missing from SPA.

The DPA was used recently and found to explain successfully X-ray edge spectroscopy results for $3d$ transition-metal solids as one moves across the periodic table.[236] These transitions form a perfect test case for DPA because the only difference between those transitions is caused by the spin–orbit splitting (several electron volts) of the $2p^{1/2}$ and $2p^{3/2}$ levels. In a ground-state KS calculation, this leads to a 2 : 1 branching ratio for the two peaks, based simply on degeneracy, as all matrix elements are identical for the two transitions. Experimentally this ratio is observed for Fe, but large deviations occur for other elements. These deviations were replicated in full TDDFT calculations and attributed to strong core–hole correlations. The SPA, while nicely accounting for the shifts in transition frequencies relative to bare KS transitions, yields only the ideal 2 : 1 branching ratio. However, the DPA model gives a much simpler interpretation. The sensitivity of oscillator strengths to off-diagonal matrix elements means that, even when the off-diagonal elements are much smaller than diagonal elements (of order 1 eV), they cause rotations

Table 10 Transition Frequencies and Oscillator Strengths (OS) Calculated Using the Double-Pole Approximation (DPA) for the Lowest $^1B_{3u}$ Transitions in Naphthalene[a]

	KS		DPA		Full TDDFT	
	ω	OS	ω	OS	ω	OS
1^1B_{3u}	4.117	(1.02)	4.245	(0.001)	4.191	(0)
2^1B_{3u}	4.131	(1.00)	6.748	(2.02)	5.633	(1.14)

[a]The PBE functional was used with an aug-TZVP basis set on top of a PBE/TZVP/RI ground state structure.

in the 2-level space, and alter greatly the branching ratio. Thus a KS branching ratio occurs even with strong diagonal "correlation," so long as off-diagonal XC contributions are truly negligible. But even small off-diagonal correlation can lead to large deviations from KS branching ratios.

We can use DPA to understand the lowest $^1B_{3u}$ transitions in naphthalene. The TDDFT matrix elements for the PBE calculation of the two nearly degenerate KS transitions, $1a_u \rightarrow 2b_{3g}$ and $2b_{1u} \rightarrow 2b_{2g}$ are listed in Table 10, along with their corresponding KS transition frequencies. Contour plots of the four orbitals involved are shown in Figure 7. We note first that these two KS transitions are essentially degenerate, and therefore we cannot treat them at all within SPA. The degeneracy is lifted by the off-diagonal elements, which cause the transitions to repel each other, and strongly rotate the oscillator strength between the levels, removing almost all of the oscillator strength from the lower peak.[235] The DPA yields almost the correct frequency and oscillator strength (i.e., none) for the lower transition, but the higher one is overestimated, with too much oscillator strength. This overestimation arises from coupling to other higher transitions neglected in the DPA. In fact, in the DPA for this example, the higher transition lands right on top of the third transition, so strong coupling occurs there too. This naphthalene example illustrates (1) that solution of the full TDDFT equations is typically required for large molecules having many coupled transitions, and (2) that simple models can aid in the interpretation of such complex results. The message we convey here is that while models developed for well-separated transitions can provide some insight for specific transitions in large molecules, the number and density of transitions make such models only semiquantitative at best.

ATOMS AS A TEST CASE

In this section, we look more closely at how well TDDFT performs for a few noble-gas atoms. As explained earlier, TDDFT's behavior for atoms is far from representative of its behavior for large molecules, but the examination of TDDFT on atoms does allow careful study of the electronic spectra without

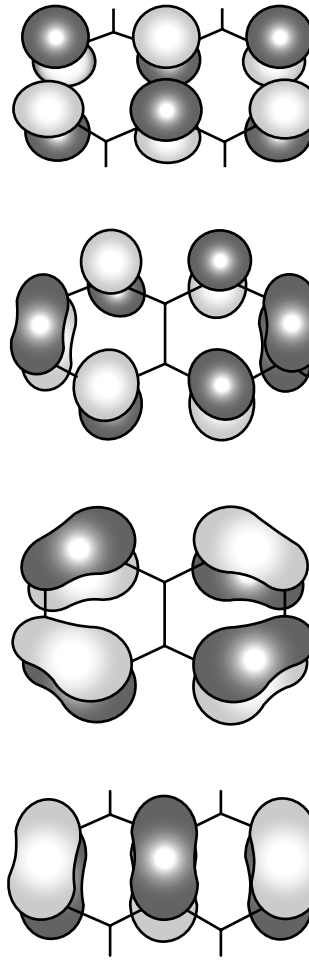

Figure 7 Four orbitals involved in the first two $^1B_{3u}$ transitions (contour value ± 0.07 a.u.). Starting from the bottom, the orbitals shown are the $2b_{1u}$, $1a_u$, $2b_{2g}$, and $2b_{3g}$ orbitals, respectively. The PBE functional and an aug-TZVP basis set were used to derive these orbitals.

other complications. Most importantly, we have essentially exact ground-state KS potentials from Umrigar and co-workers[156,237] for the He, Be, and Ne atoms, allowing us to dissect the sources of error in TDDFT calculations.

Quantum Defect

The KS orbital energy level diagram of the helium atom is shown in Figure 8. The zero is set at the onset of the continuum and is marked with a

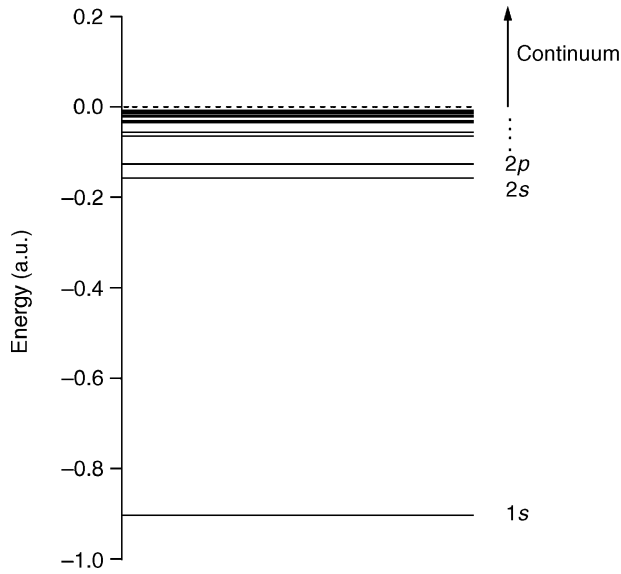

Figure 8 Singlet energy level diagram for the helium atom. The Rydberg series of transition frequencies clustered below the ionization threshold can be seen. The frequencies cluster together, making it difficult to assess the quality of the TDDFT calculated spectra. As discussed in the text, the quantum defect is preferable for this purpose.

dotted line. For closed-shell atoms and for any spherical one-electron potential that decays as $-1/r$ at large distances, the bound-state transitions form a Rydberg series with frequencies

$$\omega_{nl} = I - \frac{1}{2(n - \mu_{nl})^2} \qquad [61]$$

where I is the ionization potential, and μ_{nl} is called the quantum defect (QD). Quantum defect theory was developed by Ham[238] and Seaton[239] before the Hohenberg–Kohn theorem.[1]

The great value of the quantum defect is its ability to capture all the information about the entire Rydberg series of transitions in a single slowly varying function of energy, $\mu_l(E = \omega - I)$, which can often be fit by a straight line or parabola. We compile extremely accurate singlet and triplet values from wave function calculations[201] for the helium atom in Table 11, along with results[156] from the exact ground-state KS potential shown in Figure 2. For each column, the transition frequencies are on the left, while the corresponding quantum defects are on the right. Note how small the differences between transitions become as one climbs up the ladder, and yet the quantum defect remains finite and converges to a definite value.

Table 11 Transition Energies (ω) and Quantum Defects (QD) for He Atom s-Rydberg Series (a.u.)[a]

	Singlet[b]		Triplet[b]		KS[c]	
Transition	ω	QD	ω	QD	ω	QD
$1s \rightarrow 2s$	0.7578	0.1493	0.7285	0.3108	0.7459	0.2196
$1s \rightarrow 3s$	0.8425	0.1434	0.8350	0.3020	0.8391	0.2169
$1s \rightarrow 4s$	0.8701	0.1417	0.8672	0.2994	0.8688	0.2149
$1s \rightarrow 5s$	0.8825	0.1409	0.8883	0.2984	0.8818	0.2146
$1s \rightarrow 6s$	0.8892	0.1405	0.8926	0.2978	0.8888	0.2144
$1s \rightarrow 7s$	0.8931	0.1403	0.8926	0.2975	0.8929	0.2143

[a]The ionization energy is 0.90372 a.u.

[b]Accurate nonrelativistic calculations from Ref. 201.

[c]The differences between the KS eigenvalues obtained with the exact potential from Ref. 156.

All of the information concerning the levels in Figure 8 and the transitions of Table 11 is contained in the QD shown in Figure 9. This figure illustrates that the quantum defect is a smooth function of energy and is well approximated (in these cases) as a straight line. The quantum defect is thus an extremely compact and sensitive test of approximations used to compute transition frequencies. We recommend that any approximate ground-state KS potential suggested for use in TDDFT should have its quantum defect

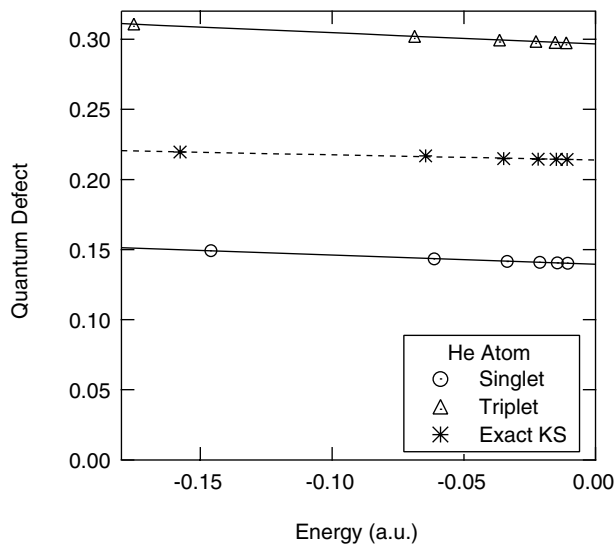

Figure 9 Exact *s* KS quantum defect and the exact singlet and triplet quantum defects of He and their fits. The quantum defect is a smooth function of energy. Knowing the quantum defect for a few transitions allows us to find it for all transitions and hence their frequencies.

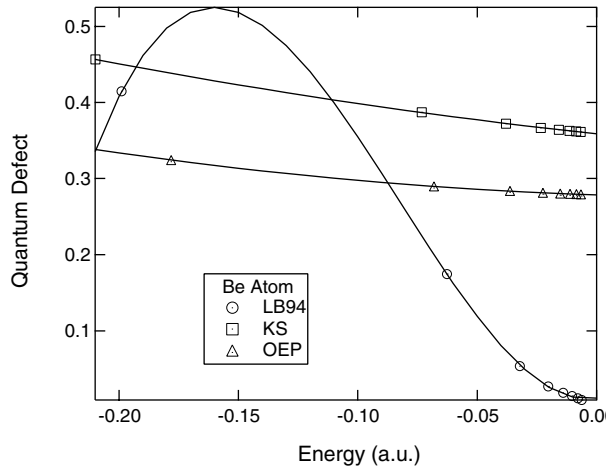

Figure 10 The Be *p* quantum defect of LB94, exact exchange (OEP), and KS, and their best fits. While both functionals give the correct asymptotic behavior of the KS potential, we can learn more about their performance by calculating the quantum defect.

compared with the exact KS quantum defect. Any approximate XC kernel should produce accurate corrections to the ground-state KS quantum defect, which are typically on the scale of Figure 9.

To demonstrate the power of QD analysis, we test two common approximations to the ground-state potential, both of which produce asymptotically correct potentials (exact exchange[240] (see the discussion on approximate functionals above and LB94[230]). Exact exchange calculations are more CPU demanding than are traditional DFT calculations, but they are becoming popular because of the high quality of the potential.[241,242] In comparison, LB94 provides an asymptotically correct potential at little extra cost beyond traditional DFT.[218,229,243] In Figure 10 we show the *p* Be quantum defect obtained with LB94, OEP, and exact KS potentials. Note the high quality of the exact exchange potential; the quantum defect curve is almost identical to the exact one, offset by about 0.1. Contrarily, the quantum defect of LB94 is poor for all cases studied.[244,245] Figure 10 shows that just having an asymptotically correct potential alone is not sufficient to get a good quantum defect.

Testing TDDFT

To see how well TDDFT really does, we can plot quantum defects for atoms, using the He atom as our prototype in this section. In Figure 11, we plot first the KS quantum defect and the exact singlet and triplet lines, as was done in Figure 9. We consider the Hartree approximation, which is equivalent to setting the XC kernel to zero. This approximation changes the position of the singlet curve but leaves the triplet curve unchanged from its KS

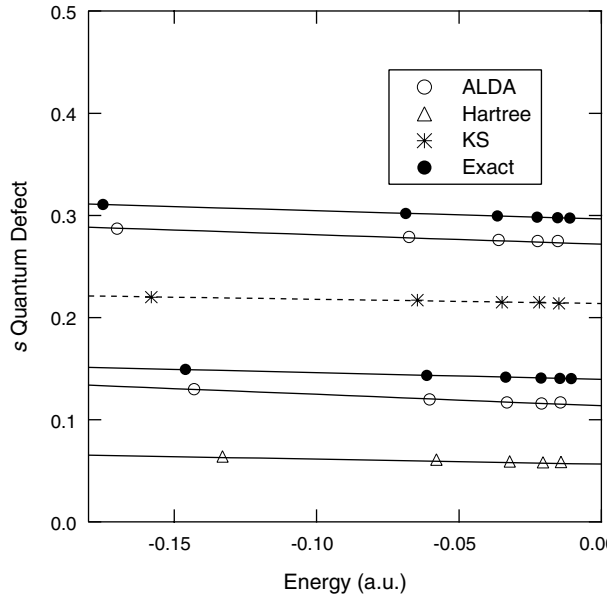

Figure 11 Corrections due to using the Hartree and ALDA kernel on the exact KS *s* quantum defect of He. The Hartree kernel affects only the singlet defect, shifting them to values that are too low. If a good XC kernel is then used, both the triplet and singlet quantum defects should move from the Hartree kernel toward the exact QD values.[245] In this case, ALDA does a good job and is performing well.

value because the direct term includes no spin flipping. The Hartree approximation definitely improves the KS for the singlet. Finally, we include ALDA XC corrections. Only if these latter corrections significantly improve the results compared to the Hartree curves can we say TDDFT is really working here. Clearly it does, reducing the Hartree error enormously.

The results of Figure 11 are also typical of He *p* transitions, and Be *s* and *p* transitions; however, for unknown reasons, the $s \rightarrow d$ transitions fail badly for both of these systems.[244,246]

Saving Standard Functionals

The incorrect long-range behavior of the potential from standard density functionals is a problem only when Rydberg excitations are needed. It would be unsatisfactory to perform a completely different type of calculation such as OEP in order to include such excitations, especially if the cost of that calculation is untenable.

It is possible, with some thought and care, however, to extract the Rydberg series from the short-ranged LDA potential by using quantum defect

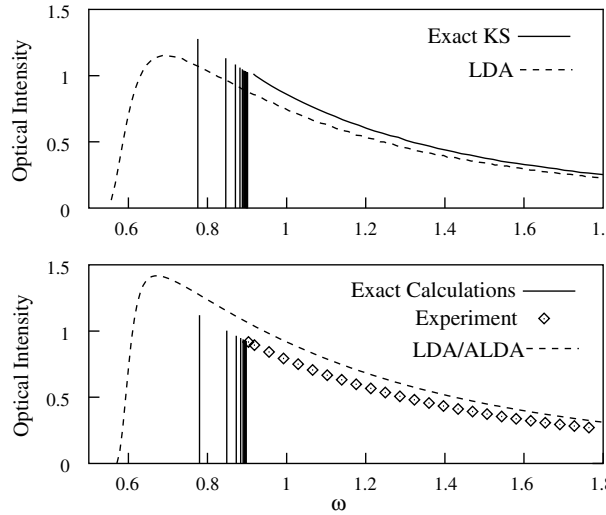

Figure 12 Optical intensities (in inverse hartrees) as a function of ω (in hartrees) for the He atom. (*Top panel*) The exact KS and LDA spectra. (*Lower panel*) The TDDFT corrected spectra. LDA/ALDA results are from Ref. 247 but unshifted. The exact calculations are from Ref. 248, multiplied by the density of states factor (see text), and the experimental results are from Ref. 249.

theory. To see this, consider Figure 12, which shows both the bare KS response and the TDDFT-corrected response as a function of ω for the He atom. The δ-function absorptions at the discrete transitions have been replaced by straight lines, whose height represents the oscillator strength of the absorption multiplied by the appropriate density of states.[250] In the top panel, just the KS transitions are shown for both the exact KS potential and the LDA potential of Figure 3. The exact curve has a Rydberg series converging to 0.904 h (24.592 eV), which is the exact ionization threshold for He. The LDA curve, on the other hand, has a threshold at just below 0.6 h. Nonetheless, its optical absorption clearly mimics that of the exact system, even in the Rydberg series region, and is accurate to about 20%. The TDDFT ALDA kernel corrections are small and overcorrect the bare LDA results, but the LDA/ALDA spectra still follows the exact one closely.

Why do the LDA spectra look so similar to the exact one? Is this just a coincidence? Returning to Figure 3, we notice that the LDA (or a GGA) potential runs almost exactly parallel to the true potential for $r \lesssim 2$, i.e., where most of the density is. Thus, the scattering orbitals of the LDA potential, with transition energies between 0.6 and 0.9 h, almost match exactly the Rydberg orbitals of the exact KS potential with the same energy.[253] When defined carefully, i.e., when we use phase space factors for the continuum relative to bound states, the oscillator strengths for both the LDA and exact KS

transitions are about the same. This similarity is no coincidence but, due to the lack of a derivative discontinuity in LDA, the potential LDA differs from the exact one by roughly a constant.

The "fruitfly" of TDDFT benchmarks is the $\pi \rightarrow \pi^*$ transition in benzene. This transition occurs at about 5 eV in a ground-state LDA calculation, and ALDA shifts it correctly to about 7 eV.[233] Unfortunately, this value lies in the LDA continuum, which starts at about 6.5 eV! This shift is an example of the same general phenomenon we saw above for He, where LDA has pushed some oscillator strength into the continuum, but its overall spectra remains about right.

We can take the observation that the LDA potential is roughly a constant shift from the exact KS potential in a core region and go one step further to deduce the energies of individual transitions. While the existence of a quantum defect requires a long-ranged potential, its value is determined by the phase shift caused by the deviation from $-1/r$ behavior in the interior of the atom. The *quantum defect extractor* (QDE)[251] is a formula for extracting the effective quantum defect from a scattering orbital of a short-ranged KS potential, such as that of LDA. The QDE is

$$\frac{d \ln \phi}{dr} = \frac{1}{n^*} - \frac{n^*}{r} - \frac{1}{r} \frac{U(-n^*; 2; 2r/n^*)}{U(1 - n^*; 2; 2r/n^*)} \qquad [62]$$

Here $k = \sqrt{2|E|}$ is written as $k = (n^*)^{-1}$, with $n^* = (n - \mu_n)$, where n numbers the bound state, and μ_n is the quantum defect; U is the confluent hypergeometric function.[252] If the extractor is applied to an orbital of a long-ranged potential, it rapidly approaches its quantum defect.

The results of the QDE for the He atom, applied to both the exact KS potential and the LDA potential are plotted in Figure 13. The LDA potential

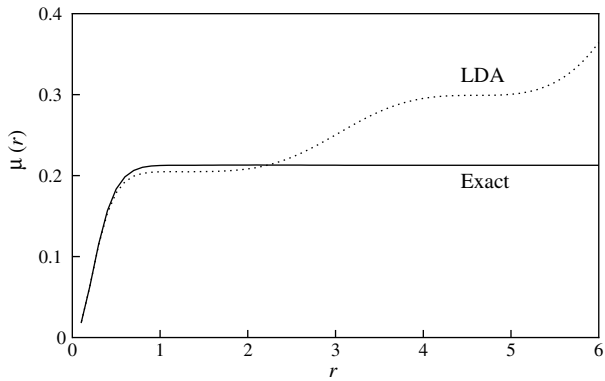

Figure 13 Solution of Eq. [62] for μ as a function of r for the He atom. The $n = 20$ orbital was used for the exact case, and the scattering orbital or energy $E = I + \epsilon_{1s}^{\mathrm{LDA}}$ was used for the LDA.

runs parallel to the exact potential in the region $1 < r < 2$ (where μ_∞ can already be extracted accurately), and orbitals corresponding to the same *frequency* (exact and LDA) are therefore spatially very similar in that region. Thus, the difference between the exact energy-normalized 20*s* orbital (which is essentially identical to the zero energy state in the region $0 < r < 6$) and the LDA scattering orbital of energy $I + \epsilon_{1s}^{\mathrm{LDA}} = 0.904 - 0.571 = 0.333\,\mathrm{h}$ is small in the region $1 < r < 2$, as can be seen in Ref. 251.

We show in Figure 13 the solution of Eq. [62] when this LDA scattering orbital is employed. Clearly, the plateau of the LDA curve in the $1 < r < 2$ region is an accurate estimate of the quantum defect. The value of μ on this plateau is 0.205, which is an underestimate by less than 4%.

Thus, given the ionization potential of the system, LDA gives a very accurate prediction of the asymptotic quantum defect. The ionization potential is needed to choose the appropriate LDA scattering orbital, but the results are not terribly sensitive to it. We repeated the same procedure with the LDA ionization potential [defined as $E_{\mathrm{LDA}}(\mathrm{He}) - E_{\mathrm{LDA}}(\mathrm{He}^+) = 0.974\,\mathrm{h}$] instead of the exact ionization potential, and found $\mu_\infty^{\mathrm{LDA}} = 0.216$, overestimating the exact μ_∞ by just 1%.

Electron Scattering

In this final section, we mention recent progress in developing a theory for low-energy electron scattering from molecules because scattering was one of the original motivations for developing TDDFT. One approach to calculating electron scattering would be to evolve a wave packet using the TDKS equations, but a more direct approach has been developed[254,255] in terms of the response function χ of the $N + 1$ electron system (assuming it is bound).

This latter approach to computing electron scattering uses similar technology to the discrete transition case described in detail earlier. Initial results for the simplest case of electron scattering from He^+ suggest a level of accuracy comparable to bound–bound transitions, at least for low energies (the most difficult case for traditional methods, due to bound-free correlation[256]). Using the exact ground-state potential and ALDA produces more accurate answers than when using static exchange,[254] a traditional low-cost method that is often used for larger molecules.[257,258]

In contrast to He^+, this method fails when applied to electron scattering from hydrogen because the approximate solution of the TDDFT equations (very similar to the single-pole approximation discussed above) fails, as a result of stronger correlations in hydrogen scattering. To overcome this strong correlation problem, a much simpler, but still general, method has been developed.[259] It uses an old scattering trick[260] to deduce scattering phase shifts from bound-state energies when the system is placed in a box[261] and yields excellent results for a very demanding case.

BEYOND STANDARD FUNCTIONALS

We surveyed and illustrated in the previous sections some of the many present successful applications of TDDFT. In those applications, standard approximations (local, gradient-corrected, and hybrid) were used for both the ground-state calculation and the excitations, via the adiabatic approximation. In this section, we survey several important areas in which the standard functionals have been found to *fail*, and we explain what might be done about it.

The errors in standard TDDFT are due to locality in both space and time, both of which are intimately related. In fact, all memory effects, i.e., dependence on the history of the density,[185] implying a frequency dependence in the XC kernel, can be subsumed into an initial-state dependence,[181] but probably not vice versa. Several groups are attempting to incorporate such effects into new approximate functionals,[262–273] but none have yet shown universal applicability.

The failure of the adiabatic approximation is most noticeable when higher order excitations are considered; these excitations are found to be missing in the usual linear response treatment.[191] The failure of the local approximation in space is evident, for example, when TDDFT is applied to extended systems, e.g., polymers or solids. Local approximations yield short-ranged XC kernels that become irrelevant compared to Hartree contributions in the long-wavelength limit. The Coulomb repulsion between electrons generally requires long-ranged $(1/r)$ exchange effects when long-wavelength response is being calculated.

Several approaches to correcting these problems have been developed and applied in places where the standard formulation has failed. These approaches fall into two distinct categories. First, where approximations that are local in the *density* fail, one can try approximations that are local (or semilocal) in the *current density*. In fact, for TDDFT, the gradient expansion, producing the leading corrections to ALDA, *only* works if the current is the basic variable.[274] Using the gradient expansion itself is called the Vignale–Kohn (VK) approximation,[275,276] and it has been tried on a variety of problems. The second category involves constructing orbital-dependent approximations with explicit frequency dependence.[277,278] This can work well for specific cases, but it is difficult to construct general density functional approximations from these examples. More importantly, solution of the OEP equations is typically far more CPU expensive than for the simple KS equations, making OEP impractical for large molecules.

Double Excitations

Casida[191] first pointed out that double excitations appear to be missing[279] from TDDFT linear response within any adiabatic approximation. Experience[280,281] shows that, as in naphthalene, adiabatic TDDFT will

sometimes produce a single excitation in about the right region, in place of two lines, where a double excitation has mixed strongly with a single excitation.

When a double excitation lies close to a single excitation, elementary quantum mechanics shows that f_{XC} must have a strong frequency dependence.[277] Post-adiabatic TDDFT methodologies have been developed[277,282,283] recently for including a double excitation when it is close to an optically active single excitation, and such post-adiabatic methodologies appear to work well for small dienes.[277,284] By going beyond linear response, one might hope that nontrivial double excitations are naturally included in, e.g., ALDA. It has been proven that, in the higher order response in ALDA, the double excitations occur simply as the sum of single excitations.[285] Thus, the scientific community does not currently know how best to approximate these excitations. The problem with higher order excitations is particularly severe for quantum wells, where the external potential is parabolic, leading to multiple near degeneracies between levels of excitation.[282]

For example, based on a HF reference, the 2^1A_g state of naphthalene has, according to the RICC2 results, a considerable admixture of double excitations. This admixture is consistent with the fact that the CIS method yields an excitation energy that is too high by 1.5 eV compared to experiment. The TDDFT results are much closer to experiment, yet still too high by several tenths of an electron volt.

Polymers

An early triumph of the VK functional was its success in predicting the static polarizabilities of long-chain conjugated polymers. These polarizabilites are greatly underestimated by both LDA and GGA functionals, with the error growing rapidly with the number of monomer units in the polymer.[289] In contrast, HF does rather well and does not overpolarize. The VK correction to LDA yields excellent results in many (but not all) cases, showing that a current-dependent functional can sometimes correct the overpolarization problem. Naturally, orbital-dependent functionals also account for this effect,[290] but they do at a much higher computational cost. A comparison of the methods is given in Figure 14.

Solids

When using TDDFT to calculate the optical response of insulators, local approximations have again been shown to fail badly. Most noticeably, local approximations do not describe excitonic effects,[291] or the exciton spectrum within the band gap. Moreover, the computed gap is usually much smaller than experiment because adiabatic approximations cannot change the gap size from its KS value.

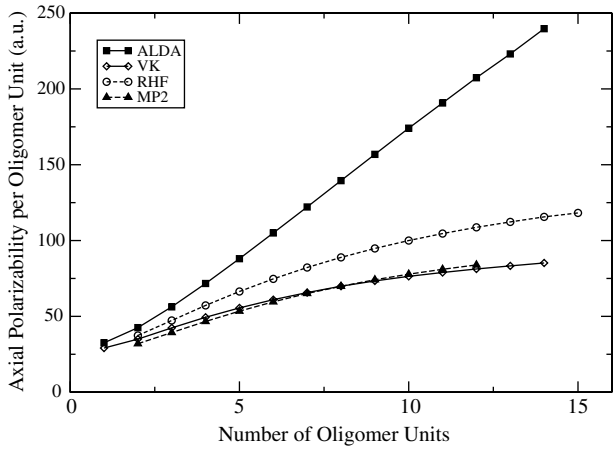

Figure 14 ALDA and VK static axial polarizability of polyacetylene compared with RHF and MP2 results from Refs. 286–288. ALDA overestimates the polarizability severely compared to the more accurate MP2 calculation. Restricted Hartree–Fock is also incorrect. The VK functional gives almost exact agreement with the MP2 results, at least in this case.

One approach to calculating optical responses of insulators is to use the approximation in TDCDFT. This has proven successful, although a single empirical factor was needed for results to agree with experiment.[292–294] An alternative approach to fixing TDDFT for solids is to study the many-body problem.[295] and determine which expressions the XC kernel must include in order to yield an accurate absorption spectrum.[296,297] However, all the schemes presently available require an expensive GW calculation in the first place.[298] The GW method is a common approximation to the self-energy in many-body Green's function theory. A recent review of how many-body techniques can improve TDDFT be found in Ref. 299.

Charge Transfer

Whenever a method is shown to work well, it inevitably gets applied to many scientific investigations, and specific failures then appear. Charge-transfer excitations are of great importance in photochemistry, especially of biological systems, but many workers are now finding abysmal results with TDDFT for such cases.[280,300,301]

The genesis of the failure of TDDFT can be traced to the fact that TDDFT is a linear response theory. When an excitation moves charge from one area in a molecule to another, both ends of that molecule will geometrically relax. While charge transfer between molecules can be well approximated by ground-state density functional calculations of the total energies of the species involved, TDDFT must deduce the correct transitions by

(infinitesimal) perturbations around the ground state, without relaxation. Thus, linear response is a poor method to use for problems involving charge transfer and many researchers are attempting to find practical solutions around it.[88,302–305]

OTHER TOPICS

We now discuss several topics of specialized interest where TDDFT is being applied and where development has been beyond simple extraction of excitations from linear response theory. First we will show how TDDFT can be used to construct entirely new approximations to the ground-state XC energy, which is particularly useful for capturing the long-range fluctuations that produce dispersion forces between molecules that are notoriously absent from most ground-state approximations. We will then survey strong field applications in which TDDFT is being used to model atoms and molecules in strong laser fields. Finally, we discuss the more recent and hot area of molecular electronics. Here, many workers are using ground-state DFT to calculate transport characteristics, but a more careful formulation can be done only within (and beyond) TDDFT.

Ground-State XC Energy

A more sophisticated ground-state approximate energy functional can be constructed[306–310] using the frequency-dependent response function of linear response TDDFT. We now introduce the basic formula and then discuss some of the systems this method is being used to study.

To construct the ground-state energy functional we use the long known adiabatic connection fluctuation–dissipation (ACFD) formula:

$$E_{\mathrm{XC}}[n_0] = \frac{1}{2}\int_0^1 d\lambda \int d^3r \int d^3r' \frac{P^{\lambda}(r,r')}{|\mathbf{r}-\mathbf{r}'|} \qquad [63]$$

where the pair density is

$$P^{\lambda}(r,r') = -\left(\sum_{\sigma\sigma'}\int_0^{\infty}\frac{d\omega}{\pi}\chi^{\lambda}_{\sigma\sigma'}[n_0](\mathbf{r}\mathbf{r}';i\omega)\right) - n_0(\mathbf{r})\delta^{(3)}(\mathbf{r}-\mathbf{r}') \qquad [64]$$

and the coupling constant λ is defined so as to multiply the electron–electron repulsion in the Hamiltonian but where the external potential is adjusted to keep the density fixed.[311,312] The quantity $\chi^{\lambda}_{\sigma\sigma'}$ is given by Eq. [42] with the XC kernel $f^{\lambda}_{\mathrm{XC}\sigma\sigma'}$. Any approximation to the XC kernel yields a sophisticated XC energy $E_{\mathrm{XC}}[n]$.

Note that when we set XC effects to zero in conventional DFT, we end up with the highly inaccurate Hartree method of 1928. However, when calculating the linear response, if the XC kernel is zero (i.e., if it is within the random phase approximation), the XC energy calculated by Eq. [63] still gives useful results.[306]

The ACFD procedure is far more demanding computationally than is conventional DFT, but as the previous paragraph has shown, even poor approximations to the XC kernel can still lead to good results. Using Eq. [63] to find the XC energy allows one to capture effects such as dynamical correlation or van der Waals interactions, which are missing from conventional ground-state DFT approximations and which are important in biological and other systems.

The energy decay coefficient between two atoms or molecules (C_6 in $E \rightarrow -C_6/R^6$, where R is their separation) can be evaluated accurately (within about 20%) using a local approximation to the frequency-dependent polarizability.[308,313–315] The van der Waals binding energy curve for two helium atoms is shown in Figure 15. Using the fluctuation–dissipation formula, Eq. [63], with the PBE0 XC kernel gives more accurate results than those calculated with the semilocal functionals (BP86, PBE). The frequency integral in Eq. [63] has been performed explicitly, albeit approximately, yielding

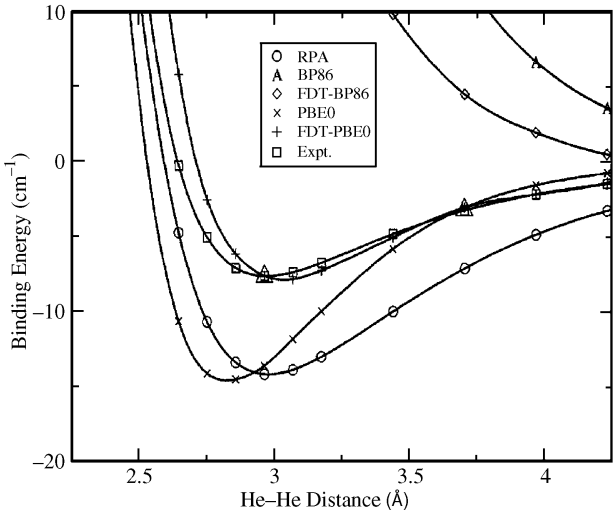

Figure 15 Binding energy for the helium dimer interacting via van der Waals (vdW) forces, from Ref. 306. New XC energy functional may be constructed from any ground-state functional using the fluctuation–dissipation theorem (FDT). Curves from the standard ground-state functionals BP86[5,316] and PBE[7] are given, along with FDT curves constructed from these two functionals as input. The FDT is needed to describe vdW interaction accurately. A BP86 ground state density is used.

an explicit nonlocal density functional[308,310,313,317–322] applicable at all separations, which shows great promise for including dispersion forces in standard DFT calculations. TDDFT response functions have also been used in the framework of symmetry-adapted perturbation theory to generate accurate binding energy curves of van der Waals molecules.[323]

One can also use Eq. [63] for bond lengths.[324,325] In fact, Eq. [63] provides a KS density functional that allows bond breaking without artificial symmetry breaking.[309] In the paradigm case of the H_2 molecule, the binding energy curve has no Coulson–Fischer point, and the bond dissociation correctly gives two isolated H atoms. Unfortunately, while simple approximations provide correct results near equilibrium and at infinite bond lengths, they produce an unphysical repulsion at large, but finite separations. This repulsion can be traced back[309] to the lack of double excitations in any adiabatic f_{XC}. Study of the basis set convergence of E_{XC} has also revealed an obvious flaw in the ALDA kernel at short distances.[306]

Further research is needed to find accurate XC kernels. One method[307] that can be used to test these new kernels is to examine the uniform electron gas because the frequency-dependent susceptibility can be found easily with the well-known Lindhard function. Different approximate XC kernels may thus be tested,[326] and their results can be compared to results from highly accurate Monte Carlo simulations.

Strong Fields

We now turn our attention to the nonperturbative regime. Due to advances in laser technology over the past decade, many experiments are now possible where the laser field is stronger than the nuclear attraction.[11] The time-dependent field cannot be treated perturbatively, and even solving the time-dependent Schrödinger equation in three dimensions for the evolution of two interacting electrons is barely feasible with present-day computer technology.[327]

Wave function methods are prohibitive for more than a few electrons in the regime of (not too high) laser intensities where the electron–electron interaction is still important. TDDFT is essentially the only practical scheme available[328–334] for dealing with many electrons in these kinds of time-dependent fields. There exists a host of phenomena that TDDFT might be able to predict including: high harmonic generation, multiphoton ionization, above-threshold ionization, above-threshold dissociation, etc., but these predictions will be possible only if accurate approximations are available.

With the recent advent of atto-second laser pulses, the electronic time scale has become accessible experimentally. Theoretical tools needed to analyze the dynamics of excitation processes on the atto-second time scale will consequently become more and more important to scientists studying such fast processes. An example is the time-dependent electron localization

function[335,336] (TDELF), which allows one to compute the time-resolved formation, modulation, and breaking of chemical bonds, thus providing a visual understanding of the dynamics of excited electrons, as, for example, in Ref. 337. The natural way of calculating the TDELF is from the TDKS orbitals.

High harmonic generation (HHG) is the production of many harmonics (sometimes hundreds) of the input frequency from medium intensity lasers. Here TDDFT calculations have been successful for some atoms[338–340] and molecules.[341,342] Several experiments have used the HHG response of molecules to determine their vibrational modes,[343] and calculations have been performed using traditional scattering theory.[344] If HHG response develops into a new spectroscopy, the electron scattering theory discussed above may be of utility to treat large molecules.

Multiphoton ionization (MPI) occurs when an atom or molecule loses more than one electron in an intense electromagnetic field. It was discovered to be a nonsequential process, meaning that the probability of double ionization can be much greater than the product of two independent ionization events, thus leading to a "knee" in the double ionization probability as a function of intensity.[345–347] TDDFT calculations have been unable to reproduce this knee accurately, and it has been shown that a correlation-induced derivative discontinuity is needed in the time-dependent KS potential[186] for the method to give proper results.

Above-threshold ionization (ATI) refers to the probability of ionization when the laser frequency is below the ionization potential, i.e., it does not occur in linear response.[348,349] Both ATI and MPI require knowledge of the correlated wave function, which is not directly available in a KS calculation, hence neither are given well in a TDDFT calculation.

Because the ionization threshold plays a crucial role in most strong field phenomena, Koopman's theorem, which relates the energy level of the KS HOMO to the ionization energy, should be satisfied. As standard functionals fail to satisfy Koopman's theorem due to their poor potentials (see Figure 3), this suggests the use of self-interaction free methods such as OEP[159,174] or LDA-SIC.

The field of quantum control[350] involving the femto-second control of chemical bonding has concentrated mainly on the motion of the nuclear wave packet on a given set of precalculated potential energy surfaces. With the advent of atto-second pulses, control of electronic dynamics has come within reach. A marriage of optimal control theory together with TDDFT appears to be the ideal theoretical tool to tackle these problems.[351,352] The ability of TDDFT to predict the coherent control of quantum wells using terahertz lasers has been shown,[353–355] although, once again, the lack of access to the true wave function is a difficulty. Many difficulties and challenges remain in order to develop a general-purpose theory, including the coupling between nuclei and electrons.[356–358]

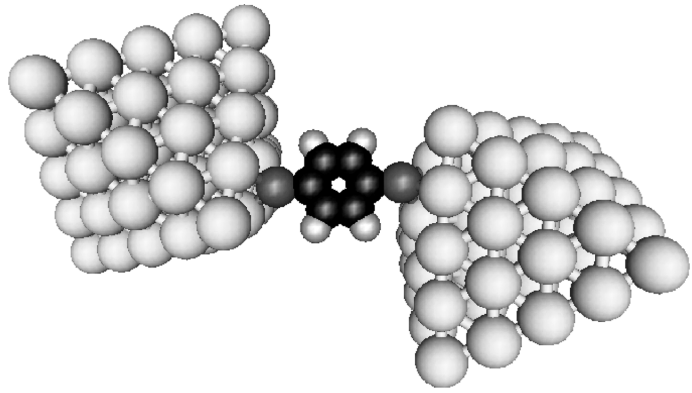

Figure 16 Schematic representation of a benzene-1,4-di-thiol molecule between two gold contacts. The molecule plus gold pyramids (55 atoms each) constitute the *extended molecule* as used in the DFT calculations for the Landauer approach.

Electron Transport

Electron transport through single molecules may become a key component of future nanotechnology.[359] Present theoretical formulations rely on ground-state density functionals to describe the stationary nonequilibrium current-carrying state,[360] but suggestions have been made to consider this as a time-dependent problem[361–364] and use TD(C)DFT for a full description of the situation. Imagine the scenario of Figure 16 where a conducting molecule is sandwiched between two contacts that are connected to semi-infinite leads. The Landauer formula for the current is

$$I = \frac{1}{\pi}\int_{-\infty}^{\infty} dE\, T(E)[f_L(E) - f_R(E)] \qquad [65]$$

where $T(E)$ is the transmission probability for a given energy and $f_{L/R}(E)$ is the Fermi distribution function for the left/right lead. The transmission probability of the system can be written using nonequilibrium Green's functions (NEGF). Ground-state DFT is used to find the KS orbitals and energies of the extended molecule and also used to find the self-energies of the leads. These orbitals and energies are then fed into the NEGF model to determine $T(E)$ and hence the current.

The NEGF scheme has had a number of successes, most notably for atomic-scale point contacts and metallic wires. Generally, it does well for systems where the conductance is high, but it was found that the conductance is overestimated by 1–3 orders of magnitude for molecular wires.

Various explanations for this overestimation and the problems with DFT combined with NEGF in general have been suggested. First, the use of the KS

orbitals and energy levels has no theoretical basis. The KS orbitals are those orbitals for the noninteracting problem that reproduce the correct ground-state density. They should not be thought of as the true single-particle excitations of the true system. However, as we have seen, the KS orbitals often reproduce the single-particle excitations qualitatively, so it is not clear to what extent their use in NEGF affects the conductance. Second, the geometry of the conducting molecules was also suggested as a source of error. DFT first relaxes the molecule to find its geometry, whereas in the experiments the molecule may be subject to stresses that could rotate parts of it and/or squash parts together. Calculations[365] have shown that the geometry corrections are small. Finally, the approximation that the nonequilibrium XC functional is the same as for the static case has been suggested as a major source of error. In fact, neither the HK theorem nor the RG theorem are strictly valid for current-carrying systems in homogeneous electric fields. A dynamical correction to the LDA functional for the static case has been derived using the Vignale–Kohn functional TDCDFT, but these dynamical corrections were found to yield only small improvements to ALDA.[366]

In a similar vein, the lack of the derivative discontinuity and the existence of self-interaction errors (SIE) in the approximations to the XC functional may be the source of this overestimation problem.[365] In Hartree–Fock calculations (and also in OEP calculations[290] with EXX, exact exchange) that have no SIE, the conductances are found to be much lower.[367] Calculations have also been done on a simple model[368] containing a KS potential with a derivative discontinuity. The current-voltage (I-V) curves for this model system are significantly different from those predicted by LDA. The discrepancy was found to be most severe when the molecule was not coupled strongly to the leads, but goes away when it is bonded covalently. Recent OEP calculations of the transmission along a chain consisting of H atoms verify these features.[367]

Quantitative results can be found for molecular devices despite these problems. By examining the bias at which a KS energy level gets moved between the two chemical potentials of the leads (from Eq. [65] this gives a peak in the conductance), one can predict[369] positions of these peaks qualitatively, although the magnitude of the conductance may be incorrect by orders of magnitude.

Because electron transport is a nonequilibrium process, we anticipate that static DFT will not be able to accurately predict some features of electron transport. A number of methods have been developed that allow one to use TDDFT for these purposes. For example, Kurth et al.[370] present a practical scheme using TDDFT to calculate current. The basic idea is to "pump" the system into a nonequilibrium initial state by some external bias and then allow the KS orbitals to evolve in time via the TDKS equations. The RG theorem then allows one to extract the longitudinal current using the continuity equation. Using transparent boundary conditions that solve problems with

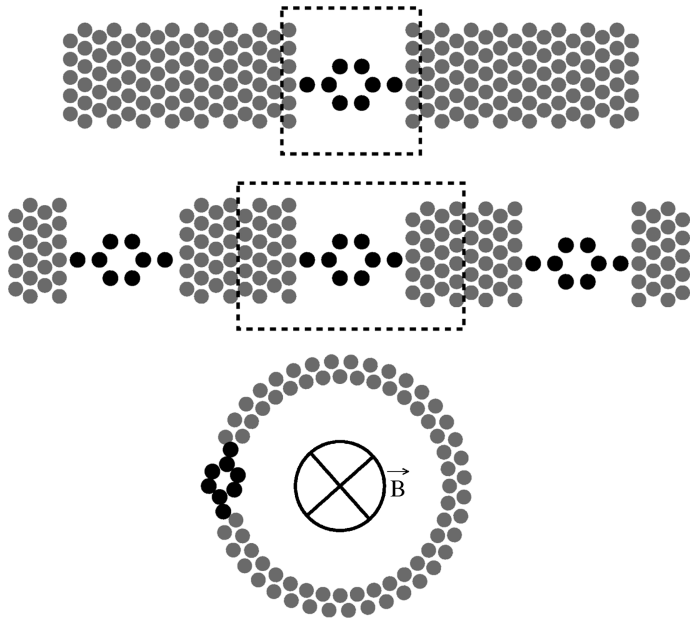

Figure 17 Ring geometry for gauge transformation of electric fields. Black dots represent a conducting molecule while gray dots represent the electrically conducting leads. (*Top panel*) Single molecule in a bias electric field attached to semi-infinite leads. (*Middle panel*) Same system with periodic boundary conditions, while the lower panel shows how the middle panel can be imagined as a ring with the electric field gauge transformed to a magnetic one.

propagating KS orbitals in the semi-infinite leads, and using an iterative procedure to get the correct initial state, the authors were able to find a steady-state current.

An alternative TDDFT formulation for electron transport uses periodic boundary conditions and includes dissipation.[371] In the Landauer–Büttiker formalism, dissipation effects arising from electron–electron interaction and electron–phonon interaction can be neglected because the molecule is smaller than the scattering length. However, there would be scattering in the leads. Imagine a molecule in the ring geometry of Figure 17, with a spatially constant electric field; via a gauge transformation, the electric field can be replaced by a constant time-dependent magnetic field through the center of the ring. If no dissipation exists, the electrons keep accelerating indefinitely and never reach a steady state.

In the classical Boltzmann equation for electron transport, scattering is included via a dissipation term using τ, the average collision time. A master equation approach is basically a generalization of the Boltzmann equation to a fully quantum mechanical system. The master equation is based on the

Louville equation in quantum mechanics, and, for a quantum mechanical density coupled to a heat bath (or reservoir), it is written as

$$\frac{d}{dt}\hat{\rho}(t) = -\imath[H, \hat{\rho}(t)] + \mathbf{C}[\hat{\rho}(t)] \qquad [66]$$

where **C** is a superoperator acting on the density whose elements are calculated using Fermi's golden rule with $V_{\text{el-ph}}$ in a certain approximation (weak coupling and instantaneous processes). A KS master equation[364] can be derived, modifying C for single-particle reduced-density matrices, so that it gives the correct steady state. The TDKS equations are then used to propagate forward in time until the correct steady-state density is found, and the current is then extracted from this. Recent calculations have shown that this master equation approach can give correct behavior, such as hysteresis in I-V curves.[363,372]

SUMMARY

We have conveyed some of the spirit and excitement of development and uses of TDDFT in this review. We explained what TDDFT is and where it comes from. While it often works well for many molecular excitations, its usefulness lies neither in high accuracy nor reliability but instead in its qualitative ability to yield roughly correct absorption spectra for molecules of perhaps several hundred atoms. We emphasize that there are usually many excitations of the same symmetry, all coupled together, and that under these circumstances the theory will be of greatest use. TDDFT is now a routine tool that produces accurate results with reasonable confidence for many molecular systems.

That said, we have discussed some of the areas where TDDFT (in its current incarnation) is not working, such as double excitations, charge transfer, and extended systems. But there has been significant progress in all of these, both in understanding the origin of the problem and finding alternative approaches using orbital-dependent expressions that may ultimately yield a practical solution. We also examined how well TDDFT works for a few cases where the exact ground-state solution is known, describing the accuracy of different functionals, and we surveyed some applications beyond simple linear response for optical absorption, such as ground-state functionals from the adiabatic connection, strong fields, and electron transport. In each of these areas, more development is needed before TDDFT calculations can become a routine tool with the accuracy needed by scientists and engineers.

Many wonder how long DFT's preeminence in electronic structure theory can last. For sure, Kohn–Sham DFT is a poor player that struts and frets its hour upon the stage of electronic structure and then is heard no more.[373] After all, its predecessor, Thomas–Fermi theory,[374,375] is now obsolete, being

too inaccurate for modern needs. Although many alternatives for electronic excitations, such as GW, are becoming computationally feasible for interesting systems, we believe DFT, and TDDFT, should dominate for a few decades yet.

ACKNOWLEDGMENTS

We thank Michael Vitarelli for his early work on the review and Meta van Faassen, Max Koentopp, and Roberto Car for providing figures. K.B. gratefully acknowledges support of the U.S. Department of Energy, under grant number DE-FG02-01ER45928, and the NSF, under grant CHE-0355405. This work was supported, in part, by the Center for Functional Nanostructures (CFN) of the Deutsche Forschungsgemeinschaft (DFG) within project C3.9, the EXC!TiNG Research and Training Network of the European Union and the NANOQUANTA Network of Excellence.

REFERENCES

1. P. Hohenberg and W. Kohn, *Phys. Rev.*, **136**, B 864 (1964). Inhomogeneous Electron Gas.
2. W. Kohn and L. J. Sham, *Phys. Rev.*, **140**, A 1133 (1965). Self-Consistent Equations Including Exchange and Correlation Effects.
3. R. M. Dreizler and E. K. U. Gross, *Density Functional Theory: An Approach to the Quantum Many-Body Problem*, Springer, Berlin, 1990.
4. M. Levy, *Phys. Rev. A*, **26**, 1200 (1982). Electron Densities in Search of Hamiltonians.
5. A. D. Becke, *Phys. Rev. A*, **38**, 3098 (1988). Density-Functional Exchange-Energy Approximation with Correct Asymptotic Behavior.
6. C. Lee, W. Yang, and R. G. Parr, *Phys. Rev. B*, **37**, 785 (1988). Development of the Colle-Salvetti Correlation-Energy Formula into a Functional of the Electron Density.
7. J. P. Perdew, K. Burke, and M. Ernzerhof, *Phys. Rev. Lett.*, **77**, 3865 (1996). Generalized Gradient Approximation Made Simple. [Erratum: *Phys. Rev. Lett.*, **78**, 1396 (1997).]
8. A. D. Becke, *J. Chem. Phys.*, **98**, 5648 (1993). Density-Functional Thermochemistry. III. The Role of Exact Exchange.
9. F. Furche and J. P. Perdew, *J. Chem. Phys.*, **124**, 044103 (2006). The Performance of Semi-Local and Hybrid Density Functional in 3d Transition Metal Chemistry.
10. See www.turbomole.com.
11. M. A. L. Marques and E. K. U. Gross, *Annu. Rev. Phys. Chem.*, **55**, 427 (2004). Time-Dependent Density-Functional Theory.
12. F. Furche and K. Burke, in *Annual Reports in Computational Chemistry, Vol. 1*, D. Spellmeyer, Ed., Elsevier, Amsterdam, 2005, pp. 19–30. Time-Dependent Density Functional Theory in Quantum Chemistry.
13. N. T. Maitra, K. Burke, H. Appel, E. K. U. Gross, and R. van Leeuwen, in *Reviews in Modern Quantum Chemistry: A Celebration of the Contributions of R. G. Parr*, K. D. Sen, Ed., World Scientific, Singapore 2001. Ten Topical Questions in Time-Dependent Density Functional Theory.
14. K. Burke and E. K. U. Gross, in *Density Functionals: Theory and Applications*, D. Joubert, Ed., Springer, Berlin, 1998. A Guided Tour of Time-Dependent Density Functional Theory.
15. E. K. U. Gross, J. F. Dobson, and M. Petersilka, *Topics in Current Chemisty*, **181**, 81 (1996). Density Functional Theory of Time-Dependent Phenomena.
16. E. Runge and E. K. U. Gross, *Phys. Rev. Lett.*, **52**, 997 (1984). Density-Functional Theory for Time-Dependent Systems.

17. F. Furche, Ph.D. thesis, Universität Karlsruhe, 2002. Dichtefunktionalmethoden für Elektronisch Angeregte Moleküle. Theorie, Implementierung und Anwendung.
18. K. Eichkorn, F. Weigend, O. Treutler, and R. Ahlrichs, *Theor. Chem. Acc.*, **97**, 119 (1997). Auxiliary Basis Sets for Main Row Atoms and Transition Metals and Their Use to Approximate Coulomb Potentials.
19. H. Goto, N. Harada, J. Crassous, and F. Diederich, *J. Chem. Soc., Perkin Trans.*, **2**, 1719 (1998). Absolute Configuration of Chiral Fullerenes and Covalent Derivatives from Their Calculated Circular Dichroism Spectra.
20. B. J. Coe, J. L. Harries, M. Helliwell, L. A. Jones, I. Asselberghs, K. Clays, B. S. Brunschwig, J. A. Harris, J. Garin, and J. Orduna, *J. Am. Chem. Soc.*, **128**, 12192 (2006). Pentacyanoiron (II) as an Electron Donor Group for Nonlinear Optics: Medium-Responsive Properties and Comparisons with Related Pentaammineruthenium(II) Complexes.
21. C. H. Yang, W. L. Su, K. H. Fang, S. P. Wang, and I. W. Sun, *Organometallics*, **25**, 4514 (2006). Studies of the 5′-Substituted Phenylisoquinoline-Based Iridium Complexes Using Density Functional Theory.
22. A. Vargas, M. Zerara, E. Krausz, A. Hauser, and L. M. L. Daku, *J. Chem. Theory Comput.*, **2**, 1342 (2006). Density-Functional Theory Investigation of the Geometric, Energetic, and Optical Properties of the Cobalt(II)tris(2,2′-bipyridine) Complex in the High-Spin and the Jahn-Teller Active Low-Spin States.
23. A. Sakamoto, A. Hirooka, K. Namiki, M. Kurihara, M. Murata, M. Sugimoto, and H. Nishihara, *Inorg. Chem.*, **44**, 7547 (2005). Photon-, Electron-, and Proton-Induced Isomerization Behavior of Ferrocenylazobenzenes.
24. S. R. Stoyanov, J. M. Villegas, A. J. Cruz, L. L. Lockyear, J. H. Reibenspies, and D. P. Rillema, *J. Chem. Theory Comput.*, **1**, 95 (2005). Computational and Spectroscopic Studies of Re(I) Bipyridyl Complexes Containing 2,6-Dimethylphenylisocyanide (CNx) Ligand.
25. F. Gutierrez, C. Rabbe, R. Poteau, and J. P. Daudey, *J. Phys. Chem. A*, **109**, 4325 (2005). Theoretical Study of Ln(III) Complexes with Polyaza-aromatic Ligands: Geometries of $[LnL(H_2O)(n)]^{3+}$ Complexes and Successes and Failures of TD-DFT.
26. J. Neugebauer, E. J. Baerends, M. Nooijen, and J. Autschbach, *J. Chem. Phys.*, **122**, 234305 (2005). Importance of Vibronic Effects on the Circular Dichroism Spectrum of Dimethyloxirane.
27. E. Lanthier, C. Reber, and T. Carrington, *Chem. Phys.*, **329**, 90 (2006). Vibronic Coupling in Square Planar Complexes of Palladium(II) and Platinum(II).
28. G. Fronzoni, R. Francesco, M. Stener, and M. Causa, *J. Phys. Chem. B*, **110**, 9899 (2006). X-ray Absorption Spectroscopy of Titanium Oxide by Time Dependent Density Functional Calculations.
29. W. Hieringer and E. J. Baerends, *J. Phys. Chem. A*, **110**, 1014 (2006). First Hyperpolarizability of a Sesquifulvalene Transition Metal Complex by Time-Dependent Density-Functional Theory.
30. N. G. Park, G. C. Choi, J. E. Lee, and Y. S. Kim, *Current Appl. Phys.*, **5**, 79 (2005). Theoretical Studies of Cyclometalated Phenylpyrazol Ir(III) Complex Using Density Functional Theory.
31. J. M. Villegas, S. R. Stoyanov, W. Huang, L. L. Lockyear, J. H. Reibenspies, and D. P. Rillema, *Inorg. Chem.*, **43**, 6383 (2004). Synthesis, Characterization, and Photochemical and Computational Investigations of Ru(II) Heterocyclic Complexes Containing 2,6-Dimethylphenylisocyanide (CNx) Ligand.
32. B. J. Coe, J. A. Harris, B. S. Brunschwig, J. Garin, J. Orduna, S. J. Coles, and M. B. Hursthouse, *J. Am. Chem. Soc.*, **126**, 10418 (2004). Contrasting Linear and Quadratic Nonlinear Optical Behavior of Dipolar Pyridinium Chromophores with 4-(Dimethylamino)Phenyl or Ruthenium(II) Ammine Electron Donor Groups.
33. S. R. Stoyanov, J. M. Villegas, and D. P. Rillema, *Inorg. Chem. Comm.*, **7**, 838 (2004). The Charge Transfer Band Solvent-Dependence of [Ru(bpy)(2)(CNx)Cl](+) CNx = 2,6-Dimethylphenylisocyanide: A Polarizable Continuum Model/Time-Dependent Density Functional Theory Study.

34. F. De Angelis, S. Fantacci, and A. Selloni, *Chem. Phys. Lett.*, **389**, 204 (2004). Time-Dependent Density Functional Theory Study of the Absorption Spectrum of [Ru (4,4′-COOH-2,2′-bpy)(2)(NCS)(2)] in Water Solution: Influence of the pH.

35. F. E. Jorge, J. Autschbach, and T. Ziegler, *Inorg. Chem.*, **42**, 8902 (2003). On the Origin of the Optical Activity in the d-d Transition Region of Tris-Bidentate Co(III) and Rh(III) Complexes.

36. R. K. Pandey and S. Mukamel, *J. Chem. Phys.*, **124**, 094106 (2006). Simulation of X-ray Absorption Near-Edge Spectra and X-ray Fluorescence Spectra of Optically Excited Molecules.

37. G. Fronzoni, A. Stener, A. Reduce, and P. Decleva, *J. Phys. Chem. A*, **108**, 8467 (2004). Time-Dependent Density Functional Theory Calculations of Ligand K Edge and Metal L Edge X-ray Absorption of a Series of Oxomolybdenum Complexes.

38. S. Y. Yang, Y. H. Kan, G. C. Yang, Z. M. Su, and L. Zhao, *Chem. Phys. Lett.*, **429**, 180 (2006). TD-DFT Investigation on the Low-Lying Excited States of Spiro-Bithiophene.

39. N. Manoj, G. Ajayakumar, K. R. Gopidas, and C. H. Suresh, *J. Phys. Chem. A*, **110**, 11338 (2006). Structure Absorption Spectra Correlation in a Series of 2,6-Dimethyl-4-arylpyrylium Salts.

40. E. Fabiano, F. Della Sala, G. Barbarella, S. Lattante, M. Anni, G. Sotgiu, C. Hättig, R. Cingolani, and G. Gigli, *J. Phys. Chem. B*, **110**, 18651 (2006). Optical Properties of *N*-Succinimidyl Bithiophene and the Effects of the Binding to Biomolecules: Comparison between Coupled-Cluster and Time-Dependent Density Functional Theory Calculations and Experiments.

41. C. Lapouge and J. P. Cornard, *J. Phys. Chem. A*, **109**, 6752 (2005). Time Dependent Density Functional Theory Study of Electronic Absorption Properties of Lead(II) Complexes with a Series of Hydroxyflavones.

42. S. Fratiloiu, F. C. Grozema, and L. D. A. Siebbeles, *J. Phys. Chem. B*, **109**, 5644 (2005). Optical Properties and Delocalization of Excess Negative Charges on Oligo(phenylene-vinylene)s: A Quantum Chemical Study.

43. M. Belletete, G. Durocher, S. Hamel, M. Cote, S. Wakim, and M. Leclerc, *J. Chem. Phys.*, **122**, 104303 (2005). A First Principles Calculations and Experimental Study of the Ground- and Excited-State Properties of Ladder Oligo(p-aniline)s.

44. M. Weimer, W. Hieringer, F. Della Sala, and A. Görling, *Chem. Phys.*, **309**, 77 (2005). Electronic and Optical Properties of Functionalized Carbon Chains with the Localized Hartree-Fock and Conventional Kohn-Sham Methods.

45. L. M. Ramaniah and M. Boero, *Phys. Rev. A*, **74**, 042505 (2006). Structural, Electronic, and Optical Properties of the Diindenoperylene Molecule from First-Principles Density-Functional Theory.

46. D. L. Kokkin and T. W. Schmidt, *J. Phys. Chem. A*, **110**, 6173 (2006). On the Electronic Properties of Dehydrogenated Polycyclic Aromatic Hydrocarbons.

47. M. K. Shukla and J. Leszczynski, *J. Phys. Chem. A*, **108**, 10367 (2004). Electronic Transitions of Thiouracils in the Gas Phase and in Solutions: Time-Dependent Density Functional Theory (TD-DFT) Study.

48. M. Odelius, B. Kirchner, and J. Hutter, *J. Phys. Chem. A*, **108**, 2044 (2004). s-Tetrazine in Aqueous Solution: A Density Functional Study of Hydrogen Bonding and Electronic Excitations.

49. J. E. Rogers, K. A. Nguyen, D. C. Hufnagle, D. G. McLean, W. J. Su, K. M. Gossett, A. R. Burke, S. A. Vinogradov, R. Pachter, and P. A. Fleitz, *J. Phys. Chem. A*, **107**, 11331 (2003). Observation and Interpretation of Annulated Porphyrins: Studies on the Photophysical Properties of meso-Tetraphenylmetalloporphyrins.

50. T. L. J. Toivonen, T. I. Hukka, O. Cramariuc, T. T. Rantala, and H. Lemmetyinen, *J. Phys. Chem. A*, **110**, 12213 (2006). DFT and TDDFT Study Related to Electron Transfer in Nonbonded Porphine$\cdots C_{60}$ complexes.

51. A. G. Marinopoulos, L. Wirtz, A. Marini, V. Olevano, A. Rubio, and L. Reining, *Appl. Phys. A*, **78**, 1157 (2004). Optical Absorption and Electron Energy Loss Spectra of Carbon and Boron Nitride Nanotubes: A First-Principles Approach.

52. Y. Miyamoto, A. Rubio, and D. Tomanek, *Phys. Rev. Lett.*, **97**, 126104 (2006). Real-Time Ab Initio Simulations of Excited Carrier Dynamics in Carbon Nanotubes.

53. O. T. Ehrler, J. M. Weber, F. Furche, and M. M. Kappes, *Phys. Rev. Lett.*, **91**, 113006 (2003). Photoelectron Spectroscopy of C_{84} Dianions.

54. O. T. Ehrler, F. Furche, J. M. Weber, and M. M. Kappes, *J. Chem. Phys.*, **122**, 094321 (2005). Photoelectron Spectroscopy of Fullerene Dianions C_{76}^{2-}, C_{78}^{2-}, and C_{84}^{2-}.

55. A. G. Marinopoulos, L. Reining, A. Rubio, and N. Vast, *Phys. Rev. Lett.*, **91**, 046402 (2003). Optical and Loss Spectra of Carbon Nanotubes: Depolarization Effects and Intertube Interactions.

56. A. D. Quartarolo, N. Russo, and E. Sicilia, *Chem.-Eur. J.*, **12**, 6797 (2006). Structures and Electronic Absorption Spectra of a Recently Synthesised Class of Photodynamic Therapy Agents.

57. S. B. Nielsen and T. I. Solling, *Chem. Phys. Chem.*, **6**, 1276 (2005). Are Conical Intersections Responsible for the Ultrafast Processes of Adenine, Protonated Adenine, and the Corresponding Nucleosides?

58. I. Tavernelli, U. F. Rohrig, and U. Rothlisberger, *Mol. Phys.*, **103**, 963 (2005). Molecular Dynamics in Electronically Excited States Using Time-Dependent Density Functional Theory.

59. A. Tsolakidis and E. Kaxiras, *J. Phys. Chem. A*, **109**, 2373 (2005). A TDDFT Study of the Optical Response of DNA Bases, Base Pairs, and Their Tautomers in the Gas Phase.

60. M. Wanko, M. Hoffmann, P. Strodet, A. Koslowski, W. Thiel, F. Neese, T. Frauenheim, and M. Elstner, *J. Phys. Chem. B*, **109**, 3606 (2005). Calculating Absorption Shifts for Retinal Proteins: Computational Challenges.

61. Y. L. Ren, J. Wan, X. Xu, Q. Y. Zhang, and G. F. Yang, *J. Phys. Chem. B*, **110**, 18665 (2006). A Time-Dependent Density Functional Theory Investigation of the Spectroscopic Properties of the Beta-Subunit in C-Phycocyanin.

62. J. Guthmuller and D. Simon, *J. Phys. Chem. A*, **110**, 9967 (2006). Linear and Nonlinear Optical Response of Aromatic Amino Acids: A Time-Dependent Density Functional Investigation.

63. M. D. Kundrat and J. Autschbach, *J. Phys. Chem. A*, **110**, 4115 (2006). Time Dependent Density Functional Theory Modeling of Chiroptical Properties of Small Amino Acids in Solution.

64. L. Shen, H. F. Ji, and H. Y. Zhang, *J. Mol. Struct. THEOCHEM*, **758**, 221 (2006). Theoretical Study on Photophysical and Photosensitive Properties of Aloe Emodin.

65. M. Schmitt, R. Brause, C. M. Marian, S. Salzmann, and W. L. Meerts, *J. Chem. Phys.*, **125**, 124309 (2006). Electronically Excited States of Tryptamine and Its Microhydrated Complex.

66. H. Kang, C. Jouvet, C. Dedonder-Lardeux, S. Martrenchard, C. Charriere, G. Gregoire, C. Desfrancois, J. P. Schermann, M. Barat, and J. A. Fayeton, *J. Chem. Phys.*, **122**, 084307 (2005). Photoinduced Processes in Protonated Tryptamine.

67. D. Varsano, R. Di Felice, M. A. L. Marques, and A. Rubio, *J. Phys. Chem. B*, **110**, 7129 (2006). A TDDFT Study of the Excited States of DNA Bases and Their Assemblies.

68. H. Tachikawa and T. Iyama, *J. Photochem. Photobiol. B: Biol.*, **76**, 55 (2004). TD-DFT Calculations of the Potential Energy Curves for the trans-cis Photo-Isomerization of Protonated Schiff Base of Retinal.

69. M. A. L. Marques, X. Lopez, D. Varsano, A. Castro, and A. Rubio, *Phys. Rev. Lett.*, **90**, 258101 (2003). Time-Dependent Density-Functional Approach for Biological Chromophores: The Case of the Green Fluorescent Protein.

70. X. Lopez, M. A. L. Marques, A. Castro, and A. Rubio, *J. Am. Chem. Soc.*, **127**, 12329 (2005). Optical Absorption of the Blue Fluorescent Protein: A First-Principles Study.

71. F. Cordova, L. J. Doriol, A. Ipatov, M. E. Casida, C. Filippi, and A. Vela, arXiv:0708.1381v1 (2007). Troubleshooting Time-Dependent Density-Functional Theory for Photochemical Applications: Oxirane.

72. A. K. De and T. Ganguly, *Chem. Phys. Lett.*, **428**, 213 (2006). Theoretical Predictions for Occurrence of Charge Transfer Complex within the Two Synthesized Bichromophores Considering the Role of Their Spacers in Interactions with the Pi-Orbitals of the Redox Centers.

73. B. J. Coe, J. A. Harris, B. S. Brunschwig, I. Asselberghs, K. Clays, J. Garin, and J. Orduna, *J. Am. Chem. Soc.*, **127**, 13399 (2005). Three-Dimensional Non-Linear Optical Chromophores Based on Metal-to-Ligand Charge-Transfer from Ruthenium(II) or Iron(II) Centers.

74. A. Karton, M. A. Iron, M. E. van der Boom, and J. M. L. Martin, *J. Phys. Chem. A*, **190**, 5454 (2005). NLO Properties of Metallabenzene-Based Chromophores: A Time-Dependent Density Functional Study.

75. J. Wan, X. Xu, Y. L. Ren, and G. F. Yang, *J. Phys. Chem. B*, **109**, 11088 (2005). A Time Dependent Density Functional Theory Study of Alpha-84 Phycocyanobilin in C-phycocyanin.

76. B. Toffoli, M. Stener, G. Fronzoni, and P. Decleva, *J. Chem. Phys.*, **124**, 214313 (2006). Photoionization Cross Section and Angular Distribution Calculations of Carbon Tetrafluoride.

77. D. Jacquemin, J. Preat, V. Wathelet, and E. A. Perpete, *Chem. Phys.*, **328**, 324 (2006). Time-Dependent Density Functional Theory Determination of the Absorption Spectra of Naphthoquinones.

78. R. J. Cave, K. Burke, and E. W. Castner Jr., *J. Phys. Chem. A*, **106**, 9294 (2002). A Theoretical Investigation of the Ground and Excited States of Coumarin 151 and Coumarin 120.

79. L. Shen, H. F. Ji, and H. Y. Zhang, *Chem. Phys. Lett.*, **409**, 300 (2005). A TD-DFT Study on Triplet Excited-State Properties of Curcumin and Its Implications in Elucidating the Photo Sensitizing Mechanisms of the Pigment.

80. D. Jacquemin, E. A. Perpete, G. Scalmani, M. J. Frisch, X. Assfeld, I. Ciofini, and C. Adamo, *J. Chem. Phys.*, **125**, 164324 (2006). Time-Dependent Density Functional Theory Investigation of the Absorption, Fluorescence, and Phosphorescence Spectra of Solvated Coumarins.

81. B. Champagne, M. Guillaume, and F. Zutterman, *Chem. Phys. Lett.*, **425**, 105 (2006). TDDFT Investigation of the Optical Properties of Cyanine Dyes.

82. D. Jacquemin, M. Bouhy, and E. A. Perpete, *J. Chem. Phys.*, **124**, 204321 (2006). Excitation Spectra of Nitro-Diphenylaniline: Accurate Time-Dependent Density Functional Theory Predictions for Charge-Transfer Dyes.

83. F. Labat, P. P. Laine, I. Ciofini, and C. Adamo, *Chem. Phys. Lett.*, **417**, 445 (2006). Spectral Properties of Bipyridyl Ligands by Time-Dependent Density Functional Theory.

84. A. Chakraborty, S. Kar, D. N. Nath, and N. Guchhait, *J. Phys. Chem. A*, **110**, 12089 (2006). Photoinduced Intramolecular Charge Transfer Reaction in (E)-3-(4-Methylamino-phenyl)-acrylic Acid Methyl Ester: A Fluorescence Study in Combination with TDDFT Calculation.

85. N. Ben Amor, S. Zalis, and C. Daniel, *Int. J. Quantum Chem.*, **106**, 2458 (2006). Theoretical Analysis of Low-Lying Charge Transfer States in [Ru(X) (Me)(CO)(2)(Me-DAB)] (X = Cl, I; DAB = 1,4-diaza-1,3-butadiene) Complexes by TDDFT and CASSCF/CASPT2 Methods.

86. R. Gelabert, M. Moreno, and J. M. Lluch, *J. Phys. Chem. A*, **110**, 1145 (2006). Charge-Transfer π-π^* Excited State in the 7-Azaindole Dimer. A Hybrid Configuration Interactions Singles/Time-Dependent Density Functional Theory Description.

87. L. Bernasconi, M. Sprik, and R. Hutter, *Chem. Phys. Lett.*, **394**, 141 (2004). Hartree-Fock Exchange in Time Dependent Density Functional Theory: Application to Charge Transfer Excitations in Solvated Molecular Systems.

88. C. J. Jamorski and M. E. Casida, *J. Phys. Chem. B*, **108**, 7132 (2004). Time-Dependent Density-Functional Theory Investigation of the Fluorescence Behavior as a function of Alkyl Chain Size for the 4-(*N*,*N*-Dimethylamino)benzonitrile-Like Donor-Acceptor Systems 4-(*N*, *N*-Diethylamino)benzonitrile and 4-(*N*,*N*-Diisopropylamino)benzonitrile.

89. A. Dreuw and M. Head-Gordon, *J. Am. Chem. Soc.*, **126**, 4007 (2004). Failure of Time-Dependent Density Functional Theory for Long-Range Charge-Transfer Excited States: The Zincbacteriochlorin-Bacteriochlorin and Bacteriochlorophyll-Spheroidene Complexes.

90. D. Rappoport and F. Furche, *J. Am. Chem. Soc.*, **126**, 1277 (2004). Photoinduced Intramolecular Charge Transfer in 4-(Dimethyl)aminobenzonitrile—A Theoretical Perspective.
91. D. J. Tozer, *J. Chem. Phys.*, **119**, 12697 (2003). Relationship between Long-Range Charge-Transfer Excitation Energy Error and Integer Discontinuity in Kohn-Sham Theory.
92. C. J. Jamorski and H. P. Luthi, *J. Chem. Phys.*, **119**, 12852 (2003). Rational Classification of a Series of Aromatic Donor-Acceptor Systems within the Twisting Intramolecular Charge Transfer Model, a Time-Dependent Density-Functional Theory Investigation.
93. L. E. Roy and T. Hughbanks, *Inorg. Chem.*, **45**, 8273 (2006). Electronic Transitions in $[Re_6S_8X_6]^{4-}$ (X = Cl, Br, I): Results from Time-Dependent Density Functional Theory and Solid-State Calculations.
94. J. C. Idrobo, S. Ogut, and J. Jellinek, *Phys. Rev. B*, **72**, 085445 (2005). Size Dependence of the Static Polarizabilities and Absorption Spectra of Ag_n ($n = 2 - 8$) Clusters.
95. L. Jensen, J. Autschbach, and G. C. Schatz, *J. Chem. Phys.*, **122**, 224115 (2005). Finite Lifetime Effects on the Polarizability within Time-Dependent Density-Functional Theory.
96. S. S. M. C. Godinho, P. C. do Couto, and B. J. C. Cabral, *J. Chem. Phys.*, **122**, 044316 (2005). Polarization Effects and Charge Separation in AgCl-Water Clusters.
97. M. Stener, G. Fronzoni, and R. De Francesco, *Chem. Phys.*, **309**, 49 (2005). Core Excitations in MgO: A DFT Study with Cluster Models.
98. G. F. Zhao, Y. Lei, and Z. Zeng, *Chem. Phys.*, **327**, 261 (2006). Absorption Spectra of Small Silver Clusters Ag_n ($n = 4$, 6, 8): A TDDFT Study.
99. M. L. del Puerto, M. L. Tiago, and J. R. Chelikowsky, *Phys. Rev. Lett.*, **97**, 096401 (2006). Excitonic Effects and Optical Properties of Passivated CdSe Clusters.
100. O. Lehtonen and D. Sundholm, *Phys. Rev. B*, **74**, 045433 (2006). Optical Properties of Silaadamantane Nanoclusters from Density-Functional Theory.
101. Y. Z. Lan, W. D. Cheng, D. S. Wu, J. Shen, S. P. Huang, H. Zhang, Y. J. Gong, and F. F. Li, *J. Chem. Phys.*, **124**, 094302 (2006). A Theoretical Investigation of Hyperpolarizability for Small Ga_nAs_m ($n + m = 4 - 10$) Clusters.
102. S. S. M. C. Godinho, P. C. do Couto, and B. J. C. Cabral, *Chem. Phys. Lett.*, **419**, 340 (2006). Photochemistry of AgCl-Water Clusters: Comparison with Cl^--Water Clusters.
103. N. A. Besley and A. J. Blundy, *J. Phys. Chem. B*, **110**, 1701 (2006). Electronic Excited States of Si(100) and Organic Molecules Adsorbed on Si(100).
104. E. Broclawik, A. Gora, P. Liguzinski, P. Petelenz, and H. A. Witek, *J. Chem. Phys.*, **124**, 054709 (2006). Quantum Chemical Modeling of Electrochromism of Tungsten Oxide Films.
105. G. Durand, M. C. Heitz, F. Spiegelman, C. Meier, R. Mitric, V. Bonacic-Koutecky, and J. Pittner, *J. Chem. Phys.*, **121**, 9898 (2004). Different Approaches for the Calculation of Electronic Excited States of Nonstoichiometric Alkali Halide Clusters: The Example of Na_3F.
106. B. Gervais, E. Giglio, E. Jacquet, A. Ipatov, P. G. Reinhard, and E. Suraud, *J. Chem. Phys.*, **121**, 8466 (2004). Simple DFT Model of Clusters Embedded in Rare Gas Matrix: Trapping Sites and Spectroscopic Properties of Na Embedded in Ar.
107. R. Baer and N. Siam, *J. Chem. Phys.*, **121**, 6341 (2004). Real-Time Study of the Adiabatic Energy Loss in an Atomic Collision with a Metal Cluster.
108. A. Pohl, P. G. Reinhard, and E. Suraud, *Phys. Rev. A*, **70**, 023202 (2004). Angular Distribution of Electrons Emitted from Na Clusters.
109. R. Rao, J. Sutin, R. Clegg, E. Gratton, M. H. Nayfeh, S. Habbal, A. Tsolakidis, and R. M. Martin, *Phys. Rev. B*, **69**, 205319 (2004). Excited States of Tetrahedral Single-Core Si_{29} Nanoparticles.
110. F. Della Sala, R. Rousseau, A. Görling, and D. Marx, *Phys. Rev. Lett.*, **92**, 183401 (2004). Quantum and Thermal Fluctuation Effects on the Photoabsorption Spectra of Clusters.
111. R. Baer, D. Neuhauser, and S. Weiss, *Nano Lett.*, **4**, 85 (2004). Enhanced Absorption Induced by a Metallic Nanoshell.

112. J. I. Martinez, A. Castro, A. Rubio, and J. A. Alonso, *J. Chem. Phys.*, **125**, 074311 (2006). Photoabsorption Spectra of Ti_8C_{12} Metallocarbohedrynes: Theoretical Spectroscopy within Time-Dependent Density Functional Theory.

113. J. I. Martinez, A. Castro, A. Rubio, J. M. Poblet, and J. A. Alonso, *Chem. Phys. Lett.*, **398**, 292 (2004). Calculation of the Optical Spectrum of the Ti_8C_{12} and V_8C_{12} Met-Cars.

114. J. Lalevee, X. Allonas, and P. Jacques, *J. Mol. Struct. THEOCHEM*, **767**, 143 (2006). Electronic Distribution and Solvatochromism Investigation of a Model Radical (2,2,6,6-Tetramethylpiperidine *N*-oxyl:tempo) through TD-DFT Calculations Including PCM Solvation.

115. J. Neugebauer, M. J. Louwerse, E. J. Baerends, and T. A. Wesolowski, *J. Chem. Phys.*, **122**, 094115 (2005). The Merits of the Frozen-Density Embedding Scheme to Model Solvatochromic Shifts.

116. A. Masternak, G. Wenska, J. Milecki, B. Skalski, and S. Franzen, *J. Phys. Chem. A*, **109**, 759 (2005). Solvatochromism of a Novel Betaine Dye Derived from Purine.

117. C. Zazza, A. Grandi, L. Bencivenni, and M. Aschi, *J. Mol. Struct. THEOCHEM*, **764**, 87 (2006). On the Performance of Gradient-Corrected Approximation Functional and Polarizable Continuum Model in the Study of 1,2,3-Triazine in Water.

118. A. Chakraborty, S. Kar, and N. Guchhait, *Chem. Phys.*, **324**, 733 (2006). Photophysical Properties of trans-3-(4-Monomethylamino-phenyl)-acrylonitrile: Evidence of Twisted Intramolecular Charge Transfer (TICT) Process.

119. J. Guthmuller and D. Simon, *J. Chem. Phys.*, **124**, 174502 (2006). Water Solvent Effect on the First Hyperpolarizability of *p*-Nitrophenol and *p*-Nitrophenylphosphate: A Time-Dependent Density Functional Study.

120. J. Sebek, Z. Kejik, and P. Bour, *J. Phys. Chem. A*, **110**, 4702 (2006). Geometry and Solvent Dependence of the Electronic Spectra of the Amide Group and Consequences for Peptide Circular Dichroism.

121. D. Jacquemin, E. A. Perpete, G. Scalmani, M. J. Frisch, M. Ciofini, and C. Adamo, *Chem. Phys. Lett.*, **421**, 272 (2006). Absorption and Emission Spectra in Gas Phase and Solution Using TD-DFT: Formaldehyde and Benzene as Case Studies.

122. G. Scalmani, M. J. Frisch, B. Mennucci, J. Tomasi, R. Cammi, and V. Barone, *J. Chem. Phys.*, **124**, 094107 (2006). Geometries and Properties of Excited States in the Gas Phase and in Solution: Theory and Application of a Time-Dependent Density Functional Theory Polarizable Continuum Model.

123. L. Bernasconi, J. Blumberger, M. Sprik, and R. Vuilleumier, *J. Chem. Phys.*, **121**, 11885 (2004). Density Functional Calculation of the Electronic Absorption Spectrum of Cu^+ and Ag^+ Aqua Ions.

124. B. C. Mort and J. Autschbach, *J. Phys. Chem. A*, **109**, 8617 (2005). Magnitude of Zero-Point Vibrational Corrections to Optical Rotation in Rigid Organic Molecules: A Time-Dependent Density Functional Study.

125. P. J. Stephens, D. M. McCann, J. R. Cheeseman, and M. J. Frisch, *Chirality*, **17**, S52 (2005). Determination of Absolute Configurations of Chiral Molecules Using Ab Initio Time-Dependent Density Functional Theory Calculations of Optical Rotation: How Reliable are Absolute Configurations Obtained for Molecules with Small Rotations?

126. M. Dierksen and S. Grimme, *J. Chem. Phys.*, **124**, 174301 (2006). A Theoretical Study of the Chiroptical Properties of Molecules with Isotopically Engendered Chirality.

127. J. Autschbach, L. Jensen, G. C. Schatz, Y. C. E. Tse, and M. Krykunov, *J. Phys. Chem. A*, **110**, 2461 (2006). Time-Dependent Density Functional Calculations of Optical Rotatory Dispersion Including Resonance Wavelengths as a Potentially Useful Tool for Determining Absolute Configurations of Chiral Molecules.

128. F. E. Jorge, J. Autschbach, and T. Ziegler, *J. Am. Chem. Soc.*, **127**, 975 (2005). On the Origin of Optical Activity in tris-Diamine Complexes of Co(III) and Rh(III): A Simple Model Based on Time-Dependent Density Function Theory.

129. L. Jensen, M. Swart, P. T. van Duijnen, and J. Autschbach, *Int. J. Quantum Chem.*, **106**, 2479 (2006). Circular Dichroism Spectrum of $[Co(en)_3]^{3+}$ in Water: A Discrete Solvent Reaction Field Study.

130. P. J. Stephens, D. M. McCann, E. Butkus, S. Stoncius, J. R. Cheeseman, and M. J. Frisch, *J. Org. Chem.*, **69**, 1948 (2004). Determination of Absolute Configuration Using Concerted Ab Initio DFT Calculations of Electronic Circular Dichroism and Optical Rotation: Bicyclo [3.3.1] nonanediones.

131. M. Seth, T. Ziegler, A. Banerjee, J. Autschbach, S. J. A. van Gisbergen, and E. J. Baerends, *J. Chem. Phys.*, **120**, 10942 (2004). Calculation of the A Term of Magnetic Circular Dichroism Based on Time Dependent-Density Functional Theory I. Formulation and Implementation.

132. N. N. Lathiotakis, N. Helbig, and E. K. U. Gross, *Phys. Rev. A*, **72**, 030501 (2005). Open Shells in Reduced-Density-Matrix-Functional Theory.

133. M. Watanabe, H. Suzuki, Y. Tanaka, T. Ishida, T. Oshikawa, and A. Tori-i, *J. Org. Chem.*, **69**, 7794 (2004). One-Pot Synthesis of Helical Aromatics: Stereoselectivity, Stability Against Racemization, and Assignment of Absolute Configuration Assisted by Experimental and Theoretical Circular Dichroism.

134. G. Marconi, S. Monti, F. Manoli, A. D. Esposti, and A. Guerrini, *Helv. Chim. Acta*, **87**, 2368 (2004). Circular-Dichroism Studies on Artemisinin and Epiartemisinin and Their Beta-cyclodextrin Complexes in Solution.

135. K. Watanabe, M. Araidai, and K. Tada, *Thin Solid Films*, **464–65**, 354 (2004). Field Emission and Electronic Structures of Carbon Allotropes.

136. G. Gurtubay, W. Ku, J. M. Pitarke, and A. G. Eguiluz, *Comput. Mater. Sci.*, **30**, 104 (2004). Effects of the Crystal Structure in the Dynamical Electron Density-Response of hcp Transition Metals.

137. K. Hirose, Y. Meir, and N. S. Wingreen, *Physica E*, **22** 486 (2004). Time-Dependent Density Functional Theory of Excitation Energies of Closed-Shell Quantum Dots.

138. S. Botti, F. Sottile, N. Vast, V. Olevano, L. Reining, H. C. Weissker, A. Rubio, G. Onida, R. Del Sole, and R. W. Godby, *Phys. Rev. B*, **69**, 155112 (2004). Long-Range Contribution to the Exchange-Correlation Kernel of Time-Dependent Density Functional Theory.

139. B. Insuasty, C. Atienza, C. Seoane, N. Martin, J. Garin, J. Orduna, R. Alcala, and B. Villacampa, *J. Org. Chem.*, **69**, 6986 (2004). Electronic and Structural Effects on the Nonlinear Optical Behavior in Push-Pull TTF/Tricarbonyl Chromiun Arene Complexes.

140. F. F. Jian and P. S. Zhao, *J. Mol. Struct.*, **705**, 133 (2004). Experimental and Ab Initio Calculational Studies on 2,3-Diketo-benzopiperazine.

141. N. Kobko, A. Masunov, and S. Tretiak, *Chem. Phys. Lett.*, **392**, 444 (2004). Calculations of the Third-Order Nonlinear Optical Responses in Push-Pull Chromophores with a Time-Dependent Density Functional Theory.

142. A. M. Masunov and S. Tretiak, *J. Phys. Chem. B*, **108**, 899 (2004). Prediction of Two-Photon Absorption Properties for Organic Chromophores Using Time-Dependent Density-Functional Theory.

143. W. Guan, G. C. Yang, L. K. Yan, and Z. M. Su, *Inorg. Chem.*, **45**, 7864 (2006). Prediction of Second-Order Optical Nonlinearity of Trisorganotin-Substituted beta-Keggin Polyoxotungstate.

144. G. C. Yang, Z. M. Su, and C. S. Qin, *J. Phys. Chem. A*, **110**, 4817 (2006). Theoretical Study on the Second-Order Nonlinear Optical Properties of Asymmetric Spirosilabifluorene Derivatives.

145. M. Makowska-Janusik, S. Tkaczyk, and I. V. Kityk, *J. Phys. Chem. B*, **110**, 6492 (2006). Origin of the Photoinduced Optical Second Harmonic Generation Arising in *N*-Phenyl Microcrystalline Films.

146. P. N. Day, K. A. Nguyen, and R. Pachter, *J. Chem. Phys.*, **125**, 094103 (2006). Calculation of Two-Photon Absorption Spectra of Donor-pi-Acceptor Compounds in Solution Using Quadratic Response Time-Dependent Density Functional Theory.

147. G. C. Yang, C. S. Qin, Z. M. Su, and S. Dong, *J. Mol. Struct.: THEOCHEM*, **726**, 61 (2005). Calculations of Two-Photon Absorption Cross-Sections of Stibene and bis(Styryl) Benzene Derivatives by Means of TDDFT-SOS Method.

148. C. Katan, F. Terenziani, O. Mongin, M. H. V. Werts, L. Porres, T. Pons, J. Mertz, S. Tretiak, and M. Blanchard-Desce, *J. Phys. Chem. A*, **109**, 3024 (2005). Effects of (Multi)branching of Dipolar Chromophores on Photophysical Properties and Two-Photon Absorption.

149. P. N. Day, K. A. Nguyen, and R. Pachter, *J. Phys. Chem. B*, **109**, 1803 (2005). TDDFT Study of One- and Two-Photon Absorption Properties: Donor-pi-Acceptor Chromophores.

150. K. Ohta and K. Kamada, *J. Chem. Phys.*, **124**, 124303 (2006). Theoretical Investigation of Two-Photon Absorption Allowed Excited States in Symmetrically Substituted Diacetylenes by Ab Initio Molecular-Orbital Method.

151. A. E. Clark, *J. Phys. Chem. A*, **110**, 3790 (2006). Time-Dependent Density Functional Theory Studies of the Photoswitching of the Two-Photon Absorption Spectra in Stilbene, Metacyclophenadiene, and Diarylethene Chromophores.

152. O. Rubio-Pons, Y. Luo, and H. Agren, *J. Chem. Phys.*, **124**, 094310 (2006). Effects of Conjugation Length, Electron Donor and Acceptor Strengths on Two-Photon Absorption Cross Sections of Asymmetric Zinc-Porphyrin Derivatives.

153. J. F. Kauffman, J. M. Turner, I. V. Alabugin, B. Breiner, S. V. Kovalenko, E. A. Badaeva, A. Masunov, and S. Tretiak, *J. Phys. Chem. A*, **110**, 241 (2006). Two-Photon Excitation of Substituted Enediynes.

154. C. Fiolhais, F. Nogueira, and M. Marques, Eds., *A Primer in Density Functional Theory*, Springer, New York, 2003.

155. M. Levy, *Proc. Natl. Acad. Sci. (U.S.A.)*, **76**, 6062 (1979). Universal Variational Functionals of Electron Densities, First Order Density Matrices, and Natural Spin-Orbitals and Solution of the v-Representability Problem.

156. C. J. Umrigar and X. Gonze, *Phys. Rev. A*, **50**, 3827 (1994). Accurated Exchange-Correlation Potentials and Total-Energy Components for the Helium Isoelectronic Series.

157. J. P. Perdew, R. G. Parr, M. Levy, and J. L. Balduz, Jr., *Phys. Rev. Lett.*, **49**, 1691 (1982). Density-Functional Theory for Fractional Particle Number: Derivative Discontinuities of the Energy.

158. E. Engel, in *A Primer in Density Functional Theory*, C. Fiolhais, F. Nogueira, and M. Marques, Eds., Springer, New York, 2003, pp. 56–122. Orbital-Dependent Functionals for the Exchange-Correlation Energy: A Third Generation of Density Functionals.

159. T. Grabo, T. Kreibich, S. Kurth, and E. K. U. Gross, in *Strong Coulomb Correlations in Electronic Structure: Beyond the Local Density Approximation*, V. I. Anisimov, Ed., Gordon and Breach, Tokyo, 2000, pp. 203–311. Orbital Functionals in Density Functional Theory: The Optimized Effective Potential Method.

160. A. Görling, *J. Chem. Phys.*, **123**, 062203 (2005). Orbital- and State-Dependent Functionals in Density-Functional Theory.

161. D. M. Ceperley and B. J. Alder, *Phys. Rev. Lett.*, **45**, 566 (1980). Ground State of the Electron Gas by a Stochastic Method.

162. J. P. Perdew and A. Zunger, *Phys. Rev. B*, **23**, 5048 (1981). Self-Interaction Correction to Density-Functional Approximations for Many-Electron Systems.

163. S. H. Vosko, L. Wilk, and M. Nusair, *Can. J. Phys.*, **58**, 1200 (1980). Accurate Spin-Dependent Electron Liquid Correlation Energies for Local Spin-Density Calculations—A Critical Analysis.

164. J. P. Perdew and Y. Wang, *Phys. Rev. B*, **46**, 12947 (1992). Pair Distribution Function and Its Coupling-Constant Average for the Spin-Polarized Electron Gas. [Erratum: *Phys. Rev. B*, **56**, 7018 (1997).]

165. S. K. Ma and K. A. Brueckner, *Phys. Rev.*, **165**, 18 (1968). Correlation Energy of an Electron Gas with a Slowly Varying High Density.

166. E. H. Lieb and S. Oxford, *Int. J. Quantum Chem.*, **19**, 427 (1981). Improved Lower Bound on the Indirect Coulomb Energy.

167. K. Burke, M. Ernzerhof, and J. P. Perdew, *Chem. Phys. Lett.*, **265**, 115 (1997). The Adiabatic Connection Method: A Non-Empirical Hybrid.

168. A. D. Becke, *J. Chem. Phys.*, **98**, 1372 (1993). A New Mixing of Hartree-Fock and Local Density-Functional Theories.

169. J. P. Perdew, L. A. Constantin, E. Sagvolden, and K. Burke, *Phys. Rev. Lett.*, **97**, 223002 (2006). Relevance of the Slowly-Varying Electron Gas to Atoms, Molecules, and Solids.

170. J. P. Perdew, M. Ernzerhof, and K. Burke, *J. Chem. Phys.*, **105**, 9982 (1996). Rationale for Mixing Exact Exchange with Density Functional Approximations.

171. K. Burke, F. G. Cruz, and K. C. Lam, *J. Chem. Phys.*, **109**, 8161 (1998). Unambiguous Exchange-Correlation Energy Density.

172. N. I. Gidopoulos, P. G. Papaconstantinou, and E. K. U. Gross, *Physica B*, **318**, 328 (2002). Ensemble-Hartree-Fock Scheme for Excited States. The Optimized Effective Potential Method.

173. M. Petersilka, U. J. Gossmann, and E. K. U. Gross, in *Electronic Density Functional Theory: Recent Progress and New Directions*, J. F. Dobson, G. Vignale, and M. P. Das, Eds., Plenum, New York, 1998, pp. 177–198. Time-Dependent Optimized Effective Potential in the Linear Response Regime.

174. C. A. Ullrich, U. J. Gossman, and E. K. U. Gross, *Phys. Rev. Lett.*, **74**, 872 (1995). Time-Dependent Optimized Effective Potential.

175. F. Della Sala and A. Görling, *J. Chem. Phys.*, **115**, 5718 (2001). Efficient Localized Hartree-Fock Methods as Effective Exact-Exchange Kohn-Sham Methods for Molecules.

176. F. Della Salla and A. Görling, *J. Chem. Phys.*, **116**, 5374 (2002). The Asymptotic Region of the Kohn-Sham Exchange Potential in Molecules.

177. E. R. Davidson and D. Feller, *Chem. Rev.*, **86**, 681 (1986). Basis Set Selection for Molecular Calculations.

178. M. Häser and R. Ahlrichs, *J. Comput. Chem.*, **10**, 104 (1989). Improvements on the Direct SCF Method.

179. H. Y. Afeefy, J. F. Liebman, and S. E. Stein, in NIST Chemistry WebBook, Neutral Thermochemical Data, June 2005. Available: http://webbook.nist.gov.

180. E. K. U. Gross and W. Kohn, in *Advances in Quantum Chemistry*, *Vol. 21: Density Functional Theory of Many-Fermion Systems*, S. B. Trickey, Ed., Academic, San Diego, 1990, pp. 255–291. Time-Dependent Density Functional Theory.

181. N. T. Maitra, K. Burke, and C. Woodward, *Phys. Rev. Lett.*, **89**, 023002 (2002). Memory in Time-Dependent Density Functional Theory.

182. N. T. Maitra and K. Burke, *Phys. Rev. A*, **63**, 042501 (2001). Demonstration of Initial-State Dependence in Time-Dependent Density Functional Theory. [Erratum: *Phys. Rev. A*, **64** 039901.]

183. K. L. Liu and S. H. Vosko, *Can. J. Phys.*, **67**, 1015 (1989). A Time-Dependent Spin-Density Functional Theory for the Dynamic Spin Susceptibility.

184. I. D'Amico and G. Vignale, *Phys. Rev. B*, **59**, 7876 (1999). Exact Exchange-Correlation Potential for a Time-Dependent Two Electron System.

185. P. Hessler, N. T. Maitra, and K. Burke, *J. Chem. Phys.*, **117**, 72 (2002). Correlation in Time-Dependent Density Functional Theory.

186. M. Lein and S. Kümmel, *Phys. Rev. Lett.*, **94**, 143003 (2005). Exact Time-Dependent Exchange-Correlation Potentials for Strong-Field Electron Dynamics.

187. A. Castro, M. A. L. Marques, and A. Rubio, *J. Chem. Phys.*, **121**, 3425 (2004). Propagators for the Time-Dependent Kohn-Sham Equations.

188. R. van Leeuwen, *Phys. Rev. Lett.*, **82**, 3863, (1999). Mapping from Densities to Potentials in Time-Dependent Density-Functional Theory.

189. M. Petersilka, U. J. Gossmann, and E. K. U. Gross, *Phys. Rev. Lett.*, **76**, 1212 (1996). Excitation Energies from Time-Dependent Density-Functional Theory.

190. K. Burke, *Lect. Notes Phys.*, **706**, 181 (2006). Exact Conditions in TDDFT.

191. M. E. Casida, in *Recent Developments and Applications in Density Functional Theory*, J. M. Seminario, Ed., Elsevier, Amsterdam, 1996, pp. 391–439. Time-Dependent Density Functional Response Theory of Molecular Systems: Theory, Computational Methods, and Functionals.

192. R. Bauernschmitt and R. Ahlrichs, *Chem. Phys. Lett.*, **256**, 454 (1996). Treatment of Electronic Excitations within the Adiabatic Approximation of Time Dependent Density Functional Theory.

193. E. Schrödinger, *Phys. Rev.*, **28**, 1049 (1926). An Undulatory Theory of the Mechanics of Atoms and Molecules.

194. A. Zangwill and P. Soven, *Phys. Rev. A*, **21**, 1561 (1980). Density-Functional Approach to Local-Field Effects in Finite Systems: Photoabsorption in the Rare Gases.

195. T. Ando, *Z. Phys. B.*, **26**, 263 (1977). Inter-Subband Optical Absorption in Space-Charge Layers on Semiconductor Surfaces.

196. I. Vasiliev, S. Öğüt, and J. R. Chelikowsky, *Phys. Rev. Lett.*, **82**, 1919 (1999). Ab Initio Excitation Spectra and Collective Electronic Response in Atoms and Clusters.

197. M. A. L. Marques, A. Castro, G. F. Bertsch, and A. Rubio, *Comput. Phys. Commun.*, **151**, 60 (2003). Octopus: A First-Principles Tool for Excited Electron-Ion Dynamics.

198. *CPMD*, Copyright IBM Corp 1990–2006, Copyright MPI für Festkörperforschung 1997–2001. Available: http://www.cpmd.org.

199. F. Furche, *J. Chem. Phys.*, **114**, 5982 (2001). On the Density Matrix Based Approach to Time-Dependent Density Functional Theory.

200. M. Rubio, M. Merchán, E. Ortí, and B. O. Roos, *Chem. Phys.*, **179**, 395 (1994). A Theoretical Study of the Electronic Spectrum of Naphthalene.

201. G. W. F. Drake in *Atomic Molecular, and Optical Physics Handbook*, G. W. F. Drake, Ed., AIP, Woodbury, NY, 1996, pp. 154–171. High Precision Calculations for Helium.

202. F. Weigend, F. Furche, and R. Ahlrichs, *J. Chem. Phys.*, **119**, 12753 (2003). Gaussian Basis Sets of Quadruple Zeta Valence Quality for Atoms H to Kr.

203. R. A. Kendall, T. H. Dunning, and R. J. Harrison, *J. Chem. Phys.*, **96**, 6796 (1992). Electron Affinities of the First-Row Atoms Revisited. Systematic Basis Sets and Wave Functions.

204. A. Schäfer, H. Horn, and R. Ahlrichs, *J. Chem. Phys.*, **97**, 2571 (1992). Fully Optimized Contracted Gaussian Basis Sets for Atoms Li to Kr.

205. W. J. Hehre, R. Ditchfield, and J. A. Pople, *J. Chem. Phys.*, **56**, 2257 (1972). Self-Consistent Molecular Orbital Methods. XII. Further Extensions of Gaussian-Type Basis Sets for Use in Molecular Orbital Studies of Organic Molecules.

206. P. C. Hariharan and J. A. Pople, *Theoret. Chim. Acta*, **28**, 213 (1973). The Influence of Polarization Functions on Molecular Orbital Hydrogenation Energies.

207. F. Weigend and R. Ahlrichs, *Phys. Chem. Chem. Phys.*, **7**, 3297 (2005). Balanced Basis Sets of Split Valence, Triple Zeta Valence and Quadruple Zeta Valence Quality for H to Rn: Design and Assessment of Accuracy.

208. T. H. Dunning Jr., *J. Chem. Phys.*, **90**, 1007 (1989). Gaussian Basis Sets for Use in Correlated Molecular Calculations. I. The Atoms Boron through Neon and Hydrogen.

209. J. W. Mintmire and B. I. Dunlap, *Phys. Rev. A*, **25**, 88 (1982). Fitting the Coulomb Potential Variationally in Linear-Combination-of-Atomic-Orbitals Density-Functional Calculations.

210. K. Eichkorn, O. Treutler, H. Öhm, M. Häser, and R. Ahlrichs, *Chem. Phys. Lett.*, **240**, 283 (1995). Auxiliary Basis Sets to Approximate Coulomb Potentials.

211. D. Rappoport and F. Furche, *J. Chem. Phys.*, **122**, 064105 (2005). Analytical Time-Dependent Density Functional Derivative Methods within the RI-J Approximation, an Approach to Excited States of Large Molecules.

212. F. Furche and R. Ahlrichs, *J. Chem. Phys.*, **117**, 7433 (2002). Adiabatic Time-Dependent Density Functional Methods for Excited State Properties.

213. O. Christiansen, H. Koch, and P. Jørgensen, *Chem. Phys. Lett.*, **243**, 409 (1995). The Second-Order Approximate Coupled Cluster Singles and Doubles Model CC2.

214. C. Hättig and F. Weigend, *J. Chem. Phys.*, **113**, 5154 (2000). CC2 Excitation Energy Calculations on Large Molecules Using the Resolution of the Identity Approximation.

215. C. Hättig and A. Köhn, *J. Chem. Phys.*, **117**, 6939 (2002). Transition Moments and Excited State First-Order Properties in the Second-Order Coupled Cluster Model CC2 Using the Resolution of the Identity Approximation.

216. M. Parac and S. Grimme, *Chem. Phys.*, **292**, 11 (2003). A TDDFT Study of the Lowest Excitation Energies of Polycyclic Aromatic Hydrocarbons.

217. M. Grüning, O. V. Gritsenko, S. J. A. van Gisbergen, and E. J. Baerends, *J. Chem. Phys.*, **116**, 9591 (2002). On the Required Shape Corrections to the Local Density and Generalized Gradient Approximations to the Kohn-Sham Potentials for Molecular Response Calculations of (Hyper)polarizabilities and Excitation Energies.

218. Q. Wu, P. W. Ayers, and W. Yang, *J. Chem. Phys.*, **119**, 2978 (2003). Density-Functional Theory Calculations with Correct Long-Range Potentials.

219. F. Della Sala and A. Görling, *Int. J. Quantum Chem.*, **91**, 131 (2003). Excitation Energies of Molecules by Time-Dependent Density Functional Theory Based on Effective Exact Exchange Kohn-Sham Potentials.

220. A. J. Sadlej, *Theor. Chim. Acta*, **79**, 123 (1991). Medium-Size Polarized Basis-Sets for High-Level-Correlated Calculations of Molecular Electric Properties. II. 2nd-Row Atoms—Si through Cl.

221. T. Grabo, M. Petersilka, and E. K. U. Gross, *J. Mol. Struct. THEOCHEM*, **501**, 353 (2000). Molecular Excitation Energies from Time-Dependent Density Functional Theory.

222. C. Jamorski, M. E. Casida, and D. R. Salahub, *J. Chem. Phys.*, **104**, 5134 (1996). Dynamic Polarizabilities and Excitation Spectra from a Molecular Implementation of Time-Dependent Density Functional Response Theory: N_2 as a Case Study.

223. M. E. Casida, C. Jamorski, K. C. Casida, and D. R. Salahub, *J. Chem. Phys.*, **108**, 4439 (1998). Molecular Excitation Energies to High-Lying Bound States from Time-Dependent Density-Functional Response Theory: Characterization and Correction of the Time-Dependent Local Density Approximation Ionization Threshold.

224. J. Oddershede, N. E. Grüner, and G. H. F. Diercksen, *Chem. Phys.*, **97**, 303 (1985). Comparison between Equation of Motion and Polarization Propagator Calculations.

225. K. P. Huber and G. Herzberg, *Molecular Spectra and Molecular Structure IV: Constants of Diatomic Molecules*, Van Nostrand Reinhold, New York, 1979.

226. A. Savin, C. J. Umrigar, and X. Gonze, *Chem. Phys. Lett.*, **288**, 391 (1998). Relationship of Kohn-Sham Eigenvalues to Excitation Energies.

227. D. J. Tozer and N. C. Handy, *J. Chem. Phys.*, **108**, 2545 (1998). The Development of New Exchange-Correlation Functionals.

228. Q. Wu and W. Yang, *J. Chem. Phys.*, **118**, 2498 (2003). A Direct Optimization Method for Calculating Density Functionals and Exchange-Correlation Potentials from Electron Densities.

229. M. E. Casida and D. R. Salahub, *J. Chem. Phys.*, **113**, 8918 (2000). Asymptotic Correction Approach to Improving Approximate Exchange-Correlation Potentials: Time-Dependent Density-Functional Theory Calculations of Molecular Excitation Spectra.

230. R. van Leeuwen and E. J. Baerends, *Phys. Rev. A*, **49**, 2421 (1994). Exchange-Correlation Potential with Correct Asymptotic Behavior.

231. J. B. Krieger, Y. Li, and G. J. Iafrate, in *Density Functional Theory*, R. Dreizler and E. K. U. Gross, Eds., NATO ASI Series B, Plenum, New York, 1995, pp. 191–216. Recent Developments in Kohn-Sham Theory for Orbital Dependent Exchange-Correlation Energy Functionals.

232. M. Petersilka, E. K. U. Gross, and K. Burke, *Int. J. Quantum Chem.*, **80**, 534 (2000). Excitation Energies from Time-Dependent Density Functional Theory Using Exact and Approximate Functionals.

233. I. Vasiliev, S. Öğüt, and J. R. Chelikowsky, *Phys. Rev. B*, **65**, 115416 (2002). First-Principles Density-Functional Calculations for Optical Spectra of Clusters and Nanocrystals.

234. H. Appel, E. K. U. Gross, and K. Burke, *Phys. Rev. Lett.*, **90**, 043005 (2003). Excitations in Time-Dependent Density-Functional Theory.

235. H. Appel, E. K. U. Gross, and K. Burke, *Int. J. Quantum Chem.*, **106**, 2840 (2006). Double-Pole Approximation in Time-Dependent Density Functional Theory.

236. A. Scherz, E. K. U. Gross, H. Appel, C. Sorg, K. Baberschke, H. Wende, and K. Burke, *Phys. Rev. Lett.*, **95**, 253006 (2005). Measuring the Kernel of Time-Dependent Density Functional Theory with X-ray Absorption Spectroscopy of 3d Transition Metals.

237. C. J. Umrigar and X. Gonze, in *High Performance Computing and Its Application to the Physical Sciences*, Proceedings of the Mardi Gras 1993 Conference, D. A. Browne, Ed., World Scientific, Singapore, 1993, pp. 43–59. Comparison of Approximate and Exact Density Functionals: A Quantum Monte Carlo Study.

238. F. Ham, *Solid State Phys.*, **1**, 127 (1955). The Quantum Defect Method.

239. M. J. Seaton, *Mon. Not. R. Astron. Soc.*, **118**, 504 (1958). The Quantum Defect Method.

240. J. D. Talman and W. F. Shadwick, *Phys. Rev. A*, **14**, 36 (1976). Optimized Effective Atomic Central Potential.

241. A. Görling, *Phys. Rev. Lett.*, **83**, 5459 (1999). New KS Method for Molecules Based on an Exchange Charge Density Generating the Exact Local KS Exchange Potential.

242. S. Ivanov, S. Hirata, and R. J. Bartlett, *Phys. Rev. Lett.*, **83**, 5455 (1999). Exact Exchange Treatment for Molecules in Finite-Basis-Set Kohn-Sham Theory.

243. M. Gruning, O. V. Gritsenko, S. J. A. van Gisbergen, and E. J. Baerends, *J. Chem. Phys.*, **114**, 652 (2001). Shape Corrections to Exchange-Correlation Potentials by Gradient-Regulated Seamless Connection of Model Potentials for Inner and Outer Region.

244. M. van Faassen and K. Burke, *J. Chem. Phys.*, **124**, 094102 (2006). The Quantum Defect: The True Measure of TDDFT Results for Atoms.

245. M. van Faassen, *Int. J. Quantum Chem.*, **106**, 3235 (2006). The Quantum Defect as a Powerful Tool for Studying Rydberg Transition Energies from Density Functional Theory.

246. M. van Faassen and K. Burke, *Chem. Phys. Lett.*, **431**, 410 (2006). A New Challenge for Time-Dependent Density Functional Theory.

247. M. Stener, P. Decleva, and A. Görling, *J. Chem. Phys.*, **114**, 7816 (2001). The Role of Exchange and Correlation in Time-Dependent Density-Functional Theory for Photoionization.

248. A. Kono and S. Hattori, *Phys. Rev. A*, **29**, 2981 (1984). Accurate Oscillator Strengths for Neutral Helium.

249. J. A. R. Samson, Z. X. He, L. Yin, and G. N. Haddad, *J. Phys. B*, **27**, 887 (1994). Precision Measurements of the Absolute Photoionization Cross Sections of He.

250. H. Friedrich, *Theoretical Atomic Physics*, **2**nd ed., Springer, New York 1998.

251. A. Wasserman and K. Burke, *Phys. Rev. Lett.*, **95**, 163006 (2005). Rydberg Transition Frequencies from the Local Density Approximation.

252. M. Abramowitz and I. A. Stegun, Eds., *Handbook of Mathematical Functions*, Dover, New York, 1972.

253. A. Wasserman, N. T. Maitra, and K. Burke, *Phys. Rev. Lett.*, **91**, 263001 (2003). Accurate Rydberg Transitions from LDA Potentials.

254. A. Wasserman, N. T. Maitra, and K. Burke, *J. Chem. Phys.*, **122**, 133103 (2005). Electron-Molecule Scattering from Time-Dependent Density Functional Theory.

255. A. Wasserman and K. Burke, *Lect. Notes Phys.*, **706**, 493 (2006). Scattering Amplitudes from TDDFT.

256. R. K. Nesbet, *Phys. Rev. A*, **62**, 040701 (2000). Bound-Free Correlation in Electron Scattering by Atoms and Molecules.

257. S. Tonzani and C. H. Greene, *J. Chem. Phys.*, **122**, 014111 (2005). Electron-Molecule Scattering Calculations in a 3D Finite Element R-Matrix Approach.

258. S. Tonzani and C. H. Greene, *J. Chem. Phys.*, **124**, 054312 (2006). Low-Energy Electron Scattering from DNA and RNA Bases: Shape Resonances and Radiation Damage.

259. M. van Faassen, A. Wasserman, E. Engel, F. Zhang, and K. Burke, *Phys. Rev. Lett.*, **99**, 043005 (2007). Time-Dependent Density Functional Calculation of e-H Scattering.

260. U. Fano, *Nuovo Cimento*, **12**, 154 (1935). On the Absorption Spectrum of Noble Gases at the Arc Spectrum Limit. [Translation: cond-mat/0502210 (2005).]

261. V. A. Mandelshtam, T. R. Ravuri, and H. S. Taylor, *Phys. Rev. Lett.*, **70**, 1932 (1993). Calculation of the Density of Resonance States Using the Stabilization Method.

262. E. K. U. Gross and W. Kohn, *Phys. Rev. Lett.*, **55**, 2850 (1985). Local Density-Functional Theory of Frequency-Dependent Linear Response. [Erratum: *Phys. Rev. Lett.*, **57**, 923 (1986).]

263. J. F. Dobson, M. Bünner, and E. K. U. Gross, *Phys. Rev. Lett.*, **79**, 1905 (1997). Time-Dependent Density Functional Theory beyond Linear Response: An Exchange-Correlation Potential with Memory.

264. C. A. Ullrich and K. Burke, *J. Chem. Phys.*, **121**, 28 (2004). Excitation Energies from Time-Dependent Density-Functional Theory beyond the Adiabatic Approximation.

265. C. A. Ullrich and I. V. Tokatly, *Phys. Rev. B*, **73**, 235102 (2006). Nonadiabatic Electron Dynamics in Time-Dependent Density-Functional Theory.

266. C. A. Ullrich, *J. Chem. Phys.*, **125**, 234108 (2006). Time-Dependent Density-Functional Theory beyond the Adiabatic Approximation: Insights from a Two-Electron Model System.

267. G. Vignale, *Int. J. Mod. Phys. B*, **15**, 1714 (2001). Time-Dependent Density Functional Theory beyond the Adiabatic Approximation.

268. J. M. Tao and G. Vignale, *Phys. Rev. Lett.*, **97**, 036403 (2006). Time-Dependent Density-Functional Theory beyond the Local-Density Approximation.

269. Y. Kurzweil and R. Baer, *J. Chem. Phys.*, **121**, 8731 (2004). Time-Dependent Exchange-Correlation Current Density Functionals with Memory.

270. Y. Kurzweil and R. Baer, *Phys. Rev. B*, **72**, 035106 (2005). Generic Galilean-Invariant Exchange-Correlation Functionals with Quantum Memory.

271. Y. Kurzweil and R. Baer, *Phys. Rev. B*, **73**, 075413 (2006). Quantum Memory Effects in the Dynamics of Electrons in Gold Clusters.

272. I. V. Tokatly, *Phys. Rev. B*, **71**, 165104 (2005). Quantum Many-Body Dynamics in a Lagrangian Frame: I. Equations of Motion and Conservation Laws.

273. I. V. Tokatly, *Phys. Rev. B*, **71**, 165105 (2005). Quantum Many-Body Dynamics in a Lagrangian Frame: II. Geometric Formulation of Time-Dependent Density Functional Theory.

274. G. Vignale, *Lect. Notes Phys.*, **706**, 75 (2006). Current Density Functional Theory.

275. G. Vignale and W. Kohn, *Phys. Rev. Lett.*, **77**, 2037 (1996). Current-Dependent Exchange-Correlation Potential for Dynamical Linear Response Theory.

276. G. Vignale, C. A. Ullrich, and S. Conti, *Phys. Rev. Lett.*, **79**, 4878 (1997). Time-Dependent Density Functional Theory beyond the Adiabatic Local Density Approximation.

277. N. T. Maitra, F. Zhang, R. J. Cave, and K. Burke, *J. Chem. Phys.*, **120**, 5932 (2004). Double Excitations in Time-Dependent Density Functional Theory Linear Response.

278. A. Marini, R. Del Sole, and A. Rubio, *Lect. Notes Phys.*, **706**, 161 (2006). Approximate Functional from Many-Body Perturbation Theory.

279. B. G. Levine, C. Ko, J. Quenneville, and T. J. Martinez, *Mol. Phys.*, **104**, 1039 (2006). Conical Intersections and Double Excitations in Time Dependent Density Functional Theory.

280. D. J. Tozer, R. D. Amos, N. C. Handy, B. O. Roos, and L. Serrano-Andres, *Mol. Phys.*, **97**, 859 (1999). Does Density Functional Theory Contribute to the Understanding of Excited States of Unsaturated Organic Compounds?

281. D. J. Tozer and N. C. Handy, *Phys. Chem. Chem. Phys.*, **2**, 2117 (2000). On the Determination of Excitation Energies Using Density Functional Theory.

282. F. Zhang and K. Burke, *Phys. Rev. A*, **69**, 052510 (2004). Adiabatic Connection for Near Degenerate Excited States.

283. M. E. Casida, *J. Chem. Phys.*, **122**, 054111 (2005). Propagator Corrections to Adiabatic Time-Dependent Density-Functional Theory Linear Response Theory.

284. R. J. Cave, F. Zhang, N. T. Maitra, and K. Burke, *Chem. Phys. Lett.*, **389**, 39 (2004). A Dressed TDDFT Treatment of the 2^1A_g States of Butadiene and Hexatriene.

285. S. Tretiak and V. Chernyak, *J. Chem. Phys.*, **119**, 8809 (2003). Resonant Nonlinear Polarizabilities in the Time-Dependent Density Functional (TDDFT) Theory.

286. M. van Faassen, P. L. de Boeij, R. van Leeuwen, J. A. Berger, and J. G. Snijders, *Phys. Rev. Lett.*, **88**, 186401 (2002). Ultranonlocality in Time-Dependent Current-Density-Functional Theory: Application to Conjugated Polymers.

287. M. van Faassen, P. L. de Boeij, R. van Leeuwen, J. A. Berger, and J. G. Snijders, *J. Chem. Phys.*, **118**, 1044 (2003). Application of Time-Dependent Current-Density-Functional Theory to Nonlocal Exchange-Correlation Effects in Polymers.

288. M. van Faassen, *Int. J. Mod. Phys. B*, **20**, 3419 (2006). Time-Dependent Current-Density-Functional Theory Applied to Atoms and Molecules.

289. S. J. A. van Gisbergen, P. R. T. Schipper, O. V. Gritsenko, E. J. Baerends, J. G. Snijders, B. Champagne, and B. Kirtman, *Phys. Rev. Lett.*, **83**, 694 (1999). Electric Field Dependence of the Exchange-Correlation Potential in Molecular Chains.

290. S. Kümmel, L. Kronik, and J. P. Perdew, *Phys. Rev. Lett.*, **93**, 213002 (2004). Electrical Response of Molecular Chains from Density Functional Theory.

291. Y. H. Kim, M. Stadele, and A. Görling, *Int. J. Quantum Chem.*, **91**, 257 (2003). Optical Excitations of Si by Time-Dependent Density Functional Theory Based on Exact-Exchange Kohn-Sham Band Structure.

292. F. Kootstra, P. L. de Boeij, and J. G. Snijders, *J. Chem. Phys.*, **112**, 6517 (2000). Efficient Real-Space Approach to Time-Dependent Density Functional Theory for the Dielectric Response of Nonmetallic Crystals.

293. F. Kootstra, P. L. de Boeij, and J. G. Snijders, *Phys. Rev. B*, **62**, 7071 (2000). Application of Time-Dependent Density-Functional Theory to the Dielectric Function of Various Nonmetallic Crystals.

294. P. L. de Boeij, F. Kootstra, J. A. Berger, R. van Leeuwen, and J. G. Snijders, *J. Chem. Phys.*, **115**, 1995 (2001). Current Density Functional Theory for Optical Spectra: A Polarization Functional.

295. G. Onida, L. Reining, and A. Rubio, *Rev. Mod. Phys.*, **74**, 601 (2002). Electronic Excitations: Density-Functional versus Many-Body Green's-Function Approaches.

296. F. Sottile, V. Olevano, and L. Reining, *Phys. Rev. Lett.*, **91**, 056402 (2003). Parameter-Free Calculation of Response Functions in Time-Dependent Density-Functional Theory.

297. A. Marini, R. Del Sole, and A. Rubio, *Phys. Rev. Lett.*, **91**, 256402 (2003). Bound Excitons in Time-Dependent Density-Functional Theory: Optical and Energy-Loss Spectra.

298. A. Marini and A. Rubio, *Phys. Rev. B*, **70**, 081103 (2004). Electron Linewidths of Wide-Gap Insulators: Excitonic Effects in LiF.

299. M. Marques, C. A. Ullrich, F. Noguiera, A. Rubio, K. Burke, and E. K. U. Gross, Eds., *Time-Dependent Density Functional Theory*, Springer, Heidelberg, 2006.

300. A. Dreuw, J. Weisman, and M. Head-Gordon, *J. Chem. Phys.*, **119**, 2943 (2003). Long-Range Charge-Transfer Excited States in Time-Dependent Density Functional Theory Require Non-Local Exchange.

301. O. Gritsenko and E. J. Baerends, *J. Chem. Phys.*, **121**, 655 (2004). Asymptotic Correction of the Exchange Correlation Kernel of Time-Dependent Density Functional Theory for Long-Range Charge-Transfer Excitations.

302. N. T. Maitra, *J. Chem. Phys.*, **122**, 234104 (2005). Undoing Static Correlation: Long-Range Charge Transfer in Time-Dependent Density Functional Theory.

303. N. T. Maitra and D. G. Tempel, *J. Chem. Phys.*, **125**, 184111 (2006). Long-Range Excitations in Time-Dependent Density Functional Theory.

304. W. Hieringer and A. Görling, *Chem. Phys. Lett.*, **419**, 557 (2006). Failure of Time-Dependent Density Functional Methods for Excitations in Spatially Separated Systems.

305. M. E. Casida, F. Gutierrez, J. G. Guan, F. X. Gadea, D. Salahub, and J. P. Daudey, *J. Chem. Phys.*, **113**, 7062 (2000). Charge-Transfer Correction for Improved Time-Dependent Local Density Approximation Excited-State Potential Energy Curves: Analysis within the Two-Level Model with Illustration for H_2 and LiH.

306. F. Furche and T. van Voorhis, *J. Chem. Phys.*, **122**, 164106 (2005). Fluctuation-Dissipation Theorem Density-Functional Theory.

307. M. Lein, E. K. U. Gross, and J. P. Perdew, *Phys. Rev. B* , **61**, 13431 (2000). Electron Correlation Energies from Scaled Exchange-Correlation Kernels: Importance of Spatial vs. Temporal Nonlocality.

308. Y. Andersson, D. C. Langreth, and B. I. Lunqvist, *Phys. Rev. Lett.*, **76**, 102 (1996). van der Waals Interactions in Density-Functional Theory.

309. M. Fuchs, Y. M. Niquet, X. Gonze, and K. Burke, *J. Chem. Phys.*, **122**, 094116 (2005). Describing Static Correlation in Bond Dissociation by Kohn-Sham Density Functional Theory.

310. M. Dion, H. Rydberg, E. Schröder, D. C. Langreth, and B. I. Lundqvist, *Phys. Rev. Lett.*, **92**, 246401 (2004). van der Waals Density Functional for General Geometries.

311. D. C. Langreth and J. P. Perdew, *Solid State Commun.*, **17**, 1425 (1975). The Exchange-Correlation Energy of a Metallic Surface.

312. O. Gunnarsson and B. I. Lundqvist, *Phys. Rev. B*, **13**, 4274 (1976). Exchange and Correlation in Atoms, Molecules, and Solids by the Spin-Density-Functional Formalism.

313. Y. Andersson, B. I. Lunqvist, and D. C. Langreth, *Phys. Rev. Lett.*, **77**, 2029 (1996). Density Functional for van der Waals Forces at Surfaces.

314. V. P. Osinga, S. J. A. van Gisbergen, J. G. Snijders, and E. J. Baerends, *J. Chem. Phys.*, **106**, 5091 (1997). Density Functional Results for Isotropic and Anisotropic Multipole Polarizabilities and C_6, C_7, and C_8 van der Waals Dispersion Coefficients for Molecules.

315. W. Kohn, Y. Meir, and D. E. Makarov, *Phys. Rev. Lett.*, **80**, 4153 (1998). van der Waals Energies in Density Functional Theory.

316. J. P. Perdew, *Phys. Rev. B*, **33**, 8822 (1986). Density Functional Approximation for the Correlation Energy of the Inhomogeneous Gas. [Erratum: *Phys. Rev. B*, **34**, 7406 (1986).]

317. Y. Andersson, E. Hult, H. Rydberg, P. Apell, B. I. Lundqvist, and D. C. Langreth, in *Electronic Density Functional Theory: Recent Progress and New Directions*, J. F. Dobson, G. Vignale, and M. P. Das, Eds., Plenum, New York, 1997, pp. 243–260. van der Waals Interactions in Density Functional Theory.

318. H. Ryberg, B. I. Lundqvist, D. C. Langreth, and M. Dion, *Phys. Rev. B*, **62**, 6997 (2000). Tractable Nonlocal Correlation Density Functional for Flat Surfaces and Slabs.

319. H. Rydberg, M. Dion, N. Jacobson, E. Schröder, P. Hyldgaard, S. I. Simak, D. C. Langreth, and B. I. Lundqvist, *Phys. Rev. Lett.*, **91**, 126402 (2003). van der Waals Density Functional for Layered Structures.

320. S. D. Chakarova Käck, E. Schröder, B. I. Lundqvist, and D. C. Langreth, *Phys. Rev. Lett.*, **96**, 146107 (2006). Application of van der Waals Density Functional to an Extended System: Adsorption of Benzene and Naphthalene on Graphite.

321. A. Puzder, M. Dion, and D. C. Langreth, *J. Chem. Phys.*, **124**, 164105 (2006). Binding Energies in Benzene Dimers: Nonlocal Density Functional Calculations.

322. T. Thonhauser, A. Puzder, and D. C. Langreth, *J. Chem. Phys.*, **124**, 164106 (2006). Interaction Energies of Monosubstituted Benzene Dimers via Nonlocal Density Functional Theory.

323. A. J. Misquitta, B. Jeziorski, and K. Szalewicz, *Phys. Rev. Lett.*, **91**, 033201 (2003). Dispersion Energy from Density-Functional Theory Description of Monomers.

324. F. Furche, *Phys. Rev. B*, **64**, 195120 (2001). Molecular Tests of the Random Phase Approximation to the Exchange-Correlation Energy Functional.

325. M. Fuchs and X. Gonze, *Phys. Rev. B*, **65**, 235109 (2002). Accurate Density Functionals: Approaches Using the Adiabatic-Connection Fluctuation-Dissipation Theorem.

326. M. Lien and E. K. U. Gross, *Lect. Notes Phys.*, **706**, 423 (2006). Back to the Ground State: Electron Gas.

327. J. Parker, L. R. Moore, D. Dundas, and K. T. Taylor, *J. Phys. B: At. Mol. Opt. Phys.*, **33**, L691 (2000). Double Ionization of Helium at 390 nm.

328. T. Kreibich, R. van Leeuwen, and E. K. U. Gross, *Chem. Phys.*, **304**, 183 (2004). Time-Dependent Variational Approach to Molecules in Strong Laser Fields.

329. T. Kreibich, N. I. Gidopoulos, R. van Leeuwen, and E. K. U. Gross, *Prog. Theoret. Chem. Phys.*, **14**, 69 (2003). Towards Time-Dependent Density-Functional Theory for Molecules in Strong Laser Pulses.

330. M. Petersilka and E. K. U. Gross, *Laser Phys.*, **9**, 1 (1999). Strong-Field Double Ionization of Helium: A Density-Functional Perspective.

331. M. Lein, E. K. U. Gross, and V. Engel, *Laser Phys.*, **12**, 487 (2002). The Effect of the Electron-Electron Interaction in Above-Threshold Double Ionization.

332. M. Lein, T. Kreibich, E. K. U Gross, and V. Engel, *Phys. Rev. A*, **65**, 033403 (2002). Strong-Field Ionization Dynamics of a Model H_2 Molecule.

333. M. Lien, V. Engel, and E. K. U. Gross, *Optics Express*, **8**, 411 (2001). Phase-Space Analysis of Double Ionization.

334. M. Lein, E. K. U. Gross, and V. Engel, *Phys. Rev. Lett.*, **85**, 4707 (2000). Intense-Field Double Ionization of Helium: Identifying the Mechanism.

335. T. Burnus, M. A. L. Marques, and E. K. U. Gross, *Phys. Rev. A*, **71**, 010501 (2005). Time-Dependent Electron Localization Function.

336. M. Erdmann, E. K. U. Gross, and V. Engel, *J. Chem. Phys.*, **121**, 9666 (2004). Time-Dependent Electron Localization Functions for Coupled Nuclear-Electronic Motion.

337. Available: http://www.physik.fu-berlin.de/~ag-gross/tdelf.

338. C. A. Ullrich, S. Erhard, and E. K. U. Gross, in *Super Intense Laser Atom Physics IV*, H. G. Muller and M. V. Fedorov, Eds., Kluwer, 1996, pp. 267–284. Time-Dependent Density-Functional Approach to Atoms in Strong Laser Pulses.

339. S. Erhard and E. K. U. Gross, in *Multiphoton Processes 1996*, P. Lambropoulus and H. Walther, Eds., IOP, 1997, pp. 37–45. High Harmonic Generation in Hydrogen and Helium Atoms Subject to One- and Two-Color Laser Pulses.

340. A. Castro, M. A. L. Marques, J. A. Alonso, G. F. Bertsch, and A. Rubio, *Eur. Phys. J. D*, **28**, 211 (2004). Excited States Dynamics in Time-Dependent Density Functional Theory—High-Field Molecular Dissociation and Harmonic Generation.

341. X. Chu and S. I. Chu, *Phys. Rev. A*, **6302**, 3411 (2001). Self-Interaction-Free Time-Dependent Density-Functional Theory for Molecular Processes in Strong Fields: High-Order Harmonic Generation of H_2 in Intense Laser Fields.

342. R. Baer, D. Neuhauser, P. R. Ždánská, and N. Moiseyev, *Phys. Rev. A*, **68**, 043406 (2003). Ionization and High-Order Harmonic Generation in Aligned Benzene by a Short Intense Circularly Polarized Laser Pulse.

343. N. L. Wagner, A. Wüest, I. P. Christov, T. Popmintchev, X. Zhou, M. M. Murnane, and H. C. Kapteyn, *Proc. Nat. Acad. Sci. (U.S.A.)*, **103**, 13279 (2006). Monitoring Molecular Dynamics Using Coherent Electrons from High Harmonic Generation.

344. Available: http://online.itp.ucsb.edu/online/atto06/moletomo/.

345. B. Walker, B. Sheehy, L. F. DiMauro, P. Agostini, K. J. Schafer, and K. C. Kulander, *Phys. Rev. Lett.*, **73**, 1227 (1994). Precision Measurement of Stong Field Double Ionization of Helium.

346. D. N. Fittinghoff, P. R. Bolton, B. Chang, and K. C. Kulander, *Phys. Rev. Lett.*, **69**, 2642 (1992). Observation of Nonsequential Double Ionization of Helium with Optical Tunnelling.

347. K. Kondo, A. Sagisaka, T. Tamida, Y. Nabekawa, and S. Watanabe, *Phys. Rev. A*, **48**, R2531 (1993). Wavelength Dependence of Nonsequential Double Ionization in He.

348. A. Pohl, P. G. Reinhard, and E. Suraud, *Phys. Rev. Lett.*, **84**, 5090 (2000). Towards Single-Particle Spectroscopy of Small Metal Clusters.

349. H. S. Nguyen, A. D. Bandrauk, and C. A. Ullrich, *Phys. Rev. A*, **69**, 063415 (2004). Asymmetry of Above-Threshold Ionization of Metal Clusters in Two-Color Laser Fields: A Time-Dependent Density-Functional Study.

350. S. A. Rice and M. Zhao, *Optical Control of Molecular Dynamics*, Wiley, New York, 2000.

351. J. Werschnik and E. K. U. Gross, *J. Opt. B: Quantum Semiclass. Opt.*, **7**, S300 (2005). Tailoring Laser Pulses with Spectral and Fluence Constraints Using Optimal Control Theory.

352. A. G. Urena, K. Gasmi, S. Skowronek, A. Rubio, and P. M. Echenique, *Eur. Phys. J. D*, **28**, 193 (2004). Laser-Induced Control of (Multichannel) Intracluster Reactions—The Slowest is Always the Easiest to Take.

353. H. O. Wijewardane and C. A. Ullrich, *Appl. Phys. Lett.*, **84**, 3984 (2004). Coherent Control of Intersubband Optical Bistability in Quantum Wells.

354. C. A. Ullrich and G. Vignale, *Phys. Rev. Lett.*, **87**, 037402 (2001). Theory of the Linewidth of Intersubband Plasmons in Quantum Wells.

355. C. A. Ullrich and G. Vignale, *Phys. Rev. B*, **61**, 2729 (2000). Collective Charge-Density Excitations of Noncircular Quantum Dots in a Magnetic Field.

356. R. Baer and D. Neuhauser, *J. Chem. Phys.*, **125**, 074709 (2006). Theoretical Studies of Molecular Scale Near-Field Electron Dynamics.

357. E. Livshits and R. Baer, *J. Phys. Chem. A*, **110**, 8443 (2006). Time-Dependent Density-Functional Studies of the D_2 Coulomb Explosion.

358. Y. B. Band, S. Kallush, and R. Baer, *Chem. Phys. Lett.*, **392**, 23 (2004). Rotational Aspects of Short-Pulse Population Transfer in Diatomic Molecules.

359. A. Nitzan and M. A. Ratner, *Science*, **300**, 1384 (2003). Electron Transport in Molecular Wire Junctions.

360. M. Brandbyge, J. L. Mozos, P. Ordejon, J. Taylor, and K. Stokbro, *Phys. Rev. B*, **65**, 165401 (2002). Density Functional Method for Nonequilibrium Electron Transport.

361. G. Stefanucci and C. O. Almbladh, *Phys. Rev. B*, **69**, 195318 (2004). Time-Dependent Partition-Free Approach in Resonant Tunneling Systems.

362. M. di Ventra and T. N. Todorov, *J Phys. Cond. Matt.*, **16**, 8025 (2004). Transport in Nanoscale Systems: The Microcanonical versus Grand-Canonical Picture.

363. R. Gebauer and R. Car, *Phys. Rev. B*, **70**, 125324 (2004). Kinetic Theory of Quantum Transport at the Nanoscale.

364. K. Burke, R. Car, and R. Gebauer, *Phys. Rev. Lett.*, **94**, 146803 (2005). Density Functional Theory of the Electrical Conductivity of Molecular Devices.

365. F. Evers, F. Weigend, and M. Koentopp, *Phys. Rev. B*, **69**, 25411 (2004). The Conductance of Molecular Wires and DFT Based Transport Calculations.

366. N. Sai, M. Zwolak, G. Vignale, and M. Di Ventra, *Phys. Rev. Lett.*, **94**, 186810 (2005). Dynamical Corrections to the DFT-LDA Electron Conductance in Nanoscale Systems.

367. S. H. Ke, H. U. Baranger, and W. Yang, *J. Chem. Phys.*, **126**, 201102 (2007). The Dramatic Role of the Exchange-Correlation Potential in ab initio Electron Transport Calculations.

368. C. Toher, A. Filippetti, S. Sanvito, and K. Burke, *Phys. Rev. Lett.*, **95**, 146402 (2005). Self-Interaction Errors in Density Functional Calculations of Electronic Transport.

369. M. Koentopp, K. Burke, and F. Evers, *Phys. Rev. B Rapid Commun.*, **73**, 121403 (2006). Zero-Bias Molecular Electronics: Exchange-Correlation Corrections to Landauer's Formula.

370. S. Kurth, G. Stefanucci, C. O. Almbladh, A. Rubio, and E. K. U. Gross, *Phys. Rev. B*, **72**, 035308 (2005). Time-Dependent Quantum Transport: A Practical Scheme Using Density Functional Theory.

371. R. Gebauer, K. Burke, and R. Car, *Lect. Notes Phys.*, **706**, 463 (2006). Kohn-Sham Master Equation Approach to Transport Through Single Molecules.

372. R. Gebauer and R. Car, *Int. J. Quantum Chem.*, **101**, SI 564, (2005). Electron Transport with Dissipation: A Quantum Kinetic Approach.

373. W. Shakespeare, in *Mr. William Shakespeares Comedies, Histories, and Tragedies*, J. Heminges and H. Condell, Eds., Stationers Company, London, 1623, pp. 152–282. The Tragedie of Hamlet, Prince of Denmarke.

374. L. H. Thomas, *Proc. Camb. Phil. Soc.*, **23**, 542 (1926). The Calculation of Atomic Fields.

375. E. Fermi, *Zeit. Fur Physik*, **48**, 73 (1928). A Statistical Method for the Determination of Some Atomic Properties and the Application of This Method to the Theory of the Periodic System of Elements.

CHAPTER 4

Computing Quantum Phase Transitions

Thomas Vojta

Department of Physics, Missouri University of Science and Technology, Rolla, Missouri

PREAMBLE: MOTIVATION AND HISTORY

A phase transition occurs when the thermodynamic properties of a material display a singularity as a function of the external parameters. Imagine, for instance, taking a piece of ice out of the freezer. Initially, its properties change only slowly with increasing temperature, but at 0° C, a sudden and dramatic change occurs. The thermal motion of the water molecules becomes so strong that it destroys the crystal structure. The ice melts, and a new phase of water forms, the liquid phase. At the phase transition temperature of 0° C the solid (ice) and the liquid phases of water coexist. A finite amount of heat, the so-called latent heat, is required to transform the ice into liquid water at 0° C. Phase transitions involving latent heat are called first-order transitions. Another well-known example of a phase transition is the ferromagnetic transition of iron. At room temperature, iron is ferromagnetic, i.e., it displays a spontaneous magnetization. With rising temperature, the magnetization decreases continuously due to thermal fluctuations of the spins. At the transition temperature (the so-called Curie point) of 770° C, the magnetization vanishes, and iron is paramagnetic at higher temperatures. In contrast to the previous example, there is no phase coexistence at the transition temperature; the ferromagnetic and paramagnetic phases instead become indistinguishable.

Reviews in Computational Chemistry, Volume 26
edited by Kenny B. Lipkowitz and Thomas R. Cundari

Consequently, there is no latent heat. This type of phase transition is called a continuous (second-order) transition or critical point.

Phase transitions play an essential role in shaping the world. The large-scale structure of the universe is the result of phase transitions during the early stages of its development after the Big Bang. Phase transitions also occur during the production of materials, in growth processes, and in chemical reactions. Understanding phase transitions has thus been a prime endeavor of science. More than a century has gone by from the first (modern) discoveries of phase transitions in gases and liquids by Andrews[1] and van der Waals[2] until a consistent picture of the nature of those transitions started to emerge. However, the theoretical concepts established during this development, viz., scaling and the renormalization group[3,4] now belong to the central paradigms of modern physics and chemistry.

The examples of phase transitions mentioned above occur at nonzero temperature. At these so-called thermal or classical transitions, the ordered phase (the ice crystal or the ferromagnetic state of iron) is destroyed by thermal fluctuations. In the last two decades or so, considerable attention has focused on a very different class of phase transitions. These new transitions occur at zero temperature when a nonthermal parameter such as pressure, chemical composition, or magnetic field is changed. The fluctuations that destroy the ordered phase in these transitions cannot be of a thermal nature. Instead, they are quantum fluctuations that are a consequence of Heisenberg's uncertainty principle. For this reason, these zero-temperature transitions are called quantum phase transitions.

As an illustration of this phenomenon, consider the magnetic phase diagram[5] of the compound $LiHoF_4$ in Figure 1. In zero external magnetic field, $LiHoF_4$ undergoes a phase transition from a paramagnet to a ferromagnet

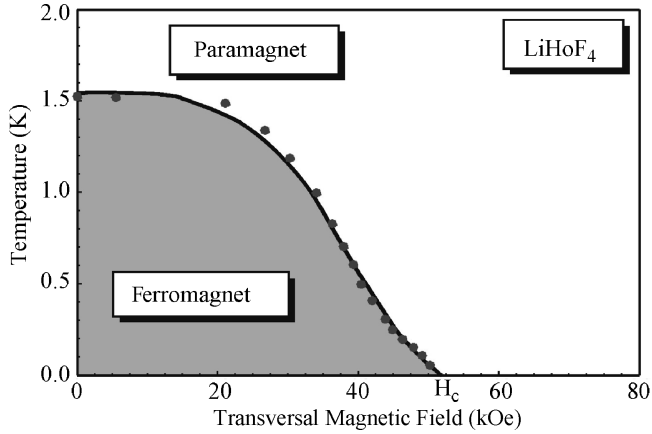

Figure 1 Phase diagram of $LiHoF_4$ as function of temperature and transverse magnetic field.

at about 1.5 K. This transition is a thermal continuous phase transition analogous to the Curie point of iron discussed above. Applying a magnetic field perpendicular to the ordering direction of the ferromagnet induces quantum fluctuations between the spin-up and spin-down states and thus reduces the transition temperature. At a field strength of $H_c \approx 50$ kOe (corresponding to a field of $B_c \approx 5$ T), the transition temperature drops to zero. Thus, at 50 kOe $LiHoF_4$ undergoes a quantum phase transition from a ferromagnet to a paramagnet. At first glance, quantum phase transitions would seem to be a purely academic problem since they occur at isolated values in parameter space and at zero temperature, which is not accessible in a real experiment. However, it is now clear that the opposite is true; quantum phase transitions do have important, experimentally relevant consequences, and they are believed to provide keys to many new and exciting properties of condensed matter, including the quantum Hall effects, exotic superconductivity, and non-Fermi liquid behavior in metals.

The purpose of this chapter is twofold: In the following two sections, Phase Transitions and Critical Behavior and Quantum vs. Classical Phase Transitions, we give a concise introduction into the theory of quantum phase transitions, emphasizing similarities with and differences from classical thermal transitions. After that, we point out the computational challenges posed by quantum phase transitions, and we discuss a number of successful computational approaches together with prototypical examples. However, this chapter is not meant to be comprehensive in scope. We rather want to help scientists who are taking their first steps in this field to get off on the right foot. Moreover, we want to provide experimentalists and traditional theorists with an idea of what simulations can achieve in this area (and what they cannot do, ... yet). Those readers who want to learn more details about quantum phase transitions and their applications should consult one of the recent review articles[6–9] or the excellent textbook on quantum phase transitions by Sachdev.[10]

PHASE TRANSITIONS AND CRITICAL BEHAVIOR

In this section, we briefly collect the basic concepts of the modern theory of phase transitions and critical phenomena to the extent necessary for the purpose of this chapter. A detailed exposition can be found in, e.g., the textbook by Goldenfeld.[11]

Landau Theory

Most modern theories of phase transitions are based on Landau theory.[12] Landau introduced the concept of an *order parameter*, a thermodynamic quantity that vanishes in one phase (the disordered phase) and is nonzero and generally nonunique in the other phase (the ordered phase). For the ferromagnetic

phase transition, the total magnetization is an order parameter, for example. In general, the order parameter can be a scalar, a vector, or even a tensor. Landau theory can be understood as a unification of earlier mean-field theories such as the van der Waals theory of the liquid–gas transition[2] or Weiss's molecular field theory of ferromagnetism.[13] It is based on the crucial assumption that the free energy is an analytic function of the order parameter m and can thus be expanded in a power series:

$$F = F_L(m) = F_0 + rm^2 + wm^3 + um^4 + O(m^5) \qquad [1]$$

Close to the phase transition, the coefficients r,w,u vary slowly with respect to the external parameters such as temperature, pressure, and electric or magnetic field. For a given system, the coefficients can be determined either by a first-principle calculation starting from a microscopic model, or, phenomenologically, by comparison with experimental data. The correct equilibrium value of the order parameter m for each set of external parameter values is found by minimizing F_L with respect to m.

Let us now discuss the basic properties of phase transitions that result from the Landau free energy, Eq. [1]. If the coefficient r is sufficiently large, the minimum of F_L is located at $m = 0$, i.e., the system is in the disordered phase. In contrast, for sufficiently small (negative) r, the minimum is at some nonzero m, putting the system into the ordered phase. Depending on the value of w, the Landau free energy describes a first-order or a continuous transition. If $w \neq 0$, the order parameter jumps discontinuously from $m = 0$ to $m \neq 0$, i.e., the transition is of first order. If $w = 0$ (as is often the case due to symmetry), the theory describes a continuous transition or critical point at $r = 0$. In this case, r can be understood as the distance from the critical point, $r \propto T - T_c$. Within Landau theory, the behavior close to a critical point is superuniversal, meaning that all continuous phase transitions display the same behavior. For instance, the order parameter vanishes as $m = (-r/2u)^{1/2}$ when the critical point $r = 0$ is approached from the ordered phase, implying that the critical exponent β, which describes the singularity of the order parameter at the critical point via $m \propto |r|^{\beta} \propto |T - T_c|^{\beta}$, always has the mean-field value $\frac{1}{2}$.

In experiments, the critical exponent values are usually different from what Landau theory predicts; and while they show some degree of universality, it is weaker than the predicted superuniversality. For instance, all three-dimensional Ising ferromagnets (i.e., ferromagnets with uniaxial symmetry and a scalar order parameter) fall into the same universality class with $\beta \approx 0.32$ while all two-dimensional Ising magnets have $\beta \approx \frac{1}{8}$. All three-dimensional Heisenberg magnets [for which the order parameter is a three-component vector with $O(3)$ symmetry] also have a common value of $\beta \approx 0.35$, but this value for Heisenberg magnets is different from that in Ising magnets.

The failure of Landau theory to describe the critical behavior correctly was the central puzzle in phase transition theory over many decades. It was

only solved in the 1970s with the development of the renormalization group.[3,4] We now understand that Landau theory does not include adequately the fluctuations of the order parameter about its average value. The effects of these fluctuations in general decrease with increasing dimensionality and with increasing number of order parameter components. This observation suggests that Landau theory might actually be correct for systems in sufficiently high space dimension d. In fact, the fluctuations lead to two different critical dimensionalities, d_c^+ and d_c^-, for a given phase transition. If d is larger than the upper critical dimension d_c^+, fluctuations are unimportant for the critical behavior, and Landau theory gives the correct critical exponents. If d is between the upper and the lower critical dimensions, $d_c^+ > d > d_c^-$, a phase transition still exists but the critical behavior is different from Landau theory. For dimensionalities below the lower critical dimension, fluctuations become so strong that they completely destroy the ordered phase. For the ferromagnetic transition at nonzero temperature, $d_c^+ = 4$, and $d_c^- = 2$ or 1 for Heisenberg and Ising symmetries, respectively.

Scaling and the Renormalization Group

To go beyond Landau theory, the order parameter fluctuations need to be included. This can be achieved by writing the partition function as a functional integral

$$Z = e^{-F/k_B T} = \int D[\phi] e^{-S[\phi]/k_B T} \qquad [2]$$

where $S[\phi]$ is the Landau–Ginzburg–Wilson (LGW) free energy or "action," a generalization of the Landau free energy, Eq. [1], for a fluctuating field $\phi(\mathbf{x})$ representing the local order parameter. It is given by

$$S[\phi] = \int d^d x [c(\nabla\phi(\mathbf{x}))^2 + F_L(\phi(\mathbf{x})) - h\phi(\mathbf{x})] \qquad [3]$$

Here, we have also included an external field h conjugate to the order parameter (in the case of the ferromagnetic transition, h is a uniform magnetic field). The thermodynamic average m of the order parameter is given by the average $\langle\phi\rangle$ of the field with respect to the statistical weight $e^{-S[\phi]/k_B T}$.

In the disordered phase, the thermodynamic average of the order parameter vanishes, but its fluctuations are nonzero. When the critical point is approached, the spatial correlations of the order parameter fluctuations, as characterized by the correlation function $G(\mathbf{x} - \mathbf{y}) = \langle\phi(\mathbf{x})\phi(\mathbf{y})\rangle$, become long-ranged. Close to the critical point, their typical length scale, the correlation length ξ, diverges as

$$\xi \propto |r|^{-\nu} \qquad [4]$$

where ν is called the correlation length critical exponent. This divergence was observed in 1873 in a famous experiment by Andrews:[1] A fluid becomes milky when approaching its critical point because the length scale of its density fluctuations reaches the wavelength of light. This phenomenon is called critical opalescence.

Close to the critical point, ξ is the only relevant length scale in the system. Therefore, the physical properties must be unchanged, if all lengths in the system are rescaled by a common factor b, and at the same time the external parameters are adjusted in such a way that the correlation length retains its old value. This gives rise to a homogeneity relation for the free energy density $f = -(k_B T/V)\log Z$,

$$f(r,h) = b^{-d} f(rb^{1/\nu}, hb^{y_h}) \qquad [5]$$

The scale factor b is an arbitrary number, and y_h is another critical exponent. Analogous homogeneity relations for other thermodynamic quantities can be obtained by taking derivatives of f. These homogeneity laws were first obtained phenomenologically[14] and are sometimes summarily called the scaling hypothesis. Within the framework of the modern renormalization group theory of phase transitions,[3,4] the scaling laws can be derived from first principles. The diverging correlation length is also responsible for the above-mentioned universality of the critical behavior. Close to the critical point, the system effectively averages over large volumes rendering microscopic system details irrelevant. As a result, the universality classes are determined only by symmetries and the spatial dimensionality.

In addition to the critical exponents ν and y_h defined above, other exponents describe the dependence of the order parameter and its correlations on the distance from the critical point and on the field conjugate to the order parameter. The definitions of the most commonly used critical exponents are summarized in Table 1. These exponents are not all independent from each other. The four thermodynamic exponents α, β, γ, δ all derive from the

Table 1 Definitions of Critical Exponents

	Exponent	Definition[a]	Conditions
Specific heat	α	$c \propto \lvert r\rvert^{-\alpha}$	$r \to 0, h = 0$
Order parameter	β	$m \propto (-r)^{\beta}$	$r \to 0-, h = 0$
Susceptibility	γ	$\chi \propto \lvert r\rvert^{-\gamma}$	$r \to 0, h = 0$
Critical isotherm	δ	$h \propto \lvert m\rvert^{\delta}\mathrm{sgn}(m)$	$r = 0, h \to 0$
Correlation length	ν	$\xi \propto \lvert r\rvert^{-\nu}$	$r \to 0, h = 0$
Correlation function	η	$G(\mathbf{x}) \propto \lvert\mathbf{x}\rvert^{-d+2-\eta}$	$r = 0, h = 0$
Dynamical	z	$\xi_t \propto \xi^z$	
Activated dynamical	ψ	$\ln \xi_t \propto \xi^{\psi}$	

[a] m is the order parameter, and h is the conjugate field. The variable r denotes the distance from the critical point, and d is the space dimensionality. The exponent y_h defined in Eq. [5] is related to δ via $y_h = d\delta/(1+\delta)$.

free energy, Eq. [5], which contains only two independent exponents. They are therefore connected by the scaling relations

$$\begin{aligned} 2 - \alpha &= 2\beta + \gamma \\ 2 - \alpha &= \beta(\delta + 1) \end{aligned} \qquad [6]$$

The correlation length and correlation function exponents are related by

$$\begin{aligned} 2 - \alpha &= d\nu \\ \gamma &= (2 - \eta)\nu \end{aligned} \qquad [7]$$

Exponent relations involving the dimensionality d explicitly are called hyperscaling relations. They only hold below the upper critical dimension d_c^+. Above d_c^+ they are destroyed by dangerously irrelevant variables.[11]

In addition to the diverging length scale ξ, a critical point is characterized by a diverging time scale, the correlation time ξ_t. It leads to the phenomenon of *critical slowing down*, i.e., very slow relaxation toward equilibrium near a critical point. At generic critical points, the divergence of the correlation time follows a power law $\xi_t \propto \xi^z$ where z is the dynamical critical exponent. At some transitions, in particular in the presence of quenched disorder, the divergence can be exponential, $\ln \xi_t \propto \xi^\psi$. The latter case is referred to as activated dynamical scaling in contrast to the generic power-law dynamical scaling.

Finite-Size Scaling

The question of how a finite system size influences a critical point is important for the application of computational methods and also for many experiments, for example, in layered systems or nanomaterials. In general, a sharp phase transition can exist only in the thermodynamic limit, i.e., in an infinite system. A finite system size results in a rounding and shifting of the critical singularities. A quantitative description of finite-size effects is provided by finite-size scaling theory.[15–17] Finite-size scaling starts from the observation that the inverse system size acts as an additional parameter (analogous to r or h) that takes the system away from the critical point. Because the correlation length of the infinite system ξ_∞ is the only relevant length scale close to the critical point, finite-size effects in a system of linear size L must be controlled by the ratio L/ξ_∞ only. We can therefore generalize the classical homogeneity relation of Eq. [5] for the free energy density by including the system size

$$f(r, h, L) = b^{-d} f(rb^{1/\nu}, hb^{y_h}, Lb^{-1}) \qquad [8]$$

By taking derivatives and/or setting the arbitrary scale factor b to appropriate values, Eq. [8] can be used to derive scaling forms of various observables. For instance, by setting $b = L$ and $h = 0$, we obtain $f(r, L) = L^{-d}\Theta_f(rL^{1/\nu})$ where

$\Theta_f(x)$ is a dimensionless scaling function. This can also be used to find how the critical point shifts as a function of L in geometries that allow a sharp transition at finite L (e.g., layers of finite thickness). The finite-L phase transition corresponds to a singularity in the scaling function at some nonzero argument x_c. The transition thus occurs at $r_c L^{1/\nu} = x_c$, and the transition temperature $T_c(L)$ of the finite-size system is shifted from the bulk value T_c^0 by

$$T_c(L) - T_c^0 \propto r_c = x_c L^{-1/\nu} \qquad [9]$$

Note that the simple form of finite-size scaling summarized above is only valid below the upper critical dimension d_c^+ of the phase transition. Finite-size scaling can be generalized to dimensions above d_c^+, but this requires taking dangerously irrelevant variables into account. One important consequence is that the shift of the critical temperature, $T_c(L) - T_c^0 \propto L^{-\varphi}$ is controlled by an exponent φ that in general is different from $1/\nu$.

Finite-size scaling has become one of the most powerful tools for analyzing computer simulation data of phase transitions. Instead of treating finite-size effects as errors to be avoided, one can simulate systems of varying size and test whether or not homogeneity relations such as Eq. [8] are fulfilled. Fits of the simulation data to the finite-size scaling forms of the observables then yield values for the critical exponents. We will discuss examples of this method later in the chapter.

Quenched Disorder

Realistic systems always contain some amount of quenched (frozen-in) disorder in the form of vacancies, impurity atoms, dislocations, or other types of imperfections. Understanding their influence on the behavior of phase transitions and critical points is therefore important for analyzing experiments. In this section, we focus on the simplest type of disorder (sometimes called weak disorder, random-T_c disorder, or, from the analogy to quantum field theory, random-mass disorder) by assuming that the impurities and defects do not change qualitatively the bulk phases that are separated by the transition. They only lead to spatial variations of the coupling strength and thus of the local critical temperature. In ferromagnetic materials, random-T_c disorder can be achieved, for example, by diluting the lattice, which means by replacing magnetic atoms with nonmagnetic ones. Within a LGW theory such as Eq. [3], random T_c disorder can be modeled by making the parameter r (which measures the distance from the critical point) a random function of spatial position, $r \to r + \delta r(\mathbf{x})$.

The presence of quenched disorder naturally leads to the following questions:

- Will the phase transition remain sharp or will it be rounded?
- Will the order of the transition (first order or continuous) remain the same as in the clean case?

- If the transition is continuous, will the "dirty" system show the same critical behavior as the clean one or will the universality class change?
- Will only the transition itself be influenced or will the behavior also be changed in its vicinity?

An important early step toward answering these questions came from the work of Harris[18] who considered the stability of a critical point against disorder. He showed that if a clean critical point fulfills the exponent inequality

$$d\nu > 2 \qquad [10]$$

now called the Harris criterion, it is perturbatively stable against weak disorder. Note, however, that the Harris criterion only deals with the average behavior of the disorder at large length scales; effects due to qualitatively new behavior at finite length scales (and finite disorder strength) are not covered. Thus, the Harris criterion is a necessary condition for the stability of a clean critical point, not a sufficient one.

The Harris criterion can serve as the basis for a classification of critical points with quenched disorder according to the behavior of the average disorder strength with increasing length scale. Three classes can be distinguished:[19] (1) The first class contains critical points fulfilling the Harris criterion. At these phase transitions, the disorder strength *decreases* under coarse graining, and the system becomes homogeneous at large length scales. Consequently, the critical behavior of the dirty system is identical to that of the clean system. Macroscopic observables are self-averaging at the critical point, i.e., the relative width of their probability distributions vanishes in the thermodynamic limit.[20,21] A prototypical example is the three-dimensional classical Heisenberg model whose clean correlation length exponent is $\nu \approx 0.711$ fulfilling the Harris criterion. (2) In the second class, the system remains inhomogeneous at all length scales with the relative strength of the disorder approaching a finite value for large length scales. The resulting critical point still displays conventional power-law scaling, but it is in a new universality class with exponents that differ from those of the clean system (and fulfill the inequality $d\nu > 2$). Macroscopic observables are *not* self-averaging, but in the thermodynamic limit, the relative width of their probability distributions approaches a size-independent constant. An example in this class is the classical three-dimensional Ising model. Its clean correlation length exponent, $\nu \approx 0.629$, does not fulfill the Harris criterion. Introduction of quenched disorder, for example, via dilution, thus leads to a new critical point with an exponent of $\nu \approx 0.684$. (3) At critical points in the third class, the relative magnitude of the disorder counterintuitively *increases* without limit under coarse graining. At these so-called infinite-randomness critical points, the power-law scaling is replaced by activated (exponential) scaling. The probability distributions of macroscopic variables become very broad (even on a logarithmic scale) with their width diverging with system size. Infinite-randomness

critical points have been found mainly in quantum systems, starting with Fisher's seminal work on the random transverse field Ising model[22,23] by means of the Ma–Dasgupta–Hu renormalization group.[24]

The above classification is based on the behavior of the *average* disorder strength at large length scales. In recent years it has become clear, however, that an important role is often played by strong disorder fluctuations and the rare spatial regions that support them. These regions can show local order even if the bulk system is in the disordered phase. Their fluctuations are very slow because they require changing the order parameter in a large volume. Griffiths[25] showed that the contributions of the rare regions lead to a singular free energy not only at the phase transition point but in an entire parameter region around it. At generic thermal (classical) transitions, the rare region contributions to thermodynamic observables are very weak since the singularity in the free energy is only an essential one.[26,27] In contrast, at many quantum phase transitions, rare disorder fluctuations lead to strong power-law quantum Griffiths singularities that can dominate the thermodynamic behavior.[22,23,28,29] In some systems, rare region effects can become so strong that they destroy the sharp phase transition by smearing.[30] A recent review of rare region effects at classical, quantum, and nonequilibrium phase transitions can be found in Ref. 31.

QUANTUM VS. CLASSICAL PHASE TRANSITIONS

In this section, we give a concise introduction into the theory of quantum phase transitions, emphasizing similarities with and differences from classical thermal transitions.

How Important Is Quantum Mechanics?

The question of how important quantum mechanics is for understanding continuous phase transitions has several facets. On the one hand, one may ask whether quantum mechanics is even needed to explain the existence and properties of the bulk phases separated by the transition. This question can be decided only on a case-by-case basis, and very often quantum mechanics is essential as, e.g., for the superconducting phase. On the other hand, one can ask how important quantum mechanics is for the behavior close to the critical point and thus for the determination of the universality class to which the transition belongs. It turns out that the latter question has a remarkably clear and simple answer: Quantum mechanics does *not* play any role in determining the critical behavior if the transition occurs at a finite temperature; it does play a role, however, at zero temperature.

To understand this remarkable observation, it is useful to distinguish fluctuations with predominantly thermal or quantum character (depending on whether their thermal energy $k_B T$ is larger or smaller than the quantum energy scale $\hbar\omega_c$, where ω_c is the typical frequency of the fluctuations). As discussed in the last section, the typical time scale ξ_t of the fluctuations generally diverges as a continuous transition is approached. Correspondingly, the typical frequency scale ω_c goes to zero and with it the typical energy scale

$$\hbar\omega_c \propto |r|^{\nu z} \qquad [11]$$

Quantum fluctuations will be important as long as this typical energy scale is larger than the thermal energy $k_B T$. If the transition occurs at some finite temperature T_c, quantum mechanics will therefore become unimportant if the distance r from the critical point is smaller than a crossover distance r_x given by $r_x \propto T_c^{1/\nu z}$. Consequently, we find that the critical behavior asymptotically close to the transition is always classical if the transition temperature T_c is nonzero. This justifies calling all finite-temperature phase transitions "classical transitions," even if they occur in an intrinsically quantum mechanical system. Consider, as an example, the superconducting transition of mercury at 4.2 K. Here, quantum mechanics is obviously important on microscopic scales for establishing the superconducting order parameter, but classical thermal fluctuations dominate on the macroscopic scales that control the critical behavior. In other words, close to criticality the fluctuating clusters become so big (their typical size is the correlation length ξ) that they behave classically.

In contrast, if the transition occurs at zero temperature as a function of a nonthermal parameter such as pressure or magnetic field, the crossover distance r_x vanishes; in this situation quantum mechanics is important for the critical behavior. Consequently, transitions at zero temperature are called quantum phase transitions as described earlier. In Figure 2, we show the resulting schematic phase diagram close to a quantum critical point. Sufficiently close to the finite-temperature phase boundary, the critical behavior is purely classical, as discussed above. However, the width of the classical critical region vanishes with vanishing temperature. Thus, an experiment along path (a) at sufficiently low temperatures will mostly observe quantum behavior, with a very narrow region of classical behavior (which may be unobservable) right at the transition. The disordered phase comprises three regions, separated by crossover lines. In the quantum disordered region at low temperatures and when $B > B_c$, quantum fluctuations destroy the ordered phase, and the effects of temperature are unimportant. In contrast, in the thermally disordered region, the ordered phase is destroyed by thermal fluctuations while the corresponding ground state shows long-range order. Finally, the so-called quantum critical region is located at $B \approx B_c$ and extends (somewhat counterintuitively) to comparatively high temperatures. In this regime, the system is critical with respect to B, and the critical singularities are cut-off exclusively

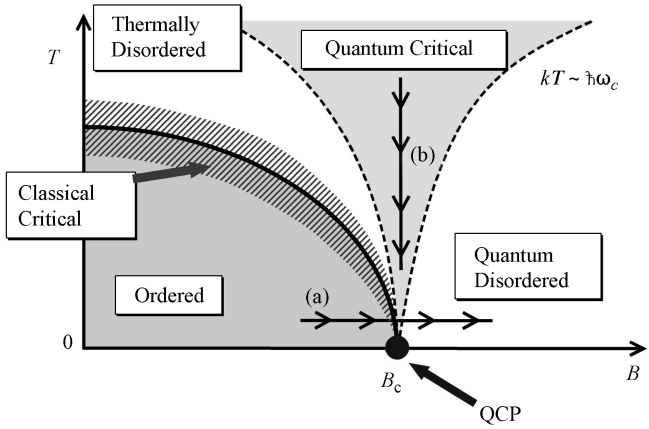

Figure 2 Schematic phase diagram close to a quantum critical point for systems having an ordered phase at nonzero temperature. The solid line is the finite-temperature phase boundary while the dashed lines are crossover lines separating different regions within the disordered phase. QCP denotes the quantum critical point.

by the temperature. An experiment along path (b) thus explores the temperature scaling of the quantum critical point. The phase diagram in Figure 2 applies to systems that have an ordered phase at finite temperatures. Some systems, such as Heisenberg magnets in two dimensions, display long-range order only at exactly zero temperature. The corresponding schematic phase diagram is shown in Figure 3. Even though the system is always in the disordered phase at any nonzero temperature, the quantum critical point still controls the crossovers between the three different regions discussed above.

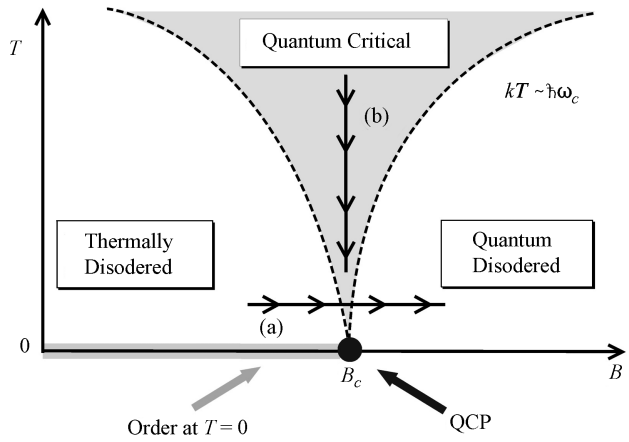

Figure 3 Same as Figure 2 but for systems that display long-range order only at exactly zero temperature.

Quantum Scaling and Quantum-to-Classical Mapping

In classical statistical mechanics, static and dynamic behaviors decouple. Consider a classical Hamiltonian $H(p_i, q_i) = H_{\text{kin}}(p_i) + H_{\text{pot}}(q_i)$ consisting of a kinetic part H_{kin} that depends only on the momenta p_i and a potential part H_{pot} that depends only on the coordinates q_i. The classical partition function of such a system, $Z = \int dp_i e^{-H_{\text{kin}}/k_B T} \int dq_i e^{-H_{\text{pot}}/k_B T}$, factorizes into kinetic and potential parts that are independent of each other. The kinetic contribution to the free energy generally does not display any singularities since it derives from a product of Gaussian integrals. One can therefore study the thermodynamic critical behavior in classical systems using time-independent theories such as the Landau–Ginzburg–Wilson theory discussed above. The dynamical critical behavior can be found separately.

The situation is different in quantum statistical mechanics. Here, the kinetic and potential parts of the Hamiltonian do not commute with each other. Consequently, the partition function $Z = \text{Tr} e^{-\hat{H}/k_B T}$ does not factorize, and one must solve for the dynamics together with the thermodynamics. The canonical density operator $e^{-\hat{H}/k_B T}$ takes the form of a time–evolution operator in imaginary time, if one identifies $1/k_B T = -it/\hbar$. Thus, quantum mechanical analogs of the LGW theory, Eq. [3], need to be formulated in terms of space- and time-dependent fields. A simple example of such a quantum LGW action takes the form

$$S[\phi] = \int_0^{1/k_B T} d\tau \int d^d x [a(\partial_\tau \phi(\mathbf{x}, \tau))^2 + c(\nabla \phi(\mathbf{x}, \tau))^2 + F_L(\phi(\mathbf{x}, \tau)) - h\phi(\mathbf{x}, \tau)] \quad [12]$$

with τ being the imaginary time variable. This action describes, for example, the magnetization fluctuations of an Ising model in a transverse field.

This LGW functional also illustrates another remarkable feature of quantum statistical mechanics. The imaginary time variable τ effectively acts as an additional coordinate whose extension becomes infinite at zero temperature. A quantum phase transition in d-space dimensions is thus equivalent to a classical transition in $d + 1$ dimensions. This property is called the *quantum-to-classical mapping*. In general, the resulting classical system is anisotropic because space and time coordinates do not enter in the same fashion. A summary of the analogies arising from the quantum-to-classical mapping is given in Table 2.

The homogeneity law, Eq. [5], for the free energy can be generalized easily to the quantum case (see, e.g., Ref. 10). For the generic case of power-law dynamical scaling, it takes the form

$$f(r, h, T) = b^{-(d+z)} f(rb^{1/\nu}, hb^{y_h}, Tb^z) \quad [13]$$

Table 2 Analogies between Important Quantities in Quantum-to-Classical Mapping

Quantum System	Classical System
d space, 1 time dimensions	$d+1$ space dimensions
Coupling constant	Classical Temperature T
Inverse physical temperature $1/k_B T$	Finite size L_t in the "time" direction
Spatial correlation length ξ	Spatial correlation length ξ
Inverse energy gap Δ	Correlation length ξ_t in "time" direction

After Ref. 6.

The appearance of the imaginary time direction also modifies the hyperscaling relations of Eq. [7]: The spatial dimensionality d has to be replaced by $d + z$. If space and time enter the theory symmetrically (as in the example given in Eq. [12]), the dynamical exponent is $z = 1$, but in general, it can take any positive value. Note that the quantum-to-classical mapping is valid for the thermodynamics only. Other properties such as the real-time dynamics at finite temperatures require more careful considerations. Moreover, the interpretation of the quantum partition function as being a classical one in a higher dimension is only possible if the statistical weight is real and positive. If this is not the case (consider, e.g., Berry phase terms in the spin functional integral), the quantum-to-classical mapping cannot be applied directly.

The quantum-to-classical mapping can be exploited for computational studies of quantum phase transitions. If one is only interested in finding the universal critical behavior at the quantum critical point (i.e., in the critical exponents) and not in nonuniversal quantities, it is often easier to perform a simulation of the equivalent classical system instead of the original quantum system. We will come back to this point later in the chapter.

Beyond the Landau–Ginzburg–Wilson Paradigm

It has become clear in recent years that some quantum phase transitions cannot be described satisfactorily by the LGW approach, i.e., by considering long-wavelength fluctuations of a local order parameter only. In this section we briefly discuss mechanisms that can invalidate the LGW approach.

Generic Scale Invariance

The derivation of the LGW theory as a regular expansion of the free energy in terms of the order parameter fluctuations relies on those fluctuations being the only gapless (soft) modes in the system. If other soft modes exist, such as those due to conservation laws or broken continuous symmetries, they lead to long-range power-law correlations of various quantities even away from the critical point. This phenomenon is called generic scale invariance.[32–34] If one insists on deriving an LGW theory in the presence of other gapless modes, the resulting functional has singular coefficients and is thus ill-defined. One should instead work with a coupled theory that keeps all soft

modes at the same footing. This mechanism is discussed in detail in Ref. 9, and it is important for metallic quantum ferromagnets as an example.

Deconfined Quantum Criticality

Certain two-dimensional $S = \frac{1}{2}$ quantum antiferromagnets can undergo a direct continuous quantum phase transition between two ordered phases, an antiferromagnetic Néel phase and the so-called valence-bond ordered phase (where translational invariance is broken). This is in contradiction to Landau theory, which predicts phase coexistence, an intermediate phase, or a first-order transition, if any. The continuous transition is the result of topological defects that become spatially deconfined at the critical point and are not contained in an LGW description. Recently, there has been a great interest in the resulting deconfined quantum critical points.[35]

Heavy-Fermion Quantum Criticality

Nonconventional quantum critical point scenarios may also be important for understanding the magnetic transitions in heavy-fermion systems. In experiments,[36] many of these materials show pronounced deviations from the predictions of the standard LGW theory of metallic quantum phase transitions.[37,38] The breakdown of the conventional approach in these systems may be due to Kondo fluctuations. The standard theory[37,38] assumes that the heavy quasi-particles (which arise from Kondo hybridization between f electrons and conduction electrons) remain intact across the transition. However, there is now some fairly direct experimental evidence (from de-Haas–van-Alphen and Hall measurements) for the Kondo effect breaking down right at the magnetic transition in some materials. This phenomenon cannot be described in terms of the magnetic order parameter fluctuations contained in the LGW theory. Several alternative scenarios are being developed, including the so-called local critical point,[39] and the fractionalized Fermi liquid leading to one of the above-mentioned deconfined quantum critical points.[40,41] A complete field theory for these transitions has not yet been worked out.

Impurity Quantum Phase Transitions

An interesting type of quantum phase transition are boundary transitions where only the degrees of freedom of a subsystem become critical while the bulk remains uncritical. The simplest case is the so-called impurity quantum phase transitions where the free energy contribution of the impurity (or, in general, a zero-dimensional subsystem) becomes singular at the quantum critical point. Such transitions occur in anisotropic Kondo systems, quantum dots, and in spin systems coupled to dissipative baths as examples. Impurity quantum phase transitions require the thermodynamic limit in the bulk (bath) system but are completely independent from possible phase transitions of the bath. A recent review of impurity quantum phase transitions can be found in Ref. 42.

QUANTUM PHASE TRANSITIONS: COMPUTATIONAL CHALLENGES

Computational studies of quantum phase transitions generally require a large numerical effort because they combine several formidable computational challenges. These include (1) the problem of many interacting degrees of freedom, (2) the fact that phase transitions arise only in the thermodynamic limit of infinite system size, (3) critical slowing down and supercritical slowing down at continuous and first-order transitions, respectively, and (4) anisotropic space–time scaling at quantum critical points. In disordered systems, there is the additional complication (5) of having to simulate large numbers of disorder configurations to obtain averages and probability distributions of observables. In the following, we discuss these points in detail.

1. *The Quantum Many-Particle Problem* Computational studies of quantum phase transitions require simulating interacting quantum many-particle systems. The Hilbert space dimension of such systems increases exponentially with the number of degrees of freedom. Thus, ''brute-force'' methods such as exact diagonalization are limited to very small systems that are usually insufficient for investigating properties of phase transitions. In many research areas of many-particle physics and chemistry, sophisticated approximation methods have been developed to overcome this problem, but many of those approximations are problematic in the context of quantum phase transitions. Self-consistent field (SCF) or single-particle-type approximations such as Hartree–Fock or density functional theory (see, e.g., Refs. 43–45), by construction, neglect fluctuations because they express the many-particle interactions in terms of an effective field or potential. Because fluctuations have proven to be crucial for understanding continuous phase transitions (as discussed in the section above on Phase Transitions and Critical Behavior), these methods must fail at least in describing the critical behavior close to the transition. They may be useful for approximately locating the transition in parameter space, though. Other approximation methods, such as the coupled cluster-method,[46] go beyond the self-consistent field level by including one or several classes of fluctuations. However, since the set of fluctuations included is limited and has to be selected by hand, these methods are not bias free. Quantum critical states are generally very far from any simple reference state so they are particularly challenging for these techniques. One important class of methods that are potentially numerically exact and bias free are quantum Monte Carlo methods.[47–49] They will be discussed in more detail later in this chapter. However, quantum Monte Carlo methods for fermions suffer from the notorious sign problem that originates in the antisymmetry of the many-fermion wave function and hampers the simulation severely. Techniques developed for dealing with the sign problem often reintroduce biases into the method, via, for instance,

forcing the nodes of the wave function to coincide with those of a trial wave function.

2. *Thermodynamic Limit* Sharp phase transitions only arise in the thermodynamic limit of infinite system size, but this does not mean one has to actually simulate infinitely large systems. The critical behavior of a continuous phase transition can be extracted by simulating finite systems using finite-size scaling (see section on Phase Transitions and Critical Behavior). This still requires sufficiently large system sizes, however, that are in the asymptotic finite-size scaling regime where corrections to scaling forms such as Eq. [8] are small. In general, it is not clear a priori how large the system sizes have to be to reach this asymptotic regime, so, one must simulate a range of system sizes and test the validity of the scaling forms a posteriori.

3. *Critical and Supercritical Slowing Down* As discussed in the section on Phase Transitions and Critical Behavior, critical points display critical slowing down, i.e., the system dynamics becomes arbitrarily slow when one approaches the transition. First-order transitions can display an even more dramatic supercritical slowing down where the correlation time increases exponentially with the length scale. The same slowing down problem occurs in many Monte Carlo methods, in particular if the updates (elementary moves) are local. This means that the necessary simulation times diverge when approaching the transition point. Critical and supercritical slowing down can be overcome by more sophisticated Monte Carlo methods including cluster update techniques[50,51] for critical points and flat-histogram methods[52,53] for first-order transitions.

4. *Anisotropic Space–Time Scaling at Quantum Critical Points* Many commonly used quantum Monte Carlo algorithms work at finite temperatures and require an extrapolation to zero temperature to extract information on quantum phase transitions. The data analysis in such simulations thus implies finite-size scaling not only for the spatial coordinates but also for the imaginary time direction. This finite-size scaling will in general be anisotropic in space and time with an unknown dynamical exponent z. Therefore, system size and (inverse) temperature have to be varied independently, increasing greatly the numerical effort.

5. *Disordered Systems* Computational studies of disordered systems in general require the simulation of a large number (from 100s to several 10,000s) of samples or disorder configurations to explore the averages or distribution functions of macroscopic observables. This is particularly important for finite-disorder and infinite-disorder critical points (which occur in many quantum systems) because at these critical points, the probability distributions of observables remain broad or even broaden without limit with increasing system size. The numerical effort for simulating a disordered quantum many-particle system can thus be several orders of magnitude larger than that for the corresponding clean system.

CLASSICAL MONTE CARLO APPROACHES

We describe here computational approaches to quantum phase transitions that rely on the quantum-to-classical mapping. The number of transitions that can be studied by these approaches is huge; our discussion is therefore not meant to be comprehensive. Following an introduction to the method, we discuss a few representative examples, mostly from the area of magnetic quantum phase transitions.

Method: Quantum-to-Classical Mapping and Classical Monte Carlo Methods

In the section on Quantum vs. Classical Phase Transitions, we pointed out that the partition function of a d-dimensional quantum many-particle system can be written as a functional integral over space and (imaginary) time-dependent fields. If the statistical weight in this representation is real and positive, it can be interpreted as the statistical weight of a classical system in $d + 1$ dimensions with the extra dimension corresponding to the imaginary time direction. This classical system can now be simulated very efficiently using the well-developed machinery of classical Monte Carlo methods.[54,55] Often, this quantum-to-classical mapping is exact only for the asymptotic low-energy degrees of freedom. Therefore, this approach works best if one is mostly interested in the universal critical behavior at the transition, i.e., in the overall scaling scenario and the values of the critical exponents, rather than in nonuniversal quantities that depend on microscopic details such as the critical coupling constants or numerical values of observables.

In some simple cases, the classical system arising from the quantum-to-classical mapping belongs to one of the well-known universality classes of classical phase transitions whose critical behavior has been studied in great detail in the literature. In these cases, the quantum problem can be solved by simply "translating" the known classical results and by calculating specific observables, if desired. The first two examples discussed below will be of this type. However, more often than not, the classical system arising from the quantum-to-classical mapping is unusual and anisotropic (space and imaginary time directions do not appear in a symmetric fashion). In these cases, the behavior of the classical system has likely not been studied before, but it can nonetheless be simulated efficiently by classical Monte Carlo methods.

Transverse-Field Ising Model

The first example we consider is arguably the simplest model displaying a quantum phase transition—the quantum Ising model in a transverse field. It can be viewed as a toy model for the magnetic quantum phase transition of $LiHoF_4$ discussed in the introductory section. For this system, we explain

the quantum-to-classical mapping in detail, identify the equivalent classical model and then discuss the results for the quantum critical behavior.

The transverse-field Ising model is defined on a d-dimensional hypercubic (i.e., square, cubic, etc.) lattice. Each site is occupied by a quantum spin-$\frac{1}{2}$. The spins interact via a ferromagnetic nearest-neighbor exchange interaction $J > 0$ between their z components. The transverse magnetic field h_x couples to the x components of the spins. The Hamiltonian of the model is given by

$$\hat{H} = -J \sum_{\langle i,j \rangle} \hat{S}_i^z \hat{S}_j^z - h_x \sum_i \hat{S}_i^x \qquad [14]$$

For $J \gg h_x$, the system is in a ferromagnetic state, with a nonzero spontaneous magnetization in the z direction. In contrast, for $J \ll h_x$, the z magnetization vanishes, and the system is a paramagnet. The two phases are separated by a quantum phase transition at $J \sim h_x$. The starting point for our investigation of the critical behavior of this transition is the partition function $Z = \mathrm{Tr}\, e^{-\hat{H}/k_B T}$. We now show how to map this partition function onto that of a classical system. The procedure is analogous to Feynman's path integral for the quantum mechanical propagator.[56]

Because the z and x components of the spin operators do not commute, the partition function cannot be factorized simply into an interaction part and a transverse-field part. However, we can use the Trotter product formula,[57] $e^{\hat{A}+\hat{B}} = \lim_{N\to\infty}(e^{\hat{A}/N} e^{\hat{B}/N})^N$, for Hermitean operators $\hat{A}$ and $\hat{B}$ to slice the imaginary time direction and then factorize the exponential in each slice. The partition function now reads

$$Z = \mathrm{Tr} \lim_{N\to\infty} \left(\exp \varepsilon J \sum_{\langle i,j \rangle} \hat{S}_i^z \hat{S}_j^z \exp \varepsilon h_x \sum_i \hat{S}_i^x \right)^N \qquad [15]$$

where $\varepsilon = 1/(k_B T N)$ is the step in imaginary time direction. We now insert resolutions of the unit operator in terms of $\hat{S}^z$ eigenstates between each pair of time slices as well as resolutions of the unit operator in terms of $\hat{S}^x$ eigenstates between the interaction and field terms within each slice. Applying all $\hat{S}^z$ operators onto $\hat{S}^z$ eigenstates and all $\hat{S}^x$ operators onto $\hat{S}^x$ eigenstates, we can express the partition function in terms of the eigenvalues (which are classical variables) only. The sums over the $\hat{S}^x$ eigenvalues can be easily carried out, and up to a constant prefactor, the partition function is given by

$$Z \propto \lim_{N\to\infty} \sum_{\{S_{i,n}\}} \exp \varepsilon J \sum_{\langle i,j \rangle, n} S_{i,n} S_{j,n} + K \sum_{i,n} S_{i,n} S_{i,n+1} \qquad [16]$$

where $S_{i,n} = \pm 1$ is the $\hat{S}^z$ eigenvalue of the spin at site i and time slice n. The interaction K in imaginary time direction takes the form $K = \frac{1}{2} \ln \coth(\varepsilon h_x)$.

This representation of the partition function of the transverse-field Ising model is identical to the partition function of an anisotropic classical Ising model in $d+1$ dimensions with coupling constants εJ in the d-space dimensions and K in the timelike direction. The classical Hamiltonian reads

$$\frac{H_{\mathrm{cl}}}{k_B T} = -\varepsilon J \sum_{\langle i,j\rangle,n} S_{i,n} S_{j,n} - K \sum_{i,n} S_{i,n} S_{i,n+1} \qquad [17]$$

Because the interactions are short ranged (nearest neighbor only) in both space- and timelike directions, the anisotropy does not play a role in the critical behavior of this classical model. We thus conclude that the quantum phase transition of the d-dimensional quantum Ising model in a transverse field falls into the universality class of the $(d+1)$-dimensional classical Ising model. This establishes the quantum-to-classical mapping (for a slightly different derivation based on transfer matrices; see Ref. 10).

The classical model arising from the mapping is a well-studied model of classical statistical mechanics in this example. We can thus simply translate the known results. Specifically, the one-dimensional transverse-field Ising model is equivalent to the two-dimensional classical Ising model that was solved exactly in a seminal study[58] by Onsager more than 60 years ago. The exponent values are $\alpha = 0$, $\beta = \frac{1}{8}$, $\gamma = \frac{7}{4}$, $\delta = 15$, $\nu = 1$, $\eta = \frac{1}{4}$. Since space and time directions are equivalent, the dynamic exponent is $z = 1$. The critical behavior of various thermodynamic quantities can now be obtained from the homogeneity relation of Eq. [13]. For instance, by differentiating Eq. [13] twice with respect to h, we obtain the homogeneity relation for the magnetic susceptibility

$$\chi(r, h, T) = b^{\gamma/\nu} \chi(r b^{1/\nu}, h b^{y_h}, T b^z) \qquad [18]$$

Note that the field h appearing in Eq. [18] is a field conjugate to the order parameter, i.e., it is a magnetic field in the z direction, not the transverse field h_x. By setting $r = 0$, $h = 0$ and $b = T^{-1/z}$, we find the temperature dependence of the zero-field susceptibility at criticality to be $\chi(T) \propto T^{-\gamma/\nu z} = T^{-7/4}$. Other thermodynamic observables can be determined analogously. The energy gap Δ, an important property of the quantum system close to criticality, is related to the correlation length ξ_t of the equivalent classical system in imaginary time direction via $\Delta^{-1} \propto \xi_t$.

The two-dimensional transverse-field Ising model maps onto the three-dimensional classical Ising model, which is not exactly solvable. However, the critical behavior has been determined with high precision using Monte Carlo and series expansion methods (see, e.g., Ref. 59). The exponent values are $\beta \approx 0.326$, $\gamma \approx 1.247$, $\nu \approx 0.629$. The other exponents can be found from the scaling and hyperscaling relations of Eqs. [6] and [7]. In dimensions three and higher, the transverse-field Ising model displays mean-field critical

behavior because the equivalent classical model is at or above the upper critical dimension $d_c^+ = 4$. (Precisely at d_c^+, there will be the usual logarithmic corrections.[11])

Bilayer Heisenberg Quantum Antiferromagnet

A (single-layer) two-dimensional Heisenberg quantum antiferromagnet consists of quantum spins-$\frac{1}{2}$ on the sites of a square lattice. They interact via the Hamiltonian

$$\hat{H} = J_{\parallel} \sum_{\langle i,j \rangle} \hat{\mathbf{S}}_i \cdot \hat{\mathbf{S}}_j \qquad [19]$$

where $J_{\parallel} > 0$ is the nearest-neighbor exchange interaction. In contrast to Eq. [14], the interaction is isotropic in spin space. This model describes, for example, the magnetic properties of the CuO planes in undoped high-T_c cuprate perovskites. Even though quantum fluctuations (caused by the noncommutativity of the spin components) reduce the staggered magnetization from its classical value of $\frac{1}{2}$ to about 0.3, the ground state displays long-range antiferromagnetic (Néel) order as will be discussed in the section on Quantum Monte Carlo Methods. To induce a quantum phase transition to a paramagnetic state, one has to increase the quantum fluctuations. This can be done, e.g., by considering two identical layers with the corresponding spins in the two layers coupled antiferromagnetically by an interaction $J_{\perp} > 0$ (see Figure 4 for a sketch of the system).

The Hamiltonian of the resulting bilayer Heisenberg quantum antiferromagnet reads

$$\hat{H} = J_{\parallel} \sum_{\langle i,j \rangle} (\hat{\mathbf{S}}_{i,1} \cdot \hat{\mathbf{S}}_{j,1} + \hat{S}_{i,2} \cdot \hat{\mathbf{S}}_{j,2}) + J_{\perp} \sum_i \hat{\mathbf{S}}_{i,1} \cdot \hat{\mathbf{S}}_{i,2} \qquad [20]$$

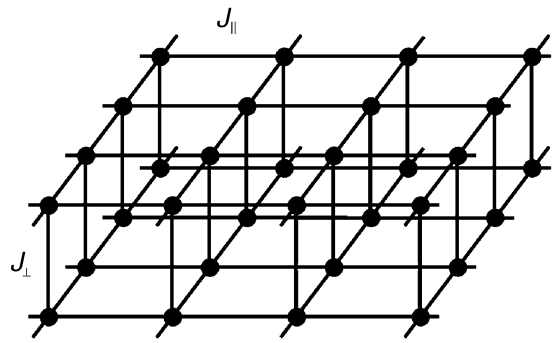

Figure 4 Sketch of the bilayer Heisenberg quantum antiferromagnet. Each lattice site is occupied by a quantum spin-$\frac{1}{2}$.

where the second index of the spin operator distinguishes the two layers. For $J_\perp \gg J_\parallel$, the corresponding spins in the two layers form singlets that are magnetically inert (i.e., $J_\perp$ increases the fluctuations away from the classical Néel state). Thus, the system is in the paramagnetic phase. In contrast, for $J_\perp \ll J_\parallel$, each layer orders antiferromagnetically, and the weak interlayer coupling establishes global antiferromagnetic long-range order. There is a quantum phase transition between the two phases at some $J_\perp \sim J_\parallel$.

We now map this quantum phase transition onto a classical transition. Chakravarty and co-workers[60] showed that the low-energy behavior of two-dimensional quantum Heisenberg antiferromagnets is generally described by a $(2+1)$-dimensional quantum rotor model with the Euclidean action

$$S = \frac{1}{2g} \int_0^{1/k_B T} d\tau \left[\sum_i \left(\partial_\tau \mathbf{n}_i(\tau)\right)^2 - \sum_{\langle i,j \rangle} \mathbf{n}_i(\tau) \cdot \mathbf{n}_j(\tau) \right] \qquad [21]$$

or by the equivalent continuum nonlinear sigma model. Here $\mathbf{n}_i(\tau)$ is a three-dimensional unit vector representing the *staggered* magnetization. For the bilayer Hamiltonian Eq. [20], the rotor variable $\mathbf{n}_i(\tau)$ represents $\hat{\mathbf{S}}_{i,1} - \hat{\mathbf{S}}_{i,2}$ while the conjugate angular momentum represents $\hat{\mathbf{S}}_{i,1} + \hat{\mathbf{S}}_{i,2}$ (see Chapter 5 of Ref. 10). The coupling constant g is related to the ratio $J_\parallel/J_\perp$. By reinterpreting the imaginary time direction as an additional space dimension, we can now map the rotor model Eq. [21] onto a three-dimensional classical Heisenberg model with the Hamiltonian

$$\frac{H_{\mathrm{cl}}}{k_B T} = -K \sum_{\langle i,j \rangle} \mathbf{n}_i \cdot \mathbf{n}_j \qquad [22]$$

Here the value of K is determined by the ratio $J_\parallel/J_\perp$ and tunes the phase transition. (Since the interaction is short ranged in space and time directions, the anisotropy of Eq. [21] does not play a role in the critical behavior.)

As in the first example, the classical system arising from the quantum-to-classical mapping is a well-known model of classical statistical mechanics. While it is not exactly solvable, its properties are known with high precision from classical Monte Carlo simulations.[61,62] The critical exponents of the phase transition are $\alpha \approx -0.133$, $\beta \approx 0.369$, $\gamma \approx 1.396$, $\delta \approx 4.783$, $\nu \approx 0.711$, and $\eta \approx 0.037$. Because space and time directions enter Eq. [22] symmetrically, the dynamical exponent is $z = 1$. The critical behavior of observables can be obtained from the homogeneity relation of Eq. [13] as before. Note that the field h appearing in the homogeneity relation is *not* a uniform magnetic field but rather the field conjugate to the antiferromagnetic order parameter, i.e., it is a staggered magnetic field. Including a uniform magnetic field in the quantum-to-classical mapping procedure leads to complex

weights in the partition function. As a result, the uniform magnetic field has no analog in the classical problem. Investigating the effects of a uniform field beyond linear response theory is thus outside the quantum-to-classical mapping approach.

Dissipative Transverse-Field Ising Chain

The quantum-to-classical mapping in the two examples above resulted in systems where space and time directions appear symmetrically, implying a dynamical exponent $z = 1$ from the outset. We now turn to an example where space and time directions scale differently, and where the dynamical exponent has to be determined from the simulation data.

The dissipative transverse-field Ising chain consists of a one-dimensional transverse-field Ising model, as discussed in the first example above, with each spin coupled to a heat bath of harmonic oscillators. The Hamiltonian reads

$$\hat{H} = -J \sum_{\langle i,j \rangle} \hat{S}_i^z \hat{S}_j^z - h_x \sum_i \hat{S}_i^x + \sum_{i,k} [c_k \hat{S}_i^z (a_{i,k}^\dagger + a_{i,k}) + \omega_{i,k} a_{i,k}^\dagger a_{i,k}] \qquad [23]$$

Here $a_{i,k}^\dagger$ and $a_{i,k}$ are the creation and destruction operators of harmonic oscillator k coupled to spin i. The oscillator frequencies $\omega_{i,k}$ and coupling constants c_k are chosen such that the spectral function $J(\omega) = 4\pi \sum_k c_k^2 \delta(\omega - \omega_{i,k}) = 2\pi\alpha\omega$ for ω less than some cutoff ω_c, but vanishes otherwise. This defines Ohmic (linear) dissipation with dimensionless dissipation strength α.

The quantum-to-classical mapping for this system follows the same "Feynman path integral" procedure used in the first example. The harmonic oscillator degrees of freedom lead to Gaussian integrals and can thus be integrated out exactly. The resulting classical Hamiltonian reads

$$\frac{H_{\mathrm{cl}}}{k_B T} = -\varepsilon J \sum_{\langle i,j \rangle, n} S_{i,n} S_{j,n} - K \sum_{i,n} S_{i,n} S_{i,n+1} - \alpha \sum_{i,n \neq m} \left(\frac{\pi}{N}\right)^2 \frac{S_{i,n} S_{i,m}}{\sin^2(\pi/N|n-m|)} \qquad [24]$$

Here $S_{i,n} = \pm 1$ are classical Ising variables at site i and imaginary time step n. The time interval ε is related to the inverse temperature via $\varepsilon = 1/(k_B T N)$, and the coupling constant K is given by $K = \frac{1}{2} \ln \coth(\varepsilon h_x)$, as before. The coupling to the Ohmic baths has introduced a long-range interaction in the time direction that behaves as $1/\tau^2$ in the Trotter limit $N \to \infty$. This long-range interaction breaks the symmetry between space and time directions.

The classical Hamiltonian, Eq. [24], can now be studied using classical Monte Carlo algorithms. To reduce the computational effects of critical slowing down close to the transition, cluster algorithms are helpful. However, the commonly used Swendsen–Wang[50] and Wolff[51] algorithms are not very efficient for long-range interactions because they have to go over

all neighbors of each site when building a cluster. Luijten and Blöte[63] developed a version of the Swendsen–Wang algorithm that is suitable and efficient for long-range interactions. Werner et al.[64] used this algorithm to simulate the Hamiltonian of Eq. [24]. Since space and time directions are not equivalent, the data analysis via finite-size scaling is not entirely trivial. An efficient way for determining the critical point and the dynamical exponent z self-consistently was suggested by Guo, Bhatt and Huse[65] as well as by Rieger and Young.[66] It is based on analyzing dimensionless observables such as the Binder cumulant:

$$B = 1 - \frac{\langle m^4 \rangle}{3\langle m^2 \rangle^2} \qquad [25]$$

where m is the magnetization (i.e., the order parameter). This quantity approaches well-known limits in both bulk phases: In the ordered phase, all spins are correlated, and the magnetization has small fluctuations around a nonzero value, so, $\langle m^4 \rangle \approx \langle m^2 \rangle^2$, and the Binder ratio approaches $\frac{2}{3}$. In the disordered phase, the system consists of many independent fluctuators. Consequently, $\langle m^4 \rangle$ can be decomposed using Wick's theorem giving $\langle m^4 \rangle \approx 3\langle m^2 \rangle^2$, and the Binder ratio approaches zero. Since the Binder ratio is dimensionless, the finite-size scaling homogeneity relation for this quantity reads

$$B(r, L, L_t) = B(rb^{1/\nu}, Lb^{-1}, L_t b^{-z}) \qquad [26]$$

where L and L_t are the linear system sizes in space and time direction, respectively. Setting the arbitrary scale factor $b = L$ leads to the scaling form

$$B(r, L, L_t) = \Phi_B(rL^{1/\nu}, L_t/L^z) \qquad [27]$$

with Φ_B a dimensionless scaling function. The following important characteristic holds: For fixed L, B has a peak as a function of L_t. The peak position $L_t^{\max}$ marks the optimal sample shape, where the ratio L_t/L behaves roughly like the corresponding ratio of the correlation lengths in time and space directions. (If the aspect ratio deviates from the optimum one, the system can be decomposed into independent units either in space or in time direction, and thus B decreases.) At the critical point, the peak value $B^{\max}$ is independent of L. Thus, plotting B vs. $L_t/L_t^{\max}$ at the critical point should collapse the data, without the need for a value of the dynamical exponent z. Instead, z can be extracted from the relation $L_t^{\max} \propto L^z$. An example of such an analysis is shown in Figure 5. Once the dynamical exponent z is found, the other exponents can be derived from one-parameter finite-size scaling as in the classical case.[15–17]

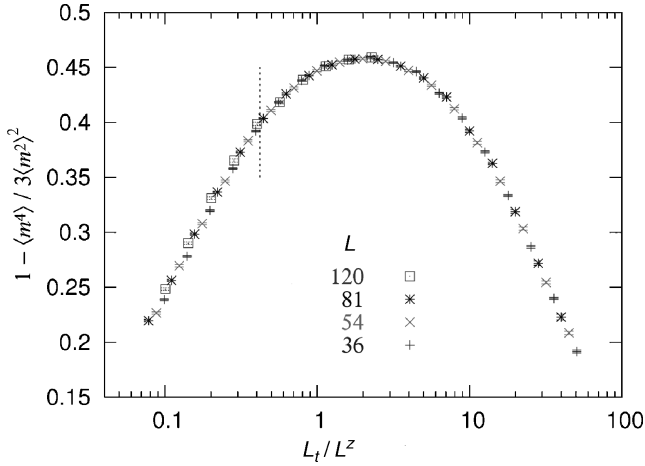

Figure 5 Scaling analysis of the Binder cumulant B of the classical Hamiltonian, Eq. [24], at criticality ($\alpha = 0.6$, $\varepsilon J = 0.00111$, $K = 1.153$) with a dynamical exponent $z = 2$. (Taken with permission from Ref. 64.)

Werner et al.[64] used these techniques to investigate the phase diagram of the Hamiltonian and the quantum phase transition between the ferromagnetic and paramagnetic phases. They found the critical behavior to be universal (i.e., independent of the dissipation strength α for all $\alpha \neq 0$). The exponent values are $\nu \approx 0.638, \eta \approx 0.015$, and $z \approx 1.985$, which agree well with the results of perturbative renormalization group calculations.[67,68] The other exponents can be found from the scaling and hyperscaling relations of Eqs. [6] and [7].

Diluted Bilayer Quantum Antiferromagnet

We have seen that dissipation can lead to an effective long-range interaction in time and thus break the symmetry between space and time directions in the last example. Another mechanism to break this symmetry is quenched disorder (i.e., impurities and defects), because this disorder is random in space but perfectly correlated in the time direction.

Consider the bilayer Heisenberg quantum antiferromaget, Eq. [20]. Random disorder can be introduced by randomly removing spins, for example, from the system (in an experiment, one would randomly replace magnetic atoms with nonmagnetic atoms). If the substitutions in the two layers are made independent of one another, the resulting unpaired spins lead to complex weights in the partition function that cannot be expressed in terms of a classical Heisenberg model. Here, we therefore consider dimer dilution, that is, the case where the corresponding spins in the two layers are removed together. The Hamiltonian of the dimer-diluted bilayer Heisenberg quantum

antiferromagnet is given by

$$\hat{H} = J_{\parallel} \sum_{\langle i,j \rangle} \mu_i \mu_j (\hat{\mathbf{S}}_{i,1} \cdot \hat{\mathbf{S}}_{j,1} + \hat{\mathbf{S}}_{i,2} \cdot \hat{\mathbf{S}}_{j,2}) + J_{\perp} \sum_i \mu_i \hat{\mathbf{S}}_{i,1} \cdot \hat{\mathbf{S}}_{i,2} \qquad [28]$$

where the μ_i are independent random variables that can take the values 0 and 1 with probability p and $1 - p$, respectively. The zero temperature phase diagram of this model has been worked out by Sandvik[69] and Vajk and Greven[70] and is shown in Figure 6. For small $J_{\perp}$, magnetic long-range order survives up to the percolation threshold of the lattice, $p_p \approx 0.4072$, and a multicritical point exists at $J_{\perp}/J_{\parallel} \approx 0.16$, $p = p_p$. Thus, the dimer-diluted bilayer Heisenberg antiferromagnet has two quantum phase transitions, the generic transition for $p < p_p$ and a quantum percolation transition at $p = p_p$, $J_{\perp} < 0.16 J_{\parallel}$.

The quantum-to-classical mapping follows the same procedure as for the clean bilayer quantum Heisenberg model above. The result is an unusual diluted three-dimensional classical Heisenberg model. Because the impurities in the quantum system are quenched (time-independent), the equivalent classical Heisenberg model has line defects parallel to the imaginary time direction. The classical Hamiltonian is given by

$$\frac{H_{\mathrm{cl}}}{k_B T} = -K \sum_{\langle i,j \rangle, n} \mu_i \mu_j \, \mathbf{n}_{i,n} \cdot \mathbf{n}_{j,n} - K \sum_{i,n} \mu_i \, \mathbf{n}_{i,n} \cdot \mathbf{n}_{i,n+1} \qquad [29]$$

where i and j are the spatial indices while n is the index in the timelike direction. The line defects break the symmetry between space and time directions; we thus expect anisotropic scaling with a dynamical exponent $z \neq 1$.

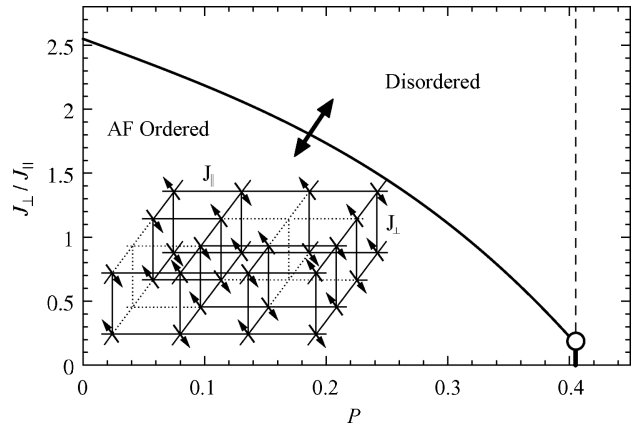

Figure 6 Phase diagram of the dimer-diluted bilayer Heisenberg antiferromagnet, as a function of $J_{\perp}/J_{\parallel}$ and dilution p. The dashed line is the percolation threshold; the open dot is the multicritical point. (Taken with permission from Ref. 71.)

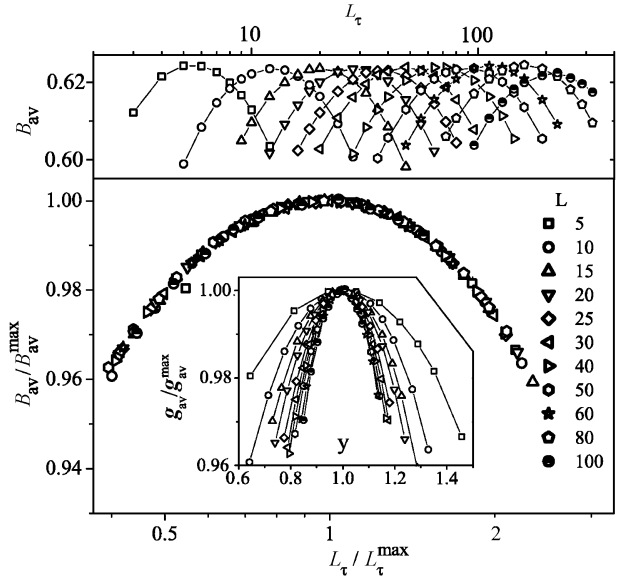

Figure 7 (*Upper panel*) Binder cumulant of the classical Hamiltonian, Eq. [29], at the critical point as a function of L_t for various L and impurity concentration $p = \frac{1}{5}$. (*Lower panel*) Power-law scaling plot of the Binder cumulant. (*Inset*) Activated scaling plot of the Binder cumulant. (Taken with permission from Ref. 71.)

Sknepnek, Vojta and Vojta[71] and Vojta and Sknepnek[72] have performed large-scale Monte Carlo simulations of the classical Hamiltonian, Eq. [29], by means of the Wolff cluster algorithm.[51] Because of the disorder, all simulations involve averages over a large number (up to several 10,000) of disorder configurations. Let us first discuss the generic transition ($p < p_p$). As explained above, the scaling behavior of the Binder cumulant can be used to self-consistently find the critical point and the dynamical exponent z. A typical result of these calculations is presented in Figure 7. It shows the Binder cumulant at the critical point for a system with impurity concentration $p = 1/5$. As seen in the main panel of this figure, the data scale very well when analyzed according to power-law scaling while the inset shows that they do not fulfill activated (exponential) scaling. Analogous data were obtained for impurity concentrations $\frac{1}{8}$, $\frac{2}{7}$, and $\frac{1}{3}$. The dynamical exponent of the generic transition now follows from a power-law fit of the maximum position L_t^{max} vs. L, as shown in Figure 8. Taking the leading corrections to scaling into account gives a universal value $z \approx 1.31$. The correlation length exponent can be determined from the off-critical finite-size scaling of the Binder cumulant, giving $\nu \approx 1.16$. Note that this value fulfills the inequality $d\nu > 2$ as required for a sharp transition in a disordered system (see discussion on quenched disorder in the section on Phase Transitions and Critical Behavior). Analyzing the magnetization and susceptibility data at criticality yields $\beta/\nu \approx 0.53$, $\gamma/\nu \approx 2.26$.

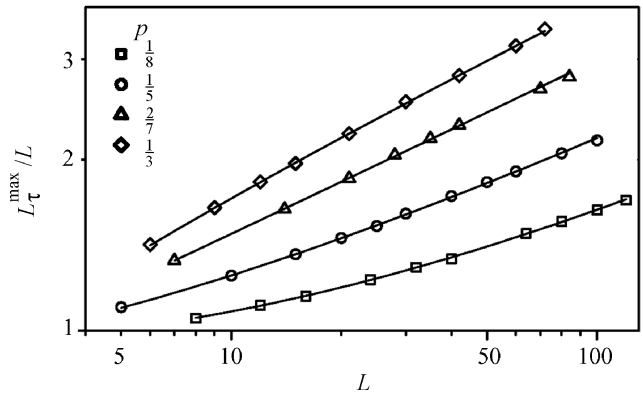

Figure 8 $L_t^{\max}$ vs. L for four impurity concentrations. The solid lines are fits to $L_t^{\max} = aL^z(1 + bL^{-\omega})$ with $z = 1.31$, $\omega = 0.48$. (Taken with permission from Ref. 71.)

Vojta and Sknepnek[72] also performed analogous calculations for the quantum percolation transition at $p = p_p$, $J_\perp < 0.16J_\parallel$ and the multicritical point at $p = p_p$, $J_\perp = 0.16J_\parallel$. A summary of the critical exponents for all three transitions is found in Table 3. The results for the percolation transition are in reasonable agreement with theoretical predictions of a recent general scaling theory[73] of percolation quantum phase transitions: $\beta/\nu = 5/48$, $\gamma/\nu = 59/16$ and a dynamical exponent of $z = D_f = \frac{91}{48}$ (coinciding with the fractal dimension of the critical percolation cluster).

Random Transverse-Field Ising Model

To illustrate the rich behavior of quantum phase transitions in disordered systems, we now consider the random transverse-field Ising model, a random version of our first example. It is given by the Hamiltonian

$$\hat{H} = -\sum_{\langle i,j \rangle} J_{ij}\hat{S}_i^z\hat{S}_j^z - \sum_i h_i^x\hat{S}_i^x \qquad [30]$$

Table 3 Critical Exponents of the Generic Transition, Percolation Transition, and Multicritical Point of the Dimer-Diluted Bilayer Quantum Heisenberg Antiferromagnet

Exponent	Generic Transition	Multicritical Point	Percolation Transition
z	1.31	1.54	1.83
β/ν	0.53	0.40	0.15
γ/ν	2.26	2.71	3.51
ν	1.16		

From Ref. 72.

where both $J_{ij} > 0$ and $h_i^x > 0$ are random functions of the lattice site. In one space dimension, the critical behavior of the quantum phase transition can be determined exactly[22,23] by means of the Ma–Dasgupta–Hu "strong-disorder" renormalization group.[24] This calculation predicts an exotic infinite-randomness critical point, characterized by the following unusual properties: (1) the effective disorder increases without limit under coarse graining (i.e., with increasing length scale), (2) instead of the usual power-law dynamical scaling one now has activated scaling, $\ln \xi_t \propto \xi^{\psi}$, with $\psi = \frac{1}{2}$, (3) the probability distributions of observables become very broad, even on a logarithmic scale, with their widths diverging when approaching the critical point, (4) average and typical correlations behave differently: At criticality, the average correlation function $C_{\mathrm{av}}(r)$ falls off with a power of the distance r, while the typical correlations decay much faster, as a stretched exponential $\ln C_{\mathrm{typ}}(r) \propto r^{-\psi}$. These results have been confirmed by extensive and efficient numerical simulations[74,75] based on mapping the spin systems onto free fermions.[76]

In dimensions $d > 1$, an exact solution is not available because the strong disorder renormalization group can be implemented only numerically.[19] Moreover, mapping the spin system onto free fermions is restricted to one dimension. Therefore, simulation studies have mostly used Monte Carlo methods. The quantum-to-classical mapping for the Hamiltonian in Eq. [30] can be performed analogously to the clean case. The result is a disordered classical Ising model in $d + 1$ dimensions with the disorder perfectly correlated in one dimension (in $1 + 1$ dimensions, this is the famous McCoy–Wu model[77,78]). The classical Hamiltonian reads

$$\frac{H_{\mathrm{cl}}}{k_B T} = -\sum_{\langle i,j\rangle,n} (\varepsilon J_{ij}) S_{i,n} S_{j,n} - \sum_{i,n} K_i S_{i,n} S_{i,n+1} \qquad [31]$$

with $J_{ij} > 0$ and $K_i = \frac{1}{2} \ln \coth(\varepsilon h_i^x) > 0$ being independent random variables.

Pich et al.[79] performed Monte Carlo simulations of this Hamiltonian in $2 + 1$ dimensions using the Wolff cluster algorithm.[51] As in the two examples above, they used the scaling behavior of the Binder cumulant to find the critical point and to analyze the dynamical scaling. The resulting scaling plot is shown in Figure 9. The figure shows that the curves do not scale when analyzed according to the usual power-law dynamical scaling, $\xi_t \propto \xi^z$, but rather get broader with increasing system size. In the inset, the data for $L \geq 12$ scale quite well according to activated scaling, $\ln \xi_t \propto \xi^{\psi}$, with $\psi \approx 0.42$. Pich et al.[79] also studied the behavior of the correlation function at criticality. They found a power-law decay of the average correlations and a stretched exponential decay of the typical correlations, as in one dimension. These results provide strong simulational evidence for the quantum critical point in the two-dimensional random transverse-field Ising model being of exotic infinite randomness type. This agrees with the prediction of the numerically implemented strong-disorder renormalization group[19] and with a general classification of

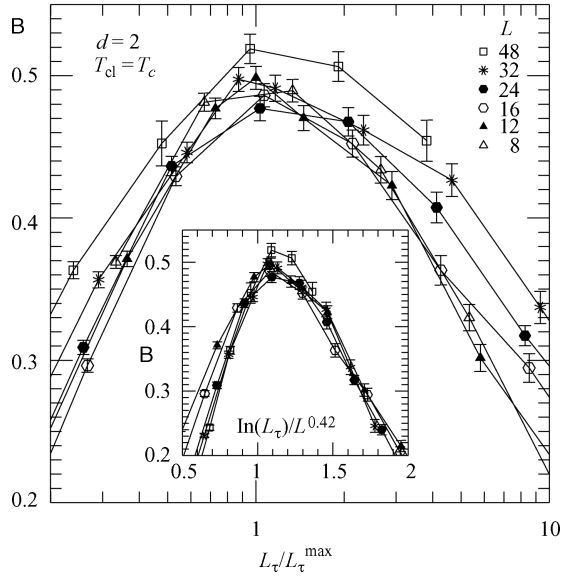

Figure 9 Binder cumulant of the classical Hamiltonian in Eq. [31] at the critical point. (*Main panel*) Power-law scaling plot. (*Inset*) Scaling plot according to activated scaling. (Taken with permission from Ref. 79.)

phase transitions in disordered systems according to the effective dimensionality of the defects.[31]

Dirty Bosons in Two Dimensions

The examples discussed so far are all *magnetic* quantum phase transitions. Our last example in this section on quantum-to-classical mapping is a quite different transition, viz. the superconductor–insulator transition in two-dimensional dirty boson systems. Experimentally, this transition can be realized in helium absorbed in a porous medium or in granular superconducting films as an example.

The minimal model for describing the superconductor–insulator transition in the general case of both charge and phase fluctuations being relevant is the boson Hubbard model with a random local chemical potential.[80,81] The Hamiltonian (defined on a square lattice) takes the form

$$\hat{H}_{\mathrm{BH}} = \frac{U}{2}\sum_i \hat{N}_i^2 - \sum_i (\mu + v_i - zt)\,\hat{N}_i - t\sum_{\langle i,j\rangle} (\hat{\Phi}_i^\dagger \hat{\Phi}_j + \hat{\Phi}_j^\dagger \hat{\Phi}_i) \qquad [32]$$

Here, U is the onsite repulsion, μ is the chemical potential, z is the number of nearest neighbors, and v_i represents the random onsite potential. The hopping strength is given by t, and $\hat{\Phi}_i^\dagger$, $\hat{\Phi}_i$ are the boson creation and destruction operators at site i. The number operator is given by $\hat{N}_i = \hat{\Phi}_i^\dagger \hat{\Phi}_i$.

If the boson density is an integer (per site), and, in the absence of disorder, charge (amplitude) fluctuations are small. If we set $\hat{\Phi}_i = |\hat{\Phi}_i| \, e^{i\hat{\theta}_i}$ and integrate out the amplitude fluctuations, we obtain a phase-only model that can be written as an O(2) quantum rotor model:

$$\hat{H}_{\mathrm{QR}} = -\frac{U}{2}\sum_i \frac{\partial^2}{\partial\theta_i^2} - t\sum_{\langle i,j\rangle}\cos(\theta_i - \theta_j) \qquad [33]$$

This Hamiltonian describes, among other systems, an array of coupled Josephson junctions.

In the spirit of this section, we now discuss the quantum-to-classical mapping for the dirty boson problem. We first consider the case of integer boson density and no disorder, i.e., the Hamiltonian in Eq. [33]. In this case, the quantum-to-classical mapping can be performed analogously to the transverse-field Ising model: The partition function is factorized using the Trotter product formula leading to a path integral representation. By reinterpreting the imaginary time direction as an extra dimension and rescaling space and time appropriately (which does not change universal properties), we finally arrive at an isotropic three-dimensional classical XY model with the Hamiltonian

$$\frac{H_{\mathrm{cl}}}{k_B T} = -K\sum_{\langle i,j\rangle}\cos(\theta_i - \theta_j) \qquad [34]$$

where θ_i is a classical angle in the interval $[0, 2\pi]$. This is again a well-known model of classical statistical mechanics that can be simulated efficiently using Monte Carlo cluster algorithms and series expansions (see, e.g., Ref. 82). The resulting critical exponents are $\alpha \approx -0.015$, $\beta \approx 0.348$, $\gamma \approx 1.318$, $\delta \approx 4.780$, $\nu \approx 0.672$, and $\eta \approx 0.038$. Since space and time enter symmetrically, the dynamical exponent is $z = 1$.

The general case of noninteger boson density and/or the presence of the random potential is more realistic. However, it leads to broken time-reversal symmetry for the quantum rotors because the particle number is represented by the quantity canonically conjugate to the phase variable, that is, by angular momentum. The quantum-to-classical mapping procedure sketched above, therefore, leads to complex weights in the partition function, and the system cannot be interpreted in terms of a classical XY model. Wallin et al.[81] found an alternative quantum-to-classical mapping that avoids the complex weight problem. They expressed the partition function in terms of the integer-valued angular momentum variables of the rotors. The resulting link current (Villain[83]) representation is a classical $(2+1)$-dimensional Hamiltonian:

$$\frac{H_{\mathrm{cl}}}{k_B T} = \frac{1}{K}\sum_{i,\tau}\left[\frac{1}{2}\mathbf{J}_{i,\tau}^2 - (\tilde{\mu} + \tilde{v}_i)J_{i,\tau}^{\tau}\right] \qquad [35]$$

Here, i and τ are the site indices in space- and the timelike direction, respectively. The dynamic variable $\mathbf{J} = (J^x, J^y, J^\tau)$ is a three-dimensional "current" with integer-valued components. It must be divergenceless, i.e., the sum over all currents entering a particular site must vanish; $\tilde{\mu}$ and $\tilde{v}_i$ represent the chemical and random potentials, renormalized by U.

To perform Monte Carlo simulations of the classical Hamiltonian, one must construct updates that respect the zero divergence condition for the currents. This prevents using the usual type of cluster algorithms.[50,51] For this reason, early simulations[81] used algorithms with local updates that suffered from significant critical slowing down. Alet and Sorensen[84] developed a cluster algorithm in which the link currents are updated by moving a "worm" through the lattice. This algorithm is efficient and performs comparably to the Wolff algorithm[51] for classical spin systems. Alet and Sorensen first confirmed the three-dimensional XY universality class for the clean case at integer boson density using this algorithm. In the presence of the random potential, they found a different universality class with exponents $\nu \approx 1.15$ and $z \approx 2$.

QUANTUM MONTE CARLO APPROACHES

If one is only interested in the universal critical behavior of a quantum phase transition, then the quantum-to-classical mapping method discussed in the last section (if available) is usually the most efficient approach. If one is also interested in nonuniversal quantities such as critical coupling constants or numerical values of observables, however, the quantum system has to be simulated directly. This can be done, for example, by quantum Monte Carlo methods that are the topic of this section.

The name *quantum Monte Carlo* refers to a diverse class of algorithms used for simulating quantum many-particle systems by stochastic means (for an overview see Ref. 47). Some of these algorithms, such as variational Monte Carlo[85,86] and diffusion Monte Carlo,[87,88] aim at computing the ground-state wave function (and are thus zero-temperature methods). Other algorithms including path-integral (world-line) Monte Carlo[89,90] sample the density matrix at finite temperatures. Before discussing quantum phase transitions, it is useful to illustrate the wide spectrum of problems that can be attacked by quantum Monte Carlo methods today along with the challenges involved.

One branch of quantum Monte Carlo research aims at providing a quantitative first-principle description of atoms, molecules, and solids beyond the accuracy of density functional theory.[48,49] If the basic physics and chemistry of the material in question is well understood at least *qualitatively*, as is the case for many bulk semiconductors, for example, good trial wave functions such as the Jastrow–Slater type can be constructed. These functions can

then be used in variational or diffusion Monte Carlo simulations to provide accurate results for the correlation energy and for other quantities. In contrast, different problems arise for materials whose behavior is not even qualitatively understood, such as when dealing with many strongly correlated electron systems. These systems are often studied by using simple models that capture the new properties of a whole class of materials without adding too many (realistic) details. However, the absence of even a qualitative understanding of such systems severely hampers the construction of trial wave functions with the right properties (symmetries, etc.). Ideally, this class of problems should be studied by (bias-free) methods that do not rely on trial wave functions at all.

Studies involving the simulation of quantum phase transitions belong to the second class of problems. While variational or diffusion Monte Carlo calculations can be very useful in locating approximately the quantum phase transition of a particular system in parameter space, they are much less suitable for studying the quantum critical state itself (because it is generally far away from any simple reference state). Significant progress in simulating quantum phase transitions of boson and spin systems has been achieved by path-integral (world-line) Monte Carlo[89,90] and the related stochastic series expansion (SSE) method[91,92] in recent years. Fermion systems pose a much harder problem to solve because the antisymmetry of the many-fermion wave function generically leads to the notorious sign problem, an issue that we shall return to at the end of the section. In the following we introduce briefly the world-line and SSE methods and then discuss a few representative examples of quantum phase transitions in boson and spin systems.

World-Line Monte Carlo

The world-line Monte Carlo algorithm is a finite-temperature method that samples the canonical density matrix of a quantum many-particle system. It may appear counterintuitive at first glance to use a finite-temperature method to study quantum phase transitions that occur at zero temperature, but a finite-temperature method is suitable for the following two reasons: (1) One of the (experimentally) most interesting regions of the phase diagram close to a quantum critical point is the quantum critical region located at the critical coupling strength but at comparatively high temperatures (see the section on Quantum vs. Classical Phase Transitions). Finite-temperature methods are thus required to explore it. (2) Assessing the dependence of observables on temperature is an efficient tool for determining the dynamical scaling behavior of the quantum critical point (analogous to finite-size scaling, but in the imaginary time direction).

The general idea[89,90] of the world-line Monte Carlo algorithm is similar to that of the quantum-to-classical mapping discussed in the last section. The Hamiltonian is split into two or more terms $\hat{H} = \sum_i \hat{H}_i$ such that the matrix

elements of each exponential term $e^{-\varepsilon \hat{H}_i}$ can be calculated easily. Even if the $\hat{H}_i$ do not commute, we can use the Trotter product formula to decompose the canonical density operator

$$e^{-\hat{H}/k_B T} = \lim_{N\to\infty} \left(\prod_i e^{-\varepsilon \hat{H}_i} \right)^N \qquad [36]$$

with $\varepsilon = 1/k_B TN$. Inserting complete sets of states between the different factors leads to a representation of the Boltzmann factor in terms of matrix elements of the $e^{-\varepsilon \hat{H}_i}$. If all of these matrix elements are positive, their product can be interpreted as a statistical weight, and Monte Carlo algorithms can be constructed to sample this weight. (If some of the matrix elements are negative, we have an instance of the notorious sign problem in quantum Monte Carlo.) The N factors of the Trotter decomposition can be interpreted as N time slices in the imaginary time direction, and the spin or particle configurations form "world lines" in the resulting $(d+1)$-dimensional space–time. This gives the method its name. A specific implementation of the world-line Monte Carlo method will be discussed in our first example later in this tutorial. More details of this technique can also be found in Chapter 3 of Ref. 47.

Applications of the world-line algorithm to quantum phase transitions require three extrapolations: (1) to infinite system size, (2) to temperature $T \to 0$, and (3) to imaginary time step $\varepsilon \to 0$. The first two extrapolations can be handled conveniently by finite-size scaling in the space and time directions, respectively. The systematic error of the Trotter decomposition arising from a finite ε was originally controlled by an explicit extrapolation from simulations with different values of ε. In 1996, Prokofev et al. showed that (at least for quantum lattice models) the algorithm can be formulated in continuous time, taking the limit $\varepsilon \to 0$ from the outset.[93] World-line Monte Carlo algorithms with local updates of spin or particle configurations suffer from critical slowing down close to quantum critical points. This problem is overcome by using the loop algorithm[94] and its continuous time version.[95] These algorithms, which are generalizations of the classical cluster algorithms[50,51] to the quantum case, have been reviewed in detail in Ref. 96. Further improvements for systems without spin-inversion or particle-hole symmetry include the worm algorithm[97] and the directed loop method.[98]

Stochastic Series Expansion

The stochastic series expansion (SSE) algorithm[91,92] is a generalization of Handscomb's power-series method[99] for the Heisenberg model. To derive an SSE representation of the partition function, we start from a Taylor expansion in powers of the inverse temperature. We then decompose the

Hamiltonian into two or more terms $\hat{H} = \sum_i \hat{H}_i$ such that the matrix elements with respect to some basis can be calculated easily, giving

$$Z = \mathrm{Tr}\, e^{-\hat{H}/k_B T} = \sum_{n=0}^{\infty} \frac{1}{n!} \left(\frac{1}{k_B T}\right)^n \mathrm{Tr}(-\hat{H})^n = \sum_{n=0}^{\infty} \frac{1}{n!} \left(\frac{1}{k_B T}\right)^n \mathrm{Tr}\left(-\sum_i \hat{H}_i\right)^n \quad [37]$$

Inserting complete sets of basis states between the different $\hat{H}_i$ factors then leads to a similar representation of the partition function and a similar world-line picture as in the world-line Monte Carlo method. Because there is no Trotter decomposition involved, the method is free of time discretization errors from the outset. Early applications of the SSE method employed local updates, but more efficient cluster-type updates have been developed more recently to overcome the critical slowing down. They include the operator-loop update[100] and the previously mentioned directed-loop algorithm.[98]

The source code for some of the algorithms discussed above is available on the Internet as part of the ALPS (Algorithms and Libraries for Physics Simulations) project.[101] SSE programs for the Heisenberg model can also be found on the homepage of A. Sandvik.[102]

Spin-$\frac{1}{2}$ Quantum Heisenberg Magnet

We will use our first example, the spin-$\frac{1}{2}$ quantum Heisenberg magnet, to further illustrate the world-line quantum Monte Carlo method. The model we present is the quantum XXZ model:

$$\hat{H} = \sum_{\langle i,j \rangle} [J_x(\hat{S}_i^x \hat{S}_j^x + \hat{S}_i^y \hat{S}_j^y) + J_z \hat{S}_i^z \hat{S}_j^z] = \sum_{\langle i,j \rangle} \left[\frac{J_x}{2}(\hat{S}_i^+ \hat{S}_j^- + \hat{S}_i^- \hat{S}_j^+) + J_z \hat{S}_i^z \hat{S}_j^z\right] \quad [38]$$

where $\hat{S}_i^x$, $\hat{S}_i^y$, $\hat{S}_i^z$ are the components of the quantum spin-$\frac{1}{2}$ operator at site i, $\hat{S}_i^+$, $\hat{S}_i^-$ are the associate raising and lowering operators, and the sum is over all pairs of nearest neighbors. We now divide the Hamiltonian into pieces such that the matrix elements of each piece can be evaluated easily. For the XXZ Hamiltonian, a convenient choice is the so-called checkerboard decomposition.[103] We illustrate it by considering one space dimension (see also Figure 10). We then write $\hat{H} = \hat{H}_1 + \hat{H}_2$ where $\hat{H}_1$ contains the bonds

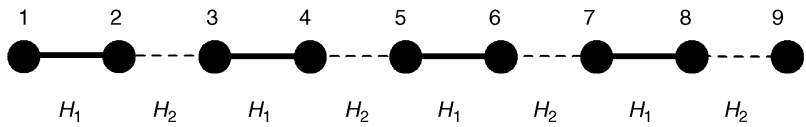

Figure 10 Checkerboard decomposition of the one-dimensional XXZ Hamiltonian.

between sites i and $i+1$ for all even i while $\hat{H}_2$ contains those for all odd i. To find a world-line representation we now insert this decomposition into the Trotter formula [36]. Since $\hat{H}_1$ and $\hat{H}_2$ each consist of independent two-site terms, the matrix elements in a $\hat{S}^z$ basis of $e^{-\varepsilon \hat{H}_i}$ factorize completely into terms of the type

$$e^{-\varepsilon J_z S^z_{i,n} S^z_{i+1,n}} \left\langle S^z_{i,n} S^z_{i+,n} \left| \exp -\varepsilon \frac{J_x}{2} (\hat{S}^+_i \hat{S}^-_{i+1} + \hat{S}^-_i \hat{S}^+_{i+1}) \right| S^z_{i,n+1} S^z_{i+,n+1} \right\rangle \qquad [39]$$

where n is the Trotter index. The remaining matrix elements are easily calculated. They read [with $\hat{h} = J_x(\hat{S}^+_i \hat{S}^-_{i+1} + \hat{S}^-_i \hat{S}^+_{i+1})/2$) as

$$\begin{aligned} \langle ++|e^{-\varepsilon \hat{h}}|++\rangle &= \langle --|e^{-\varepsilon \hat{h}}|--\rangle = 1 \\ \langle +-|e^{-\varepsilon \hat{h}}|+-\rangle &= \langle -+|e^{-\varepsilon \hat{h}}|-+\rangle = \cosh\left(\frac{\varepsilon J_x}{2}\right) \\ \langle +-|e^{-\varepsilon \hat{h}}|-+\rangle &= \langle -+|e^{-\varepsilon \hat{h}}|+-\rangle = -\sinh\left(\frac{\varepsilon J_x}{2}\right) \end{aligned} \qquad [40]$$

All other matrix elements are zero. The only nonvanishing matrix elements are those between states with the same total spin in the two Trotter slices, reflecting the spin conservation of the Hamiltonian. Note that the off-diagonal matrix elements are negative if J_x is antiferromagnetic ($J_x > 0$). This prevents interpreting the matrix elements as a statistical weight and is indicative of the sign problem. However, for our one-dimensional chain, or more generally, on any bipartite lattice, we can eliminate the sign problem by rotating every other spin by 180°, which changes the sign of J_x.

The allowed spin configurations can be easily visualized in a $(1+1)$-dimensional space–time picture by drawing lines connecting space–time points where the z component of the spin points up (see Figure 11). Because the number of such sites is conserved, the resulting "world lines" are continuous. Moreover, the periodic boundary conditions implied by the trace require that the world lines also connect continuously from the last imaginary time slice to the first.

As the last ingredient for the Monte Carlo algorithm, we have to specify the Monte Carlo moves within the restricted class of allowed spin configurations. Single spin flips are not allowed, as they break the continuous world lines. Instead, the simplest Monte Carlo moves consist of proposing a local deformation of the world line (an example is shown in Figure 11) and accepting or rejecting it with a suitable (Metropolis) probability that is determined by the changes in the matrix elements involved. As discussed above, algorithms based on such local moves suffer from critical slowing down near a quantum critical point. In the more efficient loop algorithm,[94–96] one

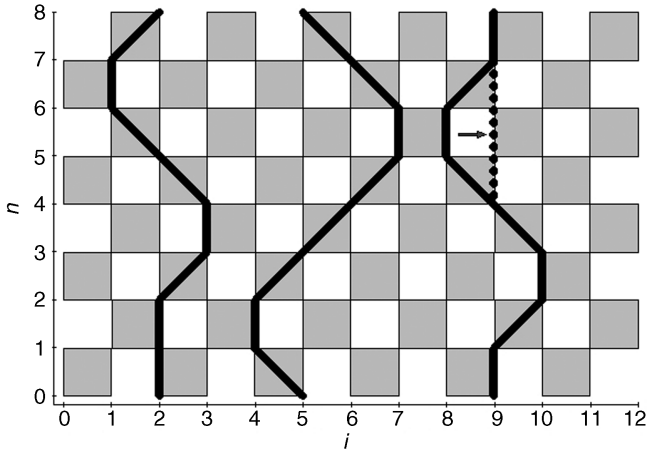

Figure 11 World-line configuration for the XXZ Hamiltonian of [38]. The world lines (thick lines) connect space–time points where the z component of the spin points up. They can be either straight or cross the shaded squares, which show where the imaginary time evolution operators $e^{-\varepsilon \hat{H}_1}$ and $e^{-\varepsilon \hat{H}_2}$ act. The dotted line shows the configuration change after a local Monte Carlo update.

builds large world-line loops and then changes the spin direction along the entire loop.

Let us now focus on the special case of the isotropic ($J_x = J_z > 0$) Heisenberg quantum antiferromagnet on the square lattice (see also the Hamiltonian of Eq. [19]). This model has played an important role in the history of high-temperature superconductivity studies because it describes the magnetic properties of the copper oxide planes in the undoped parent cuprate perovskites. An important early problem was establishing, beyond doubt, that the ground state of the square lattice Heisenberg model is antiferromagnetically (Néel) ordered and finding the value of the staggered magnetization. Reger and Young[104] performed world-line Monte Carlo simulations of the square lattice Heisenberg antiferromagnet using a two-dimensional version of the algorithm described above. Since the ground state of the Heisenberg model for any finite system size is rotationally invariant, the expectation value of the staggered magnetization vanishes. To determine the macroscopic value, which assumes that the symmetry has been broken spontaneously, Reger and Young[104] computed both the (staggered) structure factor $S(\mathbf{Q})$ at the ordering wave vector $\mathbf{Q} = (\pi, \pi)$ and the correlation function $C_{L/2}$ between spins as far apart as possible on the lattice. Both quantities reduce to $m_s^2/3$, where m_s is the staggered magnetization in the thermodynamic limit. Figure 12 shows the extrapolation of $S(\mathbf{Q})$ and $C_{L/2}$ to infinite system size (the extrapolations $T \to 0$ and $\varepsilon \to 0$ have already been carried out). From the intercept with the vertical axis, Reger and Young found $m_s = 0.30 \pm 0.02$ establishing

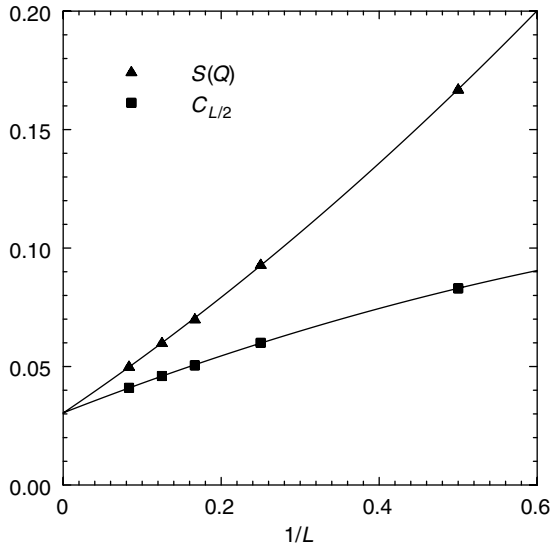

Figure 12 World-line Monte Carlo results for the square lattice Heisenberg antiferromagnet: Structure factor S and the long-distance limit C of the correlation function as functions of the linear system size L. The intercept on the vertical axis can be used to find the staggered magnetization. (Taken with permission from Ref. 104.)

clearly that the ground state is antiferromagnetically ordered. In later work, the staggered magnetization value was further refined by simulations using a continuous time loop algorithm,[95] giving the value $m_s = 0.3083 \pm 0.0002$.

Bilayer Heisenberg Quantum Antiferromagnet

While quantum fluctuations reduce the staggered magnetization of a single-layer Heisenberg quantum antiferromagnet from its classical value of $\frac{1}{2}$, they are not strong enough to induce a quantum phase transition. As discussed in the section on Classical Monte Carlo Approaches, the strength of the quantum fluctuations can be tuned if one considers a system of two identical, antiferromagnetically coupled layers defined by the bilayer Hamiltonian of Eq. [20]. If the interlayer coupling $J_\perp$ is large compared to the in-plane coupling $J_\parallel$, the corresponding spins in the two layers form magnetically inert singlets. In contrast, for $J_\perp \ll J_\parallel$, the system orders antiferromagnetically. There is a quantum phase transition between these two phases at some critical value of the ratio $J_\perp/J_\parallel$.

In the section on Classical Monte Carlo Approaches we used the quantum-to-classical mapping to discuss the universal critical behavior of this quantum phase transition and found it to belong to the three-dimensional classical Heisenberg universality class. However, this approach does not give

quantitative answers for nonuniversal observables such as the critical value of the ratio $J_\perp/J_\parallel$, which can only be obtained by a true quantum algorithm. Sandvik and Scalapino[105] have performed quantum Monte Carlo simulations of the bilayer Heisenberg quantum antiferromagnet employing the stochastic series expansion method. By analyzing the staggered structure factor and the staggered susceptibility, they found a critical ratio of $(J_\perp/J_\parallel)_c = 2.51 \pm 0.02$ (see the vertical axis in Figure 6). More recently, Wang and co-workers[106] performed a high-precision study of the same model using the stochastic series expansion algorithm with operator loop update.[100] Using the Binder cumulant, the spin stiffness and the uniform susceptibility, they obtained a value of $(J_\perp/J_\parallel)_c = 2.5220 \pm 0.0001$ for the critical coupling. In addition, they computed the correlation length exponent and found $\nu = 0.7106 \pm 0.0009$, which agrees within error bars with the best value of the three-dimensional classical Heisenberg exponent[62] (as expected from the quantum-to-classical mapping).

Diluted Heisenberg Magnets

In the example above, we saw that increased quantum fluctuations (as induced by the interlayer coupling $J_\perp$ in the bilayer system) can cause a quantum phase transition in the two-dimensional Heisenberg quantum antiferromagnet. Another way to increase the fluctuations is by dilution, i.e., by randomly removing spins from the lattice. The phases and phase transitions of diluted Heisenberg quantum antiferromagnets have been studied extensively during the last few years and many interesting features have emerged.

Consider the site-diluted square lattice Heisenberg model given by the Hamiltonian

$$\hat{H} = J \sum_{\langle i,j \rangle} \mu_i \mu_j \hat{S}_i \cdot \hat{S}_j \qquad [41]$$

where the μ_i are independent random variables that can take the values 0 and 1 with probability p and $1-p$, respectively. As discussed above, the ground state of the clean system ($p = 0$) is aniferromagnetically ordered. It is clear that the tendency toward magnetism decreases with increasing impurity concentration p, but the location and nature of the phase transition toward a nonmagnetic ground state remained controversial for a long time. The most basic question to ask is whether the magnetic order vanishes before the impurity concentration reaches the percolation threshold of the lattice $p_p \approx 0.4072$ (the transition would then be caused by quantum fluctuations) or whether it survives up to p_p (in which case the transition would be of percolation type). Magnetic long-range order is impossible above p_p because the lattice is decomposed into disconnected finite-size clusters. Early studies, both

analytical and numerical, gave values between 0.07 and 0.35 for the critical impurity concentration, suggesting a transition driven by quantum fluctuations.

Sandvik[107] performed quantum Monte Carlo simulations of the Heisenberg Hamiltonian on the critical infinite percolation cluster ($p = p_p$) using the stochastic series expansion method with operator loop update.[100] He computed the staggered structure factor and from it the staggered ground-state magnetization of the cluster. Figure 13 shows the extrapolation of this quantity to infinite system size. The data demonstrate that the ground state is magnetically ordered, with a sizable staggered magnetization of about $m_s = 0.150$ (roughly half the value of the undiluted system). This means that even right at the percolation threshold p_p, the quantum fluctuations are not strong enough to destroy the magnetic long-range order. The phase transition to a paramagnetic ground state occurs right at p_p. It is driven by the geometry of the underlying lattice and is thus of percolation type. More recently, Wang and Sandvik[108] studied the dynamical quantum critical behavior of this transition (the static behavior is given by classical percolation). They found a dynamical critical exponent of $z \approx 3.7$, which is much larger than the value $z = D_f = \frac{91}{48}$ found for the dimer diluted bilayer[72,73] (see discussion in the

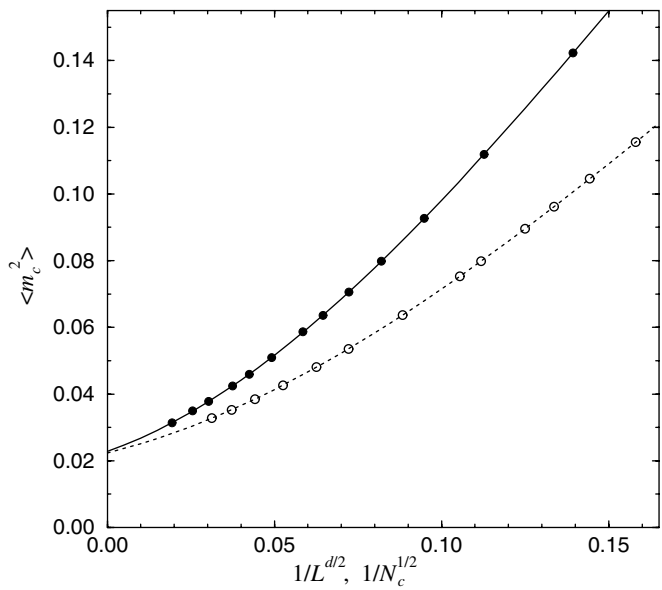

Figure 13 Squared staggered ground-state magnetization of the Heisenberg model on a site-diluted lattice at $p = p_p$. The two curves correspond to two different ways of constructing the percolation clusters in the simulation. (*Solid circles*) Largest cluster on $L \times L$ lattices. (*Open Circles*) Clusters with a fixed number N_c sites. (Taken with permission from Ref. 107.)

section on Classical Monte Carlo Approaches). This difference is most likely caused by unpaired spins (uncompensated Berry phases) that exist in the site-diluted single layer (but not in the dimer-diluted bilayer) and prevent the quantum-to-classical mapping onto a classical Heisenberg model.

Because the ground state of the diluted Heisenberg model remains long-range ordered up to the percolation threshold, one has to increase the quantum fluctuations to induce a quantum phase transition for $p < p_p$. One way to achieve this is by going to the dimer-diluted bilayer, as in the clean system, and tuning the fluctuations with the interlayer coupling $J_\perp$. (The quantum phase transitions in this system were discussed in the section on Classical Monte Carlo Approaches.) Yu et al.[109] found a different way of increasing the quantum fluctuations. They suggested introducing an *inhomogeneous* bond dilution, which is a scenario where not all bonds (interactions) are removed with the same probability. If the occupation probabilities for different types of bonds are chosen in such a way that the system preferably forms dimers and ladders, a nontrivial quantum phase transition to a paramagnetic ground state can be achieved while the underlying lattice is still in the percolating phase.

Superfluid–Insulator Transition in an Optical Lattice

Having considered several examples of magnetic quantum phase transitions, we now turn to the superfluid–insulator transition in many-boson systems. In the section on Classical Monte Carlo Approaches we discussed how the universal critical behavior of this transition can be determined by mapping the Bose–Hubbard model, Eq. [32], onto the classical $(d+1)$-dimensional link current Hamiltonian, Eq. [35], which can then be simulated using classical Monte Carlo methods.

It is now possible to observe this transition experimentally in ultracold atomic gases. For instance, in the experiments by Greiner et al.,[110] a gas of ^{87}Rb atoms was trapped in a simple cubic optical lattice potential. This system is well described by the Bose–Hubbard Hamiltonian, Eq. [32], with an additional overall harmonic confining potential, and, the particle density as well as the interparticle interactions can be controlled easily. To study the properties of the gas in the experiment, the trapping and lattice potential were switched off, and absorption images of the freely evolving atomic cloud were taken to give direct information about the single-particle momentum distribution.

To provide quantitative predictions about how to detect the superfluid–insulator transition in these experiments, Kashurnikov, Prokof'ev and Svistunov[111] performed quantum Monte Carlo simulations of the single-particle density matrix $\rho_{ij} = \langle \hat{\Phi}_i^\dagger \hat{\Phi}_j \rangle$. They used the Bose–Hubbard model with harmonic confining potential and carried out world-line Monte Carlo simulations with the continuous-time Worm algorithm.[97] The diagonal elements of the density matrix provide the real-space particle density, and

the momentum distribution can be obtained by Fourier transforming ρ_{ij}. The real-space density of several example systems is shown in Figure 14. These plots show the development with increasing density of a shell-type structure with insulator phases visible as plateaus at integer local density. Specifically, system (a) is in the superfluid phase. If the Hubbard interaction U is raised to about the critical value of the superfluid–insulator transition [system (b)],

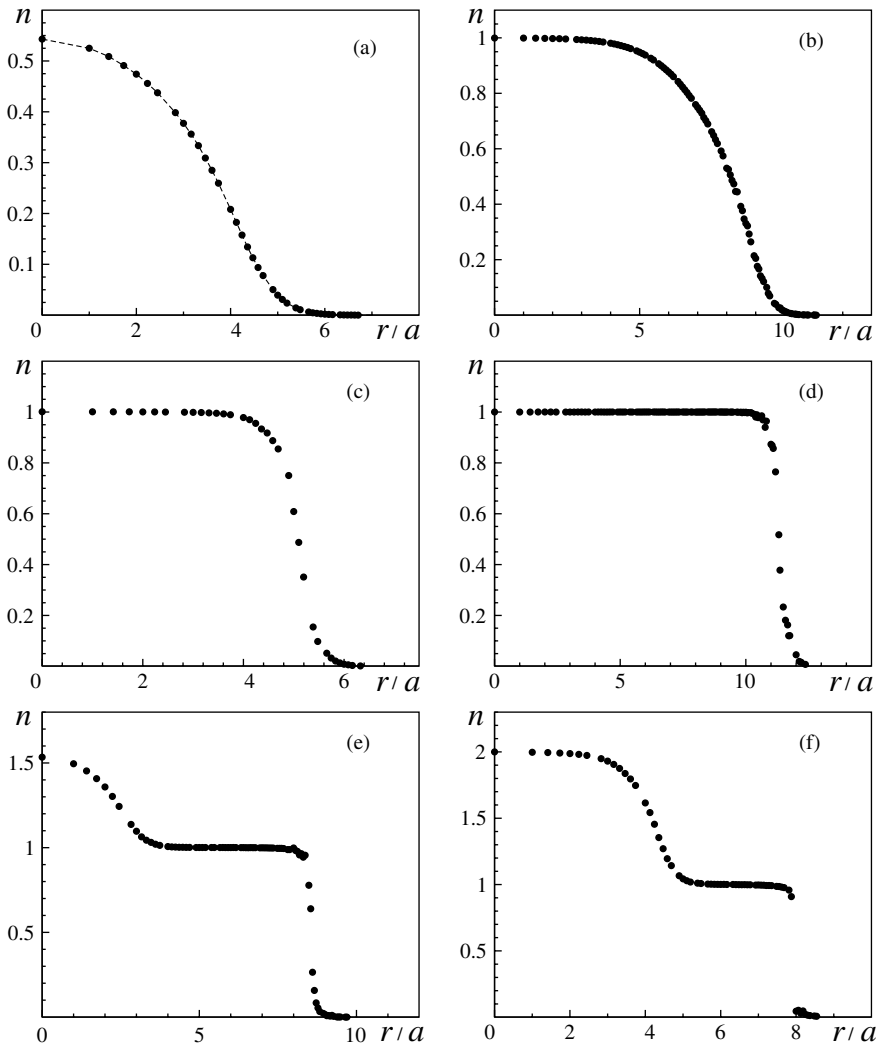

Figure 14 Superfluid–insulator transition in an optical lattice: Particle density (per lattice site) as a function of distance from the trap center for various parameters and filling factors. (Taken with permission from Ref. 111.)

an insulating domain appears at the center of the trap (if the density there is close to commensurate). Increasing U further reduces the correlation length [system (c)] because the system moves away from the transition. Systems (d)–(f) show how the second shell forms when the density is increased.

The corresponding momentum distributions are shown in Figure 15. The superfluid sample (a) shows a single narrow peak at zero momentum. (The broadening of the δ-function contribution of the condensate expected in a superfluid arises from the harmonic confining potential.) When a domain of the insulating phase appears, the momentum distribution develops a pronounced fine structure [clearly visible in systems (b) and (c)]. System (e) is similar to (a) except for the large momentum tail due to the insulating shell.

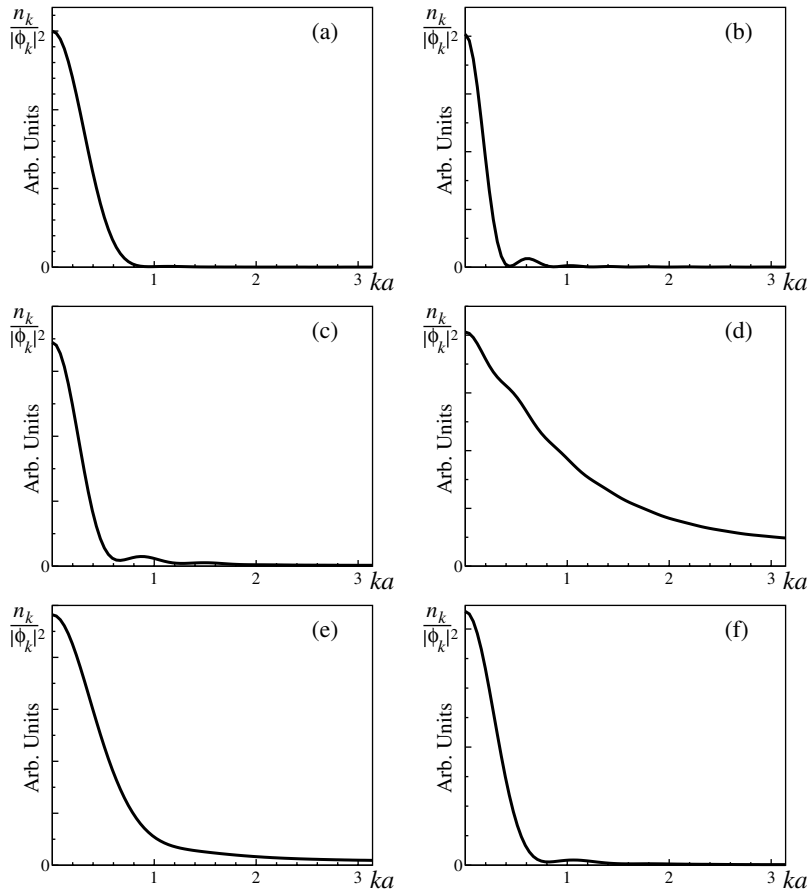

Figure 15 Superfluid–insulator transition in an optical lattice: Single-particle momentum distribution. Panels (a)–(f) correspond to the systems shown in Figure 14. (Taken with permission from Ref. 111.)

System (f) again displays the fine structure associate with the appearance of an insulating domain in the second shell. These quantitative results can be used to identify the superfluid–insulator transition in experiments.

Fermions

So far, we have discussed quantum Monte Carlo approaches to quantum phase transitions in boson and spin systems. In these systems, the statistical weight in the Monte Carlo procedure is generally positive definite, so there is no sign problem. Note that for spin systems, this is only true if there is no frustration. Frustrated spin systems in general do have a sign problem.

Unfortunately, the sign problem generally exists for fermions because it is rooted in the antisymmetry of the many-fermion wave function. The problem can be understood by recognizing that boson and spin operators on different lattice sites commute. The signs of the matrix elements appearing in a quantum Monte Carlo scheme are thus determined locally. Contrarily, fermion operators on different lattice sites anticommute, thus leading to extra nonlocal minus signs. In fact, it was shown that a generic solution to the sign problem is almost certainly impossible to obtain by proving that the sign problem belongs to the NP (nondeterministic polynomial) hard computational complexity class.[112] This means that a generic solution of the sign problem would also solve all other NP hard problems in polynomial time.

One way of circumventing (if not solving) the sign problem is to force the nodes of the many-fermion wave function to coincide with that of a trial wave function. The resulting fixed-node quantum Monte Carlo method[88,113] has been successful in determining with high precision the ground-state properties of real materials. It is clear that the accuracy of the method depends crucially on the quality of the trial wave function. This implies that the fixed-node Monte Carlo method will work well if the ground-state properties are understood at least qualitatively. However, quantum critical states are, in general, very far from any simple reference state, which means that simple trial wave functions cannot be constructed easily. Fixed-node methods are therefore not well suited for studying the properties of fermionic systems close to quantum phase transitions (although they may be useful for locating the transition in parameter space).

While a general solution of the fermionic sign problem is likely impossible to find, several nontrivial fermionic systems exist for which the sign problem can be avoided. Hirsch et al.[90] developed a world-line Monte Carlo simulation scheme for fermions that, in strictly one dimension, avoids the sign problem. (Generalizations to higher dimensions still suffer from the sign problem.) A more general quantum Monte Carlo approach to fermions is the so-called determinantal Monte Carlo method.[114] Its basic idea is to decouple the fermion–fermion interactions by means of a Hubbard–Stratonovich transformation,[115] leading to a system of noninteracting fermions coupled to a

bosonic field. The fermions can now be integrated out in closed form, and the partition function is given as the sum over configurations of the bosonic field with the weight being a fermionic determinant. This sum can be performed by Monte Carlo sampling. In general, the fermionic determinant will have a fluctuating sign, again reflecting the fermionic sign problem. In some special cases, however, the determinant can be shown to be positive definite. For instance, the determinant is positive definite for the two-dimensional repulsive Hubbard model on bipartite lattices at exactly half filling (because of particle-hole symmetry).[116] For the attractive Hubbard model, sign-problem free algorithms can even be constructed for all filling factors, and such algorithms have been used to study the superconducting transition in two and three spatial dimensions. In two dimensions, the transition is classified as being of the Kosterlitz–Thouless type.[117–119] In three dimensions, the model displays a conventional second-order transition, and an interesting crossover takes place between the Bardeen–Cooper–Schrieffer (BCS) and the Bose–Einstein condensation (BEC) scenarios.[120] Another attack on the sign problem is by the so-called meron-cluster algorithm that can be applied to certain fermionic Hamiltonians.[121] It has been used, for example, to study the effects of disorder superconductivity in fermion models with attractive interactions.[122]

Despite this progress, the utility of quantum Monte Carlo simulations for studying quantum phase transitions in fermionic systems is still rather limited. Many of the most interesting problems, such as the ferromagnetic and antiferromagnetic quantum phase transitions[9,36,123] in transition-metal compounds and heavy-fermion materials, are still too complex to be attacked directly by microscopic quantum Monte Carlo methods.

OTHER METHODS AND TECHNIQUES

In this section we discuss briefly—without any pretense of completeness—further computational approaches to quantum phase transitions. The conceptually simplest method for solving a quantum many-particle problem is (numerically) exact diagonalization. However, as already discussed in the section on Quantum Phase Transitions: Computational Challenges, the exponential increase of the Hilbert space dimension with the number of degrees of freedom severely limits the possible system sizes. One can rarely simulate more than a few dozen particles even for simple lattice systems. Systems of this size are too small to study quantum phase transitions (which are a property of the thermodynamic limit of infinite system size) with the exception of, perhaps, certain simple one-dimensional systems. Even in one dimension, however, more powerful methods have largely superceded exact diagonalization.

One of these techniques is the density matrix renormalization group (DMRG) proposed by White in 1992.[124] In this method, one builds the

eigenstates of a large many-particle system iteratively from the low-energy states of smaller blocks, using the density matrix to decide which states to keep and which to discard. In one space dimension, this procedure works very well and gives accuracies comparable to exact diagonalization for much larger system sizes. Since its introduction, the DMRG has quickly become a method of choice for many one-dimensional quantum many-particle problems including various spin chains and spin ladders with and without frustration. Electronic systems such as Hubbard chains and Hubbard ladders can be studied efficiently as well because the DMRG is free of the fermionic sign problem. An extensive review of the DMRG method and its applications can be found in Ref. 125.

In the context of our interest in quantum phase transitions, however, we note that the accuracy of the DMRG method suffers greatly in the vicinity of quantum critical points. This was shown explicitly in two studies of the one-dimensional Ising model in a transverse field, as given by the Hamiltonian of Eq. [14].[126,127] Legaza and Fath[127] studied chains of up to 300 sites and found that the relative error of the ground-state energy at the quantum critical point is several orders of magnitude larger than off criticality. (This is caused by the fact that the quantum critical system is gapless; it thus has many low-energy excitations that must be retained in the procedure.) Andersson, Boman and Östlund[128] studied the behavior of the correlation function in a DMRG study of gapless free fermions (or equivalently, a spin-$\frac{1}{2}$ XX model). They found that the DMRG result reproduces the correct power law at small distances, but it always drops exponentially at large distances. The fake correlation length grows as $M^{1.3}$ with the number of states M retained in each DMRG step. When studying a critical point, this fake correlation length should be larger than the physical correlation length, which increases greatly the numerical effort. While the standard DMRG method does not work very well in dimensions larger than one, an interesting generalization[129,130] has arisen recently in the quantum information community. It is based on so-called projected entangled-pair states (PEPS). First applications to quantum many-particle systems look promising (e.g., Ref. 131 reports a study of bosons in a two-dimensional optical lattice), but the true power of the method has not been explored fully.

Another useful technique for studying one-dimensional spin systems involves mapping the system onto *noninteracting* fermions. This method was developed by Lieb, Schultz and Mattis[76] in the 1960's and was applied to the nonrandom transverse-field Ising model of Eq. [14] by Katsura[132] and Pfeuty.[133] The resulting fermionic Hamiltonian can be solved analytically by Fourier transformation in the nonrandom case. Young and Rieger[74,75] applied the same method to the random transverse-field Ising chain, Eq. [30]. The mapping onto fermions now results in a disordered system; the fermionic Hamiltonian must therefore be diagonalized numerically. However, since one is simulating a *noninteracting* system, the numerical effort is still much

smaller than with other methods. Using this approach, Young and Rieger confirmed numerically the analytical result[22,23] that the quantum critical point in the random transverse-field Ising chain is of exotic infinite-randomness type.

The investigation of quantum phase transitions in disordered systems has benefited in recent years from the strong-disorder renormalization group that was introduced originally by Ma, Dasgupta, and Hu.[24] The basic idea of their method is to successively integrate out local high-energy degrees of freedom in perturbation theory. The quality of this method improves with increasing disorder strength, in contrast to many other techniques; and it becomes asymptotically exact at infinite-randomness critical points (where the effective disorder strength diverges). This approach has been applied to a variety of classical and quantum disordered systems, ranging from quantum spin chains to chemical reaction-diffusion models with disorder. A recent review can be found in Ref. 134. In one space dimension, the strong-disorder renormalization group can often be solved analytically in closed form, as is the case for the random transverse-field Ising chain[22,23] or the random $S = \frac{1}{2}$ antiferromagnetic Heisenberg chain as examples.[24,135] In higher dimensions, or for more complicated Hamiltonians, the method can only be implemented numerically. For instance, Montrunich et al.[19] studied the quantum phase transition in the two-dimensional random transverse-field Ising model. In analogy with the one-dimensional case,[22,23] they found an infinite randomness critical point, but the critical exponents take different values. Schehr and Rieger[136] studied the interplay between dissipation, quantum fluctuations, and disorder in the random transverse-field Ising chain coupled to dissipative baths. In agreement with theoretical predictions,[30,31] they found that the dissipation freezes the quantum dynamics of large, locally ordered clusters, which then dominate the low-energy behavior. This leads to a smearing of the quantum phase transition.[30]

Let us also mention a class of methods that are not numerically exact but have greatly fostered our understanding of quantum many-particle systems: the dynamical mean-field theory (DMFT). Its development started with the pioneering work of Metzner and Vollhardt[137] on the Hubbard model in infinite dimensions. The basic idea behind this approach is a natural generalization of the classical mean-field theories to quantum problems: The quantum many-particle Hamiltonian is reduced to a quantum impurity problem coupled to one or several self-consistent baths.[138] This impurity problem is then solved self-consistently, either by approximate analytical methods or by numerical methods. In contrast to classical mean-field theories such as Hartree–Fock, the DMFT contains the full local quantum dynamics. (This means that the DMFT suppresses spatial fluctuations but keeps the local imaginary time fluctuations.) DMFT methods have now been applied to a wide variety of problems ranging from model Hamiltonians of strongly correlated electrons to complex materials. For instance, the DMFT was instrumental in understanding the Mott metal–insulator phase transition in the Hubbard

model; and, more recently, it was combined with realistic band structure calculations to investigate many-particle effects and strong correlations in real materials. Reviews of these developments can be found in Refs. 139 and 140.

Let us finally point out that we have focused on bulk quantum phase transitions. Impurity quantum phase transitions[42] require a separate discussion that is beyond the scope of this chapter (Note, however, that within the DMFT method a bulk quantum many-particle system is mapped onto a self-consistent quantum impurity model.) Some of the methods discussed here such as quantum Monte Carlo can be adapted to impurity problems. Moreover, there are powerful special methods dedicated to impurity problems, most notably Wilson's numerical renormalization group.[141–143]

SUMMARY AND CONCLUSIONS

We have discussed quantum phase transitions in this chapter. These are transitions that occur at zero temperature when a nonthermal external parameter such as pressure, magnetic field, or chemical composition is changed. They are driven by quantum fluctuations, which are a consequence of Heisenberg's uncertainty principle. At first glance, it might appear that investigating such special points in the phase diagram at the absolute zero of temperature is purely of academic interest, however, it has become clear in recent years that the presence of quantum phase transitions has profound consequences for the experimental behavior of many condensed-matter systems. In fact, quantum phase transitions have emerged as a new ordering principle for low-energy phenomena that allows us to explore regions of the phase diagram where more conventional pictures, based on small perturbations about simple reference states, are not sufficient.

In the first part of the tutorial, we provided a concise introduction to the theory of quantum phase transitions. We contrasted the contributions of thermal and quantum fluctuations, and we explained how their interplay leads to a very rich structure of the phase diagram in the vicinity of a quantum phase transition. It turns out that the Landau–Ginzburg–Wilson (LGW) approach, which formed the basis for most modern phase transition theories, can be generalized to quantum phase transitions by including the imaginary time as an additional coordinate of the system. This leads to the idea of the quantum-to-classical mapping, which relates a quantum phase transition in d-space dimensions to a classical one in $d + 1$ dimensions. We also discussed briefly situations in which the LGW order parameter approach can break down, a topic that has attracted considerable interest lately.

The second part of this chapter was devoted to computational approaches to quantum phase transitions with the emphasis being on Monte Carlo methods. If one is mainly interested in finding the universal critical

behavior (i.e., the overall scaling scenario, the critical exponents, and the critical amplitude ratios), using a purely classical simulation scheme based on quantum-to-classical mapping is often most efficient. We illustrated this approach for the transverse-field Ising model with and without dissipation, for the bilayer Heisenberg antiferromagnet, and for dirty bosons in two dimensions. If one is interested in nonuniversal questions such as quantitative results for critical coupling constants or observables, a true quantum algorithm must be used. We have reviewed several quantum Monte Carlo approaches to quantum spin and boson Hamiltonians and discussed their results for the quantum phase transitions in these systems. We have also considered fermionic systems and the extra complications brought about by the generic appearance of the notorious sign problem.

It is probably fair to say that Monte Carlo simulations of model systems that are free of the sign problem (bosons, spin systems without frustration, and some special fermionic systems) have become so powerful that the properties of their quantum phase transitions can be determined quantitatively with high precision (see, e.g., the accuracy of some of the exponent values quoted in the preceding sections). For many frustrated spin systems, in contrast, the results are limited to a qualitative level, and for quantum phase transitions in generic fermionic systems (with sign problem), direct computational attacks are still of limited utility.

ACKNOWLEDGMENTS

The author has benefited greatly from discussions with many friends and colleagues, in particular, D. Belitz, A. Castro-Neto, A. Chubukov, P. Coleman, K. Damle, V. Dobrosavljevic, P. Goldbart, M. Greven, S. Haas, J. A. Hoyos, F. Iglói, T. R. Kirkpatrick, A. Millis, D. Morr, M. Norman, P. Phillips, H. Rieger, S. Sachdev, A. Sandvik, J. Schmalian, Q. Si, R. Sknepnek, G. Steward, J. Toner, M. Vojta, and A. P. Young.

Some of the work described here has been supported by the National Science Foundation under grant nos. DMR-0339147 and PHY99-07949, by Research Corporation and by the University of Missouri Research Board. Parts of this work have been performed at the Aspen Center for Physics and the Kavli Institute for Theoretical Physics, Santa Barbara.

REFERENCES

1. T. Andrews, *Phil. Trans. R. Soc. A*, **159**, 575 (1869). The Bakerian Lecture: On the Continuity of the Gaseous and Liquid States of Matter.
2. J. D. van der Waals, PhD Thesis, University of Leiden, 1873. On the Continuity of the Gas and Liquid State.
3. K. G. Wilson, *Phys. Rev. B*, **4**, 3174 (1971). Renormalization Group and Critical Phenomena. I. Renormalization Group and the Kadanoff Scaling Picture.
4. K. G. Wilson and J. Kogut, *Phys. Rep.*, **12**, 75 (1974). The Renormalization Group and the ε Expansion.

5. D. Bitko, T. F. Rosenbaum, and G. Aeppli, *Phys. Rev. Lett.*, **77**, 940 (1996). Quantum Critical Behavior for a Model Magnet.
6. S. L. Sondhi, S. M. Girvin, J. P. Carini, and D. Shahar, *Rev. Mod. Phys.*, **69**, 315 (1997). Continuous Quantum Phase Transitions.
7. T. Vojta, *Ann. Phys. (Leipzig)*, **9**, 403 (2000). Quantum Phase Transitions in Electronic Systems.
8. M. Vojta, *Rep. Prog. Phys.*, **66**, 2069 (2003). Quantum Phase Transitions.
9. D. Belitz, T. R. Kirkpatrick, and T. Vojta, *Rev. Mod. Phys.*, **77**, 579 (2005). How Generic Scale Invariance Influences Classical and Quantum Phase Transitions.
10. S. Sachdev, *Quantum Phase Transitions*, Cambridge University Press, Cambridge, UK, 2000.
11. N. Goldenfeld, *Lectures on Phase Transitions and the Renormalization Group*, Westview Press, Boulder, CO, 1992.
12. D. Ter Haar, Ed., *Collected Papers of L. D. Landau*, Pergamon, Oxford, 1965.
13. P. Weiss, *J. Phys. (Paris)*, **6**, 661 (1907). L'Hypothèse du Champ Moléculaire et la Propriété Ferromagnétique.
14. B. Widom, *J. Chem. Phys.*, **43**, 3892 (1965). Surface Tension and Molecular Correlations near the Critical Point.
15. M. E. Fisher and M. N. Barber, *Phys. Rev. Lett.*, **28**, 1516 (1972). Scaling Theory for Finite-Size Effects in the Critical Region.
16. M. N. Barber, in *Phase Transitions and Critical Phenomena*, Vol. 8, C. Domb and J. L. Lebowitz, Eds., Academic, New York, 1983, pp. 145–266. Finite-Size Scaling.
17. J. Cardy, Ed., *Finite-Size Scaling*, North Holland, Amsterdam, 1988.
18. A. B. Harris, *J. Phys. C*, **7**, 1671 (1974). Effect of Random Defects on the Critical Behaviour of Ising Models.
19. O. Motrunich, S. C. Mau, D. A. Huse, and D. S. Fisher, *Phys. Rev. B*, **61**, 1160 (2000). Infinite-Randomness Quantum Ising Critical Fixed Points.
20. A. Aharony and A. B. Harris, *Phys. Rev. Lett.*, **77**, 3700 (1996). Absence of Self-Averaging and Universal Fluctuations in Random Systems near Critical Points.
21. S. Wiseman and E. Domany, *Phys. Rev. Lett.*, **81**, 22 (1998). Finite-Size Scaling and Lack of Self-Averaging in Critical Disordered Systems.
22. D. S. Fisher, *Phys. Rev. Lett.*, **69**, 534 (1992). Random Transverse-Field Ising Spin Chains.
23. D. S. Fisher, *Phys. Rev. B*, **51**, 6411 (1995). Critical Behavior of Random Transverse-Field Ising Spin Chains.
24. S. K. Ma, C. Dasgupta, and C. K. Hu, *Phys. Rev. Lett.*, **43**, 1434 (1979). Random Antiferromagnetic Chain.
25. R. B. Griffiths, *Phys. Rev. Lett.*, **23**, 17 (1969). Nonanalytic Behavior above the Critical Point in a Random Ising Ferromagnet.
26. M. Randeria, J. Sethna, and R. G. Palmer, *Phys. Rev. Lett.*, **54**, 1321 (1985). Low-Frequency Relaxation in Ising Spin-Glasses.
27. A. J. Bray and D. Huifang, *Phys. Rev. B*, **40**, 6980 (1989). Griffiths Singularities in Random Magnets: Results for a Soluble Model.
28. M. Thill and D. Huse, *Physica A*, **214**, 321 (1995). Equilibrium Behaviour of Quantum Ising Spin Glass.
29. H. Rieger and A. P. Young, *Phys. Rev.*, *B* **54**, 3328 (1996). Griffiths Singularities in the Disordered Phase of a Quantum Ising Spin Glass.
30. T. Vojta, *Phys. Rev. Lett.*, **90**, 107202 (2003). Disorder Induced Rounding of Certain Quantum Phase Transitions.
31. T. Vojta, *J. Phys. A*, **39**, R143 (2006). Rare Region Effects at Classical, Quantum and Nonequilibrium Phase Transitions.

32. B. M. Law and J. C. Nieuwoudt, *Phys. Rev. A*, **40**, 3880 (1989). Noncritical Liquid Mixtures Far from Equilibrium: The Rayleigh Line.
33. G. Grinstein, *J. Appl. Phys.*, **69**, 5441 (1991). Generic Scale Invariance in Classical Non-equilibrium Systems.
34. J. R. Dorfman, T. R. Kirkpatrick, and J. V. Sengers, *Ann. Rev. Phys. Chem. A*, **45**, 213 (1994). Generic Long-Range Correlations in Molecular Fluids.
35. T. Senthil, A. Vishwanath, L. Balents, S. Sachdev, and M. P. A. Fisher, *Science*, **303**, 1490 (2004). Deconfined Quantum Critical Points.
36. G. R. Stewart, *Rev. Mod. Phys.*, **73**, 797 (2001). Non-Fermi-Liquid Behavior in d- and f-Electron Metals.
37. J. A. Hertz, *Phys. Rev. B*, **14**, 1165 (1976). Quantum Critical Phenomena.
38. A. J. Millis, *Phys. Rev. B*, **48**, 7183 (1983). Effect of a Nonzero Temperature on Quantum Critical Points in Itinerant Fermion Systems.
39. Q. Si, S. Rabello, K. Ingersent, and J. L. Smith, *Nature*, **413**, 804 (2001). Locally Critical Quantum Phase Transitions in Strongly Correlated Metals.
40. T. Senthil, S. Sachdev, and M. Vojta, *Phys. Rev. Lett.*, **90**, 216403 (2003). Fractionalized Fermi Liquids.
41. T. Senthil, M. Vojta, and S. Sachdev, *Phys. Rev. B* **69**, 035111 (2004). Weak Magnetism and Non-Fermi Liquids Near Heavy-Fermion Critical Points.
42. M. Vojta, *Phil. Mag.*, **86**, 1807 (2006). Impurity Quantum Phase Transitions.
43. R. M. Dreizler and E. K. U. Gross, *Density Functional Theory*, Springer, Berlin, 1990.
44. L. J. Bartolotti and K. Flurchick, in *Reviews in Computational Chemistry*, K. B. Lipkowitz and D. B. Boyd, Eds., VCH, New York, 1995, Vol. 7, pp. 187–216. An Introduction to Density Functional Theory.
45. F. M. Bickelhaupt and E. J. Baerends, in *Reviews in Computational Chemistry*, K. B. Lipkowitz and D. B. Boyd, Eds., Wiley-VCH, New York, 2000, Vol. 15, pp. 1–86. Kohn–Sham Density Functional Theory: Predicting and Understanding Chemistry.
46. T. D. Crawford and H. F. Schaefer III, in *Reviews in Computational Chemistry*, K. B. Lipkowitz and D. B. Boyd, Eds., Wiley-VCH, New York, 2000, Vol. 14, pp. 33–136. An Introduction to Coupled Cluster Theory for Computational Chemists.
47. M. P. Nightgale and C. J. Umrigar, Eds., *Quantum Monte Carlo Methods in Physics and Chemistry*, Springer, New York, 1998.
48. J. B. Anderson, in *Reviews in Computational Chemistry*, K. B. Lipkowitz and D. B. Boyd, Eds., Wiley-VCH, New York, 1999, Vol. 13, pp. 132–182. Quantum Monte Carlo: Atoms, Molecules, Clusters, Liquids, and Solids.
49. W. M. C. Foulkes, L. Mitas, R. J. Needs, and G. Rajagopal, *Rev. Mod. Phys.*, **73**, 33 (2001). Quantum Monte Carlo Simulations of Solids.
50. R. Swendsen and J.-S. Wang, *Phys. Rev. Lett.*, **58**, 86 (1987). Nonuniversal Critical Dynamics in Monte Carlo Simulations.
51. U. Wolff, *Phys. Rev. Lett.*, **62**, 361 (1989). Collective Monte Carlo Updating for Spin Systems.
52. B. A. Berg and T. Neuhaus, *Phys. Rev. Lett.*, **68**, 9 (1992). Multicanonical Ensemble: A New Approach to Simulate First-Order Phase Transitions.
53. F. Wang and D. P. Landau, *Phys. Rev. Lett.*, **86**, 2050 (2001). Efficient, Multiple-Range Random Walk Algorithm to Calculate the Density of States.
54. M. E. J. Newman and G. T. Barkema, *Monte Carlo Methods in Statistical Physics*, Oxford University Press, Oxford, UK, 1999.
55. D. P. Landau and K. Binder, *A Guide to Monte Carlo Simulations in Statistical Physics*, Cambridge University Press, Cambridge, UK, 2005.
56. R. P. Feynman and A. R. Hibbs, *Quantum Physics and Path Integrals*, McGraw-Hill, New York, 1965.

57. H. F. Trotter, *Proc. Am. Math. Soc.*, **10**, 545 (1959). On the Product of Semigroups of Operators.

58. L. Onsager, *Phys. Rev.*, **65**, 117 (1944). Crystal Statistics. I. A Two-Dimensional Model with an Order-Disorder Transition.

59. A. M. Ferrenberg and D. P. Landau, *Phys. Rev. B*, **44**, 5081 (1991). Critical Behavior of the Three-Dimensional Ising Model: A High-Resolution Monte Carlo Study.

60. S. Chakravarty, B. I. Halperion, and D. R. Nelson, *Phys. Rev. B*, **39**, 2344 (1989). Two-Dimensional Quantum Heisenberg Antiferromagnet at Low Temperatures.

61. C. Holm and W. Janke, *Phys. Rev. B*, **48**, 936 (1993). Critical Exponents of the Classical Three-Dimensional Heisenberg Model: A Single-Cluster Monte Carlo Study.

62. M. Campostrini, M. Hasenbusch, A. Pelissetto, P. Rossi, and E. Vicari, *Phys. Rev. B*, **65**, 144520 (2002). Critical Exponents and Equation of State of the Three-Dimensional Heisenberg Universality Class.

63. E. Luijten and H. W. J. Blöte, *Int. J. Mod. Phys. C*, **6**, 359 (1995). Monte Carlo Method for Spin Models with Long-Range Interactions.

64. P. Werner, K. Völker, M. Troyer, and S. Chakravarty, *Phys. Rev. Lett.*, **94**, 047201 (2005). Phase Diagram and Critical Exponents of a Dissipative Ising Spin Chain in a Transverse Magnetic Field.

65. M. Guo, R. N. Bhatt, and D. A. Huse, *Phys. Rev. Lett.*, **72**, 4137 (1994). Quantum Critical Behavior of a Three-Dimensional Ising Spin Glass in a Transverse Magnetic Field.

66. H. Rieger and A. P. Young, *Phys. Rev. Lett.*, **72**, 4141 (1994). Zero-Temperature Quantum Phase Transition of a Two-Dimensional Ising Spin Glass.

67. S. Pankov, S. Florens, A. Georges, G. Kotliar, and S. Sachdev, *Phys. Rev. B*, **69**, 054426 (2004). Non-Fermi-Liquid Behavior from Two-Dimensional Antiferromagnetic Fluctuations: A Renormalization-Group and Large-N Analysis.

68. S. Sachdev, P. Werner, and M. Troyer, *Phys. Rev. Lett.*, **92**, 237003 (1992). Universal Conductance of Nanowires near the Superconductor-Metal Quantum Transition.

69. A. Sandvik, *Phys. Rev. Lett.*, **89**, 177201 (2002). Multicritical Point in a Diluted Bilayer Heisenberg Quantum Antiferromagnet.

70. O. P. Vajk and M. Greven, *Phys. Rev. Lett.*, **89**, 177202 (2002). Quantum versus Geometric Disorder in a Two-Dimensional Heisenberg Antiferromagnet.

71. R. Sknepnek, T. Vojta, and M. Vojta, *Phys. Rev. Lett.*, **93**, 097201 (2004). Exotic versus Conventional Scaling and Universality in a Disordered Bilayer Quantum Heisenberg Antiferromagnet.

72. T. Vojta and R. Sknepnek, *Phys. Rev. B*, **74**, 094415 (2006). Quantum Phase Transitions of the Diluted O(3) Rotor Model.

73. T. Vojta and J. Schmalian, *Phys. Rev. Lett.*, **95**, 237206 (2005). Percolation Quantum Phase Transitions in Diluted Magnets.

74. A. P. Young and H. Rieger, *Phys. Rev. B*, **53**, 8486 (1996). Numerical Study of the Random Transverse-Field Ising Spin Chain.

75. A. P. Young, *Phys. Rev. B*, **56**, 11691 (1997). Finite-Temperature and Dynamical Properties of the Random Transverse-Field Ising Spin Chain.

76. E. Lieb, T. Schultz, and D. Mattis, *Ann. Phys. (N.Y)*, **16**, 407 (1961). Two Soluble Models of an Antiferromagnetic Chain.

77. B. M. McCoy and T. T. Wu, *Phys. Rev. Lett.*, **21**, 549 (1968). Random Impurities as the Cause of Smooth Specific Heats near the Critical Temperature.

78. B. M. McCoy and T. T. Wu, *Phys. Rev.*, **176**, 631 (1968). Theory of a Two-Dimensional Ising Model with Random Impurities. I. Thermodynamics.

79. C. Pich, A. P. Young, H. Rieger, and N. Kawashima, *Phys. Rev. Lett.*, **81**, 5916 (1998). Critical Behavior and Griffiths–McCoy Singularities in the Two-Dimensional Random Quantum Ising Ferromagnet.

80. M. P. A. Fisher, P. B. Weichman, G. Grinstein, and D. S. Fisher, *Phys. Rev. B*, **40**, 546 (1989). Boson Localization and the Superfluid-Insulator Transition.

81. M. Wallin, E. S. Sorensen, S. M. Girvin, and A. P. Young, *Phys. Rev. B*, **49**, 12115 (1994). Superconductor–Insulator Transition in Two-Dimensional Dirty Boson Systems.

82. M. Campostrini, M. Hasenbusch, A. Pelissetto, P. Rossi, and E. Vicari, *Phys. Rev. B*, **63**, 214503 (2001). Critical Behavior of the Three-Dimensional XY Universality Class.

83. J. Villain, *J. Phys. (Paris)*, **36**, 581 (1975). Theory of One- and Two-Dimensional Magnets with an Easy Magnetization Plane. II. The Planar, Classical, Two-Dimensional Magnet.

84. F. Alet and E. S. Sorensen, *Phys. Rev. E*, **68**, 026702 (2003). Directed Geometrical Worm Algorithm Applied to the Quantum Rotor Model.

85. W. L. McMillan, *Phys. Rev.*, **138**, A442 (1965). Ground State of Liquid ^{4}He.

86. D. Ceperley, G. V. Chester, and M. H. Kalos, *Phys. Rev. B*, **16**, 3081 (1977). Monte Carlo Simulation of a Many-Fermion Study.

87. R. C. Grimm and R. G. Storer, *J. Comput. Phys.*, **7**, 134 (1971). Monte Carlo Solution of Schrödinger's Equation.

88. J. B. Anderson, *J. Chem. Phys.*, **63**, 1499 (1975). A Random-Walk Simulation of the Schrödinger Equation: H_3^+.

89. M. Suzuki, *Commun. Math. Phys.*, **51**, 183 (1976). Generalized Trotter's Formula and Systematic Approximants of Exponential Operators and Inner Derivations with Applications to Many-Body Problems.

90. J. E. Hirsch, R. L. Sugar, D. J. Scalapino, and R. Blankenbecler, *Phys. Rev. B*, **26**, 5033 (1982). Monte Carlo Simulations of One-Dimensional Fermion Systems.

91. A. W. Sandvik and J. Kurkijärvi, *Phys. Rev. B*, **43**, 5950 (1991). Quantum Monte-Carlo Method for Spin Systems.

92. A. W. Sandvik, *J. Phys. A*, **25**, 3667 (1992). A Generalization of Handscomb's Quantum Monte-Carlo Scheme—Application to the 1D Hubbard Model.

93. N. V. Prokofev, B. V. Svistunov, and I. S. Tupitsyn, *JETP Lett.*, **64**, 911 (1996). Exact Quantum Monte Carlo Process for the Statistics of Discrete Systems.

94. H. G. Evertz, G. Lana, and M. Marcu, *Phys. Rev. Lett.*, **70**, 875 (1993). Cluster Algorithm for Vertex Models.

95. B. B. Beard and U. J. Wiese, *Phys. Rev. Lett.*, **77**, 5130 (1996). Simulations of Discrete Quantum Systems in Continuous Euclidean Time.

96. H. G. Evertz, *Adv. Phys.*, **52**, 1 (2003). The Loop Algorithm.

97. N. V. Prokof'ev, B. V. Svistunov, and I. S. Tupitsyn, *JETP*, **87**, 310 (1998). Exact, Complete, and Universal Continuous-Time Worldline Monte Carlo Approach to the Statistics of Discrete Quantum Systems.

98. O. F. Syljuasen and A. W. Sandvik, *Phys. Rev. E*, **66**, 046701 (2002). Quantum Monte Carlo with Directed Loops.

99. D. Handscomb, *Proc. Cambridge Philos. Soc.*, **58**, 594 (1962). The Monte Carlo Method in Quantum Statistical Mechanics.

100. A. W. Sandvik, *Phys. Rev. B*, **59**, 14157(R) (1999). Stochastic Series Expansion Method with Operator-Loop Update.

101. ALPS Project (Algorithms and Libraries for Physics Simulations). Available: http://alps.comp-phys.org.

102. A. W. Sandvik, Available: http://physics.bu.edu/~sandvik.

103. M. Barma and B. S. Shastry, *Phys. Rev. B*, **18**, 3351 (1978). Classical Equivalents of One-Dimensional Quantum-Mechanical Systems.

104. J. D. Reger and A. P. Young, *Phys. Rev. B*, **37**, 5978 (1988). Monte Carlo Simulations of the Spin-1/2 Heisenberg Antiferromagnet on a Square Lattice.

105. A. W. Sandvik and D. J. Scalapino, *Phys. Rev. Lett.*, **72**, 2777 (1994). Order-Disorder Transition in a Two-Layer Quantum Antiferromagnet.

106. L. Wang, K. S. D. Beach, and A. W. Sandvik, *Phys. Rev. B*, **73**, 014431 (2006). High-Precision Finite-Size Scaling Analysis of the Quantum Critical Point of S = 1/2 Heisenberg Antiferromagnetic Bilayers.

107. A. W. Sandvik, *Phys. Rev. B*, **66**, 024418 (2002). Classical Percolation Transition in the Diluted Two-Dimensional S = 1/2 Heisenberg Antiferromagnet.

108. L. Wang and A. W. Sandvik, *Phys. Rev. Lett.*, **97**, 117204 (2006). Low-Energy Dynamics of the Two-Dimensional S = 1/2 Heisenberg Antiferromagnet on Percolating Clusters.

109. R. Yu, T. Roscilde, and S. Haas, *Phys. Rev. Lett.*, **94**, 197204 (2005). Quantum Percolation in Two-Dimensional Antiferromagnets.

110. M. Greiner, O. Mandel, T. Esslinger, T. W. Hänsch, and I. Bloch, *Nature*, **415**, 39 (2002). Quantum Phase Transition from a Superfluid to a Mott Insulator in a Gas of Ultracold Atoms.

111. V. A. Kashurnikov, N. V. Prokof'ev, and B. V. Svistunov, *Phys. Rev. A*, **66**, 031601(R) (2002). Revealing the Superfluid-Mott-Insulator Transition in an Optical Lattice.

112. M. Troyer and U.-J. Wiese, *Phys. Rev. Lett.*, **94**, 170201 (2005). Computational Complexity and Fundamental Limitations in Fermionic Quantum Monte Carlo Simulations.

113. D. Ceperley and B. J. Alder, *Phys. Rev. Lett.*, **45**, 566 (1980). Ground State of the Electron Gas by a Stochastic Method.

114. R. Blankenbecler, D. J. Scalapino, and R. L. Sugar, *Phys. Rev. D*, **24**, 2278 (1981). Monte Carlo Calculations for Coupled Boson-Fermion Systems. I.

115. J. Hubbard, *Phys. Rev. Lett.*, **3**, 77 (1959). Calculation of Partition Functions.

116. J. E. Hirsch, *Phys. Rev. Lett.*, **51**, 1900 (1983). Monte Carlo Study of the Two-Dimensional Hubbard Model.

117. R. T. Scalettar, E. Y. Loh, J. E. Gubernatis, A. Moreo, S. R. White, D. J. Scalapino, R. L. Sugar, and E. Dagotto, *Phys. Rev. Lett.*, **62**, 1407 (1989). Phase Diagram of the Two-Dimensional Negative-U Hubbard Model.

118. A. Moreo and D. J. Scalapino, *Phys. Rev. Lett.*, **66**, 946 (1991). Two-Dimensional Negative-U Hubbard Model.

119. T. Paiva, R. R. dos Santos, R.T. Scalettar, and P. J. H. Denteneer, *Phys. Rev. B*, **69**, 184501 (2004). Critical Temperature for the Two-Dimensional Attractive Hubbard Model.

120. A. Sewer, X. Zotos, and H. Beck, *Phys. Rev. B*, **66**, 140504(R) (2002). Quantum Monte Carlo Study of the Three-Dimensional Attractive Hubbard Model.

121. S. Chandrasekharan and U.-J. Wiese, *Phys. Rev. Lett.*, **83**, 3116 (1999). Meron-Cluster Solution of Fermion Sign Problems.

122. J.-W. Lee, S. Chandrasekharan, and H. U. Baranger, *Phys. Rev. B*, **72**, 024525 (2005). Quantum Monte Carlo Study of Disordered Fermions.

123. H. von Löhneysen, A. Rosch, M. Vojta, and P. Wölfle, *Rev. Mod. Phys.*, **79**, 1015 (2007). Fermi-Liquid Instabilities at Magnetic Quantum Phase Transitions.

124. S. R. White, *Phys. Rev. Lett.*, **69**, 2863 (1992). Density Matrix Formulation for Quantum Renormalization Groups.

125. U. Schollwöck, *Rev. Mod. Phys.*, **77**, 259 (2005). The Density Matrix Renormalization Group.

126. A. Drzewinski and J. M. J. van Leeuwen, *Phys. Rev. B*, **49**, 403 (1994). Renormalization of the Ising Model in a Transverse Field.

127. Ö. Legeza and G. Fath, *Phys. Rev. B*, **53**, 14349 (1996). Accuracy of the Density-Matrix Renormalization-Group Method.

128. M. Andersson, M. Boman, and S. Östlund, *Phys. Rev. B*, **59**, 10493 (1999). Density-Matrix Renormalization Group for a Gapless System of Free Fermions.

129. F. Verstraete and J. I. Cirac, arXiv:cond-mat/0407066. Renormalization Algorithms for Quantum Many-Body Systems in Two and Higher Dimensions.

130. F. Verstraete, M. M. Wolf, D. Perez-Garcia, and J. I. Cirac, *Phys. Rev. Lett.*, **96**, 220601 (2006). Criticality, the Area Law, and the Computational Power of Projected Entangled Pair States.

131. V. Murg, F. Verstraete, and J. I. Cirac, *Phys. Rev. A*, **75**, 033605 (2007). Variational Study of Hard-Core Bosons in a Two-Dimensional Optical Lattice Using Projected Entangled Pair States.

132. S. Katsura, *Phys. Rev.*, **127**, 1508 (1962). Statistical Mechanics of the Anisotropic Linear Heisenberg Model.

133. P. Pfeuty, *Ann. Phys. (NY)*, **57**, 79 (1970). The One-Dimensional Ising Model with a Transverse Field.

134. F. Igloi and C. Monthus, *Phys. Rep.*, **412**, 277 (2005). Strong-Disorder Renormalization Group Approach of Random Systems.

135. D. S. Fisher, *Phys. Rev. B*, **50**, 3799 (1994). Random Antiferromagnetic Quantum Spin Chains.

136. G. Schehr and H. Rieger, *Phys. Rev. Lett.*, **96**, 227201 (2006). Strong-Disorder Fixed Point in the Dissipative Random Transverse-Field Ising Model.

137. W. Metzner and D. Vollhardt, *Phys. Rev. Lett.*, **62**, 324 (1989). Correlated Lattice Fermions in $d = \infty$ Dimensions.

138. A. Georges and G. Kotliar, *Phys. Rev. B*, **45**, 6479 (1992). Hubbard Model in Infinite Dimensions.

139. A. Georges, G. Kotliar, W. Krauth, and M. J. Rozenberg, *Rev. Mod. Phys.*, **68**, 13 (1996). Dynamical Mean-Field Theory of Strongly Correlated Fermion Systems and the Limit of Infinite Dimensions.

140. G. Kotliar, S. Y. Savrasov, K. Haule, V. S. Oudovenko, O. Parcollet, and C. A. Marianetti, *Rev. Mod. Phys.*, **78**, 865 (2006). Electronic Structure Calculations with Dynamical Mean-Field Theory.

141. K. G. Wilson, *Rev. Mod. Phys.*, **47**, 773 (1975). The Renormalization Group: Critical Phenomena and the Kondo Problem.

142. H. R. Krishnamurthy, J. W. Wilkins, and K. G. Wilson, *Phys. Rev. B*, **21**, 1003 (1980). Renormalization-Group Approach to the Anderson Model of Dilute Magnetic Alloys. I. Static Properties for the Symmetric Case.

143. R. Bulla, T. Costi, and T. Pruschke, *Rev. Mod. Phys.*, **80**, 395 (2008). The Numerical Renormalization Group Method for Quantum Impurity Systems.

CHAPTER 5

Real-Space and Multigrid Methods in Computational Chemistry

Thomas L. Beck

Departments of Chemistry and Physics, University of Cincinnati, Cincinnati, Ohio

INTRODUCTION

Real-space methods are iterative numerical techniques for solving partial differential equations on grids in coordinate space. The physical responses due to many chemical phenomena are restricted to domains that are relatively local in space, and real-space methods are well suited to exploit that physical locality. In real-space methods, the iterative updates of the desired functions require information only in a small neighborhood near the updated point. The drawback with this approach is that, if the iterations are performed only on a single (finest) grid, the solver tends to stall due to the long-wavelength components of the errors. Multigrid methods overcome this stalling by utilizing information from a wide range of length scales. With the incorporation of multiscale ideas, solvers can often be designed for which the cost scales linearly with system size. In the last 15 years, real-space and multigrid methods have been developed for a wide range of problems in computational chemistry. Those problems include electronic structure, Poisson and Poisson–Boltzmann equations, and transport models. This review will first give a tutorial introduction to real-space and multigrid methods and then present some case studies illustrating how these techniques have been applied in chemistry, nanomaterials, and biology.

Reviews in Computational Chemistry, Volume 26
edited by Kenny B. Lipkowitz and Thomas R. Cundari

Physical Systems: Why Do We Need Multiscale Methods?

Modern computational chemistry research frequently examines problems that require treating multiple-length and time scales. It is instructive to consider first two example systems that exemplify the need to develop methods for handling multiple scales. These two examples come from recent research projects in the author's group; they are limited in scope but representative of challenging computational problems in biophysics and nanoscience.

Consider first ion channels and transporters, which are large proteins embedded in biological membranes.[1–3] Their function is to control the flux of ions across the membrane selectively. In *channels*,[4] ions move based on diffusion driven by an electrochemical potential gradient. The transport down the gradient is typically controlled by a gating mechanism, which in turn requires conformational transitions in the protein. The pore is often extremely small, on the order of the size of the ions, and very specific physical/chemical interactions lead to selectivity. *Transporters* are also membrane proteins, but they can move one ion uphill in electrochemical potential if a gradient in another ion is maintained. [That gradient in the second ion is created by a separate membrane *pump* that utilizes chemical energy in the form of adenosine 5′-triphosphate (ATP).] The ions or molecules moved by a transporter can either propagate in the same direction (co-transport) or in the opposite direction (exchange).

One interesting and recent example of channel and transporter behavior is the chloride channel family;[5,6] the three-dimensional X-ray structure (see Figure 1) of a bacterial homolog was discovered,[7,8] leading to extensive modeling efforts over the last several years.[9–18] (Several discussions of computational methods for ion channels have appeared recently; see Refs. 4, 19–27 for some examples.) The bacterial chloride channel homolog reveals a complicated homodimeric architecture. Each monomer contains a large number of α helices that possess a wide range of tilt angles relative to the membrane normal. The arrangement of those helices leads to an hourglass structure with two aqueous vestibules separated by a narrow filter region. The N-terminal domains of the helices tend to point toward the selectivity filter, creating a large positive electrostatic potential in the central part of the pore. Several small anions can move through the pore—these anion channels and transporters are less selective than the cation (K^+ and Na^+) counterparts,[28] probably due to the fact that chloride ions are the dominant anions in biological fluids.[29]

Recently, it has been discovered that the bacterial chloride channel homolog is not a channel as previously thought but is rather a transporter that exchanges two chloride ions for one proton.[30–32] The exchange mechanism leads to a net charge displacement of three! Following this surprising finding, two members of the eukaryotic chloride channel family (ClC-4 and ClC-5) were also shown to be chloride/proton antiporters,[33,34] and plants utilize related transporters for nitrogen uptake.[35] So the question arises, how does this protein

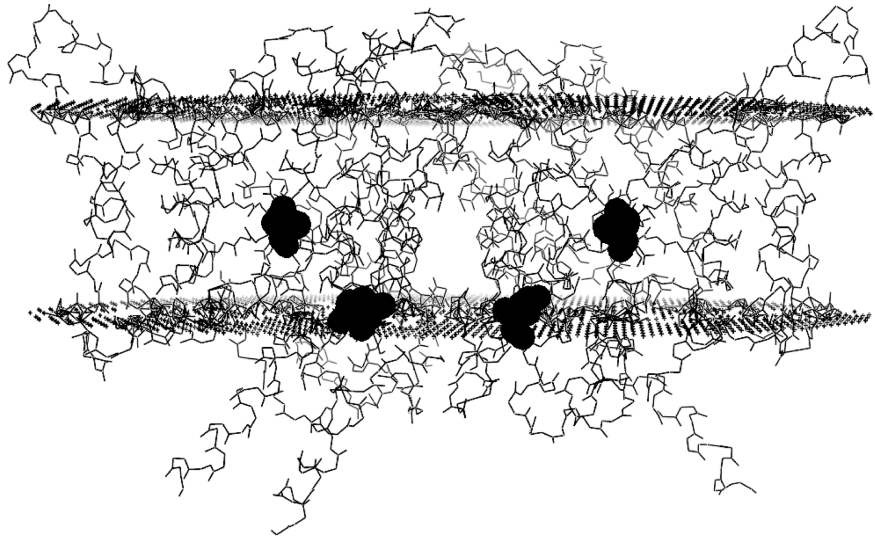

Figure 1 Bacterial chloride channel homolog (PDB code 1KPL). This transporter exists as a homodimer—the plane separating the two dimers is oriented vertically in the middle of this figure. The extracellular side is on top. The viewing direction is from the side, and the two shaded areas are the rough locations of the boundaries of the membrane. The two darkly shaded groups in each of the monomers are weak acid groups (glutamates, E148 on top and E203 on the bottom), which are important for proton transport through the structure. The E148 group also acts as a gate for chloride ion transport.

"magically" perform this ion exchange? Both experiments[31,36] and modeling studies[17] have begun to address this issue.

Several aspects of this membrane protein system require the use of multiscale modeling. Anion transport through the pore definitely requires a molecular-level treatment because the pore in the selectivity filter is close in size to that of a single chloride ion, and protein fluctuations clearly play a role during ion motion.[20] Electrostatic forces are crucial in anion selection, and the corresponding interaction energies are very large. If a single ion is placed at a central binding site in the pore, the free energy relative to that in water is tens of kT energy units lower; a second anion is required to enter the pore to destabilize the first anion through repulsive interactions. Experiments indicate such multiion transport.[37] One motivation for implementing a multiscale approach, therefore, is that while the local interactions in the pore must be handled at the molecular level, parts of the protein and the membrane far from the pore may be treated in a time-saving, coarse-grained fashion. A second motivation is simply that we need efficient solutions of the Poisson equation in determining the electrostatic interactions for a given configuration. A third motivating point concerns the gating mechanism: A glutamate (weak acid) residue is strategically situated at the extracellular entrance to the filter, and this gate

apparently swings open upon protonation.[8,17] The time scales for the opening and closing events can occur on the order of microseconds, and these times are beyond the capabilities of existing molecular dynamics simulations (more than 100,000 atoms must be simulated for a full atomic-level simulation that includes the membrane).

In addition to these justifications for multiscale modeling, a quantum treatment may be needed in at least two places for this type of problem. First, the transporter exchanges a proton for two chloride ions. How does the proton hop through what appears to be a largely hydrophobic protein domain? Quantum mechanics may be required here to account for the nuclear tunneling of the proton through potential barriers and for treating the specific interactions of that proton with chemical groups along its pathway.[38] Second, extensive work has shown that anion solvation phenomena tend to be more complex than for their cation counterparts.[39–42] The well-known Hofmeister series for specific ion effects exhibits remarkable behavior for a wide range of physical properties in ionic solutions,[39] and these behaviors are not explained by simple ionic solution statistical mechanical models. Anion polarizability is typically omitted or modeled crudely in ionic solutions, but recent efforts indicate a range of Hofmeister effects can be rationalized when the polarizability is properly included. So, we should include quantum effects for proton motion and anion polarizability even if these ions are embedded in such a large system.

A second model system that shows the need for implementing multiscale modeling strategies concerns electron transport through molecular electronic devices. Chemically synthesized molecular transistors assembled reliably onto electrode substrates could lead to large advances in computing capabilities, and to better understand electron transport in such devices, several groups have recently been modeling current–voltage behavior for molecules sandwiched between electrodes (Figure 2).[43–48] One such example is the benzene dithiol molecule attached chemically to two gold electrodes. This system

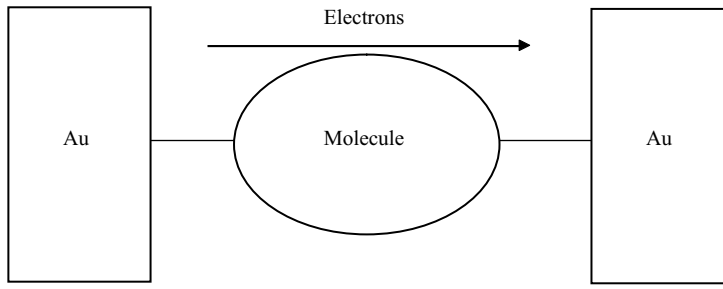

Figure 2 Schematic illustrating electron flow through a molecule sandwiched between two gold electrodes. A gradient in the electron electrochemical potential creates the driving force for the transport. The quantum states of the molecule and the coupling of the molecule to the two electrodes determine the conductance properties.

has been examined experimentally[49] and has provided a benchmark model for computational studies. Since we are interested in electron propagation through the molecule, clearly a quantum treatment is necessary. (See Chapter 3 in this volume by Elliott, Furche, and Burke[50] on using time-dependent density functional theory for exactly this system.)

Electron transport through nanoscale devices is often handled at the Landauer theory level,[51] where the electrons are assumed to move coherently from one electrode to the other without inelastic collisions. The current can be determined by computing the transmission function $T(E, V)$, which depends on energy for a given applied voltage. The functional form of $T(E, V)$ arises from the quantum states of the molecule that is coupled to the two electrodes. The most general computational methods used to compute those states have employed Green's function techniques to obtain the current self-consistently.[43–48,51]

This problem brings to the fore the need for treating multiple-length scales for an accurate determination of the current. Details of the chemical bonding of the molecule to the electrode atoms are crucial for determining both peak locations and widths in $T(E, V)$. The densities of states in the metal electrodes affect the coupling of the molecule to the electron bath. The applied potential, if large, can lead to significant changes in $T(E, V)$, implying nonlinear effects. Accordingly, this problem requires an accurate quantum chemical treatment for the molecule and for parts of the electrodes, even though this central domain may include up to tens or hundreds of atoms, depending on the size of the molecular device. Contrarily, the distant regions of the electrodes can be treated at a much coarser or a mean-field level of theory since they just provide the source of electrons that propagate through the device. Even with accurate quantum calculations at the density functional theory (DFT) level, predictions of currents may be off by two orders of magnitude in relation to experiment,[47,49] presenting major challenges at both the basic theory and computational levels for such problems.

Why Real Space?

A chapter in an earlier volume in this series devoted to quantum Monte Carlo (QMC)[52] methods noted that "there are many ways to skin a cat"; this chapter discusses yet another! In quantum chemistry, the dominant theme over many decades has been basis set calculations.[53] The basis sets consist of localized Slater-type orbitals or Gaussian functions that are adapted to provide accurate representations of the electron states in atoms. The main advantage of this approach is that the basis sets typically do not have to be terribly large in size since they already contain a lot of the detailed atomic information. A disadvantage is that it can be difficult to obtain an unambiguously converged result due to factors such as basis set superposition errors.[54]

The predominant computational motif for solid-state physicists, in contrast, has centered on expansions of wave functions in plane-wave basis sets.[55–57] Advantages of this approach include: (1) simplicity of the basis, (2) ability to use efficient fast Fourier transform (FFT) operations during minimization, (3) systematic convergence to the exact result with increasing basis set size (for a given model), and (4) lack of *Pulay forces* during molecular dynamics simulations.[56] While this basis is well suited for periodic systems, a disadvantage is that it is entirely delocalized in coordinate space—the basis functions have uniform magnitudes over all space. Thus, if we are interested in a localized system, a lot of effort must be expended to add up many functions so as to get a result of zero for regions that are far away from the molecule or cluster.

Real-space methods[58–62] are conceptually situated somewhere between the two limits of traditional basis functions and plane waves. The desired functions (electrostatic potential, wave functions, electron density, etc.) are represented directly on a grid in coordinate space, and several techniques exist for real-space representations of the partial differential equations to be solved on those grids. The simplest is finite differences (FD);[58–61] here the functions are Taylor expanded about a grid point, and those expansions are manipulated to obtain approximate representations of the derivatives. An important technical point is that this approach is *not necessarily variational* in the sense of yielding a result above the ground-state energy. The computed energy can lie above or below the ground-state energy depending on the sign of terms omitted in the expansion. The calculations do converge to the exact result as the grid spacing is reduced, however.

Another real-space approach is to use a finite-element (FE) basis.[62–64] The equations that result are quite similar to the FD method, but because localized basis functions are used to represent the solution, the method is variational. In addition, the FE method tends to be more easily ''adaptable'' than the FD method; a great deal of effort has been devoted to FE grid (or mesh) generation techniques in science and engineering applications.[65–67] Other real-space-related methods include discrete variable representations,[68–70] Lagrange meshes,[71,72] and wavelets.[73–83]

The main feature of real-space methods is that, if we represent the Laplacian operator (Poisson equation) or Hamiltonian (eigenvalue problem) on a grid, the application of the operator to the function requires information only from a local region in space. We will develop these concepts below, but here we note that only several neighboring grid points are required in general to solve such problems (depending on the approximation order). The matrix representation of these operators is thus highly banded, and application of the operator to one function requires a number of operations that is the width of the band times the number of grid points.

As we noted above, in an FD or FE solution, the exact result emerges as the grid spacing is reduced; in that respect we can call these methods *fully numerical* in the same spirit as the plane-wave approach from physics. An added advantage

of real-space methods is that it is not terribly difficult to place different resolution domains in different parts of space.[62,64,84–88] That is, the methods can utilize adaptivity, and this can be done without sacrificing the numerical efficiency of the real-space solver. In contrast, plane-wave methods utilize FFT operations at their core, and it is difficult (although not impossible[89]) to develop adaptive meshes for these processes. Finally, real-space methods, due to their near locality, are ideal for parallel computing. We can partition the problem into domains in space—most of the operations are contained within each of the domains, with relatively low communication overhead across the boundaries.

The real strength of real-space methods comes into play when we combine the localized computational representation together with the physical localization that exists in most chemical systems. For example, it is well known in chemistry that relatively localized orbitals can represent accurately directional chemical bonds in large molecules, thus allowing us to employ localized (often nonorthogonal) orbitals as we minimize the total electronic energy.[55,90] Those localized orbitals are set to zero outside a specified domain in space. So, by operating solely in real space, we can exploit this physical locality directly. Despite the claims in chaos theory that a butterfly flapping its wings on the other side of the globe might affect the weather here, small chemical changes at a point in space typically do not have a great influence far away due to screening. Kohn calls this the *near-sightedness* principal of matter.[91] The combination of a localized computational representation and physical locality can lead to linear-scaling algorithms for electronic structure,[55,92] a major aim in computational chemistry.

This chapter discusses numerical methods for solving several important differential equations in computational chemistry. It does not cover the conceptually related problem of coarse-grained modeling of large amplitude motions in polymers and biological macromolecules.[93–97]

REAL-SPACE BASICS

As outlined above, several means of representing partial differential equations in real space exist. Here, for the most part, we choose the simplest (the FD representation), restrict ourselves to second-order-accurate representations, and operate in one dimension so as to bring out all the important concepts and avoid getting wrapped up in details. A short introduction to FE representations is also included.

Equations to Be Solved

We consider here two of the most basic equations in computational chemistry: the Poisson equation and the Schrödinger equation. The Poisson equation yields the electrostatic potential due to a fixed distribution of

charges, and the time-independent Schrödinger equation produces the wave functions and energy levels for stationary quantum systems. The Poisson equation in one dimension is

$$\frac{d^2\phi(x)}{dx^2} = -4\pi\rho(x) \qquad [1]$$

where $\phi(x)$ is the electrostatic potential, and $\rho(x)$ is the charge density. The Schrödinger eigenvalue equation is

$$-\frac{1}{2}\frac{d^2\psi(x)}{dx^2} + V(x)\psi(x) = E\psi(x) \qquad [2]$$

where $\psi(x)$ is the wave function, $V(x)$ is the potential, and E is the energy eigenvalue. Atomic units are assumed throughout this chapter. In typical electronic structure theory, such as Hartree–Fock or density functional calculations, the potential $V(x)$ depends on the charge density produced by all the electrons and nuclei; thus, the calculation is termed *self-consistent* since, at convergence, the effective potential ceases to change. Prior to convergence, a solver must go back and forth between updates of the wave functions and the effective potential that depends on those wave functions.

We begin with a word on the general properties of these equations and how they can be "derived." Even though the FD representation is not variational in the sense of bounds on the ground-state energy, the iterative process by which we obtain the solution to the partial differential equations (PDEs) can be viewed variationally, i.e., we minimize some functional (see below) with respect to variations of the desired function until we get to the lowest "action" or "energy." This may seem rather abstract, but it turns out to be practical since it leads directly to the iterative relaxation methods to be discussed below. (See Ref. 98 for a more complete mathematical description of minimization and variational methods in relation to the FE method.)

For the Poisson problem, we make up an action functional $S[\phi]$ that, when minimized, yields the Poisson equation:

$$S[\phi] = -\frac{1}{2}\int \phi \frac{d^2\phi}{dx^2}\,dx - 4\pi \int \rho\phi\,dx \qquad [3]$$

A *functional* yields a number when the function over the whole domain (ϕ here) is specified. We then write a pseudodynamical equation (actually a steepest-descent equation) for the updates of ϕ:

$$\frac{\partial\phi}{\partial\tau} = -\frac{\delta S[\phi]}{\delta\phi} \qquad [4]$$

The expression on the right side of Eq. [4] is called a functional derivative. The easiest way to think about the functional derivative is to develop an FD representation for the right-hand side of Eq. [4] (see below). To do this we take the usual derivative with respect to the value of the potential at one point on the grid, divide by the grid spacing, and take the limit of decreasing grid spacing. When those steps are taken, we get Eq. [5]:

$$\frac{\partial\phi}{\partial\tau} = \frac{\partial^2\phi}{\partial x^2} + 4\pi\rho \qquad [5]$$

This equation, when iterated, will repeatedly move downhill on the action surface until the minimum is reached. Notice that this equation looks like a diffusion equation with a source term. It can be proved mathematically that, for this case, there is only one extremum, and it is a minimum. At the minimum (which is the point where the potential stops changing),

$$\frac{\partial\phi}{\partial\tau} = \frac{\partial^2\phi}{\partial x^2} + 4\pi\rho = 0 \qquad [6]$$

and we obtain the Poisson equation. PDEs like the Poisson equation are called elliptic equations. Other PDEs of importance are parabolic (diffusion) and hyperbolic (wave) equations.[99]

Solution of the Schrödinger equation can be viewed similarly.[65] The quantum energy functional (analog of the Poisson action functional above) is

$$E[\psi] = -\frac{1}{2}\int \psi^* \frac{d^2\psi}{dx^2}\,dx - \int \psi^* V\psi\,dx \qquad [7]$$

We seek to minimize this energy, but for this case we need a constraint during the minimization, namely for the normalization of the wave function. (If we are seeking many wave functions, we then need to have constraints for orthonormality—each eigenfunction must be normalized and orthogonal to all the other wave functions.) The augmented functional with the Lagrange multiplier constraint is

$$E_c[\psi] = -\frac{1}{2}\int \psi^* \frac{d^2\psi}{dx^2}\,dx + \int \psi^* V\psi\,dx - E\int \psi^*\psi\,dx \qquad [8]$$

Now our steepest-descent update equation becomes

$$\frac{\partial\psi}{\partial\tau} = -\frac{\delta E_c[\psi]}{\delta\psi^*} = \frac{1}{2}\frac{\partial^2\psi}{\partial x^2} - [V - E]\psi \qquad [9]$$

which when iterated to the minimum, yields the Schrödinger equation.

Finite-Difference Representations

How do we represent the above equations with FD methods on a grid? The answer is that a function is Taylor expanded about a central point x_i in the forward and backward directions:

$$f(x_i+h) \approx f(x_i) + f^{(1)}(x_i)h + \tfrac{1}{2}f^{(2)}(x_i)h^2 + \tfrac{1}{6}f^{(3)}(x_i)h^3 + \tfrac{1}{24}f^{(4)}(x_i)h^4 + \ldots \quad [10a]$$

$$f(x_i-h) \approx f(x_i) - f^{(1)}(x_i)h + \tfrac{1}{2}f^{(2)}(x_i)h^2 - \tfrac{1}{6}f^{(3)}(x_i)h^3 + \tfrac{1}{24}f^{(4)}(x_i)h^4 + \ldots \quad [10b]$$

where the grid spacing is h. The two equations are added together and then solved for $f^{(2)}(x_i)$, resulting in

$$f^{(2)}(x_i) \approx \tfrac{1}{h^2}[f(x_i-h) - 2f(x_i) + f(x_i+h)] - \tfrac{1}{12}f^{(4)}(x_i)h^2 + \ldots \quad [11]$$

This shows that the error in our 3-point formula for the second derivative is of order h^2. Higher order forms can be easily derived,[100] with a gain in accuracy of two orders with each pair of extra terms. Such high-order forms have been used extensively in electronic structure calculations.[58–60] It is clear from the above approximation that the sign and magnitude of $f^{(4)}(x_i)$ over the domain will be important for determining the value of the total energy.

Using the above formula for the second derivative, we can represent the Poisson equation as

$$\frac{1}{h^2}[\phi(x_{i-1}) - 2\phi(x_i) + \phi(x_{i+1})] = -4\pi\rho(x_i) \quad [12]$$

which in matrix form with six points is

$$\frac{1}{h^2}\begin{bmatrix} -2 & 1 & 0 & 0 & 0 & 0 \\ 1 & -2 & 1 & 0 & 0 & 0 \\ 0 & 1 & -2 & 1 & 0 & 0 \\ 0 & 0 & 1 & -2 & 1 & 0 \\ 0 & 0 & 0 & 1 & -2 & 1 \\ 0 & 0 & 0 & 0 & 1 & -2 \end{bmatrix} \begin{bmatrix} \phi(x_1) \\ \phi(x_2) \\ \phi(x_3) \\ \phi(x_4) \\ \phi(x_5) \\ \phi(x_6) \end{bmatrix} = -4\pi \begin{bmatrix} \rho(x_1) \\ \rho(x_2) \\ \rho(x_3) \\ \rho(x_4) \\ \rho(x_5) \\ \rho(x_6) \end{bmatrix} \quad [13]$$

In an iterative procedure that applies the appropriate update matrix to the function many times, the boundary values of the function (at points 1 and 6 above) are typically fixed (or periodic boundaries are enforced). We can write Eq. [13] in the simple matrix form

$$LU = f \quad [14]$$

where L is the Laplacian matrix, U is the potential that solves Eq. [14], and f is -4π times the charge density.

During the solution process, the progress can be monitored by computing the residual

$$r = f - Lu \qquad [15]$$

and plotting its magnitude averaged over the domain. As the residual is reduced in magnitude toward 0, we approach the exact solution on the grid (but not the exact solution of the PDE, since there are numerical errors in our FD approximation.) The lowercase u is used to signify the *current approximation* to the exact solution U.

This chapter is directed at describing a new development in computational chemistry, but it should be noted that, already in Pauling and Wilson's classic quantum chemistry text from 1935,[101] there is a section on variational methods that includes a discussion of FD approximations for the Schrödinger equation!

Finite-Element Representations

Here again we consider a simple Poisson problem, but the same general procedure can be applied to the eigenvalue or total energy minimization problems. As we discussed above, one approach is to minimize the action functional of Eq. [3], using an FD representation of the Laplacian inside the integral (or summation on a grid when the integral is discretized) and specified boundary conditions (e.g., fixed or periodic). Alternatively, we can integrate by parts the action term involving the Laplacian in Eq. [3] to obtain

$$S[\phi] = \frac{1}{2}\int \left(\frac{d\phi}{dx}\right)^2 dx - 4\pi \int \rho\phi \, dx \qquad [16]$$

assuming that the values of the potential or its derivative vanish on the boundaries.[65] We can then minimize this alternate form of the action with respect to variations in the potential ϕ.[98] Once the minimum is reached, the potential ϕ is the solution. If we assume that we have that minimizing solution ϕ, an approximate form of the potential can be represented as $\phi + \varepsilon v$, where v is any function that vanishes on the boundaries. If we substitute this general form into Eq. [16], take the derivative with respect to ε, and set ε equal to 0, we obtain the following variational expression:

$$\int \left(\frac{d\phi}{dx}\right)\left(\frac{dv}{dx}\right) dx = 4\pi \int \rho v \, dx \qquad [17]$$

If Eq. [17] is true for all arbitrary v, then ϕ satisfies Poisson's equation. This equation is called the variational boundary value problem for the Poisson

equation[98] and is true for all continuously differentiable functions v that exist in the domain and vanish on the boundaries.

The next step in the development of the FE method is to represent the solution in a finite-dimensional space as a superposition of basis functions. The basis functions are quite different from those typically employed in quantum chemistry (Gaussians or linear combinations of atomic orbitals—LCAOs). The FE basis is taken as polynomial functions that are strictly zero outside of a small local domain centered at a given grid point (or *node*). We then represent the function approximately as a linear combination of these localized basis functions:

$$\phi_n = \sum_{i=1}^{n} b_i \chi_i \qquad [18]$$

and we minimize the action functional with respect to variations of the coefficients b_i in the expansion. If the above expansion is inserted into the formula for the action, we obtain

$$\begin{aligned} S[v_n] &= \frac{1}{2}\int \left(\frac{d\phi_n}{dx}\right)\left(\frac{d\phi_n}{dx}\right) dx - 4\pi \int \rho\phi_n \, dx \\ &= \frac{1}{2}\int \left(b_1 \frac{d\chi_1}{dx} + b_2 \frac{d\chi_2}{dx} + \ldots\right)\left(b_1 \frac{d\chi_1}{dx} + b_2 \frac{d\chi_2}{dx} + \ldots\right) \\ &\qquad dx - 4\pi \int \rho(b_1\chi_1 + b_2\chi_2 + \ldots)\, dx \\ &= \frac{1}{2}\sum_{i,j=1}^{n} K_{ij} b_i b_j - \sum_{i=1}^{n} F_j b_j \end{aligned} \qquad [19]$$

where

$$K_{ij} = \int \frac{d\chi_i}{dx}\frac{d\chi_j}{dx}\, dx \qquad [20]$$

and

$$F_j = 4\pi \int \rho\chi_j \, dx \qquad [21]$$

If we then minimize this function by varying the coefficients b_i, this leads to a matrix equation of the form

$$K\mathbf{a} = F \qquad [22]$$

where the vector **a** solves the minimization problem. We see that Eq. [22] is very similar to the FD matrix Eq. [13], since the localized nature of the basis leads to a highly banded matrix K. The last piece of the puzzle concerns how to choose the polynomial basis functions χ_i. Brenner and Scott[102] work through a simple example using piecewise linear functions for the basis, and for that basic case the analogy between the FD and FE formulations is apparent. Higher order polynomial forms for the basis functions are described in the review of Pask and Sterne.[62]

Besides the basis set nature of the FE approach, the essential difference between the FE and FD methods is manifested in Eq. [17] and the nature of the boundary conditions. For the FE case, the general boundary condition $\phi(0) = c_1$ is required on one side of the domain, while a second boundary condition $\phi'(1) = c_2$ is automatically implied by satisfaction of the variational condition. (These two constants were assumed to be 0 for some of the discussion above.) The first boundary condition is termed *essential*, while the second is called *natural*. The FE method is called a *weak* formulation, in contrast to the FD method, which is labeled a *strong* formulation (requiring both boundary conditions from the start and twice differentiable functions). A clear statement of these issues is given in the first chapter of Ref. 103, and the equivalence of the strong and weak formulations is proven there. Most electronic structure applications of FE methods have utilized zero or periodic boundary conditions.

We can now see that a similar matrix representation is obtained for both the FD and FE methods due to their near-local nature. If the grid is highly structured and a low-order representation is assumed, the two representations become virtually indistinguishable. The FE method has the advantages that it is variational from the beginning, and it allows for greater flexibility in the arrangement of the mesh. On the other hand, the FD method is nonvariational in the sense of convergence from above, but the numerical representation is highly structured and generally more banded (fewer terms to represent the action of the Laplacian operator) than for the FE case. Thus, the preferred choice between the FD and FE representations depends on the nature of the problem, and the tastes of the practitioner.

Iterative Updates of the Functions, or Relaxation

To solve the Poisson equation iteratively, we make an initial guess for the function values over the domain and then update Eq. [5] numerically. We first write the spatial part of Eq. [5] in FD form:

$$\frac{\partial \phi(x_i)}{\partial \tau} = \frac{1}{h^2}[\phi(x_{i-1}) - 2\phi(x_i) + \phi(x_{i+1})] + 4\pi\rho(x_i) \qquad [23]$$

Next, we replace the denominator on the left side ($d\tau$) by τ and call this the time-step size. Eq. [23] can then be written as an update equation:

$$\phi^{n+1}(x_i) = \phi^n(x_i) + \frac{\tau}{h^2}[\phi^n(x_{i-1}) - 2\phi^n(x_i) + \phi^n(x_{i+1})] + 4\pi\tau\rho(x_i) \qquad [24]$$

where n labels the iteration number. This equation can be rearranged to give

$$\phi^{n+1}(x_i) = (1-\omega)\phi^n(x_i) + \frac{\omega}{2}[\phi^n(x_{i-1}) + \phi^n(x_{i+1}) + 4\pi\rho(x_i)h^2] \qquad [25]$$

where $\omega = 2\tau/h^2$. The update equation above is called the weighted Jacobi method. If $\omega = 1$, it is termed the Jacobi method.[99,104,105] As will be shown below, there is a limit on the value of ω; if it becomes too large, the values of the function diverge during repeated iterations.

One simple modification leads to two other update schemes. As the solver scans through the grid, the values at grid points are typically updated in sequence. Thus, when we update the function at the (i) point, the $(i-1)$ value has already been changed. Eq. [25] can then be altered to

$$\phi^{n+1}(x_i) = (1-\omega)\phi^n(x_i) + \frac{\omega}{2}[\phi^{n+1}(x_{i-1}) + \phi^n(x_{i+1}) + 4\pi\rho(x_i)h^2] \qquad [26]$$

This relaxation scheme is named successive overrelaxation (SOR), and if $\omega = 1$, it is the Gauss–Seidel method. This slight change alters the underlying spectral properties of the update matrix, most often favorably. It turns out that Gauss–Seidel iterations are particularly well suited for multigrid calculations—they tend to efficiently smooth the errors on wavelengths characteristic for a given grid level.[105]

The same methods can be applied to the Schrödinger equation, but the eigenvalue E needs to be updated after each iteration, and the wave function must be normalized.[106] If the lowest n states are desired, the wave functions must be orthogonalized (Gram–Schmidt procedure) and then normalized. Given normalized approximate eigenfunctions, the approximate eigenvalues are given by Eq. [27]:

$$E_i = \int \psi_i \left[-\frac{1}{2}\frac{d^2}{dx^2} + V \right] \psi_i \, dx = \langle \psi_i | H | \psi_i \rangle \qquad [27]$$

This formula can be approximated on the grid by utilizing the FD methods discussed above.

What Are the Limitations of Real-Space Methods on a Single Fine Grid?

If we iterate toward the solution as discussed above, the residual decreases quickly at first, but then the convergence slows considerably. This

behavior gets worse as the grid spacing decreases. To address why this happens, we will look at the solution of the Laplace equation [Poisson equation with $\rho(\mathbf{r}) = 0$], since it illustrates the important features of the slowing down. The analysis will be performed for the weighted Jacobi method discussed above.

The update or relaxation Eq. [25] can be written as a matrix equation. We are interested in the mathematical properties of the update matrix, so we will calculate the eigenvalues of that matrix. Let the update matrix act upon a plane wave with wavevector k. Then our eigenvalue equation is

$$\frac{\omega}{2}e^{ik(x-h)} + (1-\omega)e^{ikx} + \frac{\omega}{2}e^{ik(x+h)} = \lambda_k e^{ikx} \qquad [28]$$

where λ_k is the eigenvalue of the update matrix. Using the relation $e^{ix} = \cos x + i \sin x$, and a trigonometric identity, we find

$$\lambda_k = 1 - 2\omega \sin^2\left(\frac{kh}{2}\right) \qquad [29]$$

We can imagine that if the eigenvalues of this matrix exceed one in magnitude, the iterations will numerically "explode." This implies that $\omega \leq 1$ for the weighted Jacobi method. When you write your first relaxation code, it is easy to test this assertion, and indeed it is true! It turns out that, for the SOR algorithm, the stability criterion is $\omega \leq 2$. This corresponds effectively to a larger "time step" during the iterations and can lead to greater efficiency. An added bonus of Gauss–Seidel and SOR methods is that, since the updated values are used rather than the previous values, we need not store an extra vector for the old and new function values. Thus, the memory requirements are reduced.[105]

For small k, we can expand the sin function to give

$$\lambda_k \approx 1 - \left(\frac{\omega k^2 h^2}{2}\right) \qquad [30]$$

Small k corresponds to a long-wavelength mode, and the above approximation tells us that the eigenvalues corresponding to the longest wavelength modes in the errors approach 1 as the grid spacing is reduced toward zero. This means that errors with the longer wavelengths do not get removed efficiently. (The error reduction efficiency is related to the eigenvalue raised to a power of the number of iterations.) This, in a nutshell, is the origin of "critical slowing down," which motivated the development of multigrid (MG) methods.[105]

MULTIGRID METHODS

The MG method was developed in the late 1960s and early 1970s. Early multilevel ideas from Fedorenko were fully developed by Brandt, Hackbusch, and others into highly efficient PDE solvers.[105,107–109] This method cleverly utilizes multiple grid levels to accelerate the convergence rate of iterative solvers. The trick is to design a coarse-grid representation such that, if we had the exact numerical solution on the fine grid, nothing would happen during the coarse-grid correction process. This is termed *zero correction at convergence*.

How Does Multigrid Overcome Critical Slowing Down?

The basic idea of the original MG method is to set up a series of coarser grids, with each next-coarser grid typically having a grid spacing twice that on the finer level. After a few iterations on the fine grid, the problem is passed to the coarser level, iterated there, and then moved to a yet coarser level. This is repeated until the coarsest grid is reached. For some problems, such as the Poisson equation, the coarsest grid can contain only one interior point. In other problems, like the eigenvalue problem, the coarsest level must contain enough resolution to at least approximately represent the wiggles in the eigenfunctions, so there can be limits on how coarse we can go.

Why does this process work? The main explanation is that components of the error having wavelengths roughly the size of a small multiple of the grid spacing on a given level get removed efficiently by the relaxation process.[105] A careful analysis of the spectral properties of the Gauss–Seidel method shows that errors with those wavelengths get decimated quickly. Thus, by proceeding through a range of coarser levels, errors with *all* wavelengths can be removed. This is one of the few cases in computational science where it almost seems as if we get something for nothing—in three dimensions, the cost of the updates on the next coarser level is one eighth that on the fine level, yet by going to the coarser level, we are solving the hardest part of the problem.

Full Approximations Scheme (FAS) Multigrid, and Full Multigrid (FMG)

The question one might ask is: Can we design a coarse-grid problem that possesses the important zero correction at convergence property? Here we will discuss the full approximation scheme (FAS) multigrid method, since it is general in scope.[105,107,108] The FAS approach can be employed to solve both linear and nonlinear problems, and many of the problems in which we are interested are nonlinear in nature (Poisson–Boltzmann, eigenvalue, etc.).

We first introduce some of the basic operations in an MG process. We have already discussed the FD representation, but we need operations that pass functions between the grid levels. Those are *restriction* (fine to coarse)

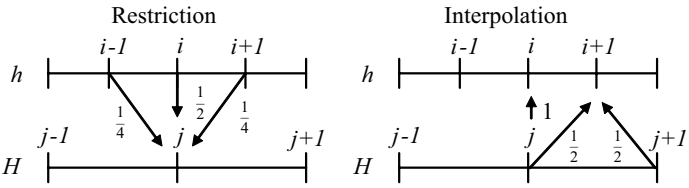

Figure 3 Illustration of the restriction and interpolation operations. Full weighting restriction (left) averages the three fine-grid values to yield the coarse-grid value. Interpolation injects the values from the coarse grid, which are included in the fine grid, and averages two coarse values to generate the intermediate fine-grid value.

and *interpolation* (coarse to fine); see Figure 3. Every numerical operation we perform in an MG solver has a numerical order associated with it. It turns out we need not be particularly worried about the orders of the restriction and interpolation operators (the orders of these two operations must add up to the order of the differential equation, which in all of the cases of interest here is 2).[105,108] In our own work, we have typically used *full weighting* restriction and linear interpolation (or sometimes cubic interpolation in the eigenvalue problem). These operations sound like involved mathematical tasks but are actually quite simple.

Full weighting restriction is just a trapezoid-rule numerical integration: Take the central point on the fine grid and average it with the two closest neighbors (as in Eq. [31] for one dimension):

$$f_j^H = \tfrac{1}{4} f_{i-1}^h + \tfrac{1}{2} f_i^h + \tfrac{1}{4} f_{i+1}^h \qquad [31]$$

Here the fine-grid point i coincides with the coarse-grid point j. The three fine-level points yield the coarse-grid value when averaged. Of course, in two and three dimensions, the trapezoid rule gets slightly more complicated and involves more points, but those values can be easily worked out from the one-dimensional example. The weights in the integration formula add up to 1. Symbolically we represent the restriction operator as I_h^H, where h is the fine-grid spacing, and H is the coarse-grid spacing.

Linear interpolation is also simple. For the points on the fine grid that coincide with the coarse-grid points, simply inject the function value:

$$f_i^h = f_j^H \qquad [32]$$

For the intermediate points, average the two neighboring coarse-grid points:

$$f_{i+1}^h = \tfrac{1}{2}(f_j^H + f_{j+1}^H) \qquad [33]$$

In this last formula the coarse-grid index j is located at the point just to the left of the fine-grid point (Figure 3). In higher dimensions, the best way to enact the interpolation is to perform the operation as a series of interpolations on lines, that is, as a series of one-dimensional operations. This has the same approximation order and is easy to code. The symbol used for the interpolation operator is I_H^h.

Now that we have the two transfer operations in hand, how do we design the coarse-grid problem? Consider again the matrix representation of the Poisson equation:

$$L^h U^h = f^h \qquad [34]$$

Here we use the uppercase U^h to represent the exact numerical solution on the fine grid. We now pass that exact solution to the coarse grid by restriction and examine the same type of equation:

$$L^H u^H = f^H \qquad [35]$$

where

$$u^H = I_h^H U^h \qquad [36]$$

and

$$f^H = I_h^H f^h \qquad [37]$$

The difficulty here is that u^H does not solve the coarse-grid equation (which is why lowercase was used for this function above). This situation immediately becomes a problem because once we have the exact solution on the fine grid, nothing should happen on the coarse grid. Brandt introduced a clever solution to this problem called the FAS method.[107,108]

We modify the coarse-grid equation (Eq. [35]), with an added function τ^H, the *defect correction*, defined as follows (assuming we have the exact fine-grid solution U^h for now—of course, we do not have that function during the solution process, but this argument illustrates a key point):

$$\tau^H = L^H I_h^H U^h - I_h^H L^h U^h \qquad [38]$$

This term is added to the right side of the coarse-grid equation [35] to obtain

$$L^H U^H = f^H + \tau^H = I_h^H f^h + L^H I_h^H U^h - I_h^H L^h U^h = L^H I_h^H U^h \qquad [39]$$

since

$$L^h U^h = f^h \qquad [40]$$

Thus, we have an identity, and iterations on the coarse grid will not change the function. This development by Brandt thus satisfies the zero correction at convergence condition. In general, τ^H is not zero even when the solution has converged to the exact result, so its inclusion is crucial. The defect correction τ^H is a difference between the coarse-grid Laplacian acting on the coarse-grid function and the restriction of the fine-grid Laplacian acting on the fine-grid function. It tends to be large in places where the final result changes rapidly; for example, if we have a single-point charge located at a grid point, the potential that solves the Poisson equation varies dramatically near that point, and a peak in τ^H is observed.

So far we have been concerned with only two grid levels, with grid spacings h (fine) and H (coarse). We now need one addition to the above discussion. If we use many grid levels, the coarse-grid defect correction on levels two or more removed from the fine level must include a term that restricts the previous level's defect correction. Here we label the general coarse-grid level k (typically l is used then for the finest level):

$$\tau^k = L^k I_{k+1}^k u^{k+1} - I_{k+1}^k L^{k+1} u^{k+1} + I_{k+1}^k \tau^{k+1} \qquad [41]$$

In Eq. [41] we input the current approximation u^k for the function on a given level, which is what is done in the solver as it progresses toward the exact solution, U^l. The coarsest grid level is labeled by the smallest k. It is a good exercise to show that Eq. [41] is required on levels two or more removed from the finest level. Notice that the defect correction on level k requires information only from the next-finer $(k+1)$ level.

Once the coarsest level is reached, some iterations are performed there, and then the solver begins to head back to the fine level (Figure 4). The final part of the FAS-MG process to be discussed is the *correction* step. Once the iterations are completed on the coarsest level, the next-finer level is updated as follows:

$$u^{k+1} \leftarrow u^{k+1} + I_k^{k+1}(u^k - I_{k+1}^k u^{k+1}) \qquad [42]$$

This step interpolates the change in the coarse-grid function during iterations onto the next-finer level and corrects the current approximation there.

Once corrected, a few iterations are performed on the current level, the next-finer level is corrected, and the process is repeated until the finest level is reached. The whole procedure of starting on the fine level, proceeding to coarser levels, and then correcting and iterating along a path back to the fine

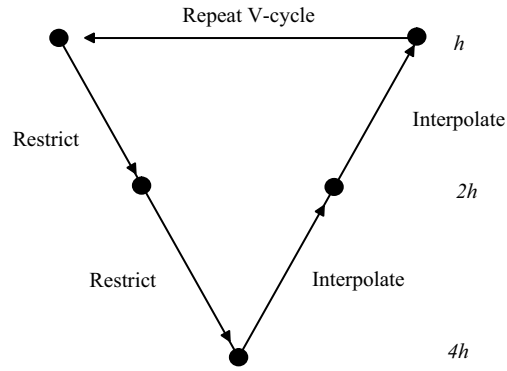

Figure 4 The V-cycle in a multigrid solver. An initial guess is made on the fine level, iterations are performed, and then the approximate solution is passed to the coarser level. This process is repeated until the coarsest grid is reached. The solver then progresses through interpolation (correction) steps back to the finest level. The V-cycle can be repeated.

level, is termed a V-cycle (Figure 4). The solver can loop back around the V-cycle as many times as desired until a specified magnitude of the residual is obtained. If the MG Poisson solver is working properly, the residual should be reduced by an order of magnitude during each V-cycle. The author still remembers the first working Poisson MG code he wrote, and how dramatic the difference in convergence rate is once the multiple levels are incorporated! See Figure 5.

In the preceding discussion, we started on the finest level with some initial approximation and then proceeded through the V-cycle. This approach works fine, but there is a way to obtain a good initial approximation with little computational cost called the FMG method (Figure 6). In this approach, iterations are first performed by taking the coarsest level as the starting point (making it the current finest grid). The current approximation is then interpolated to the next level, and one or more V-cycles are performed there. This process is repeated until the finest grid is reached, at which point a very good preliminary estimate of the solution on the finest level is generated. The total cost of this "preconditioning" is very low, and it is almost always a good idea to use FMG if we have little or no prior knowledge about the solution on the fine level. If we do have a good initial guess at the solution, it then makes sense to use that guess and start with V-cycles on the finest level.

For the Poisson problem, the total number of grid points for all the grid levels in three dimensions is only a small constant (greater than one) times the number of fine-grid points (indicated by N_g).[58] It is observed that the convergence rate does not depend on the system size, and the residual decreases exponentially with the number of iterations, i.e., a plot of the log of the residual vs. the number of iterations decreases linearly. Thus, the

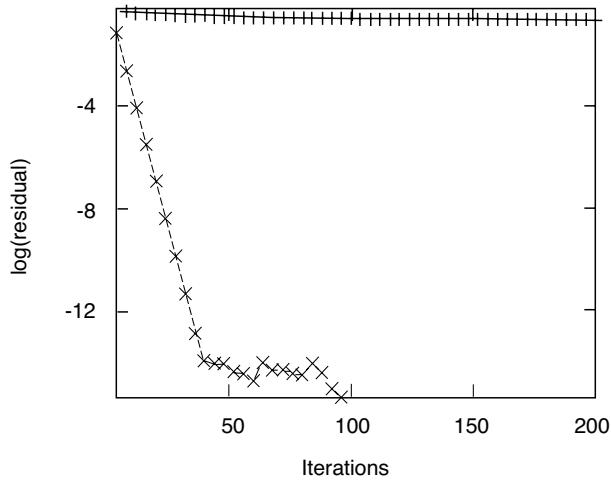

Figure 5 Convergence rates for a simple one-dimensional Poisson problem in a finite domain with 65 points. The potential was fixed at 0 on the boundaries, and two discrete charges were placed in the domain. The figure plots the number of fine-grid relaxation iterations vs. the log(10) of the residual. The top curve (crosses) is for Gauss–Seidel relaxation on the fine grid alone. The lower curve (x's) is for repeated cycling through MG V-cycles with 6 levels. The apparent "stalling" after 40 iterations for the MG process occurs because machine-precision zero has been reached for the residual.

computer time required scales linearly with system size, which is the best we can do for an electrostatic problem. We do point out, though, that on uniform grids, FFT methods for solving the Poisson problem scale as $N_g \log N_g$, and the log term grows very slowly with system size. So FFT and MG are competitive methods for obtaining the Poisson potential over the whole domain of a uniform grid.[58]

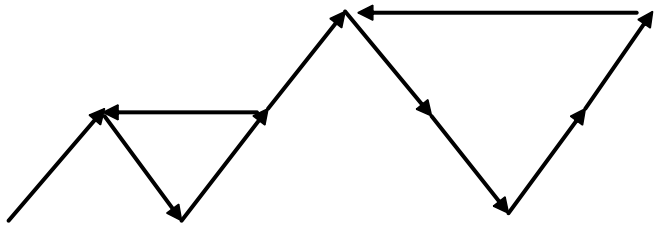

Figure 6 Full multigrid cycle (FMG); see also Figure 4. Instead of starting with an initial guess on the finest level and performing V-cycles from that point, iterations are begun on the coarsest level and the solver progresses toward the finest level. By the time the left side of the finest-level V-cycle has been reached, an excellent initial approximation to the function has been obtained for little computational cost.

EIGENVALUE PROBLEMS

It was mentioned earlier that aspects of eigenvalue problems exist that make them more difficult to solve than the Poisson equation. Typically, we would like to solve for the first q eigenfunctions for a given Hamiltonian operator. This is what is done in a Kohn–Sham DFT calculation,[110,111] where those q states are populated with $2q$ electrons, and the self-consistent solution process minimizes the total electronic energy when converged. The most difficult part of a DFT calculation is the eigenvalue problem, which can be solved directly or cast in a different format, such as a density-matrix formulation.[112,113] Even though the Hamiltonian operator is a linear operator, solving the eigenvalue part of the problem is a nonlinear process since we seek both the eigenvalues and the eigenfunctions.[106]

First consider iterations on a single, fine grid. The relaxation step, Eq. [9], is similar to the Poisson problem. Following the relaxation, additional operations must be performed, however. Those operations correspond to orthonormalizing the eigenfunctions in a Gram–Schmidt procedure and updating the eigenvalues (Eq. [27]). The Gram–Schmidt orthogonalization method is discussed in applied mathematics texts (see Ref. 114 as an example). In this step, the dot products of eigenvectors (the values of the wave function on the grid) with all other eigenvectors must be computed. This operation thus scales as q^2N_g, or N_e^3, where N_e is the number of electrons. (The number of eigenfunctions q is typically $N_e/2$, and the number of grid points required increases linearly with the number of electrons.) This is a major bottleneck for eigenvalue problems in which the eigenfunctions span the whole physical domain. Notice also that the updates of all the eigenvalues by Eq. [27] and the relaxation step for the eigenfunctions both scale as qN_g or N_e^2. It is clear from this discussion that the only possible way to obtain linear scaling in real space is to utilize localized functions of some sort.

Multigrid for the Eigenvalue Problem

We do not lay out in great detail here the FAS-MG method for the eigenvalue problem. An original effort in this direction was developed in 1983 by Brandt, McCormick, and Ruge.[106] Their article presents a clear discussion of the FAS method applied to eigenvalue problems. The algorithm contains all the basic features discussed above for the Poisson equation but adds several necessary modifications. Those additions will be summarized here briefly; the reader is referred to the original article for the technical details.[106]

One complication in the eigenvalue problem that becomes apparent when writing a solver is that the wave functions are oscillatory for states above the ground state. This suggests that the coarsest grid that may be used must still have enough resolution to at least approximately represent the eigenfunction variations. This in turn slows down the convergence rates relative to the

Poisson problem. A second complication is that constraints must be imposed during coarse-scale iterations to at least approximately maintain eigenfunction orthonormality. An interesting feature of the FAS approach is that such global constraints can be imposed on coarse levels (when they are properly formulated). An important point to note is that, even if we had the exact eigenfunctions on the fine level, they are no longer orthogonal or normalized when restricted to the coarse level. A third complication is that the eigenvalues must be updated during coarse-scale iterations. They are calculated on coarse levels with the following formula:

$$E_i = \frac{\langle H^k \psi_i^k - \tau_i^k | \psi_i^k \rangle}{\langle \psi_i^k | \psi_i^k \rangle} \qquad [43]$$

It is an interesting analytical exercise to show that, at convergence, the eigenvalues computed in this way are the same on all levels. This is why no level index k is placed on the eigenvalue. On the finest level, since $\tau_i^l = 0$, we get back the usual formula for the eigenvalue.

A final feature of the Brandt, McCormick, and Ruge[106] algorithm that deserves comment is the Ritz projection operation performed on the finest level. In the Ritz projection, the Hamiltonian matrix is constructed using as a basis the current approximation for the eigenfunctions. This Hamiltonian matrix is thus of dimension $q \times q$. The matrix is then diagonalized by standard matrix methods. New eigenvalues are obtained, and the eigenfunctions are updated using the dimension-q vector from the diagonalization routine. What this operation does is to "purify" the occupied subspace of the q eigenfunctions—it makes the errors orthogonal to the occupied subspace. The problem with this step, as with the Gram–Schmidt orthogonalization process, is that it scales as $q^2 N_g$ (to construct the Hamiltonian matrix), or N_e^3, so we are back to the same scaling problem. In spite of the cubic scaling, this algorithm is efficient and has been utilized in the development of DFT-MG solvers.[58,115]

Following the original FAS algorithm of Brandt and co-workers, modifications were proposed by Costiner and Ta'asan[116,117] to move the costly orthogonalization and Ritz projection to coarser levels. For small to medium-sized systems, where the eigenfunctions span the whole physical domain, their method effectively scales as qN_g. This method has been incorporated into a computational algorithm recently for the Kohn–Sham equations.[118,119] The original Costiner–Ta'asan algorithm did not converge properly for large quantum chemical problems, and the method was subsequently modified to regain proper convergence.[119]

Self-Consistency

Quantum chemical calculations require self-consistent solution, and we illustrate this here with a standard Kohn–Sham DFT calculation. We make

an initial guess at the wave functions or charge density, the Poisson equation is solved to yield the electrostatic potential, and the exchange–correlation potential is computed. This yields the effective potential in the Kohn–Sham approach, and then we solve the eigenvalue problem approximately to get new approximations to the eigenfunctions. In an MG approach, we can then make a choice as to how to proceed. The first way, which follows closely standard electronic structure methods, is to perform an MG V-cycle for the eigenvalue problem, holding the effective potential fixed during the iterations. Then, at the end of the V-cycle, the charge density and effective potential can be updated on the finest level. The solver goes back and forth between solution of the eigenvalue problem and generation of the effective potential.

A second strategy would be to update the effective potential on coarse levels *during* the V-cycle so that the eigenfunctions and effective potential evolve together.[116] This approach fits nicely into the overall MG philosophy and has been implemented successfully in DFT calculations.[119,120] However, it was found in Ref. 119 that simultaneously updating the potential on coarse levels does not lead to a significant improvement in overall efficiency. The reasons for this are not entirely clear.

LINEAR SCALING FOR ELECTRONIC STRUCTURE?

It was argued above that many chemical systems exhibit some degree of localization. What this means is that if one atom moves by a small amount, the electrons and nuclei relax in a way that screens out, over some length scale, the effects of that movement. This concept can be quantified by looking at the one-electron density matrix.[110] In a Kohn–Sham calculation, the electron density at a point $\mathbf{r}$ is given by

$$\rho(\mathbf{r}) = 2\sum_{i=1}^{N_e/2} |\psi_i(\mathbf{r})|^2 \qquad [44]$$

A generalization of Eq. [44] yields the one-electron density matrix:

$$\gamma(\mathbf{r}, \mathbf{r}') = 2\sum_{i=1}^{N_e/2} \psi_i(\mathbf{r})\psi_i^*(\mathbf{r}') \qquad [45]$$

The total energy in Hartree–Fock theory or DFT can be expressed entirely in terms of this density matrix. It can be shown that, for systems with a band gap (that is, a separation between the highest occupied molecular orbital (HOMO) and the lowest unoccupied molecular orbital (LUMO) energies)[121] or for

metals at finite temperature,[122] the density matrix defined above decays exponentially with distance:

$$\gamma(\mathbf{r}, \mathbf{r}') \propto \exp(-c|\mathbf{r} - \mathbf{r}'|) \qquad [46]$$

where c is a constant that depends on the magnitude of the band gap and/or the temperature. (Metals at zero temperature are more difficult to handle since the decay with distance is then only algebraic.[55]) Thus, in principle, we should be able to represent the density matrix in some basis of localized functions and discard information beyond a specified cutoff. This truncation should have little impact on computed energies if it is chosen to be large enough to include most of the relevant physical information (oscillations in the density matrix).

The MG eigenvalue method discussed above possesses computational scaling that is more than linear in several parts of the algorithm. A goal of modern computational chemistry is to drive that scaling down to near linear, and a great deal of effort has been directed at achieving this optimal scaling.[92] Attempts at linear scaling have been made in traditional basis set algorithms,[123–126] and in real-space solvers;[90,112,113,127] here we discuss the real-space approaches. If the wave functions span the whole physical domain, the basic relaxation step scales as qN_g, or N_e^2. The only way to reduce this scaling is to enforce some form of localization on the orbitals being updated. If the orbitals are restricted to have nonzero values only within some specified distance from a chosen center, the relaxation step will then scale as the number of orbitals times the constant number of grid points within the local domain.

Even more challenging are the N_e^3-scaling orthogonalization and Ritz projection steps. If the problem is reformulated in a localized-orbital representation, those costly operations can be reduced or eliminated, at the expense of other processes that crop up. One MG approach to solving this problem was developed by Fattebert and Bernholc,[90] who utilized localized, nonorthogonal orbitals to represent the electronic states. In this method the total electronic energy is minimized while enforcing the localization constraint. The formulation requires computation of the overlap matrix and its inverse and leads to a generalized eigenvalue problem in the basis of the localized orbitals. Thus, there still remain N_e^3 operations in the solver, but their prefactor tends to be small. Fattebert and Bernholc[90] observed that the cubic-scaling operations comprise only a small amount of the total work for large systems. This localized-orbital method has been generalized to an FAS-MG form by Feng and Beck.[127]

Two apparent drawbacks of the localized-orbital approach exist. First, the convergence of the total energy stalls at a value above the exact numerical solution depending on the size of the cutoff radius for the orbitals.[128] This makes sense because physical information is lost in the truncation. Second, the convergence rate appears to slow somewhat with increasing system size.[127] The observed convergence rates are still good, and competitive with other numerical methods, but this slowdown does not fit with standard MG orthodoxy—the

convergence rates should not depend on size for a properly functioning multiscale solver. An excellent discussion of the various linear-scaling approaches to electronic structure is presented in the book by Martin.[55]

OTHER NONLINEAR PROBLEMS: THE POISSON—BOLTZMANN AND POISSON—NERNST—PLANCK EQUATIONS

Poisson–Boltzmann Equation

A second nonlinear problem to consider is the Poisson–Boltzmann (PB) mean-field theory of ionic solution electrostatics.[129–134] This approximate theory has found wide application in biophysics involving problems such as protein–protein and protein–membrane interactions. At a qualitative level, the PB equation arises from replacement of the exact mobile-ion charge distribution by its average, assuming that the average is given by the Boltzmann factor for the ions interacting with the mean electrostatic potential:

$$\nabla \cdot [\varepsilon(\mathbf{r})\nabla\phi(\mathbf{r})] = -4\pi[\rho_f(\mathbf{r}) + zn_+ \exp(-\beta z\phi(\mathbf{r}) - \nu(\mathbf{r})) - zn_- \exp(\beta z\phi(\mathbf{r}) - \nu(\mathbf{r}))] \quad [47]$$

where a three-dimensional representation has been used, and $\beta = 1/kT$. Besides assuming an average distribution of mobile ions determined by the Boltzmann factor, this equation assumes that the underlying medium (water, membrane, protein) is a continuum dielectric with spatially varying dielectric constant $\varepsilon(\mathbf{r})$. For example, in a membrane protein calculation, it is common to use values of 80 for water, 4–20 for the protein interior, and 2 for the hydrophobic part of the membrane. On the right-hand side (rhs) of Eq. [47] there are three contributions to the charge density: one for fixed, discrete charges (the partial or full charges on the protein atoms), and one each for the distributed positive and negative mobile ions. The charge z is the magnitude of the charge on the mobile ions. (The physical assumptions underlying the PB equation generally imply accurate results only for $z = 1$.) The added potential $\nu(\mathbf{r})$ excludes ions from parts of space such as the membrane or protein interior domains. The variables n_+ and n_- are the bulk concentrations of the positive and negative ions in the aqueous solution far from the region of interest (where the potentials have decayed to zero due to screening).

If the electric potential happens to be small, the exponential terms in Eq. [47] can be linearized to produce

$$\nabla \cdot [\varepsilon(\mathbf{r})\nabla\phi(\mathbf{r})] = -4\pi[\rho_f(\mathbf{r}) + \beta z^2(n_+ + n_-)\phi(\mathbf{r})] \quad [48]$$

in regions of space outside the excluded volume zones specified by $v_(\mathbf{r})$. If Eq. [48] is solved in an isotropic region in which the dielectric constant does not vary in space, that dielectric constant can be moved to the other side, and the coefficient of the potential in the linearized term becomes

$$\kappa^2 = \frac{4\pi\beta z^2}{\varepsilon}(n_+ + n_-) \qquad [49]$$

which is the square of the inverse Debye screening length. If Eq. [48] is solved for a single point charge in spherical coordinates, the exponential screening is apparent:

$$\phi(r) = \frac{Z}{\varepsilon}\frac{e^{-\kappa r}}{r} \qquad [50]$$

The quantity $1/\kappa$ determines the length scale over which the potential decays due to screening from the ion cloud in this Debye–Hückel theory.

The physical effects missing from Eq. [47] are: (1) the surrounding medium is treated as a continuum, (2) the ions are assumed to be points with no excluded volume, and (3) there are no correlation effects between the ions. The PB theory has been modified to treat some of these missing effects;[135] Eq. [47] can also be derived as the mean-field limit of an exact statistical field theory,[136–139] or from more traditional statistical mechanical procedures in the theory of liquids.[140,141] Once the potential is computed by solving Eq. [47], the free energy of the ion distribution can be calculated.[136,137]

The PB equation is nonlinear in a way quite different from the eigenvalue problem. Although we are solving for a single function $\phi(\mathbf{r})$ over the whole domain as in the Poisson equation, a strong nonlinearity arises due to the exponential terms on the right side of Eq. [47]. Treatment of nonlinearities in MG solvers has been discussed extensively in the early work of Brandt and co-workers[107,108] and in Ref. 105. The FAS-MG method described above is designed to handle both linear and nonlinear problems. We do not go through all the technical details of solving the PB equation with MG methods, but note below some of the stumbling blocks that had to be overcome. Further details can be found in Refs. 58 and 142–147. Other biophysical electrostatics methods will also be discussed in the applications section below.

Discrete charges in Eq. [47] lead to large electrostatic potentials. Therefore, the nonlinearity can be substantial near those charges, while away from the discrete charges, the potential gets screened by the mobile ions, and the nonlinearity is smaller. Several points need to be highlighted. First, the fine grid must be of high enough resolution to contain at least several points over the distance corresponding to the Debye screening length; if this condition is not met, the solver can become unstable. Second, as noted in Ref. 58, the continuum form of Eq. [47], as written, does not conserve charge

over the domain (when discretized on a lattice). A lattice field theory[136–138] includes a normalization step that does lead to exact charge balance in the examined domain, by adjusting the bulk densities self-consistently. This is an important point because the lack of conservation may become more pronounced on coarser levels without the normalization. Third, the defect correction must contain terms related to the nonlinearity. Fourth, the driving term f^h (see Eq. [40]) includes the nonlinear terms during the relaxation steps. Finally, discontinuities in the dielectric constant can lead to numerical difficulties. We have found, however, that for typical dielectric constants in biological problems (80 for water, 2 for the internal parts of membranes, and 4–20 for protein interiors), these issues can be handled directly in FAS solvers[58,142,148] without the special techniques developed in Ref. 149.

Poisson–Nernst–Planck (PNP) Equations for Ion Transport

All of the problems discussed so far pertain to static or equilibrium solutions of partial differential equations. Many problems in chemistry are nonequilibrium in nature, however, and here we discuss briefly one approximate means of modeling transport (the PNP theory),[4,19,150] and techniques used for solving the relevant equations with MG methods. The underlying equations first involve solution of the diffusion equation in the presence of an external potential, and then solution of the Poisson equation to generate a new potential. The two equations must be solved repeatedly—one equation affects the other. If the transport process is steady state (i. e., the particle densities do not change with time), the problem can then be recast as two Poisson-type equations that must be solved self-consistently. The nonlinearity arises from the coupling of the two equations. Typical applications would include the study of ion transport through a semiconductor device or through an ion channel in biology.

The conservation law for the ion transport is

$$\frac{\partial \rho(\mathbf{r}, t)}{\partial t} = -\nabla \cdot \mathbf{j}(\mathbf{r}, t) \qquad [51]$$

where $\rho(\mathbf{r}, t)$ is the particle number density, and $\mathbf{j}(\mathbf{r}, t)$ is the current. There is a conservation equation for each of the chemical species, but we omit those labels here. The diffusion (or Smoluchowski) equation results from the assumption that the particles move in a medium where their motion is rapidly damped and thermalized;[151] this is the Brownian motion assumption. Then

$$\mathbf{j}(\mathbf{r}, t) = D(\mathbf{r})[\nabla \rho(\mathbf{r}, t) + \beta \nabla \phi(\mathbf{r}) \rho(\mathbf{r}, t)] \qquad [52a]$$

$$= D(\mathbf{r}) \exp[-\beta \phi(\mathbf{r})] \nabla \exp[\beta \phi(\mathbf{r})] \rho(\mathbf{r}, t) \qquad [52b]$$

A particle charge of 1 has been assumed here. Three regimes for this equation are possible. First, if there is no current [$\mathbf{j}(\mathbf{r}, t) = 0$], Eq. [52] along with the Poisson equation [which determines the potential $\phi(\mathbf{r})$] lead to the PB equation; this is the equilibrium situation. Second, if the particle densities are not changing [$\rho(\mathbf{r}, t) = \text{constant}$], the steady-state (Nernst–Planck) case is obtained:

$$\nabla \cdot \mathbf{j}(\mathbf{r}, t) = 0 \qquad [53]$$

By insertion of Eq. [52b] for $\mathbf{j}(\mathbf{r}, t)$ into this equation, it is easy to see that a Poisson-type equation is obtained (actually a Laplace equation, with the rhs equal to zero). If the diffusion coefficient is a constant over the domain, then that variable drops out. Notice that, in Eq. [52b], an effective "dielectric constant" [$\exp(-\beta\phi(\mathbf{r}))$] appears, and this expression can vary over orders of magnitude due to large variations in the potential. Finally, if we seek a solution to the time-dependent problem, we must solve the full Smoluchowski equation iteratively. The particle density then depends explicitly on time.

The well-known PNP transport equations correspond to the steady-state case. Any transients are assumed to have died out, so the particle number densities are constant; transport still occurs in a way that maintains those constant particle densities. The PNP-type equations have found wide application in semiconductor physics[152] and more recently in ion channel biophysics. A recent study has moved beyond the steady-state regime to examine real-time transport related to enzyme kinetics.[153]

At the PNP level, our group has developed an efficient FAS-MG solver for the coupled equations, and we found that the choice of relaxation and interpolation schemes plays a crucial role in stability and efficiency. The Poisson part of the problem is standard and requires no special considerations. The Nernst–Planck part, however, contains strongly varying functions (as discussed above), and this is where focus on the relaxation and interpolation operations is required.

The Laplace equation for the diffusion part of the PNP equations (for one of the ionic species) can be written as

$$\nabla[\theta(\mathbf{r})\nabla\psi(\mathbf{r})] = 0 \qquad [54]$$

where

$$\theta(\mathbf{r}) = \exp[-\beta z\phi(\mathbf{r})] \qquad [55]$$

and

$$\psi(\mathbf{r}) = \exp[\beta z\phi(\mathbf{r})]\rho(\mathbf{r}, t) \qquad [56]$$

The particle charge z has been added to show that these functions depend strongly on the charge. The equation is discretized at the point $\mathbf{r}_i$ by employing Gauss's law for a small cube of volume $V = h^3$, where h is the grid spacing:

$$\frac{V}{h}\sum_{J=1}^{6}\tfrac{1}{2}[\theta(\mathbf{r}_i + h\mathbf{j}) + \theta(\mathbf{r}_i)]\left[\frac{\psi(\mathbf{r}_i + h\mathbf{j}) - \psi(\mathbf{r}_i)}{h}\right] = 0 \qquad [57]$$

where the vectors $\boldsymbol{j}$ are directed to the six faces of the cube. The right-hand side is not zero on coarser levels in an FAS solver due to the defect correction. If Eq. [55] and [56] are substituted into Eq. [57], and the resulting equation solved for the density, the following expression is obtained:

$$\rho(\mathbf{r}_i) = \frac{\sum_{j=1}^{6}\left[1 + \exp\left\{\frac{z}{kT}(\phi(\mathbf{r}_i + h\mathbf{j}) - \phi(\mathbf{r}_i))\right\}\right]\rho(\mathbf{r}_i + h\mathbf{j})}{\sum_{j=1}^{6}\left[1 + \exp\left\{-\frac{z}{kT}(\phi(\mathbf{r}_i + h\mathbf{j}) - \phi(\mathbf{r}_i))\right\}\right]} \qquad [58]$$

This formula involves only the exponential of *differences* of the potential (between neighboring grid points), and thus it is relatively well behaved. So long as the potential is relatively smooth, a further approximation can be made:

$$\rho(\mathbf{r}_i) = \frac{\sum_{j=1}^{6}\left[1 + \frac{z}{2kT}(\phi(\mathbf{r}_i + h\mathbf{j}) - \phi(\mathbf{r}_i))\right]\rho(\mathbf{r}_i + h\mathbf{j})}{\sum_{j=1}^{6}\left[1 - \frac{z}{2kT}(\phi(\mathbf{r}_i + h\mathbf{j}) - \phi(\mathbf{r}_i))\right]} \qquad [59]$$

Recall that a term for the defect correction must be added to the numerator for coarse-grid iterations in an FAS V-cycle. On the finer grids, Eq. [59] works well since the potential does not vary much between grid points. On coarser grids, however, the linearization may not be feasible, and use of Eq. [58] may be necessary instead (this, of course, depends on the actual physical problem being examined). For the steady-state case, Eqs. [58] and [59] are also possible choices for the interpolation operator. Successive overrelaxation (SOR) was utilized by us for the relaxation steps, and the old and new charge densities were mixed with a weighting factor during the self-consistent updates to ensure stability.

The above-described algorithm was developed and tested successfully on several simple model systems. The method was further tested on the more challenging gramicidin A channel; our results correspond well with the published results in Refs. 154 and 155. The main conclusion from our work is that the FAS-MG approach leads to one order-of-magnitude improvement in

the convergence rate relative to SOR on a single level. The code is available upon request.[156]

SOME ADVICE ON WRITING MULTIGRID SOLVERS

It may be helpful to share a few lessons we have learned in writing grid-based codes. The first advice is to start with very simple problems; a good place to start in fact is with the Poisson equation in one dimension, with a finite domain (see Fig. 5). The potential can be fixed at 0 on the edges of the domain, and if a single-point charge is placed somewhere in the domain, the solution $\phi(x)$ is in the shape of a V (oriented normally or upside down depending on the charge). The first step is to write a relaxation code and test it on a modest-sized domain: say 65 grid points including the boundary points. The relaxations will converge to the exact numerical answer rather quickly. (Hundreds or even thousands of iterations may be required but, with such a small number of grid points, the calculation is, nonetheless, fast.)

There are two measures of error in a numerical grid solution.[108] One is the error between the current approximation on the grid and the exact grid result. That difference is a measure of the progress to the *numerical* solution. The other error measure is the difference between the exact numerical solution and the analytical solution (where that exists). There is no reason to converge the numerical solution beyond the point where the first error is smaller than the second. It is useful at the initial stages, however, to make sure the grid equations are correct and the code is error free by continuing iterations until machine precision zero is obtained for the residual.

It is then best to write a two-level MG-FAS code. This involves writing new routines for calculation of the defect correction and the interpolation and restriction operations. For the Poisson problem, if Gauss–Seidel iteration is employed on each level, and only a few relaxations are performed, the residual should decrease by roughly one order of magnitude per full V-cycle. With only two levels, the residual reduction will likely be smaller than this theoretical expectation. It is recommended to allow for repeated V-cycles as in Figure 4 to test whether the code can converge the residual to machine precision zero. Once a two-level code is written, most of the important steps are in place, and it is easy to go to many levels. As discussed earlier, an additional term is required in the defect correction for levels two or more removed from the finest level. For the Poisson problem, it is good to use a coarsest grid with only one central point.

One key recommendation for writing MG codes is to make the code as modular as possible, with separate routines for each operation. Once relaxation, restriction, defect correction, and interpolation codes are developed, these can be used repeatedly for a wide range of problems. Also, preplanning and organization before starting to write the code can save a great deal of time and effort.

After successfully writing a one-dimensional Poisson code, the next step is to move to two or three dimensions. A good model problem is to solve the three-dimensional Poisson equation for a single charge at the center of the domain. The boundary values for the potential can be set to the analytical $1/r$ values and fixed. The numerical solution is finite at the origin since the charge is smeared over the grid volume h^3; the computed solution approaches the $1/r$ potential quickly as we move away from the origin, however, even with a second-order numerical approximation for the Laplacian. At any rate, once you have a working three-dimensional solver for this problem, your Poisson code is ready to go for general problems.

A next stage might be to adapt the Poisson code to run on a parallel cluster using Message Passing Interface (MPI) coding. A first step here is to partition the fine-scale domain into subdomains; the communication between the subdomains is limited to the boundary areas. If higher order Laplacians are used, however, the communication overhead increases.

Eigenvalue problems present a higher level of complexity. We recommend going back to one dimension when starting to write an eigenvalue code following the algorithm of Brandt, McCormick, and Ruge.[106] Additional routines are required to enforce wave function constraints (Gram–Schmidt orthogonalization, Ritz projection, etc.). The one-dimensional harmonic oscillator is a good model problem on which to work initially. Remember that the number of coarse levels can be limited—the coarsest level must still have enough resolution to represent, at least partially, the oscillations in the eigenfunction corresponding to the highest eigenvalue.

One issue encountered repeatedly by the author is the treatment of boundaries. On several occasions, the solver apparently worked, but then stalled at some finite residual. Almost invariably, that stalling was traced back to a slight error on the boundaries in one of the routines (restriction, interpolation, relaxation, etc). So a word of warning is: If the solver stalls before complete convergence, look first at the boundaries and how they have been handled in the code!

The author has found several basic sources to be instructive, especially in the early stages of learning about multigrid techniques. This is strictly a personal bias, but the book by Briggs, Henson, and MeCormick[105] and the early review studies by Brandt[107,108] have been particularly helpful and are recommended. They lay out both the theory and applications in clear language and are less mathematically oriented than some other multigrid sources.

APPLICATIONS OF MULTIGRID METHODS IN CHEMISTRY, BIOPHYSICS, AND MATERIALS NANOSCIENCE

In this section, we discuss recent progress in algorithms and some case studies of the application of real-space and MG methods in computational

chemistry. Because the applications have covered a wide range of topics over the last decade, this section cannot review the whole field. Rather, some representative examples will be considered from the electronic structure, electrostatics, and transport areas. The focus will be on methods that utilize MG techniques in conjunction with real-space representations, but several of the publications discussed have employed alternative real-space techniques for solving the eigenvalue (and/or total energy minimization), electrostatic, and transport problems.

Electronic Structure

In June of 2005 a CECAM workshop was held in Lyon, France, on the topics of real-space, embedding, and linear-scaling techniques for electronic structure. A special issue of *Physica Status Solidi B*[157] is devoted to the proceedings of that meeting, and several review articles appear there that thoroughly cover current methods development activities and applications. Accordingly, that is a good place to start when entering the literature of real-space methods for electronic structure. Another review covers earlier developments in the field,[58] and a recent book provides an excellent introduction to real-space methods applied to nanostructure modeling.[158]

The initial stages of real-space methods development focused on the underlying representations (FD and FE) and test studies on small systems[59,63,159–163] (e.g., diatomic molecules) to determine the accuracy of the methods, convergence with approximation order, and the rate of convergence to the exact numerical result as a function of the number of self-consistency iterations. Here we discuss the substantial progress over the last several years, which has centered on linear-scaling algorithms, alternative representations, and applications to large systems at the nanoscale. The review will be organized based on the methods of representation: finite differences, finite elements, and other approaches (such as wavelets, atomic orbitals, etc.).

In the discussion to follow, we note the difference between solving the eigenvalue problem and minimizing the total electronic energy in some orbital or density matrix representation. This distinction is important for labeling the various algorithms. If we solve the Kohn–Sham equations of DFT as an *eigenvalue* problem in real space, the wave functions must satisfy restrictions (as discussed above), namely they cover the whole physical domain and they must be normalized and orthogonal since they are the eigenfunctions of a Hermitian operator. Given those restrictions, the scaling of any real-space numerical method must go formally as cq^2N_g, where c is a constant prefactor, q is the number of eigenfunctions (typically equal to $N_e/2$), and N_g is the number of grid points in the domain. With specialized techniques (below), this scaling may be effectively reduced to cqN_g, which corresponds to the cost of updating all the wave functions on the grid.

Enforcing some localization constraint on the solved-for orbitals leads to a different kind of problem than the eigenvalue problem. The total energy can be expressed in terms of the localized orbitals, and then solving the electronic structure problem corresponds to minimizing that total energy with respect to variations of the values of the functions on the grid. Often the localized orbitals are allowed to be nonorthogonal. So for the present discussion, the relevant definitions are: (1) *wave functions* or *eigenfunctions* are solutions to the Kohn–Sham system of equations; they possess the properties of normalization and orthogonality, and they span the whole physical domain, and (2) *orbitals* may be localized functions on the grid that are used to represent the total electronic energy. They are often used to construct the density matrix. For case 2 we do not solve the eigenvalue problem in its standard form. Another common term from quantum chemistry is *basis function*; basis functions are used to "build up" the eigenfunctions or orbitals from simpler functions. The basis functions could be finite elements, Gaussian functions, or atomic-like functions. The FD method is *not* a basis function method since it results from a Taylor expansion of the function about a grid point.

The FD representation is the simplest approach and is thus the easiest to implement in MG solvers. It leads to a highly structured and banded Hamiltonian matrix, as can be inferred from Eq. [13] for the Poisson problem. That highly structured form is helpful when passing functions between grids of different resolution, which makes MG code development more straightforward. Several early works in real-space electronic structure employed FD representations, usually using high-order forms.[59–61,159,160,163] The high-order FD representation can yield accurate DFT results on grids with reasonable spacings (roughly 0.2–0.3 au).

After initial testing on small systems, Chelikowsky's group extended their real-space code (now called PARSEC) for a wide range of challenging applications.[164] The applications include quantum dots, semiconductors, nanowires, spin polarization, and molecular dynamics to determine photoelectron spectra, metal clusters, and time-dependent DFT (TDDFT) calculations for excited-state properties. PARSEC calculations have been performed on systems with more than 10,000 atoms. The PARSEC code does not utilize MG methods but rather employs Chebyshev-filtered subspace acceleration[165,166] and other efficient techniques[167] during the iterative solution process. When possible, symmetries may be exploited to reduce the numbers of atoms treated explicitly.

Two of the first efforts to adapt MG methods for DFT calculations were made by the groups of Bernholc[60,61,163] and Beck.[58,85,115,159–162] The method developed by Briggs, Sullivan, and Bernholc[60] employed an alternative FD representation called the Mehrstellen discretization. In this discretization, both the kinetic and potential portions contain off-diagonal contributions in the real-space Hamiltonian, as opposed to the standard high-order FD representation, where the kinetic energy piece contains off-diagonal terms, but the

potential is diagonal. The advantage of the Mehrstellen form is that the spatial range of the kinetic or potential pieces is smaller than that for the corresponding high-order form; this allows for lower communication overhead in a parallel implementation. A disadvantage is that more multiplications are required to update an orbital value at a grid point relative to the same order in the high-order FD form.[58] The MG algorithm of Ref. 60 leads to a significant efficiency gain relative to iterations on a single level, but the eigenvalue problem was linearized during the MG V-cycles. The method in this original work was applied to the study of several large systems, including 64-atom Si and diamond supercells for testing purposes. A similar algorithm was developed by Ancilotto, Blandin and Toigo.[168]

Iyer, Merrick, and Beck utilized a high-order FD representation and first developed a one-way multiple-grid approach.[159] A significant acceleration in the solution process was found proceeding from coarse to fine grids. Some residual stalling occurred, however. Lee, Kim, and Martin[169] proposed a related one-way multiple-level approach. While these methods accelerate the solution process, the earlier discussion of the FAS method helps to explain why this is not a true MG solver. Imagine there are only two levels, and iterations are performed on the coarser level until the problem is nearly converged. The problem is then interpolated to the finest level and iterations are performed there. The coarse-level processing removes a significant fraction of the long-wavelength errors, but not all of them. One way to look at this is that the initial coarse iterations are performed with no defect correction from a finer level. Even if the exact solution is obtained on the coarse level, residual errors remain on the finest level that are due to the neglect of the defect correction (which does not exist until the finest level is reached and iterations are performed there). Thus, true MG efficiency can only be obtained with V-cycle processes as displayed in Figures 4–6. In subsequent work, Wang and Beck[115] adapted the nonlinear FAS eigenvalue method of Brandt, McCormick, and Ruge[106] to the Kohn–Sham DFT problem. Calculations were performed on simple atomic and diatomic molecular problems at the all-electron level, and excellent convergence rates were observed in relation to linearized MG approaches.

Fattebert and Bernholc[90] developed a near-linear scaling approach by minimizing the total energy represented with localized nonorthogonal orbitals. Multiscale preconditioning was used to accelerate the solution process. Localization removes the computational overhead of orthogonalizing all of the eigenfunctions, but some N_e^3 operations remain due to required solution of a generalized eigenvalue problem and inversion of an overlap matrix. Those cubic-scaling operations are only of the form q^3, however, so for modest-sized systems they do not dominate, and near-linear scaling is observed. The method was applied initially to electronic structure calculations on the C_{60} molecule and carbon nanotubes. Feng and Beck[127] generalized the Fatterbert–Bernholc algorithm by deriving the nonlinear FAS formulation for the same set of equations. The performance of the FAS algorithm was tested on convergence rates

for benzene, C_{20}, and C_{60}. Further applications of the linear-scaling approach, including electron transport studies, are described in a recent review of nanostructure modeling by Bernholc et al.[170] Fattebert and Gygi[128,171–174] have extended the localized orbital algorithm of Ref. 90 to molecular dynamics simulations of large systems, including Si, disordered dense hydrogen, and liquid water.

As another route to lower the effective scaling of traditional eigenvalue solvers, Costiner and Ta'asan[117] took the FAS eigenvalue method[106] a step further by moving the expensive orthogonalization and Ritz projection steps to coarse levels. Their work was discussed above briefly. A general lesson from the FAS "philosophy" is that global constraints or other global operations (involving integrals over the whole physical domain) can be processed efficiently on coarse levels without destroying the convergence of the algorithm. Wijesekera, Feng, and Beck[118] adapted the Costiner–Ta'asan method to DFT and found that, while the algorithm converges nicely for highly symmetric systems with clear eigenvalue structure in the spectrum, it failed to converge for larger DFT problems with less symmetry. This failure is linked to harsher and less symmetric potentials in the DFT problem relative to the model potentials in Refs. 116 and 117. In a recent study,[119] the convergence of the algorithm was restored by performing Ritz projections for *clusters* of eigenfunctions on the finest level. The effective scaling of the algorithm is qN_g for medium-sized systems (cubic scaling will take over for very large systems). Convergence rates were tested for benzene, benzene dithiol, C_{20}, and several monomeric and dimeric amino acids. While this method does not scale linearly (since the eigenfunctions span the whole physical domain), it converges fully to the exact numerial grid result. Methods that truncate the orbitals and/or the density matrix inevitably throw away some physical information, which can lead to stalling in the energy convergence at values above the exact grid result.

One other aspect of the nonlinear FAS approach for self-consistent electronic structure deserves comment. When all the eigenfunctions and eigenvalues are updated on coarse levels, as in the FAS method, it is also possible to update the effective potential *simultaneously* there[116] rather than cycling back and forth between the eigenvalue problem and generation of the effective potential (which is typically done in traditional electronic structure methods). This is potentially a very attractive feature of the multiscale approach. It is a common problem for instabilities to arise in self-consistent electronic structure calculations. This is often due to charge sloshing[56,57] in large systems, where the electron density can undergo large oscillations during the self-consistency iterations. Mixing of the old and new charge densities can eliminate that problem. Other forms of charge preconditioning can also help.[112] We have found in our own work that the multiscale approach, by handling the long-wavelength modes of the error on coarse grids, can eliminate a significant amount of the charge-sloshing problem. Wang et al.[120] and Wijesekera,

Feng, and Beck[119] have developed MG methods that allow for the simultaneous update of the potential on coarse levels. Wang et al.[120] found rapid convergence for a method in which the charge density and resulting potential were updated on coarse levels. Wijesekera, Feng, and Beck employed the simultaneous algorithm proposed by Costiner and Ta'asan but did not observe a significant efficiency gain in relation to the sequential approach. This topic deserves further exploration for large-scale calculations.

There have been several other advances in real-space FD methodology. The Multigrid Instead of k-Space (MIKA) project has developed several variants of real-space solvers, including FD representations and MG methods. The review article by Torsti et al.[73] discusses recent algorithm development work in that group thoroughly; here we just mention their large-scale applications concerning quantum dots, quantum Hall effects, surface nanostructures, positron interactions with matter, all-electron finite elements, electron transport through nanodevices, and new wavelet algorithms. Hirose, Ono, and co-workers have developed alternative large-scale (order-N_e) FD methods for modeling nanostructures[158,175,176] and have applied these methods to study electron transport through sodium bulk/wire contacts and C_{60} bridges. They have also proposed a "double-grid" technique for efficient pseudopotential calculations. Hoshi and Fujiwara[177–179] have developed linear-scaling FD methods and, more recently, highly efficient numerical schemes for simulating nanostructure processes.

One advantage of real-space calculations is the ability to place domains of higher resolution in localized regions of space[84,85] without sacrificing algorithm efficiency. This is particularly difficult to accomplish in the context of plane-wave calculations due to their nonlocality. As an alternative to placing a *localized* mesh refinement at a specific location on a coarser mesh,[84,85] several groups have developed methods for curving the grids to generate higher resolution near nuclei.[87,88] It is sensible to have higher resolution near the nuclear locations because, even with pseudopotentials to remove the core electrons, the potential varies most rapidly there. The grid-curving methods have been found to enhance accuracy without a large gain in computational cost. Two potential disadvantages of these methods are that the Laplacian operator can become less banded relative to FD discretization on a Cartesian grid, and the grid curving transformation can be rather nonlocal (see the grid pictures in Ref. 88). These drawbacks appear to have been enough to limit the further development of the grid curving approaches. Local refinements embedded in coarser domains, which maintain the same Cartesian structure, are likely a better alternative.

An ambitious goal is to model materials at the all-electron level. Typically, for large-scale materials calculations in DFT, the core electrons are removed and replaced by a nonlocal pseudopotential. Mortensen, Hansen, and Jacobsen[180] have taken the first steps to perform all-electron DFT calculations with FD difference representations and MG acceleration. They employ the projection augmented wave method in the frozen-core approximation.

Their code is termed Gpaw, and their computational method was tested on 20 small-molecule examples and bulk-aluminum solids.

The FD representation and MG methods of solution have found application in other related areas as well. Schmid et al.[181,182] developed a Car–Parrinello scheme for updating the electron wave functions, computing forces, and moving the nuclei in a molecular dynamics simulation. In this algorithm, MG methods are used for solving the Poisson equation. Kümmel[183] has employed MG methods to solve orbital-dependent DFT problems, namely the optimized effective-potential (OEP) approach. The OEP method addresses the problem of self-interaction, which occurs in DFT formulations. FD representations have found wide application in time-dependent DFT (TDDFT) calculations, yielding accurate electronic excitation energies for complex systems. Besides the PARSEC code[164] discussed above, the `octopus` code[184] developed by Castro et al. is largely centered around TDDFT methodology for finite or periodic systems. The real-space real-time grid propagation scheme of Yabana and Bertsch[185] can be applied to highly nonlinear response properties of materials. Finally, novel FD kinetic energy representations have been developed to yield better accuracy and to overcome the nonvariational character of the standard FD representation.[186–189]

A great deal of progress has been made in recent years in developing FE methods for large-scale DFT calculations. That progress has been reviewed thoroughly by Pask and Sterne.[62] Their review also presents several applications to problems such as Si and GaAs crystals and positron distributions in the vicinity of a Cu precipitate in Fe. The positron study involved the computation of a single eigenstate (for the positron) moving in the potential of 5488 atoms. In the FE method, a local polynomial basis set is utilized to represent the wave functions or orbitals. A more general but related ''blip-function'' representation has been employed in the CONQUEST code.[112,190] That representation allows for the utilization of nonpolynomial, yet still near-local, basis functions. As discussed above, the resulting matrix representations of the FD and FE methods are quite similar, however, reflecting the real-space bandedness of the Laplacian and/or Hamiltonian. Moreover, the same length-scale preconditioning issues arise for both methods.[102]

The CONQUEST code[112] has been developed with linear-scaling applications in mind for large systems. The underlying algorithm is thus formulated in a density matrix representation, and the orbitals are truncated in space to utilize the physical ''nearsightedness'' condition for insulators. Methods for computing forces on nuclei during molecular dynamics propagation have been incorporated. This computational approach has been tested on large Si crystals (512 atoms) and other related semiconductor systems. Reference 112 presents numerical results for a 23,000-atom system consisting of a Ge hut on top of a Si(001) crystal. The CONQUEST code presently allows for the use of both blip-function and localized atomic-orbital bases. The latter approach reduces the size of the basis significantly but can lead to other basis

set convergence issues; a similar strategy has been employed in the SIESTA code (below).[191–193] When comparing the various codes and sizes of applications, it is important to remember that different systems examined can lead to very different grid size requirements; for example, O atoms may require a grid spacing three times smaller than Si atoms due to the harsher pseudopotential near the O nucleus, and this, in turn, implies 27 times more grid points.

Tsuchida and Tsukada have developed an adaptive FE algorithm for large-scale electronic structure calculations.[194–196] They utilize a three-dimensional cubic Hermite basis to represent the electron orbitals and have extended their method to linear-scaling complexity.[197] MG techniques were employed in the solution of the Poisson problem, and accurate forces suitable for molecular dynamics simulations were computed. The method was tested on diamond and cubic BN lattices and the C_{60} molecule. The FE code has also been applied to simulate liquid formamide at the ab initio level.[196] Those simulations were used to assess the accuracy of previous simulations using empirical force fields. The current version of the Tsuchida–Tsukada code is called FEMTECK;[197] this code incorporates their recently developed linear-scaling technology.

The MIKA project has developed FE solvers in addition to FD methods.[73] The FE portion of their code is based on the Elmer package. The *p*-element basis employed is based on underlying Legendre polynomials. It is pointed out in Ref. 73 that high-order polynomials are better suited for smooth functions. Near a nucleus, for example, where the wave function varies rapidly, it is better to use lower order elements. The MIKA project FE code has been tested successfully on small-to-medium-sized molecular cases. More recently it has been applied to examine electron currents through nanostructures.[198]

In other FE work, the Kaxiras[199] and Vashishta[200,201] groups have developed multiscale methods that seamlessly link a central ab initio DFT region with coarser classical molecular dynamics levels and terminate with a continuum FE domain. These new algorithms allow for the accurate modeling of a central atomic resolution domain while still incorporating forces from more distant regions treated at a continuum mechanics level; crucial applications of this kind of work are stress distributions and the propagation of cracks through solids. Finally, Yamakawa and Hyodo[202] have developed a hybrid Gaussian/FE mixed basis for all-electron DFT calculations, and the new method was successfully tested on several small-molecule cases. The use of Gaussians for the core electrons allows for a coarser FE grid for the valence electrons.

We complete this section with a listing of other algorithmic developments in real-space electronic structure. As mentioned above, the PARSEC code has incorporated alternative techniques for accelerating the solution of the eigenvalue problem based on Chebyshev-filtered subspace methods,[165,166] thus circumventing the need for multiscale methods. Jordan and Mazziotti[167] have developed new spectral difference methods for real-space electronic structure that can yield the same accuracies as the FD representation with

less computational work. These techniques have been incorporated in the PARSEC and HARES codes. High-order evolution operator forms and collective approximations for response can enhance the convergence to the exact numerical solution in DFT calculations significantly;[203,204] these new methods lead to at least one order-of-magnitude improvement in convergence rates relative to second-order schemes.

Several groups have developed linear-scaling approaches that generally rely on the spatial localization of the density matrix. Some of those algorithms have been discussed above in relation to particular applications: CONQUEST,[112] MGMol (Fattebert),[128,174] our own FAS solver,[127] MIKA,[73] Hoshi and Fujiwara's code,[177] FEMTECK,[197] and Ono and Hirose's code.[158] Vashishta and co-workers[205,206] have developed a divide-and-conquer/cellular decomposition algorithm for large-scale, linear-scaling DFT. Other linear-scaling codes include the SIESTA[191–193] and ONETEP[207] programs. SIESTA utilizes a localized, numerical atomic-orbital basis, as do the Seijo–Barandiaran Mosaico[208] and Ozaki OpenMX codes,[209,210] while ONETEP employs plane-wave ideas to generate a localized psinc basis. These methods incorporate mixtures of real-space and alternative representations. Other real-space representations based on Lagrange functions[71,72] or discrete variable representations (DVRs)[68–70,211,212] appear to offer advantages over the FD and FE methods. Linear-scaling Gaussian codes have also been developed.[123–125] Earlier linear-scaling developments are thoroughly summarized by Goedecker.[92] Applications of linear-scaling codes to very large problems have appeared recently.[206]

Real-space methods have found recent application in QM/MM methods, which couple central quantum regions with more distant molecular mechanics domains.[213,214] Wavelet applications to electronic structure are at an earlier stage of development than are the methods discussed here, but they continue to hold a great deal of promise due to their inherent multiscale nature. Several recent studies suggest that wavelets will find wide application in future electronic structure codes.[73–80,82,83]

Electrostatics

Real-space numerical solutions to problems in electrostatics have been a predominant theme in biochemistry and biophysics for some time.[129–131,133,215] In condensed-matter physics, on the other hand, FFT methods for periodic systems have dominated electrostatic calculations.[56] One reason for this difference is that computations in chemical and biophysical electrostatics typically focus on large, but finite, molecules bathed in a solution. Thus, periodic boundary conditions are often not appropriate. Also, increased resolution near molecular surfaces is much easier to enact with a real-space approach. The early biophysics computational work focused on solving the PB equation for solvation free energies of molecules and ions. Recent efforts have been directed at more efficient solvers and

applications to large-scale systems.[58,129,134] We reiterate here that continuum electrostatic methods can yield insights into solvation phenomena, but care should be taken in applying these methods because they do not account for ion correlations, finite ion sizes, and specific interactions between ions and solvent, all of which can be important for detailed free energy studies. (MG methods have been developed to go beyond the mean-field PB level of theory while still maintaining the grid representation.[135]) In this section we describe some of the recent progress in real-space electrostatic calculations. After discussion of continuum dielectric approaches, applications of MG methods used to compute electrostatic forces in molecular-level simulations will be presented, along with some alternative views of electrostatic calculations.

In the 1990s, several groups developed FD-MG solvers for the nonlinear PB equation.[58,142–148,216] As noted above, a significant nonlinearity arises due to the exponential terms for the equilibrium charge densities, and these nonlinearities can lead to numerical difficulties. This earlier work has been summarized, along with some of the potential pitfalls in PB calculations, by Coalson and Beck,[142] Beck,[58] and Baker.[134] Once a solution is obtained, the output of a PB calculation consists of the potential over the domain, from which the continuous charge distributions of the mobile ions can be computed. In addition, the potential yields an approximation for the free energy of the ion "gas," so potentials of mean force (PMFs) can be computed for interactions between large biological molecules.

Significant effort has been directed at deriving more accurate, efficient, and parallel solutions of the PB equation.[217–221] Those efforts have included adaptive FE approaches that automatically refine the mesh based on a posteriori error estimates from a coarse-level calculation. A discretize–solve–estimate–refine procedure is repeated until a solution of nearly uniform quality is obtained over the whole domain. Holst, Baker, and Wang[220] found this FE algorithm to outperform standard uniform-mesh discretization in terms of overall accuracy and efficiency. In a second study, Baker, Holst and Wang[221] tested the algorithm on challenging electrostatics problem in biophysics, namely a 36-mer DNA structure and three proteins.

Baker et al.[218] subsequently extended the adaptive focusing method to FD representations and developed a massively parallel version of their code. The algorithm obtains linear-scaling complexity due to the use of multiscale techniques. They applied the method to examination of electrostatic effects in extremely large biological nanosystems including a million-atom microtubule and the ribosome. Examination of the electrostatic potential profile for the microtubule structure identified potential drug binding sites. Similarly, the studies of the ribosome revealed interesting electrostatic effects near the active site. The potential utility of this efficient PB solver in dynamics simulations of large structures was noted.

In work simulating flexible polyelectrolyte structures with free energies determined by solution of the PB equation, Tsonchev et al.[148] modeled the

polyelectrolytes moving in the background of an ion gas. In these Monte Carlo simulations, the PB equation was solved for each test conformation, and the solution produced the free energy for the conformation. The PB equation was solved with an FD-MG algorithm (and compared with more standard solution techniques). The most efficient method presented in Ref. 148 was the MG algorithm coupled with a configurational-bias Monte Carlo (CBMC) procedure for simulating the flexible chains. In that approach, a linearized form of the PB potential (the Debye–Hückel potential),

$$\frac{v_{\mathrm{DH}}(r)}{kT} = Z^2 \lambda_B \frac{e^{-\kappa r}}{r} \qquad [60]$$

was employed to guide the generation of a new trial chain in the CBMC process. In Eq. [60], Z is the charge, λ_B is a physical parameter termed the Bjerrum length (which is about 7 Å in water), and κ is the inverse of the Debye–Hückel screening length. Then, following chain growth, the full PB equation was solved to yield a correction to the free energy beyond the Debye–Hückel level. That is, the simulation moves on the free energy surface determined by the nonlinear PB level of theory. Tens of thousands of numerical solutions of the PB equation were required. Simulations were performed for a range of polyelectrolyte charge densities both above and below the Manning condensation limit. This kind of simulation is similar in spirit to the Born–Oppenheimer ab initio simulation methods discussed above in the electronic structure section; in those methods the nuclei move based on forces determined by the ground-state electronic surface (Hellman–Feynman forces).[182] Here the mobile ion distribution is assumed to relax quickly for a given polymer configuration, and the free energy of the configuration is computed from that equilibrium distribution. These ideas have also been applied to simulations of large-scale colloid systems and proteins.[222–225] In addition, the accuracy of the PB approximation for ions near DNA has been addressed by Ponomarev, Thayer, and Beveridge.[226]

While real-space grid methods have been applied to continuum dielectric problems for some time, their utilization for computations of electrostatic forces in molecular-level simulations is rather new. Long-ranged forces such as the Coulomb potential present difficult challenges for molecular simulation, and those components of molecular dynamics codes typically consume a large fraction of the computational time. Significant efforts have been directed at improving the speed and scaling of electrostatics calculations.

The Coulomb potential in simulations of periodic systems is typically computed with the Ewald method.[227] This clever idea from 1921 partitions the problem into a locally screened potential and a long-range part that can be handled with a momentum space sum. The method formally scales as $N^{3/2}$ if an optimal width parameter is used for the often-used Gaussian screening functions. The locally screened part of the potential decays rapidly with

distance from a given nucleus, so that part of the calculation scales linearly with system size. An alternative to the momentum-space sum is to discretize the continuous Gaussian functions on a grid and solve the long-ranged part with either an FFT[228] or real-space MG method.[229] This approach results in $N \log N$ (FFT) or N (MG) scaling and is called the particle-mesh-Ewald (PME) method. It is now a standard for large-scale biomolecular simulations, and the method has been extended to include fixed and induced dipolar interactions.[230]

It should be emphasized that the proper handling of long-ranged electrostatics has been shown to be crucial for accurate free energy calculations in molecular simulations. Errors of many kilo calories/mole can occur if the electrostatic potential is artificially truncated. In addition, if proper self-energy corrections are included, accurate free energies for charged systems can be obtained with remarkably few solvent (water) molecules in the simulation box.[227,231,232] In fact, it makes more sense physically in modeling ion free energies to calculate those free energies for a charged system, since neutralization with an ion of the opposite charge necessarily creates a high-concentration environment. These issues have not been widely recognized until recently.

Finally, we list some interesting developments related to alternative forms of electrostatics calculations. Pask and Sterne[233] pointed out that real-space electrostatic calculations for periodic systems require no information from outside the central box. Rather, we only need the charge density within the box and the appropriate boundary conditions to obtain the electrostatic potential for the infinite system. These ideas were used earlier in an initial MG effort to compute Madelung constants in crystals.[160] So long as charge balance exists inside the box, the computed potential is stable and yields an accurate total electrostatic energy. Thus, questions about conditional summation of the $1/r$ potential to obtain the physical electrostatic energy are unnecessary. This has also been noted in the context of Ewald methods for the simulation of liquids (See Chapter 5 in Ref. 227).

Thompson and Ayers[234] presented an interesting new technique for solving the Poisson equation "inside the box." The electrostatic potential is expanded in a set of sine functions, which leads to simple analytic forms for the Coulomb energy for systems of electrons in a box. The method is closely related to FFT methods and scales linearly with system size. Both finite and periodic systems were considered. Juselius and Sundholm[235] developed a FE method for electrostatics that employs Lagrange interpolating polynomials as the basis. Rather than utilizing an iterative approach (as in the MG method), innovative procedures for direct numerical integration on the grid result in $N^{3/2}$ computational complexity. A parallel implementation was shown to scale linearly with system size since the matrix multiplications in the innermost loop are independent.

In the spirit of real-space methods, where all of the function updates in solving the Poisson equation are near-local in space, Maggs and Rossetto[236]

have developed a new local view of electrostatic interactions. In this approach, the electric field is the physical quantity of interest, and the canonical partition function is written in terms of this field. The Hamiltonian for the total electrostatic energy is then a grid sum of the field variable squared, times a constant. The field has a value for each neighbor link on the grid. The basic algorithm consists of solution of Gauss's law for a starting charge configuration, provides updates of the fields by shifts of the link variables, and updates the particle locations using a Monte Carlo procedure. This algorithm has been modified to overcome sampling difficulties inherent in the original approach.[237–239]

Transport Problems

Most of the problems considered above involved solving for the electron distribution given a static nuclear configuration or solving for the static Poisson or equilibrium PB electrostatic potential. In the field of ab initio simulation, the nuclei are propagated classically in real time based on forces determined by the other nuclear locations and the electron distribution, but the electrons are generally assumed to move on the ground-state surface. In many important physical systems, such as molecular electronic devices and membrane proteins, the system exists out of equilibrium, however. Thus, we must deal with electron or ion transport. These nonequilibrium cases are at a much earlier stage of development than their equilibrium counterparts, both in terms of fundamental theory and numerical applications. Here we briefly review some recent progress in modeling electron and ion transport through nanosystems.

Modeling electron transport requires a quantum treatment, as discussed in the introduction to this chapter. It is beyond the scope of this review to discuss details of the nonequilibrium Green's function approach, which is the most rigorous ab initio method at the present time.[51] Suffice it to say that the Green's function methods allow for modeling of a molecular device coupled to electrodes at the DFT level. Several computational methods have been developed to carry out the transport calculations.[43,44,46–48,175] Real-space methods are ideally suited for this purpose because the physical system involves two semi-infinite metal surfaces, with a localized molecule sandwiched between them. The use of a localized-orbital representation allows for relatively easy construction of the necessary Green's functions that enter the Landauer theory of transport. An alternative is to set up the electrode system as a scattering problem, with incident, penetrating, and reflected waves that assume a plane-wave form in the bulk electrodes. A clear description of this second approach is detailed by Hirose et al.,[158] along with its relationship to the Green's function method (with a further discussion of the alternative Lippman–Schwinger scattering theory[240]). Real-space methods have found application in both the Green's function and scattering wave function approaches.

Taylor, Guo, and Wang[43] utilized a localized nonorthogonal atomic-orbital (Fireball) basis to represent the states in a DFT calculation in an early effort at an ab initio nonequilibrium Green's function approach for electron transport. The localized representation is crucial for the computation of the separate contact and molecule Green's functions. MG methods were used to solve the Poisson equation during the self-consistency cycles. Attention was focused on the role of boundary conditions in the construction of the density matrix and Green's functions. The authors applied the method successfully to a carbon nanotube–metal interface. The conductance was found to be roughly half that for infinite perfect metallic nanotubes due to the contact resistance. In a similar vein, localized numerical atomic orbitals developed for the SIESTA code were employed in a self-consistent Green's function method for transport (TranSIESTA);[44,45] the method was applied to carbon and gold nanowires, nanotubes, and molecular electronic devices. Xue and Ratner[46] proposed a related algorithm based on a Gaussian basis function representation and then studied current–voltage behavior of potential molecular electronic devices.

In terms of real-space grid calculations, Nardelli, Fattebert, and Bernholc[48] extended the linear-scaling DFT MG method of Fattebert and Bernholc to transport calculations. In their first application of the method, the transmission function, *T(E),* was computed at zero bias, which yields the linear response conductance. The method was applied to study electron transport through nanotubes in contact with metal surfaces, and in more recent work, the Bernholc group extended this approach to finite-potential contacts.[170] The method has been generalized to an FAS-MG form by Feng and Beck.[47] In addition, Feng and Beck explored the use of a new constrained current approach[241,242] for electron transport, which differs from the full Green's function method in that the current is *imposed* on the system and the driving potential drop must then be computed. It was found, however, that the charge density is invariant to a change of sign of the current, indicating that the method will always predict zero potential drop. Bokes and Godby[243,244] presented a maximum entropy theory that rationalizes this observation. Further work is necessary to relate the constrained current/maximum entropy picture to the Green's function approach.

In related work, Sasaki, Ono, and Hirose developed a linear-scaling FD code for semi-infinite systems[176] that was used to examine electron transport through atomic nanowires and, more recently, to study conduction properties of C_{60} bridges. Doping with Li atoms was found to increase the conductivity through the bridge significantly. In addition to FD representations for the electron states, FE methods have been utilized for transport calculations applied to nanostructures.[73,198] The group developing the real-space `octopus` code for TDDFT calculations[184] is planning applications to molecular electronic transport.

We close the discussion of real-space applications in transport calculations with a brief overview of work on ion (as opposed to electron) transport.

We discussed above solution of the PNP equations, which couple Poisson and diffusion problems to solve for the steady-state transport.[4,20] The PNP theory is a mean-field theory where, like in the PB equation, the ions are assumed to be pointlike and uncorrelated. In addition, the surrounding solvent is treated as a dielectric continuum. These methods are thus adequate for studying transport through pores that are much larger than the size of the ions, but unsatisfactory for some of the most important ion channels in biology where the pore size is comparable to the ion size. Nevertheless, by incorporating physically reasonable diffusion constants and dielectric profiles, decent results can be obtained in some cases, and if the pores are larger, accurate results are possible.

In the field of continuum-modeled ion transport through channels, pioneering work has been done by the Eisenberg[4] and Coalson[20] groups. Kurnikova et al.[245,246] first developed a numerical real-space three-dimensional solver for the PNP equations and applied that method to examining cation transport through the gramicidin channel. In their work, a successive overrelaxation method (on a single grid) was employed to obtain convergence. MG methods can significantly accelerate the rate of convergence to the solution, as discussed above.

More recently, Cheng et al.[153] developed an FE numerical technique to model diffusion in large biomolecular systems. Their simulations do not assume steady-state diffusion, but rather, solve the time-dependent Smoluchowski equation directly; the steady-state limit may emerge as the solution progresses. Rates for inhibitor binding to acetylcholinesterase were computed for several ionic strengths. Electrostatic steering was found to be important.

If we want to go beyond the rather severe physical limitations of the PNP theory, a first step is to model the transport via Brownian dynamics.[11,132,247–249] Here the ions are modeled discretely, but the solvent and surrounding macromolecules are treated as dielectric continua. Additionally, when considering ion transport through channels, the protein is typically maintained in a fixed configuration. Ion correlations are accounted for with this approach, however, at least approximately. Even though it is a challenging goal to model ion transport at the all-atom level, efforts are progressing on this front as well.[250,251] The necessary system size for ion channels as an example is often over 100,000 atoms, and one ion transit event can be expected to occur on the tens of nanoseconds time scale. To compute currents accurately, simulations approaching microseconds are thus required.

EXISTING REAL-SPACE AND MULTIGRID CODES

Compiled here are existing electronic structure, electrostatics, and transport codes that utilize real-space and MG or multiscale methods. The vitality of this field of computational science is self-evident.

Electronic Structure

- SIESTA: General-purpose electronic structure code. Uses localized numerical atomic orbitals and real-space grids for computation of Hartree and gradient-corrected exchange–correlation potentials. Linear-scaling capabilities. Can perform ab initio molecular dynamics simulations. Available: http://www.uam.es/departamentos/ciencias/fismateriac/siesta/. The Mosaico code has been implemented in the SIESTA package.
- MIKA: Real-space MG code. Recent developments in the MIKA code and affiliated methodology are thoroughly discussed by Torsti et al.[73] Available: http://www.csc.fi/physics/mika.
- ONETEP: Plane-wave-based method that utilizes a psinc localized/orthogonal basis. Linear-scaling capabilities. Thorough discussion presented by Skylaris et al.[113] Available: http://www.onetep.soton.ac.uk/.
- PARSEC: High-order FD code from the Chelikowsky group. Many applications and capabilities summarized by Kronik et al.[164] Available: http://www.ices.utexas.edu/~mtiago/parsec/index.html.
- MGmol: Real-space MG code for MD simulations developed by J.-L. Fattebert at Lawrence Livermore National Laboratory. Available: http://www.llnl.gov/casc/MolecularDynamics/.
- Bernholc group code: Real-space MG code with applications to a wide range of nanosystems. Available: http://nemo.physics.ncsu.edu/~luw/.
- ACRES: Adaptive-grid real-space code from the Kaxiras group. A modified version is called HARES. Available: http://cst-www.nrl.navy.mil/~singh/acres/info.html.
- GPaw: All-electron real-space code using projected augmented wave method and frozen core approximation. Available: http://www.camd.dtu.dk/software.aspx.
- OpenMX: Linear-scaling method that utilizes variationally optimized atomic orbitals. Available: http://www.openmx-square.org/.
- FEMTECK: Finite-element code from Tsuchida's group. Linear-scaling capabilities. Available: http://unit.aist.go.jp/rics/research-e.html.
- MADNESS: Wavelet code from Oak Ridge National Laboratory. Available: http://www.csm.ornl.gov/ccsg/html/projects/madness.html.
- `octopus`: Real-space code specifically directed at time-dependent DFT (TDDFT) calculations. Available: http://www.tddft.org/programs/octopus.

Electrostatics

- APBS: Adaptive PB solver developed by Holst/Baker/McCammon et al. FE methods with adaptivity to solve PB equation for biomolecular

complexes. Also time-dependent diffusional processes (below). Available: http://apbs.sourceforge.net/.

- UHBD: Solves the linearized or nonlinear PB equation. Available: http://mccammon.ucsd.edu/uhbd.html.
- Charmm PB: APBS codes utilized in the CHARMM package. Available: http://biowulf.nih.gov/apps/charmm/charmmdoc/c33b2/apbs.html, or FD approach http://biowulf.nih.gov/apps/charmm/charmmdoc/c33b2/pbeq.html.
- DelPhi: Code to solve the linearized PB equation. Available: http://wiki.c2b2.columbia.edu/honiglab_public/index.php/Main_Page.
- PME in AMBER: Sagui's group has contributed MG solvers to the PME forcefields. Available: http://amber.scripps.edu/.

Transport

- APBS (above): Models for ion and large biomolecule transport.
- PNP solver: Beck group MG-PNP solver for ion transport is freely available on request. Contact thomas.beck@uc.edu.
- TranSIESTA: General-purpose electronic structure code (above), adapted to electron transport calculations.
- MIKA: General-purpose real-space electronic structure code (above), adapted to electron transport calculations.
- `octopus`: Real-space electronic structure code (above) with emphasis on TDDFT and electron transport codes planned.

This list is not complete, but it should provide a good entry into available software for real-space calculations. It is interesting to note that the real-space field has gone from a few developmental studies to a wide range of relatively mature codes in about 15 years.

SOME SPECULATIONS ON THE FUTURE

This last section presents a few speculations on research directions that may be pursued in the future.

Chemistry and Physics: When Shall the Twain Meet?

Chemists are steeped in the tradition of wave functions and basis set calculations.[53] This mindset has come about mainly because the wave function/orbital picture has been extremely helpful in the development of chemical ideas. Physicists, on the other hand, have traditionally focused on periodic

systems, convergent plane-wave expansions, and alternative statistical representations such as the Thomas–Fermi theory for electron densities.[55] It is interesting that most of the recent real-space developments have come out of academic physics groups and national laboratories around the world, with the initial motivation often being the modeling of nanostructures. It is likely that the real-space, localized orbital ideas will have growing influence in chemistry in the future since a great deal of modern chemical research is directed at nanosystems and biological macromolecules. Sometimes it takes a decade or more for a major shift to take hold.

Elimination of Molecular Orbitals?

As discussed above, wave functions and basis set expansions have had a wide influence in chemistry. But long ago, Coulson suggested that quantum chemical computations should focus instead on the one- and two-electron density matrices[252] because these physical quantitites yield a much-reduced, yet complete, description of the electronic structure. This goal has been pursued off and on since Coulson's comments, and there continue to be developments in this area.[253] It is likely that this way of looking at electronic structure will have a large impact in the future, perhaps coupled with ideas from quantum Monte Carlo methods and stochastic differential equations.[254] An even more aggressive step away from wave functions is the integral formulation of DFT.[110,255,256] While there has been significant interest in this formal theory, and some developments of orbital-free methods,[257,258] this appproach has not reached its full potential in computational electronic structure. It is the one approach to DFT that is truly in the spirit of the Hohenberg–Kohn theorem because the only object that enters the theory is the physical electron density.

Larger Scale DFT, Electrostatics, and Transport

Ever-larger systems are being examined in biochemical and biophysical research, as exemplified by studies on microtubules and the ribosome,[218] and new algorithms and more powerful massively parallel machines will propagate this trend. In terms of increased complexity, the author believes that more and more biological phenomena will be shown to require a quantum treatment, at least in a local region of space. An example discussed in this chapter is the solvation of anions in ion channels and in water where the polarizability is an important physical quantity linked to the pervasive Hofmeister series that continues to crop up in a wide array of biological and colloid systems.[39] Quantum effects are also important for studies of reaction dynamics where tunneling occurs as outlined by Truhlar et al. in a previous volume of this series.[259] It might seem that ever-larger computers will lead the way, but the author predicts that novel algorithms and new physical ideas will "win out" over hardware advances in how we model complex chemical and biological phenomena. Of course, these

advances can occur together, and they often mutually influence each other. It is comforting to note that several new physical ideas for solving the Poisson equation have appeared in the last few years, and this equation and various traditional methods of solution are as old as the hills!

Reiteration of "Why Real Space?"

One predominant theme in this chapter is computational and physical locality. It has been argued that the conjunction of physical localization due to screening and computational locality resulting from real-space approaches is the physically "preferred" way to proceed for large-scale modeling. That conclusion is not likely to change in the near or even far future. Multiscale solvers are required in order to overcome "critical slowing down" in the solution process once this locality has been exploited. The adaptivity feature of real-space methods (without loss of efficiency) provides another bonus. For these reasons, it appears that real-space approaches for accurate modeling of large systems will be a major theme in computational chemistry for years to come.

To end this tutorial, we mention a new physical theory of liquid solutions that presents a statistical mechanical version of real-space partitioning. In this quasi-chemical theory,[227] the space around a distinguished solute is divided into inner-shell and outer-shell domains. The final result for the solvation free energy does not depend on the choice for the cutoff. Approximations may be inserted once the basic theory is formulated, however, and that is where errors may crop up in the computation of free energies. For example, a quantum chemical treatment can be employed for the inner-shell region, where specific interactions may be strong if considering a system like a multiply charged ion in water. The more distant regions may then be treated at a classical molecular dynamics level or even a dielectric continuum level. The key chemical interactions are modeled accurately in this way, while the more averaged distant contributions are treated approximately. Accurate solvation free energies for ions have been obtained with this theory. The important point here is that real-space computational approaches need to be incorporated into a physically motivated and accurate statistical mechanical theory to predict reliably the free energies that are the driving forces for chemical processes.

ACKNOWLEDGMENTS

This research was supported by the National Science Foundation (CHE-0112322, CHE-0709560) and the Department of Defense (Army) MURI program (DAAD19-02-1-0227). I thank Achi Brandt, Rob Coalson, Lawrence Pratt, Michael Paulaitis, and members of my research group for stimulating discussions and collaborations. I also thank Jean-Luc Fattebert and Eduardo Hernandez for reading and commenting on the manuscript prior to publication. I especially thank Zhifeng Kuang for his contributions to the chloride channel research and to the development of the PNP code discussed in this chapter.

REFERENCES

1. B. Hille, *Ion Channels of Excitable Membranes*, Sinauer Associates, Sunderland, 2001.
2. W. D. Stein, *Channels, Carriers, and Pumps: An Introduction to Membrane Transport*, Academic, New York, 1990.
3. F. M. Ashcroft, *Ion Channels and Disease*, Academic, New York, 2000.
4. M. Saraniti, S. Aboud, and R. Eisenberg, in *Reviews in Computational Chemistry*, K. B. Lipkowitz, T. R. Cundari, and V. J. Gillet, Eds., Wiley, Hoboken, NJ, 2006, Vol. 22, pp. 229–293. The Simulation of Ionic Charge Transport in Biological Ion Channels: An Introduction to Numerical Methods.
5. T. J. Jentsch, I. Neagoe, and O. Scheel, *Curr. Opin. Neurobiol.*, **15**, 319–325 (2005). CLC Chloride Channels and Transporters.
6. M. Pusch, G. Zifarelli, A. R. Murgia, A. Picollo, and E. Babini, *Exp. Physiol.*, **91**, 149–152 (2006). Channel or Transporter? The CLC Saga Continues.
7. R. Dutzler, E. B. Campbell, M. Cadene, B. T. Chait, and R. MacKinnon, *Nature*, **415**, 287–294 (2002). X-ray Structure of a ClC Chloride Channel at 3.0 Angstrom Reveals the Molecular Basis of Anion Selectivity.
8. R. Dutzler, E. B. Campbell, and R. MacKinnon, *Science*, **300**, 108–112 (2003). Gating the Selectivity Filter in ClC Chloride Channels.
9. J. Yin, Z. Kuang, U. Mahankali, and T. L. Beck, *Proteins: Struct., Func., Bioinform.*, **57**, 414–421 (2004). Ion Transit Pathways and Gating in ClC Chloride Channels.
10. O. Moran, S. Traverso, L. Elia, and M. Pusch, *Biochemistry*, **42**, 5176–5185 (2003). Molecular Modeling of *p*-Chlorophenoxyacetic Acid Binding to the CLC-0 Channel.
11. B. Corry, M. O'Mara, and S. H. Chung, *Biophys. J.*, **86**, 846–860 (2004). Conduction Mechanisms of Chloride Ions in ClC-type Channels.
12. D. Bisset, B. Corry, and S. H. Chung, *Biophys. J.*, **89**, 179–186 (2005). The Fast Gating Mechanism in ClC-0 Channels.
13. J. Cohen and K. Schulten, *Biophys. J.*, **86**, 836–845 (2004). Mechanism of Anionic Conduction Across ClC.
14. F. L. Gervasio, M. Parrinello, M. Ceccarelli, and M. L. Klein, *J. Mol. Biol.*, **361**, 390–398 (2006). Exploring the Gating Mechanism in the ClC Chloride Channel via Metadynamics.
15. D. L. Bostick and M. L. Berkowitz, *Biophys. J.*, **87**, 1686–1696 (2004). Exterior Site Occupancy Infers Chloride-Induced Proton Gating in a Prokaryotic Homolog of the ClC Chloride Channel.
16. G. V. Miloshevsky and P. C. Jordan, *Biophys. J.*, **86**, 825–835 (2004). Anion Pathway and Potential Energy Profiles Along Curvilinear Bacterial ClC Cl− Pores: Electrostatic Effects of Charged Residues.
17. Z. Kuang, U. Mahankali, and T. L. Beck, *Proteins: Struct., Funct., Bioinform.*, **68**, 26–33 (2007). Proton Pathways and H^+/Cl^- Stoichiometry in Bacterial Chloride Transporters.
18. M. H. Cheng, A. B. Mamonov, J. W. Dukes, and R. D. Coalson, *J. Phys. Chem. B*, **111**, 5956–5965 (2007). Modeling the Fast Gating Mechanism in the ClC-0 Chloride Channel.
19. B. Roux, T. Allen, S. Berneche, and W. Im, *Quart. Rev. Biophys.*, **37**, 15–103 (2004). Theoretical and Computational Models of Biological Ion Channels.
20. R. D. Coalson and M. G. Kurnikova, *IEEE Trans. Nanobiosci.*, **4**, 81–93 (2005). Poisson-Nernst-Planck Theory Approach to the Calculation of Current through Biological Ion Channels.
21. A. Warshel, *Proc. Natl. Acad. Sci. U.S.A.*, **102**, 1813–1814 (2005). Inverting the Selectivity of Aquaporin 6: Gating versus Direct Electrostatic Interaction.
22. A. Burykin and A. Warshel, *FEBS Lett.*, **570**, 41–46 (2004). On the Origin of the Electrostatic Barrier for Proton Transport in Aquaporin.

23. M. Kato, A. V. Pisliakov, and A. Warshel, *Proteins: Struct., Funct., Bioinform.*, **64**, 829–844 (2006). The Barrier for Proton Transport in Aquaporins as a Challenge for Electrostatic Models: The Role of Protein Relaxation in Mutational Calculations.
24. A. Burykin and A. Warshel, *Biophys. J.*, **85**, 3696–3706 (2003). What Really Prevents Proton Transport through Aquaporin? Charge Self-Energy versus Proton Wire Proposals.
25. S. Braun-Sand, A. Burykin, Z. T. Chu, and A. Warshel, *J. Phys. Chem. B*, **109**, 583–592 (2005). Realistic Simulations of Proton Transport along the Gramicidin Channel: Demonstrating the Importance of Solvation Effects.
26. M. Kato, A. V. Pisliakov, and A. Warshel, *Proteins: Struct., Funct., Bioinform.*, **64**, 829–844 (2006). The Barrier for Proton Transport in Aquaporins as a Challenge for Electrostatic Models: The Role of Protein Relaxation in Mutational Calculations.
27. S. H. Chung, O. S. Anderson and V. Krishnamurthy, Eds., *Biological Membrane Ion Channels: Dynamics, Structure, and Applications*, Springer, New York, 2007.
28. D. A. Doyle, J. Morais Cabral, R. A. Pfuetzner, A. Kuo, J. M. Gulbis, S. L. Cohen, B. T. Chait, and R. MacKinnon, *Science*, **280**, 69–77 (1998). The Structure of the Potassium Channel: Molecular Basis of K^+ Conduction and Selectivity.
29. M. Maduke, C. Miller, and J. A. Mindell, *Annu. Rev. Biophys. Biomol. Struct.*, **29**, 411–438 (2000). A Decade of CLC Chloride Channels: Structure, Mechanism, and Many Unsettled Questions.
30. A. Accardi and C. Miller, *Nature*, **427**, 803–807 (2004). Secondary Active Transport Mediated by a Prokaryotic Homologue of ClC Cl-Channels.
31. A. Accardi, S. Lobet, C. Williams, C. Miller, and R. Dutzler, *J. Mol. Biol.*, **362**, 691–699 (2006). Synergism between Halide Binding and Proton Transport in a CLC-type Exchanger.
32. C. Miller, *Nature*, **440**, 484–489 (2006). ClC Chloride Channels Viewed through a Transporter Lens.
33. O. Scheel, A. A. Zdebik, S. Lourdel, and T. J. Jentsch, *Nature*, **436**, 424–427 (2005). Voltage-Dependent Electrogenic Chloride/Proton Exchange by Endosomal CLC Proteins.
34. A. Picollo and M. Pusch, *Nature*, **436**, 420–423 (2005). Chloride/Proton Antiporter Activity of Mammalian CLC Proteins ClC-4 and ClC-5.
35. A. De Angeli, D. Monachello, G. Ephritikhine, J. M. Frachisse, S. Thomine, F. Gambale, and H. Barbier-Brygoo, *Nature*, **442**, 939–942 (2006). The Nitrate/Proton Antiporter AtCLCa Mediates Nitrate Accumulation in Plant Vacuoles.
36. A. Accardi, M. Walden, W. Nguitragool, H. Jayaram, C. Williams, and C. Miller, *J. Gen. Physiol.*, **126**, 563–570 (2005). Separate Ion Pathways in a Cl^-/H^+ Exchanger.
37. M. Pusch, U. Ludewig, A. Rehfeldt, and T. J. Jentsch, *Nature*, **373**, 527–531 (1995). Gating of the Voltage-Dependent Chloride Channel CIC-0 by the Permeant Anion.
38. G. A. Voth, *Acc. Chem. Res.*, **39**, 143–150 (2006). Computer Simulation of Proton Solvation and Transport in Aqueous and Biomolecular Systems.
39. W. Kunz, P. Lo Nostro, and B. W. Ninham, *Curr. Opin. Coll. Interface Sci.*, **9**, 1–18 (2004). The Present State of Affairs with Hofmeister Effects.
40. P. Jungwirth, B. J. Finlayson-Pitts, and D. J. Tobias, *Chem. Rev.*, **106**, 1137–1139 (2006). Introduction: Structure and Chemistry at Aqueous Interfaces.
41. H. I. Petrache, I. Kimchi, D. Harries, and V. A. Parsegian, *J. Am. Chem. Soc.*, **127**, 11546–11547 (2005). Measured Depletion of Ions at the Biomembrane Interface.
42. P. Jungwirth and D. J. Tobias, *Chem. Rev.*, **106**, 1259–1281 (2006). Specific Ion Effects at the Air/Water Interface.
43. J. Taylor, H. Guo, and J. Wang, *Phys. Rev. B*, **6324**, 245407 (2001). Ab Initio Modeling of Quantum Transport Properties of Molecular Electronic Devices.
44. M. Brandbyge, J. L. Mozos, P. Ordejon, J. Taylor, and K. Stokbro, *Phys. Rev. B*, **65**, 165401 (2002). Density-Functional Method for Nonequilibrium Electron Transport.

45. K. Stokbro, J. Taylor, M. Brandbyge, J. L. Mozos, and P. Ordejon, *Comput. Mat. Sci.*, **27**, 151–160 (2003). Theoretical Study of the Nonlinear Conductance of Di-thiol Benzene Coupled to Au(111) Surfaces via Thiol and Thiolate Bonds.

46. Y. Q. Xue and M. A. Ratner, *Phys. Rev. B*, **68**, 115406 (2003). Microscopic Study of Electrical Transport through Individual Molecules with Metallic Contacts. I. Band Lineup, Voltage Drop, and High-Field Transport.

47. G. G. Feng, N. Wijesekera, and T. L. Beck, *IEEE Trans. Nanotech.*, **6**, 238–244 (2007). Real-Space Multigrid Method for Linear-Response Quantum Transport in Molecular Electronic Devices.

48. M. B. Nardelli, J. L. Fattebert, and J. Bernholc, *Phys. Rev. B*, **64**, 245423 (2001). O(N) Real-Space Method for Ab Initio Quantum Transport Calculations: Application to Carbon Nanotube-Metal Contacts.

49. M. A. Reed, C. Zhou, C. J. Muller, T. P. Burgin, and J. M. Tour, *Science*, **278**, 252–254 (1997). Conductance of a Molecular Junction.

50. P. Elliott, F. Furche, and K. Burke, in *Reviews in Computational Chemistry*, K. B. Lipkowitz and T. R. Cundari, Eds., Wiley, Hoboken, NJ, 2009, Vol. 26, pp. 91–165. Excited States from Time-Dependent Density Functional Theory.

51. S. Datta, *Electronic Transport in Mesoscopic Systems*, Cambridge University Press, Cambridge, UK, 1995.

52. J. B. Anderson, in *Reviews in Computational Chemistry*, K. B. Lipkowitz and D. B. Boyd, Eds., Wiley-VCH, New York, 1999, Vol. 13, pp. 133–182. Quantum Monte Carlo: Atoms, Molecules, Clusters, Liquids, and Solids.

53. A. Szabo and N. S. Ostlund, *Modern Quantum Chemistry: Introduction to Advanced Electronic Structure Theory*, 1st, rev. ed., McGraw-Hill, New York, 1989.

54. N. R. Kestner and J. E. Combariza, in *Reviews in Computational Chemistry*, K. B. Lipkowitz and D. B. Boyd, Eds., Wiley-VCH, New York, 1999, Vol. 13, pp. 99–132. Basis Set Superposition Errors: Theory and Practice. See also I. N. Levine, *Quantum Chemistry*, 5th ed., Prentice-Hall, Upper Saddle River, NJ, 2000.

55. R. M. Martin, *Electronic Structure: Basic Theory and Practical Methods*, Cambridge University Press, Cambridge, UK, 2004.

56. M. C. Payne, M. P. Teter, D. C. Allan, T. A. Arias, and J. D. Joannopoulos, *Rev. Mod. Phys.*, **64**, 1045–1097 (1992). Iterative Minimization Techniques for Ab Initio Total-Energy Calculations—Molecular-Dynamics and Conjugate Gradients.

57. G. Kresse and J. Furthmuller, *Phys. Rev. B*, **54**, 11169–11186 (1996). Efficient Iterative Schemes for Ab Initio Total-Energy Calculations Using a Plane-Wave Basis Set.

58. T. L. Beck, *Rev. Mod. Phys.*, **72**, 1041–1080 (2000). Real-Space Mesh Techniques in Density-Functional Theory.

59. J. R. Chelikowsky, N. Troullier, and Y. Saad, *Phys. Rev. Lett.*, **72**, 1240–1243 (1994). Finite-Difference-Pseudopotential Method—Electronic-Structure Calculations without a Basis.

60. E. L. Briggs, D. J. Sullivan, and J. Bernholc, *Phys. Rev. B*, **54**, 14362–14375 (1996). Real-Space Multigrid-Based Approach to Large-Scale Electronic Structure Calculations.

61. E. L. Briggs, D. J. Sullivan, and J. Bernholc, *Phys. Rev. B*, **52**, R5471–R5474 (1995). Large-Scale Electronic-Structure Calculations with Multigrid Acceleration.

62. J. E. Pask and P. A. Sterne, *Model. Simul. Mater. Sci. Eng.*, **13**, R71–R96 (2005). Finite Element Methods in Ab Initio Electronic Structure Calculations.

63. S. R. White, J. W. Wilkins, and M. P. Teter, *Phys. Rev. B*, **39**, 5819–5833 (1989). Finite-Element Method for Electronic-Structure.

64. J. L. Fattebert, R. D. Hornung, and A. M. Wissink, *J. Comput. Phys.*, **223**, 759–773 (2007). Finite Element Approach for Density Functional Theory Calculations on Locally-Refined Meshes.

65. L. R. Ramdas Ram-Mohan, *Finite Element and Boundary Element Applications in Quantum Mechanics*, Oxford, University Press, Oxford, UK, 2002.

66. V. D. Liseikin, *Grid Generation Methods*, Springer, Heidelberg, 1999.

67. I. Babuska, Ed., *Modeling, Mesh Generation, and Adaptive Numerical Methods for Partial Differential Equations*, Springer, Heidelberg, 1995.

68. H. S. Lee and M. E. Tuckerman, *J. Phys. Chem. A*, **110**, 5549–5560 (2006). Ab Initio Molecular Dynamics with Discrete Variable Representation Basis Sets: Techniques and Application to Liquid Water.

69. H. S. Lee and M. E. Tuckerman, *J. Chem. Phys.*, **125**, 154507 (2006). Structure of Liquid Water at Ambient Temperature from Ab Initio Molecular Dynamics Performed in the Complete Basis Set Limit.

70. Y. Liu, D. A. Yarne, and M. E. Tuckerman, *Phys. Rev. B*, **68**, 125110 (2003). Ab Initio Molecular Dynamics Calculations with Simple, Localized, Orthonormal Real-Space Basis Sets.

71. K. Varga and S. T. Pantelides, *Phys. Stat. Sol. B*, **243**, 1110–1120 (2006). Lagrange-Function Approach to Real-Space Order-N Electronic-Structure Calculations.

72. D. Baye, *Phys. Stat. Sol. B*, **243**, 1095–1109 (2006). Lagrange-Mesh Method for Quantum-Mechanical Problems.

73. T. Torsti, T. Eirola, J. Enkovaara, T. Hakala, P. Havu, V. Havu, T. Hoynalanmaa, J. Ignatius, M. Lyly, I. Makkonen, T. T. Rantala, J. Ruokolainen, K. Ruotsalainen, E. Rasanen, H. Saarikoski, and M. J. Puska, *Phys. Stat. Sol. B*, **243**, 1016–1053 (2006). Three Real-Space Discretization Techniques in Electronic Structure Calculations.

74. S. Goedecker and C. Chauvin, *J. Theor. Comput. Chem.*, **2**, 483–495 (2003). Combining Multigrid and Wavelet Ideas to Construct More Efficient Multiscale Algorithms.

75. T. D. Engeness and T. A. Arias, *Phys. Rev. B*, **65**, 165106 (2002). Multiresolution Analysis for Efficient, High Precision All-Electron Density-Functional Calculations.

76. T. A. Arias, *Rev. Mod. Phys.*, **71**, 267–311 (1999). Multiresolution Analysis of Electronic Structure: Semicardinal and Wavelet Bases.

77. T. Yanai, R. J. Harrison, and N. C. Handy, *Mol. Phys.*, **103**, 413–424 (2005). Multiresolution Quantum Chemistry in Multiwavelet Bases: Time-Dependent Density Functional Theory with Asymptotically Corrected Potentials in Local Density and Generalized Gradient Approximations.

78. R. J. Harrison, G. I. Fann, T. Yanai, Z. T. Gan, and G. Beylkin, *J. Chem. Phys.*, **121**, 11587–11598 (2004). Multiresolution Quantum Chemistry: Basic Theory and Initial Applications.

79. T. Yanai, G. I. Fann, Z. T. Gan, R. J. Harrison, and G. Beylkin, *J. Chem. Phys.*, **121**, 6680–6688 (2004). Multiresolution Quantum Chemistry in Multiwavelet Bases: Hartree–Fock Exchange.

80. T. Yanai, G. I. Fann, Z. T. Gan, R. J. Harrison, and G. Beylkin, *J. Chem. Phys.*, **121**, 2866–2876 (2004). Multiresolution Quantum Chemistry in Multiwavelet Bases: Analytic Derivatives for Hartree–Fock and Density Functional Theory.

81. R. J. Harrison and G. Beylkin, *Abst. Papers Am. Chem. Soc.*, **225**, U464–U464 (2003). Multiresolution Quantum Chemistry in Multiwavelet Bases.

82. R. J. Harrison, G. I. Fann, T. Yanai, and G. Beylkin, *Comput. Sci.—ICCS 2003, Pt Iv, Proc.*, **2660**, 103–110 (2003). Multiresolution Quantum Chemistry in Multiwavelet Bases.

83. R. Schneider and T. Weber, *Appl. Numer. Math.*, **56**, 1383–1396 (2006). Wavelets for Density Matrix Computation in Electronic Structure Calculation.

84. J. L. Fattebert, *J. Comput. Phys.*, **149**, 75–94 (1999). Finite Difference Schemes and Block Rayleigh Quotient Iteration for Electronic Structure Calculations on Composite Grids.

85. T. L. Beck, *J. Comput. Chem.*, **20**, 1731–1739 (1999). Multigrid High-Order Mesh Refinement Techniques for Composite Grid Electrostatics Calculations.

86. D. Bai and A. Brandt, *SIAM J. Sci. Stat. Comput.*, **8**, 109–134 (1987). Local Mesh Refinement Multilevel Techniques.

87. F. Gygi and G. Galli, *Phys. Rev. B*, **52**, R2229–R2232 (1995). Real-Space Adaptive-Coordinate Electronic-Structure Calculations.

88. N. A. Modine, G. Zumbach, and E. Kaxiras, *Phys. Rev. B*, **55**, 10289–10301 (1997). Adaptive-Coordinate Real-Space Electronic-Structure Calculations for Atoms, Molecules, and Solids.

89. F. Gygi, *Phys. Rev. B*, **48**, 11692–11700 (1993). Electronic-Structure Calculations in Adaptive Coordinates.

90. J. L. Fattebert and J. Bernholc, *Phys. Rev. B*, **62**, 1713–1722 (2000). Towards Grid-Based O(N) Density-Functional Theory Methods: Optimized Nonorthogonal Orbitals and Multigrid Acceleration.

91. W. Kohn, *Phys. Rev. Lett.*, **76**, 3168–3171 (1996). Density Functional and Density Matrix Method Scaling Linearly with the Number of Atoms.

92. S. Goedecker, *Rev. Mod. Phys.*, **71**, 1085–1123 (1999). Linear Scaling Electronic Structure Methods.

93. R. Faller, in *Reviews in Computational Chemistry*, K. B. Lipkowitz and T. R. Cundari, Eds., Wiley, Hoboken, NJ, 2007, Vol. 23, pp. 233–262. Coarse-Grain Modeling of Polymers.

94. W. G. Noid, J. W. Chu, G. S. Ayton, and G. A. Voth, *J. Phys. Chem. B*, **111**, 4116–4127 (2007). Multiscale Coarse-Graining and Structural Correlations: Connections to Liquid-State Theory.

95. J. Zhou, I. F. Thorpe, S. Izvekov and G. A. Voth, *Biophys. J.*, 92, 4289–4303 (2007). Coarse-Grained Peptide Modeling Using a Systematic Multiscale Approach.

96. J. W. Chu, S. Izveko, and G. A. Voth, *Mol. Simul.*, **32**, 211–218 (2006). The Multiscale Challenge for Biomolecular Systems: Coarse-Grained Modeling.

97. D. Bai and A. Brandt, in *Multiscale Computational Methods in Chemistry and Physics*, A. Brandt, J. Bernholc, and K. Binder, Eds., IOS Press, Amsterdam, 2000, pp. 250–266. Multiscale Computation of Polymer Models.

98. B. D. Reddy, *Introductory Functional Analysis with Applications to Boundary Value Problems and Finite Elements*, Springer, Heidelberg, 1998.

99. K. W. Morton and D. F. Mayers, *Numerical Solution of Partial Differential Equations*, 2nd ed., Cambridge University Press, Cambridge, UK, 2005.

100. R. W. Hamming, *Numerical Methods for Scientists and Engineers*, Dover, New York, 1962.

101. L. Pauling and E. B. Wilson, *Introduction to Quantum Mechanics with Applications to Chemistry*, Dover, New York, 1935.

102. S. C. Brenner and L. R. Scott, *The Mathematical Theory of Finite Elements*, Springer, Heidelberg, 1994.

103. T. J. R. Hughes, *The Finite Element Method: Linear Static and Dynamic Finite Element Analysis*, Dover, Mineola, NY, 2000.

104. W. H. Press, S. A. Teukolsky, W. T. Vetterling, and B. P. Flannery, *Numerical Recipes in C*, 2nd ed., Cambridge University Press, Cambridge, UK, 1992.

105. W. L. Briggs, V. E. Henson, and S. F. McCormick, *A Multigrid Tutorial*, 2nd ed., SIAM, Philadelphia, 2000.

106. A. Brandt, S. McCormick, and J. Ruge, *SIAM J. Sci. Stat. Comput.*, **4**, 244–260 (1983). Multigrid Algorithms for Differential Eigenproblems.

107. A. Brandt, *Math. Comput.*, **31**, 333–390 (1977). Multi-level Adaptive Solutions to Boundary-Value Problems.

108. A. Brandt, *Multigrid Techniques: 1984 Guide with Applications to Fluid Dynamics*, Gesellschaft fur Mathematik und Datenverarbeitung, Bonn, 1984.

109. W. Hackbusch, *Multi-grid Methods and Applications*, Springer, New York, 1985.

110. R. G. Parr and W. Yang, *Density Functional Theory of Atoms and Molecules*, Oxford University Press, New York, 1989.

111. F. M. Bickelhaupt and E. J. Baerends, in *Reviews in Computational Chemistry*, K. B. Lipkowitz and D. B. Boyd, Eds., Wiley, Hoboken, NJ, 2000, Vol. 15, pp. 1–86. Kohn–Sham Density Functional Theory: Predicting and Understanding Chemistry.

112. D. R. Bowler, R. Choudhury, M. J. Gillan, and T. Miyazaki, *Phys. Stat. Sol. B*, **243**, 989–1000 (2006). Recent Progress with Large-Scale Ab Initio Calculations: The CONQUEST Code.

113. C. K. Skylaris, P. D. Haynes, A. A. Mostofi, and M. C. Payne, *Phys. Stat. Sol. B*, **243**, 973–988 (2006). Implementation of Linear-Scaling Plane Wave Density Functional Theory on Parallel Computers.

114. P. Dennery and A. Krzywicki, *Mathematics for Physicists*, Dover, Mineola, NY, 1995.

115. J. Wang and T. L. Beck, *J. Chem. Phys.*, **112**, 9223–9228 (2000). Efficient Real-Space Solution of the Kohn–Sham Equations with Multiscale Techniques.

116. S. Costiner and S. Ta'asan, *Phys. Rev. E*, **52**, 1181–1192 (1995). Simultaneous Multigrid Techniques for Nonlinear Eigenvalue Problems—Solutions of the Nonlinear Schrödinger–Poisson Eigenvalue Problem in 2 and 3 Dimensions.

117. S. Costiner and S. Ta'asan, *Phys. Rev. E*, **51**, 3704–3717 (1995). Adaptive Multigrid Techniques for Large-Scale Eigenvalue Problems—Solutions of the Schrödinger-Problem in 2 and 3 Dimensions.

118. N. Wijesekera, G. G. Feng, and T. L. Beck, *J. Theor. Comput. Chem.*, **2**, 553–561 (2003). Multiscale Algorithms for Eigenvalue Problems.

119. N. Wijesekera, G. Feng, and T. L. Beck, *Phys. Rev. B*, **75**, 115101 (2007). Efficient Multiscale Algorithms for Solution of Self-Consistent Eigenvalue Problems in Real Space.

120. J. Wang, Y. Wang, S. Y. Yu, and D. Kolb, *J. Phys.: Cond. Matt.*, **17**, 3701–3715 (2005). Nonlinear Algorithm for the Solution of the Kohn–Sham Equations in Solids.

121. S. Ismail-Beigi and T. A. Arias, *Phys. Rev. Lett.*, **82**, 2127–2130 (1999). Locality of the Density Matrix in Metals, Semiconductors, and Insulators.

122. S. Goedecker, *Phys. Rev. B*, **58**, 3501–3502 (1998). Decay Properties of the Finite-Temperature Density Matrix in Metals.

123. V. Weber and M. Challacombe, *J. Chem. Phys.*, **125**, 104110 (2006). Parallel Algorithm for the Computation of the Hartree-Fock Exchange Matrix: Gas Phase and Periodic Parallel ONX.

124. A. M. N. Niklasson, V. Weber, and M. Challacombe, *J. Chem. Phys.*, **123**, 044107 (2005). Nonorthogonal Density-Matrix Perturbation Theory.

125. S. Goedecker and G. E. Scuseria, *Comput. Sci. Eng.*, **5**, 14–21 (2003). Linear Scaling Electronic Structure Methods in Chemistry and Physics.

126. C. Ochsenfeld, J. Kussmann, and D. S. Lambrecht, in *Reviews in Computational Chemistry*, K. B. Lipkowitz and T. R. Cundari, Eds., Wiley-VCH, Hoboken, NJ, 2007, Vol. 23, pp. 1–82. Linear-Scaling Methods in Quantum Chemistry.

127. G. C. Feng and T. L. Beck, *Phys. Stat. Sol. B*, **243**, 1054-1062 (2006). Nonlinear Multigrid Eigenvalue Solver Utilizing Nonorthogonal Localized Orbitals.

128. J. L. Fattebert and F. Gygi, *Comput. Phys. Commun.*, **162**, 24–36 (2004). Linear Scaling First-Principles Molecular Dynamics with Controlled Accuracy.

129. G. Lamm, in *Reviews in Computational Chemistry*, K. B. Lipkowitz, R. Larter, and T. R. Cundari, Eds., Wiley-VCH, Hoboken, NJ, 2003, Vol. 19, pp. 147–365. The Poisson–Boltzmann Equation.

130. J. D. Madura, M. E. Davis, M. K. Gilson, R. C. Wade, B. A. Luty, and J. A. McCammon, in *Reviews in Computational Chemistry*, K. B. Lipkowitz and D. B. Boyd, Eds., Wiley-VCH, Hoboken, NJ, 1994, Vol. 5, pp. 229–268. Biological Applications of Electrostatic Calculations and Brownian Dynamics Simulations.

131. C. J. Cramer and D. G. Truhlar, in *Reviews in Computational Chemistry*, K. B. Lipkowitz and D. B. Boyd, Eds., Wiley-VCH, Hoboken, NJ, 1995, Vol. 6, pp. 1–72. Continuum Solvation Models: Classical and Quantum Mechanical Implementations.

132. J. D. Madura, J. M. Briggs, R. C. Wade, M. E. Davis, B. A. Luty, A. Ilin, J. Antosiewicz, M. K. Gilson, B. Bagheri, L. R. Scott, and J. A. McCammon, *Comput. Phys. Commun.*, **91**, 57–95 (1995). Electrostatics and Diffusion of Molecules in Solution: Simulations with the University of Houston Brownian Dynamics Program.

133. W. L. Briggs and J. Antosiewicz, in *Reviews in Computational Chemistry*, K. B. Lipkowitz and D. B. Boyd, Eds., Wiley-VCH, New York, 1999, Vol. 13, pp. 249–311. Simulation of pH-Dependent Properties of Proteins Using Mesoscopic Models.

134. N. A. Baker, in *Reviews in Computational Chemistry*, K. B. Lipkowitz, R. Larter, and T. R. Cundari, Eds., Wiley-VCH, Hoboken, NJ, 2005, Vol. 21, pp. 349–379. Biomolecular Applications of Poisson–Boltzmann Methods.

135. S. Tomac and A. Graslund, *J. Comput. Chem.*, **19**, 893–901 (1998). Multi-Multigrid Solution of Modified Poisson-Boltzmann Equation for Arbitrarily Shaped Molecules.

136. R. D. Coalson and A. Duncan, *J. Chem. Phys.*, **97**, 5653–5661 (1992). Systematic Ionic Screening Theory of Macroions.

137. R. D. Coalson, A. M. Walsh, A. Duncan, and N. Bental, *J. Chem. Phys.*, **102**, 4584–4594 (1995). Statistical-Mechanics of a Coulomb Gas with Finite-Size Particles—A Lattice Field-Theory Approach.

138. R. D. Coalson and A. Duncan, *J. Phys. Chem.*, **100**, 2612–2620 (1996). Statistical Mechanics of a Multipolar Gas: A Lattice Field Theory Approach.

139. S. F. Edwards and A. Lenard, *J. Math. Phys.*, **3**, 778–792 (1962). Exact Statistical Mechanics of a One-Dimensional System with Coulomb Forces. II. The Method of Functional Integration.

140. J. G. Kirkwood, *J. Chem. Phys.*, **2**, 767–781 (1934). On the Theory of Strong Electrolyte Solutions.

141. J. G. Kirkwood and J. C. Poirier, *J. Phys. Chem.*, **58**, 591-596 (1954). The Statistical Mechanical Basis of the Debye-Hückel Theory of Strong Electrolytes.

142. R. D. Coalson and T. L. Beck, in *Encyclopedia of Computational Chemistry*, P. von Rague Schleyer, Ed., Wiley, New York, 1998, pp. 2086–2100. Numerical Methods for Solving Poisson and Poisson-Boltzmann Type Equations.

143. M. Holst and F. Saied, *J. Comput. Chem.*, **14**, 105–113 (1993). Multigrid Solution of the Poisson–Boltzmann Equation.

144. M. Holst, R. E. Kozack, F. Saied, and S. Subramaniam, *J. Biomol. Struct. Dyn.*, **11**, 1437–1445 (1994). Protein Electrostatics—Rapid Multigrid-Based Newton Algorithm for Solution of the Full Nonlinear Poisson–Boltzmann Equation.

145. M. Holst, R. E. Kozack, F. Saied, and S. Subramaniam, *Proteins: Struct., Funct., Gen.*, **18**, 231–245 (1994). Treatment of Electrostatic Effects in Proteins—Multigrid-Based Newton Iterative Method for Solution of the Full Nonlinear Poisson–Boltzmann Equation.

146. M. Holst, R. E. Kozack, F. Saied, and S. Subramaniam, *Biophys. J.*, **66**, A130–A130 (1994). Multigrid-Based Newton Iterative Method for Solving the Full Nonlinear Poisson–Boltzmann Equation.

147. M. J. Holst and F. Saied, *J. Comput. Chem.*, **16**, 337–364 (1995). Numerical-Solution of the Nonlinear Poisson–Boltzmann Equation—Developing More Robust and Efficient Methods.

148. S. Tsonchev, R. D. Coalson, A. P. Liu, and T. L. Beck, *J. Chem. Phys.*, **120**, 9817–9821 (2004). Flexible Polyelectrolyte Simulations at the Poisson–Boltzmann Level: A Comparison of the Kink-Jump and Multigrid Configurational-Bias Monte Carlo Methods.

149. R. E. Alcouffe, A. Brandt, J. E. Dendy, and J. W. Painter, *SIAM J. Sci. Stat. Comput.*, **2**, 430–454 (1981). The Multi-Grid Method for the Diffusion Equation with Strongly Discontinuous Coefficients.

150. R. D. Coalson and M. G. Kurnikova, *IEEE Trans. Nanobiosci.*, **4**, 81–93 (2005). Poisson–Nernst–Planck Theory Approach to the Calculation of Current through Biological Ion Channels.

151. N. G. van Kampen, *Stochastic Processes in Physics and Chemistry*, rev. ed., Elsevier, Amsterdam, 1992.

152. M. Lundstrom, *Fundamentals of Carrier Transport*, 2nd ed., Cambridge University Press, Cambridge, UK, 2000.

153. Y. H. Cheng, J. K. Suen, D. Q. Zhang, S. D. Bond, Y. J. Zhang, Y. H. Song, N. A. Baker, C. L. Bajaj, M. J. Holst, and J. A. McCammon, *Biophys. J.*, **92**, 3397–3406 (2007). Finite Element Analysis of the Time-Dependent Smoluchowski Equation for Acetylcholinesterase Reaction Rate Calculations.

154. M. G. Kurnikova, R. D. Coalson, P. Graf, and A. Nitzan, *Biophys. J.*, **76**, 642–656 (1999). A Lattice Relaxation Algorithm for Three-Dimensional Poisson–Nernst–Planck Theory with Application to Ion Transport through the Gramicidin A Channel.

155. A. E. Cardenas, R. D. Coalson, and M. G. Kurnikova, *Biophys. J.*, **79**, 80–93 (2000). Three-Dimensional Poisson–Nernst–Planck Theory Studies: Influence of Membrane Electrostatics on Gramicidin A Channel Conductance.

156. Z. Kuang and T. L. Beck, (2007). The PNP code is available on request. Contact thomas.beck@uc.edu.

157. E. Artacho, T. L. Beck and E. Hernandez, *Phys. Stat. Sol. B*, **243**, 971–972 (2006), Preface.

158. K. Hirose, T. Ono, Y. Fujimoto, and S. Tsukamoto, *First-Principles Calculations in Real-Space Formalism: Electronic Configurations and Transport Properties of Nanostructures*, Imperial College Press, London, 2005.

159. K. A. Iyer, M. P. Merrick, and T. L. Beck, *J. Chem. Phys.*, **103**, 227–233 (1995). Application of a Distributed Nucleus Approximation in Grid Based Minimization of the Kohn–Sham Energy Functional.

160. M. P. Merrick, K. A. Iyer, and T. L. Beck, *J. Phys. Chem.*, **99**, 12478–12482 (1995). Multigrid Method for Electrostatic Computations in Numerical Density-Functional Theory.

161. T. L. Beck, *Int. J. Quant. Chem.*, **65**, 477–486 (1997). Real-Space Multigrid Solution of Electrostatics Problems and the Kohn–Sham Equations.

162. T. L. Beck, K. A. Iyer, and M. P. Merrick, *Int. J, Quant. Chem.*, **61**, 341–348 (1997). Multigrid Methods in Density Functional Theory.

163. J. Bernholc, J. Y. Yi, and D. J. Sullivan, *Faraday Discussions*, **91**, 217–228 (1991). Structural Transitions in Metal-Clusters.

164. L. Kronik, A. Makmal, M. L. Tiago, M. M. G. Alemany, M. Jain, X. Y. Huang, Y. Saad, and J. R. Chelikowsky, *Phys. Stat. Sol. B*, **243**, 1063–1079 (2006). PARSEC—The Pseudopotential Algorithm for Real-Space Electronic Structure Calculations: Recent Advances and Novel Applications to Nano-Structures.

165. Y. K. Zhou, Y. Saad, M. L. Tiago, and J. R. Chelikowsky, *J. Comput. Phys.*, **219**, 172–184 (2006). Self-Consistent-Field Calculations Using Chebyshev-Filtered Subspace Iteration.

166. Y. K. Zhou, Y. Saad, M. L. Tiago, and J. R. Chelikowsky, *Phys. Rev. E*, **74**, 066704 (2006). Parallel Self-Consistent-Field Calculations via Chebyshev-Filtered Subspace Acceleration.

167. D. K. Jordan and D. A. Mazziotti, *J. Chem. Phys.*, **120**, 574–578 (2004). Spectral Differences in Real-Space Electronic Structure Calculations.

168. F. Ancilotto, P. Blandin, and F. Toigo, *Phys. Rev. B*, **59**, 7868–7875 (1999). Real-Space Full-Multigrid Study of the Fragmentation of Li-11(+) Clusters.

169. I. H. Lee, Y. H. Kim, and R. M. Martin, *Phys. Rev. B*, **61**, 4397–4400 (2000). One-Way Multigrid Method in Electronic-Structure Calculations.

170. J. Bernholc, W. Lu, S. M. Nakhmanson, P. H. Hahn, V. Meunier, M. B. Nardelli, and W. G. Schmidt, *Mol. Phys.*, **105**, 147–156 (2007). Atomic Scale Design of Nanostructures.

171. J. L. Fattebert and F. Gygi, *J. Comput. Chem.*, **23**, 662–666 (2002). Density Functional Theory for Efficient Ab Initio Molecular Dynamics Simulations in Solution.

172. J. L. Fattebert and F. Gygi, *Int. J. Quant. Chem.*, **93**, 139–147 (2003). First-Principles Molecular Dynamics Simulations in a Continuum Solvent.

173. F. Gygi, J. L. Fattebert, and E. Schwegler, *Comput. Phys. Commun.*, **155**, 1–6 (2003). Computation of Maximally Localized Wannier Functions Using a Simultaneous Diagonalization Algorithm.

174. J. L. Fattebert and F. Gygi, *Phys. Rev. B*, **73**, 115124 (2006). Linear-Scaling First-Principles Molecular Dynamics with Plane-Waves Accuracy.

175. T. Ono and K. Hirose, *Phys. Rev. Lett.*, **98**, 026804 (2007). First-Principles Study of Electron-Conduction Properties of C-60 Bridges.

176. T. Sasaki, T. Ono, and K. Hirose, *Phys. Rev. E*, **74**, 056704 (2006). Order-N First-Principles Calculation Method for Self-Consistent Ground-State Electronic Structures of Semi-Infinite Systems.

177. T. Hoshi and T. Fujiwara, *J. Phys.: Cond. Matter*, **18**, 10787–10802 (2006). Large-Scale Electronic Structure Theory for Simulating Nanostructure Processes.

178. T. Hoshi and T. Fujiwara, *J. Phys. Soc. Jpn.*, **69**, 3773–3776 (2000). Theory of Composite-Band Wannier States and Order-N Electronic-Structure Calculations.

179. T. Hoshi and T. Fujiwara, *J. Phys. Soc. Jpn.*, **66**, 3710–3713 (1997). Fully Self-Consistent Electronic-Structure Calculation Using Nonorthogonal Localized Orbitals Within a Finite-Difference Real-Space Scheme and Ultrasoft Pseudopotential.

180. J. J. Mortensen, L. B. Hansen, and K. W. Jacobsen, *Phys. Rev. B*, **71**, 035109 (2005). Real-Space Grid Implementation of the Projector Augmented Wave Method.

181. R. Schmid, *J. Comput.Chem.*, **25**, 799–812 (2004). Car-Parrinello Simulations with a Real Space Method.

182. R. Schmid, M. Tafipolsky, P. H. Konig, and H. Kostler, *Phys. Stat. Sol. B*, **243**, 1001–1015 (2006). Car-Parrinello Molecular Dynamics Using Real Space Wavefunctions.

183. S. Kümmel, *J. Comput. Phys.*, **201**, 333–343 (2004). Damped Gradient Iteration and Multigrid Relaxation: Tools for Electronic Structure Calculations Using Orbital Density-Functionals.

184. A. Castro, H. Appel, M. Oliveira, C. A. Rozzi, X. Andrade, F. Lorenzen, M. A. L. Marques, E. K. U. Gross, and A. Rubio, *Phys. Stat. Sol. B*, **243**, 2465–2488 (2006). Octopus: A Tool for the Application of Time-Dependent Density Functional Theory.

185. K. Yabana, T. Nakatsukasa, J. I. Iwata, and G. F. Bertsch, *Phys. Stat. Sol. B*, **243**, 1121–1138 (2006). Real-Time, Real-Space Implementation of the Linear Response Time-Dependent Density-Functional Theory.

186. S. K. Gray and E. M. Goldfield, *J. Chem. Phys.*, **115**, 8331–8344 (2001). Dispersion Fitted Finite Difference Method with Applications to Molecular Quantum Mechanics.

187. C. K. Skylaris, O. Dieguez, P. D. Haynes, and M. C. Payne, *Phys. Rev. B*, **66**, 073103 (2002). Comparison of Variational Real-Space Representations of the Kinetic Energy Operator.

188. C. K. Skylaris, A. A. Mostofi, P. D. Haynes, C. J. Pickard, and M. C. Payne, *Comput. Phys. Commun.*, **140**, 315–322 (2001). Accurate Kinetic Energy Evaluation in Electronic Structure Calculations with Localized Functions on Real Space Grids.

189. P. Maragakis, J. Soler, and E. Kaxiras, *Phys. Rev. B*, **64**, 193101 (2001). Variational Finite-Difference Representation of the Kinetic Energy Operator.

190. E. Hernandez, M. J. Gillan, and C. M. Goringe, *Phys. Rev. B*, **55**, 13485–13493 (1997). Basis Functions for Linear-Scaling First-Principles Calculations.

191. E. Artacho, D. Sanchez-Portal, P. Ordejon, A. Garcia, and J. M. Soler, *Phys. Stat. Sol. B*, **215**, 809–817 (1999). Linear-Scaling Ab-Initio Calculations for Large and Complex Systems.

192. M. Calleja, C. Rey, M. M. G. Alemany, L. J. Gallego, P. Ordejon, D. Sanchez-Portal, E. Artacho, and J. M. Soler, *Phys. Rev. B*, **60**, 2020–2024 (1999). Self-Consistent Density-Functional Calculations of the Geometric, Electronic Structures, and Magnetic Moments of Ni-Al Clusters.

193. P. Ordejon, *Phys. Stat. Sol. B*, **217**, 335–356 (2000). Linear Scaling Ab Initio Calculations in Nanoscale Materials with SIESTA.

194. E. Tsuchida and M. Tsukada, *Phys. Rev. B*, **54**, 7602–7605 (1996). Adaptive Finite-Element Method for Electronic-Structure Calculations.

195. E. Tsuchida and M. Tsukada, *J. Phys. Soc. Jpn.*, **67**, 3844–3858 (1998). Large-Scale Electronic-Structure Calculations Based on the Adaptive Finite-Element Method.

196. E. Tsuchida, *J. Chem. Phys.*, **121**, 4740–4746 (2004). Ab Initio Molecular-Dynamics Study of Liquid Formamide.

197. E. Tsuchida, *J. Phys. Soc. Jpn.*, **76**, 034708 (2007). Augmented Orbital Minimization Method for Linear Scaling Electronic Structure Calculations.

198. P. Havu, V. Havu, M. J. Puska, and R. M. Nieminen, *Phys. Rev. B*, **69**, 115325 (2004). Nonequilibrium Electron Transport in Two-Dimensional Nanostructures Modeled Using Green's Functions and the Finite-Element Method.

199. G. Lu, E. B. Tadmor, and E. Kaxiras, *Phys. Rev. B*, **73**, 024108 (2006). From Electrons to Finite Elements: A Concurrent Multiscale Approach for Metals.

200. E. Lidorikis, M. E. Bachlechner, R. K. Kalia, A. Nakano, P. Vashishta, and G. Z. Voyiadjis, *Phys. Rev. Lett.*, **87**, 086104 (2001). Coupling Length Scales for Multiscale Atomistics-Continuum Simulations: Atomistically Induced Stress Distributions in Si/Si3N4 Nanopixels.

201. S. Ogata, E. Lidorikis, F. Shimojo, A. Nakano, P. Vashishta, and R. K. Kalia, *Comput. Phys. Commun.*, **138**, 143–154 (2001). Hybrid Finite-Element/Molecular-Dynamics/Electronic-Density-Functional Approach to Materials Simulations on Parallel Computers.

202. S. Yamakawa and S. Hyodo, *Phys. Rev. B*, **71**, 035113 (2005). Gaussian Finite-Element Mixed-Basis Method for Electronic Structure Calculations.

203. M. Aichinger and E. Krotscheck, *Comput. Mater. Sci.*, **34**, 188–212 (2005). A Fast Configuration Space Method for Solving Local Kohn–Sham Equations.

204. E. R. Hernandez, S. Janecek, M. Kaczmarski, and E. Krotscheck, *Phys. Rev. B*, **75**, 075108 (2007). Evolution-Operator Method for Density Functional Theory.

205. F. Shimojo, R. K. Kalia, A. Nakano, and P. Vashishta, *Comput. Phys. Commun.*, **167**, 151–164 (2005). Embedded Divide-and-Conquer Algorithm on Hierarchical Real-Space Grids: Parallel Molecular Dynamics Simulation Based on Linear-Scaling Density Functional Theory.

206. A. Nakano, R. K. Kalia, K. Nomura, A. Sharma, P. Vashishta, F. Shimojo, A. C. T. van Duin, W. A. Goddard, R. Biswas, and D. Srivastava, *Comput. Mater. Sci.*, **38**, 642–652 (2007). A Divide-and-Conquer/Cellular-Decomposition Framework for Million-to-Billion Atom Simulations of Chemical Reactions.

207. P. D. Haynes, C. K. Skylaris, A. A. Mostofi, and M. C. Payne, *Phys. Stat. Sol. B*, **243**, 2489–2499 (2006). ONETEP: Linear-Scaling Density-Functional Theory with Local Orbitals and Plane Waves.

208. L. Seijo and Z. Barandiaran, *J. Chem. Phys.*, **121**, 6698–6709 (2004). Parallel, Linear-Scaling Building-Block and Embedding Method Based on Localized Orbitals and Orbital-Specific Basis Sets.

209. T. Ozaki and H. Kino, *J. Chem. Phys.*, **121**, 10879–10888 (2004). Variationally Optimized Basis Orbitals for Biological Molecules.

210. T. Ozaki, *Phys. Rev. B*, **67**, 115108 (2003). Variationally Optimized Atomic Orbitals for Large-Scale Electronic Structures.

211. H. S. Lee and M. E. Tuckerman, *J. Chem. Phys.*, **126**, 164501 (2007). Dynamical Properties of Liquid Water from Ab Initio Molecular Dynamics Performed in the Complete Basis Set Limit.

212. J. A. Morrone, K. E. Hasllinger, and M. E. Tuckerman, *J. Phys. Chem. B*, **110**, 3712–3720 (2006). Ab Initio Molecular Dynamics Simulation of the Structure and Proton Transport Dynamics of Methanol-Water Solutions.

213. H. Takahashi, T. Hori, H. Hashimoto, and T. Nitta, *J. Comput. Chem.*, **22**, 1252–1261 (2001). A Hybrid QM/MM Method Employing Real Space Grids for QM Water in the TIP4P Water Solvents.

214. H. Takahashi, N. Matubayasi, M. Nakahara, and T. Nitta, *J. Chem. Phys.*, **121**, 3989–3999 (2004). A Quantum Chemical Approach to the Free Energy Calculations in Condensed Systems: The QM/MM Method Combined with the Theory of Energy Representation.

215. B. Honig and A. Nicholls, *Science*, **268**, 1144–1149 (1995). Classical Electrostatics in Biology and Chemistry.

216. H. Oberoi and N. M. Allewell, *Biophys. J.*, **65**, 48–55 (1993). Multigrid Solution of the Nonlinear Poisson–Boltzmann Equation and Calculation of Titration Curves.

217. M. Holst, N. Baker, and F. Wang, *J. Comput. Chem.*, **22**, 475–475 (2001). Adaptive Multilevel Finite Element Solution of the Poisson–Boltzmann Equation I. Algorithms and Examples.

218. N. A. Baker, D. Sept, S. Joseph, M. J. Holst, and J. A. McCammon, *Proc. Natl. Acad. Sci. USA*, **98**, 10037–10041 (2001). Electrostatics of Nanosystems: Application to Microtubules and the Ribosome.

219. N. A. Baker, D. Sept, M. J. Holst, and J. A. McCammon, *IBM J. Res. Devel.*, **45**, 427–438 (2001). The Adaptive Multilevel Finite Element Solution of the Poisson–Boltzmann Equation on Massively Parallel Computers.

220. M. Holst, N. Baker, and F. Wang, *J. Comput. Chem.*, **21**, 1319–1342 (2000). Adaptive Multilevel Finite Element Solution of the Poisson–Boltzmann Equation I. Algorithms and Examples.

221. N. Baker, M. Holst, and F. Wang, *J. Comput. Chem.*, **21**, 1343–1352 (2000). Adaptive Multilevel Finite Element Solution of the Poisson–Boltzmann Equation II. Refinement at Solvent-Accessible Surfaces in Biomolecular Systems.

222. F. Fogolari, A. Brigo, and H. Molinari, *Biophys. J.*, **85**, 159–166 (2003). Protocol for MM/PBSA Molecular Dynamics Simulations of Proteins.

223. B. Z. Lu, W. Z. Chen, C. X. Wang, and X. J. Xu, *Proteins: Struct., Funct., Gen.*, **48**, 497–504 (2002). Protein Molecular Dynamics with Electrostatic Force Entirely Determined by a Single Poisson–Boltzmann Calculation.

224. B. Z. Lu, X. L. Cheng, T. J. Hou, and J. A. McCammon, *J. Chem. Phys.*, **123**, 084904 (2005). Calculation of the Maxwell Stress Tensor and the Poisson–Boltzmann Force on a Solvated Molecular Surface Using Hypersingular Boundary Integrals.

225. J. L. Smart, T. J. Marrone, and J. A. McCammon, *J. Comput. Chem.*, **18**, 1750–1759 (1997). Conformational Sampling with Poisson–Boltzmann Forces and a Stochastic Dynamics Monte Carlo Method: Application to Alanine Dipeptide.

226. S. Y. Ponomarev, K. M. Thayer, and D. L. Beveridge, *Proc. Natl. Acad. Sci. USA*, **101**, 14771–14775 (2004). Ion Motions in Molecular Dynamics Simulations on DNA.

227. T. L. Beck, M. E. Paulaitis, and L. R. Pratt, *The Potential Distribution Theorem and Models of Molecular Solutions*, Cambridge University Press, Cambridge, UK, 2006.

228. T. Darden, D. York, and L. Pedersen, *J. Chem. Phys.*, **98**, 10089–10092 (1993). Particle Mesh Ewald—An N log(N) Method for Ewald Sums in Large Systems.

229. C. Sagui and T. Darden, *J. Chem. Phys.*, **114**, 6578–6591 (2001). Multigrid Methods for Classical Molecular Dynamics Simulations of Biomolecules.

230. A. Toukmaji, C. Sagui, J. Board, and T. Darden, *J. Chem. Phys.*, **113**, 10913–10927 (2000). Efficient Particle-Mesh Ewald Based Approach to Fixed and Induced Dipolar Interactions.

231. G. Hummer, L. R. Pratt, and A. E. Garcia, *J. Phys. Chem.*, **100**, 1206–1215 (1996). Free Energy of Ionic Hydration.

232. G. Hummer, L. R. Pratt, and A. E. Garcia, *J. Phys. Chem. A*, **102**, 7885–7895 (1998). Molecular Theories and Simulation of Ions and Polar Molecules in Water.

233. J. E. Pask and P. A. Sterne, *Phys. Rev. B*, **71**, 113101 (2005). Real-Space Formulation of the Electrostatic Potential and Total Energy of Solids.

234. D. C. Thompson and P. W. Ayers, *Int. J. Quant. Chem.*, **106**, 787–794 (2006). Thinking Inside the Box: Novel Linear Scaling Algorithm for Coulomb Potential Evaluation.

235. J. Juselius and D. Sundholm, *J. Chem. Phys.*, **126**, 094101 (2007). Parallel Implementation of a Direct Method for Calculating Electrostatic Potentials.

236. A. C. Maggs and V. Rossetto, *Phys. Rev. Lett.*, **88**, 196402 (2002). Local Simulation Algorithms for Coulomb Interactions.

237. A. Duncan, R. D. Sedgewick, and R. D. Coalson, *Phys. Rev. E*, **71**, 046702 (2005). Improved Local Lattice Approach for Coulombic Simulations.

238. A. Duncan, R. D. Sedgewick, and R. D. Coalson, *Comput. Phys. Commun.*, **175**, 73–77 (2006). Fast Fourier Transform Simulation Techniques for Coulomb Gases.

239. A. Duncan, R. D. Sedgewick, and R. D. Coalson, *Phys. Rev. E*, **73**, 016705 (2006). Local Simulation Algorithms for Coulomb Gases with Dynamical Dielectric Effects.

240. M. Di Ventra and N. D. Lang, *Phys. Rev. B*, **65**, 045402 (2002). Transport in Nanoscale Conductors from First Principles.

241. D. S. Kosov, *J. Chem. Phys.*, **116**, 6368–6375 (2002). Schrödinger Equation for Current Carrying States.

242. D. S. Kosov, *J. Chem. Phys.*, **119**, 1–5 (2003). Kohn–Sham Equations for Nanowires with Direct Current.

243. P. Bokes and R. W. Godby, *Phys. Rev. B*, **68**, 125414 (2003). Maximum-Entropy Theory of Steady-State Quantum Transport.

244. P. Bokes, H. Mera, and R. W. Godby, *Phys. Rev. B*, **72**, 165425 (2005). Current-Constraining Variational Approaches to Quantum Transport.

245. M. G. Kurnikova, R. D. Coalson, P. Graf, and A. Nitzan, *Biophys. J.*, **76**, A211–A211 (1999). A Lattice Relaxation Algorithm for 3D Poisson–Nernst–Planck Theory with Application to Ion Transport through the Gramicidin A Channel. (Meeting abstract).

246. M. G. Kurnikova, R. D. Coalson, P. Graf, and A. Nitzan, *Biophys. J.*, **76**, 642–656 (1999). A Lattice Relaxation Algorithm for Three-Dimensional Poisson–Nernst–Planck Theory with Application to Ion Transport through the Gramicidin A Channel.

247. P. Graf, A. Nitzan, M. G. Kurnikova, and R. D. Coalson, *J. Phys. Chem. B*, **104**, 12324–12338 (2000). A Dynamic Lattice Monte Carlo Model of Ion Transport in Inhomogeneous Dielectric Environments: Method and Implementation.

248. M. H. Cheng, A. B. Mamonov, J. W. Dukes and R. D. Coalson, *J. Phys. Chem. B*, **111**, 5956–5665 (2007). Modeling the Fast Gating Mechanism in the CIC-O Chloride Channel.

249. P. Graf, M. G. Kurnikova, R. D. Coalson, and A. Nitzan, *J. Phys. Chem. B*, **108**, 2006–2015 (2004). Comparison of Dynamic Lattice Monte Carlo Simulations and the Dielectric Self-Energy Poisson–Nernst–Planck Continuum Theory for Model Ion Channels.

250. H. W. de Haan, I. S. Tolokh, C. G. Gray, and S. Goldman, *Phys. Rev. E*, **74**, 030905 (2006). Nonequilibrium Molecular Dynamics Calculation of the Conductance of the KcsA Potassium Ion Channel.

251. P. S. Crozier, R. L. Rowley, N. B. Holladay, D. Henderson, and D. D. Busath, *Phys. Rev. Lett.*, **86**, 2467–2470 (2001). Molecular Dynamics Simulation of Continuous Current Flow through a Model Biological Membrane Channel.

252. A. J. Coleman and V. I. Yukalov, *Reduced Density Matrices: Coulson's Challenge*, Springer, Heidelberg, 2000.

253. D. A. Mazziotti, in *Reduced-Density-Matrix Mechanics, with Applications to Many-Electron Atoms and Molecules*, D. A. Mazziotti, Ed., Wiley, Hoboken, NJ, 2007, Vol. 134, pp. 21–59. Variational Two-Electron Reduced-Density-Matrix Theory.

254. J. M. Thijssen, *Computational Physics*, Cambridge University Press, Cambridge, UK, 1999.

255. R. A. Harris and L. R. Pratt, *J. Chem. Phys.*, **82**, 856–859 (1985). Discretized Propagators, Hartree, and Hartree–Fock Equations, and the Hohenberg–Kohn Theorem.

256. R. A. Harris and L. R. Pratt, *J. Chem. Phys.*, **82**, 5084–5088 (1985). Discretized Propagators in Hartree and Hartree–Fock Theory. 2. Responses to Static Electric and Magnetic-Fields.

257. T. J. Frankcombe, G. J. Kroes, N. I. Choly, and E. Kaxiras, *J. Phys. Chem. B*, **109**, 16554–16562 (2005). Orbital-Free Density Functional Theory Applied to $NaAlH_4$.

258. B. Zhou and E. A. Carter, *J. Chem. Phys.*, **122**, 184108 (2005). First Principles Local Pseudopotential for Silver: Towards Orbital-Free Density-Functional Theory for Transition Metals.

259. A. Fernando-Ramos, B. A. Ellingson, B. C. Garrett, and D. G. Truhlar, in *Reviews in Computational Chemistry*, K. B. Lipkowitz and T. R. Cundari, Eds., Wiley-VCH, Hoboken, NJ, 2007, Vol. 23, pp. 125–232. Variational Transition State Theory with Multidimensional Tunneling.

CHAPTER 6

Hybrid Methods for Atomic-Level Simulations Spanning Multiple–Length Scales in the Solid State

Francesca Tavazza, Lyle E. Levine, and Anne M. Chaka

National Institute of Standards and Technology, Gaithersburg, Maryland

INTRODUCTION

When investigating the properties of the solid state, very different length scales must be probed, depending upon the quantities of interest. For instance, when studying the mechanical behavior of materials, micro- and macroscale (hundreds of nanometers and larger) phenomena such as long-range stress fields must be considered. On the other hand, when effects such as bond breaking, atomic (re)arrangements, or defect properties are of primary importance, simulations at the nanoscale (one to hundreds of nanometers) or atomic (angstrom) scale are required.[1,2] For a given problem, it is the trade-off between the need for detailed information and the computational cost that determines which computational methodology provides the optimal approach. Thus, depending upon the length scale under examination, different computational methodologies should be used. Continuum mechanics are usually the optimum tool to simulate events occurring at the macroscale because there is no need to consider the behavior of each individual atom, while it is crucial to include all of the long-range effects. In contrast, atomistic simulations using classical potentials are generally the best

Reviews in Computational Chemistry, Volume 26
edited by Kenny B. Lipkowitz and Thomas R. Cundari

approach for studying nanoscale phenomena, where atomic behavior becomes important but including quantum-level effects is less vital than modeling relatively large systems (up to many millions of atoms). Lastly, quantum mechanical simulations are often the most appropriate way to investigate atomic-scale processes where the detailed electronic behavior can be crucial.

We begin by briefly reviewing some of the computational methodologies most commonly used in studies of the solid state, starting with the finite-element method (FEM). The FEM (see Refs. 3–6 among many) is the computational technique most commonly used to investigate macroscale processes such as stress–strain and thermal behaviors; it is based upon the idea of discretizing the continuum into a set (mesh) of discrete subdomains (elements). The partial differential equations that determine the material behavior are solved at each mesh point (node). The behavior away from the nodes is then determined using an interpolation scheme.

Atomistic modeling using semiempirical classical potentials (e.g., see Refs. 7–13) is widely used to model phenomena at the nanoscale. In this approach, the interatomic potential energy function is computed either using a relatively simple analytic functional form or an interpolation of empirical data points. In both cases, the information describing the specific material is entered into the model through empirical parameters that are determined by fitting experimental or ab-initio data. The equilibrium atomic configuration of the system is then found using minimization procedures such as conjugate gradient[14] or Monte Carlo techniques (see Refs. 15–17 among many). Using semiempirical classical potentials, the dynamical evolution of the system can be determined as well, by deriving the forces acting on the atoms from the expression for the energy, and applying a molecular dynamics (MD) approach.[18–21] In this level of theory, no quantum mechanical behavior is explicitely included, so results are only as good as the parametrization used, which also means that transferability can be a problem.

Finally, the atomic scale can be investigated by using tight-binding (TB), density functional theory (DFT), or even lower level ab initio calculations. All of these methodologies are within the quantum mechanical framework, with TB[22–24] being the least accurate (because of the many approximations) but also the least computationally demanding. TB describes the electronic states starting from the limit of isolated-atom orbitals, and is well suited for the investigation of materials characterized by fairly localized electrons, such as transition metals and their alloys, or by covalent bonding, such as semiconductors and insulators. A significant advantage of TB, beyond its computational speed, is that it can be easily coupled with molecular dynamics (TBMD), providing a computationally efficient way to investigate the dynamical evolution of a system, while retaining the most important aspects of its quantum behavior. In most applications, TB is used in its semiempirical form, i.e., the energy is approximated as the sum of a "band structure" energy and a "repulsive" energy, where only the band structure energy is actually found through a quantum mechanical calculation.

The repulsive part of the total energy is approximated by the sum of short-range two-body interactions with empirically fitted parameters. Also, empirical parameters enter into the determination of the band structure energy as well, substituting for the explicit calculation of the two-center integrals $\langle \phi_{R_i}/H/\phi_{R_j} \rangle$ (ϕ_{R_i} is the wave function of atom i with position $\mathbf{R_i}$ and H the Hamiltonian). Therefore, transferability can be a problem in this methodology just as it is for semiempirical classical potentials. DFT is an ab initio approach where the energy of an interacting system of fermions is found using its density, not its many-body wave function. DFT is based on the Hohenberg–Kohn theorems,[25] which demonstrate a one-to-one correspondence between the ground-state electron density and the ground-state wave function of a many-particle system. This ground-state density minimizes the total electronic energy of the system. Moreover, the most commonly used form of DFT is the Kohn–Sham DFT,[25] where the many-body problem of interacting electrons in a real potential is reduced to a problem of noninteracting electrons moving in an effective potential.

Traditionally, multiscale material behavior has been investigated following a ''serial'' approach, where the empirical parameters required for large-length-scale simulations are obtained from more exact calculations of smaller systems. For example, as mentioned above, parameters for classical potentials or semiempirical TB are often determined through the fitting of ab initio data. However, the unspoken assumption behind this approach is that different length scales can be decoupled without significantly affecting the results of the calculations. In other words, it is assumed that a process can be correctly simulated considering just one length scale at a time: A process modeled by a quantum mechanical method will not be significantly affected by being simulated in a very small system, while one modeled with classical methods will not suffer from the absence of both an atomic quantum description and long-range forces, and so on. This assumption is very reasonable when studying a great number of physical problems, but it does not hold, for instance, for microscopic phenomena that are driven by macroscopic forces, or, conversely, for macroscopic phenomena that are significantly affected by small-scale effects. More generally, a serial approach is not suitable for describing mechanisms characterized by a continuous exchange of information between the different length scales. Physical mechanisms of this kind are defined as *multiscale* phenomena and include problems such as crack formation and propagation, stress-induced defect processes, nanoindentation, and so on. For instance, when a crack is propagating inside a solid, localized electronic rearrangements may affect the strength of the interatomic bonding; the bonding, in turn, dictates the atomic restructuring, and the atomic structure controls the macroscopic mechanical properties of the material. Therefore, to correctly simulate multiscale phenomena, it is necessary to simultaneously include detailed descriptions at both the atomic and macroscopic levels.

Despite impressive improvements in computer capabilities over recent years, it is still not possible to simulate macroscopically large systems with

atomic-level resolution. Therefore, the avenue most commonly explored to bypass such an impasse is the use of *hybrid methodologies*. Here, different length scales are simulated simultaneously in a coupled fashion. The main obstacle to overcome when producing such a hybrid simulation method is developing an efficient and physically correct coupling scheme. Hybrid methodologies, coupling schemes, and applications will be discussed in detail in the next section.

A related topic is the issue of time scales. Dynamic simulations of atomic behavior generally require time steps that are short enough to capture the vibrational modes of the system, whereas changes at the macroscopic scale usually occur over vastly longer time scales. Coupling between such widely varying time scales is a very important challenge, but it is not within the scope of this review. However, the problem of multiple-time-scale simulations will be discussed briefly in the discussion of dynamical methods.

The need for coupled methodologies is definitely not limited to the physics of the solid state, and the subject has a long history. The first application of hybrid methods to the solid state are the works of Gehlen et al.[26] and Sinclair,[27] where continuum elasticity was used to provide realistic boundary conditions for atomistic simulations. However, only recently, hybrid methodologies have become widespread in solid-state physics, primarily because of the explosion of interest in nanotechnology. Coupled methods have been a key investigation technique for quite some time in many other fields as well. In chemistry, for instance, combining quantum mechanics (QM) and molecular mechanical (MM) potentials was started by Warshell and Levitt in 1976[28] and has been common practice ever since. Several reviews of hybrid QM/MM methods can be found.[29–32] However, these methodologies are not necessarily well suited for studying many of the materials of interest in the solid state, metals in particular. This is because QM/MM methods are designed for covalently bonded organic molecules, i.e., materials where the bond is strongly localized, while in metals bonds are strongly delocalized. Hybrid methodologies have also been extensively applied to the investigation of fluid behavior. In this field, we find extensive use of static coupling between continuum and atomistic regimes, as in the Navier–Stokes/Monte Carlo method of Dejong et al.[33] or Garcia et al.,[34] or the coupling of Monte Carlo to fluid simulations proposed by Sommerer et al.[35] and Bogaerts et al.,[36] just to mention a few. Even more coupling schemes have been developed to explore the dynamics of fluids. Among many, we want to mention the continuum-to-molecular dynamics methods developed by O'Connell et al.,[37] by Hadjiconstantinou and Patera,[38] Hadjiconstatinou,[39] by Li et al.,[40] and more recently by Wang and He.[41] Hybrid methodologies based solely on the exchange of fluxes have been proposed as well, such as those by Flekkoy et al.[42,43] Magnetism,[44] electromagnetism,[45] toxicology,[46] biology, and so on are just a few other examples of fields that currently make systematic use of hybrid methodologies.

Lastly, it is important to mention that hybrid methodologies are not the only possible avenue to follow when investigating phenomena that require very large systems and/or very long times together with atomistic resolution, at least locally. Several other approaches have been proposed, including kinetic Monte Carlo,[47–52] histogram reweighting Monte Carlo,[53–56] replica exchange Monte Carlo,[57–60] and, especially worth mentioning, the "accelerated molecular dynamics" of Art Voter and co-workers.[61–64] It is beyond the scope of this review to discuss such methods, so we redirect the interested reader to the more specific studies listed above.

General Remarks about Hybrid Methods

Hybrid methodologies are designed to investigate phenomena that require large system sizes but also contain smaller critical regions that must be treated with a level of theory that is too computationally expensive to be used for the whole simulation. The basic assumption for the applicability of a coupled methodology is the "locality" of the process that needs to be described at a higher level. In other words, the simulation of such a process should not be significantly affected by the fact that the higher level theory is used only on a smaller region of space, and that far away the system is treated using a different computational approach.

The most critical component of any hybrid methodology is the interface between the different computational models. Such a region is usually referred to as the "hand-shake" region. Here, unphysical forces (ghost forces) may arise because intrinsically incompatible descriptions of the material are matched to each other. Such an incompatibility originates largely from the difference in interaction range between the computational models. More specifically, in a continuum description, the displacement of any point inside an element is completely determined by the displacements of that element's nodes, while in an atomistic description, the displacement of one atom directly affects all atoms that are within the cutoff of the potential, not only its nearest neighbors. Similarly, in classical atomistic simulations, the energy of one atom does not directly depend upon the position of atoms that are beyond the potential interaction range (cutoff), while in quantum mechanical calculations it depends upon the positions of all atoms in the system. To clarify how this produces ghost forces, let us consider the following. Atomistic-to-continuum hybrid methodologies usually add pseudoatoms on the continuum side of the interface to provide a complete set of neighbors to the atoms near the interface itself. This is done to avoid dealing with the nonphysical surface that would be created by sharply terminating the atomistic region. These pseudoatoms are seen by the atoms in the atomistic calculation but are treated as part of the continuum. Let us consider a real atom and a pseudoatom such that their distance is larger than the nearest-neighbor distance but smaller than the classical potential cutoff distance. Displacing the

pseudoatom will generate a force on the real atom because of the range of the classical potential. However, displacing the real atom will not produce a force on the pseudoatom because of the nearest-neighbor nature of the continuum interactions. It is such a mismatch in the forces that results in the formation of ghost forces.

For hybrid methodologies dealing with dynamical processes, the need to connect different computational models creates a second, very significant, problem: Wave reflections may occur at the artificial boundary. Such a reflection arises because of the mismatch in wave spectra between the regions; a classical atomistic region, for instance, emits waves that are significantly shorter than those that can be captured by a continuum finite-element (FE) region.

Depending upon how the coupling between computational methods has been handled, different classes of hybrid methodologies can be defined. A possible classification is in terms of the nature of the hand-shake region: Is it a sharp interface between the computational domains or an extended area (as in the example above)? Methodologies can also be divided depending upon how the energy functional is constructed, whether a single energy functional is used for the whole system or a different functional is constructed for each domain, in which case an iterative procedure is then used to find equilibrium. Lastly, coupling methodologies can also be separated into adaptive refinement methods and domain decomposition methods. Adaptive refinement methods are coupling schemes where a single macroscale model is considered over the whole system; such a model is more highly refined over the area of interest than away from it. Conversely, domain decomposition methods employ a macroscale model only far from the area of interest, while in the vicinity of it they make use of an atomistic model. In this review, examples of all of these approaches will be presented.

Complete-Spectrum Hybrid Methods

In this review, methods are divided into two main classes: methodologies dealing with the coupling of classical atomistic simulations to continuum ones and methodologies coupling classical atomistic models to quantum mechanical formulations. However, it is important to mention that a few methods have been designed to cover the whole span from the continuum to the quantum scale. Examples of these methods are the *coupling of length scales* (CLS) method of Abraham et al., the *orbital-free density functional theory—quasi-continuum* method (OFDFT-QC), the method developed by Ogata et al., and the *transparent interface* method by Cheng et al. All of these methodologies will be discussed in this review, with each coupling scheme in its appropriate section, i.e., the part of the method that deals with continuum/atomistic coupling will be presented in the Atomistic/Continuum Coupling section, and the part dealing with classical/quantum coupling in the Classical/Quantum Coupling section.

About this Review

The application of hybrid methodologies to the solid state is surging and new coupling schemes are being introduced at a rapid pace. Several review works are available on this topic.[47,48,65–77] However, these works invariably concentrate on a narrow range of hybrid methods that are examined in great detail. Instead, this review was written to introduce newcomers to the field by providing a broad, easily understandable discussion of the full range of hybrid methodologies that are currently available for solid-state studies (for static or dynamical problems, for continuum-to-classical or classical-to-quantum coupling, and so on), so that they could easily choose the most appropriate approach for their specific problem. Although a significant number of methodologies is covered, we obviously could not include every method that has ever been developed. However, we tried to present at least one methodology for each major approach.

To retain coherence with the more detailed descriptions found in the references, the equations and descriptions in this chapter closely follow the referenced works whenever possible. In particular, this means that the variable definitions are not uniform throughout the chapter but are defined with respect to each specific coupling methodology. Also, since it is expected that many readers will refer primarily to individual sections, several commonly used acronyms are defined more than once and a table of acronyms is included at the end of this chapter.

ATOMISTIC/CONTINUUM COUPLING

Zero-Temperature Equilibrium Methods

In this section, we will discuss methods designed to find lattice static solutions, i.e., determining equilibrium atomic positions for a given geometry and externally imposed forces or displacements. These methods are usually significantly faster than dynamical ones, so they are a very convenient choice when static properties, such as energy differences between equilibrium configurations, are the object of the investigation. Our goal in this section is the exploration of atomistic-to-continuum *coupling procedures*, so the individual modeling methods will only be described to the extent necessary to understand the coupling. A great deal of attention will be devoted to the unphysical effects that intrinsically arise with any sort of hybrid methodology. In addition to the methodologies included in this review, several other coupling schemes have been proposed, as, for instance, those discussed in Refs.[78–80.]

Atomistic/Continuum Coupling to Simulate Static Loads

A simple case of atomistic/continuum coupling is the methodology devised by Kwon and Jung to study the atomic behavior of materials under static loads.[81] In this case, the coupling to a continuum description is

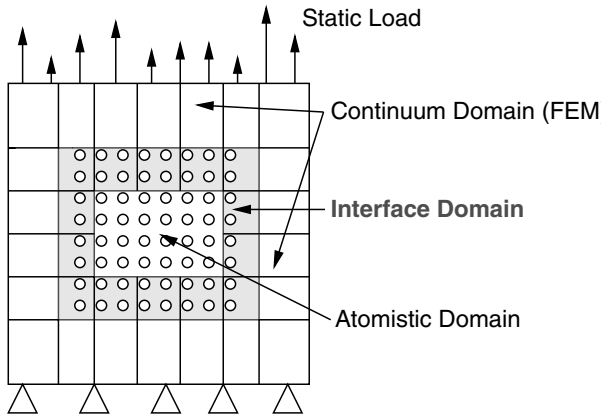

Figure 1 Schematic representation of the coupling between the atomistic and continuum domains. The finite-element method (FEM) is used in the continuum region. The arrows represent the static load on the system. The shaded area indicates the interface domain.

introduced only as a way to simplify the application of static loads, allowing the loads to be imposed as boundary conditions on an FE model instead of on the atomistic system.

Figure 1 schematically displays the coupling procedure. The system is subdivided into three zones: the atomistic domain, modeled by an interatomic potential such as the embedded atom method (EAM)[9,10] or Morse potential,[11] the continuum domain, where an FE approach is used, and an interface domain, where atoms and FE meshes overlap.

No single energy functional is defined for the whole system; instead, the atomistic and FE models are solved independently in a staggered manner, and the computation continues iteratively until convergence is achieved. Each iteration consists of several steps. First, the equations for the FE region are solved, and new positions are determined for the FE nodes. Next, the displacements for the interface atoms are computed by interpolating the FE nodal displacements at the atomic positions. Keeping the interface atoms fixed in their new positions, the displacements for all of the other atoms are then calculated using the interatomic potential. Once all of the new displacements have been computed, the interatomic forces on the interface atoms are determined. Next, the equivalent nodal forces on the finite elements containing the interface atoms are calculated. With the nodal forces computed, the new FE solution is obtained and the next iteration is started.

This method has been tested by studying atomic rearrangements for two-dimensional (2D) systems with a dislocation under shear, tensile, and compressive forces. The atomistic domain was modeled with the Morse potential. A 2D system was chosen only for computational convenience; nothing in the algorithm is limited to such a dimensionality.

FEAt Method

The *finite-element combined with atomistic modeling* (FEAt) method,[82–86] developed by Kohlhoff et al. in 1988, is one of the oldest atomistic/continuum coupling methods, and it was inspirational in the development of several other coupling schemes (e.g., the one used in the CADD methodology discussed below).

This method is based on three main ideas: first, to only use displacements in the coupling procedure; second, to use a *mutual-displacement boundary conditions* scheme; and third, to match the elastic constants in order to equilibrate the stresses between the atomistic and the continuum domains. The reason for the first assumption is that, because of the local nature of the continuum and the nonlocal nature of the atomistic regime, the stress principles governing the two regions are significantly different, and they should not enter the coupling procedure. In other words, the use of forces is explicitly avoided in this scheme, so no direct interaction occurs between the stress fields of the two media. We will now illustrate the mutual-displacement boundary conditions scheme. As shown in Figure 2, the atomistic core region is connected to the large continuum domain through a transition region (shaded area in the figure) where the two representations overlap, i.e., in this area atoms and nodes coincide. The transition region is subdivided into two zones: one (labeled II in the figure) provides the boundary conditions for the continuum, and the other (labeled III) provides the boundary conditions for the atomistic region. More specifically, in zone II the displacements of the finite-element nodes are determined by the displacements of the atoms with which they coincide, while in zone III the nodal displacements dictate how the atoms in that zone should move. This procedure ensures equality of the displacement fields in the atomistic region and in the continuum.

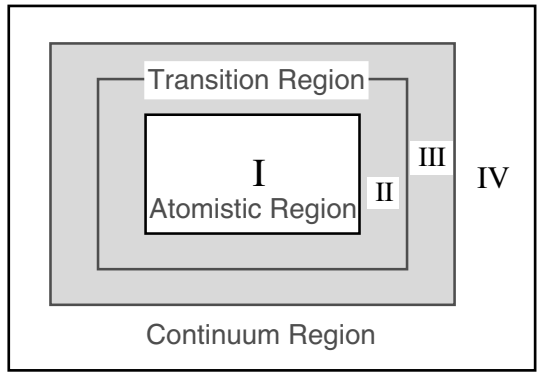

Figure 2 Schematic representation of the FEAt coupling scheme. The atomistic region (I) is embedded inside a continuum region (IV) and the two zones are coupled through an extended interface zone (shaded area). The transition region is divided into two zones (II and III), each providing boundary condition for either the continuum (zone II) or the atomistic region (zone III).

Sizewise, for three-dimensional problems zone II is actually a surface (a line for a 2D problem), while zone III should be sufficiently wide to provide a complete set of neighbors to those atoms in III that interact with atoms in II. This means that the width of zone III should be at least equal to the cutoff distance of the interatomic potential that is being used in the calculations. However, for density-dependent potentials or potentials containing three-body terms, the zone III width should be twice that distance.

Lastly, as pointed out earlier, no matching of the forces between the atomistic and the continuum regions has been introduced. Therefore, it is necessary to impose additional conditions to guarantee stress equilibrium between the two domains. To do so, the elastic energy is first expanded in a Taylor series with respect to the strain ϵ:

$$E(\epsilon) = E(0) + \left.\frac{\partial E}{\partial \epsilon_{ij}}\right|_0 \epsilon_{ij} + \frac{1}{2}\left.\frac{\partial^2 E}{\partial \epsilon_{ij}\epsilon_{kl}}\right|_0 \epsilon_{ij}\epsilon_{kl} + \frac{1}{6}\left.\frac{\partial^3 E}{\partial \epsilon_{ij}\epsilon_{kl}\epsilon_{mn}}\right|_0 \epsilon_{ij}\epsilon_{kl}\epsilon_{mn} + \dots \qquad [1]$$

then all coefficients are set equal in the atomistic and continuum regions (the strains had already been set equal because of the coupling procedure). This condition is therefore equivalent to the matching of the elastic constants between the two media:

$$\begin{aligned} c_{ij} &= \left.\frac{\partial E}{\partial \epsilon_{ij}}\right|_0 \qquad \text{first order} \\ c_{ijkl} &= \left.\frac{\partial^2 E}{\partial \epsilon_{ij}\epsilon_{kl}}\right|_0 \qquad \text{second order} \\ c_{ijklmn} &= \left.\frac{\partial^3 E}{\partial \epsilon_{ij}\epsilon_{kl}\epsilon_{mn}}\right|_0 \qquad \text{third order} \\ &\dots \end{aligned} \qquad [2]$$

The main approximation of the FEAt coupling method is therefore given by the truncation of the Taylor series expansion [1]. Within the framework of linear local elasticity theory, it is enough to retain (and match) terms only up to the second order. However, if nonlinear elastic effects need to be included, third-order elastic constants must also be matched. Moreover, because the first-order elastic constants in the continuum are zero by definition, such a matching condition requires the interatomic potential to yield zero stress in a perfect lattice.

Applications The FEAt methodology has been extensively applied to the study of crack propagation in body-centered cubic (bcc) metals (iron and

tungsten), both on cleavage and non-cleavage planes. Failure mechanisms for brittle fracture in nickel have been investigated as well, under mixed-mode loading conditions.[82–86]

The Quasi-continuum Method

The quasi-continuum (QC) method was first introduced in 1996 by Tadmor et al.[87,88] for the investigation of deformation in solids. Ever since, this method has been one of the most powerful and widely applied hybrid methodologies. Its primary applications include the study of dislocation nucleation, cracks, interfaces, grain boundary structure and deformation, nanoindentation phenomena, and so on. Various applications are discussed in more detail below. Since its appearance, the model has been improved and expanded,[89–94] and these more complete versions are briefly presented here. If additional details are needed, several specialized reviews are available.[71,95–98]

The idea behind the QC method is to consider the atomistic description (classical or quantum mechanically based) as being the correct way to model a material. Continuum assumptions are then progressively introduced to reduce the degrees of freedom of the system, making it computationally tractable. However, a fully atomistic resolution can be maintained wherever it is needed. The reduction of degrees of freedom occurs only through the introduction of kinematic constraints, i.e., where most of the atomic displacements are completely determined by the calculated positions of a much smaller subset of atoms. As a consequence, and this is one of the key features of the model, the coupling between the continuum and the atomistic regions is almost or completely seamless (depending upon which implementation of the method is considered). The coupling is seamless because the only difference between the two regions is the degree of coarsening, i.e., the constitutive properties of the continuum, as well as those of the atomic region, are always obtained from the atomistic level. This feature also garantees that key properties of the material, such as crystal symmetries and slip invariance, are automatically included. This makes the QC treatment of the continuum region significantly different from traditional continuum calculations, where constitutive properties are derived from assumed phenomenological forms.

A second key feature of the method is adaptive meshing,[99] i.e., the ability to shift the location of the atomistic/continuum boundary and to refine or coarsen the continuum grid during a single simulation. This feature makes the QC method particularly suited for investigating phenomena such as the diffusion of defects.

Lastly, any underlying atomistic model can be used, whether quantum mechanically or classically based. In practice, semi empirical interatomic potentials such as EAM[9,10] and Stillinger–Weber[8] (three-body interaction) potentials have usually been used to model the atomistic regime.

The reduction of the degrees of freedom in the QC method is based on the assumption that, under a smoothly changing deformation gradient, it is not

necessary to directly compute the displacement of every atom to determine the equilibrium configuration of the system. Under such circumstances, a subset of atoms can be used to represent the whole system. The displacement of such atoms, called representative atoms or *repatoms*, is therefore explicitly treated, while the displacement of the remaining atoms is approximated through interpolation. For an interpolation scheme, the QC method makes use of the finite-element method (FEM). Here, the solid is partitioned into a finite number of regions ("elements"). The deformation within each element is interpolated from the corresponding nodal displacements. A repatom is chosen for each element, and around it a small cluster of atoms (*crystallite*) is considered. This crystallite is distorted according to the continuum displacement field, and the energy of the repatom is computed using the atomistic model of choice. Figure 3 shows an example of such a coarsening mechanism. Of all of the atoms in the system (open circles) only a few (solid circles) are chosen as repatoms. In some QC formulations, the repatoms coincide with the FEM nodes. The density of the repatoms is adjusted according to the severity of the deformation gradient (in the example, there are many more repatoms near the dislocation core than away from it).

Mathematically, if a semiempirical model is used, then the total energy of the system, $E^{\text{tot}}(\mathbf{u})$, can be written as the sum of the energies of each atom:

$$E^{\text{tot}}(\mathbf{u}) = \sum_{i=1}^{N} E_i(\mathbf{u}) \qquad [3]$$

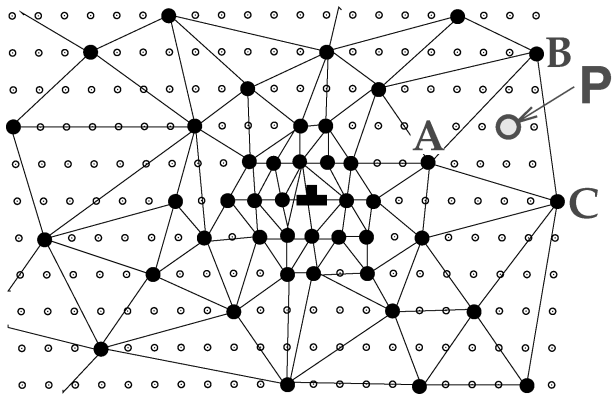

Figure 3 Example of repatom selection near a dislocation core. The repatoms (solid circles) become the nodes of a linear triangular mesh for the FEM. The density of the repatoms increases close to the dislocation core because the deformation gradient is larger.

where $\mathbf{u}$ is the atomic displacement field for the entire sample and N is the total number of atoms in the system. The first approximation of the QC method is to replace Eq. [3] with

$$E^{\text{tot},h} = \sum_{i=1}^{N} E_i(\mathbf{u}^h) \qquad [4]$$

where $\mathbf{u}^h$ are exactly calculated displacements for the repatoms (if coinciding with the FEM nodes) and interpolated displacements for all other atoms. An important point is that the displacement of nonrepresentative atoms inside an element (atom P in Figure 3, e.g.) is completely determined by the displacements of the nodes defining the element itself (atoms A, B, and C in the figure). Thus,

$$\mathbf{u}^h(\mathbf{X}_P) = \sum_j N_j(\mathbf{X}_P)\mathbf{u}_j \qquad j = A, B, C \qquad [5]$$

where N_j are the finite-element shape functions and $\mathbf{X}_P$ is the position of such a non-representative atom. This makes computing the total energy of the system (Eq. [4]) much faster than in the explicit case (Eq. [3]). However, because the summation in Eq. [4] still includes all of the atoms in the system, further approximations are needed to make the computations feasible for large systems. Depending upon which approximation is chosen, different formulations of the method (local, nonlocal, or mixed) are obtained.

Local QC The local formulation of the QC method[65,87,88] is the most straightforward and computationally efficient way to relate the atomic positions to the continuum displacement field. This formulation is based on two main approximations. First, the total energy of the system is obtained by adding the energies of each element, instead of each atom. Second, the element energy is computed using the Cauchy–Born rule,[100,101] i.e., assuming uniform deformation inside the element. More specifically, the Cauchy–Born rule states that the deformed structure of a crystal subject to a uniform deformation gradient $\mathbf{F}$ can be found by simply applying $\mathbf{F}$ to the undeformed crystal lattice basis $\mathbf{A}_i$ and then reconstructing the crystal from the altered basis vectors $\mathbf{a}_i$ (i.e., $\mathbf{a}_i = \mathbf{F}\mathbf{A}_i$). Therefore, one atom (repatom) is chosen inside each element (near the quadrature point), such that its crystallite is completely enclosed in the element itself [see Figure 4(a)], so that the same deformation gradient can reasonably be assumed for the entire crystallite. Then, its energy is found by calculating the energy of the corresponding perfect, periodic crystal that is generated using the deformed basis vectors $\mathbf{a}_i = F\mathbf{A}_i$, where $\mathbf{F}$ is the deformation gradient for the chosen repatom. Finally,

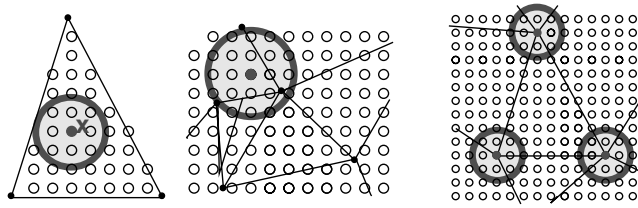

Figure 4 Schematic of sampling choices for various QC formulations. (a) Local QC: The repatom and its crystallite are completely contained inside one element (X indicates the quadrature point). (b) Nonlocal QC in the energy formulation: The repatom is still contained inside the element, but its crystallite is not. (c) Fully nonlocal QC: The repatoms coincide with the FEM nodes, and the atoms comprising their crystallites are individually considered in the energy calculation.

the energy of the element is obtained by multiplying the energy of the repatom by the number of atoms in the element, or, more precisely:

$$E^{\text{tot},h'} = \sum_{e=1}^{N_{\text{elements}}} \Omega_e \varepsilon_e(\mathbf{F_e}) \qquad [6]$$

$$\varepsilon_e(\mathbf{F}) = \frac{E_0(\mathbf{F})}{\Omega_0} \qquad [7]$$

where Ω_e is the volume of element e, ε_e is its energy density, Ω_0 is the unit cell volume, and E_0 is the energy of the unit cell.

Clearly, this method for computing the element energy is very fast. Also, because it only requires the energy of a single unit cell with periodic boundary conditions (PBC), the local QC method allows the use of quantum mechanical models, such as tight-binding[22–24] and DFT, that cannot be written as a sum over individual atom energies. However, the local QC approximation is reasonable only for displacements that vary slowly from one element to the next. The Cauchy–Born rule, for one, does not allow relaxation of the basis atoms inside the unit cell. More importantly, inhomogeneous structural features such as surfaces, interfaces, and stacking faults can not be modeled.

Fully Nonlocal QC The nonlocal formulation of the QC method was developed for modeling inhomogeneous structural features. A first formulation was presented in the original QC studies;[87,88] this method was later expanded (see, e.g., Ref. 89) and, finally, the fully nonlocal QC (FNL-QC) method was developed by Knap and Ortiz.[102–104] The key point of the nonlocal formulation is that each atom within the representative crystallite is displaced according to the actual continuum displacement field at its position. Thus, the displacement field considered when computing the energy (or force) of a repatom can be nonuniform. In the original formulation, the repatoms are

placed near the quadrature point of each element (as they are in the local QC method), so nonuniform displacement fields are included in the calculations if a given element is smaller than its crystallite [Figure 4(b)]. In such a case, the crystallite includes atoms belonging to different elements and therefore experiences different displacement fields. In later formulations, however, the repatoms are placed at the nodes of the finite-element grid [Figure 4(c)], so they are always experiencing nonuniform displacement fields.

The nonlocal QC method has been formulated in both *energy-based* and *force-based* forms. In the first, the energy of the system is approximated by the weighted sum of the energies of the repatoms:

$$E^{\text{tot},h} = \sum_{\alpha=1}^{N_{\text{rep}}} n_\alpha E_\alpha(\mathbf{u}_h) \qquad [8]$$

$$n_\alpha = \text{weight function such that} \sum_{\alpha=1}^{N_{\text{rep}}} n_\alpha = N \qquad [9]$$

and, again, the energy of each repatom is obtained by selecting a cluster of atoms around the repatom, displacing each atom in the cluster as dictated by the interpolated displacement field at that point and then computing the energy of the cluster using the classical potential of choice. Forces on all of the repatoms can then be obtained as derivatives of Eq. [8] with respect to the repatom positions.

In the forced-based form,[102–104] the equilibrium configuration is found by working directly with an approximate expression for the forces. Again, a spherical cluster (crystallite) is defined around each repatom, and every atom in it is displaced according to the interpolated displacement field at that point. To avoid the overlapping of such clusters in regions of high repatom density, the clusters are suitably truncated. The optimal cluster size is a balance between computational efficiency and error in the approximation and was found by Knap and Ortiz[102] to be on the order of first or second neighbor shells.

The main advantage of the nonlocal QC method is that it reduces exactly to the lattice static solution when refined down to the atomic scale. The main disadvantage of this formulation is its computational cost, as compared to the local approach. Each energy or force evaluation requires the mapping of a cluster of atoms and their neighbors to their deformed configuration at each repatom, followed by the interatomic potential evaluation necessary to compute the energy or forces for the cluster. Another problem with this formulation is that surface or interface effects can be significantly overestimated. If a repatom near an inhomogeneous structural feature belongs to a large element, its high energy is going to be multiplied by a large weight, and its contribution to Eq. [8] will be artificially large, leading to an overestimate of the final

energy. An obvious, but computationally expensive solution to this problem is to only consider very small (ideally atomic size) elements very close to highly inhomogeneous features.

QC-Mixed: Coupled Local/Nonlocal QC A way to exploit the accuracy of the nonlocal QC method in regions where atomic resolution is needed or inhomogeneities are present, without paying the high computational price that this formulation requires, is to couple it to the local formulation. Thus, the local approach is used where the elastic displacement field is changing slowly, and the nonlocal method is used only in proximity to defects, surfaces, interfaces, and so on. This general prescription leads to a very effective methodology, the coupled local/nonlocal QC method. Here, each repatom is treated either as being local or nonlocal, and the total energy of the system is given by the sum of the repatom energies:

$$E^{\text{tot},b} = \sum_{\alpha=1}^{N_{\text{nonloc}}} n_\alpha E_\alpha(\mathbf{u}_b) + \sum_{e=1}^{N_{\text{loc}}} \Omega_e \varepsilon_e(\mathbf{F}_e) \qquad [10]$$

The disadvantage of this formulation is the creation of a local/nonlocal interface, i.e., a region across which the computational methodology is abruptly changed. This does not happen in the two previous formulations. Even though a detailed prescription is given (Ref. 95, e.g.) for avoiding double counting the energy contributions from interface repatoms, it is not possible to avoid the formation of unphysical forces (ghost forces) if a unique energy functional is considered for the whole system (e.g., as in eq. [10]).

Ghost Forces If a coupled local/nonlocal QC method is used in its standard formulation (with a unique energy functional for the whole system), then the mismatch between the local (continuum) and nonlocal (atomistic) formulations produces nonphysical forces in the hand-shake region. As a result, atoms close to the local/nonlocal interface have nonzero forces acting on them even for a perfect crystal in its ground state, i.e., local displacements at the interface will unphysically lower the total energy of the system. These forces, named ghost forces, come into play because of the asymmetry in the contributions to the repatom energies between the local and nonlocal cases. The origin of such an asymmetry is the following. Since a *nonlocal* repatom treats all of the repatoms in its crystallite as neighbors (even those that do not belong to adjacent elements), their displacements affect the nonlocal repatom's energy. However, the energy of a *local* repatom depends only on the displacements of the adjacent repatoms. This asymmetry leaves unbalanced forces. A more explicit treatment of these forces can be found in Ref. 71.

Ghost Force Reduction Methods (QC-GFC, SCF-HACG, . . .) Several methods have been developed to alleviate or eliminate the effect of ghost

forces. For example, the QC developers themselves[95,99] suggested adding corrective forces as static loads. In this methodology, the exact ghost forces are calculated for the initial reference state, and then the negative of these forces is applied, throughout the entire simulation, to the atoms in the interface region. The energy functional is then obtained by adding a term associated with the work done by these dead-load forces to the standard QC energy functional. However, if the meshing is changed during the simulation, the ghost forces have to be recalculated after each remeshing step, and the procedure becomes much more computationally intensive. Also, and more importantly, these correction forces are nonconservative,[105] which leads to major problems with energy conservation during molecular dynamic simulations.

Alternatively, Mortensen et al.[106] suggest using two different approximate force expressions for the local nodes and the nonlocal repatoms. The two expressions will differ from the negative derivative of the energy only in the interface region. As with the previous method, this approach involves nonconservative forces.

A different solution to the ghost forces problem was suggested by Shimokawa et al.,[105] and then later generalized by E et al.[107] In the Shimokawa approach, atoms at the local/nonlocal interface are considered *quasi-nonlocal*, i.e., they act as local atoms when interacting with "real" local repatoms and as nonlocal atoms when interacting with nonlocal repatoms. E et al.[107] expanded this idea and determined a necessary and sufficient geometric condition for locally uniform first-order accuracy at the local/nonlocal interface that contains the quasi-local approach as a special case and guarantees the elimination of the ghost forces.

An alternative scheme to eliminate ghost forces (QC-ghost forces corrected or QC-GFC[71]) is to abandon the requirement of a unique energy functional for the entire system and, as done in the force-based FNL-QC formulation, to seek equilibrium by determining the atomic configuration for which the forces on all the repatoms is zero. In this case, the local and nonlocal regions are not directly coupled, except through the overlapping of their domains.

Similarly, the newly proposed SCF-HACG method (self-consistent-field approach for the hybrid atomistic coarse-grained treatment of multiscale processes), by Diestler et al.,[108] also suggests dividing the system into two regions, the *near region* (the area of most interest, where significant changes occur) and the *far region*. These regions are iteratively relaxed using a Monte Carlo algorithm, until the whole system has self-consistently reached equilibrium. Only the far region is coarse grained; the remainder is described strictly at the atomic scale. A two-stage Monte Carlo algorithm is used, where, in stage I, the nodes of the coarse-grained far region are held fixed while the near region atoms are subjected to random displacements. In stage II, the atoms in the near region are kept fixed in the final configuration of stage I, while the far-region nodes are given random trial displacements sequentially. More details

on the potential energy governing the acceptance of the trial displacements, the functional form of the force, and the "all-local" approximation used in determining the change in potential energy accompanying the trial move of each node are given in Refs. 108 and 109. Lastly, it must be noted that this methodology also allows for a finite-temperature treatment of the system (see discussion below).

QC and FNL-QC Applications The QC method has been applied to the study of a wide variety of materials and mechanical problems. From a materials stand point, it has been used to model both metals [especially face-centered cubic (fcc)] and semiconductors (mostly Si[110–112]). As examples, some of the most recent works that utilized QC methods to investigate the behavior of metals include studies of copper,[106,113–118] nickel,[119,120] aluminum,[104,113,120–123] silver,[116] palladium,[116] gold,[103,120] and fcc metals in general.[124] With respect to mechanical behavior, the phenomena most commonly investigated using QC methods are grain boundary structures,[113,114,121] nanoindentation and dislocation nucleation,[115,116,119–121,123] cracks,[118,122] interfaces,[117,118] the formation and strength of dislocation junctions,[124] and cross slip and mobility of dislocations.[106] References to several other application studies can be found, for instance, in Ref. 71.

A more complete, and continously updated list of QC-related publications can be found on the Web at http://www.qcmethod.com/qc_publications. html.

Extensions of the QC Method Because of its versatility, the QC method has been widely applied and, naturally, extended as well. While its original formulation was for zero-temperature static problems only, several groups have modified it to allow for finite-temperature investigations of equilibrium properties as well. A detailed discussion of some of these methodologies is presented in the discussion of finite-temperature methods below. Also, Dupoy et al. have extended it to include a finite-temperature alternative to molecular dynamics (see below). Lastly, the quasi-continuum method has also been coupled to a DFT description of the system in the OFDFT-QC (orbital-free DFT-QC) methodology discussed below.

Coupled Atomistic and Discrete Dislocation Method

The coupled atomistic and discrete dislocation (CADD) method was developed by Shilkrot, Miller, Dewalt, and Curtin[71,125–128] as a continuum/atomistic hybrid methodology where defects (specifically dislocations) are allowed to move, can exist in both the atomistic and the continuum region, and, lastly, are permitted to cross the boundary between such domains. The methodology has later been expanded to model finite temperature as well.[129]

Similarly to the FEAt and CLS methods, CADD is based on a spatial separation of the physical problem into regions, which are modeled by either

atomistic potentials or a continuum finite-element method. However, neither FEAt nor CLS allow for the existence of continuum dislocations in the finite-element region, nor can they easily modify the size of the atomistic region to model a propagating defect. The quasi-continuum method (see above) is able to follow a moving defect because of an adaptive remeshing algorithm, but it does not support a continuum description of dislocations. This means that in the QC model, each dislocation has to be completely embedded in an atomistic region, therefore substantially limiting the number of dislocations that can be treated because of their computational cost. In the CADD methodology, not only the presence and movement of continuum discrete dislocations in the continuum regime is possible, but also their interactions with each other and with atoms in the atomistic region.

In its current implementation, the CADD method can only deal with 2D problems, i.e., problems where the dislocations all have a line direction perpendicular to the modeled plane. However, the method does not contain any limitation on the dislocation character (edge, screw, or mixed) because periodic boundary conditions along the z direction are used in the atomistic region and three degrees of freedom (displacements u_x, u_y, and u_z) are considered in the two-dimensional (x-y) continuum region. The extension of the methodology to the 3D case is not trivial and is currently being explored.

It must also be noted that this is an iterative method (no unique energy functional exists) that covers both the atomistic and the continuum regions. This is because of the methodology adopted to minimize the ghost forces, which will discussed in more detail below. A modified conjugate-gradient algorithm is used to search for the point of zero forces on all degrees of freedom in order to drive the system to equilibrium. While doing so, atomic coordinates and dislocation positions are updated simultaneously.

There are four main components to the CADD approach: the atomistic model, the discrete dislocation framework, the coupling between these regions, and the method for detecting and passing dislocations through the atomistic/continuum boundary. The atomistic model most commonly used in CADD simulations is the EAM.[9,10] However, more complex atomistic approaches could be utilized as well. The adopted discrete dislocation framework is that of van der Giessen and Needleman.[130] It is beyond the scope of this review to illustrate such a methodology and how it is incorporated into the CADD model, so we refer the interested reader to the original studies[71,125–128] and references within. That also applies to the description of the algorithm used to detect and move dislocations through the atomistic/continuum boundary. In the following we will describe the coupling mechanism between zones.

The general boundary value problem that the CADD method wishes to solve is the following: A body, containing N continuum dislocations, is divided into an atomistic region Ω_A and a continuum region Ω_C. Such a system is subject to a known traction $\mathbf{T} = \mathbf{T}_0$ and initial displacements $\mathbf{u} = \mathbf{u}_0$. The

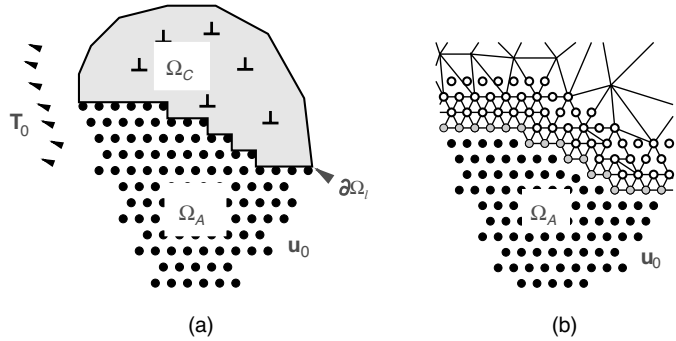

Figure 5 Schematic representation of the continuum/atomistic coupling in the CADD method. In (a) the system is portrayed: The atomic region Ω_A and the continuum one Ω_C are joined at an interface $\partial\Omega_I$ defined by a line of atoms (not necessarily straight) and are subject to a prescribed traction, $\mathbf{T}_0$, and initial displacements, $\mathbf{u}_0$. In (b) the continuum/atomistic interface is displayed in detail: Solid circles represent real atoms in the bulk, gray circles represent real atoms on the interface, and unfilled circles represent pad atoms. Pad atoms are situated in the continuum region. The finite-element mapping is shown in the continuum region as well.

atomistic and continuum domains are joined at an interface ($\partial\Omega_I$) that is defined by a line of atoms [Figure 5(a)]. Because tractions applied on boundary atoms are inherently discrete, they are more intuitively treated as lumped forces $\mathbf{f}_A$ on individual atoms. The CADD approach solves this boundary value problem for the equilibrium stress σ, strain ϵ, displacement fields $\mathbf{u}$, and discrete dislocation positions $\mathbf{d}^i$ in the continuum, and, simultaneously, for the equilibrium positions of the atoms, as a function of the imposed boundary conditions.

In the atomistic region, any number of defects can be present (dislocations, grain boundaries, vacancies, etc.), and the only assumption is that near the atomistic/continuum interface the atoms should behave in a way that approaches the linear elastic response used to describe the continuum. The only exceptions to this rule are the atoms constituting the core of a dislocation moving across the atomistic/continuum interface. In the continuum domain, the only allowed defects are continuum dislocations. Summarizing, the degrees of freedom in the continuum region are given by the dislocation positions $\mathbf{d}^i$ and by the finite-element nodal displacements $\mathbf{U}_C$ and $\mathbf{U}_I$ (where C indicates a continuum quantity and I indicates an interface quantity). In the atomistic region, the degrees of freedom are simply given by the atomic positions, $\mathbf{r}_A$ and $\mathbf{r}_I$ (A is for "quantity associated with the atomistic region," while, again, I indicates a quantity associated with the atomistic/continuum interface). To minimize the effect of the atomistic/continuum transition, the discretization of the continuum region matches the atomistic lattice at the interface: The interface atoms $\mathbf{r}_I$ also act as interface nodes with displacement $\mathbf{U}_I$.

To connect the two regions while making sure that the real atoms near and at the interface are correctly coordinated, pad atoms are added to the system in the continuum region [see Figure 5(b)]. This treatment of the handshake region is inspired by the one used in the FEAt method. The pad thickness is crucial for obtaining correct results, and not only should it be larger than the range of the atomistic interactions $\mathbf{r}_{\text{cut}}$, but the real atoms must continue to be correctly coordinated even after dislocations have crossed the boundary between the atomistic and continuum zones, a phenomenon that generates slip steps at the interface. The positions, $\mathbf{r}_P$, of the pad atoms are obtained by interpolating the FE nodal displacements to their reference positions, i.e., they are considered a ''continuum region'' quantity and are instantaneously perceived as fixed by the real atoms. However, the expression for the total energy of the atomistic domain includes interactions with the pad atoms:

$$E^a = \sum_{i\in(A,I,P)} E_i(\mathbf{r}_A, \mathbf{r}_I, \mathbf{r}_P)\mathbf{f}_A \cdot \mathbf{u}_A \qquad [11]$$

where $\mathbf{u}_A$ are the atomic displacements, $\mathbf{f}_A$ are the lumped forces, and the sum includes the pad atoms even though they are not degrees of freedom. The full atomistic forces on the atoms are then obtained by taking the partial derivatives of E^a with respect to positions $\mathbf{r}_A$ and $\mathbf{r}_I$. It is important to notice that only the partial derivatives of E^a with respect to the pad atom positions would contain unphysical forces, but they are not needed because the pad atom displacements are completely determined by those of the FE nodes. The total energy functional for the continuum domain is given by a sum over the energies, E_μ, of the finite elements, μ, plus boundary work terms:

$$E^c = \sum_{\mu} E_\mu(\mathbf{U}_I, \mathbf{U}_C, \mathbf{d}^i) - \int_{\partial\Omega_T} \mathbf{T}_0\mathbf{u}\, dA \qquad [12]$$

It is important to mention that the displacement of the interfacial nodes, $\mathbf{U}_I$, are not degrees of freedom in the continuum calculation: Because the interfacial nodes coincide with interface atoms, $\mathbf{r}_I$, they are moved as atoms and appear as fixed nodes with prescribed displacements to the other elements of the continuum region. Lastly, it must be remarked that this formulation of the continuum/atomistic coupling does not allow for the use of a unique energy functional because E^a includes the elastic energy of the pad atoms, whose energy is already implicitly contained in the continuum energy, E^c.

Before concluding the analysis of the hybrid coupling utilized in the CADD method, it is important to briefly discuss the issue of ghost forces. As in all of the other coupled methodologies, in CADD the main cause for such spurious forces is that the atomistic region is inherently nonlocal since the range of realistic interatomic potentials is larger than the nearest-neighbor

distance. The continuum region, however, is local since stresses at a point are completely determined by the deformation at that point. Moreover, CADD, as well as most of the other continuum/atomistic hybrid methodologies, assumes linear elasticity in the entire continuum region, and something very close to it in the atomistic region near the atomistic/continuum interface. However, core regions of real dislocations are strongly nonlinear, and hence such an assumption is significantly violated when a dislocation comes close to the atomistic/continuum interface. This issue is particularly important here because CADD's main purpose is dealing with dislocations, and, in particular, allowing dislocation motion through such an interface. To significantly reduce the spurious forces that arise when a dislocation crosses the atomistic/continuum boundary, the CADD's authors devised a specific method, the template method, to be added to the above-described treatment of the interface.[128] It is beyond the scope of this review to give a detailed description of such a methodology, we'll just mention that it is based on the idea of generating a template of true atomistic positions for the dislocation core, which is consistent with a far-field anisotropic linear elasticity solution, and using it as a discrete atomistic displacement field whenever the core of the dislocation is close to the atomic/continuum interface.

Applications The CADD method has been successfully applied to the investigation of Brinell nanoindentation to large penetration depth (up to 60Å) in hexagonal (2D) aluminum[131] and to the study of edge dislocation pile-ups interacting with a grain boundary in Al, under different loading conditions.[132]

Atomic Size Finite Element Method

The atomic size finite-element method (AFEM)[133,134] is an iterative procedure built on the idea that the use of a unified theoretical framework for atomistic and continuum calculations will lead to a seamless coupling between the two length scales. To accomplish that, the atomistic calculations are performed using the same formal structure that is used in the continuum FEM. A second important point in this methodology is the use, during the energy minimization, of both the first and the second derivatives of the system total energy, which leads to a much faster convergence than standard conjugate-gradient methods.

In the atomistic part of the procedure, particles are used as FEM nodes, even though, as will become clearer in the following, an AFEM element is quite different from the standard FEM definition. As for any zero-temperature equilibrium method, the objective is to determine the state of lowest energy, i.e., the system configuration such that

$$\frac{\partial E_{\text{tot}}}{\partial \mathbf{x}} = 0 \qquad [13]$$

To do so, a Taylor expansion of the energy is considered, up to the quadratic term:

$$E_{\text{tot}}(\mathbf{x}) \sim E_{\text{tot}}(\mathbf{x}_0) + \left.\frac{\partial E_{\text{tot}}}{\partial \mathbf{x}}\right|_{\mathbf{x}=\mathbf{x}_0} (\mathbf{x}-\mathbf{x}_0) + \frac{1}{2}(\mathbf{x}-\mathbf{x}_0)^{\mathrm{T}} \left.\frac{\partial^2 E_{\text{tot}}}{\partial \mathbf{x}\,\partial \mathbf{x}}\right|_{\mathbf{x}=\mathbf{x}_0} (\mathbf{x}-\mathbf{x}_0) \quad [14]$$

where $\mathbf{x}_0 = (\mathbf{x}_1^{(0)}, \mathbf{x}_2^{(0)}, \ldots, \mathbf{x}_N^{(0)})^{\mathrm{T}}$ is an initial guess of the equilibrium state. Substituting Eq. [14] into Eq. [13], and defining $\mathbf{u} = \mathbf{x} - \mathbf{x}_0$ as the atomic displacement, produces an equation typical of the continuum FEM:

$$\mathbf{K}\mathbf{u} = \mathbf{P} \quad [15]$$

where, following the FEM nomenclature, $\mathbf{K} = \partial^2 E_{\text{tot}}/\partial \mathbf{x}\ \partial \mathbf{x}|_{\mathbf{x}=\mathbf{x}_0}$ is the stiffness matrix, and $\mathbf{P} = \partial E_{\text{tot}}/\partial \mathbf{x}|_{\mathbf{x}=\mathbf{x}_0}$ is the nonequilibrium force vector. The main difference between the AFEM and the standard FEM is in the definition and properties of the elements. In AFEM an element i is defined as the ensemble of atoms that contribute to the computation of the atomic energy E_i [similar to the definition of crystallite in the fully nonlocal quasi-continuum method (discussed above)]. Clearly, the size and shape of the elements depend on the atomic structure and chosen interatomic potential. However, in AFEM the "elements" overlap in space, to account for multibody atomistic interactions, while in the FNL-QC method the crystallites were suitably truncated to avoid overlapping. This means that, in AFEM, the energy is not partitioned into elements, as it is in standard FEM, and that all of the atoms inside an element contribute to the energy calculations, not only the nodes. Equation [15] is then solved iteratively until $\mathbf{P}$ reaches zero. When both atomistic and continuum region are considered (i.e., the AFEM is used in an hybrid methodology), the total energy of the system is minimized simultaneously with respect to both atomic positions (in AFEM) and FEM nodes (in continuum FEM).

Applications The AFEM methodology has been applied to the investigation of properties of single carbon nanotubes (e.g., deformation under compression), and of woven nanostructures of carbon nanotubes.[134] The same methodology has also been applied to simulate postbuckling[135] and critical strain[136] of carbon nanotubes.

Green's Function Boundary Condition Methods

In the following, we explore the possibility of imposing boundary conditions as a way to relieve incompatibility stresses at the interfaces between computational domains, while, at the same time, allowing the use of a minimal atomistic region. More specifically, boundary condition (BC) methods can be

used to simulate phenomena where the elasticity solution does not change with the defect size (outside of a predefined core region) and phenomena where, instead, the elasticity solution evolves in the neighborhood of the defect. Simulations of a dislocation core, or of kinks on a dislocation, are examples of the first class of phenomena, while the investigation of crack propagation is an example of the second class. Green's function boundary condition (GFBC) methods are well suited for the investigation of the former class of processes, while boundary condition methodologies that couple finite-element-continuum domains to atomistic regions are designed for modeling the latter. This second class of boundary condition methods is examined below. Several groups have proposed GFBC methodologies,[137–141] and, in the following, as an example, we will discuss the one suggested by Sinclair et al.[140] and then expanded by Rao et al.[141]

The simplest approach to simulate an infinite dislocation line is to consider an atomistic cell of cylindrical shape, aligned along the dislocation line itself, and embed it into a fixed continuum region [Figure 6(a)]. Such a configuration is usually referred to as 2D because the thickness of the cell along

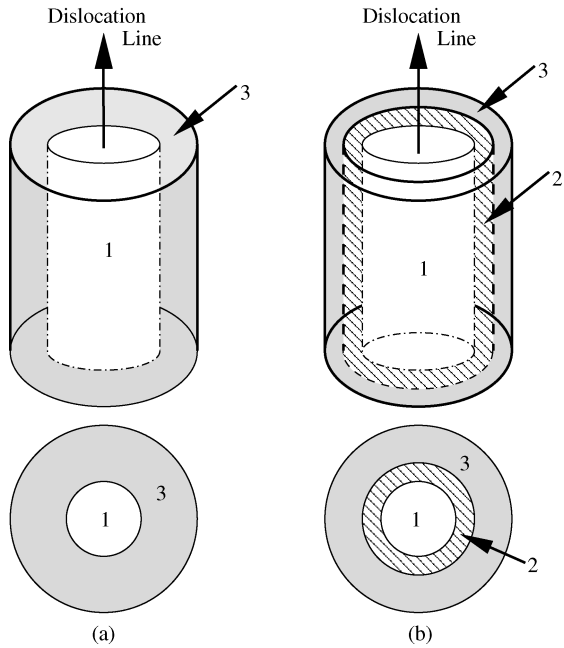

Figure 6 Simulation cells for studying dislocation cores in the 2D case. (a) In the fixed boundary approach, region 1 is the atomistic region, where atoms are allowed to relax, while region 3 is the fixed outer shell mimicking the continuum medium. (b) In the GFBC method of Rao et al.,[141] an intermediate shell (region 2) is inserted between the atomistic (region 1) and the continuum domains (region 3).

the dislocation line direction is minimal, just the amount needed to fully describe the crystal structure. The use of such a configuration allows for the modeling of a single straight dislocation, but not of complex defects such as dislocation interaction or kinks. The thickness of the continuum region (region 3 in the figure) corresponds to the maximum range of the classical potential, i.e., all of the atoms in the core (region 1) are given a computationally complete set of neighbors. Periodic boundary conditions are applied along the direction of the dislocation line, and atoms inside the atomistic region are allowed to relax during the simulation. Because the external shell is kept fixed at all times, we can label this approach as *fixed boundary*. The downside of such a simple approach is that incompatibility forces arise at the continuum/atomistic interface and become negligible only when very large atomistic regions are considered.

To overcome this difficulty, and to allow for the use of a much smaller core region, Rao et al.[141] took the GFBC method originally developed by Sinclair et al.[140] for 2D simulations and extended it to the 3D case. For simplicity, let us examine the 2D scenario (the same principle applies to 3D simulations as well). Now, a cylindrical shell of thickness equal to the range of the classical potential [region 2 in Figure 6(b)] is inserted in between the atomistic and the continuum domains. Because of its thickness, such a shell contains all of the atoms in the continuum domain on which atoms in region 1 may exert a force. The simulation is started by placing all of the atoms in the system (regions 1, 2, and 3) into positions determined using a linear elastic displacement field. Then, atoms in region 1 are individually relaxed, while atoms in region 2 and 3 are displaced collectively, according to the Green's function solution for a line force acting on a perfect lattice.[142,143] Equilibrium is reached through an iterative procedure, where region 1 is relaxed first, and then the forces still acting on atoms in region 2 are used to determine a corrective displacement field on all three regions from a superposition of Green's functions. Details on the relaxation procedure, the Green's function solutions, and the extention of the methodology to the 3D case can be found in the original studies. Using such a computational technique, Rao et al.[141] managed to reduce simulation cell sizes by as much as 90%.

Applications Sinclair et al.[140] used the GFBC method to investigate [100] edge dislocations in α iron, while Rao et al.[141] applied their expanded version to the study of straight screw dislocations in Ni, kinks (isolated or as a periodic array) on a screw dislocation in bcc Fe, screw dislocations in Mo, and 3D cross-slip core structures of screw dislocations in fcc metals.[141,144,145]

Finite-Temperature Equilibrium Methods

In the following, we present some finite-temperature static/semistatic methods that utilize a coupled atomistic/continuum description of the system. As with the zero-temperature case, they are a better choice than dynamical

methods if only equilibrium properties are investigated, because they (1) are usually computationally faster than dynamical ones, (2) can probe a larger part of the configurational space, and (3) are not affected by the spurious wave reflections at the atomistic/continuum interface as happens with most dynamical methods. The key difference between zero-temperature and finite-temperature equilibrium methods is that in the former it is sufficient to minimize the effective energy, while in the latter an effective free energy must be constructed and then minimized. However, if dealing with the free energy directly is computationally too expensive, alternative routes can also be used. One of the most popular of these is the Monte Carlo (MC) method,[15–17] where a random sampling of the phase space is used to reach equilibrium, instead of directly minimizing the free energy. To conclude, it is worth noticing that most of the methods discussed in this section can be considered as extentions of the zero-temperature quasi-continuum (QC) method (see above).

Basic Approximations

The majority of the finite-temperature equilibrium methods that we are about to discuss make use of a few key approximations in order to minimize the computational load. To begin with, an harmonic approximation of the atomistic potential is used,[110,146] both when computing the Helmholtz free energy directly and when determining the effective energy to use in MC calculations. In the harmonic approximation of the potential, only terms up to the second order are retained in the Taylor expansion of the total potential energy.

A second, very important, approximation is the local harmonic approximation (LHA),[147–149] which states that all of the atoms in the system can be treated as independent oscillators, i.e., the Einstein model can be used to describe the material, all of the atoms have the same vibrational frequencies, and the correlation between the vibrations of different atoms is neglected. The introduction of this approximation greatly simplifies the calculations, but also significantly diminishes the accuracy of the results. Therefore, the next three computational methods are discussed in order of increasing theoretical accuracy, with the first method being the least accurate (and therefore the most computationally tractable) because it uses the LHA for describing both the representative and slave atoms. The second method is an intermediate treatment (the LHA is used only for slave atoms), and the third method is the most accurate since it does not use the LHA at all.

A third approximation often used is the high-temperature classical limit,[147] where $\sinh(h\omega_{ik}/4\pi k_B T) \approx h\omega_{ik}/4\pi k_B T$. Using such an approximation greatly simplifies computing the Helmholtz free energy or the effective energy, but it is not valid at temperatures above one half of the melting point.[146,149] Lastly, we would like to mention that the methods presented here are just some of the proposed methodologies that expand the QC idea to finite temperature (for others, see, e.g., Ref. 146).

QC Free Energy Functional Method

Diestler et al. have proposed several extensions of the QC method for the case of finite temperature.[109,150–152] In their earlier work, this group suggested Monte Carlo approaches,[150–152] while more recently they developed a free energy functional treatment for the investigation of finite-temperature quasi-static multiscale processes [109]. Here we'll discuss such a free energy functional methodology, while an example of the QC Monte Carlo approach will be discussed in the next section.

This treatment is based on the idea of replacing the zero-temperature QC potential energy function (e.g., Eq. [10]) with a free energy functional, F_c. The nonzero-temperature equilibrium is then found by minimizing such a free energy using a standard conjugate gradient algorithm [14]. The method is designed for investigating systems under constant temperature, T, and density conditions, so the relevant free energy to be minimized is the Helmholtz free energy, F,

$$F = E - TS \qquad [16]$$

where E is the energy of the system and S is the entropy. Assuming that both the local and nonlocal elements comprising the finite-element coarse-graining mesh that covers the entire system are subject only to homogeneous deformation, then the Helmholtz free energy for the coarse-grained system can be approximated by

$$F = \sum_{e=1}^{N_e} N_a^e f_e \qquad [17]$$

where the summation is over all of the N_e elements, N_a^e is the number of atoms in element e, and f_e is the Helmholtz free energy per atom. Using the local harmonic approximation[147–149] (see next section), the Helmholtz free energy per atom is approximated by

$$f_e = u_e + 3k_B T \ln\left[\frac{h(\det \mathbf{D}_e)^{1/6}}{2\pi k_B T}\right] \qquad [18]$$

where h is Plank's constant, u_e is the potential energy per atom at zero temperature (using the Lennard-Jones interatomic potential, e.g.), and $\mathbf{D}_e$ is the dynamical matrix associated with the representative atom, again calculated for the zero-temperature system. Computationally, the evaluation of f_e for a local element is not too demanding: u_e is obtained by applying the Cauchy–Born rule, and, likewise, $\mathbf{D}_e$ is computed as the dynamical matrix associated with an atom in an infinite crystal subject to the same deformation as the

representative atom under investigation. However, if the element is nonlocal, then the representative atom has neighbors in both its and other elements. Since the positions of atoms in different elements depend on the configurations of all the nodes of those elements, clearly the evaluation of f_e for nonlocal representative atoms is computationally much more involved.

Applications Up to now this method has only been applied to the computation of stresses in the simple case of a 3D, fcc Lennard-Jones crystal.[109] To avoid dealing with ghost forces, the method's authors choose to treat all the elements as local, irrespective of their true status. Such a crude approximation worked well in this test case, possibly because of the simplicity of the problem under examination.

Quasi-continuum Monte Carlo

Shenoy et al.[98,153] in 1999 proposed the quasi-continuum Monte Carlo (QCMC) method as a way to extend the quasi-continuum method to the study of equilibrium properties of materials at finite temperature. The objective of this treatment is to construct a computationally manageable expression for a temperature-dependent effective energy for a system maintained at fixed temperature. Such an energy would then be used instead of the zero-temperature effective energy (e.g., Eq. [10]) in a Monte Carlo formulation of the QC method.

In a Metropolis–Monte Carlo approach, the probability of finding the system in a specific configuration $\{\mathbf{u_i}\}$ is given by

$$P(\{\mathbf{u}_i\}) \propto e^{-\beta H(\{\mathbf{u}_i\},T)} \qquad [19]$$

where T is the temperature, $\beta = 1/k_B T$, k_B is Boltzmann's constant, and H is the system energy. In the QCMC method, the idea is to construct an effective energy that would depend only on the positions of the representative atoms, while the contribution of all the remaining atoms (called *slave atoms* in this treatment) is averaged over. To do so, the authors started from the assumption that the partition function of the system is unchanged when averaging out the slave atoms:

$$Z = \int d\mathbf{u}^R \, d\mathbf{u}^S e^{-\beta H(\{\mathbf{u}_i^R\},(\{\mathbf{u}_i^S\}))} = \int d\mathbf{u}^R e^{-\beta H^{\text{eff}}(\{\mathbf{u}_i^R\},T)} \qquad [20]$$

where the index R indicates quantities related to representative atoms, and S those related to slave atoms. Equation [20] leads to the definition of an effective energy as

$$e^{-\beta H^{\text{eff}}(\{\mathbf{u}_i^R\},T)} = \int d\mathbf{u}^S e^{-\beta H(\{\mathbf{u}_i^R\},(\{\mathbf{u}_i^S\}))} \qquad [21]$$

which is, by construction, only dependent on the representative atoms (all the slave degrees of freedom have been integrated out). In this model, the displacements of the slave atoms are assumed to be

$$\mathbf{u}_i^S = \sum_j \mathbf{u}_j^R N_j(\mathbf{X}_i^S) + \boldsymbol{\eta}_i \qquad [22]$$

which means that they are not completely determined in terms of the displacements of the representative atoms by finite-element interpolation [$\mathbf{u}_i^S = \sum_j \mathbf{u}_j^R N_j(\mathbf{X}_i^S)$], as they were in the zero-temperature QC Eq. [5], but they also depend on a fluctuational variable, $\boldsymbol{\eta}_i$, which accounts for temperature-driven random fluctuations in the finite-element shape functions. Using Eq. [22], expanding H in terms of the random fluctuations, terminating the expansion to the second order, and going through a rather involved derivation (for details we refer to Ref. 153), an approximate form of the effective energy function is obtained:

$$H_{\mathrm{QC}}(\{\mathbf{u}_i^R\}, T) = H_{\mathrm{QC}}(\{\mathbf{u}_i^R\}, 0) + 3k_B T \sum_e \nu_e^s \ln\left\{\frac{\hbar[\det \mathbf{D}(\mathbf{F}_e)]^{1/6}}{k_B T}\right\} \qquad [23]$$

where the first term accounts for the internal energy of the deformed crystal, while the second term contains the entropic contribution due to the slave degrees of freedom that were integrated out. In Eq. [23] $D(\mathbf{F}_e)$, is the local dynamical matrix of an atom in a crystal undergoing an homogeneous deformation gradient $\mathbf{F}$, and ν_e^s is the number of slave atoms in element e. In obtaining Eq. [23], several approximations were made, the most important one being the use of the local harmonic approximation (LHA; see discussion above), i.e., slave atoms are assumed to have harmonic displacements around their equilibrium positions. This means that all of the slave atoms in one element have the same vibrational frequencies, i.e., the correlation between the vibrations of different atoms is neglected. However, while the introduction of the local harmonic approximation in deriving Eq. [23] has notably expedited the calculation of the effective energy function, the energy determination still requires a larger computational effort than performing QC calculations at zero temperature. The most important limitation of this approach comes from the use of the local harmonic approximation as well: Because of it, the method is reliable only at low temperatures and has a tendency to underestimate the temperature dependence of defect free energies.

QC k-space Quasi-harmonic Model

An alternative approach to the calculation of the Helmholtz free energy is the k-space quasi-harmonic model (QC-QHMK)[110,154,155] introduced in 2001 by Aluru et al. This method, still a generalization of the quasi-continuum

methodology, is more accurate than the previous two because it does not make use of the local harmonic approximation, i.e., it preserves the coupling of the vibrations of different atoms. The key idea is to keep the amount of computation manageable by calculating the Helmholtz free energy in the reciprocal space while using Bloch's theorem[156] with the Born–von Karman boundary conditions.[157] The authors applied it to the investigation of the effect of temperature and strain on phonon and elastic properties in silicon.

Because of the reciprocal representation (details on the calculation can be found in Refs. 110,154, and 155), the dynamical matrix **D** for a representative atom α is reduced to a 6×6 matrix of the form

$$\mathbf{D}(\mathbf{k}) = \frac{1}{M}\begin{bmatrix} \Sigma_{\beta=1}^{N}\Phi_{j,k}^{11}(\alpha,\beta)e^{i\mathbf{k}\cdot\mathbf{R}_{\beta\alpha}^{0}} & \Sigma_{\beta=1}^{N}\Phi_{j,k}^{12}(\alpha,\beta)e^{i\mathbf{k}\cdot(\mathbf{R}_{\beta\alpha}^{0}-\mathbf{F}^{-1}\xi)} \\ \Sigma_{\beta=1}^{N}\Phi_{j,k}^{21}(\alpha,\beta)e^{i\mathbf{k}\cdot(\mathbf{R}_{\beta\alpha}^{0}+\mathbf{F}^{-1}\xi)} & \Sigma_{\beta=1}^{N}\Phi_{j,k}^{22}(\alpha,\beta)e^{i\mathbf{k}\cdot\mathbf{R}_{\beta\alpha}^{0}} \end{bmatrix} \quad [24]$$
$$\alpha = 1 \qquad j,k = 1,2,3$$

where $\mathbf{k}$ is the wave vector, $\Phi_{j,k}^{pq}(\alpha,\beta)$ is the force constant matrix, α is the representative atom (center atom), and β loops over all the atoms in the crystal. For more detail on this derivation, we refer to the original study.[110,154,155] The free energy of a representative atom α can therefore be written as

$$F_\alpha = U_\alpha^0 + \frac{1}{2V_B}\left(\frac{1}{2}\int_{\mathbf{k}}\sum_{s=1}^{6}\hbar\omega_s(\mathbf{k})\,d\mathbf{k} + k_BT\int_{\mathbf{k}}\sum_{s=1}^{6}\ln(1-e^{\hbar\omega_s(\mathbf{k})/k_BT})\,d\mathbf{k}\right) \quad [25]$$

where U_α^0 is the total potential energy of atom α evaluated using the equilibrium position of the system, V_B is the volume of the first Brillouin zone of the reciprocal lattice, and the factor 2 is due to the fact that the silicon lattice is made by two interpenetrating Bravais lattices. More importantly, $\omega_s(\mathbf{k}) = \sqrt{\lambda_s(\mathbf{k})}$, where $\lambda_s(\mathbf{k})$ are the eigenvalues of the 6×6 dynamical matrix **D** and s is the index of the polarization for the crystal. In deriving Eq. [25], the authors also used the fact that $\mathbf{k}$ can be assumed continuous for a bulk material. Lastly, in the QC-QHMK model, the vibrational component of the Helmholtz free energy (second term on the right-hand side in Eq. [25]) is evaluated for all the atoms corresponding to the continuum nodes by considering a bulk, nonlocal silicon crystal subjected to a homogeneous deformation given by the local deformation gradient (Cauchy–Born rule[158,159]).

Dynamical Methods

In this section, we discuss hybrid methodologies that explore the dynamical evolution of systems composed of a continuum region (usually described using finite-element methods) coupled to a discrete one [modeled using molecular dynamics (MD) algorithms and semiempirical classical potentials].

Dynamical hybrid methods face even greater challenges than equilibrium ones. In addition to dealing with the same difficulties in achieving a smooth matching in the hand-shake region, as discussed earlier, dynamical methods must also take into consideration the pathological wave reflection that occurs at the boundary between the discrete and the continuum regions. Such a reflection occurs because the distribution of wavelengths emitted by the MD region includes waves significantly shorter than those that can be captured by the continuum FE region. Because an energy-conserving formulation is usually used, the wave must go somewhere and, therefore, gets reflected back into the MD region, leading to fictitious heat generation in the atomistic region. The ability to minimize (or, even better, eliminate) such a reflection is therefore a key point in developing a successful dynamical hybrid methodology.

Lastly, to be effective, dynamical simulations should cover as long a time as possible. Therefore, the size of the time step is a significant issue in the effectiveness of the methodology. In most hybrid implementations, the size of the finite-element mesh is graded down to the atomic lattice size at the boundary between continuum and MD domains to reduce wave reflection (see discussions on domain decomposition and quasi-continuum coarse-grain alternative below). Because the time step in an FE simulation is governed by the smallest element in the mesh, this procedure requires the use of the same size time step in both the discrete and continuum domains, even though the large-scale physical quantities evolve much more slowly than the short-scale ones. However, a few methods, such as the bridging scale technique of Wagner and Liu discussed in the section on adaptive model refinement techniques, have particularly addressed this issue and allow for the possibility of using multiple time scales in hybrid simulations.

Domain Decomposition Methods

Domain decomposition methods are hybrid methodologies where the various computational methods are spatially separated, i.e., a higher level of theory (e.g., atomistic models) is used in the area of interest (near a vacancy, defect, crack tip, and so on), and a lower level of theory (e.g., continuum models) is used everywhere else. This is the most intuitive approach to the coupling problem, and often the easiest to implement computationally. Among these methodologies are some of the most widely used coupling schemes in the solid state (like the CLS method). However, the existence of spatial boundaries between computational methods may lead to hand-shake problems larger than those created by other approaches. In the following, a few examples of such an approach will be given.

Coupling of Length Scales Method: Atomistic/Continuum Part The FE/MD/TB coupling of length scales (CLS) method,[66,67,160–164] also known as MAAD (macroscopic, atomistic, ab initio dynamics), is one of the few methodologies to provide a dynamical coupling of three different regimes: the macroscopic

one, described using continuum mechanics, the mesoscopic one, modeled with classical atoms interacting through empirical potentials, and, lastly, the microscopic one, where a quantum mechanics description is necessary to correctly reproduce bond breaking. A good representation of quantum mechanical effects such as bond breaking was very important to the CLS developers because the method was aimed at the investigation of phenomena such as fracture and crack propagation. In this section, we will delineate the basic principles of the methodology, and we will provide a description of the FE/MD coupling, while details on the MD/TB coupling will be discussed below.

The CLS methodology uses an FE description to model the continuum, classical MD to simulate the evolution of the mesoscopic regime, and a TB molecular dynamics approach to include quantum effects in the overall treatment. The FE description is at the linear elastic level because its use is limited to regions where the atoms are only slightly perturbed from equilibrium. The classical molecular dynamics makes use of semiempirical potentials such as the Stillinger–Weber (SW) potential[8] for Si. Lastly, the tight-binding method was chosen instead of other, more accurate, quantum descriptions because of its computational speed.

The key idea in the CLS approach is to define a unified Hamiltonian H_{tot} across all three regions. This guarantees energy conservation, which is crucial for a realistic description of dynamics at finite temperature. Also, a single Hamiltonian requires a sharp interface between the regions. The Hamiltonian degrees of freedom are the atomic positions, $\mathbf{r}$, and velocities, $\dot{\mathbf{r}}$, for the MD and TB regions, and the *nodal* displacements, $\mathbf{u}$, and their time rates of change, $\dot{\mathbf{u}}$, for the FE region. Such a Hamiltonian has the form

$$\begin{aligned} H_{\text{tot}} = {} & H_{\text{FE}}(\{\mathbf{u}, \dot{\mathbf{u}}\} \in \text{FE}) + H_{\text{FE/MD}}(\{\mathbf{u}, \dot{\mathbf{u}}, \mathbf{r}, \dot{\mathbf{r}}\} \in \text{FE/MD}) \\ & + H_{\text{MD}}(\{\mathbf{r}, \dot{\mathbf{r}}\} \in \text{MD}) + H_{\text{MD/TB}}(\{\mathbf{r}, \dot{\mathbf{r}}\} \in \text{MD/TB}) \\ & + H_{\text{TB}}(\{\mathbf{r}, \dot{\mathbf{r}}\} \in \text{TB}) \end{aligned} \quad [26]$$

where $H_{\text{FE/MD}}$ and $H_{\text{MD/TB}}$ are the Hamiltonians that dictate the dynamics in the two hand-shake regions. The equations of motion are then obtained by taking the derivative of Eq. [26] with respect to all of the appropriate variables.

The matching of the FE and the MD modeling across the FE/MD interface is accomplished by fine-graining the FE grid down to the atomic size, so that a one-to-one correspondence between the MD atoms and FE nodes is achieved (Figure 7). Away from the interface and into the FE region, the mesh expands. In the FE domain, the one-to-one mapping is not necessary at distances larger than twice the cutoff of the classical potential, and, on the MD side, beyond the first line of elements. This asymmetry is due to the different locality of the two methods. Also, an assumption of no diffusion across the interface is made,

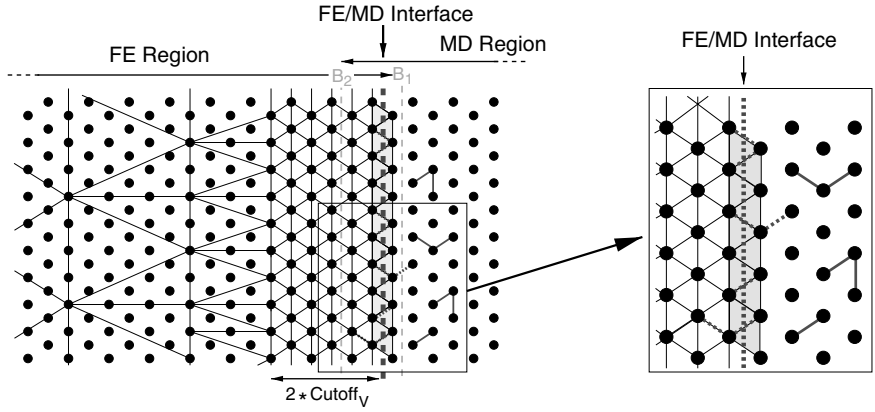

Figure 7 Schematic illustration of the hand-shake treatment near the FE/MD interface in the CLS method. A one-to-one atom-to-node mapping is considered in the FE zone up to a distance equal to twice the classical potential cutoff. After that, the mesh expands. Elements that are partially contained in the MD zone are displayed as shaded and contribute less than their entire energy to the Hamiltonian. Similarly, on the MD side, bonds crossing the interface (dashed lines) contribute less than their full weight, while bonds completely enclosed in the MD area (solid lines) have weight equal to one. B_1 and B_2 are the boundaries of the hand-shake region.

so that atoms remain near the corresponding mesh point on either side of the interface at all times. The way the hand-shake Hamiltonian is constructed is based on the idea that the interactions at the interface can be approximated to first order by an average of the two descriptions. This means that bonds completely contained in the MD region, or elements in the FE one, contribute with a full weight to the Hamiltonian, while bonds or elements only partially contained in their natural region contribute with a reduced weight to the overall Hamiltonian. More specifically, when considering as semiempirical potential the SW one, the hand-shake Hamiltonian becomes

$$\begin{aligned} H_{\mathrm{FE/MD}} = & \frac{1}{2}\sum_{i}^{N} m_i v_i^2 + \frac{1}{2}\sum_{i,j}^{N_{\mathrm{at}}} w_{ij} V_{ij}^{(2)}(\mathbf{r}_{ij}) \\ & + \frac{1}{6}\sum_{i,j,k}^{N_{\mathrm{at}}} w_{ijk} V_{ijk}^{(3)}(\mathbf{r}_{ij}, \mathbf{r}_{ik}) \\ & + \frac{1}{2}\sum_{l}^{N_e}\sum_{i,j}^{N_{\mathrm{ne}}} w_l \mathbf{u}_i^l \mathbf{k}_{ij}^l \mathbf{u}_j^l \end{aligned} \qquad [27]$$

where N, N_{at}, N_e, N_{ne}, are the total number of particles, atoms, elements, and nodes per element, respectively ($N < N_{\mathrm{at}} + N_{\mathrm{nodes}}$ because of the atom/node

overlap). Also, m_i and v_i indicate both the atomic and the nodal masses and velocities, respectively, while $V_{ij}^{(2)}$ and $V_{ijk}^{(3)}$ are the two- and three-body terms of the SW potential. Lastly, $\mathbf{u}^l$ and $\mathbf{k}^l$ are the FE displacement vector and stiffness matrix, respectively, for element l. The weights w_l, w_{ij}, and w_{ijk} are determined by matching the elastic constants of the hand-shake region to those of the "bulk" MD and FE systems and are given by (see Figure 7 for the definition of B_1 and B_2)

$$w_i = \begin{cases} 1 & \text{if } i \text{ or } j \text{ is to the right of } B_1 \\ \frac{3}{4} & \text{if } i \text{ and } j \text{ are between } B_1 \text{ and the FE/MD interface} \\ \frac{1}{2} & \text{if } i \text{ or } j \text{ crosses the FE/MD interface} \\ \frac{1}{4} & \text{if } i \text{ and } j \text{ are between } B_2 \text{ and the FE/MD interface} \\ 0 & \text{if } i \text{ or } j \text{ is to the left of } B_2 \end{cases} \quad [28]$$

$$w_i = \begin{cases} 1 & \text{if } l \text{ is to the left of } B_2 \\ \frac{1}{2} & \text{if } l \text{ crosses the FE/MD interface} \\ 0 & \text{if } l \text{ is to the right of the FE/MD interface} \end{cases} \quad [29]$$

The three-body weights, w_{ijk}, are defined similarly to the two-body ones, w_{ij}.

As discussed previously, an important issue that all dynamic multiscale methodologies must deal with is the phonon spectrum mismatch between the atomistic and coarse-grained regions. In the CLS method, this effect is handled by weakly coupling the FE degrees of freedom to a Brownian motion heat bath that is set to the desired temperature. As a last remark, we need to mention that this hybrid scheme is computationally very efficient and reasonably simple to implement, so that several groups other than the original authors have adopted it.

Applications The developers of the CLS method applied it to the investigation of fracture and crack propagation in silicon,[164–167] while Lidorikis et al. used it to model the strain relaxation and induced-stress distribution in Si/Si_3N_4 nanopixels.[168,169]

Overlapping Domain Decomposition and Edge-to-Edge Decomposition Methods In 2003, Belytschko and Xiao introduced the overlapping domain decomposition (ODD) method and the edge-to-edge decomposition (EED) method[170] to effectively couple atomistic simulations to continuum ones, particularly targeting the modeling of large deformations in nanosystems. The ODD method was later extended to include dynamical effects as well.[171]

In the ODD method, the atomistic and continuum regions are coupled through a standard hand-shake region, and a single energy functional is considered for the complete domain. As in most methods, the continuum is

discretized using a finite-element approach, but, in contrast to other methodologies (e.g., CLS), a uniform mesh is used for the entire continuum domain, as well as for the hand-shake region. Thus, the continuum mesh does not coincide with the atomic positions in the hand-shake part of the system. This methodology is well suited for the modeling of crystalline or amorphous solids subject to deformations small enough that voids or dislocations do not develop in the continuum subdomain, i.e., no diffusion of atoms into the continuum region can be considered. The method also provides a natural way to simulate heat flow through the system.

To correctly compute the energy of the hand-shake region, a scaling parameter for this region is defined as $\alpha = l(\mathbf{X})/l_0$, where $l(\mathbf{X})$ is the orthogonal projection of the position $\mathbf{X}$ onto the edge of the continuum domain, and l_0 is the length of this orthogonal projection to the edge of the atomistic domain (see Figure 8), so that

$$\alpha = \begin{cases} 1 & \text{in the continuum} - \text{only region, } (\Omega_0^C - \Omega_0^{\text{hand shake}}) \\ [0,1] & \text{in the hand} - \text{shake region, } \Omega_0^{\text{hand shake}} \\ 0 & \text{in the atomistic} - \text{only region, } (\Omega_0^A - \Omega_0^{\text{hand shake}}) \end{cases} \quad [30]$$

Using such a parameter, the Hamiltonian for the whole system is constructed as a linear combination of the atomistic and continuum Hamiltonians:

$$\begin{aligned} H &= (1-\alpha)H^A + \alpha H^C \\ &= \sum_I \left[1 - \alpha(\mathbf{X}_I)\right] \frac{\mathbf{p}_I^A \mathbf{p}_I^A}{2m_I} + (1-\alpha)W^A + \sum_N \alpha(\mathbf{X}_N) \frac{\mathbf{p}_N^C \mathbf{p}_N^C}{2M_N} + \alpha W^C \end{aligned} \quad [31]$$

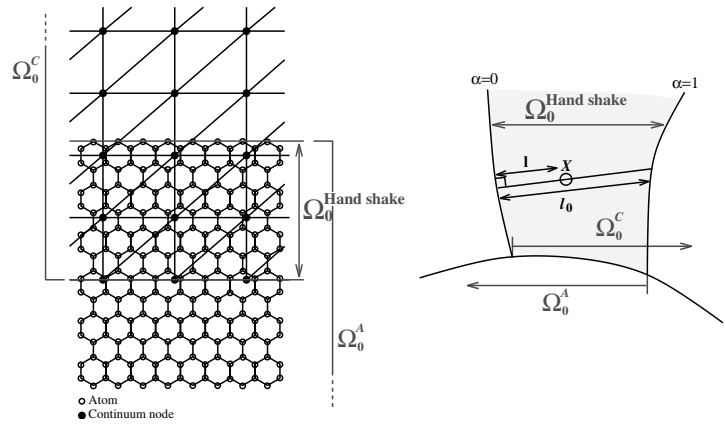

Figure 8 Coupling between the atomistic and the continuum domains in the ODD method.

where $\mathbf{p}^A$ is the atomic momentum, m_I is the atomic mass, W^A is the atomistic external potential, $\mathbf{p}^C$ and M_I are the nodal momentum and mass for the continuum model once it is discretized by a finite-element method and W^C is the total potential of the continuum model. The index I varies over all of the atoms, while the index N spans all of the nodes covering the continuum region. Explicit expressions for W^A and W^C are given in Ref. 171; for the scope of this review it is sufficient to specify that W^A should only be due to a constant external force, such as electrostatic forces, and a pairwise interatomic potential, while the constitutive equation for the finite-element method is constructed via the Cauchy–Born rule as in the quasi-continuum approach, or via the exponential Cauchy–Born rule[158] if monolayer crystalline membranes such as nanotubes are simulated. Lastly, the coupling of the two regimes (atomistic and continuum) is completed by requiring that the atomic displacements should conform to the continuum displacements at the discrete positions of the atoms.

The constraints are first applied to all components of the displacements by the Lagrange multiplier method; then the modifications needed for the augmented Lagrangian method are added. Lastly, the equations of motion for the Lagrange multiplier method are obtained. A detailed derivation of such equations of motion can be found in Ref. 171, together with the explicit recipe for the Verlet algorithm used to integrate such equations.

One of the issues in dynamical multiscale coupling is the tailoring of the time step to the different subdomains. If the same time step is used in both the atomistic and the continuum regions, computations will be wasted in the continuum model. However, if in the hand-shake region the size of the FEM elements is reduced to coincide with the individual atoms, it is difficult to tailor the time step. Therefore, the authors of the ODD method chose to use a uniform mesh for the continuum domain, so that a much larger time step could be used in the continuum model than in the atomistic one. A description of such a multiple-time-step algorithm is provided in the paper.[169]

With regard to the problem of phonon reflections from the interface, the authors provide test results that show that the ODD method dramatically reduces spurious wave reflections at the atomistic/continuum interface without any additional filtering procedure. If the overlapping subdomain is large enough, they find that the high-frequency wave reflection is almost completely eliminated.

Lastly, we will briefly describe the EED method introduced in Ref. 170. While this method is found to be almost as effective as the ODD for static applications, it is not suited for dynamical ones because it causes significant reflection of the high-frequency part of the wave at the atomic/continuum interface. In the EED method, no hand-shake region is defined and the coupling of the two regions occurs through an interface (Figure 9). Three types of "particles" are defined: nodes in the continuum region, atoms in the atomistic domain, and, virtual atoms that are introduced in the continuum domain to model the bond angle bending for bonds between the continuum and the

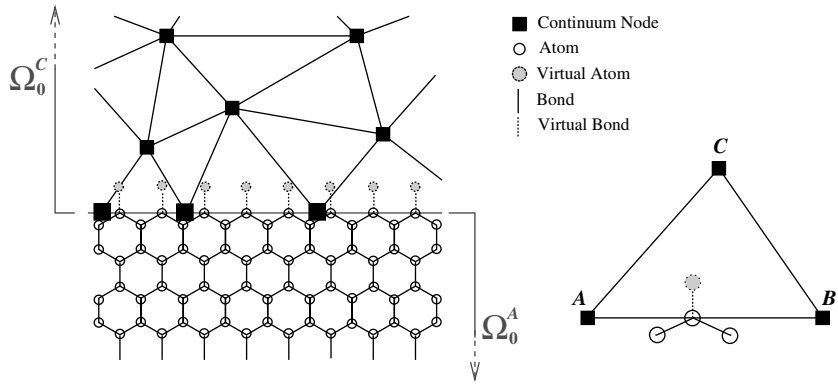

Figure 9 Coupling between the atomistic and continuum domains in the EED method: In contrast to the ODD case, no hand-shake region is considered, and the coupling of the two regions occurs through an interface.

molecular domains. The virtual atoms are connected to the real ones through virtual bonds. The internal potential energy for the entire system is the sum of the continuum (W^C) and atomistic (W^A) potential energies. The bond angle-bending potential resulting from the bond angle change between the virtual bonds is included in the atomistic potential energy. The motion of a virtual atom is completely determined by the displacements $\mathbf{u}$ of the nodes A, B, and C of its element (for a given choice of the shape functions N):

$$\mathbf{u}_f(\mathbf{X}, t) = \sum_I N_I(\mathbf{X})\mathbf{u}_I(t) \qquad I = A, B, C \tag{32}$$

The coupling between the two regions is then completed by imposing the same constraints as in the ODD method and, as before, the equations of motion can be obtained using the Lagrange multiplier method and the augmented Lagrangian method.

Applications The ODD and EED methods were tested and compared studying the semistatic bending of a graphite sheet and two nested carbon nanotubes.[170] The authors applied the dynamic ODD method to the study of wave propagation and dynamic crack propagation in a graphene sheet,[171] and, also, to the investigation of defects in carbon nanotubes.[172] A very detailed study of the coupling terms used in the ODD method is presented in Ref. 173. A further extension of the method is presented in Ref. 174.

Adaptive Model Refinement Techniques

The adaptive model refinement techniques, also called bridging scale/multigrid methods, are based on the idea of covering the entire computational

domain with a macrogrid on which a macroscale model is applied. Such a macroscale model is then locally refined in the area, or areas, of interest. This kind of approach avoids having to deal with spatial transitions in the computational technique and, therefore, minimizes the hand-shake problems.

Heterogeneous Multiscale Method The heterogeneous multiscale method (HMM)[175,176] provides a general framework for dealing with multiscale phenomena and can be easily applied to the coupling of continuum and atomistic (molecular dynamics) simulations at finite temperature.

The basic goal of this methodology is to enable simulations of macroscopic processes in cases where explicit macroscale models are invalid in at least part of the macroscopic system. In those regions, microscale models are used to supply the missing data. In the HMM, the computational saving comes from reducing both the spatial and the temporal domains. The spatial reduction is, as in all hybrid methodologies, due to the possibility of applying the higher level of theory only to a limited part of the whole system, while the reduction in temporal domain originates from the fact that this method naturally decouples the atomistic time scale from the continuum one, therefore allowing the use of a much larger time step in the macroscopic calculation. The HMM can also be used to model isolated defects, such as dislocations or cracks, that require the use of a higher level of theory only in the vicinity of the defect itself. The different possible applications of the HMM are schematically displayed in Figure 10 and include macroscopic processes with unknown constitutive relations (a), and isolated defects [(b) and (c)]. How to treat the problem of an isolated defect depends upon the relationship between the time scale for the defect dynamics, T_D, and the time scale for the relaxation of the defect structure, T_r. For $T_D \gg T_r$, the simulation time, Δt, for the microscopic model can be less than the macroscopic-scale time step, (TS) [case (b)]. Conversely, if T_D is comparable to T_r [case (c)], the whole time history of the defect should be computed atomistically.

In the following, we discuss in detail the application of the HMM to the study of macroscopic processes with unknown constitutive relations because the isolated-defect case can be obtained with easy modifications. Because the aim of the HMM is to accurately simulate a macroscopic process with state variable U, the main components of the methodology are: (1) a macroscopic scheme to solve the continuum equations for U and (2) a way to estimate the missing macroscopic data from a microscopic model. Therefore, the key steps in applying the heterogeneous multiscale procedure to the atomistic/continuum coupling are as follows. To begin with, because the macroscopic model is based on the conservation laws of mass, momentum, and energy, the MD must be expressed in the form of conservation laws as well, i.e., as a set of partial differential equations (PDEs). Then, the PDEs are solved numerically.

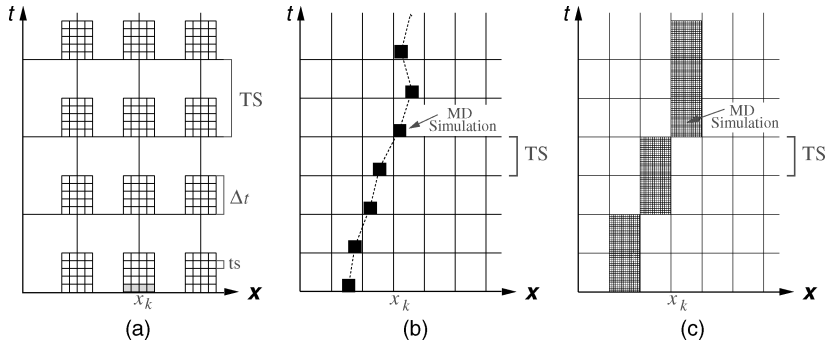

Figure 10 Schematic representation of HMM applications. In (a) simulation of a macroscopic process for which the constitutive relations have to be obtained from modeling at the microscale. The macroscopic system is solved using a grid (x_k), and only a small region around each macroscopic-solver grid point is used for the atomistic calculation (the shaded area represents the atomic cell at grid point x_k). The time step (TS) used for the macroscopic calculations is much larger than the microscopic one (ts), and times, $\Delta t \ll \text{TS}$ are necessary to equilibrate the atomistic calculations. In (b) and (c) isolated defect calculations, i.e., problems where the coupling with the microscale model is needed only in a limited part of the system (near the defect itself). If the time scale for the defect dynamics is much larger than the time scale for the relaxation of the defect structure (case b), then only a short time $\Delta t \ll \text{TS}$ is simulated using the atomistic model for each macroscopic time step, otherwise (case c) the whole time history of the defect should be computed atomistically.

At each macroscopic time step, MD calculations, constrained by the local macrostate of the system, are used to compute the missing data needed in the numerical solution of the PDEs. These data are obtained as time averages of microscopic variables after the MD simulation has equilibrated. The physical requirement to minimize/eliminate wave reflection at the boundary between the atomistic and the continuum treatment is achieved via well-chosen boundary conditions for the MD simulational cell.[177,178]

Choosing to work in Lagrangian coordinates, the conservation laws at the basis of the continuum model are

$$\begin{aligned} \partial_t \mathbf{A} - \nabla_{\mathbf{x}^0} \cdot \mathbf{v} &= 0 \qquad \text{time evolution of the deformation} \\ \partial_t \mathbf{q} - \nabla_{\mathbf{x}^0} \cdot \sigma &= 0 \qquad \text{conservation of momentum} \\ \rho_0\, \partial_t e - \nabla_{\mathbf{x}^0} \cdot \mathbf{j} &= 0 \qquad \text{conservation of energy} \end{aligned} \tag{33}$$

where $\mathbf{A}$, $\mathbf{v}$, $\mathbf{q}$, e are the deformation gradient, velocity, momentum, and total energy per atom, respectively, ρ_0 is the initial density, σ is the first Piola–Kirchhoff stress tensor, $\mathbf{j}$ is the energy flux, and $\mathbf{x}^0$ is the reference coordinate of the solid. The position after deformation is then $\mathbf{x} = \mathbf{x}^0 + \mathbf{u}(\mathbf{x}^0, t)$. To

express MD (Newton's law) in the form of Eqs. [33], the authors first define the distributions[179]

$$\begin{aligned}
\tilde{\rho}(\mathbf{x}^0, t) &= \sum_i m_i\, \delta(\mathbf{x}^0 - \mathbf{x}_i^0) \\
\tilde{\mathbf{v}}(\mathbf{x}^0, t) &= \sum_i \mathbf{v}_i(t)\delta(\mathbf{x}^0 - \mathbf{x}_i^0) \\
\tilde{e}(\mathbf{x}^0, t) &= \frac{1}{2}\sum_i \left\{ m_i \mathbf{v}_i^2 + \sum_{j\neq i} \phi[\mathbf{x}_i(t) - \mathbf{x}_j(t)] \right\} \delta(\mathbf{x}^0 - \mathbf{x}_i^0)
\end{aligned} \tag{34}$$

and the fluxes

$$\begin{aligned}
\tilde{\sigma}_{\alpha,\beta}(\mathbf{x}^0, t) &= -\frac{1}{2}\sum_{i\neq j} f_\alpha(\mathbf{x}_i - \mathbf{x}_j)(x_{i\beta}^0 - x_{j\beta}^0) \\
&\quad \times \int_0^1 \delta\{\mathbf{x}^0 - [\mathbf{x}_j^0 + \lambda(\mathbf{x}_i^0 - \mathbf{x}_j^0)]\} d\lambda \\
\tilde{\mathbf{j}}(\mathbf{x}^0, t) &= -\frac{1}{4}\sum_{i\neq j} (\mathbf{v}_i + \mathbf{v}_j) \cdot \mathbf{f}(\mathbf{x}_j - \mathbf{x}_i)(\mathbf{x}_i^0 - \mathbf{x}_j^0) \\
&\quad \times \int_0^1 \delta\{\mathbf{x}^0 - [\mathbf{x}_j^0 + \lambda(\mathbf{x}_i^0 - \mathbf{x}_j^0)]\} d\lambda
\end{aligned} \tag{35}$$

where ϕ is the interaction potential and $\mathbf{f}(\mathbf{x}_j - \mathbf{x}_i)$ is the force between the ith and the jth particles. We then have

$$\begin{aligned}
\partial_t \tilde{\mathbf{q}} - \nabla_{\mathbf{x}^0} \cdot \tilde{\sigma} &= 0 \\
\rho_0 \partial_t \tilde{e} + \nabla_{\mathbf{x}^0} \cdot \tilde{\mathbf{j}} &= 0
\end{aligned} \tag{36}$$

Equations [36] are numerically solved using any appropriate macroscopic solver. In Ref. 176 the authors used the Nessyahu and Tadmor algorithm, which is formulated over a staggered grid.[180] With this specific macrosolver, the fluxes $\tilde{\sigma}$ and $\tilde{j}$ are required as input data at each macroscopic time step and for each grid point $\mathbf{x}_k$. These fluxes are obtained by performing local MD simulations that are constrained by the local macroscopic variables **A**, **v**, and e. After the MD system equilibrates, the fluxes are evaluated by time/ensemble averaging. It is important to notice that the microscopic model does not have to be solved everywhere, but rather only over a small region near where the data estimation is carried out. The first step in setting up the local MD simulations is finding an atomic configuration that is consistent with the local macroscopic variables. This is accomplished using the Cauchy–Born rule (see discussion of the QC method above), i.e., generating the basis vectors for the deformed

cell, $\tilde{\mathbf{E}}$, by applying the deformation gradient $\mathbf{A}$ to the basis vectors of the undeformed cell, $\mathbf{E}$:

$$\tilde{\mathbf{E}} = \mathbf{AE} \qquad [37]$$

Several other requirements have to be taken into account to keep the MD simulations consistent with the macroscopic fields, and they are discussed in Ref. 176. The final step is to average the microscopic fluxes to obtain the fluxes needed by the macroscopic scheme.

Two final remarks need to be made. First, even when the MD simulation time is short compared to the macroscopic time scale, it can still be very long when compared with the microscopic time step if a substantial energy barrier must be overcome during the microscopic relaxation. Second, the choice of the MD cell size is a delicate balance between accuracy and computational efficiency; as the cell size increases, the error decreases (as $L^{-1.5}$, for a cell of volume $V = L^3$), but the computational time significantly increases.

Applications The HMM has been applied to the study of friction between two-dimensional atomically flat crystal surfaces, dislocation dynamics in the Frenkel–Kontorova model (i.e., considering a one-dimensional chain of atoms in a periodic potential, coupled by linear springs[181]), and crack propagation in an inhomogeneous medium.[175,176]

Bridging Scale The bridging scale technique by Wagner and Liu[73,182–184] is a multiple-scale method explicitly developed to eliminate the elastic wave reflection at the continuum-discrete interface. At the same time, because this methodology couples finite elements, or other continuous interpolation functions, to MD simulations without grading the continuum nodal spacing down to the atomic lattice size, it permits the use of a larger time step in the FE simulation than in the MD one.

The key idea of this technique is to decompose the total displacement field $\mathbf{u}$ into a coarse and a fine scale:

$$\mathbf{u} = \overline{\mathbf{u}} + \mathbf{u}' \qquad [38]$$

where $\overline{\mathbf{u}}$ is the coarse-scale component and $\mathbf{u}'$ is the fine-scale one. The coarse scale is that part of the solution that can be represented by a set of basis functions (finite element or mesh-free shape functions):

$$\overline{\mathbf{u}}(X_\alpha) = \sum_I N_I^\alpha \mathbf{d}_I \quad (\text{or } \overline{\mathbf{u}} = \mathbf{Nd} \text{ in matrix representation}) \qquad [39]$$

where $N_I^\alpha = N_I(\mathbf{X}_\alpha)$ is the shape function associated with node I evaluated at the initial atomic position $\mathbf{X}_\alpha$, and $\mathbf{d}_I$ is the FE nodal displacement associated

with node I. The sum is over all of the coarse-scale nodes. The fine-scale $\mathbf{u}'$ is defined as that part of the solution whose projection onto the coarse scale is zero; in other words, it is the part of the total solution that the coarse scale cannot represent. Because the coarse and fine scales are orthogonal to each other, it is possible to obtain a set of multiscale equations of motion for the MD and FE systems that are coupled only through the interatomic forces $\mathbf{f}$ (the negative derivative of the interatomic potential energy U):

$$\mathbf{M}_A\ddot{\mathbf{q}} = \mathbf{f} \quad [40]$$

$$\mathbf{M}\ddot{\mathbf{d}} = \mathbf{N}^{\mathrm{T}}\mathbf{f} \quad [41]$$

where $\mathbf{q}$ is the MD displacement, $\mathbf{M}_A$ is a diagonal matrix with the atomic masses on the diagonal, d is the coarse scale displacement, and $\mathbf{M}$ is the coarse-scale mass matrix defined as

$$\mathbf{M} = \mathbf{N}^{\mathrm{T}}\mathbf{M}_A\mathbf{N} \quad [42]$$

Equations [40] and [41] were obtained considering that the coarse and the fine scales coexist everywhere in the system. However, the goal is to explicitly simulate the fine scale only in a small region of the domain, while solving the FE equation of motion *everywhere* in the system, and including the effects of the fine scale that lies outside the MD region, at least in an average way. This reduction of the fine-scale degrees of freedom can be achieved in the bridging-scale technique by applying a generalized Langevin equation (GLE)[185–188] boundary condition. A detailed derivation of the final equations of motion is beyond the scope of this review and can be found in Refs. 73 and 182; here, it will suffice to say that the process of eliminating the unnecessary fine-scale degrees of freedom results in a modified MD equation of motion that includes an external force, named the impedance force, $\mathbf{f}^{\mathrm{imp}}$, which contains the time history kernel $\theta(t-\tau)$ and acts to dissipate fine-scale energy from the MD simulation into the surrounding continuum. The numerical result is a highly desiderable nonreflective boundary between the MD and FE regions. The final form for the coupled equations of motion for the two regions is

$$\mathbf{M}_A\ddot{\mathbf{q}} = \mathbf{f} + \mathbf{f}^{\mathrm{imp}} + \mathbf{R} \quad [43]$$

$$\mathbf{M}\ddot{\mathbf{d}} = \mathbf{N}^{\mathrm{T}}\mathbf{f} \quad [44]$$

Clearly, Eq. [43] is the modified MD equation of motion; the first term is the standard nonlinear interatomic force, the second term is the impedance force discussed above, and the third term is a stochastic force representing the exchange of thermal energy between the MD region and the surrounding eliminated fine-scale degrees of freedom. In other words, this last term acts

as a heat bath on the MD region. For simplicity, in the earlier applications of the bridging-scale method this term was set to zero, indicating a zero-temperature simulation. Recently, though, a finite-temperature form for this term was derived by Karpov et al.[189] It is worth mentioning that the impedance force also depends on the coarse-scale solution, $\bar{\mathbf{u}}$. This indicates truly two-way information passing between the two regions; not only does the MD region affect the FE evolution, but also coarse-scale information originating in the continuum can be passed onto the MD region. A substantial difference between this method and many others is that here the FE equation of motion is solved *everywhere* in the system, i.e., also where MD is applied. This eliminates the need to mesh the size of the elements down to the atomic scale, and therefore allows the use of a staggered time integration scheme.[182] Lastly, it must be noted that no ad hoc treatment is used to couple the MD and FE regions, instead the MD lattice behaves as if part of a larger lattice due to the GLE (the GLE is a mathematically exact representation of the MD degrees of freedom that are not explicitely solved for), even though ghost atoms are introduced in the MD simulation to ensure that the reduced atomistic system does not relax due to spurious free-surface effects. These atoms' displacements are determined by interpolating the FE displacements of the elements in which they lie, not by integrating the MD equation of motion. Recent extentions of the bridging-scale method include the coupling of the continuum region to a quantum mechanical one (tight binding), instead of a classical atomistic one, for quasi-static applications.[190]

Applications The bridging method has been successfully used to model both quasi-static and dynamical phenomena. In its quasi-static formulation it has been used to model nanoindentation (on a crystalline gold substrate)[191] and carbon nanostructures: single graphene sheets and multilayered graphite,[192] and buckling of a multiwalled carbon nanotube.[184,193] Dynamically, the bridging method has been applied to the investigation of crack propagation[183] in fcc materials (3D), and dynamic shear banding[194] (1D and 2D). More recently the model has been further expanded to describe solids with moving dislocations in one dimension.[195]

Other Adaptive Model Refinement Methodologies The use of the *adaptive refinement* idea is absolutely not limited to the two methods presented in the previous sections. Several other groups have developed methodologies based upon this principle. Among many, we would like to mention the coupling scheme proposed by Klein and Zimmerman[196] and the one suggested by To and co-workers,[197,198] where the bridging-scale method is combined with the perfectly matched layer method,[199] to eliminate the spurious wave reflection at the computational boundaries during the fine-scale part of the simulation. This methodology is then widened to allow the simulation of nonequilibrium multiscale phenomena.[200] Lastly, a whole

class of adaptive modeling algorithms is presented in the work of Oden and co-workers.[201,202]

Coarse-Grain Molecular Dynamics

The course-grain molecular dynamics (CGMD) methodology could be classified as a modification of the "adaptive model refinement" approach: In this methodology a coarse-grained (CG) prescription is used that is statistical in nature.[66,67,203,204] It must be noted that this is a very unique, and interesting, approach to designing a hybrid method. The CGMD was developed by Rudd and Broughton[66,67,203,204] especially to model thermally activated phenomena that require several length scales with an atomistic model at the finest resolution, i.e., phenomena that intrinsically need a hybrid approach, finite-temperature conditions, and a dynamical treatment (MD) to be simulated.

In common with many other hybrid techniques, the CGMD methodology uses a coarse-grain mesh that divides a solid into cells of different sizes; in important regions, a mesh node is assigned to each equilibrium atomic position, while elsewhere a single cell contains several atoms. The main difference between this approach and many others is that here the energy functional is defined as a constrained ensemble average of the atomistic energy under fixed thermodynamic conditions. The equations of motion for the mean displacement field are Hamilton's equations of motion for this conserved energy functional, and are solved using a standard MD procedure. Because the CGMD equations of motion agree with the atomistic ones when the mesh nodes and the atomic sites coincide, the coupling between the atomistic regions and the generalized FE ones is very good. It is not, however, completely seamless because, as the mesh increases, some short-wavelength degrees of freedom are not supported by the coarse mesh. However, these degrees of freedom are not completely lost because their thermodynamic average effect has been retained. As the authors observe, this approximation is expected to be good for systems initially in thermal equilibrium and such that only adiabatic changes in the missing degrees of freedom are considered. More specifically, for this approximation to be valid, the relaxation time of those missing degrees of freedom should be fast compared to the driving forces in the CG regions. No other types of ghost forces are present in the model, i.e., the atoms at the interface do not experience a net force when in their equilibrium positions or if the displacement corresponds to uniform strain and the uniformly strained system is in equilibrium.

The CGMD prescription for constructing the mean displacement field at the nodes of the coarse-grain grid is as follows:

$$\mathbf{u}_j = \text{displacement of the mesh node } j = \sum_{\mu} f_{\mu j}\mathbf{u}_{\mu} \qquad [45]$$

where $\mathbf{u}_{\mu} = \mathbf{x}_{\mu} - \mathbf{x}_{\mu 0}$ is the displacement of atom μ ($\mathbf{x}_{\mu 0}$ is its equilibrium position) and $f_{\mu j}$ is a weighting function analogous to the FEM interpolation

functions. A similar relation applies to the momenta, $\mathbf{p}_{\mu j}$. The CG energy is then defined as the average energy of the canonical ensemble on this constrained (Eq. [45]) phase space:

$$E(\mathbf{u}_k, \dot{\mathbf{u}}_k) = \langle H_{\mathrm{MD}} \rangle_{\mathbf{u}_k, \dot{\mathbf{u}}_k}$$
$$= \int d\mathbf{x}_\mu \, d\mathbf{p}_\mu \, H_{\mathrm{MD}} \, e^{-\beta H_{\mathrm{MD}}} \Delta / Z \qquad [46]$$

$$Z(\mathbf{u}_k, \dot{\mathbf{u}}_k) = \int d\mathbf{x}_\mu \, d\mathbf{p}_\mu \, e^{-\beta H_{\mathrm{MD}}} \Delta \qquad [47]$$

$$\Delta = \prod_j \delta(\mathbf{u}_j - \sum_\mu \mathbf{u}_\mu f_{j\mu}) \delta\left(\dot{\mathbf{u}}_j - \sum_\mu \frac{\mathbf{p}_\mu f_{j\mu}}{m_\mu}\right) \qquad [48]$$

where $\beta = 1/(kT)$ (T = temperature), Z is the partition function, and $\delta(\mathbf{u})$ is a three-dimensional delta function. The delta functions enforce the mean-field constraint (Eq. [45]). The explicit form of the full CG energy (Eq. [46]) for a monoatomic harmonic or anharmonic solid is derived in Ref. 204.

Applications Test applications of the method include calculation of the phonon spectra for solid argon and tantalum in three dimensions.

Quasi-continuum Coarse-Grain Alternative to Molecular Dynamics

In order to extend the quasi-continuum method (discussed above) to include not only finite-temperature effects but also a dynamical description of the system, Dupoy et al. introduced the "molecular dynamics without all the atoms" method in 2005.[205] This procedure, which essentially is a coarse-grain (CG) alternative to molecular dynamics, is based on the *potential of mean force* (PMF) concept, which was first introduced by Kirkwood in 1935.[206] Here, a variety of equilibrium and nonequilibrium properties of large systems are calculated using only a limited number of degrees of freedom. However, the tricky part in applying the PMF method is making it computationally efficient. Dupoy et al. proposed to expedite the calculation of the PMF by coupling it to the QC method, i.e., making use of finite-element interpolation to determine the position of the *constrained atoms* and introducing the local harmonic approximation[147–149] (see above) and the Cauchy–Born rule[88,100,101] (see above) when determining the state of the system under strain.

The basic structure of this methodology is the following. Following the QC procedure, the atoms of an N-atom system are separated into *representative* and *constrained* ones. The representative atoms are the only atoms actively considered in the simulations. Their positions are indicated as $\{\mathbf{q}^r\}$, their number as N_r, and they can be either *nonlocal*, if only interacting with other representative atoms, or local, if interacting with constrained atoms as well. The *constrained* atoms are atoms whose position $\{\mathbf{q}^c\}$ is not directly determined in the

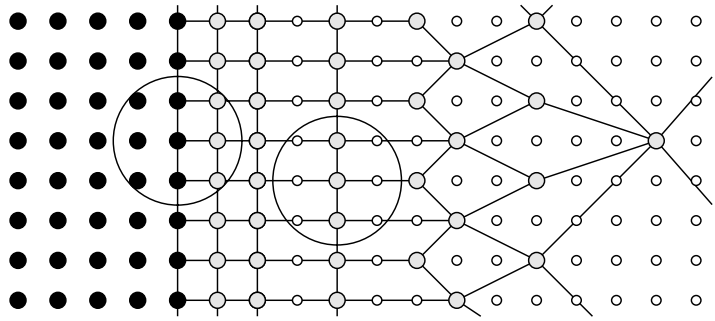

Figure 11 Schematic representation of the system considered. Black dots indicate *nonlocal representative* atoms (they only interact with other representative atoms), gray dots indicate *local representative* atoms (they interact with both representative and constrained atoms), and, finally, small white dots represent *constrained* atoms. The large circles represent the range of the atomic potential (centered on a local or on a nonlocal representative atom).

simulations but is obtained by interpolating the positions of the closest representative atoms using an FE scheme (Figure 11). More precisely, it is their thermally averaged position that is obtained through interpolation.

The Hamiltonian that is considered for the CG system is

$$H_{\mathrm{CG}}(\{\mathbf{q}^r\},\{\mathbf{p}^r\},\beta) = \sum_{i=1}^{N_r} \frac{(\mathbf{p}_i^r)^2}{2m_i^r} + V_{\mathrm{CG}}(\{\mathbf{q}^r\},\beta) \qquad [49]$$

where $V_{\mathrm{CG}}(\{\mathbf{q}^r\},\beta)$ is the CG potential energy, $\beta = 1/k_B T$, $\mathbf{p}_i^r = m_i^r \dot{\mathbf{q}}_i^r$ are the momenta of the representative atoms, and m_i^r their effective masses. By imposing the conditions that the total mass of the CG system should be equal to that of the full-atom system, and that both systems should have the same momentum free energy, the effective masses are determined to be $m_i^r = \alpha^{n_i - 1} m$, where n_i is the number of atoms represented by representative atom i, and α is found solving the equation

$$\sum_{i=1}^{n_r} \alpha^{n_i - 1} = N \qquad [50]$$

Similar to the quasi-continuum Monte Carlo approach (see above), the CG potential energy is the PMF for the constrained degrees of freedom[153,206]

$$V_{\mathrm{CG}}(\{\mathbf{q}^r\},\beta) = -\frac{1}{\beta}\ln \int e^{-\beta V(\{\mathbf{q}^r\},\{\mathbf{q}^c\})} d\{\mathbf{q}^c\} \qquad [51]$$

where V is the interatomic potential. This choice for the CG potential energy guarantees that the ensemble average of any observable A that depends only on the positions of the representative atoms is equal to the ensemble average

that would be found for the same observable in a fully atomistic and canonical system at equilibrium:

$$\langle A(\{\mathbf{q}^r\})\rangle_{\mathrm{CG}} = \langle A(\{\mathbf{q}^r\})\rangle_{N_r,V,T} = \langle A(\{\mathbf{q}^r\})\rangle_{N,V,T} \qquad [52]$$

Using this methodology, the dynamical behavior of the representative atoms is obtained by deriving the equation of motion from the coarse-grained Hamiltonian. Moreover, because the interest is on simulating the system under constant-temperature conditions, the coupling to a thermal reservoir is simulated using a Nosé–Poincaré thermostat.[207,208] More specifically, such a thermostat is applied only to the set of representative atoms, not to all the atoms in the system. By following such a procedure, the validity of Eq. [52] is preserved.

Lastly, computational efficiency needs to be discussed. However complete the formulation of the coarse-grained alternative to MD methodology is up to here, additional approximations are required to make it computationally efficient. To begin with, it is assumed that the thermally averaged positions of the constrained atoms can be expressed as a finite-element interpolation of the positions of the representative atoms, i.e., using finite-element shape functions. This is analogous to the procedure followed in the standard QC method to determine the instantaneous positions of the nonrepresentative atoms. Moreover, the computation of V_{CG} is noticibly expedited when both the local harmonic approximation and the Cauchy–Born rule are taken into account. Under such circumstances, V_{CG} becomes

$$\begin{aligned} V_{\mathrm{CG}}(\{\mathbf{q}^r\},\beta) = &\sum_{i\in \mathrm{NL}} E_i(\{\mathbf{q}^r\}) \\ &+ \sum_e \left[n_e E_{\mathrm{CB}}(\mathbf{F}_e) + \frac{n_e^c}{2\beta} \ln \frac{\mathrm{Det}(\mathbf{D}_{\mathrm{CB}}(\mathbf{F}_e))}{(2\pi/\beta)^3} \right] \end{aligned} \qquad [53]$$

where NL indicates the nonlocal representative atoms, n_e and n_e^c are the total number of atoms and the number of constrained atoms, in element e, respectively, and $E_i(\{\mathbf{q}^r\})$ is the energy of the ith nonlocal representative atom, calculated exactly as it would be in a standard MD simulation. However, unlike standard MD simulations, $E_{\mathrm{CB}}(\mathbf{F}_e)$ and $\mathrm{Det}(\mathbf{D}_{\mathrm{CB}}(\mathbf{F}_e))$ are the potential energy and the determinant of the dynamical matrix of an atom embedded in an infinite perfect crystal subject to a uniform deformation gradient, $\mathbf{F}_e$. The CG potential given in Eq. [53] is reasonably fast to compute, and is an accurate approximation for temperatures up to about half the melting temperature.

Applications Dupoy et al. applied this methodology to the study of the temperature dependence of the threshold for dislocation nucleation during nanoindentation.[205]

Boundary Conditions Methods

As already emphasized, a major problem in all of the dynamical formulations of hybrid methodologies is the occurrence of spurious reflections when phonons cross the domain boundary. One possible approach to minimize/eliminate such an unphysical phenomenon is to fine-tune the boundary conditions (BC) used in the molecular dynamics simulation. A great number of boundary condition schemes of this kind have been developed, as in Refs. 177,178,185–188, and 209–221, just to mention some. It is beyond the scope of this review to discuss them in detail, but, borrowing from Yang and Li,[221] we will briefly present the general idea behind some of the most commonly used schemes.

The most commonly used BC methods can be classified into three main categories: the exact nonreflective BC, the approximated nonreflective BC (also called the variational BC or VBC), and the damping region BC. In principle, exact nonreflective BCs can be obtained via numerical computation for crystalline systems under certain assumptions.[185–188,214–216] One possible formulation of this type of BC is discussed below. However, exact BCs are not local in both space and time, meaning that information about all of the boundary atoms at all times is, in principle, necessary to compute them. Because the decay of the history dependence is rather slow, implementing such a BC scheme can be computationally very expensive. To reduce such a computational cost, E and co-workers introduced the VBC scheme.[177,178,217,218] Here, the BCs are of a local nature and assume the general form

$$\mathbf{u}_k(t) = \sum_{j \in J} \int_0^{t_0} \alpha_j(\tau)\mathbf{u}_j(t-\tau)\, d\tau \qquad [54]$$

and are obtained by determining the time history kernel, α, that minimizes the energy flux due to the phonon reflection. In Eq. [54], k indicates any boundary atom, $\mathbf{u}(t)$ is the atomic displacement at time t, and the set J contains adjacent lattice points inside the system. Together, the set J and the time interval $(0, t_0)$ are called a stencil, and one of the main advantages of this kind of BC is the possibility of fine tuning the stencil to achieve a desired accuracy. For an extensive derivation of the VBC, we refer to Refs. 177,178,217, and 218. Lastly, the third commonly used type of BC is the damping region BC. Here [Figure 12(a)], an additional border region is added to the original system, and it acts as an absorbing layer for the outgoing phonons. Standard MD is utilized in the primary region, while an extra friction term is added to the equation of motion of atoms in the damping region

$$m\ddot{\mathbf{x}}_j = -\frac{\partial V}{\mathbf{x}_j} - \eta\dot{\mathbf{x}}_j \qquad [55]$$

where η is the friction coefficient, and it can assume different functional forms depending on the type of damping used (e.g., Holian et al. used a homogeneous viscous damping via the irreversible Berendsen thermostat[222]).

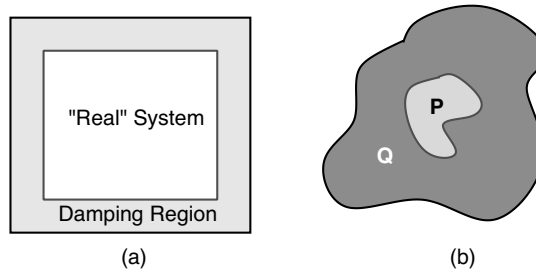

Figure 12 Schematic representation of: (a) damping region BC (the region of interest is surrounded by a border region where damping of the outgoing waves takes place), and (b) coupled system for exact nonreflective BC (P is the region of interest and may contain inhomogeneities, while Q is the defect-free medium that surrounds it).

In general, damping methods are very convenient to use because they do not require precalculations and are very easily implemented, but their effectiveness is completely dependent on the size of the damping region and, often, a significant number of atoms must be added to the system for this method to work properly. Moreover, there is no a priori way to estimate the size of the damping region. In summary, all three methods can be very effective in suppressing phonon reflection, and only the specific problem under examination dictates which one is the most convenient to use.

We conclude this section with an example of exact nonreflective BCs, the method developed by Cai et al.[214] This method is designed to minimize the wave reflection between a region of interest P, and a defect-free medium Q around it [Figure 12(b)]. The region P may contain inhomogeneities and must be large enough that, for moderate temperatures, the interactions between P and Q (P–Q), and within P (P–P), can be considered as harmonic. The idea behind this approach is to represent the effects of Q on P in terms of a set of response functions that are estimated numerically during test simulations prior to the real calculations. These response functions provide a numerical set of boundary conditions for P that preserves the correct dynamic because it contains the information related to the degrees of freedom in region Q. More in detail, the generalized Langevin equation (GLE) (the equation of motion for the degrees of freedom $x_i = 1, \ldots, N$ in P when the explicit degrees of freedom associated with medium Q have been replaced by an implicit formulation) takes the form[185–188,223]

$$m\ddot{x}_i = -\frac{\partial V}{\partial x_i} + \int_0^t d\tau \sum_{j=1}^{N} \beta_{ij}(\tau) x_j(t-\tau) + \sum_{j=1}^{N} \beta_{ij}(\tau) x_j(0) + R_i(\tau) \qquad [56]$$

where $V = V(x_i)$ is the potential energy of the entire system with the atoms in Q fixed at their equilibrium positions, $\beta_{ij}(t)$ indicates the N^2 elements of the time-dependent memory kernel matrix $\beta(t)$, and $R_i(t)$ is a linear function of the initial displacements and velocities in region Q. Physically, the functions $\beta_{ij}(t)$ represent the response of medium Q to perturbations in P, while $R_i(t)$ describes changes in P due to initial disturbances in Q. Such changes are usually treated as random forces.[185–188] The idea is to compute $\beta(t)$ from test MD simulations. To do that, an initial equilibrium situation is considered, with atoms in both P and Q at rest; then, in each simulation, a different single atom x_k in P is given a displacement ϵ at time $t = 0$, after which all of the atoms in P are kept fixed while the atoms in Q are allowed to relax. This means that the atomic positions in P are given by

$$x_j(t) = x_j(0) = \epsilon\delta_{jk} \qquad [57]$$

while the time-dependent forces acting on the atoms in P are (Eq. [56])

$$F_i(t) = -\frac{\partial V}{\partial x_i} + \epsilon\beta_{ik}(t) \qquad [58]$$

The convolution term has disappeared because region Q was initially in equilibrium. Therefore, recording the forces $F_i(t)$ as a function of time during the MD run, directly gives the N response functions $\beta_{ik}(t)\, i = 1, \ldots, N$, once the static force components $-\partial V/\partial x_i$ have been subtracted. The introduction of a time cutoff and a space cutoff does not seem to affect the validity of the method (for a more detailed discussion of this point we direct the reader to the original paper[214]). Lastly, the authors compared their approach to the coarse-grained molecular dynamics one (CGMD, see above) in the simple case of simulating the dynamics of a small section of a linear chain of identical harmonic oscillators with nearest-neighbor interactions. They found much more accurate results in most of the Brillouin zone.

Miscellanea

Due to the sheer number, it is not possible to include in this review all of the proposed hybrid methodologies that deal with the coupling of continuum and atomistic regions in dynamical simulations. However, before leaving this section, we want to mention a few more types of methodologies. First, the multigrid methods,[76,224–228] of which the recent work of Waisman and Fish[229] is a good example. Also, the MPM/MD method, where the material point method (MPM) is used instead of the finite-element method (FEM) to couple continuum mechanics to conventional molecular dynamics.[230–233] Lastly, the statistical approach suggested by Saether et al. for concurrent coupling of molecular dynamics and finite element methods.[234] For even more methods, see, for instance, Refs. 235–240.

CLASSICAL/QUANTUM COUPLING

Coupled methodologies that connect classically described domains to quantum mechanically described regions encounter the same difficulties that continuum-to-classical methods do (possible ghost forces at the artificial boundary and phonon reflection when dynamics is taken into account). Moreover, the fact that using ab initio methods makes it impossible to localize the energy onto specific atoms or bonds makes dealing with the hand-shake region even more complicated. Furthermore, methods coupling atomistic to quantum calculations also have to face problems related to dealing with the electronic degrees of freedom in the quantum mechanical domain. In principle, the presence of such degrees of freedom requires the imposition of boundary conditions on the electronic wave function at the interface between the two domains. Such a complication is particularly serious when dealing with metals because of the nearly complete delocalization of the bonds. In the following, we will explore how several methodologies have dealt with such issues in both static and dynamical phenomena.

Static and Semistatic Methods

Orbital-Free DFT–Classical Mechanics

One approach to couple classically treated regions to regions described by quantum mechanics is to use the methodology introduced by Choly et al.[241] in 2005. In this formalism, the quantum mechanical zone is modeled using orbital-free density functional theory (OFDFT), which is an approximate form of DFT where the kinetic energy of the noninteracting electrons is approximated by a functional of the density.[242–246] This allows the energy of the system to be expressed as the sum of terms that are all explicit functionals of the charge density, therefore avoiding the necessity of solving the single-particle Schrödinger equations for the fictitious particles and using the Kohn–Sham orbitals. Such a simplification allows the method to scale linearly with the system size, and, therefore, makes it capable of handling significantly more atoms than standard DFT. The memory requirements are also significantly reduced. However, the approximations introduced in describing the kinetic energy make the method less transferable than standard DFT. Lastly, OFDFT is particularly well suited for hybrid calculations because having the energy as a function of only the electronic density makes it easer to evaluate the coupling term between the quantum and the classical regions than it is when using standard DFT. Other hybrid methodologies that take advantage of OFDFT when coupling classical and quantum regions are, for instance, those of Wesolowski and Warshel[247] and of Klüner et al.[248] In the method of Choly and co-workers, the system is divided into two parts: a small OFDFT region, where the electronic behavior is important, and a much larger region

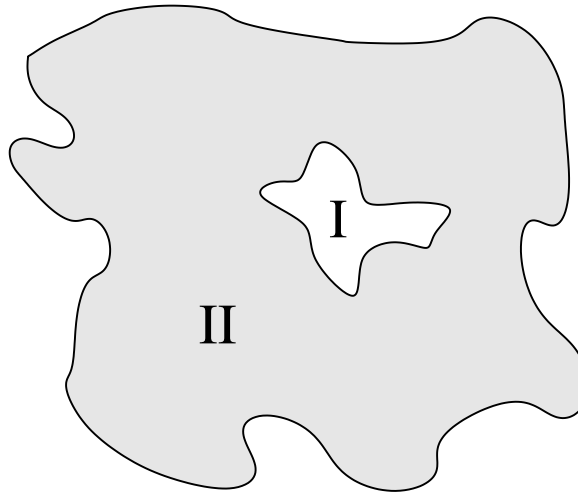

Figure 13 Smaller domain (region I) represents the part of the system where the detailed physics is relevant and that is, therefore, described using OFDFT. The larger domain (region II) is the region described by the atomistic classical potential (usually EAM). Region I is embedded into region II and is always nonperiodic, while periodic boundary conditions can be applied to region II.

(the rest of the system) that is simulated using classical potentials (Figure 13). Because OFDFT is particularly well suited for metallic systems, embedded atom method (EAM) potentials[9,10] are the preferred choice for the atomistic potentials.

This methodology adopts the single energy functional strategy, i.e., the energy of the whole system is written as the sum of the energies of the two regions (E_1 and E_2), plus a term that describes the interaction energy of these two regions (the hand-shake term):

$$E[\mathrm{I}+\mathrm{II}] = E_1[\mathrm{I}] + E_2[\mathrm{II}] + E^{\text{hand shake}}[\mathrm{I},\mathrm{II}], \qquad [59]$$

where label I indicates quantities evaluated in the smaller, higher resolution region (where OFDFT is used), and II indicates quantities evaluated in the larger, lower resolution region (where EAM is used). The energies, E_1 and E_2, are calculated using DFT (or OFDFT) and a classical potential, respectively. The coupling energy, $E^{\text{hand shake}}$ [I, II], can be computed either way, which gives rise to two possible coupling schemes.

In the first scheme, $E^{\text{hand shake}}$ [I, II] is calculated classically. Specifically, it is obtained as

$$E^{\text{hand shake}}[\mathrm{I},\mathrm{II}] = E_{\mathrm{cl}}[\mathrm{I}+\mathrm{II}] - E_{\mathrm{cl}}[\mathrm{I}] - E_{\mathrm{cl}}[\mathrm{II}] \qquad [60]$$

because, as the authors note, the classical energy can be viewed as an approximation of the DFT energy functional that has been minimized with respect to the charge density. This means that this approach contains more approximations than the one where OFDFT is used to evaluate the hand-shake energy, but, also, that it is much lighter computationally. The final expression for the total energy is obtained by substituting Eq. [60] into Eq. [59]:

$$E[\mathrm{I}+\mathrm{II}] = E_{\mathrm{cl}}[\mathrm{I}+\mathrm{II}] - E_{\mathrm{cl}}[\mathrm{I}] + E_{\mathrm{DFT}}[\mathrm{I}], \qquad [61]$$

where, according to the Hohenberg–Kohn theorem, $E_{\mathrm{DFT}}[\mathrm{I}]$ is found, within the Born–Oppenheimer approximation, by minimizing a functional of the charge density

$$E_{\mathrm{DFT}}[\mathrm{I}] = \min_{\rho}^{\mathrm{I}} E_{\mathrm{DFT}}[\rho^{\mathrm{I}}, \mathbf{R}^{\mathrm{I}}] \qquad [62]$$

where $\mathbf{R}^{\mathrm{I}}$ are the ion coordinates in region I. For a detailed discussion of how such a scheme affects the calculation of the forces, we refer to the original paper.[241]

The second coupling schemes computes $E^{\text{hand shake}}[\mathrm{I},\mathrm{II}]$ using OFDFT. The use of an orbital-free approach, instead of a standard DFT, is particularly effective in this step because the only information available on region II is its approximate charge density ρ_{II} and the positions of the atoms in $\mathbf{R}^{\mathrm{II}}$, and, as discussed above, that is all OFDFT needs to determine the energy. In this scheme, the interaction energy is given by

$$E^{\text{hand shake}}[\mathrm{I},\mathrm{II}] = E_{\mathrm{OF}}[\mathrm{I}+\mathrm{II}] - E_{\mathrm{OF}}[\mathrm{I}] - E_{\mathrm{OF}}[\mathrm{II}] \qquad [63]$$

where the computational advantage of using this approach versus simulating the whole system with OFDFT comes from the cancellation hidden in $E_{\mathrm{OF}}[\mathrm{I}+\mathrm{II}] - E_{\mathrm{OF}}[\mathrm{I}]$, when Eq. [63] is inserted in Eq. [59], and from the fact that $E_{\mathrm{OF}}[\mathrm{I}+\mathrm{II}]$ is found by minimizing the OFDFT energy functional with respect to ρ_{I} only (ρ_{I} being the charge density in region I). For details on how the method can be implemented, we refer to the original paper.[241]

DFT/OFDFT and Quasi-continuum (OFDFT-QC, QCDFT)

In the previous section, we discussed a hybrid methodology that couples orbital-free DFT (OFDFT) to classical potentials. A basic description of the OFDFT was also given. Another possibility is to couple OFDFT to quasicontinuum methods. Such an approach has been suggested by Fago et al. in 2004[249–251] and followed by Gavini et al.[252] in 2007. OFDFT lends itself very easily to coupling with QC methods because it is significantly faster than traditional Kohn–Sham DFT, and speed is crucial when millions of DFT calculations are needed during a typical hybrid simulation.

Fago et al.'s[249–251] implementation of OFDFT inside a QC method is straightforward. They utilize a local approach in the QC part (LQC, see above for details) and use OFDFT to compute the energy at each quadrature point. Therefore, the pros and cons of this method are the same as those for the standard LQC, with the difference that the energy evaluation is now more accurate than if a classical potential was used. However, even if local electronic effects are accounted for, no coupling between neighbor unit cells is included in the calculations because, in LQC, the energy of each quadrature point is calculated using the Cauchy–Born rule. Such a rule states that the energy of a quadrature point can be found by computing the energy of a perfect, infinite crystal undergoing the same uniform deformation that is applied to the quadrature point in question. Also, as pointed out earlier, the Cauchy–Born rule holds well for slowly varying elastic deformation, but breaks down in the vicinity of defects, impurities, and the like. This methodology has been applied to the study of dislocation nucleation during indentation of Al.

To bypass the limitations of the Cauchy–Born rule, in 2006, Lu et al.[253] proposed a more involved scheme to couple standard DFT to quasi-continuum calculations. In their method, the part of the system far away from the zone of interest is described using a classical (nonquantum) quasi-continuum approach (see discussion above on QC for details), i.e., considering both local (continuum) and nonlocal (atomistic) terms. Classical potentials (EAM[9,10] in the applications presented) are used to evaluate the energy within the QC calculations. A third region is considered as well, covering the part of the system that needs a more detailed description. It is in this region that density functional theory is used.

In this methodology, the coupling between the continuum and the atomistic regions is handled in the same way as it is in the standard formulation of the mixed quasi-continuum. However, the coupling scheme used to connect the quantum region to the atomistic one is that proposed by Choly et al.,[241] which we described earlier. In particular, Choly's approach offers two ways of evaluating the hand-shake energy term, and Lu et al.[253] adopted the one where the interaction energy is computed using only classical evaluations (Eq. [60]). For details on the evaluation of the forces and the relaxation scheme, we refer to the original paper.[252] The method has been applied to the investigation of the core structure of an edge dislocation in aluminum, with and without H impurities.

An even more involved scheme, which does not assume the Cauchy–Born rule and which allows seamless incorporation of defects, was proposed in 2007 by Gavini et al.[252] Here, OFDFT is used for the quantum evaluation of the energies, and three levels of coarsening are considered in the QC meshing of the system. Following the naming convention suggested by the authors (see Figure 14), they are: T_{b1}, the coarse grid, T_{b3}, the intermediate grid, and T_{b2}, the finer one. The T_{b1} mesh is the atomic mesh, i.e., the standard meshing used in QC methods: Selected atoms are chosen as representative, and, in this

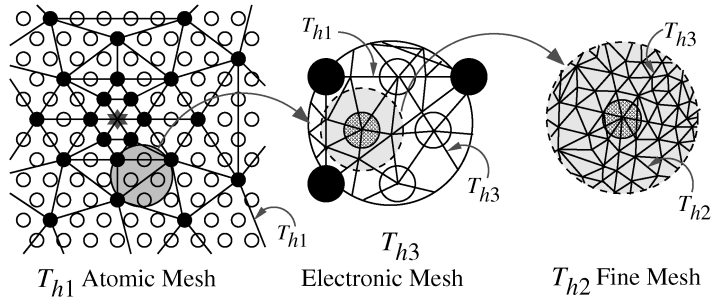

Figure 14 Three levels of mesh coarsening considered in Gavini's methodology. The star indicates the defect, vacancy, or so on that is of particular interest. The solid circles are the nodes of the atomic mesh (they coincide with atomic positions), and the open circles indicate the remaining atomic positions.

application, they coincide with the grid nodes. Also, the meshing becomes coarser as the distance from the defect (indicated by a star in the figure) increases. The T_{h2} mesh is the fine mesh, and it is a subatomic mesh present everywhere that captures the subatomic oscillations in the electronic density and potential. It is uniform in space, i.e., it does not coarsen going away from the defect. Lastly, T_{h3} (electronic mesh) is a subatomic mesh that is very fine close to the defect and increasingly coarse away from it.

Using OFDFT, the energy is an explicit functional of the electron density and atomic positions (see preceding section). Therefore, the ground-state electron density and equilibrium positions of the nuclei are found by minimizing the energy:

$$E(u, \mathbf{R}) = \sup_{\phi \in H^1(\Re^3)} L(u, \mathbf{R}, \phi) \qquad [64]$$

where $u = \sqrt{\rho}$ is the square root of the electronic density, $\mathbf{R}$ are the atomic positions, and ϕ is the electrostatic field. We refer to the original paper[253] for the explicit form of the local Lagrangian, L; for this review, it is enough to point out that L depends upon u, $\mathbf{R}$, and ϕ.

In Gavini's method, u and $\mathbf{R}$ are determined using a predictor–corrector approach

$$\begin{aligned} u^h &= u_0^h + u_c^h \\ \phi^h &= \phi_0^h + \phi_c^h \end{aligned} \qquad [65]$$

where u_0^h and ϕ_0^h are the predictors, and u_c^h, ϕ_c^h are the nonlocal corrections to be solved for. The predictor parts of the fields are computed on the fine mesh, T_{h2}, using periodic calculations performed in every element of T_{h1} and integration rules to reduce the computations from the complexity of T_{h2} to the complexity

of T_{b3}. The corrections are then computed on the electronic mesh, T_{b3}. The variational problem is then solved using conjugate gradients. More details on the method can be found in the original paper.[253] The OFDFT-QC method was demonstrated by studying one and two vacancies in large Al crystals.

First-Principles Green's Function Boundary Condition Method

The first-principles Green's function boundary condition (FP-GFBC) method introduced by Woodward et al. in 2001[254–256] is a generalization of the flexible boundary condition method (GFBC), discussed earlier. As before, the methodology is directed to the study of dislocation properties, with particular attention to core structures. As in the earlier GFBC work, the dislocation core is embedded into a medium where the lattice Green's function is used to compute a stress field consistent with the response function of the bulk material. We refer to the earlier description of the general principles of the Green's function boundary condition approach. The main difference between the two methodologies is that in the first-principles version, the core structure (region 1 in Figure 6) is modeled using an ab initio (DFT) approach instead of a classical one. Pseudopotential plane-wave methods are a particularly good choice for such a modeling because they allow for an easy calculation of the Hellmann–Feynman forces that are used to relax the core domain. It is important to remark that the possibility of using DFT, instead of an empirical potential, comes from the ability of the method to use minimal computational cell sizes without incurring significant incompatibility forces.

From a computational point of view, the use of the DFT method employed by the authors[257–261] required the use of 3D periodic boundary conditions. However, the problem under examination, the determination of the equilibrium core structure of an isolated dislocation, only allows periodicity along the direction of the dislocation line. Therefore, the authors proposed two possible simulation cells to circumvent such an impasse: One where the standard cell used in GFBC is embedded within a vacuum region that isolates it from its periodic images (Figure 15(a)], and one where a much larger region 3 is considered, instead of the vacuum [Figure 15(b)].

The authors found that the two geometries lead to quantitatively identical results, as long as the thickness of region 3 is large enough to screen out the charge dipole that forms at the outer cell boundary. However, the geometry of Figure 15(b) is significantly more efficient from a computational point of view.

Applications The FP-GFBC has been used to model dislocation core structure in Mo and Ta.[254–256]

Quantum Atomistic Static Interface Method

The quantum atomistic static interface (QuASI) methodology of Tavazza et al.[262–264] is inspired by the flexible boundary condition idea (e.g., the

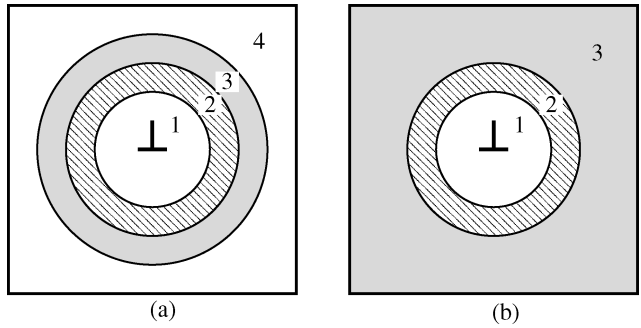

Figure 15 Two possible simulation cells for FP-GFBC: (a) vacuum region isolates the dislocation from its periodic images, while (b) region 3 is expanded up to the boundaries of the simulational cell. In the direction of the dislocation line, the cell is one periodic length thick.

FP-GFBC method), but it uses a classical potential to relax the environment around the region of interest, instead of a Green's function solution. As with the FP-GFBC, the QuASI region of interest is modeled using DFT. This method was especially developed to investigate critical regions in the neighborhood of dislocations, but not necessarily at the dislocation cores. This generality is achieved by allowing complete freedom in the placement of the quantum cluster(s) inside the classical environment [Figure 16(a)]. Such a freedom allows the detailed modeling of phenomena that are affected by the presence of nearby dislocation(s) but are spatially located outside the dislocation cores. As an example, the methodology has been used to investigate the formation of vacancies as a function of their distance from an edge dislocation. As with the GFBC and FP-GFBC methods, this methodology also makes use of an iterative approach.

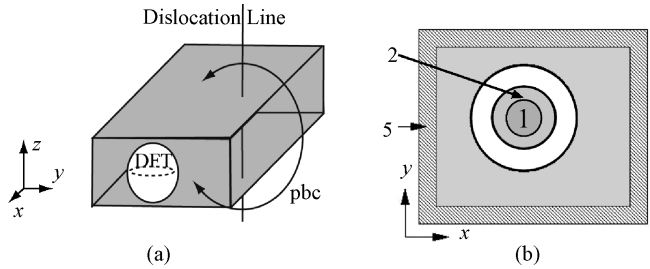

Figure 16 (a) Example of simulation cell: The gray parallelepiped constitutes the classical cell inside which is the critical region (spherical region marked DFT). (b) Schematic 2D representation of the shell structure. Shells 1, 2, and 3 correspond to the critical region, i.e., are considered in the DFT calculation. During the classical relaxation all shells are considered, but only atoms in shells 2, 3, and 4 are allowed to move.

The coupling between the ab initio and the classical simulations is made through shared atomic shells where the two atomistic approaches are used in an iterative, self-consistent manner. The small, critical region is relaxed using DFT and the much larger cell in which this is embedded is relaxed using a classical relaxation algorithm (Monte Carlo[15–17] or minimization algorithms[14]). The initial positions of all the atoms in the cell are determined by the elastic displacement field. Then, the simulations start with the DFT relaxation, followed by the classical one. Both relaxations are then repeated until convergence is achieved. The DFT sphere is composed of three concentric shells, labeled 1, 2, and 3 in Figure 16(b). During the quantum calculation, all of the atoms contained in shells 1 and 2 are relaxed, while those in shell 3 are kept fixed in positions determined by the previous classical run. During each classical simulation, atoms in shell 1 are kept fixed in positions determined by the previous DFT relaxation, while atoms in shells 2, 3, and 4 are allowed to relax. Atoms in shell 5 are kept fixed at all times in their initial positions because they constitute the most external shell of the classical cluster. With the exception of shell 5, the thickness of each shell depends on the problem under examination and needs to be determined accordingly. The thickness of shell 5 is determined solely by the cutoff used in the classical potential of choice.

Special attention is paid to the termination of the quantum cluster because the methodology is aimed at the study of metallic materials, and therefore no localized dangling bonds are available. It is beyond the scope of this review to explore the different termination strategies, and we refer the interested reader to the original papers.[261,263,264]

Applications The authors applied the QuASI methodology to the study of vacancy formation energy at different distances and directions from an edge dislocation in aluminum.[262–264]

Dynamics Methodologies

Coupling of Length Scales Method: Atomistic/Quantum Part

The general idea behind the coupling of length scales (CLS) methodology has already been discussed above, together with the basics of the FE/MD coupling. In the following, details are given on the hand-shaking procedure implemented between the atomistic and quantum regions. It is important to point out that such a procedure is specifically designed for the modeling of insulators or semiconductors because it actively takes advantage of the locality of the bonds and of the existence of well-defined dangling bonds. In particular, the authors applied their methodology to the investigation of silicon;[66,67,160–164] they employed the Stillinger–Weber (SW) potential[8] to describe classical interactions and a tight-binding (TB) methodology to model quantum interactions.

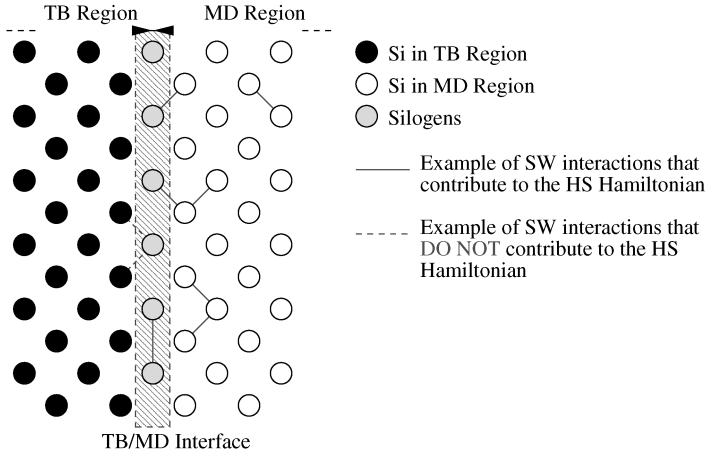

Figure 17 The TB/MD handshake (HS) region. The interface between the TB domain and the MD one runs across a line of atoms, whose properties are modified to ensure stability of the TB region. More specifically, these atoms are silogens (gray circles) and act as terminations for the TB cluster (solid circles). Si atoms in the MD region are represented by open circles.

The coupling scheme is schematically represented in Figure 17. Because of the nature of the quantum interactions, the total energy in the TB region cannot be localized on specific bonds, which makes defining the forces in the hand-shake region a nontrivial matter. In particular, it is not possible to average the MD and TB bond contributions across the interface in a computationally efficient way, as was done for the FE/MD interface. This is because the Hellman–Feynman theorem, which is at the basis of the TB force calculations, would not be applicable, and numerical derivatives of the electronic coefficients with respect to the atomic coordinates would therefore be needed. The coupling strategy is therefore different from the one employed in the FE/MD case. Now, the interface between the regions is defined as the ensemble of atoms that constitute the outer shell of the TB cluster, instead of simply being a line in between atomic planes. These atoms are called *silogens*, to indicate that their properties have been modified to make them suitable terminations for the TB cluster. More specifically, they are hydrogenlike atoms described by TB parameters that were fitted to reproduce the correct Si–Si bond length and binding energy, and to generate forces within the cluster that remain physical as the cluster itself is deformed. Also, the silogen atoms are constrained to sit where MD silicon used to be and, if more than one dangling bond needs termination, multiple silogens are placed at the same site. More details on the fitting procedure and placement criteria for the silogens can be found in the original papers.[66,67,158–162]

When computing the TB part of the Hamiltonian (H_{TB} in Eq. [26]), all of the Si–Si and Si–silogen interactions within the cluster are taken into account,

but no silogen-silogen interactions (because of the possible multiple placement on a single site). Conversely, the hand-shake term $H_{MD/TB}$ only contains classically computed terms (SW interactions), and it includes all of the SW pair interactions between a silogen and either a Si in the MD region or another silogen, and all SW three-body interactions between at least one MD silicon and a silogen–silicon pair. When computing the forces, all of the classical and TB forces acting on the same atom are added together.

Lastly, it is worthwhile noticing that the Hamiltonian given in Eq. [26] is conservative if the TB region is fixed, i.e., no dynamical allocation of the region is employed. However, a dynamical allocation of such a region may be extremely useful, for instance, in crack-propagation studies. A description of how this could be achieved is beyond the scope of this review, and we refer the interested reader to the original papers.

Learn on the Fly

The "learn-on-the-fly" (LOTF) method, suggested by Csányi et al. in 2004,[75,265–267] tackles the question of how to seamlessly couple different levels of theory in a way that is very different from everything we have examined up to this point. The method is constructed to join classical and quantum mechanical descriptions inside a dynamical simulation. The significant novelty of this approach is the fact that the focus is directly on the evaluation of the forces acting on each atom in the system, instead of on the matching of different Hamiltonians or on the constructing of a unique Hamiltonian containing the different levels of theory. In addition, the method calls for a local refitting of the classical parameters "on the fly," i.e., during the course of each simulation, to locally reproduce the quantum forces. This method could be seen as an evolution of the "serial" approach discussed at the beginning of the chapter (a higher level theory is used to determine parameters for a lower level theory calculation), in which the concurrent application of different levels of theory, the signature of hybrid approaches, enters through the evaluation of ab initio data, which occurs while the simulation is running, is repeated every so many time steps, and is local to each atom.

More specifically, this methodology employs molecular dynamics (MD) (i.e., classical simulations) to investigate the dynamical evolution of the system. However, instead of computing the forces acting on each atom from a predefined classical potential, as in standard MD, the parametrization of the potential is refitted every few time steps. This is accomplished using a predictor–corrector scheme. At the beginning of the simulation, a well-behaved potential is chosen, such that the equilibrium configuration of the system is well reproduced. Then, during the predictor part of the scheme, the classical forces acting on the atoms are computed using the parametrization given at that time (α_0), and the system is evolved along the classical trajectories for a few time steps, moving from $\mathbf{R}_0$ to $\mathbf{R}'$ in phase space. At this point, the classical and the quantum forces acting on the atoms at point $\mathbf{R}'$ are computed

(reference forces), and a new set of parameters, α_1, is found by minimizing the functional

$$\mathcal{F} = \sum |F_{\text{universal}} - F_{\{\text{classical,quantum}\}}| \qquad [66]$$

where $F_{\text{universal}}$ indicates the set of forces obtained using the new, instantaneously determined potential, and $F_{\{\text{classical,quantum}\}}$ are the reference forces. Because in most applications the quantum forces are computed only for a few atoms (those in critical regions), some atoms exist that do not have a quantum force calculated on them. For those atoms, the current classical force is used as a target in the minimization, hence the subscript {classical,quantum} in Eq. [66]. During the corrector part of the algorithm, the system is brought back to the $\mathbf{R}_0$ point in phase space, and then reevolved, this time using the forces obtained by interpolating the parameters between α_0 and α_1. The new end point, $\mathbf{R}_1$, and the corresponding parametrization, α_1, are used as initial values in the next predictor step.

The evaluation of the quantum forces can be performed using an "independent clusters" scheme. Here, for each atom in the critical region, a small cluster of atoms centered on the atom in question is considered. Such a small cluster may also be chemically terminated for improved accuracy. Using such a cluster, the quantum forces are computed, but only the ones acting on the central atom are retained. Since the clusters are independent from each other, such a scheme is well suited for parallelization. More details on this and other computational approaches for computing the exact forces are discussed in the original papers.[75,265–267]

Lastly, it must be mentioned that energy is not conserved in this methodology because the Hamiltonian is time dependent. However, it is a great candidate for constant-temperature simulations, where a thermostat is used to absorb any temperature variation.

Application The authors applied this methodology to the investigation of Si. In particular, they studied brittle fracture mechanisms (crack propagation, determination of the stress–strain curve, and so on),[75] vacancy diffusion, and gliding of a pair of partial dislocations at finite temperature.[265] In all of these applications, the authors used a tight-binding (TB) scheme to perform the quantum calculations, and the Stillinger–Weber potential (SW)[8] for the classical ones.

Coupling Method by Ogata et al.

Over the course of several years, Ogata et al. developed a full-spectrum (i.e., FE/CM/QM) hybrid methodology for chemical and physical applications.[268–270] As is the case for the LOTF method discussed in the preceding section, the current formulation of Ogata's methodology is well suited for

investigating insulators and semiconductors but not metals because of the "cluster" approach used in the quantum mechanical part of the calculations. This formulation and the quantum classical coupling are discussed below. However, because their continuum–classical coupling is strongly related to the CLS approach (discussed above), it is not individually presented in this review, and we refer the interested reader to the original papers.[268–270]

In this methodology, a single energy functional is defined for the whole system (FE/CP/QM), and the part of the Hamiltonian related to the quantum mechanics (QM) and classical potential (CP) domains is given by

$$H = \sum_{i=1}^{N} \frac{m_i}{2} \mathbf{v}_i^2 + E_{\text{pot}}(\mathbf{r}_i \in \text{CP/QM system}) \qquad [67]$$

where N is the number of atoms in the CP/QM system, m_i is their mass, and $\mathbf{v}_i$ is their velocity. E_{pot} is the CP + QM potential energy, and in this approach it is written as

$$\begin{aligned} E_{\text{pot}} = {} & E_{\text{QM}}^{\text{cluster}}(\mathbf{r}_i \in \text{cluster} + \text{handshake}) \\ & + \tilde{E}_{\text{CP}}(\mathbf{r}_i \in \text{classical domain} + \text{handshake}) \end{aligned} \qquad [68]$$

because the quantum domain consists of an atomic cluster around the area of interest, and the classical domain surrounds it. Hand-shake atoms comprise the interface between this cluster and its classical surroundings, and Eq. [68] indicates that both the cluster and the classical-domain energies depend upon such atoms. Instead of evaluating $\tilde{E}_{\text{CP}}$ directly, the authors expressed this term as

$$\tilde{E}_{\text{CP}} = E_{\text{CP}}^{\text{CP/QM system}}(\mathbf{r}_i \in \text{CP/QM system}) \qquad [69]$$

$$- E_{\text{CP}}^{\text{cluster}}(\mathbf{r}_i \in \text{cluster} + \text{handshake}) \qquad [70]$$

as suggested by Svensson et al.[271] and Eichler et al.[272] Therefore, this treatment does not require the explicit partitioning of E_{pot} into a quantum and a classical term, as is done, for instance, in the CLS method discussed above. However, it does require the classical and quantum mechanical evaluation of the cluster energy, as well as the classical evaluation of the energy of the whole QM/CM system.

In both the classical and the quantum mechanical computations of the cluster energy, it is necessary to terminate the cluster's dangling bonds, to obtain a stable structure (see Figure 18). The use of H atoms is appropriate when considering semiconductors or insulators.[273–276] The termination atoms are placed instead of the hand-shake atoms, and their position is determined

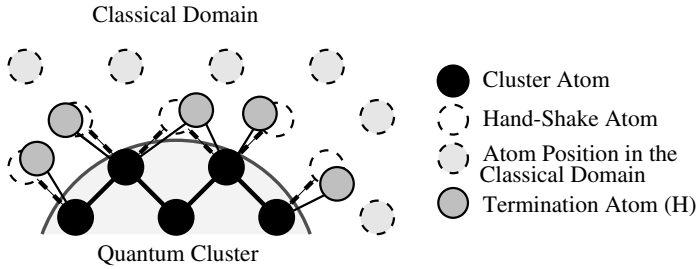

Figure 18 Schematic representation of the cluster termination procedure. When computing the cluster energy, atoms in the classical domain (dashed circles) are not included in the calculations: Some cluster bonds are therefore left unsaturated (dashed lines). For each hand-shake atom (dashed white circles) that is not included, a termination atom (gray circles) is added, with position determined by minimizing the mean-square forces acting on the cluster.

by minimizing the mean square forces that are acting on the cluster. A more detailed description of how these positions are determined can be found in Refs. 268 and 269. Lastly, both $E_{\mathrm{QM}}^{\mathrm{cluster}}$ and $E_{\mathrm{CP}}^{\mathrm{cluster}}$ are defined as the respective energies for the terminated cluster.

Once the classical and quantum energies are determined, the corresponding atomic forces are calculated and used within a molecular dynamics scheme. A velocity Verlet algorithm[277] is used for the time integration. For more details on how the method is implemented within a parallel scheme, using the message passing interface (MPI), we refer to the original paper.[268–270]

Applications This methodology has been used to investigate oxidation processes of Si(100) surfaces.[268,269] It was also used to model graphene behavior,[278] and environmental effects of H_2O on fracture initiation in Si.[279] Lastly, in 2004, the methodology was expanded to allow for the simulation of alumina systems.[280] In particular, it was used to study stress corrosion cracking of $\alpha-Al_2O_3$.

Transparent Interface Method by Cheng et al.

As a last example of coupling mechanisms between quantum mechanically described regions and classically modeled ones, we want to mention the transparent interface method developped by Cheng et al.[281–283] This method was developed to model silicon dioxide, but it can easily be generalized to describe different systems. In this methodology, a Born–Oppenheimer DFT molecular dynamics (BO-DFT-MD) approach is considered, i.e., quantum forces are used to drive molecular dynamics.[284] Also, such a methodology is designed to cover the whole span from continuum to quantum. However, in this review we are only going to present their quantum-to-classical coupling approach, while we refer the reader interested in their description of the continuum-to-classical treatment to the more specific studies listed above.

The philosophy behind the transparent interface method is to optimize the description of the interatomic forces across the interface, instead of focusing on the accurate reproduction of the total energy of the system. The method utilizes a single energy functional to describe the whole system and pseudoatoms to connect the quantum and classical regions. More in detail, a pseudoatom is placed in between each quantum-described oxygen and classically described silicon to correctly terminate the quantum wave functions, and the Hamiltonian for the whole system is given by

$$H = \sum_{\mathrm{IQ}} \frac{|\mathbf{P}_{\mathrm{IQ}}|^2}{2m_{\mathrm{IQ}}} + \sum_{\mathrm{IQ}>JQ} \frac{Z_{\mathrm{IQ}} Z_{JQ}}{|\mathbf{R}_{\mathrm{IQ}} - \mathbf{R}_{JQ}|} + E_{\mathrm{elec}}(\{\mathbf{R}_{\mathrm{IQ}}, \mathbf{R}^*_m\}; \rho[\mathbf{r}, \mathbf{r}^*]) + \sum_{\mathrm{IC}} \frac{|\mathbf{P}_{\mathrm{IC}}|^2}{2m_{\mathrm{IC}}} + U(\{\mathbf{R}_{\mathrm{IC}}\}) + U(\{\mathbf{R}_{\mathrm{IQ}}, \mathbf{R}_{\mathrm{IC}}\}) \quad [71]$$

where IQ and IC describe particles in the quantum and classical regions, respectively, $\mathbf{R}^*_m$ and $\mathbf{r}^*$ are the nuclear and electronic coordinates for the pseudoatoms, and m is the index of the pseudoatom. $E_{\mathrm{elec}} = T_e + E_{\mathrm{eI}} + E_{\mathrm{ee}}$ is the total ground-state electronic energy, i.e., the sum of the electron kinetic energy, the electron–ion interaction and the electron–electron interaction. The first three terms in Eq. [71] describe the quantum region in the presence of pseudoatoms, while the fourth and fifth terms define the kinetic and potential energy of the classical part of the system. The last term contains the sum of all the interactions between quantum and classical ions.

The pseudoatoms are introduced to terminate the wave functions of the quantum cluster in such a way that the structure and forces on the quantum cluster are as close as possible to those of the same subsystem within an all-quantum system. The pseudoatoms are therefore placed along a straight line between the quantum oxygen and the classical silicon, at a fixed distance from the oxygen [$d = 1.82\, a_0$ (Bohr)]. Also, they do not carry any kinetic energy, so as not to exert any direct influence on the dynamics of the system. Lastly, to obtain an interface as smooth as possible, the same classical potential is used for modeling both the interactions between classical and quantum ions and the interactions between classical and classical ions.

In the transparent interface method, the forces on each atom are derived from the gradient of the total potential energy in Eq. [71]. However, the constraint forces acting on quantum atoms at the boundary, due to the constaints imposed on the pseudoatoms, are neglected in this approach, leading to an approximation of the Hamiltonian equations that provides correct forces and dynamics (within the limit of a classical force field) but violates energy conservation.

More details on the explicit calculation of the forces and the implementation of the BO-DFT-MD method within a generalized gradient approximation (GGA)[285] can be found in the original papers.[281–283]

Application The transparent interface method has been tested on the $Si_2O_7H_6$ system and then applied to the study of SiO and SiO_2 molecules and their interaction with water.

CONCLUSIONS: THE OUTLOOK

The development and use of hybrid, multiscale methods for modeling solid-state processes is expanding rapidly and has been driven largely by the burgeoning activity in nanoscience and nanotechnology. Throughout this chapter, we have concentrated on the various modeling techniques that are available today, along with their strengths and weaknesses. Looking toward the future, however, it is equally important to address the question: *What more is needed*? In other words, are there important questions in computational solid-state physics that existing methodologies are incapable of answering? Perhaps not surprisingly, we find that the most sophisticated computational techniques available today can adequately address only a tiny fraction of the important problems that require solutions. For example, nearly all of the applications described in this chapter deal with geometrically simple, single-component systems composed of just a single element (often Si). While solving such problems greatly improves our fundamental understanding of important nanoscale processes, it is also true that the behavior of real-world materials and devices often critically depends upon impurities and complex interactions in multicomponent systems. Existing computational methods are woefully inadequate for modeling such systems.

Many of the important unanswered questions that we cannot adequately address can be separated into four main modeling categories: (1) multicomponent and multielement models, (2) quantitative models, (3) coupled-mechanism models, and (4) multiple time-scale models. The primary difficulty in handling multicomponent and multielement models is that atomistic simulations using classical potentials generally fare poorly when chemistry effects are important or when bonds are significantly distorted away from the configurations used to develop the potential. Multiscale models that incorporate quantum mechanics methodologies can help, but only when the important physics is concentrated within a very small volume. The LOTF method shows great promise in handling problems in this class since the classical potentials are modified on the fly using small-scale quantum calculations. It is important to emphasize, however, that multiscale models that include a QM component generally require the imposition of boundary conditions on the electronic wave function at the QM boundary. This problem is particularly severe for metals, which have highly delocalized bonding, so most CP/QM models (including LOTF) are currently restricted to modeling insulators and semiconductors.

Quantitative modeling has two primary aspects. First, a quantitative model must make *predictions* that are "qualitatively" correct, meaning that

the general mechanisms observed in the simulation would also be observed in a corresponding experiment. In general, there is no easy way to assure this correspondence except through careful comparison between experiments and model predictions. Second, a quantitative model must provide *some* indication of how accurate a given prediction is. Is the answer correct to within 10% or 1000%? Again, such uncertainty estimates can only come from careful comparison with experimental results in carefully chosen situations. For most academic applications, the large amount of effort required for quantitative modeling is not worth the trouble. For many industrial applications, however, quantitative modeling is an absolute requirement.

Coupled mechanism models are becoming increasing important as the size scales under investigation decrease. A good example is a complementary symmetry metal–oxide–semiconductor (CMOS) device. At relatively large length scales (100s of nanometers), the gate, oxide, substrate, source, and drain can mostly be considered individually for modeling purposes. As the feature sizes decrease into the 10s of nanometers range, however, effects such as local diffusion processes, elastic strain, and conductivity become closely coupled, making modeling much more difficult. Modeling methodologies that can handle such coupled processes are very limited and improvements are badly needed. For further discussion of these and related issues, we refer the reader to two workshop reports.[286,287]

Finally, although coupled time-scale models are not within the scope of this review chapter, this topic is just as important as multiple length scales when dynamical processes are being considered. As mentioned previously, models that include atoms must generally use time steps small enough to capture the vibrational modes of the system. Since the corresponding experiments almost always occur over time scales *many* orders of magnitude longer than what can be simulated, the relevance of the models to real-world behavior is often in doubt. Although good progress has been made in developing multiple time-scale methodologies, this problem remains a major stumbling block for people trying to simulate real-world processes.

In summary, tremendous progress has been made over the past couple of decades in the field of multiscale modeling of solid-state processes. Nevertheless, existing techniques can only handle a small fraction of the important problems that require solutions. There is plenty of *opportunity* at the bottom.

APPENDIX: A LIST OF ACRONYMS

1D	One dimensional
2D	Two dimensional
3D	Three dimensional

AFEM	Atomic size finite element
BC	Boundary conditions
CADD	Coupled atomistic and discrete dislocation
CG	Coarse grain
CGMD	Coarse-grain molecular dynamics
CLS	Coupling of length scales
CP	Classical potential
DFT	Density functional theory
EAM	Embedded atom method
EED	Edge-to-edge decomposition
FE	Finite element
FEM	Finite-element method
FEAt	Finite-element atomistic
FNL-QC	Fully nonlocal quasi-continuum
FP-GFBC	First-principle Green's function boundary condition
GFBC	Green's function boundary condition
GLE	Generalized Langevin equation
HMM	Heterogeneous multiscale method
HS	Hand shake
LHA	Local harmonic approximation
LOTF	Learn on the fly
LQC	Local quasi-continuum
MAAD	Macroscopic, atomistic, ab initio dynamics
MD	Molecular dynamics
MM	Molecular mechanical
MPM	Material point method
ODD	Overlapping domain decomposition
OFDFT	Orbital-free density functional theory
OFDFT-QC	Orbital-free density functional theory, quasi-continuum
PDE	Partial differential equation
PMF	Potential of mean force
QC	Quasi-continuum
QCDFT	Quasi-continuum, density functional theory
QC-GFC	Quasi-continuum, ghost forces corrected
QCMC	Quasi-continuum Monte Carlo
QC-QHMK	Quasi-continuum k-space quasi-harmonic model
QM	Quantum mechanics
QuASI	Quantum atomistic static interface
SCF-HACG	Self-consistent field, hybrid atomistic-coarse-grained
SW	Stillinger–Weber
TB	Tight binding
VBC	Variational boundary condition

REFERENCES

1. B. Q. Luan and M. O. Robbins, *Nature*, **435**, 929 (2005). The Breakdown of Continuum Models for Mechanical Contacts.
2. B. Q. Luan and M. O. Robbins, *Phys. Rev., E* **74**, 026111 (2006). Contact of Single Asperities with Varying Adhesion: Comparing Continuum Mechanics to Atomistic Simulations.
3. W. B. Bickford, *A First Course in the Finite Element Method*, Irwin, Homewood, IL, 1990, 1993.
4. D. R. J. Owen and E. Hinton, *A Simple Guide to Finite Elements*, Pineridge Press, Swansea, Wales, 1980.
5. G. Strang and G. J. Fix, *An Analysis of the Finite Element Method*, Prentice-Hall, Englewood Cliffs, NJ, 1973.
6. J. N. Reddy, *An Introduction to the Finite Element Method*, McGraw-Hill, New York, 1984, 1993, 2005.
7. J. E. Lennard-Jones, *Proc. Phys. Soc.*, **43**, 461–482 (1931). Cohesion.
8. F. H. Stillinger and T. A. Weber, *Phys. Rev. B*, **31**, 5262 (1985). Computer Simulation of Local Order in Condensed Phases of Silicon.
9. M. S. Daw and M. I. Baskes, *Phys. Rev. B*, **29**, 6443 (1984). Embedded-Atom Method: Derivation and Application to Impurities, Surfaces, and Other Defects in Metals.
10. J. K. Norskov and N. D. Lang, *Phys. Rev. B*, **21**, 2131 (1980). Effective-Medium Theory of Chemical Binding: Application to Chemisorption.
11. L. A. Girifalco and V. G. Weizer, *Phys. Rev.*, **114**, 687 (1959). Application of the Morse Potential Function to Cubic Metals.
12. J. Tersoff, *Phys. Rev. B*, **38**, 9902 (1988). Empirical Interatomic Potential for Silicon with Improved Elastic Properties.
13. D. W. Brenner, *Phys. Rev. B*, **42**, 9458 (1990). Empirical Potential for Hydrocarbons for Use in Simulating the Chemical Vapor Deposition of Diamond Films.
14. W. H. Press, S. A. Teukolsky, W. T. Vetterling, and B. P. Flannery, *Numerical Recipes in Fortran 77: The Art of Scientific Computing*, 2nd ed., Cambridge University Press, Cambridge, UK, 1996, Chapter 10. Minimization or Maximization of Functions.
15. D. P. Landau and K. Binder, *A Guide to Monte Carlo Simulations in Statistical Physics*, Cambridge University Press, Cambridge, UK, 2000.
16. R. Rubinstein, *Simulation and the Monte Carlo Method*, Wiley, New York, 1981.
17. G. S. Fishman, *Monte Carlo: Concepts, Algorithms and Applications*, Springer, New York, 1996.
18. M. P. Allen and D. J. Tildesley, *Computer Simulation of Liquids*, Oxford University Press, London 1989.
19. D. C. Rapaport, *The Art of Molecular Dynamics Simulation* Cambridge University Press, Cambridge, UK, 1996.
20. D. Frenkel and B. Smit, *Understanding Molecular Simulation*, Academic Press, San Diego 2001.
21. J. M. Haile, *Molecular Dynamics Simulation: Elementary Methods*, Wiley, New York, 2001.
22. J. C. Slater and G. F. Koster, *Phys. Rev.*, **94**, 1498 (1954). Simplified LCAO Method for the Periodic Potential Problem.
23. N. W. Ashcroft and N. D. Mermin, *Solid State Physics*, Thomson Learning, Toronto, 1976, Chapter 10. The Tight-Binding Method.
24. C. M. Goringe, D. R. Bowler, and E. Hernandez, *Rep. Prog. Phys.*, **60**, 1447 (1997). Tight-Binding Modelling of Materials.
25. R. G. Parr and W. Yang, *Density-Functional Theory of Atoms and Molecules*, Oxford University Press, New York 1989.
26. P. C. Gehlen, G. T. Hahn, and M. F. Kanninen, *Scripta Metall.*, **6**, 1087 (1972). Crack Extension by Bond Rupture in a Model of bcc Iron.

27. J. E. Sinclair, *Philos. Mag.*, **31**, 647 (1075). The Influence of the Interatomic Force Law and of Kinks on the Propagation of Brittle Cracks.

28. A. Warshel and M. Levitt, *J. Mol. Biol.*, **103**, 227 (1976). Theoretical Studies of Enzymic Reactions: Dielectric, Electrostatic and Steric Stabilization of the Carbonium Ion in the Reaction of Lysozyme.

29. *Combined QM/MM Calculations in Chemistry and Biochemistry, J. Mol. Struct. THEOCHEM* **632** (special issue).

30. J. Gao, *Reviews in Computational Chemistry*, K. B. Lipkowitz and D. B. Boyd, Eds., VCH, New York, 1996, Vol. 7, pp. 119–185. Methods and Applications of Combined Quantum Mechanical and Molecular Mechanical Potentials.

31. D. E. Ellis and O. Warschkow, *Coord. Chem. Rev.*, **238**, 31 (2003). Evolution of Classical/Quantum Methodologies: Applications to Oxide Surfaces and Interfaces.

32. F. Bessac, F. Alary, Y. Carissan, J.-L. Heully, J-P. Daudey, and R. Poteau, *J. Mol. Structure (THEOCHEM)*, **632**, 43 (2003). Effective Group Potentials: A Powerful Tool for Hybrid QM/MM Methods?

33. F. J. Dejong, J. S. Sabnis, R. C. Buggeln, and H. McDonald, *J. Spacecraft Rockets*, **29**, 312 (1992). Hybrid Navier-Stokes/Monte Carlo Method for Reacting Flow Calculations.

34. A. L. Garcia, J. B. Bell, W. Y. Crutchfield, and B. J. Alder, *J. Comput. Phys.*, **154**, 134 (1999). Adaptive Mesh and Algorithm Refinement Using Direct Simulation Monte Carlo.

35. T. J. Sommerer, M. S. Barnes, J. H. Keller, M. J. McCaughey, and M. J. Kushner, *Appl. Phys. Lett.*, **59**, 638 (1991). Monte Carlo-Fluid Hybrid Model of the Accumulation of Dust Particles at Sheath Edges in Radio-Frequency Discharges.

36. A. Bogaerts, R. Gijbels, and W. J. Goedheer, *J. Appl. Phys.*, **78**, 2233 (1995). Hybrid Monte Carlo-Fluid Model of a Direct Current Glow Discharge.

37. S. T. O'Connell and P. A. Thompson, *Phys. Rev. E*, **52**, 5792 (1995). Molecular Dynamics Continuum Hybrid Computations: A Tool for Studying Complex Fluid Flows.

38. N. G. Hadjiconstantinou and A. T. Patera, *Int. J. Mod. Phys. C*, **8**, 967 (1997). Heterogeneous Atomistic-Continuum Representations for Dense Fluid Systems.

39. N. G. Hadjiconstantinou, *J. Comput. Phys.*, **154**, 245 (1999). Hybrid Atomistic-Continuum Formulations and the Moving Contact-Line Problem.

40. J. Li, D. Y. Liao, and S. Yip, *Phys. Rev. E*, **57**, 7259 (1998). Coupling Continuum to Molecular-Dynamics Simulation: Reflecting Particle Method and the Field Estimator.

41. Y. C. Wang and G. W. He, *Chem. Eng. Sci.*, **62**, 3574 (2007). A Dynamic Coupling Model for Hybrid Atomistic-Continuum Computations.

42. E. G. Flekkoy, G. Wagner, and J. Feder, *Europhys. Lett.*, **52**, 271 (2000). Hybrid Model for Combined Particle and Continuum Dynamics.

43. E. G. Flekkoy, J. Feder, and G. Wagner, *Phys. Rev. E*, **64**, 066302 (2001). Coupling Particles and Fields in a Diffusive Hybrid Model.

44. V. V. Dobrovitski, M. I. Katsnelson, and B. N. Harmon, *J. Appl. Phys.*, **93**, 6432 (2003) and references within. Statistical Coarse Graining as an Approach to Multilength Scale Problems in Micromagnetics.

45. Z. Lin and L. Chen, Technical Report PPPL-3536, Princeton Plasma Physics Lab., NJ, 2001. A Fluid-Kinetic Hybrid Electron Model for Electromagnetic Simulations.

46. C. B. Frederick, M. L. Bush, L. G. Lomax, K. A. Black, L. Finch, J. S. Kimbell, K. T. Morgan, R. P. Subramaniam, J. B. Morris, and J. S. Ultman, *Toxicol. Appl. Pharm.*, **152**, 221 (1998). Application of a Hybrid Computational Fluid Dynamics and Physiologically Based Inhalation Model for Interspecies Dosimetry Extrapolation of Acidic Vapors in the Upper Airways.

47. G. Lu and E. Kaxiras, in *Handbook of Theoretical and Computational Nanotechnology*, Vol. X, M. Rieth and W. Schommers, Eds., American Scientific, Valencia, California 2005, pp. 1–33. An Overview of Multiscale Simulations of Materials.

48. R. M. Nieminen, *J. Phys.: Conden. Mat.*, **14**, 2859 (2002). From Atomistic Simulation towards Multiscale Modelling of Materials.
49. W. M. Young and E. W. Elcock, *Proc. Phys. Soc.*, **89**, 735 (1966). Monte Carlo Studies of Vacancy Migration in Binary Ordered Alloys: I.
50. A. B. Bortz, M. H. Kalos, and J. L. Lebowitz, *J. Comput. Phys.*, **17**, 10 (1975). A New Algorithm for Monte Carlo Simulation of Ising Spin Systems.
51. K. A. Fichthorn and W. H. Weinberg, *J. Chem. Phys.*, **95**, 1090 (1991). Theoretical Foundations of Dynamical Monte Carlo Simulations.
52. A. F. Voter, in *Radiation Effects in Solids*, K. E. Sickafus and E. A. Kotomin, Eds., Springer, NATO Publishing Unit, Dordrecht, The Netherlands, 2005. Introduction to the Kinetic Monte Carlo Method.
53. A. M. Ferrenberg and R. H. Swendsen, *Phys. Rev. Lett.*, **61**, 2635 (1988). New Monte Carlo Technique for Studying Phase Transitions.
54. A. M. Ferrenberg and R. H. Swendsen, *Phys. Rev. Lett.*, **63**, 1195 (1989). Optimized Monte Carlo Data Analysis.
55. E. P. Münger and M. A. Novotny, *Phys. Rev. B*, **43**, 5773 (1991). Reweighting in Monte Carlo and Monte Carlo Renormalization-Group Studies.
56. A. M. Ferrenberg and D. P. Landau, *Phys. Rev. B*, **44**, 5081 (1991). Critical Behavior of the Three-Dimensional Ising Model: A High-Resolution Monte Carlo Study.
57. R. H. Swendsen and J. S. Wang, *Phys. Rev. Lett.*, **57**, 2607 (1986). Replica Monte Carlo Simulation of Spin-Glasses.
58. K. Hukushima and K. Nemoto, *J. Phys. Soc. Jpn.*, **65**, 1604 (1996). Exchange Monte Carlo Method and Application to Spin Glass Simulations.
59. A. Bunker and B. Dünweg, *Phys. Rev. E*, **63**, 16701 (2000). Parallel Excluded Volume Tempering for Polymer Melts.
60. Y. Iba, *Int. J. Mod. Phy. C*, **12**, 623 (2001). Extended Ensemble Monte Carlo.
61. A. F. Voter, F. Montalenti, and T. C. Germann, *Annu. Rev. Mater. Res.*, **32**, 321 (2002). Extending the Time Scale in Atomistic Simulation of Materials.
62. A. F. Voter, *J. Chem. Phys.*, **106**, 4665 (1997). A Method for Accelerating the Molecular Dynamics Simulation of Infrequent Events.
63. A. F. Voter, *Phys. Rev. B*, **57**, R13985 (1998). Parallel Replica Method for Dynamics of Infrequent Events.
64. M. R. Srensen and A. F. Voter, *J. Chem. Phys.*, **112** 9599 (2000). Temperature-Accelerated Dynamics for Simulation of Infrequent Events.
65. E. B. Tadmor, R. Phillips, and M. Ortiz, *Int. J. Solids Struct,* **37**, 379 (2000). Hierarchical Modeling in the Mechanics of Materials.
66. R. Rudd and J. Broughton, *Phys. Stat. Sol. (b)*, **217**, 251 (2000). Concurrent Coupling of Length Scales in Solid State Systems.
67. R. Rudd, *Analog. Integrated Circuits Signal Proc.* **29**, 17 (2001). The Atomic Limit of Finite Element Modeling in MEMS: Coupling of Length Scales.
68. N. Ghoniem and K. Cho, *CMES Comput. Model. Eng. Sci.* **3**, 147 (2002). The Emerging Role of Multiscale Modeling in Nano and Micromechanics of Materials.
69. R. E. Miller, *Int. J. Multiscale Comput. Eng.*, **1**, 57 (2003). Direct Coupling of Atomistic and Continuum Mechanics in Computational Material Science.
70. H. Tan, *Comprehensive Structural Integrity: Interfacial and Nanoscale Failure*, Vol. 8, W. W. Gerberich and W. Yang, Eds., Elsevier Science, New York, 2003.
71. W. A. Curtin and R. E. Miller, *Model. Simul. Mater. Sci. Eng.*, **11**, R33 (2003). Atomistic/Continuum Coupling in Computational Materials Science.
72. W. K. Liu, E. G. Karpov, S. Zhang, and H. P. Park, *Comput. Methods Appl. Mech. Eng.*, **193**, 1529 (2004). An Introduction to Computational Nanomechanics and Materials.

73. H. S. Park and W. K. Liu, *Comput. Methods Appl. Mech. Eng.*, **193**, 1733 (2004). An Introduction and Tutorial on Multiple-Scale Analysis in Solids.

74. D. D. Vvedensky, *J. Phys: Cond. Mat.*, **16**, R1537 (2004). Multiscale Modelling of Nanostructures.

75. G. Csányi, T. Albaret, G. Moras, M. C. Payne, and A. De Vita, *J. Phys.: Cond. Mat.*, **17**, R691 (2005). Multiscale Hybrid Simulation Methods for Material Systems.

76. J. Fish, *J. Nanopart. Res.*, **8**, 577 (2006). Bridging the Scales in Nano Engineering and Science.

77. T. S. Gates, G. M. Odegard, S. J. V. Frankland, and T. C. Clancy, *Comput. Sci. Tech.*, **65**, 2416 (2005). Computational Materials: Multi-Scale Modeling and Simulation of Nanostructured Materials.

78. D. L. Shi, X. Q. Feng, H. Jiang, Y. Y. Huang, and K. C. Hwang, *Int. J. Fracture*, **134**, 369 (2005). Multiscale Analysis of Fracture of Carbon Nanotubes Embedded in Composites.

79. D. E. Segall, C. Li, and G. Xu, *Philos. Mag.*, **86**, 5083 (2006). Corroboration of a Multiscale Approach with All Atom Calculations in Analysis of Dislocation Nucleation from Surface Steps.

80. G. Xu, D. E. Segall, and C. Li, *IUTAM Symposium on Mechanical Behavior and Micro-Mechanics of Nanostructured Materials*, **144**, 181 (2007). Atomistic Corroboration of a Multiscale Approach for the Analysis of Dislocation Nucleation at a Surface Step.

81. Y. W. Kwon and S. H. Jung, *Comput. Struct.*, **82**, 1993 (2004). Atomic Model and Coupling with Continuum Model for Static Equilibrium Problems.

82. S. Kohlhoff, in *Proceedings of the International Finite-Element Method Congress*, Baden-Baden, 14–15 November 1988, Stuttgart: IKOSS. LARSTRAN a Tool in Material Sciences.

83. S. Kohlhoff and S. Schmauder, in *Atomistic Modelling in Materials Beyond Pair Potentials*, V. Vitek and D. J. Srolovitz, Eds., Plenum Press, New York, 1989, p. 411. A New Method for Coupled Elastic-Atomistic Modelling.

84. S. Kohlhoff, S. Schmauder, and P. Gumbsch, *Bonding, Structure and Mechanical Properties of Metal-Ceramic Interfaces*, Pergamon, Oxford, 1990, p. 63. Coupled Atomistic-Continuum Calculations of Near Interface Cracking in Metal/Ceramic Composites.

85. S. Kohlhoff, P. Gumbsch, and H. F. Fischmeister, *Philos. Mag. A*, **64**, 851 (1991). Crack Propagation in bcc Crystals Studied with a Combined Finite-Element and Atomistic Model.

86. P. Gumbsch, *J. Mater. Res.*, **10**, 2897 (1995). An Atomistic Study of Brittle Fracture: Toward Explicit Failure Criteria from Atomistic Modeling.

87. E. B. Tadmor, R. Phillips, and M. Ortiz, *Langmuir*, **12**, 4529 (1996). Mixed Atomistic and Continuum Models of Deformation in Solids.

88. E. B. Tadmor, M. Ortiz, and R. Phillips, *Philos. Mag.*, **73**, 1529 (1996). Quasicontinuum Analysis of Defects in Solids.

89. V. B. Shenoy, R. Miller, E. B. Tadmor, R. Phillips, and M. Ortiz, *Phys. Rev. Lett.*, **80**, 742 (1998). Quasicontinuum Models of Interfacial Structure and Deformation.

90. R. Miller, E. B. Tadmor, R. Phillips, and M. Ortiz, *Model. Simul. Mater. Sci. Eng.*, **6**, 607 (1998). Quasicontinuum Simulation of Fracture at the Atomic Scale.

91. R. Miller, M. Ortiz, R. Phillips, V. B. Shenoy, and E. B. Tadmor, *Eng. Fract. Mech.*, **61**, (1998). Quasicontinuum Models of Fracture and Plasticity.

92. D. Rodney and R. Phillips, *Phys. Rev. Lett.*, **82**, 1704 (1999). Structure and Strength of Dislocation Junctions: An Atomic Level Analysis.

93. R. B. Tew and J. A. D. Wattis, *J. Phys. A: Math. Gen.*, **34**, 7163 (2001). Quasi-Continuum Approximations for Travelling Kinks in Diatomic Lattices.

94. S. P. Xiao and W. X. Yang, *Int. J. Comput. Meth.*, **2(3)**, 293 (2005). A Nanoscale Meshfree Particle Method with the Implementation of the Quasicontinuum Method.

95. R. E. Miller and E. B. Tadmor, *J. Comput.-Aided Mater. Des.*, **9**, 203 (2002). The Quasi-Continuum Method: Overview, Applications and Current Directions.

96. M. Ortiz, A. M. Cuitino, J. Knap, and M. Koslowski, *MRS Bull.* **26**, 216 (2001). Mixed Atomistic-Continuum Models of Material Behavior: The Art of Transcending Atomistics and Informing Continua.

97. M. Ortiz and R. Phillips, *Adv. Appl. Mech.*, **36**, 1 (1999). Nanomechanics of Defects in Solids.

98. D. Rodney, *Proceedings of the NATO Conference Thermodynamics, Microstructures and Plasticity,* A. Finel, D. Maziere, and M. Veron, Eds., Kluwer, Dortrecht, 2003. Mixed Atomistic/Continuum Methods: Static and Dynamic Quasicontinuum Methods.

99. V. B. Shenoy, R. Miller, E. B. Tadmor, D. Rodney, R. Phillips, and M. Ortiz, *J. Mech. Phys. Solids*, **47**, 611 (1998). An Adaptive Methodology for Atomic Scale Mechanics: The Quasicontinuum Method.

100. J. L. Ericksen, in *Phase Transformations and Material Instabilities in Solids*, M. Gurtin, Ed., Academic Press, New York, 1984, pp. 61–77, and references therein. The Cauchy and Born Hypotheses for Crystals.

101. P. Steinmann, A. Elizondo, and R. Sunyk, *Model. Simul. Mat. Sci. Eng.*, **15**, S271 (2007). Studies of Validity of the Cauchy-Born Rule by Direct Comparison of Continuum and Atomistic Modeling.

102. J. Knap and M. Ortiz, *J. Mech. Phys. Sol.*, **49**, 1899 (2001). An Analysis of the Quasicontinuum Method.

103. J. Knap and M. Ortiz, *Phys. Rev. Lett.*, **90**, 226102 (2003). Effect of Indenter-Radius Size on Au(001) Nanoindentation.

104. J. Marian, J. Knap, and M. Ortiz, *Phys. Rev. Lett.*, **93**, 165503 (2004). Nanovoid Cavitation by Dislocation Emission in Aluminum.

105. T. Shimokawa, J. J. Mortensen, J. Schiotz, and K. W. Jacobsen, *Phys. Rev. B*, **69**, 214104 (2004). Matching Conditions in the Quasicontinuum Method: Removal of the Error Introduced at the Interface between the Coarse-Grained and Fully Atomistic Region.

106. J. J. Mortensen, J. Schitz, and K. W. Jacobsen, *Chall. Molec. Simul.*, **4**, 119 (2002). The Quasicontinuum Method Revisited.

107. W. E, J. F. Lu, and J. Z. Yang, *Phys. Rev. B*, **74**, 214115 (2006). Uniform Accuracy of the Quasicontinuum Method.

108. D. J. Diestler, H. Zhou, R. Feng, and X. C. Zeng, *J. Chem. Phys.*, **125**, 064705 (2006). Hybrid Atomistic-Coarse-Grained Treatment of Multiscale Processes in Heterogeneous Materials: A Self-Consistent-Field Approach.

109. H. Zhou, R. Feng, D. J. Diestler, and X. C. Zeng, *J. Chem. Phys.*, **123**, 164109 (2005). Coarse-Grained Free-Energy-Functional Treatment of Quasistatic Multiscale Processes in Heterogeneous Materials.

110. Z. Tang, H. Zhao, G. Li, and N. R. Aluru, *Phys. Rev. B*, **74**, 064110 (2006). Finite-Temperature Quasicontinuum Method for Multiscale Analysis of Silicon Nanostructures.

111. G. S. Smith, E. B. Tadmor, N. Bernstein, and E. Kaxiras, *Acta Materialia*, **49**, 4089 (2001). Multiscale Simulations of Silicon Nanoindentation.

112. G. S. Smith, E. B. Tadmor, and E. Kaxiras, *Phys. Rev. Lett.*, **84**, 1260 (2000). Multiscale Simulation of Loading and Electrical Resistance in Silicon Nanoindentation.

113. F. Sansoz and J. F. Molinari, *Acta Materialia*, **53**, 1931 (2005). Mechanical Behavior of Sigma Tilt Grain Boundaries in Nanoscale Cu and Al: A Quasicontinuum Study.

114. F. Sansoz and J. F. Molinari, *Thin Solid Films*, **515**, 3158 (2007). Size and Microstructure Effects on the Mechanical Behavior of FCC Bicrystals by Quasicontinuum Method.

115. D. B. Shan, L. Yuan, and B. Guo, *Mat. Sci. Eng. A*, **412**, 264 (2005). Multiscale Simulation of Surface Step Effects on Nanoindentation.

116. R. A. Iglesias and E. P. M Leiva, *Acta Materialia*, **54**, 2655 (2006). Two-Grain Nanoindentation using the Quasicontinuum Method: Two-Dimensional Model Approach.

117. Y. Hangai, N. Yoshikawa, S. V. Dmitriev, M. Kohyama, and S. Tanaka, *J. Jpn. Inst. Metals*, **69**, 194 (2005). Large Scale Atomistic Simulation of Cu/Al2O3 Interface via Quasicontinuum Analysis.

118. Y. Hangai and N. Yoshikawa, *Key Eng. Mat.*, **261–263**, 729 (2004). Quasicontinuum Models for Interface Multiscale Model.

119. F. L. Zeng and Y. Sun, *Acta Mech. Solida Sinica*, **19**, 283 (2006). Quasicontinuum Simulation of Nanoindentation of Nickel Film.

120. V. B. Shenoy, R. Phillips, and E. B. Tadmor, *J. Mech. Phys. Solids*, **48**, 649 (2000). Nucleation of Dislocations Beneath a Plane Strain Indenter.

121. F. Sansoz and V. Dupont, *Appl. Phys. Lett.*, **89**, 111901 (2006). Grain Growth Behavior at Absolute Zero During Nanocrystalline Metal Indentation.

122. S. Hai and E. B. Tadmor, *Acta Materialia*, **51**, 117 (2003). Deformation Twinning at Aluminum Crack Tips.

123. E. B. Tadmor, R. Miller, R. Phillips, and M. Ortiz, *J. Mater. Res.*, **14**, 2233 (1999). Nanoindentation and Incipient Plasticity.

124. C. S. Shin, M. C. Fivel, D. Rodney, R. Phillips, V. B. Shenoy, and L. Dupuy, *J. Phys. IV*, **11**, 19 (2001). Formation and Strength of Dislocation Junctions in FCC Metals: A Study by Dislocation Dynamics and Atomistic Simulations.

125. L. E. Shilkrot, W. A. Curtin, and R. E. Miller, *J. Mech. Phys. Solids*, **50**, 2085 (2002). A Coupled Atomistic/Continuum Model of Defects in Solids.

126. L. E. Shilkrot, R. E. Miller, and W. A. Curtin, *Phys. Rev. Lett.*, **89**, 025501 (2002). Coupled Atomistic and Discrete Dislocation Plasticity.

127. L. E. Shilkrot, R. E. Miller, and W. A. Curtin, *J. Mech. Phys. Solids*, **52**, 755 (2004). Multiscale Plasticity Modeling: Coupled Atomistics and Discrete Dislocation Mechanics.

128. M. Dewald and W. A. Curtin, *Model. Simul. Mater. Sci. Eng.*, **14**, 497 (2006). Analysis and Minimization of Dislocation Interactions with Atomistic/Continuum Interfaces.

129. B. Shiari, R. E. Miller, and W. A. Curtin, *J. Eng. Mater. Technol.*, **127**, 358 (2005). Coupled Atomistic/Discrete Dislocation Simulations of Nanoindentation at Finite Temperature.

130. E. van der Giessen and A. Needleman, *Model. Simul. Mater. Sci. Eng.*, **3**, 689 (1995). Discrete Dislocation Plasticity: A Simple Planar Model.

131. R. E. Miller, L. E. Shilkrot, and W. A. Curtin, *Acta Materialia*, **52**, 271 (2004). A Coupled Atomistics and Discrete Dislocation Plasticity Simulation of Nanoindentation into Single Crystal Thin Films.

132. M. P. Dewald and W. A. Curtin, *Model. Simul. Mater. Sci. Eng.*, **15**, S193 (2007). Multiscale Modelling of Dislocation/Grain-Boundary Interactions: I. Edge Dislocations Impinging on Σ11 (1 1 3) Tilt Boundary in Al.

133. B. Liu, Y. Huang, H. Jiang, S. Qu, and K. C. Hwang, *Comput. Meth. Appl. Mech. Eng.* **193**, 1849 (2004).The Atomic-Scale Finite Element Method.

134. B. Liu, H. Jiang, Y. Huang, S. Qu, M.-F. Yu, and K. C. Hwang, *Phys. Rev. B*, **72**, 035435 (2005). Atomic-Scale Finite Element Method in Multiscale Computation with Applications to Carbon Nanotubes.

135. A. Y. T. Leung, X. Guo, X. Q. He, H. Jiang, and Y. Huang, *J. Appl. Phys.*, **99**, 124308 (2006). Postbuckling of Carbon Nanotubes by Atomic-Scale Finite Element.

136. X. Guo, A. Y. T. Leung, H. Jiang, X. Q. He, and Y. Huang, *J. Appl. Mech.*, **74**, 347 (2007). Critical Strain of Carbon Nanotubes: An Atomic-Scale Finite Element Study.

137. P. C. Gehlen, J. P. Hirth, R. G. Hoagland, and M. F. Kanninen, *J. Appl. Phys.*, **43**, 3921 (1972). A New Representation of the Strain Field Associated with the Cube-Edge Dislocation in a Model of α-Iron.

138. R. Pasianot, E. J. Savino, Z. Y. Xie, and D. Farkas, *Mat. Res. Soc. Symp. Proc.*, **291**, 85 (1993). Simple Flexible Boundary Conditions for the Atomistic Simulation of Dislocation Core Structure and Motion.

139. J. E. Sinclair, *J. Appl. Phys.*, **42**, 5321 (1971). Improved Atomistic Model of a bcc Dislocation Core.

140. J. E. Sinclair, P. C. Gehlen, R. G. Hoagland, and J. P. Hirth, *J. Appl. Phys.*, **49**, 3890 (1978). Flexible Boundary Conditions and Nonlinear Geometric Effects in Atomic Dislocation Modeling.

141. S. I. Rao, C. Hernandez, J. P. Simmons, T. A. Parthasarathy, and C. Woodward, *Philos. Mag. A*, **77**, 231 (1998). Green's Function Boundary Conditions in Two-Dimensional and Three-Dimensional Atomistic Simulations of Dislocations.

142. A. N. Stroh, *J. Math. Phys.*, **41**, 77 (1962). Steady State Problems in Anisotropic Elasticity.

143. D. J. Bacon, D. M. Barnett, and R. O. Scattergood, *Prog. Mater. Sci.*, **23**, 51 (1979). Anisotropic Continuum Theory of Lattice Defects.

144. S. I. Rao, T. A. Parthasarathy, and C. Woodward, *Philos. Mag. A*, **79**, 1167 (1999). Atomistic Simulation of Cross-Slip Processes in Model fcc Structures.

145. S. I. Rao and C. Woodward, *Philos. Mag. A*, **81**, 1317 (2001). Atomistic Simulations of (a/2) ⟨111⟩ Screw Dislocations in bcc Mo Using a Modified Generalized Pseudopotential Theory Potential.

146. H. Jiang, Y. Huang, and K. C. Hwang, *J. Eng. Mater. Tech.*, **127**, 408 (2005). A Finite-Temperature Continuum Theory Based on the Interatomic Potential.

147. R. LeSar, R. Najafabadi, and D. J. Srolovitz, *Phys. Rev. Lett.*, **63**, 624 (1989). Finite-Temperature Defect Properties from Free-Energy Minimization.

148. J. Rickman and R. LeSar, *Annu. Rev. Mater. Res.*, **32**, 195 (2002). Free-Energy Calculations in Materials Research.

149. S. M. Foiles, *Phys. Rev. B*, **49**, 14930 (1994). Evaluation of Harmonic Methods for Calculating the Free Energy of Defects in Solids.

150. D. J. Diestler, *Phys. Rev. B*, **66**, 184104 (2002). Coarse-Grained Descriptions of Multiple Scale Processes in Solid Systems.

151. Z.-B. Wu, D. J. Diestler, R. Feng, and X. C. Zeng, *J. Chem. Phys.*, **119**, 8013 (2003). Coarse-Graining Description of Solid Systems at Nonzero Temperature.

152. D. J. Diestler, Z.-B. Wu, and X. C. Zeng, *J. Chem. Phys.*, **121**, 9279 (2004). An Extension of the Quasicontinuum Treatment of Multiscale Solid Systems to Nonzero Temperature.

153. V. Shenoy and R. Phillips, *Mat. Res. Soc. Symp. Proc.*, **538**, 465 (1999). Finite-Temperature Quasi-Continuum Methods.

154. H. Zhao, Z. Tang, G. Li, and N. R. Aluru, *J. Appl. Phys.*, **99**, 064314 (2006). Quasiharmonic Models for the Calculation of Thermodynamic Properties of Crystalline Silicon under Strain.

155. N. R. Aluru and G. Li, *Int. J. Numer. Methods Eng.*, **50**, 2373 (2001). Finite Cloud Method: A True Meshless Technique Based on a Fixed Reproducing Kernel Approximation.

156. F. Bloch, *Z. Phys.*, **52**, 555 (1928). Über die Quantenmechanik der Elektronen in Kristallgittern.

157. N. W. Ashcroft and N. D. Mermin, in *Solid State Physics*, International Edition, Saunders College, Philadelphia, 1976, Chapter 8, p. 135. Electron Levels in a Periodic Potential.

158. M. Arroyo and T. Belytschko, *J. Mech. Phys. Solids*, **50**, 1941 (2002). An Atomistic-Based Finite Deformation Membrane for Single Layer Crystalline films.

159. S. Xiao and W. Yang, *Comput. Mater. Sci.* **37**, 374 (2006). Temperature-Related Cauchy-Born Rule for Multiscale Modeling of Crystalline Solids.

160. F. F. Abraham, J. Q. Broughton, N. Bernstein, and E. Kaxiras, *Europhys. Lett.*, **44**, 783 (1998). Spanning the Continuum to Quantum Length Scales in a Dynamic Simulation of Brittle Fracture.

161. F. F. Abraham, J. Q. Broughton, N. Bernstein, and E. Kaxiras, *Comput. Phys.* **12**, 538 (1998). Spanning the Length Scales in Dynamic Simulation.

162. J. Q. Broughton, F. F. Abraham, N. Bernstein, and E. Kaxiras, *Phys. Rev. B*, **60**, 2391 (1999). Concurrent Coupling of Length Scales: Methodology and Application.

163. F. F. Abraham, *Int. J. Mod. Phys. C*, **11**, 1135 (2000). Dynamically Spanning the Length Scales from the Quantum to the Continuum.

164. F. F. Abraham, N. Bernstein, J. Q. Broughton, and D. Hess, *MRS Bull.* **25**, 27, (2000). Dynamic Fracture of Silicon: Concurrent Simulation of Quantum Electrons, Classical Atoms, and the Continuum Solid.

165. D. Hess, N. Bernstein, F. F. Abraham, and R. E. Rudd, in *Proc. DoD HPCUG Conf.*, June 1999, Monterey, CA. Coupling of Length Scales in Cracks and Micromachines.

166. R. E. Rudd and J. Q. Broughton, in *Proc. Modeling and Simulation of Microsystems*, Santa Clara, CA, Computational Publications, Boston 1998, p. 287. Coupling of Length Scales and Atomistic Simulation of a MEMS Device.

167. R. E. Rudd and J. Q. Broughton, *J. Mod. Sim. Microsys.*, **1**, 29 (1999). Atomistic Simulation of MEMS. Resonators through the Coupling of Length Scales.

168. E. Lidorikis, M. E. Bachlechner, R. K. Kalia, A. Nakano, and P. Vashishta, *Phys. Rev. Lett.*, **87**, 086104-1 (2001). Coupling Length Scales for Multiscale Atomistics-Continuum Simulations: Atomistically Induced Stress Distributions in Si/Si3N4 Nanopixels.

169. E. Lidorikis, M. E. Bachlechner, R. K. Kalia, A. Nakano, and P. Vashishta, *Phys. Rev. B*, **72**, 115338 (2005). Coupling Atomistic and Continuum Length Scales in Heteroepitaxial Systems: Multiscale Molecular-Dynamics/Finite-Element Simulations of Strain Relaxation in Si/Si3N4 Nanopixels.

170. T. Belytschko and S. P. Xiao, *Int. J. Multiscale Comput. Eng.*, **1**, 115 (2003). Coupling Methods for Continuum Model with Molecular Model.

171. S. P. Xiao and T. Belytschko, *Comput. Methods Appl. Mech. Eng.*, **193**, 1645 (2004). A Bridging Domain Method for Coupling Continua with Molecular Dynamics.

172. S. Zhang, S. L. Mielke, R. Khare, D. Troya, R. S. Ruoff, G. C. Schatz, and T. Belytschko, *Phys. Rev. B*, **71**, 115403 (2005). Mechanics of Defects in Carbon Nanotubes: Atomistic and Multiscale Simulations.

173. P.-A. Guidault and T. Belytschko, *Int. J. Numer. Methods Eng.*, **70**, 322 (2007). On the L2 and the H1 Couplings for an Overlapping Domain Decomposition Method using Lagrange Multipliers.

174. S. Zhang, R. Khare, Q. Lu, and T. Belytschko, *Int. J. Num. Meth. Eng.*, **70**, 913 (2007). A Bridging Domain and Strain Computation Method for Coupled Atomistic Continuum Modelling of Solids.

175. W. E. B. Engquist and Z. Huang, *Phys. Rev. B*, **67**, 092101 (2003). Heterogeneous Multiscale Method: A General Methodology for Multiscale Modeling.

176. X. Li and W. E, *J. Mech. Phys. Solids*, **53**, 1650 (2005). Multiscale Modeling of the Dynamics of Solids at Finite Temperature.

177. W. E and Z. Huang, *Phys. Rev. Lett.*, **87**, 135501 (2001). Matching Conditions in Atomistic-Continuum Modeling of Materials.

178. W. E and Z. Huang, *J. Comput. Phys.*, **182**, 234 (2002). A Dynamic Atomistic-Continuum Method for the Simulation of Crystalline Materials.

179. J. H. Irving and J. G. Kirkwood, *J. Chem. Phys.*, **18**, 817 (1950). The Statistical Mechanical Theory of Transport Processes. IV. The Equations of Hydrodynamics.

180. H. Nessyahu and E. Tadmor, *J. Comput. Phys.*, **87**, 408 (1990). Non-Oscillatory Central Differencing for Hyperbolic Conservation Laws.

181. M. Marder, *Condensed Matter Physics*, Wiley Interscience, New York, 2000. Corrected printing.

182. G. J. Wagner and W. K. Liu, *J. Comput. Phys.*, **190**, 249 (2003). Coupling of Atomistic and Continuum Simulations Using a Bridging Scale Decomposition.

183. H. S. Park, E. G. Karpov, P. A. Klein, and W. K. Liu, *J. Comput. Phys.*, **207**, 588 (2005). Three-Dimensional Bridging Scale Analysis of Dynamic Fracture.

184. W. K. Liu, H. S. Park, D. Qian, E. G. Karpov, H. Kadowaki, and G. J. Wagner, *Comput. Methods Appl. Mech. Eng.*, **195**, 1407 (2006). Bridging Scale Methods for Nanomechanics and Materials.

185. S. A. Adelman and J. D. Doll, *J. Chem. Phys.*, **61**, 4242 (1974). Generalized Langevin Equation Approach for Atom/Solid-Surface Scattering: Collinear Atom/Harmonic Chain Model.

186. S. A. Adelman and J. D. Doll, *J. Chem. Phys.*, **62**, 2518 (1975). Erratum: Generalized Langevin Equation Approach for Atom/Solid-Surface Scattering: Collinear Atom/Harmonic Chain Model.

187. S. A. Adelman and J. D. Doll, *J. Chem. Phys.*, **64**, 2375 (1976). Generalized Langevin Equation Approach for Atom/Solid-Surface Scattering: General Formulation for Classical Scattering Off Harmonic Solids.

188. J. D. Doll, L. E. Myers, and S. A. Adelman, *J. Chem. Phys.*, **63**, 4908 (1975). Generalized Langevin Equation Approach for Atom/Solid-Surface Scattering: Inelastic Studies.

189. E. G. Karpov, H. S. Park, and W. K. Liu, *Int. J. Numer. Meth. Eng.*, **70**, 351 (2007). A Phonon Heat Bath Approach for the Atomistic and Multiscale Simulation of Solids.

190. D. Qian, R. H. Rondhalekar, E. G. Karpov, and W. K. Liu, *Proceedings of the 6th World Congress of Computational Mechanics*, Z. H. Yao, M. W. Yuan, and W. X. Zhong, Eds., Tsinghua University Press and Springer, Tsinghua, 2004, p. 185. Multiscale Analysis of Nonlinear Mechanics in Nanoscale Materials.

191. E. G. Karpov, H. Yu, H. S. Park, W. K. Liu, Q. J. Wang, and D. Qian, *Int. J. Solids Struct.*, **43**, 6379 (2006). Multiscale Boundary Conditions in Crystalline Solids: Theory and Application to Nanoindentation.

192. S. N. Medyanik, E. G. Karpov, and W. K. Liu, *J. Comput. Phys.* **218**, 836 (2006). Domain Reduction Method for Atomistic Simulations.

193. D. Qian, G. J. Wagner, and W. K. Liu, *Comput. Methods Appl. Mech. Eng.* **193**, 1603 (2004). A Multiscale Projection Method for the Analysis of Carbon Nanotubes.

194. H. Kadowaki and W. K. Liu, *Comput. Methods Appl. Mech. Eng.*, **193**, 3267 (2004). Bridging Multi-Scale Method for Localization Problems.

195. S. Q. Tang, W. K. Liu, E. G. Karpov, and T. Y. Hou, *Chinese Phys. Lett.* **24**, 161 (2007). Bridging Atomistic/Continuum Scales in Solids with Moving Dislocations.

196. P. A. Klein and J. A. Zimmerman, *J. Comput. Phys.*, **213**, 86 (2006). Coupled Atomistic-Continuum Simulations Using Arbitrary Overlapping Domains.

197. A. C. To and S. Li, *Phys. Rev. B*, **72**, 035414 (2005). Perfectly Matched Multiscale Simulations.

198. S. Li, X. Liu, A. Agrawal, and A. C. To, *Phys. Rev. B*, **74**, 045418 (2006). Perfectly Matched Multiscale Simulations for Discrete Lattice Systems: Extension to Multiple Dimensions.

199. X. Liu and S. Li, *J. Chem. Phys.*, **126**, 124105 (2007). Nonequilibrium Multiscale Computational Model.

200. J. Berenger, *J. Comput. Phys.*, **114**, 185 (1994). A Perfectly Matched Layer for the Absorption of Electromagnetic Waves.

201. J. T. Oden, S. Prudhomme, and P. Bauman, *Comput. Methods Appl. Mech. Eng.*, **194**, 3668 (2005). On the Extension of Goal-Oriented Error Estimation and Hierarchical Modeling to Discrete Lattice Models.

202. J. T. Oden, S. Prudhomme, A. Romkes, and P. Bauman, *SIAM J. Sci. Comput.*, **28**, 2359 (2006). Multi-Scale Modeling of Physical Phenomena: Adaptive Control of Models.

203. R. Rudd and J. Broughton, *Phys. Rev. B*, **58**, R5893 (1998). Coarse-Grained Molecular Dynamics and the Atomic Limit of Finite Elements.

204. R. Rudd and J. Broughton, *Phys. Rev. B*, **72**, 144104 (2005). Coarse-Grained Molecular Dynamics: Nonlinear Finite Elements and Finite Temperature.

205. L. M. Dupuy, E. B. Tadmor, R. E. Miller, and R. Phillips, *Phys. Rev. Lett.*, **95**, 060202 (2005). Finite-Temperature Quasicontinuum: Molecular Dynamics without All the Atoms.

206. J. G. Kirkwood, *J. Chem. Phys.*, **3**, 300 (1935). Statistical Mechanics of Fluid Mixtures.

207. S. Nosé, *Mol. Phys.*, **52**, 255 (1984). A Molecular Dynamics Method for Simulations in the Canonical Ensemble.

208. S.D. Bond, B. J. Leimkuhler, and B. B. Laird, *J. Comput. Phys.*, **151**, 114 (1999). The Nose-Poincare Method for Constant Temperature Molecular Dynamics.

209. B. L. Holian and R. Ravelo, *Phys. Rev. B*, **51**, 11275 (1995). Fracture Simulations Using Large-Scale Molecular Dynamics.

210. S. J. Zhou, P. S. Lomdahl, R. Thomson, and B. L. Holian, *Phys. Rev. Lett.*, **76**, 2318 (1996). Dynamic Crack Processes via Molecular Dynamics.

211. H. Gao, *J. Mech. Phys. Solids*, **44**, 1453 (1996). A Theory of Local Limiting Speed in Dynamic Fracture.

212. P. Gumbsch, S. J. Zhou, and B. L. Holian, *Phys. Rev. B*, **55**, 3445 (1997). Molecular Dynamics Investigation of Dynamic Crack Stability.

213. D. Holland and M. Marder, *Phys. Rev. Lett.*, **80**, 746 (1998). Ideal Brittle Fracture of Silicon Studied with Molecular Dynamics.

214. W. Cai, M. de Koning, V. V. Bulatov, and S. Yip, *Phys. Rev. Lett.* **85**, 3213 (2000). Minimizing Boundary Reflections in Coupled-Domain Simulations.

215. G. J. Wagner, E. G. Karpov, and W. K. Liu, *Comput. Methods Appl. Mech. Eng.*, **193**, 1579 (2004). Molecular Dynamics Boundary Conditions for Regular Crystal Lattices.

216. E. G. Karpov, G. J. Wagner, and W. K. Liu, *Int. J. Numer. Methods Eng.*, **62**, 1250 (2005). A Green's Function Approach to Deriving Non-Reflecting Boundary Conditions in Molecular Dynamics Simulations.

217. X. Li and W. E, *Commun. Comput. Phys.*, **1**, 135 (2006). Variational Boundary Conditions for Molecular Dynamics Simulation of Solids at Low Temperature.

218. X. Li and W. E, *Phys. Rev. B*, **76**, 104107 (2007). Variational Boundary Conditions for Molecular Dynamics Simulations of Crystalline Solids at Finite Temperature: Treatment of the Thermal Bath.

219. C. Schafer, H. M. Urbassek, L. V. Zhigilei, and B. J. Garrison, *Comput. Mat. Sci.*, **24**, 421 (2002). Pressure-Transmitting Boundary Conditions for Molecular-Dynamics Simulations.

220. H. S. Park, E. G. Karpov, and W. K. Liu, *Int. J. Numer. Methods Eng.* **64**, 237 (2005). Non-reflecting Boundary Conditions for Atomistic, Continuum and Coupled Atomistic/Continuum Simulations.

221. J. Z. Yang and X. T. Li, *Phys. Rev. B*, **73**, 224111 (2006). Comparative Study of Boundary Conditions for Molecular Dynamics Simulations of Solids at Low Temperature.

222. H. J. C. Berendsen, J. P. M. Postma, W. F. van Gunsteren, A. DiNola, and J. R. Haak, *J. Chem. Phys.,* **81**, 3684 (1984). Molecular Dynamics with Coupling to an External Bath.

223. D. Wu and D. Chandler, in *Introduction to Modern Statistical Mechanics*, Oxford University Pres, New York, 1988. Thermodynamics: Fundamentals.

224. J. Fish, and V. Belsky, *Comput. Methods Appl. Mech. Eng.*, **126**, 1 (1995). Multigrid Method for Periodic Heterogeneous Media Part 1: Convergence Studies for One-Dimensional Case.

225. J. Fish, and V. Belsky, *Comput. Methods Appl. Mech. Eng.*, **126**, 17 (1995). Multigrid Method for Periodic Heterogeneous Media Part 2: Multiscale Modeling and Quality Control in Multidimensional Case.

226. J. D. Moulton, J. E. Dendy, and J. M. Hyman, *J. Comput. Phys.*, **141**, 1 (1998). The Black Box Multigrid Numerical Homogenization Algorithm.

227. D. K. Datta, R. C. Picu, and M. S. Shephard, *Int. J. Multiscale Comput. Eng.*, **2**(3), 401 (2004). Composite Grid Atomistic Continuum Method: An Adaptive Approach to Bridge Continuum with Atomistic Analysis.

228. J. Fish and W. Chen, *Comput. Methods Appl. Mech. Eng.*, **193**, 1693 (2004). Discrete-to-Continuum Bridging Based on Multigrid Principles.

229. H. Waisman and J. Fish, *Comput. Methods Appl. Mech. Eng.*, **195**, 6542 (2006). A Space-Time Multilevel Method for Molecular Dynamics Simulations.

230. B. Wang, V. Karuppiah, H. Lu, S. Roy, and R. Komanduri, *Mech. Adv. Mater. Struct.*, **12**, 471 (2005). Two-Dimensional Mixed Mode Crack Simulation Using the Material Point Method.

231. Z. Guo and W. Yang, *Int. J. Mech. Sci.*, **48**, 145 (2006). MPM/MD Handshaking Method for Multiscale Simulation and Its Application to High Energy Cluster Impacts.

232. H. Lu, N. P. Daphalapurkar, B. Wang, S. Roy, and R. Komanduri, *Philos. Mag.*, **86**, 2971 (2006). Multiscale Simulation from Atomistic to Continuum-Coupling Molecular Dynamics (MD) with the Material Point Method (MPM).

233. N. P. Daphalapurkar, H. Lu, D. Coker, and R. Komanduri, *Int. J. Fract.*, **143**, 79 (2007). Simulation of Dynamic Crack Growth Using the Generalized Interpolation Material Point (GIMP) Method.

234. E. Saether, D. Phillips, V. Yamakov, and E. Glaessgen, *Special Session on Nanostructured Materials at the 48th AIAA/ASME/ASCE/AHS/ASC Structures, Structural Dynamics and Materials Conference*, Austin, Texas, Apr. 18–21, 2005. Multiscale Modeling for the Analysis of Grain-Scale Fracture within Aluminum Microstructures.

235. B. Q. Luan, S. Hyun, J. F. Molinari, N. Bernstein, and M. O. Robbins, *Phys. Rev. E*, **74**, 046710 (2006). Multiscale Modeling of Two-Dimensional Contacts.

236. N. Chandra, S. Namilae, and A. Srinivasan, *Mater. Proc. Design: Model., Simul. Appl.*, **712**, 1571 (2004). Linking Atomistic and Continuum Mechanics Using Multiscale Models.

237. S. Namilae and N. Chandra, *J. Eng. Materials Tech.*, **127**, 222 (2005). Multiscale Model to Study the Effect of Interfaces in Carbon Nanotube-Based Composites.

238. Y. T. Gu and L. C. Zhang, *Multiscale Model. Simul.*, **5**, 1128 (2006). A Concurrent Multiscale Method Based on the Meshfree Method and Molecular Dynamics Analysis.

239. P. A. Deymier and J. O. Vasseur, *Phys. Rev. B*, **66**, 134106 (2002). Concurrent Multiscale Model of an Atomic Crystal Coupled with Elastic Continua.

240. K. Muralidharan, P. A. Deymier, and J. H. Simmons, *Model. Simul. Mater. Sci. Eng.*, **11**, 487 (2003). A Concurrent Multiscale Finite Difference Time Domain/Molecular Dynamics Method for Bridging an Elastic Continuum to an Atomic System.

241. N. Choly, G. Lu, W. E, and E. Kaxiras, *Phys. Rev. B*, **71**, 094101 (2005). Multiscale Simulations in Simple Metals: A Density-Functional-Based Methodology.

242. E. Chacon, J. E. Alvarellos, and P. Tarazona, *Phys. Rev. B*, **32**, 7868 (1985). Nonlocal Kinetic Energy Functional for Nonhomogeneous Electron Systems.

243. P. Garcia-Gonzalez, J. E. Alvarellos, and E. Chacon, *Phys. Rev. B*, **53**, 9509 (1996). Nonlocal Kinetic-Energy-Density Functionals.

244. L. W. Wang and M. P. Teter, *Phys. Rev. B*, **45**, 13196 (1992). Kinetic-Energy Functional of the Electron Density.

245. Y. A. Wang, N. Govind, and E. A. Carter, *Phys. Rev. B*, **58**, 13465 (1998). Orbital-Free Kinetic-Energy Functionals for the Nearly Free Electron Gas.

246. Y. A. Wang, N. Govind, and E. A. Carter, *Phys. Rev. B*, **60**, 16350 (1999). Orbital-Free Kinetic-Energy Density Functionals with a Density-Dependent Kernel.

247. T. A. Wesolowski and A. Warshel, *J. Phys. Chem.*, **97**, 8050 (1993). Frozen Density Functional Approach for Ab Initio Calculations of Solvated Molecules.

248. T. Klüner, N. Govind, Y. A. Wang, and E. A. Carter, *Phys. Rev. Lett.*, **88**, 209702 (2002). Klüner et al. Reply.

249. M. Fago, R. L. Hayes, E. A. Carter, and M. Ortiz, *Phys. Rev. B*, **70**, 100102(R) (2004). Density-Functional-Theory-Based Local Quasicontinuum Method: Prediction of Dislocation Nucleation.

250. R. L. Hayes, M. Fago, M. Ortiz, and E. A. Carter, *Multiscale Model. Simul.*, **4**, 359 (2005). Prediction of Dislocation Nucleation During Nanoindentation by the Orbital-Free Density Functional Theory Local Quasi-Continuum Method.

251. R. L. Hayes, G. Ho, M. Ortiz, and E. A. Carter, *Philos. Mag.*, **86**, 2343 (2006). Prediction of Dislocation Nucleation During Nanoindentation of Al_3Mg by the Orbital-Free Density Functional Theory Local Quasicontinuum Method.

252. V. Gavini, K. Bhattacharya, and M. Ortiz, *J. Mech. Phys. Solids*, **55**, 697 (2007). Quasi-Continuum Orbital-Free Density-Functional Theory: A Route to Multi-Million Atom Non-Periodic DFT Calculation.

253. G. Lu, E. B. Tadmor, and E. Kaxiras, *Phys. Rev. B*, **73**, 024108 (2006). From Electrons to Finite Elements: A Concurrent Multiscale Approach for Metals.

254. C. Woodward and S. I. Rao, *Philos. Mag. A*, **81**, 1305 (2001). Ab-Initio Simulation of Isolated Screw Dislocations in bcc Mo and Ta.

255. C. Woodward and S. I. Rao, *Phys. Rev. Lett.* **88**, 216402 (2002). Flexible Ab Initio Boundary Conditions: Simulating Isolated Dislocations in bcc Mo and Ta.

256. C. Woodward, *Mater. Sci. Eng. A*, **400–401**, 59 (2005). First-Principles Simulations of Dislocation Cores.

257. G. Kresse and J. Furthmüller, *Comput. Mater. Sci.*, **6**, 15 (1996). Efficiency of Ab-Initio Total Energy Calculations for Metals and Semiconductors Using a Plane-Wave Basis Set.

258. G. Kresse and J. Furthmüller, *Phys. Rev. B*, **54**, 11169 (1996). Efficient Iterative Schemes for Ab Initio Total-Energy Calculations Using a Plane-Wave Basis Set.

259. G. Kresse and J. Hafner, *Phys. Rev. B*, **47**, 558 (1993). Ab Initio Molecular Dynamics for Liquid Metals.

260. G. Kresse and J. Hafner, *Phys. Rev. B*, **49**, 14251 (1994). Ab Initio Molecular-Dynamics Simulation of the Liquid-Metal Amorphous Semiconductor Transition in Germanium.

261. G. Kresse and J. Hafner, *J. Phys.: Condens. Matt.*, **6**, 8245 (1994). Norm-Conserving and Ultrasoft Pseudopotentials for First-Row and Transition Elements.

262. F. Tavazza, A. M. Chaka, and L. E. Levine, *Computational Modeling and Simulation of Materials, III, Part A*, Cimtec-Techna Group, Faenza, Italy p. 657, 2004. Atomistic Insight into Dislocation Dynamics in Metal Forming.

263. F. Tavazza, L. E. Levine, and A. M. Chaka, *Int. J. Mod. Phys. C* (in press). A Hybrid, Quantum-Classical Approach for the Computation of Dislocation Properties in Real Materials: Method, Limitations and Applications.

264. F. Tavazza, R. Wagner, A. M. Chaka, and L. E. Levine, *Mater. Sci. Eng. A*, **400–401**, 72 (2005). Vacancy Formation Energy near an Edge Dislocation: A Hybrid Quantum-Classical Study.

265. G. Csányi, T. Albaret, M. C. Payne, and A. De Vita, *Phys. Rev. Lett.*, **93**, 175503 (2004). "Learn on the Fly": A Hybrid Classical and Quantum-Mechanical Molecular Dynamics Simulation.

266. M. C. Payne, G. Csányi, T. Albaret, and A. De Vita, *Chem. Phys. Chem.*, **6**, 1731 (2005). A Novel Quantum/Classical Hybrid Simulation Technique.

267. G. Moras, G. Csányi, M. C. Payne, and A. De Vita, *Physica B*, **376–377**, 936 (2006). A Novel Molecular Dynamics Approach to Large Semiconductor Systems.

268. S. Ogata, E. Lidorikis, F. Shimojo, A. Nakano, P. Vashishta, and R. K. Kalia, *Comput. Phys. Commun.*, **138**, 143 (2001). Hybrid Finite-Element Simulations on Parallel Computers.

269. S. Ogata, F. Shimojo, R. K. Kalia, A. Nakano, and P. Vashishta, *Comput. Phys. Commun.*, **149**, 30 (2002). Hybrid Quantum Mechanical/Molecular Dynamics Simulations for Parallel Computers: Density Functional Theory on Real-Space Multigrids.

270. A. Nakano, M. E. Bachlechner, R. K. Kalia, E. Lidorikis, P. Vashishta, G. Z. Voyiadjis, T. J. Campbell, S. Ogata, and F. Shimojo, *Comput. Sci. Eng.* **3**, 56 (2001). Multiscale Simulation of Nanosystems.

271. M. Svensson, S. Humbel, R. D. J. Froese, T. Matsubara, S. Sieber, and K. Morokuma, *J. Phys. Chem.*, **100**, 19357 (1996). ONIOM: A Multilayered Integrated MO + MM Method for Geometry Optimizations and Single Point Energy Predictions. A Test for Diels-Alder Reactions and $Pt(P(t\text{-}Bu)_3)_2 + H_2$ Oxidative Addition.

272. U. Eichler, C. M. Kölmel, and J. Sauer, *J. Comput. Chem.*, **18**, 463 (1996). Combining Ab Initio Techniques with Analytical Potential Functions for Structure Predictions of Large Systems: Method and Application to Crystalline Silica Polymorphs.

273. U. C. Singh and P. A. Kollman, *J. Comput. Chem.*, **7**, 718 (1986). A Combined Ab Initio Quantum Mechanical and Molecular Mechanical Method for Carrying Out Simulations on Complex Molecular Systems.

274. M. J. Field, P. A. Bash, and M. Karplus, *J. Comput. Chem.*, **11**, 700 (1990). A Combined Quantum Mechanical and Molecular Mechanical Potential for Molecular Dynamics Simulations.

275. C. S. Carmer, B. Weiner, and M. Frenklach, *J. Chem. Phys.*, **99**, 1356 (1993). Molecular Dynamics with Combined Quantum and Empirical Potentials: C2H2 Adsorption on Si(100).

276. S. Dapprich, I. Komáromi, K. S. Byun, K. Morokuma, and M. J. Frisch, *J. Mol. Struc. (THEOCHEM)*, **1**, 461 (1999). A New ONIOM Implementation in Gaussian 98.

277. M. P. Allen and D. J. Tildesley, *Computer Simulation of Liquids*, Clarendon, Oxford, 1987, Chapter 3. Molecular Dynamics.

278. A. Harada, F. Shimojo, and K. Hoshino, *J. Phys. Soc. Jpn.*, **72**, 822 (2003). Dynamic Properties of Disordered Phases of Carbon Studied by an Empirical Potential: Stringent Tests toward Hybrid Approach with the Density-Functional Theory.

279. S. Ogata, F. Shimojo, R. K. Kalia, A. Nakano, and P. Vashishta, *J. Appl. Phys.*, **95**, 5316 (2004). Environmental Effects of H_2O on Fracture Initiation in Silicon: A Hybrid Electronic-Density-Functional/Molecular-Dynamics Study.

280. S. Ogata and R. Belkada, *Comput. Mater. Sci.*, **30**, 189 (2004). A Hybrid Electronic-Density-Functional/Molecular-Dynamics Simulation Scheme for Multiscale Simulation of Materials on Parallel Computers: Applications to Silicon and Alumina.

281. M.-H. Du, A. Kolchin, and H.-P. Cheng, *J. Chem. Phys.*, **119**, 6418 (2003). Water-Silica Surface Interactions: A Combined Quantum-Classical Molecular Dynamic Study of Energetics and Reaction Pathways.

282. M.-H. Du and H.-P. Cheng, *Int. J. Quantum Chem.*, **93**, 1 (2003). Transparent Interface between Classical Molecular Dynamics and First-Principles Molecular Dynamics.

283. H. Cheng, L. Wang, M. Du, C. Cao, Y. Wan, Y. He, K. Muralidharan, G. Greenlee, and A. Kolchin, *J. Comput.-Aided Mater. Design,* **13**, 161 (2006). Quantum, Classical, and Multi-Scale Simulation of Silica–Water Interaction: Molecules, Clusters, and Extended Systems.

284. R. N. Barnett and U. Landman, *Phys. Rev. B*, **48**, 2081 (1993). Born–Oppenheimer Molecular-Dynamics Simulations of Finite Systems: Structure and Dynamics of the Water Dimer ($(H_2O)_2$).

285. J. P. Perdew, K. Burke, and M. Ernzerhof, *Phys. Rev. Lett.*, **77**, 386 (1996). Generalized Gradient Approximation Made Simple.

286. *Report of the National Nanotechnology Initiative Workshop*, January 27–29, 2004. Instrumentation and Metrology for Nanotechnology.

287. *Joint Chemical & Semiconductor Industry Research Needs for Modeling of Nanomaterials*, sponsored by Chemical Industry Vision 2020 and Semiconductor Research Corporation / SNB Consultative WG 2, June, 2006.

CHAPTER 7

Extending the Time Scale in Atomically Detailed Simulations

Alfredo E. Cárdenas[a] **and Eric Barth**[b]

[a]*Department of Chemistry, University of South Florida, Tampa, Florida*
[b]*Department of Mathematics and Computer Science, Kalamazoo College, Kalamazoo, Michigan*

INTRODUCTION

The Verlet Method

The current practice of molecular dynamics simulation dates back to the pioneering work on smooth potential models for monatomic fluids of Rahman[1] and Verlet[2] in the 1960s. In the 1970s, interest developed in applying molecular dynamics methods to more complicated molecular fluids such as water,[3] molecular fluids with internal degrees of freedom,[4] and large flexible molecules.[5] Given a potential energy function V (about which we have much more to say below) that models the interatomic forces in a molecular system with N atoms, the Newtonian equations of motion can then be expressed as

$$\mathbf{M}\ddot{\mathbf{r}} = \mathbf{F}(\mathbf{r}) = -\nabla_{\mathbf{r}} V(\mathbf{r}) \qquad [1]$$

where $\mathbf{M}$ is a diagonal mass matrix with diagonal

$$[m_1\ m_1\ m_1\ m_2\ m_2\ m_2\ \ldots\ m_N\ m_N\ m_N]$$

Reviews in Computational Chemistry, Volume 26
edited by Kenny B. Lipkowitz and Thomas R. Cundari

and m_i the mass of the ith particle. The gradient $\nabla_{\mathbf{r}} V$ is the column vector of all partial derivatives with respect to particle positions. It is easily verified that the total energy

$$E = \frac{\dot{\mathbf{r}}^T \mathbf{M} \dot{\mathbf{r}}}{2} + V(\mathbf{r}) \qquad [2]$$

is constant along solutions of Eq. [1]: $dE/dt = 0$. The system is simulated from initial positions and velocities $\mathbf{r}(t_0) = \mathbf{r}_0$, $\dot{\mathbf{r}}(t_0) = \dot{\mathbf{r}}_0$, often chosen randomly in accordance with some appropriate statistical ensemble.

Computer simulation of the system modeled by Eq. [1] requires some sort of time discretization scheme. The method proposed by Verlet propagates positions by

$$\mathbf{r}_i^{n+1} = -\mathbf{r}_i^{n-1} + 2\mathbf{r}_i^n + h^2 \mathbf{M}^{-1} \mathbf{F}_i^n \qquad [3]$$

and velocities using

$$\mathbf{v}_i^n = (\mathbf{r}_i^{n+1} - \mathbf{r}_i^{n-1})/2h \qquad [4]$$

Here the superscripts denote the indices of time steps, each of which is of size h, so

$$\mathbf{r}_i^n \approx \mathbf{r}_i(t_0 + nh) \qquad [5]$$

and $\mathbf{F}_i^n = -\nabla_{\mathbf{r}_i} V(\mathbf{r}^n)$ is a Cartesian vector that gives the sum of forces acting on particle i due to interaction with other particles, evaluated at the point $\mathbf{r}^n$.

Verlet[2] noted in his ground-breaking work the remarkable energy preservation properties of the integrator, reporting "small irregularities in the total energy ... but the error is of no consequence." The discretization method in Eqs. [2]–[4], commonly referred to as the *Verlet integrator*, is accurate to second order in time, requires only one force evaluation per step, and is *time reversible*, which is part of the reason for its excellent stability in terms of near conservation of energy. In fact, it is now known that a more general symmetry preservation—the *symplectic* property[6]—of the Verlet method, viewed as an appropriate mapping of positions and momenta, confers its excellent long-term energy stability.[7,8] For a thorough review of symplectic numerical methods, see the monograph of Sanz-Serna and Calvo.[9] The Verlet method is now regarded as the gold standard for time-stepping schemes in molecular dynamics. In conformity with modern practice, and to anticipate the algorithmic development of multiple time-step methods in the forthcoming sections of

this tutorial, we rewrite the Verlet method in the equivalent "velocity Verlet" form. The inside of the integration loop is given by

$$\mathbf{v}_i^{n+1/2} = \mathbf{v}_i^n + \frac{h}{2}\mathbf{M}^{-1}\mathbf{F}_i^n \quad [6a]$$

$$\mathbf{r}_i^{n+1} = \mathbf{r}_i^n + h\mathbf{v}_i^{n+1/2} \quad [6b]$$

$$\mathbf{v}_i^{n+1} = \mathbf{v}_i^{n+1/2} + \frac{h}{2}\mathbf{M}^{-1}\mathbf{F}_i^{n+1} \quad [6c]$$

In contrast to the constant energy regime described above, it is sometimes desirable to perform simulations at a fixed temperature. This can be accomplished by the Langevin dynamics model:[10]

$$\mathbf{M}\ddot{\mathbf{r}} = \mathbf{F}(\mathbf{r}, \mathbf{v}, t) := -\nabla_{\mathbf{r}} V(\mathbf{r}) - \gamma\mathbf{v} + \mathbf{R}(t) \quad [7]$$

where $\gamma > 0$ is a friction coefficient and $\mathbf{R}(t)$ is a vector of normally distributed random variables with zero mean and covariance $\langle R(t)R(t')^T \rangle = 2\gamma k_B T\mathbf{M}\delta(t - t')$, where k_B is Boltzmann's constant, T is the simulation temperature, and δ is the Dirac delta function. A natural extension of discretization [6] gives the following time discretization scheme:[11]

$$\mathbf{v}_i^{n+1/2} = \mathbf{v}_i^n + \frac{h}{2}\mathbf{M}^{-1}\mathbf{F}_i(\mathbf{r}^n, \mathbf{v}^{n+1/2}, t_n) \quad [8a]$$

$$\mathbf{r}_i^{n+1} = \mathbf{r}_i^n + h\mathbf{v}_i^{n+1/2} \quad [8b]$$

$$\mathbf{v}_i^{n+1} = \mathbf{v}_i^{n+1/2} + \frac{h}{2}\mathbf{M}^{-1}\mathbf{F}_i(\mathbf{r}^{n+1}, \mathbf{v}^{n+1/2}, t_{n+1}) \quad [8c]$$

Molecular Dynamics Potential

The interactions of polyatomic molecules are frequently modeled by pair potentials, both Lennard-Jones and electrostatic, between all constituent atoms. The model potential used must also account for intramolecular geometries by including the "bonded" terms: bond lengths, bond angles, and dihedral angles. The result is the molecular modeling potential function that generally is of the form

$$V(\mathbf{r}) = V^b + V^a + V^d + V^i + V^{\mathrm{LJ}} + V^{\mathrm{C}} \quad [9]$$

where V^b, V^a, V^d, and V^i are sums over various pairs, triples, and quadruples of spatially localized bonded groups of atoms representing bonds, angles, dihedral angles, and improper dihedral angles, respectively:

$$V^b = \sum_{\text{bonds}} V_{ij}^b \qquad V^a = \sum_{\text{angles}} V_{ijk}^a \qquad V^b = \sum_{\text{dihed}} V_{ijkl}^d, \ldots \quad [10]$$

Similarly V^{LJ} is the sum of Lennard-Jones contributions for all pairs of atoms, and V^{C} is the sum of the Coulombic potential over all charge–charge interaction pairs, although other mathematical functions are frequently used to account for steric and electrostatic interactions:

$$V^{LJ} = \sum_{\text{allpairs}} V_{ij}^{LJ} \qquad V^{C} = \sum_{\text{allpairs}} V_{ij}^{C}$$

The functional forms of these terms vary widely. Representative examples can be found in work by a number of authors and have been reviewed previously in this book series.[12–20] A simple, detailed model is presented in the MD Test Set project.[21]

The molecular dynamics (MD) potential energy surface of even small organic molecules is highly nonlinear, with many local minima. Minimization of the potential energy is a common task, but the nonpolynomial proliferation of local minima usually frustrates attempts to determine the lowest energy states for modeled systems.[22,23] Also, the finite-time dynamics of a nonlinear multiple-minima system can become trapped in one potential energy well, which in turn impedes complete conformational sampling. The terms in the potential must account for a wide range of spatial scales (from bonds of length $1\text{Å} = 10^{-10}$ m, to Coulombic lengths that extend throughout the modeled system) as well as time scales (the fastest bonds have a period of $10\,\text{fs} = 10^{-14}$ s, while large-scale conformational interconversions may occur on the scale of seconds). Time-stepping algorithms like the Verlet method [4] require a sufficiently short time step (0.5–1.0 fs) to resolve the fastest bonded motion, meaning that a computed trajectory that spans a time interval of one nanosecond (10^{-9} s) requires one million dynamics steps. The great majority of the computational work in MD simulations is expended in computing the forces of interaction—for N particles, the computational effort is $O(N^2)$. For simulations in which the long-range force comes only from the rapidly decaying Lennard-Jones potential, this N^2 bottleneck can be remedied by imposing *distance cutoffs* where the potential is assumed to be zero for all atomic separations greater than a predefined cutoff distance r_c.

The electrostatic $1/r^2$ forces, in contrast, are non-negligible at moderate separations, thus making Coulomb distance cutoffs unphysical and undesirable on small- to medium-sized scales. Thus, a molecule's potential energy surface has several characteristics that can impact significantly on the performance of numerical methods: multiple minima, wide range of time and space scales, and long-range interactions between many particles. For traditional molecular dynamics methods that use Eq [6], the most important limitation involves the numerical stability of the integrator. While the computational resources required for a given numerical simulation could be lessened by increasing the length of each time step, stability of the time-stepping algorithm is typically limited by the high-frequency vibrational

modes, i.e., bond stretching. The fastest period relevant to organic and biomolecules is around 10 fs (associated, e.g., with C–H, O–H, and N–H stretching). Resolving these fast motions adequately dictates that time steps of length 1 fs or less should be used. Because of this the slower and more computationally expensive force components are updated at each step, resulting in CPU limitations of simulation length and system size. Solving the problems of efficient time stepping and fast evaluation of nonbonded forces without distance cutoffs is an ongoing activity.

Multiple Time Steps

In multiple time-step (MTS) time discretization methods the short-range forces, which can change rapidly in time, are updated frequently with small time steps. The long-range forces can be treated with larger steps in time (appropriate to the time scale on which they vary). We will discuss later the fundamental impact that the high-frequency force components have on MTS methods as well. In this chapter we trace the development of MTS methods and present a tutorial that illustrates an elementary application of these techniques.

Reaction Paths

A very different set of methodologies involves trying to compute trajectories between two states of a molecular system. These "double-ended" algorithms, usually called reaction path approaches, differ from integrators of the Newton equations of motion, Eq. [6], in that only the initial positions and velocities of the particles in the system are needed. The two boundary points, i.e., the states of the system, can represent a reactant and product configuration or a transition (or intermediate) state and reactant (product) configuration. The calculated path provides a qualitative description of the structural changes as function of a parameter(s) [reaction coordinate(s)] that characterizes the reaction path. The path then represents a series of replicas of the molecular system $\{\mathbf{X}(s)\} = \{X(s_1), X(s_2), \ldots, X(s_N)\}$ parameterized according to a parameter s. In this notation, X represents the coordinates of the molecule in a given slice of the path.

Most of the reaction path approaches make use of a spatial step and accordingly are not affected by the time-scale limitation of other MD methods. For complex systems, however, the ruggedness of the potential energy surface limits the applicability and accuracy of these paths because the number of conformations in the trajectory needs to increase. Another fundamental limitation is that these methods are not applicable for the study of molecular events for which very few details are known about the conformations of products or key intermediates. It is for those processes where theoretical approaches are more helpful.

In MD trajectories it is easy to extract dynamical properties by computing an average over time. The extraction of these properties is more difficult to do in reaction path approaches because trajectories are computed in configuration space (with only coordinate information for each structure in the path). Dynamical information can be computed, though, if an ensemble of many reactive trajectories is obtained. But such an ensemble is not generally determined (this can be done with transition path sampling). Reaction path methods are very useful for determining of rates and free energy profiles for fast but rare events that are inefficiently probed with other MD algorithms because trajectories obtained with reaction path approaches filter out the waiting periods the system spends in the reactant wells, in contrast to standard MD trajectories.

The reaction path methods consist of a number of different theoretical formulations and algorithms and therefore are difficult to describe by a common framework (the second part of this chapter reviews some of the path techniques developed in the past 10 years). All of these techniques describe the system with atomic detail and use a potential function of the form of Eq. [9]. We will also describe, in more detail, one of these methods, which is based on a discretized formulation of the action of classical mechanics. In this action formalism (called stochastic difference in length, SDEL), reaction paths are obtained by linking two conformations of the system. These paths, parameterized according to arc length, can be obtained with a large length step. Therefore, this algorithm tries to solve the time-scale limitation of normal MD simulations by using a boundary value formulation of the classical equations of motion. Although this method has been used to compute approximate paths for processes that are impossible to study using normal MD simulations, it is difficult to compute dynamical properties from these paths (e.g., the time of the trajectory computed directly from the algorithm is underestimated by several orders of magnitude!). Still, the method can be used to determine large conformational changes that can be resolved by the trajectory. This chapter provides a tutorial section about how to run a program associated with this algorithm and reviews some recent applications and improvements in the methodology.

MULTIPLE TIME-STEP METHODS

In an effort to lengthen the feasible simulation time scale of molecular simulations, Streett and co-workers introduced the multiple time-step method in 1978.[24] These authors recognized that the components of the force that vary most rapidly, and hence require small time steps for numerical resolution, are typically associated with atom pair interactions at small separations. This spatial localization is important because each of the N particles in the simulation has such an interaction with only a few, say $k \ll N$, neighboring particles.

Success of the multiple time-step methodology depends on computing these $kN \ll N^2$ interactions at each step, i.e., at intervals of h Eqs. [3]–[6] and [8], while computing the remaining $N(N-k)$ pair interactions (which correspond to forces that vary more slowly) at longer time intervals τh.

Street et al.[24] originally presented the MTS method in the context of a distance truncated Lennard-Jones potential, so that the total number of computed interactions was somewhat less that N^2. For biological MD applications there is evidence that cutoffs can cause undesirable artifacts.[25,26]

Before discussing the implementation details, we need to state the general issues of multiple time-step numerical methods. The central objectives are: (1) to devise a splitting of the systematic forces into a hierarchy of two or more force classes based on the time interval over which they vary significantly, and (2) to incorporate these force classes into a numerical method in a way that realizes enhanced computational efficiency and maintains stability and accuracy of the computed solution.

Splitting the Force

Streett and co-workers[24] proposed a splitting of forces based on a distance parameter r_{split}. In the potential energy formalism we write

$$V(\mathbf{r}) = \sum_{|\mathbf{r_i}-\mathbf{r_j}|<\mathbf{r}_{\text{split}}} \mathbf{V_{ij}} + \sum_{|\mathbf{r_i}-\mathbf{r_j}|\geq\mathbf{r}_{\text{split}}} \mathbf{V_{ij}} \qquad [11]$$

$$= \mathbf{V}^{\text{fast}}(\mathbf{r}) + \mathbf{V}^{\text{slow}}(\mathbf{r}), \qquad [12]$$

with

$$\mathbf{F}^{\text{fast}}(\mathbf{r}) := -\nabla_{\mathbf{r}} V^{\text{fast}}(\mathbf{r}) \qquad \mathbf{F}^{\text{slow}}(\mathbf{r}) := -\nabla_{\mathbf{r}} V^{\text{slow}}(\mathbf{r}) \qquad [13]$$

As a practical matter, particles will move in and out of the r_{split} sphere for a given particle over the course of a simulation. To avoid discontinuities that result from a particle suddenly changing classification from the slow force component to the fast force component, the force can be decomposed into fast and slow components using a switching function $S(r)$,

$$\mathbf{F}_i = \mathbf{F}_i^{\text{fast}} + \mathbf{F}_i^{\text{slow}} = -S(r)\nabla_{\mathbf{r_i}} V - (1 - S(r))\nabla_{\mathbf{r_i}} V \qquad [14]$$

where

$$S(r) = \begin{cases} 1 & r < r_{\text{split}} - \lambda \\ 1 + R^2(2R - 3) & r_{\text{split}} - \lambda \leq r \leq r_{\text{split}} \\ 0 & r_{\text{split}} < r \end{cases} \qquad [15]$$

with $R = [r - (r_{\text{split}} - \lambda)]/\lambda$. Here λ is a "healing length" over which the switching function S varies smoothly between one and zero. The form of the switching function is somewhat arbitrary, although sufficient smoothness is required.

The forces due to bonded interaction potentials V^b, V^a, V^d, and V^i (see Eq. [10]) are included in the fast component along with the nonbonded forces that change the fastest. It is not uncommon for the two-scale splitting described here to be generalized to a hierarchy of more than two classes. We should mention that efficiency gains cannot typically be realized from the simple splitting in which bonded forces comprise one class and nonbonded forces the other. The reason is that atomic collisions cause the short-range nonbonded forces to vary over roughly the same (short) time scale as the bonded forces. The details of force splitting can be rather complicated and system dependent. Later in this work, we will address this important issue influencing efficient implementation of force splitting in MTS methods.

Numerical Integration with Force Splitting: Extrapolation vs. Impulse

The general plan for a multiple time-step numerical method is that $\mathbf{F}_i^{\text{fast}}$ will be evaluated at every step of the integration at time increments h, while $\mathbf{F}_i^{\text{slow}}$ will be evaluated less frequently, typically at time increments τh where $\tau > 1$ is an integer. The key question is: How should $\mathbf{F}_i^{\text{slow}}$ be incorporated into the numerical dynamics? In the original work of Streett et al.,[24] the slow force on particle i was approximated by a truncated Taylor series at each step j, $0 < j < \tau$, between updates at steps t_n and $t_n + \tau h$:

$$\mathbf{F}_i^{\text{slow}}(t_n + jh) = \mathbf{F}_i^{\text{slow}}(t_n) + jh\,\dot{\mathbf{F}}_i^{\text{slow}}(t_n) + \tfrac{1}{2}(jh)^2\,\ddot{\mathbf{F}}_i^{\text{slow}}(t_n) + \cdots \qquad [16]$$

A natural simplification is to truncate the Taylor series after the constant term, resulting in a constant extrapolation of the slow force. The velocity Verlet method [6] can be easily modified to implement this constant extrapolation multiple time-step method:

$$\mathbf{v}_i^{n+1/2} = \mathbf{v}_i^n + \frac{h}{2}\mathbf{M}^{-1}(\mathbf{F}_i^{\text{fast}} + \mathbf{F}_i^{\text{slow}}) \qquad [17a]$$

$$\mathbf{r}_i^{n+1} = \mathbf{r}_i^n + h\mathbf{v}_i^{n+1/2} \qquad [17b]$$

update $\mathbf{F}_i^{\text{fast}}$

if $(n+1) \bmod \tau = 0$ update $\mathbf{F}_i^{\text{slow}}$

$$\mathbf{v}_i^{n+1} = \mathbf{v}_i^{n+1/2} + \frac{h}{2}\mathbf{M}^{-1}(\mathbf{F}_i^{\text{fast}} + \mathbf{F}_i^{\text{slow}}) \qquad [17c]$$

The important feature to note is that the fast forces are computed at each step, while the slow forces are computed τ times less frequently, with updates given by

$$\mathbf{F}_i^{\text{fast}} = \mathbf{F}_i^{\text{fast}}(\mathbf{r}_i^{n+1}) \qquad \mathbf{F}_i^{\text{slow}} = \mathbf{F}_i^{\text{slow}}(\mathbf{r}_i^{n+1}) \tag{18}$$

However, the simplicity of this modification hides a potentially disastrous flaw! The Verlet method is popularly employed in virtually every molecular dynamics simulation done today because its geometric symmetry ensures that the total energy along computed solutions does not drift but remains essentially constant, respecting the underlying Newtonian physics of the model. By modifying the force updates in the multiple time-step method given above, we have disrupted the symmetry of the original method. The result is that the energy will drift significantly and systematically. The situation is improved, but not solved, by using a higher order Taylor approximation for the slow forces and a higher order integration scheme. Street et al.[24] used a third-order Taylor approximation for the slow forces along with a high-order Gear predictor–corrector integration method. In this way, the energy drift can be made small relative to the time step, so that relatively long simulations can be computed with less apparent problems from energy growth.

A new era in multiple time-step methods arrived in the early 1990s when Grubmüller et al.[27] and Tuckerman et al.[28] independently published multiple time-step methods that appeared to overcome the energy instability of extrapolation methods. Their idea is to mimic the "kick-drift" nature of the velocity Verlet method itself. In Eq. [6] the force supplies a "kick," or impulse, in the first line, and the system then "drifts" as the updated half-step velocity contributes to the position at the new step. The velocity Verlet method can be modified so that the slow force is also applied as an impulse:

$$\begin{aligned} \mathbf{v}_i^1 &= \mathbf{v}_i^n + \frac{\tau h}{2}\mathbf{M}^{-1}\mathbf{F}_i^{\text{slow}}(\mathbf{r}_i^n) \\ \mathbf{r}_i^1 &= \mathbf{r}_i^n \end{aligned} \tag{19a}$$

For $j = 1 : \tau$,

$$\mathbf{v}_i^{j+1/2} = \mathbf{v}_i^j + \frac{h}{2}\mathbf{M}^{-1}\mathbf{F}_i^{\text{fast}}(\mathbf{r}_i^j) \tag{19b}$$

$$\mathbf{r}_i^{j+1} = \mathbf{r}_i^j + h\mathbf{v}_i^{j+1/2} \tag{19c}$$

$$\mathbf{v}_i^{j+1} = \mathbf{v}_i^{j+1/2} + \frac{h}{2}\mathbf{M}^{-1}\mathbf{F}_i^{\text{fast}}(\mathbf{r}_i^{j+1}) \tag{19d}$$

end

$$\begin{aligned} \mathbf{r}_i^{n+1} &= \mathbf{r}_i^{\tau} \\ \mathbf{v}_i^{n+1} &= \mathbf{v}_i^{\tau} + \frac{\tau h}{2}\mathbf{M}^{-1}\mathbf{F}_i^{\text{slow}}(\mathbf{r}_i^{n+1}) \end{aligned} \tag{19e}$$

This modification amounts to the replacement of the middle step of Eq. [6] with an inner loop over the τ steps between slow force updates.

It can be shown that impulse multiple time-step algorithms, such as the one described here, can be formulated so as to preserve time reversibility. As a result these methods can, for suitable choices of time-step sizes, avoid systematic energy drift along computed trajectories. In the next section we discuss the question of feasible time-step size. To consume less computing resources per unit of simulation time, successful multiple time-step methods must combine force-splitting approaches and time-stepping algorithms that allow significantly lengthened time steps for the most computationally costly force components. This issue has been the focus of intense work over the past decade.

Fundamental Limitation on Size of MTS Methods

Impulse MTS methods began to show considerable success in the mid-1990s, with published results reporting computational speed-up by a factor of 5 compared to traditional MD simulation.[29,30] Two features with regard to the practical time-step sizes for MTS methods emerged. The first, which was consistent with results reported by Streett et al.[24] 20 years earlier, involved the size of the small time step used to resolve the highest frequency motion in the system. That time step needed to be somewhat smaller than the typical MD time step in order to maintain energy stability. This is of little practical concern in terms of overall computational efficiency because the forces being evaluated at each small step are assumed to be very inexpensive in CPU time. The second feature was more significant: Computed trajectories demonstrated systematic energy instability whenever the larger steps used to resolve slower force components exceeded 5 fs.[31] This is important because the possibility of achieving further efficiency gains with MTS methods require that the slowest forces be updated much less frequently. The 5 fs barrier, which for a time seemed to have put a ceiling on further developments, came to be understood as a resonance artifact[32–34] coinciding with the half-period of bond vibrations such as O–H. The impulses introduced into the dynamics at each large step excite the bonds and lead to catastrophic energy growth. This energy growth is seen initially in the highest frequency (fastest) bonded energy. As a practical matter, growth in these energy components can be used as an early diagnosis of trouble in an MTS simulation.

One obvious remedy for this problem is to choose time-step lengths so as to avoid small integer multiples of half-periods of any oscillatory motion. However, it has been demonstrated[35] that the molecular dynamics potential gives rise to motion with a continuum of periods greater than or equal to 10 fs. Furthermore, the energy instability of impulse MTS methods becomes exponentially worse at larger multiples of the half-periods. This rules out the possibility that a fortuitously chosen assortment of impulse multiple time steps longer than 5 fs could yield stable trajectories.

A number of methods have been proposed to overcome the MTS barrier, including averaging methods[36] that "mollify" the impulse, allowing time steps of up to 6 fs while maintaining the favorably small energy drift attained by impulse MTS methods with 4 fs time steps. We will omit here the details of these time-stepping algorithms but point to a reference[37] that explicitly provides implementation details.

A point of interest is that extrapolation methods such as that given above in Eq. [19] suffer from resonance artifacts to a lesser degree than impulse methods.[38] In particular, it has been demonstrated[39,40] by eigenvalue analysis of extrapolation MTS methods that the severity of the instability does not grow with the largest MTS steps. Similar eigenvalue analysis shows that impulse methods suffer from increasingly severe energy instability with increasing MTS steps. This suggests that if the relatively mild instability of extrapolation methods could be somehow managed, the 5-fs time-step barrier could be overcome. In the next section we discuss how extrapolation MTS methods, while unsuitable for simulations in which energy must be conserved, can achieve the goals of true long-time-step methods in the context of Langevin dynamics.

Langevin Stabilization

The Langevin dynamics model of Eq. [7] has been employed to meet a variety of modeling objectives. First, as a fixed-temperature method, it provides a way to carry out numerical simulations that sample from the canonical ensemble of statistical mechanics.[41] Second, the stochastic forcing function can be viewed as a model of intermolecular collisions, making the Langevin model suitable as a surrogate for explicit solvent molecules.[11] A third way the versatile Langevin formalism has been utilized is to provide energy stabilization for simulations using numerical methods that may have desirable properties but suffer from energetic drift when applied to MD equations of motion.[42,43]

Langevin stabilization as an approach to multiple time-step numerical integration was introduced by Barth and Schlick[39] in 1998. One particularly simple method described in that work can be written as a modification of Eq. [19] subject to Eq. [7]:

$$\mathbf{v}_i^{n+1/2} = \mathbf{v}_i^n + \frac{h}{2}\mathbf{M}^{-1}(\mathbf{F}_i^{\text{fast}} + \mathbf{F}_i^{\text{slow}}) \qquad [20a]$$

$$\mathbf{r}_i^{n+1} = \mathbf{r}_i^n + h\mathbf{v}_i^{n+1/2} \qquad [20b]$$

$$\text{update } \mathbf{F}_i^{\text{fast}}$$

$$\text{if } (n+1)\text{mod } \tau = 0, \quad \text{update } \mathbf{F}_i^{\text{slow}}$$

$$\mathbf{v}_i^{n+1} = \mathbf{v}_i^{n+1/2} + \frac{h}{2}\mathbf{M}^{-1}(\mathbf{F}_i^{\text{fast}} + \mathbf{F}_i^{\text{slow}}) \qquad [20c]$$

where

$$\mathbf{F}^{\text{fast}}(\mathbf{r},\mathbf{v},t) := -\nabla_{\mathbf{r}} V^{\text{fast}}(\mathbf{r}(t)) - \gamma\mathbf{v}(t) + \mathbf{R}(t) \qquad \mathbf{F}_i^{\text{slow}} = \mathbf{F}_i^{\text{slow}}(\mathbf{r}^{n+1}, \mathbf{v}^{n+1/2}, t_{n+1})$$

This method can naturally be extended to include a splitting of more than two force classes, and it is amenable to other modifications and improvements such as moving the slow force update to be more symmetrically placed in the integration loop. It was shown[39] for a three-class force splitting that for typical molecular systems, the MTS (and hence the frequency of updating the slow forces) can be extended to 48 fs or longer with resulting computational speedups of at least a factor of 10. The success of Langevin stabilization with extrapolation MTS methods has led to its use to achieve stable simulations at large time steps using mollified impulse methods as well.[44–46] A systematic comparison[47] of these methods shows that extrapolation methods hold some advantage among Langevin-stabilized MTS integrators in terms of stability at long time steps. On the other hand, the argument in favor of mollified impulse methods is that no stabilization is required at small time steps.

Further Challenges and Recent Advances

The success of Langevin-stabilized methods has yielded, for the first time, the opportunity to attain the full promise of MTS methods. As in any field of inquiry, solving one problem often clears the way for the emergence of several others, and MTS integration is no exception. As an example, the extrapolation method[39] was used successfully with 120-fs slow force update frequency in simulations of a DNA/polymerase system.[48] Remarkably, in this study computational gains were limited to a factor of 5, even though the longest-range forces were updated less frequently than the fastest forces by two orders of magnitude. The explanation for this limited gain in efficiency is due to the extreme sensitivity of DNA systems to electrostatic interactions, where medium-range forces must be treated with very short time steps in the range 1–2 fs. This highlights a difficulty with the force-splitting idea as applied to molecular dynamics of some classes of molecules such as biological systems: The time and distance scales sometimes do not naturally fall into well-separated categories. This, in turn, makes it difficult to identify force classes. For example, the highest frequency motion in a slow force class might be only marginally slower than the lowest frequency motion in a fast force class. This feature, more prominent in some systems than others, can limit the size of time step that can be used for any given force class severely, hence mitigating the hoped-for computational advantage of MTS methods.

During the development of long-time-step MTS methods, work proceeded along another path involving the fundamental problem of costly force

evaluations in MD. That research was aimed at developing summation schemes, such as fast multipole[49–52] and Ewald summation[53–55] methods for faster evaluation of electrostatic energies and forces without invoking distance cutoffs. The computational advantage of these summation schemes over direct evaluation of long-range electrostatic forces is the reduction in the complexity of the task from $O(N^2)$ to $O(N \ln N)$. Fast summation methods have been successfully integrated into the framework of force splitting in multiple time-step integration methods[29,56,57] for solvated systems. While it is often the case that fast summation methods only enjoy computational speedups compared to direct evaluation for sufficiently large systems, it is precisely these large systems that would have exhibited the largest computational speedup for long-time-step MTS methods.

The current situation is then that large time-step size allows the slowest forces to be evaluated infrequently over the course of a multiple time-step MD simulation. At the same time, these forces can be evaluated more cheaply than was possible several decades ago. Note, however, that there exist some technical limitations to the conjoined use of MTS methods and fast summation.[36,58] Because the long-range forces became both cheaper to evaluate and also because this evaluation needs to be done less frequently during a simulation, attention can now be shifted to the new "cost leader" in MD simulation: the medium-range forces. These forces are not especially slow (as in the DNA/polymerase simulation[48]), nor are they particularly amenable to efficient approximation by fast summation methods. They can, and do, require careful resolution with rather small time steps. Further efficiency gains will require new approaches to the medium-range forces. This issue is open to new research from a variety of fields: force-field modeling, force-splitting techniques, and time-stepping algorithms.

An MTS Tutorial

In this section, we present a simple model problem to illustrate impulse and extrapolation MTS methods for simulations in the constant-energy and constant-temperature regimes. The models are implemented in MATLAB, with codes given in the Appendix.

The model consists of a pair of water molecules with all atoms in a plane. The forces of interaction come from Hookean spring models of oxygen–hydrogen (O–H) bonds, as well as H–H springs to maintain the water model geometry. The angle between the two O–H bonds would correspond to a more complicated potential function in a more realistic model, but the three-spring model suits our purposes here. The atoms of each molecule also interact, via electrostatic forces, with atoms of the other molecule. To avoid the complexity of treating the system in a way that takes the pressure of the system into account, we fix in place the two oxygen atoms. This constraint is accomplished by removing the forces acting on these two atoms.

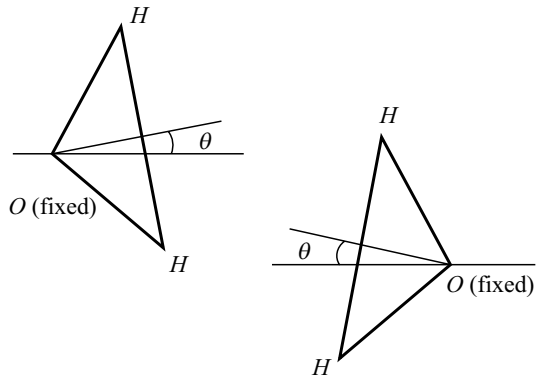

Figure 1 Planar water dimer model system. The dipole angle (measured from the horizontal) is labeled as θ.

The system is represented graphically in Figure 1. In the figure we indicate the central dipole vector for one molecule. When analyzing the simulation results, we will monitor the change of the angle θ indicated in the figure. The model uses natural units: angstroms, kilocalories per mole, and atomic mass units (AKMA). In this system of units, lengths and masses have obvious values (e.g., a hydrogen atom has approximately unit mass), but the resulting time unit is nonstandard: 4.888821×10^{-14} s. For this reason a time conversion is required so that simulation can be presented in time units of femtoseconds (fs).

To begin, we must state explicitly the potential energy function. In this example we use the CHARMM potential model:[13]

$$V_{ij}^{\text{bond}} = \frac{k_{ij}}{2}\left(\sqrt{(x_i - x_j)^2 + (y_i - y_j)^2 + (y_i - y_j)^2} - L_{ij}\right)^2 \qquad [21]$$

and

$$V_{ij}^{\text{elec}} = \frac{q_i q_j}{\sqrt{(x_i - x_j)^2 + (y_i - y_j)^2 + (y_i - y_j)^2}} \qquad [22]$$

where the spring constants and equilibrium lengths for H–H and O–H bonds are given by

$$k_{\text{HH}} = 450.0 \qquad k_{\text{OH}} = 450.0 \qquad L_{\text{OH}} = 0.9573 \qquad L_{\text{HH}} = 1.5139$$

and the electrostatic constants for hydrogen and oxygen are

$$q_{\text{H}} = 0.417 \qquad q_{\text{O}} = -0.834$$

The total potential energy for the system is obtained by summing the V^{bond} terms for all six bonds, and V^{elec} for the eight electrostatic pairs. Note that because the oxygen atoms are not subjected to any force, we need not compute interactions between them, resulting in $3 \times 3 - 1 = 8$ nonbonded pairs. The forces are then computed as the negative gradient of V^{elec}. The form of the total forces can be seen in the MATLAB code twowaters.m. We have implemented the time-stepping algorithms [6]–[20]. Simulations using the various algorithms are coordinated and dispatched by the file dyntwowat.m.

High- and Low-Frequency Motion: The Importance of Electrostatic Forces

For typical configurations of the model system, in which the molecules are separated by about 5 Å, it is seen that the forces due to the bonded interactions have magnitude on the order of 10^1, while the electrostatic forces have magnitude on the order of 10^{-3}. It is natural to wonder about the overall importance of the tiny electrostatic forces. We performed long MD simulations using [6] in the presence and absence of electrostatic forces in the model. The left view in Figure 2 shows O–H bond distance over a few dozen time steps—enough to capture several periods of the fastest motions due to the bond forces. It can be observed that the fastest oscillations have a period of approximately 9 fs. The right view in Figure 2 shows a much longer trajectory of the dipole angle θ for one of the molecules. The presence of the electrostatic forces can be seen to result in very low frequency motions—several orders of magnitude slower than the fast bond-induced motions. Without electrostatic interaction, the dipole angle remains essentially constant, with small fluctuations due to

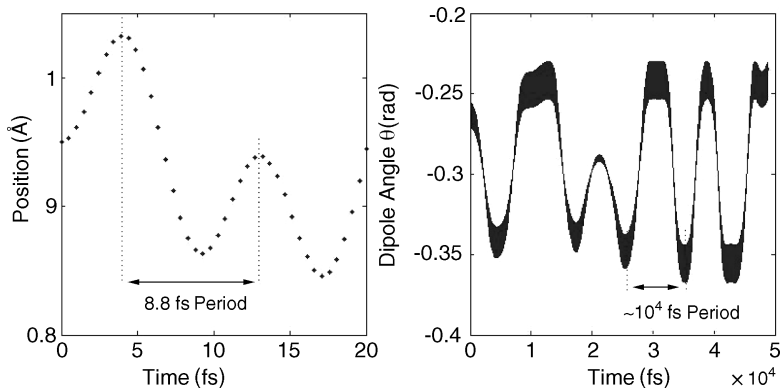

Figure 2 Model exhibits motion across a wide range of frequencies. The left view shows a short trajectory of O–H bond distance in the model system showing the period of the fastest motion to be approximately 8.8 fs. The right view shows the trajectory of one dipole angle. Note that the electrostatic interactions result in a low-frequency motion with period approximately 10 ps. This motion is absent when the electrostatic component is removed from the potential energy model.

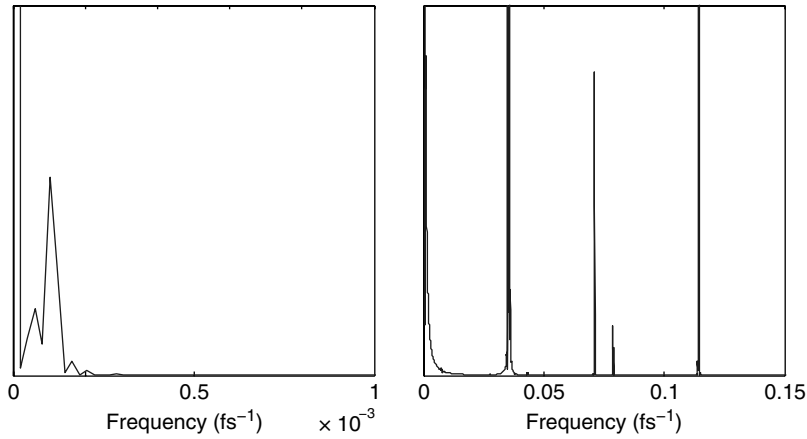

Figure 3 Power spectrum for the dipole angle of one molecule. In the right view, frequency peaks correspond to several fast motions, including the fastest of period $1/(0.114/\text{fs}) = 8.8$ fs. The left view shows an enlarged region at the low-frequency end of the scale. The slow motion due to long-range electrostatics has a period of $1/(0.0001/\text{fs}) = 10000$ fs.

molecular vibration. These low-frequency motions due to long-range forces are typical of the important motions in more elaborate biomolecular models. It is common to perform a power spectrum analysis of MD trajectories in order to identify the constituent motions of a given system. Figure 3 shows the power spectrum for the dipole angle. Notice, for example, that the highest frequency peak at $0.114\,\text{fs}^{-1}$ corresponds to a motion with period 8.8 fs. Also note that in the left view the slowest motion appears as a frequency peak of $0.0001\,\text{fs}^{-1}$, which agrees with the trajectory in Figure 2 with apparent period of 10000 fs. A MATLAB script for plotting power spectra is given in powerspectrum.m.

Behavior of Impulse MTS Method on the Model System

The model system above was designed to illustrate the simplest possible force splitting. The bonded forces constitute the fast force. The two molecules are constrained to be sufficiently distant from one another to avoid any close approaches, so the nonbond forces can be taken as the slow force. With this splitting, the impulse MTS method (Eq. [17]) was used with a step size of $h = 0.5$ fs and various values of $\tilde{\tau}$. Figure 4 shows the root mean square deviation (RMSD) energy error for the method as a function of the interval between slow force updates, which in this example correspond to integer values of τ between 1 and 20. It can be seen that the energy error from $\tau = 1$ (equivalent to the velocity Verlet algorithm) to $\tau = 8$ (corresponding to slow force updates on intervals just shorter than half the period of the fastest motion) is remarkably constant. Unstable energy behavior begins for $\tau = 9$ and is especially notable at the period of the fastest motions of the system. A power spectrum analysis of the

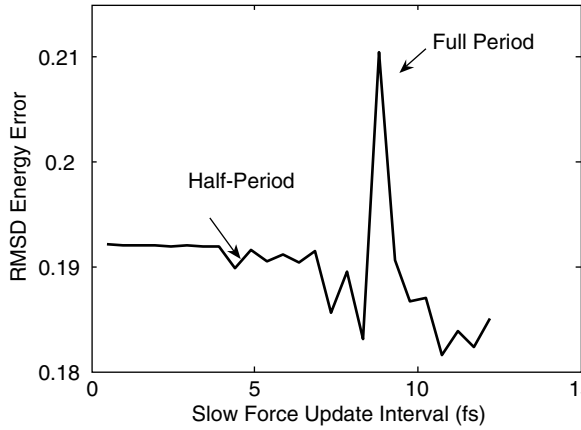

Figure 4 Sensitivity of the impulse MTS method to slow force update intervals. The energy error is essentially unchanged from that of velocity Verlet to an update interval up to 4 fs. For larger update intervals, the energy error becomes erratic, with a notable jump at the period of the fastest molecular motion.

trajectory shows that the low-frequency motion is correctly resolved by the impulse MTS method for values of τ in the stable regime.

Behavior of Langevin-Stabilized Extrapolation Method on the Model System

Langevin dynamics requires the calculation of a random force vector at every step. This is implemented for our water dimer in the MATLAB function dynlang1.m. The best value to select for the collision parameter γ is an open question. In the original work of McCammon, Gelin and Karplus,[39] the choice was 5/ps. For the water dimer model, we present results using a smaller collision parameter 2/ps (corresponding to 0.1 in the units presented here). A power spectrum analysis shows that Langevin dynamics simulations on the water dimer exhibit essentially the same frequencies as constant-energy simulations, but with broadening of the frequency peaks. This spreading of the peaks depends upon the magnitude of γ, with larger values resulting in broader peaks. This effect can be seen by comparing Figure 3 and Figure 5. We note that this broadening is especially sensitive for the low-frequency motion, where the stochastic forces can excite rotations in the dipole about the fixed atoms. This broadening can be viewed two ways, depending on the nature and aims of the simulation. If detailed time-dependent dynamical information about the very low frequency motion is needed, the stochastic forces in Langevin dynamics blur the picture somewhat. On the other hand this excitation of low-frequency modes can result in enhanced sampling of the low-frequency motion, allowing simulations to capture this important motion on a shorter simulation time scale.

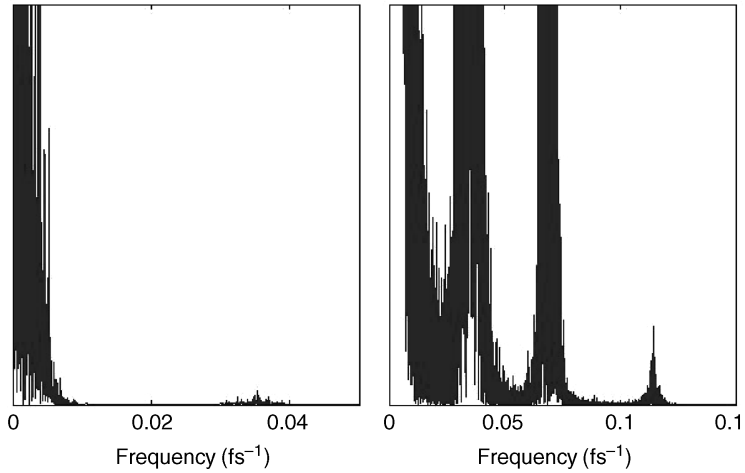

Figure 5 Power spectrum analysis of the Langevin dynamics simulation of the model system. Frequency peaks are in qualitative agreement with constant-energy simulations but somewhat broadened when compared with the data shown in Figure 2.

As pointed out earlier and shown in Figure 4, the energy of the bonded terms is an especially sensitive detector of instability arising from MTS resonance artifacts. Because the total energy is not constant in Langevin simulations, bond energy can be used to monitor the stability of a Langevin trajectory. Figure 6 shows that the energy behavior of the Langevin-stabilized

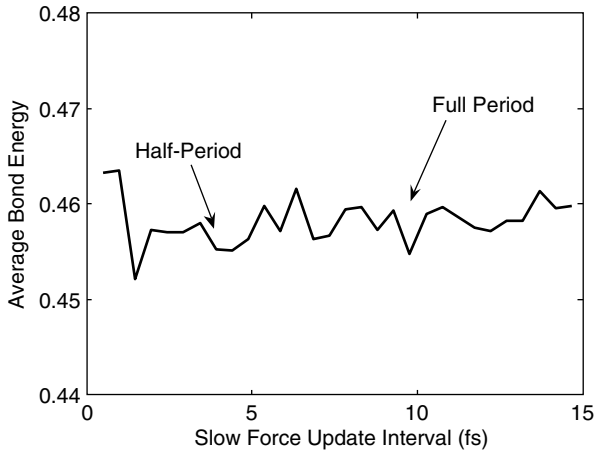

Figure 6 Average bond energy as a function of slow force update interval for a Langevin-stabilized extrapolation MTS method. These average energies, taken from long simulations, do not exhibit the sensitivity to the slow force update interval seen with impulse MTS methods in Figure 4.

extrapolation method is largely independent of τ, allowing for large MTS steps while maintaining the underlying behavior of the single-step Langevin method.

EXTENDING THE TIME SCALE: PATH METHODOLOGIES

Molecular dynamics (MD) is the most widely used computational method to study the kinetic and thermodynamic properties of atomic and molecular systems.[59–61] These properties are obtained by solving the microscopic equations of motion (Eq. [1]) for the system under consideration. The multiple time-step algorithms discussed earlier have extended the time scale that can be reached, but, the gain is still insufficient for the study of many processes; for many systems, such as biomolecules, this simulation time is inadequate to study large conformational changes or to study rare but important events as examples.

A different approach for such systems can be considered, however, that invokes a different set of methodologies that attempt to compute trajectories connecting conformations from the reactant state to conformations of the product state, i.e., the reaction path. Transition path sampling, MaxFlux, discrete path sampling, string methods, and optimization of actions are examples of methodologies that search for these transition paths. We now will review briefly the first four methods and then present the theory and implementation of the action formalism in more detail.

Transition Path Sampling

Transition path sampling (TPS) is a methodology that can be used to study slow activated processes. This technique, first developed by the Chandler group[62,63] and further improved by Bolhuis et al.,[64–67] is based on a polymer-like representation of the complete trajectory (Figure 7). TPS is an iterative method that starts by computing a dynamical pathway connecting conformations of the reactant and product state. That can be done using simpler methods that generate approximate trajectories connecting two boundary points.

Starting from this initial path, further trajectories are then generated using an iterative strategy. Specifically, a configuration snapshot (i.e., nuclear positions and velocity vectors) is taken from the previous trajectory and modified (Monte Carlo shooting method[68]) in a manner consistent with the corresponding distribution ensemble. Usually, the incorporated change is a momentum variation. Then, starting from this modified configuration, forward and backward trajectories are generated using MD, and, if this pathway connects the reactant and product state, it is used to generate another new pathway as above. An accurate sampling of trajectory space can be generated by iterating this process many times. From these trajectories, reaction mechanisms and transition

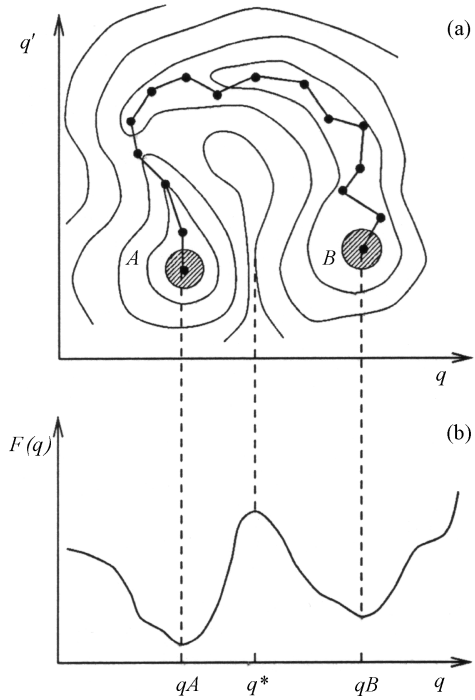

Figure 7 (a) Schematic energy diagram as a function of two coordinates q and q' with reactant region A and product region B. The chain of beads represents a discretized path in the TPS method. (b) Schematic free energy along reaction coordinate q. (Adapted from Dellago et al.[69])

states can be elucidated, and rate constants can be determined using the time derivative of the time correlation function:[64,69]

$$k_{AB}^{\mathrm{TPS}}(t) = \frac{dC(t)}{dt} \qquad C(t) = \frac{\langle h_A(\mathbf{x}_0) h_B(\mathbf{x}_t) \rangle}{\langle h_A(\mathbf{x}_0) \rangle} \qquad k_{AB}^{\mathrm{TPS}}(t) = \frac{\langle \dot{h}_B(t) \rangle_{A,H_B(T)}}{\langle h_B(t') \rangle_{A,H_B(T)}} C(t') \tag{23}$$

in which $h_A(\mathbf{x})$ and $h_B(\mathbf{x})$ are indicator functions that state if the system is in the phase space regions A or B:

$$\begin{aligned} h_A(\mathbf{x}) &= 1 \qquad \text{if } \mathbf{x} \in A \quad \text{else } h_A(\mathbf{x}) = 0 \\ h_B(\mathbf{x}) &= 1 \qquad \text{if } \mathbf{x} \in B \quad \text{else } h_B(\mathbf{x}) = 0 \end{aligned} \tag{24}$$

Here $\mathbf{x}$ is a phase space vector, $H_B(T) = \max_{0<t<T} h_B(\mathbf{x}_t)$, and $\langle \cdots \rangle_{A,H_B(T)}$ is an average over the ensembles of paths that start in A and go to B at least once during a fixed length T. An order parameter is introduced to describe

the transition, and, umbrella sampling can be used to compute the rate in Eq. [23].

The molecular processes typically studied with TPS involve a transition over a single, albeit significant barrier. TPS is more efficient than standard MD because the reactive trajectories (computed by TPS) are much shorter through phase space than the time it takes between successive transitions; more (reactive) trajectories are therefore computed with TPS than with normal MD methods.

The TPS methodology has been applied successfully to evaluate time-dependent events, such as chemical reactions and conformational changes.[65,68,70–74] Application of this algorithm to complex systems with rugged energy surfaces, however, requires the identification of basin states separated by several barriers with different heights. For these systems, the assumption of time-scale separation between the transition time and the incubation time is not easy to justify. For these complex systems, the reactive trajectories can be long, and the sampling will be limited by the time step used in the simulation. Defining the reaction coordinate or a physical descriptor that allows for the identification of the different basin and transition states present during transitions of complex molecules can be cumbersome.[75]

Maximization of the Diffusive Flux (MaxFlux)

MaxFlux is a time-independent algorithm that seeks a path that maximizes the diffusive flux (or minimizes the mean first-passage time) between two configurations at a given temperature. The algorithm is based on the work of Berkowitz and co-workers[76] who derived the optimal transition connecting reactant and product using a variational principle. If the transition is described as a stochastic process, the flux of particles along the optimal path is given by

$$j \propto \frac{\tan t}{\gamma \int \exp(\beta V) dl} \qquad [25]$$

where V is the potential of mean force of the system, γ is an isotropic and spatially independent friction coefficient, $\beta = 1/k_B T$, and dl is an infinitesimal length element along the path. In MaxFlux, the line integral in the denominator of Eq. [25] is minimized using a self-penalty walk method.[77]

MaxFlux has been used to study conformational transitions in peptides and aggregate formation by Straub et al.[78,79] It can also be used to describe slow processes controlled by diffusion.[76] A difficulty with MaxFlux is the necessity to specify the phenomenological friction constant. The magnitude of the friction constant strongly influences computed rates, and it affects the transition pathways. Equation [25] is maximized with global optimization algorithms that are both time-consuming and dependent on the initial guess for the pathway.

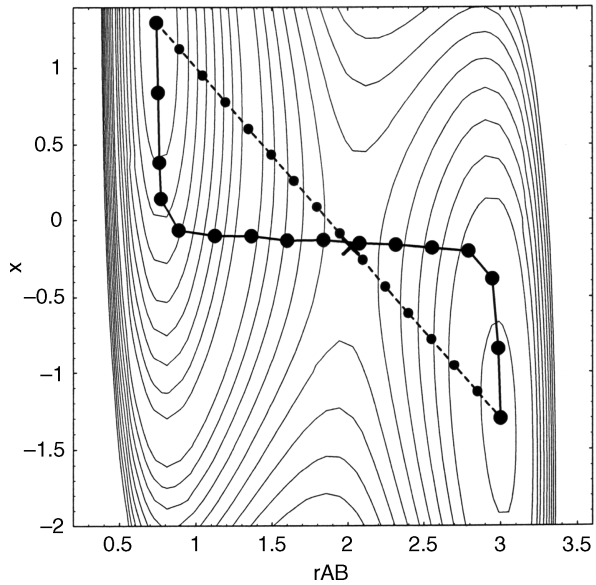

Figure 8 Minimum energy path obtained using the NEB method is shown with the larger filled circles along the continuous line. The dashed line with smaller filled circles is a linear interpolation between the initial and final state. The contour plot represents the potential surface of a 3-atom model coupled to an additional degree of freedom. (Adapted from Jónsson et al.[80])

A temperature-dependent nudged-elastic-band (NEB) algorithm, also based on maximizing the flux, was proposed recently.[80–82] In this MaxFlux-NEB algorithm, based on the differential form of Eq. [25], a discretized path is constructed with the different neighboring structures maintained equally spaced by the use of spring forces (Figure 8). The path is then minimized using a modified Verlet algorithm. This methodology has limitations similar to those of MaxFlux.

Discrete Path Sampling and String Method

Discrete path sampling (DPS)[83–87] is a methodology that samples paths along the potential energy surface (instead of the Gibbs free energy surface as in TPS). Fast paths connecting local minima and transition-state conformations are computed by DPS. The initial path connecting minima and transition states is computed using the NEB method,[88,89] and the number of paths is increased by replacing a minimum in the path with a new minimum close to the original path. That new path is accepted and used to generate additional paths only if it is faster than the original path (Figure 9). The rate constants are computed using a harmonic approximation to the local density of states for

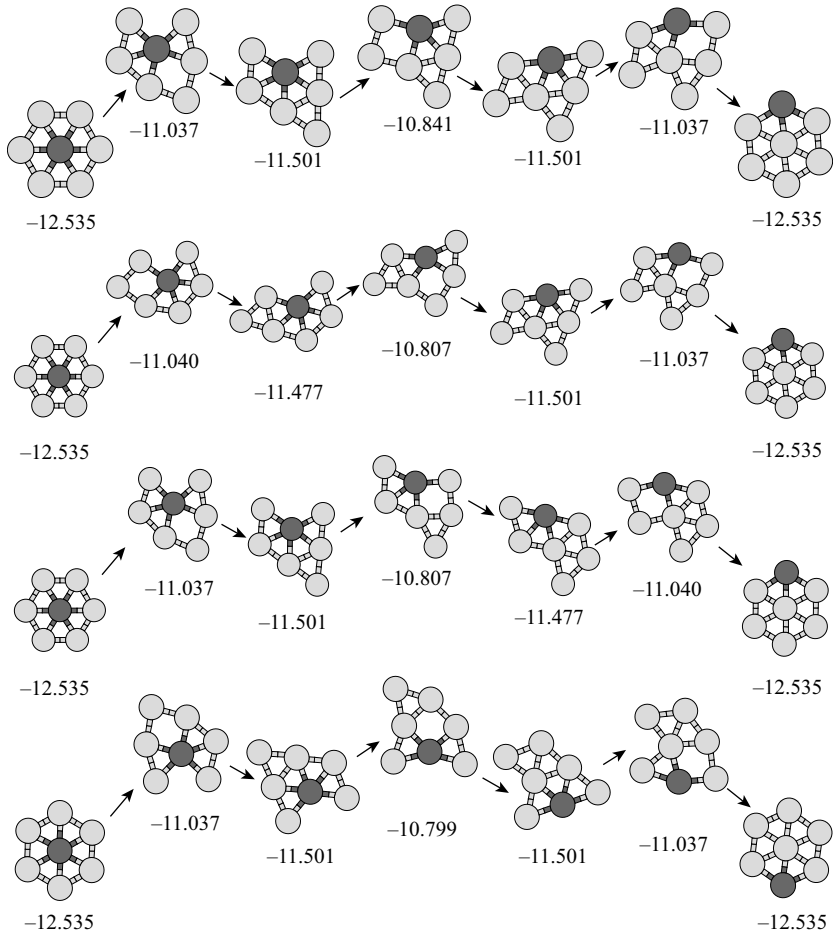

Figure 9 Configuration for the four fastest paths of an isomerization process for a two-dimensional Lennard-Jones system obtained using the discrete path sampling method. (Adapted from Wales.[87])

each stationary point of the potential energy surface. Overall phenomenological rate constants can be extracted using master equations, kinetic Monte Carlo or graph transformations, and transition-state theory. The algorithm has been applied to a small pentapeptide[83] and to the GB1 hairpin.[84] Reliance on statistical rate theory is one of the drawbacks of this methodology. A satisfactory sampling on stationary points of the potential energy for more complex systems can be difficult as well.

In the string method,[90–94] which is based on the transition path theory (TPT),[95,96] a "transition tube" in configuration space is constructed by sampling the equilibrium distribution of the system in a collection of hyperplanes.

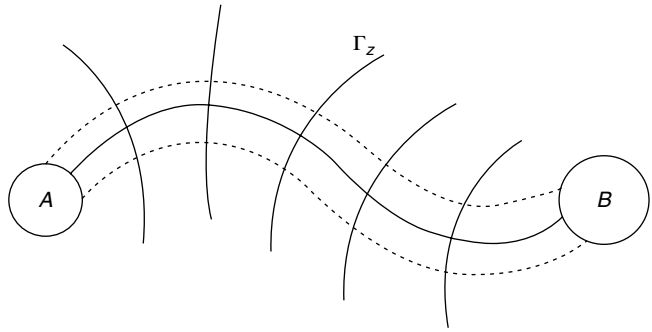

Figure 10 Transition tube between two states *A* and *B* is shown with the dashed lines. Several isocommitor surfaces Γ_z are also shown and a string (solid line perpendicular to the isocommitor surfaces. (Adapted from Ren et al.[92])

These hyperplanes are parameterized by a string connecting two metastable states (Figure 10).

The hyperplanes approximate the isocommittor surfaces (trajectories initiated at configurations on this surface have the same probability of reaching the product state before reaching the reactant state). The transition tube represents a region in configuration space in which the transition occurs with high probability. The string is a curve normal to each hyperplane passing through the center of mass on each plane and defines the center of the transition tube. It is defined as

$$\varphi(\alpha) = \langle \mathbf{x} \rangle_{P_\alpha} \qquad [26]$$

in which the average is restricted to equilibrium configurations on the hyperplane P_α (α is a parameter characterizing the hyperplanes).

The algorithm uses a variational principle that satisfies:[92]

$$\hat{\mathbf{n}}(\alpha) \parallel \varphi'(\alpha) \qquad [27]$$

to compute the string where $\hat{\mathbf{n}}(\alpha)$ is a unit vector normal to the hyperplane P_α and $\varphi'(\alpha)$ is the tangent vector of the string at α.

The string method is more sophisticated than MaxFlux and DPS, but, due to its inherent complexity, it has been used only for very simple systems such as alanine dipeptide.[92]

Optimization of Action

Another set of algorithms have been developed by Elber et al. based on the optimization of actions.[97,98] In classical mechanics, the action is a physical quantity associated with a particular system and from which the equations of

motion can be derived by computing a minimum (more exactly any extremum). This method is called the least action principle. In the optimization of an action procedure an initial guess for the trajectory is generated by connecting two boundary states, and the least action formalism is used to compute a finite-temperature trajectory.

The first formulation of this methodology was based on a discretized version of the classical action:

$$S[\mathbf{X}(t')] = \int_0^t L\, dt' \qquad [28]$$

generating the Onsager–Machlup object function:[99–103]

$$S_{\mathrm{SDET}}(\{\mathbf{X}_i\}_{i=1}^{N-1}) \equiv \sum_i \Delta t \left(\mathbf{M} \frac{\mathbf{X}_{i+1} + \mathbf{X}_{i-1} - 2\mathbf{X}_i}{\Delta t^2} + \frac{dV}{d\mathbf{X}_i} \right)^2 = \sum_i \Delta t \varepsilon_i^2 \qquad [29]$$

In these equations, $\mathbf{X}$ is the coordinate vector for the system, $\mathbf{M}$ is the diagonal mass matrix, V is the potential energy, $\mathbf{X}_0$ and $\mathbf{X}_N$ are the fixed boundary conformations in the trajectory, and ε_i is an error variable. This algorithm, called stochastic difference equation in time (SDET), has been used to compute *approximate* trajectories by using a large time step Δt for long-time events. These paths are obtained by sampling trajectory space using molecular dynamics or Monte Carlo techniques according to a Gaussian distribution of errors (the term between parentheses corresponds to a finite-difference version of Newton's equation of motion, i.e., Eq. [2]). Using similar time formalisms, Passerone and Parrinello,[104] Passerone et al.,[105] and Bai and Elber[106] have computed *exact* trajectories for relatively short but rare processes.

A variant of the SDET algorithm will be described below in more detail. In this more recent formulation called SDEL (for stochastic difference equation in length) the trajectory is parameterized as a function of its arc length and a unique path is obtained connecting the two boundary conformations.[97,98] In this sense, the SDEL algorithm is similar to DPS and string methods because trajectories are computed in configuration space instead of the space parameterized by time as in normal MD, TPS, and SDET algorithms.

Boundary Value Formulation in Length

The SDEL algorithm allows the computation of atomically detailed trajectories connecting two known conformations of the molecule over long time scales. In contrast to normal and MTS molecular dynamics algorithms, step sizes can be increased easily by two or three orders of magnitude without

significant changes in many properties of the trajectory. The trade-off between SDEL and normal and MTS MD is that trajectories obtained with such a large step size are only approximate; molecular motions that occur on a scale shorter than the step size are filtered out from the trajectories. Also, the initial and final configurations of the system under study must be known because this is a boundary value algorithm. This means that the algorithm cannot be used to predict the final conformation of a molecular system such as a protein, and, consequently, confines the applicability of the algorithm to situations in which the initial and final configurations are known by experiment or modeling. This is not an unbearable limitation because in many chemical events we are interested in determining how a system changes from a reactant state to a product state. The algorithm can be used, for example, to describe folding mechanisms,[107] i.e., how a protein folds to its native conformation starting from an unfolded structure.

The Onsager–Machlup action methodology has a critical disadvantage: the total time of the trajectory is needed in advance. Also, low-resolution trajectories do not approach a physical limit when the step size increases, in contrast to SDEL as will be shown below.

Like the Onsager–Machlup action method, the SDEL algorithm is based on the classical action. However, in this case the starting point is the action S parameterized according to the length of the trajectory:[108]

$$S = \int_{\mathbf{Y}_u}^{\mathbf{Y}_f} \sqrt{2(E - V(\mathbf{Y}))}\, dl \qquad [30]$$

where $\mathbf{Y}_u$ and $\mathbf{Y}_f$ (lower and upper limits of integration) are the mass-weighted coordinates ($\mathbf{Y} = \sqrt{\mathbf{M}}\mathbf{X}$) of the initial and final conformation of the system, respectively, E is the total energy, V is the potential energy of the system, and dl is an infinitesimal mass-weighted arc length element for the path connecting $\mathbf{Y}_u$ and $\mathbf{Y}_f$. Using the least-action principle of classical mechanics, one obtains a classical trajectory connecting these two states of the system when a stationary solution for the action is computed, i.e., $\delta S/\delta \mathbf{Y} = 0$ (the action is not necessarily a minimum[108,109]). These trajectories are calculated differently from usual MD simulations. First, the trajectory is obtained using double boundary conditions, where the initial and final coordinates of the system are required as input. In contrast, the initial positions and velocities (usually chosen randomly from a Boltzmann distribution) are needed in a standard MD algorithm. Second, the trajectory in Eq. [30] is parameterized as a function of length and not as a function of time. Finally, the total energy of the trajectory is fixed in the SDEL formulation. This contrasts with an MD trajectory where the total time is fixed once the step size and the number of steps are constrained in the calculation.

Computing exact trajectories using Eq. [30] is more expensive than in normal MD because the evaluation and optimization of the action entails knowing the entire trajectory. However, if the aim is to obtain an approximate trajectory with a large step size between successive structures, optimization of Eq. [30] becomes a more feasible task and a more stable trajectory than in a straightforward MD algorithm can be generated. An approximate trajectory is computed from Eq. [30] numerically when a large step size is used, i.e., when $\Delta l \gg dl$. Specifically, after replacing $dl \rightarrow \Delta l$ a discrete version of the action in Eq. [30] is obtained:

$$S \cong \sum_{i=0,\ldots,N} \sqrt{2(E - V(\mathbf{Y}_i))}\Delta l_{i,i+1} \qquad [31]$$

where the action is now a function of the coordinates of the N intermediate structures in the path, $\{\mathbf{Y}_i\}_{i=1}^{N}$ (with the coordinates of the structures $\mathbf{Y}_0 \equiv \mathbf{Y}_u$ and $\mathbf{Y}_{N+1} \equiv \mathbf{Y}_f$ held fixed), and $\Delta l_{i,i+1}$ is the mass-weighted distance separating consecutive structures in the trajectory ($\Delta l_{i,i+1} = |\mathbf{Y}_i - \mathbf{Y}_{i+1}|$). The trajectory that makes S stationary is determined by optimization. The optimized trajectory thus represents a sequence of structures connecting the initial and final state of the system. Explicitly, after optimization the following expression is obtained:[108]

$$\frac{\partial S}{\partial \mathbf{Y}_i} \cong \frac{\Delta^2 \mathbf{Y}_i}{\Delta l^2} - \frac{1}{2[E - V(\mathbf{Y}_i)]}[\nabla V - (\nabla V \cdot \hat{\mathbf{e}}_i) \cdot \hat{\mathbf{e}}_i] = 0 \qquad [32]$$

with

$$\frac{\Delta^2 \mathbf{Y}_i}{\Delta l^2} = \frac{2\mathbf{Y}_i - \mathbf{Y}_{i+1} - \mathbf{Y}_{i-1}}{\Delta l^2} \quad \text{and} \quad \hat{\mathbf{e}}_i \equiv \frac{\mathbf{Y}_{i+1} - \mathbf{Y}_{i-1}}{|\mathbf{Y}_{i+1} - \mathbf{Y}_{i-1}|} \qquad [33]$$

where $\hat{\mathbf{e}}_i$ is a unit vector tangential to the path at slice i, and the length step Δl can be made a constant in the calculation and therefore independent of the index i. The first term of Eq. [32] (equivalent to the acceleration term in Newton's equation of motion, Eq. [1]) depends on the step size. At larger step sizes, this ''acceleration'' contribution becomes smaller. In the limit when this inertial term can be neglected, Eq. [32] becomes

$$\begin{aligned} &\frac{\delta S}{\delta \mathbf{Y}_i} \approx -\frac{1}{2[E - V(\mathbf{Y}_i)]}[\nabla V(\mathbf{Y}_i) - (\nabla V(\mathbf{Y}_i) \cdot \hat{\mathbf{e}}_i)\hat{\mathbf{e}}_i] = 0 \\ &\rightarrow \nabla V(\mathbf{Y}_i) - [\nabla V(\mathbf{Y}_i) \cdot \hat{\mathbf{e}}_i]\hat{\mathbf{e}}_i = 0 \quad \forall i \end{aligned} \qquad [34]$$

Equation [34] generates a path in which the force is minimized in all directions except the tangential direction of the path. This is one of the definitions of the minimum energy path (MEP).[110] Equation [34] suggests that SDEL provides a physically meaningful trajectory even at low resolution (large step sizes).

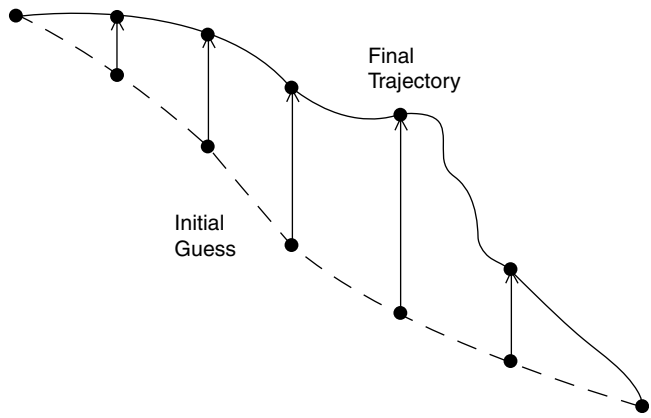

Figure 11 Simplified view of the optimization of a trajectory using SDEL. The circles denote configuration snapshots taken along the initial guess for the trajectory (dashed line). The first and last circles are the fixed boundaries of the path. The solid line is the resulting trajectory after optimization of the target function Θ. Arrows indicate the direction of the gradient of the target function for that particular coordinate slice.

The following steps are used to obtain an approximate trajectory using SDEL (Figure 11):

1. Generate an initial guess for the path connecting the initial and final coordinates of the system using an MEP algorithm, such as self-penalty walk (SPW)[77] or nudged-elastic band.[88,89]
2. Estimate the total energy of the system E (needed to evaluate and optimize the action) by averaging the total energy obtained by using several MD simulations of the system at the temperature of interest. An alternative method is to identify the highest and lowest values of the potential energy for the MEP trajectory, and then compute the average thermal energy at the top of the barrier [i.e., $E = V_{\text{high}} - V_{\text{low}} + ((3L - 6)/2)k_B T$, where L is the number of atoms in the system].
3. Obtain a stationary solution for the action S, for which $\partial S/\partial \mathbf{Y}_i = 0$, by minimizing the square of the action gradient $\Theta = \sum(\partial S/\partial \mathbf{Y}_i)^2$ with a simulated annealing protocol (Figure 11). The evaluation of the potential energy, forces, and hessians needed by the optimization algorithm can be performed by using the Amber/OPLS force field parameters including the molecular simulation package MOIL[111] as an example.
4. Examine the optimized trajectory whose accuracy is estimated by the step size Δl. The step size should be small enough to provide a smooth representation of the path. The cutoff value Δl_c depends on the particularities of the system. If $\Delta l > \Delta l_c$, the trajectory is not accepted, and more intermediate structures are added to the path. Steps 3 and 4 are then repeated.

The function $\Theta = \sum(\partial S/\partial \mathbf{Y}_i)^2$ depends on the distances $\Delta l_{i,i+1}$ (Eq. [32]), which are computed as norms in Cartesian space. Therefore, it is important to remove overall translations and rotations from the structures along the trajectory, which can be done by imposing linear constraints using the Eckart conditions:[112]

$$\sum_{j=1,\ldots,L} \mathbf{y}_{ij} = 0 \qquad \sum_{\mathrm{j}=1,\ldots,\mathrm{L}} \mathbf{y}^0_{\mathrm{ij}} \times (\mathbf{y}_{ij} - \mathbf{y}^0_{ij}) = 0 \quad \forall \mathrm{i} \tag{35}$$

where the vector $\mathbf{y}_{kl}$ is the mass-weighted Cartesian coordinate of atom l in structure k, and the vectors $\mathbf{y}^0_{ij}$ represent the coordinates of a reference structure. Equation [35] provides $6N$ linear constraints that are denoted by σ_{im} with $i = 1, \ldots, \mathrm{N}$ and $m = 1, \ldots, 6$.

The gradients of the constraints $\nabla\sigma_{im}$ and unit vectors in their directions $\boldsymbol{\eta}^0_{im} = (\nabla\sigma_{im}/|\nabla\sigma_{im}|)$ are coordinate independent. Therefore, they only need be computed once at the beginning of the calculation. These unit vectors are not necessarily orthogonal for a single structure ($\boldsymbol{\eta}^0_{il}\cdot\boldsymbol{\eta}^0_{ik} \neq \delta_{lk}$) but can be orthogonalized using a Gram–Schmidt procedure.[113] We denote this set of orthogonalized vectors by $\{\boldsymbol{\eta}_{im}\}_{i=1}^N$.

Let $\{\mathbf{Y}_i\}_{i=1}^N$ be the set of variable coordinates of the current trajectory that satisfies the constraints. Let $\{\delta\mathbf{Y}^0_i\}_{i=1}^N$ be a proposed displacement of these coordinates during the optimization process to generate a new trajectory $\{\mathbf{Y}_i + \delta\mathbf{Y}^0_i\}_{i=1}^N$. The components of the displacement that satisfy the constraints are given by

$$\delta\mathbf{Y}_i = \delta\mathbf{Y}^0_i - \sum_{m=1,\ldots,6} (\delta\mathbf{Y}^0_i \cdot \boldsymbol{\eta}_{im})\boldsymbol{\eta}_{im} \quad \forall \mathrm{i} \tag{36}$$

A new trajectory with coordinates $\{\mathbf{Y}_i + \delta\mathbf{Y}_i\}_{i=1}^N$ then satisfies the Eckart constraints.

The SDEL algorithm has been efficiently parallelized using message passing interface (MPI) libraries. In the parallelization scheme each node of a cluster of computers calculates the potential energy and derivatives for a particular path segment.[114] Internode communication is not heavy and the computing scales favorably with cluster size.

Several advantages of SDEL exist when compared to other methods:

1. *The trajectories can be computed at room temperature or any other temperature of interest and no bias potential is needed.* This differs from methods that rely on high temperature to accelerate the dynamics[115] or those that modify the potential energy function to drive the trajectory to a desired outcome.[115–117]
2. *Both the boundary conditions and the length parameterization enable one to study very slow processes.* This is demonstrated later.

3. *The algorithm is easy to run in parallel with no costly communication between processors.* Ordinary PC clusters can be used.
4. *All the trajectories are reactive as in any reaction path method.* This is in contrast to initial value normal and MTS MD methods, in which many trajectories do not end at the desired state. This also enhances the efficient use of computational resources.
5. *The SDEL formulation is general.* It is not limited to processes with large energy barriers, single barriers, or those with exponential kinetics. This makes SDEL more versatile than other reaction paths methods.
6. *The algorithm produces an interpolation between the minimum energy path (MEP) and a true classical trajectory.* Hence, even trajectories with low resolution can be useful in qualitative reaction path studies.

But the algorithm also has several disadvantages including:

1. *The trajectories are approximate.* High-frequency motions, which can be important in certain dynamical events, are not resolved.
2. *The computations are expensive.* Trajectories for systems with $\sim$1000 atoms require a parallel resource of near 20 CPU-s at current processor speeds. However, cluster of computers of this size are becoming common in computational chemistry labs.
3. *The length formulation makes it difficult to estimate the time scale of the process.* SDEL can provide information about the relative sequence of events but not absolute times. This is a limitation shared by all reaction path methods.
4. *Thermodynamic properties are approximate and quantitative kinetic properties are inaccessible.* The removal of high-frequency modes due to the large step size affects computed thermodynamic properties and transition probabilities. Enthalpic properties of slow variables, however, are affected only slightly.[98]
5. *The final solution depends on the initial guess for the trajectory.* No global optimization protocol will generate the true minimum for the target function Θ in an acceptable time for a large system. In the applications of SDEL, the initial guess is an approximate MEP obtained with a self-penalty walk algorithm and most of the solutions obtained correspond to trajectories in local minima somewhere near the initial guess. The implementation of less biased procedures, which sample trajectories connecting structures in configuration space, is a subject of ongoing research.[118]
6. *The current SDEL algorithm uses an implicit solvent model.* This is not a fatal flaw of SDEL; computations of trajectories with an atomistic description of the environment are possible. The assumption of time separation between the relaxation to equilibrium of water molecules and the solvated molecule (e.g., a protein) makes the calculations viable. The configuration for the water molecules can then be determined using a

thermal distribution for a fixed configuration of the solute molecule. A short MD simulation can be used to accomplish this as was done to include explicit water dynamics in the Onsager–Machlup action.[101,114] However, inclusion of explicit solvent using this adiabatic approximation slows the computations for large systems. A simpler way to include the effect of explicit water/molecule interactions is to extract configurations from SDEL trajectories, immerse those structures in a box with explicit water molecules and perform MD simulations until equilibration is reached.[119]

It is clear that the SDEL algorithm has appealing advantages when it is applied to long time events. Meaningful trajectories can be obtained for processes that are difficult or impractical to study by initial-value formulations and other reaction path techniques. However, the lack of kinetic information converts SDEL as a complement to other algorithms that can provide transition probabilities (albeit with limited time scale) like TPS, DPS, and string methods.

Use of SDEL to Compute Reactive Trajectories: Input Parameters, Initial Guess, and Parallelization Protocol

The SDEL algorithm is implemented in MOIL, a suite of molecular simulation programs developed in the group of Ron Elber. Linux and Windows versions of the software package can be downloaded, free of charge at http://cbsu.tc.cornell.edu/software/moil/moil.html. The Windows version has a graphics interface that is relatively easy to use. The Linux version can only be run in a command mode after installation using a makefile command. The SDEL program can be run on a standalone computer or on a parallel cluster of PCs using MPI protocols. Because the optimization of the action is computationally expensive, the use of a parallel computer is recommended for most applications dealing with systems containing more than $\sim$100 atoms. The required internode communication is low and the computation scales well with the number of nodes.[114]

Two conformations at the boundaries are required to compute a trajectory with SDEL For example, to assess protein folding, the initial unfolded conformation in the trajectory can be derived from a high-temperature molecular dynamics simulation. The final folded structure in the trajectory can be taken from the protein data bank after that native configuration has been equilibrated by MD.

The total energy of the molecular system is also required by SDEL. One can estimate this energy by performing a MD simulation of the system, using the same solvation model and force-field parameters as will be used during the SDEL run.

An initial guess for the trajectory connecting the two boundary states is required to evaluate the SDEL action, Θ. This guess is the most troublesome

step of the method. The SDEL action depends on $\sqrt{2(E - V(\mathbf{X}))}$, suggesting that each conformation in the initial trajectory must have a potential energy smaller than the total energy of the system. This, in turn, prevents the use of simple methods such as linear interpolation to compute the initial trajectory of the two boundary structures; methods such as linear interpolation usually generate intermediate structures with large potential energy due to steric repulsions.

In practice, this initial guess problem is solved by computing an approximate MEP connecting the two boundary states. That path is then used as the initial guess for SDEL. MOIL contains a program called *chmin* that computes the MEP using a simple self-penalty walk algorithm.[77] *Chmin* treats the path as a polymer chain, where each monomer is a copy of the molecular system at different times. The potential energy of the chain is the sum of the potential energies of each monomer, with the addition of a harmonic attraction term between nearest monomers, and an exponential repulsion term between next nearest monomers.

The potential energy for the structures $V(\mathbf{Y}_i)$ in the MEP should be analyzed before using this trajectory as initial guess for SDEL. Not only must the potential energy of every slice through the chain be lower than the total energy of the system, but the potential energy should also vary smoothly along the trajectory; steep peaks or decays of $V(Y_i)$ can cause a numerical instability during the optimization of the action.

The input file for SDEL, called path.inp in MOIL (Table 1), contains the names for the file (*rcrd*) with the initial guess trajectory (i.e., a binary file with extension *pth*), and the molecule's connectivity file used to extract the potential parameters for the force field. The connectivity file (with extension *wcon*) is generated by the program *conn* in MOIL.

The SDEL target function for optimization in MOIL is

$$\Theta = \sum \left(\frac{\partial S}{\partial Y_i} \right)^2 + \sum_{i=0}^{N} \gamma (\Delta l_{i,i+1} - \langle \Delta l \rangle)^2 \qquad [37]$$

Table 1 Example of Input File (path.inp) for SDEL

```
file conn name=(val.wcon) unit=10 read
file rcrd name=(valmin200.pth) bina unit=14 read
file wcrd name=(valpath.PTH) bina unit=12 wovr
#ste=5000 list=500
gama=2000.0 grid=200 pdqe=-42.2 gbsa
rmax=9999. epsi=1. v14f=8. el14=2. cpth
proc=10
tmpr=30000.0
dtop=1.0d-4
anne
action
```

with $\langle \Delta l \rangle$ being the average value of the distances $\Delta l_{i,i+1}$ between structures in the path. The second term on the right side enforces equidistance of structures along the path. The parameter γ is a constant that can be adjusted in the input file (*gama* in path.inp) to optimize calculation efficiency.

A simulated annealing protocol can be used to optimize the target function subjected to the overall translation and rotation constraints (Eq. [35]). We can denote the variable components of the initial guess for the trajectory $\{\mathbf{Y}_i^0\}_{i=1}^N$ and optimize the trajectory for K steps solving the second-order differential equation for the trajectory $\mathbf{Z} = \{\mathbf{Y}_i\}_{i=1}^N$:

$$\frac{d^2\mathbf{Z}}{d\tau^2} = -\nabla_{\mathbf{Z}}\Theta \qquad [38]$$

Using linear cooling with velocity scaling, $|d\mathbf{Z}/d\tau|^2 = \mu(\theta - \tau)$. Here τ is a fictitious time during the annealing run, θ is the total time (in practice, $\theta = K\Delta\tau$), and μ is a factor proportional to the initial temperature used at the beginning of an annealing cycle. In the input file, the flag *anne* instructs the program to use simulated annealing, *tmpr* gives the value of μ, and *dtop* is the time step $\Delta\tau$.

The SDEL program can also use a conjugate-gradient Powell algorithm[120] to minimize the target function. This algorithm is more efficient at searching for local minima than simulated annealing. As with other conjugate-gradient methods, it should be used only if the initial guess for the trajectory is presumed to be near the global minimum.

Other parameters that influence the performance of a SDEL run (Table 1) are:

#ste = the total number of optimization steps.

list = the total number of steps in each cycle of optimization (the value of K). The program also writes useful information every *list* steps.

grid = the total number of structures in the trajectory, i.e., $grid = N + 2$.

pdqe = the total energy for the molecular system in kcal/mol.

gbsa = a generalized Born model for the solvent environment.

rmax, *epsi*, *v14f*, *el14*, which are the values for the cutoff distance for nonbonded interactions, dielectric constant, and 1–4 scaling for van der Waals and electrostatics interactions, respectively.

proc = the number of computer nodes used.

cpth = the trajectory coordinates (rcrd) are input in a binary path format.

action = instructs the program to continue execution.

The program generates log files with information about the status of the run on each node during execution. The log file associated with the master node

(called pth_out_0000.log) gives the gradient of Θ at every *list* step. A value of this gradient of 10 $(\text{kcal/mol})^2$ or less typically produces a convergent trajectory. Convergence can be analyzed by comparing intermediate results for the paths, which are written after each cycle of optimization.

At the end of a run, the final trajectory is output (*file wcrd*) with path format. MOIL contains several programs that can be used to analyze the trajectory (computation of radius of gyration, native contacts, secondary structure content, etc). The Windows graphics interface of MOIL can be used to visualize the trajectory. Also, the path format can be converted to a more conventional format like *dcd* using the *ccrd* program of MOIL. *Dcd* files can be open by many molecular visualization programs such as VMD.[121]

The most common error message during a SDEL run is "*Our momentum is* < 0." This occurs any time the potential energy is larger than the total energy during the optimization process. Changes of the annealing parameters or the value of γ often fix this problem.

Applications of the Stochastic Difference Equation in Length

The SDEL algorithm has been used to study the folding dynamics of several peptides and protein systems. In those applications the solvent environment was treated implicitly using the generalized Born model.[122,123] The algorithm was first applied to study the folding of the B domain fragment of the *Staphylococcal* protein A,[97] a 60-residue three-helical protein that has been studied by many groups using different computational strategies.[107] An experimental assessment of the transition state for this folding process highlights the difficulties of atomic simulations in capturing all the features observed in the experiment.[124] The results from SDEL were similar to those of high-temperature MD simulations, showing early formation of the most stable helix. The experiment indicates that the other two helices are more involved in the early folding, hinting that some energetic frustration may exist during the folding of this protein.[125]

SDEL was also used to study the coil-helix transition of an alanine-rich peptide,[98] the conformational transition of sugar puckering in deoxyadenosine,[126] polymerase P,[127] and the B-Z DNA transition.[128] The coil to helix study[98] exemplified several properties of SDEL trajectories, like the filtering of high-frequency modes and the preservation of thermodynamics properties for slow degrees of freedom when the trajectory resolution is decreased.

An interesting application of SDEL involved the folding mechanism of cytochrome c.[129] The folding kinetics of cytochrome c has been studied extensively by a variety of experimental techniques.[130–134] The SDEL folding trajectories agree with several experimental observations including: (1) the collapse of the protein without formation of secondary structures followed by formation of the terminal helices before the middle helix (see upper side of Figure 12),

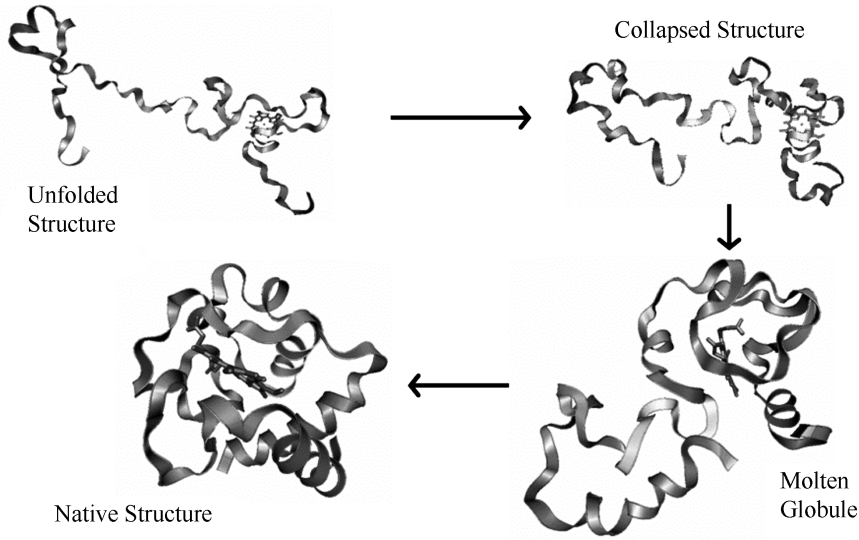

Figure 12 Ribbon view of cytochrome c at four different positions along one of the folding trajectories.

(2) subsequent formation of a molten globule conformation, the structural features of which (lower right side of Figure 12) are in agreement with fluorescence energy transfer experiments,[135] and (3) continued rearrangements prior to the protein folding to its native conformation (lower left side Figure 12).

The SDEL algorithm has also been used to study the folding of more complicated systems, such as the wild-type human Cu, Zn superoxide dismutase (SOD) dimer. SOD is a 153-residue, homodimeric, antioxidant enzyme that dismutates superoxide ion to hydrogen peroxide and oxygen.[136] It is an eight-strand, flattened, β-barrel protein with one copper and one zinc ion per monomer.[137] This protein is involved in the familial form of amyotrophic lateral sclerosis (FALS).

A 1.8-Å resolution Apo-SOD crystal structure (PDB 1HL4[138]) was used to generate SDEL trajectories of monomer folding and dimerization (Figure 13).[118] Initial analysis of a pair of trajectories showed a small population of folded but separated monomers. Interestingly, approximately 15–20% of each monomer's intrasubunit native contacts form when the subunit centers of mass are within a few angstroms of their equilibrium position, with the remaining native contacts forming when the monomers are farther away.

Recent Advances and Challenges

These applications, albeit focused on peptides and proteins, demonstrate the potential of the SDEL algorithm to study conformational dynamics of

Figure 13 Snapshots of SOD trajectory. The arrow indicates the direction of folding. The top structure is the initial unfolded conformation. The second structure is an intermediate structure in the trajectory with partial secondary structure formation. The bottom structure is the folded dimer. The monomer size and separation are not shown to scale to enhance clarity. The center-of-mass distances in the first two snapshots[121] are 280 and 50 Å greater than the equilibrium dimer distance, respectively. The disulfide bridge between Cys57 and Cys146 was conserved during the simulations.

large molecular systems at long time scales. This is the only algorithm from the methods discussed in this chapter that can be used to compute trajectories for complex processes that take milliseconds or longer, such as the folding of cytochrome c or the SOD dimer. Although the trajectories are approximate, they can provide structural data to explain experimental observations; if a more detailed and accurate description is required, snapshots taken from these SDEL trajectories can be used to extract thermodynamic information using MD, umbrella sampling, or replica exchange methodologies.

The major limitation of the SDEL algorithm is the inaccessibility of absolute times and computation of rates. A promising algorithm called milestoning

has been proposed recently to overcome this shortcoming.[139] This method computes a non-Markovian hopping between configuration space hyperplanes, the so-called milestones. The assumption being made is that there exists an equilibrium distribution on each milestone. The kinetics of a process is obtained by starting an equilibrium configuration on a milestone and measuring the time distribution needed to reach the forward or backward milestones using short MD simulations. These time distributions are then used to compute the global kinetics through a non-Markovian model. The algorithm needs a reaction coordinate to define the hyperplanes. That reaction coordinate can be an MEP or an SDEL trajectory. The equilibrium sampling is performed in the neighborhood of the curvilinear path describing the reaction coordinate. Milestoning can also be used to compute free energy profiles along reaction coordinates.[140,141] Milestoning makes the assumption that only one reaction coordinate (slow variable) exists in the system. The validity of the simulation results can be assessed by monitoring the rate as a function of the separation between the milestones, which can be changed from run to run.

A similar algorithm is partial path transition interface sampling (PPTIS).[142] This method is based on transition interface sampling (TIS),[64,68] which maps the phase space of the system with many interfaces (similar to the milestones) characterized by a one-dimensional reaction coordinate. In PPTIS rates are computed using a Markovian state model, i.e., by assuming a loss of correlation during interface hopping. This algorithm is aimed at computing the kinetics of two-state exponential process in equilibrium.

Use of milestoning or PPTIS may provide a way to recover the information that is lost when the high-frequency motions of the molecular system are filtered out by an SDEL trajectory. Hence, correct kinetic and thermodynamic properties might be extracted from the simulations. For very long and diffusive processes, like those associated with the folding of large proteins, computation of these properties will still be challenging because the transitions between hyperplanes or interfaces require longer MD simulations. At that point, a combination of MTS with these path methods could be used to improve efficiency and speed.

CONCLUSION

Computational methods used to extend the time scale of atomically detailed simulations have improved in the last 15 years. Accurate MTS simulations, with computational gains up to a factor of 10, have extended the applicability of molecular dynamics simulations and refinements in the computation of medium-range forces could provide stable results with increasing speedups. It is apparent that stability limitations will prevent the extension of these algorithms to the range of time scales that are needed to study many processes of interest, however. On the other hand, reaction path approaches can be used

to extend those time scales by using different simplifying assumptions and approximations including, for example, two-state transitions, equilibrium distributions along the path, or, removal of high-frequency motions. Therefore, path methodologies can extend the range of application of computer simulation, but they do so with loss of accuracy and dynamical information when compared with normal and MTS molecular dynamics simulations. Some path techniques utilize MD to compute rate constants and to recover part of the dynamical properties that have been filtered out. Use of MTS should improve the efficiency and practicality of these calculations in the future.

APPENDIX: MATLAB SCRIPTS FOR THE MTS TUTORIAL

```
function [t,x,v,eout]=dyntwowaters(h,nstep,x0,v0,
  tau,method)

%[t,x,v,eout]=dyntwowaters(h,nstep,x0,v0,tau,
  method)

% Dynamics front-end for model system introduced in
  Cardenas & Barth 2007

%INPUT ARGUMENTS, with some values used in Cardenas
  &Barth

% h  timestep, h=0.01
% nstep  number of integration steps
% x0 init. postions, x0=[0 0 0.95 0 0 0.95 5 -1.0 4.05 -1 5
  -0.05]'
% v0  vector of initial atom velocities, v0=zeros
  (12,1)
% tau  number of steps between slow force evaluations
% method  string specifies integration method, 'v',
  'i','b','e'

%OUTPUT ARGUMENTS
% t  vector of time values
% x  trajectory of positions
% v  trajectory of velocities
% eout  energy along computed trajectory
%
%Eric Barth
%Kalamazoo College, 2007
```

```
M1=[15.994 1.008 1.008]';
M2=kron(M1,ones(2,1));
M=[M2;M2];
gamma=.1;
temp=300;
rand('state',0)
if method(1)=='v',  %Velocity Verlet method
    [t,x,v,eout]=vv('twowaters',h,nstep,x0,v0,M);
elseif method(1)=='i',  %Impulse MTS method
    [t,x,v,eout]=impulsemts('twowaters',h,tau,
 nstep,x0,v0,M);
elseif method(1)=='b'  %Langevin Dynamics
    [t,x,v,eout]=bbk1('twowaters',h,nstep,x0,v0,M,
 gamma,temp);
elseif method(1)=='e'  %Force Extrapolation MTS with
 Langevin Dynamics
    [t,x,v,eout]=extrapmts('twowaters',h,nstep,x0,
 v0,M,tau,gamma,temp);
else
    disp('unrecognized method specification')
end
%%%%%%%%%%end of function %%%%%%%%%%%%%%%%%%%%%%


function [t,x,v,eout]=vv(fun,h,nstep,x0,v0,M);

%[t,x,v,eout]=vv(fun,h,nstep,x0,v0,M);
% velocity Verlet integrator
%
%INPUT ARGUMENTS
% fun  string containing file name of energy and force
 routine
% h  timestep
% nstep  number of steps
% x0  vector of initial atom positions
% v0  vector of initial atom velocities
% M  vector of atomic masses

%OUTPUT ARGUMENTS
% t  vector of time values
% x  trajectory of positions
% v  trajectory of velocities
% eout  energy along computed trajectory
%
%Eric Barth
%Kalamazoo College, 2007
```

```
n=length(x0);
t=0:h:h*nstep;
x=zeros(n,nstep+1);
v=zeros(n,nstep+1);
eout=zeros(1,nstep+1);
x(:,1)=x0;
v(:,1)=v0;
[e,f]=feval(fun,x0);
eout(1)=e+.5*sum(M.*v0.*v0);
for i=1:nstep
    vhalf=v(:,i)+(h/2)*f./M;
    x(:,i+1)=x(:,i)+h*vhalf;
    [e,f]=feval(fun,x(:,i+1));
    v(:,i+1)=vhalf+(h/2)*f./M;
    eout(i+1)=e+.5*sum(M.*v(:,i+1).*v(:,i+1));
end
%%%%%%%%%%end of function %%%%%%%%%%%%%%%%%%%%%%


function [t,x,v,eout]=impulsemts(fun,h,tau,nstep,
 x0,v0,M);

%[t,x,v,eout]=vv(fun,h,tau,nstep,x0,v0,M);
% impulse MTS integrator
%
%INPUT ARGUMENTS
% fun  string containing file name of energy and force
 routine
% h  timestep
% tau  number of steps between slow force evaluations
% nstep  number of steps
% x0  vector of initial atom positions
% v0  vector of initial atom velocities
% M  vector of atomic masses

%OUTPUT ARGUMENTS
% t  vector of time values
% x  trajectory of positions
% v  trajectory of velocities
% eout  energy along computed trajectory
%
%Eric Barth
%Kalamazoo College, 2007
n=length(x0);
t=0:tau*h:tau*h*nstep;
x=zeros(n,nstep+1);
v=zeros(n,nstep+1);
```

```
eout=zeros(1,nstep+1);
x(:,1)=x0;
v(:,1)=v0;
[e,f,ffast,fslow]=feval(fun,x0,0);
eout(1)=e+.5*sum(M.*v0.*v0);
for i=1:nstep
    xx=x(:,i);
    vv = v(:,i)+(tau*h/2)*fslow./M;
    for j=1:tau
        vv = vv+(h/2)*ffast./M;
        xx=xx+h*vv;
        [e,f,ffast,fslow]=feval(fun,xx,1);
        vv = vv+(h/2)*ffast./M;
    end
    x(:,i+1)=xx;
    [e,f,ffast,fslow]=feval(fun,xx,0);
    v(:,i+1)= vv+(tau*h/2)*fslow./M;
    eout(i+1)=e+.5*sum(M.*v(:,i+1).*v(:,i+1));
end
%%%%%%%%%%end of function %%%%%%%%%%%%%%%%%%%%%%%


function [t,x,v,eout]=bbk1(fun,h,nstep,x0,v0,M,
  gamma,temp);
%[t,x,v,eout]=bbk1(fun,h,nstep,x0,v0,M,gamma,
  temp);
% Langevin dynamics integrator
%
%INPUT ARGUMENTS
% fun  string containing file name of energy and force
  routine
% h  timestep
% nstep  number of steps
% x0  vector of initial atom positions
% v0  vector of initial atom velocities
% M  vector of atomic masses
% gamma  Langevin friction parameter
% temp  target temperature for Langevin dynamics

%OUTPUT ARGUMENTS
% t  vector of time values
% x  trajectory of positions
% v  trajectory of velocities
% eout  energy along computed trajectory
%
%Eric Barth
%Kalamazoo College, 2007
```

```
n=length(x0);
t=0:h:h*nstep;
x=zeros(n,nstep+1);
v=zeros(n,nstep+1);
eout=zeros(1,nstep+1);
x(:,1)=x0;
v(:,1)=v0;


[e,f]=feval(fun,x0);

eout(1)=e+.5*sum(M.*v0.*v0);
for i=1:nstep
    rf=dynlang1(n,gamma,temp,h,M);
    f=f-rf;
    vhalf=(v(:,i) +(h/2)*f./M)/(1+h/2*gamma);
    x(:,i+1)=x(:,i)+h*vhalf;
    [e,f]=feval(fun,x(:,i+1));
    f=f-rf;
    v(:,i+1)=vhalf*(1-h/2*gamma)+(h/2)*f./M;
    eout(i+1)=e+.5*sum(M.*v(:,i+1).*v(:,i+1));
end
%%%%%%%%%%end of function %%%%%%%%%%%%%%%%%%%%%%


function [t,x,v,eout]=extrapmts(fun,h,nstep,x0,v0,
  M,tau,gamma,temp);
%[t,x,v,eout]=extrapmts(fun,h,nstep,x0,v0,M,tau,
  gamma,temp);
% Force Extrapolation Langevin dynamics MTS integrator
%
%INPUT ARGUMENTS
% fun  string containing file name of energy and force
  routine
% h  timestep
% nstep  number of steps
% x0  vector of initial atom positions
% v0  vector of initial atom velocities
% M  vector of atomic masses
% tau  number of steps between slow force updates
% gamma  Langevin friction parameter
% temp  target temperature for Langevin dynamics

%OUTPUT ARGUMENTS
% t  vector of time values
% x  trajectory of positions
```

```
% v  trajectory of velocities
% eout  energy along computed trajectory
%
%Eric Barth
%Kalamazoo College, 2007

n=length(x0);
t=0:h:h*nstep;
x=zeros(n,nstep+1);
v=zeros(n,nstep+1);
eout=zeros(1,nstep+1);
x(:,1)=x0;
v(:,1)=v0;


[e,f,ffast,fslow]=feval(fun,x0,0);
%eout(1)=e+.5*sum(M.*v0.*v0);
eout(1)=e;
for i=1:nstep
    xx=x(:,i);
    vv=v(:,i);
    for j=1:tau
        rf=dynlang1(n,gamma,temp,h,M);
        fext=ffast+fslow-rf;
        vv=(vv +(h/2)*fext./M)/(1+h/2*gamma);
        xx=xx+h*vv;
        if (j==ceil(tau/2)),
          [e,f,ffast,fslow]=feval(fun,xx,0);
        else
          [e,f,ffast,fdum]=feval(fun,xx,1);
    end
    fext=ffast+fslow-rf;
    vv=vv*(1-(h/2)*gamma)+(h/2)*fext./M;
    end
    x(:,i+1)=xx;
    v(:,i+1)=vv;
    eout(i+1)=e; %report only the bond energy
    %[e,f,ffast,fslow]=feval(fun,xx,0);
end

%%%%%%%%%%end of function %%%%%%%%%%%%%%%%%%%%%%%


function [e,f,ffast,fslow]=twowaters(x,splitflag);

%[e,f,ffast,fslow]=twowaters(x,splitflag);
%Energy and Force routine used by integration methods
```

```
%
%INPUT ARGUMENTS
% x  vector of atom positions
% splitflag 0→all forces, 1→fast forces, 2→slow
  forces

%OUTPUT ARGUMENTS
% e  potential energy at for coordinate vector x
% f  total force vector
% ffast  vector of fast forces
% fslow  vector of slow forces
%
%Eric Barth
%Kalamazoo College, 2007

if nargin<2
    splitflag=0;
end;
f=zeros(12,1);
ffast=zeros(12,1);
fslow=zeros(12,1);
e=0;

if (splitflag==0 |splitflag==1),
    [e1,ffast(1:6)]=water2D(x(1:6));
    [e2,ffast(7:12)]=water2D(x(7:12));
    e=e+e1+e2;
    f=f+ffast;
end

if (splitflag==0 | splitflag==2),
    %now the electrostatics;
    qh=0.417;
    qo=-0.834;

    o1=x(1:2);
    h11=x(3:4);
    h12=x(5:6);
    o2=x(7:8);
    h21=x(9:10);
    h22=x(11:12);

    d=h11-h21;
    d2=sum(d.*d);
    e=e+qh*qh/sqrt(d2);
    fslow(3:4)=fslow(3:4)+qh*qh/d2^(3/2)*d;
    fslow(9:10)=fslow(9:10)-qh*qh*d/d2^(3/2);
```

```
d=h11-h22;
d2=sum(d.*d);
e=e+qh*qh/sqrt(d2);
fslow(3:4)=fslow(3:4)+qh*qh*d/d2^(3/2);
fslow(11:12)=fslow(11:12)-qh*qh*d/d2^(3/2);


d=h11-o2;
d2=sum(d.*d);
e=e+qh*qo/sqrt(d2);
fslow(3:4)=fslow(3:4)+qh*qo*d/d2^(3/2);
%o2 is fixed so no corresponding term for fslow
(7:8)

d=h12-h21;
d2=sum(d.*d);
e=e+qh*qh/sqrt(d2);
fslow(5:6)=fslow(5:6)+qh*qh*d/d2^(3/2);
fslow(9:10)=fslow(9:10)-qh*qh*d/d2^(3/2);

d=h12-h22;
d2=sum(d.*d);
e=e+qh*qh/sqrt(d2);
fslow(5:6)=fslow(5:6)+qh*qh*d/d2^(3/2);
fslow(11:12)=fslow(11:12)-qh*qh*d/d2^(3/2);

d=h12-o2;
d2=sum(d.*d);
e=e+qh*qo/sqrt(d2);
fslow(5:6)=fslow(5:6)+qh*qo*d/d2^(3/2);
%o2 is fixed so no corresponding term for fslow
(7:8)

d=h21-o1;
d2=sum(d.*d);
e=e+qh*qo/sqrt(d2);
fslow(9:10)=fslow(9:10)+qh*qo*d/d2^(3/2);
%o1 is fixed so no corresponding term for fslow
(1:2)

d=h22-o1;
d2=sum(d.*d);
e=e+qh*qo/sqrt(d2);
fslow(11:12)=fslow(11:12)+qh*qo*d/d2^(3/2);
%o1 is fixed so no corresponding term for fslow
(1:2)
```

```
    d=o1-o2;
    d2=sum(d.*d);
    e=e+qo*qo/sqrt(d2);
    %o1 is fixed so no corresponding term for fslow
    (1:2)
    %o2 is fixed so no corresponding term for fslow
    (7:8)

    f=f+fslow;
end
%%%%%%%%%%end of function%%%%%%%%%%%%%%%%%%%%%%%


function r=dynlang1(n,gamma,Temp,h,m);

% r=dynlang1(n,gamma,Temp,h,m);
% Langevin dynamics random forces, modified for two
   fixed atoms
%
%INPUT ARGUMENTS
% n  number of degrees of freedom
% gamma  Langevin friction parameter
% Temp  target temperature for Langevin dynamics
% h  timestep


%OUTPUT ARGUMENTS
% r random force vector
%
%Eric Barth
%Kalamazoo College, 2007


n=n-4;
m=m([3:6,9:12]);


kB=1.987191e-03;
r=randn(n,1);
r=r*sqrt(2*gamma*kB*Temp/h);
r=sqrt(m).*r;

r=[0;0;r(1:4);0;0;r(5:8)];


%%%%%%%%%%end of function%%%%%%%%%%%%%%%%%%%%%%%

%Matlab script to compute dipole angle ''theta'' from
%trajectory of positions ''x''
%
```

```
%Eric Barth
%Kalamazoo College, 2007

xc=x(9:10,:)+x(11:12,:);
xcn=sum(xc.^2);
theta=(acos(xc(1,:)./sqrt(xcn)));
%%%%%%%%%%end of script %%%%%%%%%%%%%%%%%%%%%%


function [freq,pp]=powerspectrum(data,N,h);

%[freq,pp]=powerspectrum(data,N,h);
% display data with
%      >>plot(freq,pp)
%Compute power spectrum
%Input Arguments
% data  time series data
% N  number of steps in data
% h  timestep of data
%
%Output Arguments
% freq  vector of frequencies
% pp  vector of power spectra
%
%Eric Barth
%Kalamazoo College, 2007
timfac=48.88826;  %specific to akma MD model
T=timfac*h*N;
freq = [0:N/2-1]/T;
p = abs(fft(data))/(N/2);
pp = p(1:N/2).^2;
%%%%%%%%%%end of function %%%%%%%%%%%%%%%%%%%%%%
```

ACKNOWLEDGMENT

This chapter is based in part upon work supported by the National Science Foundation under Grant No. 0447294 to A.E.C. The same author would like to acknowledge the use of the services provided by Research Computing, University of South Florida, and the help of Shawn Hamm and Adam Clarke with some of the figures.

REFERENCES

1. A. Rahman, *Phys. Rev. A*, **136**, 405 (1964). Correlations in the Motion of Atoms in Liquid Argon.
2. L. Verlet, *Phys. Rev.*, **159**, 98 (1967). Computer "Experiments" on Classical Fluids, page 99.
3. A. Rahman and F. H. Stillinger, *J. Chem. Phys.*, **55**, 3336 (1971). Molecular Dynamics Study of Liquid Water.

4. J. P. Ryckaert, G. Ciccotti, and H. J. C. Berendsen, *J. Comput. Phys.*, **23**, 327 (1977). Numerical Integration of the Cartesian Equations of Motion of a System with Constraints: Molecular Dynamics of n-Alkanes.
5. J. A. McCammon, B. R. Gelin, and M. Karplus, *Nature*, **267**, 585 (1977). Dynamics of Folded Proteins.
6. R. D. Ruth, *IEEE Trans. Nucl. Sci.*, **30**, 2669 (1983). A Canonical Integration Technique.
7. G. Benettin and A. Giorgilli, *J. Statist. Phys.*, **74**, 1117 (1994). On the Hamiltonian Interpolation of near-to-the Identity Symplectic Mappings with Application to Symplectic Integration Algorithms.
8. E. Hairer, *Ann. Numer. Math.*, **1**, 107 (1994). Backward Analysis of Numerical Integrators and Symplectic Methods.
9. J. M. Sanz-Serna and M. P. Calvo, *Numerical Hamiltonian Problems*, Chapman and Hall, London, 1994.
10. R. J. Loncharich, B. R. Brooks, and R. W. Pastor, *Biopolymers*, **21**, 523 (1992). Langevin Dynamics of Peptides: The Frictional Dependence of Isomerization Rates of *N*-Acetylalanyl-*N*′-Methylamide.
11. A. Brunger, C. L. Brooks, and M. Karplus, *Chem. Phys. Lett.*, **105**, 495 (1982). Stochastic Boundary Conditions for Molecular Dynamics Simulations of ST2 Water.
12. B. R. Brooks, R. E. Bruccoleri, B. D. Olafson, D. J. States, S. Swaminathan, and M. Karplus, *J. Comput. Chem.*, **4**, 187 (1983). CHARMM: A Program for Macromolecular Energy, Minimization, and Dynamics Calculations.
13. A. D. MacKerell Jr., D. Bashford, M. Bellott, R. L. Dunbrack Jr., J. Evanseck, M. J. Field, S. Fischer, J. Gao, H. Guo, S. Ha, D. Joseph, L. Kuchnir, K. Kuczera, F. T. K. Lau, C. Mattos, S. Michnick, T. Ngo, D. T. Nguyen, B. Prodhom, W. E. Reiher III, B. Roux, M. Schlenkrich, J. Smith, R. Stote, J. Straub, M. Watanabe, J. Wiorkiewicz-Kuczera, D. Yin, and M. Karplus, *J. Phys. Chem.*, **102**, 3586 (1998). An All-Atom Empirical Potential for Molecular Modeling and Dynamics Studies of Proteins.
14. S. J. Weiner, P. A. Kollman, D. T. Nguyen, and D. A. Case, *J. Comput. Chem.*, **7**, 230 (1986). An All Atom Force Field for Simulations of Proteins and Nucleic Acids.
15. W. D. Cornell, P. Cieplak, C. I. Bayly, I. R. Gould, K. M. Merz Jr., D. M. Ferguson, D. C. Spellmeyer, T. Fox, J. W. Caldwell, and P. A. Kollman, *J. Am. Chem. Soc.*, **117**, 5179 (1995). A Second Generation Force Field for the Simulation of Proteins and Nucleic Acids.
16. W. L. Jorgensen and J. Tirado-Rives, *J. Am. Chem. Soc.*, **1988**, 1657 (1988). The OPLS Potential Functions for Proteins. Energy Minimization for Crystals of Cyclic Peptides and Crambin.
17. J. P. Bowen and N. L. Allinger, in *Reviews in Computational Chemistry*, K. B. Lipkowitz and D. B. Boyd, Eds., VCH, Weinheim, 1991, Vol. 2, pp. 81–97. Molecular Mechanics: The Art and Science of Parameterization.
18. U. Dinur and A. T. Hagler, in *Reviews in Computational Chemistry*, K. B. Lipkowitz and D. B. Boyd, Eds., VCH, Weinheim, 1991, Vol. 2, pp. 99–164. New Approaches to Empirical Force Fields.
19. C. R. Landis, D. M. Root, and T. Cleveland, in *Reviews in Computational Chemistry*, K. B. Lipkowitz and D. B. Boyd, Eds., VCH, Weinheim, 1995, Vol. 6, pp. 73–148. Molecular Mechanics Force Fields for Modeling Inorganic and Organometallic Compounds.
20. S. L. Price, in *Reviews in Computational Chemistry*, K. B. Lipkowitz and D. B. Boyd, Eds., Wiley-VCH, New York, 2000, Vol. 14, pp. 225–289. Towards More Accurate Intermolecular Potentials for Organic Molecules.
21. E. Barth, B. Leimkuhler, and S. Reich, *Lecture Notes in Computational Science and Engineering*, **24**, 73 (2002). A Test Set for Molecular Dynamics.
22. T. Schlick, in *Reviews in Computational Chemistry*, K. B. Lipkowitz and D. B. Boyd, Eds., VCH, Weinheim, 1992, Vol. 3, pp. 1–71. Optimization Methods in Computational Chemistry.

23. A. R. Leach, in *Reviews in Computational Chemistry*, K. B. Lipkowitz and D. B. Boyd, Eds., VCH, Weinheim, 1991, Vol. 2, pp. 1–55. A Survey of Methods for Searching the Conformational Space of Small and Medium-Sized Molecules.
24. W. B. Streett, D. J. Tildesley, and G. Saville, *Mol. Phys.*, **35**, 639 (1978). Multiple Time Step Methods in Molecular Dynamics.
25. R. R. Gabdoulline and C. Zheng, *J. Comput. Chem.*, **16**, 1428 (1995). Effects of the Cutoff Center on the Mean Potential and Pair Distribution Functions in Liquid Water.
26. M. Saito, *J. Chem. Phys.*, **101**, 4055 (1994). Molecular Dynamics Simulations of Proteins in Solution: Artifacts Caused by the Cutoff Approximation.
27. H. Grubmüller, H. Heller, A. Windemuth, and K. Schulten, *Mol. Sim.*, **6**, 121 (1991). Generalized Verlet Algorithm for Efficient Molecular Dynamics Simulations with Long-Range Interactions.
28. M. Tuckerman, B. J. Berne, and G. J. Martyna, *J. Chem. Phys.*, **97**, 1990 (1992). Reversible Multiple Time Scale Molecular Dynamics.
29. R. Zhou and B. J. Berne, *J. Chem. Phys.*, **103**, 9444 (1995). A New Molecular Dynamics Method Combining the Reference System Propagator Algorithm with a Fast Multipole Method for Simulating Proteins and Other Complex Systems.
30. M. Watanabe and M. Karplus, *J. Phys. Chem.*, **99**, 5680 (1995). Simulations of Macromolecules by Multiple Time-Step Methods.
31. J. J. Biesiadecki and R. D. Skeel, *J. Comput. Phys.*, **109**, 318 (1993). Dangers of Multiple Time Step Methods.
32. T. Bishop, R. D. Skeel, and K. Schulten, *J. Comput. Chem.*, **18**, 1785 (1997). Difficulties with Multiple Time Stepping and the Fast Multipole Algorithm in Molecular Dynamics.
33. Q. Ma, J. A. Izaguirre, and R. D. Skeel, *SIAM J. Sci. Comput.*, **24**, 1951 (2003). Verlet-I/R-Respa Is Limited by Nonlinear Instability.
34. T. Schlick, M. Mandziuk, R. D. Skeel, and K. Srinivas, *J. Comput. Phys.*, **139**, 1 (1998). Nonlinear Resonance Artifacts in Molecular Dynamics Simulations.
35. T. Schlick, E. Barth, and M. Mandziuk, *Ann. Rev. Biophys. Biomol. Struct.*, **26**, 179 (1997). Biomolecular Dynamics at Long Timesteps: Bridging the Timescale Gap between Simulation and Experimentation.
36. J. A. Izaguirre, S. Reich, and R. D. Skeel, *J. Chem. Phys.*, **110**, 9853 (1999). Longer Time Steps for Molecular Dynamics.
37. J. A. Izaguirre, Q. Ma, T. Matthey, J. Willcock, T. Slabach, B. Moore, and G. Viamontes, *Lecture Notes in Computational Science and Engineering (LNCSE)*, **24**, 146 (2002). Overcoming Instabilities in Verlet-I/R-Respa with the Mollified Impulse Method.
38. E. Barth and T. Schlick, *J. Chem. Phys.*, **109**, 1633 (1998). Extrapolation Versus Impulse in Multiple-Timestepping Schemes: Linear Analysis and Applications to Newtonian and Langevin Dynamics.
39. E. Barth and T. Schlick, *J. Chem. Phys.*, **109**, 1617 (1998). Overcoming Stability Limitations in Biomolecular Dynamics: Combining Force Splitting via Extrapolation with Langevin Dynamics in Ln.
40. A. Sandu and T. Schlick, *J. Comput. Phys.*, **151**, 74 (1999). Masking Resonance Artifacts in Force-Splitting Methods for Biomolecular Simulations by Extrapolative Langevin Dynamics.
41. M. P. Allen and D. J. Tildesley, *Computer Simulation of Liquids*, Oxford Science, Oxford, UK, 1987.
42. C. S. Peskin and T. Schlick, *Commun. Pure Appl. Math.*, **42**, 1001 (1989). Molecular Dynamics by the Backwards-Euler Method.
43. G. Zhang and T. Schlick, *J. Comput. Chem.*, **14**, 1212 (1993). Lin: A New Algorithm Combining Implicit Integration and Normal Mode Techniques for Molecular Dynamics.
44. J. A. Izaguirre, D. P. Catarello, J. M. Wozniak, and R. D. Skeel, *J. Chem. Phys.*, **114**, 2090 (2001). Langevin Stabilization of Molecular Dynamics.

45. Q. Ma and J. A. Izaguirre, in *Proceedings of the 2003 ACM Symposium on Applied Computing*, ACM, 2003, pp. 178–182. Long Time Step Molecular Dynamics Using Targeted Langevin Stabilization.

46. R. D. Skeel and J. A. Izaguirre, *Mol. Phys.*, **100**, 3885 (2002). An Impulse Integrator for Langevin Dynamics.

47. J. A. Izaguirre, in *Multiscale Computational Methods in Chemistry and Physics*, A. Brandt, K. Binder, and J. Bernholc, Eds., IOS Press, Amsterdam, 2001, Vol. 177, pp. 34–47. Langevin Stabilization of Multiscale Mollified Molecular Dynamics.

48. T. Schlick and L. Yang, in *Multiscale Computational Methods in Chemistry and Physics*, A. Brandt, J. Bernholc, and K. Binder, Eds., Amsterdam, 2001, Vol. 177, pp. 293–305. Long-Timestep Biomolecular Dynamics Simulations: Ln Performance on a Polymerase Beta / DNA System.

49. L. Greengard and V. Rokhlin, *J. Comput. Phys.*, **73**, 325 (1987). A Fast Algorithm for Particle Simulations.

50. A. W. Appel, *SIAM J. Sci. Stat. Comput.*, **6**, 85 (1985). An Efficient Program for Many-Body Simulations.

51. J. Barnes and P. Hut, *Nature*, **324**, 446 (1986). A Hierarchical $O(N \log N)$ Force Calculation Algorithm.

52. Z.-H. Duan and R. Krasny, *J. Comput. Chem.*, **21**, 1 (2000). An Adaptive Treecode for Computing Nonbonded Potential Energy in Classical Molecular Systems.

53. T. Darden, D. York, and L. Pedersen, *J. Chem. Phys.*, **98**, 10089 (1993). Particle Mesh Ewald: An $N*\log(N)$ Method for Computing Ewald Sums.

54. Z.-H. Duan and R. Krasny, *J. Chem. Phys.*, **113**, 3492 (2000). An Ewald Summation Based Multipole Method.

55. R. W. Hockney and J. W. Eastwood, *Computer Simulation Using Particles*, McGraw-Hill, New York, 1981.

56. P. Procacci and M. Marchi, *J. Chem. Phys.*, **104**, 3003 (1996). Taming the Ewald Sum in Molecular Dynamics Simulations of Solvated Proteins via a Multiple Time Step Algorithm.

57. X. Qian and T. Schlick, *J. Chem. Phys.*, **116**, 5971 (2002). Efficient Multiple Timestep Integrators with Distance-Based Force Splitting for Particle-Mesh-Ewald Molecular Dynamics Simulations.

58. D. Barash, L. Yang, X. Qian, and T. Schlick, *J. Comput. Chem.*, **24**, 77 (2003). Inherent Speedup Limitations in Multiple Timestep Particle Mesh Ewald Algorithms.

59. T. Hansson, C. Oostenbrink, and W. F. van Gunsteren, *Curr. Opin. Struct. Biol.*, **12**, 190 (2002). Molecular Dynamics Simulations.

60. M. Karplus, *Acc. Chem. Res.*, **35**, 321 (2002). Molecular Dynamics Simulations of Biomolecules.

61. M. Karplus and J. Kuriyan, *Proc. Natl. Acad. Sci. U.S.A.*, **102**, 6679 (2005). Molecular Dynamics and Protein Function.

62. P. G. Bolhuis, D. Chandler, C. Dellago, and P. L. Geissler, *Annu. Rev. Phys. Chem.*, **53**, 291 (2002). Transition Path Sampling: Throwing Ropes over Rough Mountain Passes, in the Dark.

63. P. G. Bolhuis, C. Dellago, and D. Chandler, *Faraday Discuss.*, 421 (1998). Sampling Ensembles of Deterministic Transition Pathways.

64. T. S. van Erp, D. Moroni, and P. G. Bolhuis, *J. Chem. Phys.*, **118**, 7762 (2003). A Novel Path Sampling Method for the Calculation of Rate Constants.

65. P. G. Bolhuis, *Proc. Natl. Acad. Sci. U.S.A.*, **100**, 12129 (2003). Transition-Path Sampling of Beta-Hairpin Folding.

66. T. S. van Erp and P. G. Bolhuis, *J. Comput. Phys.*, **205**, 157 (2005). Elaborating Transition Interface Sampling Methods.

67. P. G. Bolhuis, *J. Phys.: Condens. Mat.*, **15**, S113 (2003). Transition Path Sampling on Diffusive Barriers.

68. P. G. Bolhuis, *Biophys. J.*, **88**, 50 (2005). Kinetic Pathways of Beta-Hairpin (Un)Folding in Explicit Solvent.

69. C. Dellago, P. G. Bolhuis, F. S. Csajka, and D. Chandler, *J. Chem. Phys.*, **108**, 1964 (1998). Transition Path Sampling and the Calculation of Rate Constants.

70. J. Juraszek and P. G. Bolhuis, *Proc. Natl. Acad. Sci. U.S.A.*, **103**, 15859 (2006). Sampling the Multiple Folding Mechanisms of Trp-Cage in Explicit Solvent.

71. P. G. Bolhuis and D. Chandler, *J. Chem. Phys.*, **113**, 8154 (2000). Transition Path Sampling of Cavitation between Molecular Scale Solvophobic Surfaces.

72. C. Dellago, P. G. Bolhuis, and D. Chandler, *J. Chem. Phys.*, **108**, 9236 (1998). Efficient Transition Path Sampling: Application to Lennard-Jones Cluster Rearrangements.

73. M. F. Hagan, A. R. Dinner, D. Chandler, and A. K. Chakraborty, *Proc. Natl. Acad. Sci. U.S. A.*, **100**, 13922 (2003). Atomistic Understanding of Kinetic Pathways for Single Base-Pair Binding and Unbinding in DNA.

74. P. L. Geissler, C. Dellago, and D. Chandler, *Phys. Chem. Chem. Phys.*, **1**, 1317 (1999). Chemical Dynamics of the Protonated Water Trimer Analyzed by Transition Path Sampling.

75. R. Radhakrishnan and T. Schlick, *Proc. Natl. Acad. Sci. U.S.A.*, **101**, 5970 (2004). Orchestration of Cooperative Events in DNA Synthesis and Repair Mechanism Unraveled by Transition Path Sampling of DNA Polymerase Beta's Closing.

76. M. Berkowitz, J. D. Morgan, J. A. McCammon, and S. H. Northrup, *J. Chem. Phys.*, **79**, 5563 (1983). Diffusion-Controlled Reactions: A Variational Formula for the Optimum Reaction Coordinate.

77. R. Czerminski and R. Elber, *Int. J. Quantum Chem.*, **38**, 167 (1990). Self-Avoiding Walk between 2 Fixed-Points as a Tool to Calculate Reaction Paths in Large Molecular-Systems.

78. S. H. Huo and J. E. Straub, *J. Chem. Phys.*, **107**, 5000 (1997). The Maxflux Algorithm for Calculating Variationally Optimized Reaction Paths for Conformational Transitions in Many Body Systems at Finite Temperature.

79. J. E. Straub, J. Guevara, S. H. Huo, and J. P. Lee, *Acc. Chem. Res.*, **35**, 473 (2002). Long Time Dynamic Simulations: Exploring the Folding Pathways of an Alzheimer's Amyloid A_{β}-Peptide.

80. H. Jónsson, G. Mills, and W. Jacobsen, in *Classical and Quantum Dynamics in Condensed Phase Simulations*, B. J. Berne, G. Ciccotti, and D. F. Coker, Eds., World Scientific, Singapore, 1998, pp. 385–404. Nudged Elastic Band Method for Finding Minimum Energy Paths of Transition.

81. R. Crehuet and M. J. Field, *J. Chem. Phys.*, **118**, 9563 (2003). A Temperature-Dependent Nudged-Elastic-Band Algorithm.

82. R. Crehuet, A. Thomas, and M. J. Field, *J. Mol. Graph. Model.*, **24**, 102 (2005). An Implementation of the Nudged Elastic Band Algorithm and Application to the Reaction Mechanism of HGXPRTase from *Plasmodium Falciparum*.

83. D. A. Evans and D. J. Wales, *J. Chem. Phys.*, **119**, 9947 (2003). The Free Energy Landscape and Dynamics of Met-Enkephalin.

84. D. A. Evans and D. J. Wales, *J. Chem. Phys.*, **121**, 1080 (2004). Folding of the Gb1 Hairpin Peptide from Discrete Path Sampling.

85. D. J. Wales, *Int. Rev. Phys. Chem.*, **25**, 237 (2006). Energy Landscapes: Calculating Pathways and Rates.

86. D. J. Wales and T. V. Bogdan, *J. Phys. Chem. B*, **110**, 20765 (2006). Potential Energy and Free Energy Landscapes.

87. D. J. Wales, *Mol. Phys.*, **100**, 3285 (2002). Discrete Path Sampling.

88. G. Henkelman, G. Johannesson, and H. Jónsson, in *Theoretical Methods in Condensed Phase Chemistry*, S. D. Schwartz, Ed. Kluwer Academic, Dordrecht, 2000, Vol. 5, pp. 269–300. Methods for Finding Saddle Points and Minimum Energy Paths.

89. S. A. Trygubenko and D. J. Wales, *J. Chem. Phys.*, **120**, 2082 (2004). A Doubly Nudged Elastic Band Method for Finding Transition States.

90. W. E, W. Ren, and E. Vanden-Eijnden, *J. Phys. Chem. B*, **109**, 6688 (2005). Finite Temperature String Method for the Study of Rare Events.

91. W. E, W. Ren, and E. Vanden-Eijnden, *Chem. Phys. Lett.*, **413**, 242 (2005). Transition Pathways in Complex Systems: Reaction Coordinates, Isocommittor Surfaces, and Transition Tubes.

92. W. Ren, E. Vanden-Eijnden, P. Maragakis, and W. E, *J. Chem. Phys.*, **123**, 134109 (2005). Transition Pathways in Complex Systems: Application of the Finite-Temperature String Method to the Alanine Dipeptide.

93. L. Maragliano, A. Fischer, E. Vanden-Eijnden, and G. Ciccotti, *J. Chem. Phys.*, **125**, 024106 (2006). String Method in Collective Variables: Minimum Free Energy Paths and Isocommittor Surfaces.

94. L. Maragliano and E. Vanden-Eijnden, *Chem. Phys. Lett.*, **426**, 168 (2006). A Temperature Accelerated Method for Sampling Free Energy and Determining Reaction Pathways in Rare Events Simulations.

95. W. E and E. Vanden-Eijnden, *J. Stat. Phys.*, **123**, 503 (2006). Towards a Theory of Transition Paths.

96. P. Metzner, C. Schutte, and E. Vanden-Eijnden, *J. Chem. Phys.*, **125**, 084110 (2006). Illustration of Transition Path Theory on a Collection of Simple Examples.

97. R. Elber, A. Ghosh, and A. Cardenas, in *Bridging the Time Scale Gap*, P. Nielaba, M. Mareschal, and G. Ciccotti, Eds., Springer, Berlin, 2002, pp. 335–365. Stochastic Difference Equation as a Tool to Compute Long Time Dynamics.

98. A. E. Cardenas and R. Elber, *Biophys. J.*, **85**, 2919 (2003). Atomically Detailed Simulations of Helix Formation with the Stochastic Difference Equation.

99. S. Machlup and L. Onsager, *Phys. Rev.*, **91**, 1512 (1953). Fluctuations and Irreversible Process. 2. Systems with Kinetic Energy.

100. L. Onsager and S. Machlup, *Phys. Rev.*, **91**, 1505 (1953). Fluctuations and Irreversible Processes.

101. R. Elber, J. Meller, and R. Olender, *J. Phys. Chem. B*, **103**, 899 (1999). Stochastic Path Approach to Compute Atomically Detailed Trajectories: Application to the Folding of C Peptide.

102. R. Olender and R. Elber, *J. Chem. Phys.*, **105**, 9299 (1996). Calculation of Classical Trajectories with a Very Large Time Step: Formalism and Numerical Examples.

103. K. Siva and R. Elber, *Proteins: Struct., Funct., Genet.*, **50**, 63 (2003). Ion Permeation through the Gramicidin Channel: Atomically Detailed Modeling by the Stochastic Difference Equation.

104. D. Passerone and M. Parrinello, *Phys. Rev. Lett.*, **8710**, 108302 (2001). Action-Derived Molecular Dynamics in the Study of Rare Events.

105. D. Passerone, M. Ceccarelli, and M. Parrinello, *J. Chem. Phys.*, **118**, 2025 (2003). A Concerted Variational Strategy for Investigating Rare Events.

106. D. Bai and R. Elber, *J. Chem. Theory Comput.*, **2**, 484 (2006). Calculation of Point-to-Point Short-Time and Rare Trajectories with Boundary Value Formulation.

107. J. E. Shea, M. R. Friedel, and A. Baumketner, in *Reviews in Computational Chemistry*, K. B. Lipkowitz, T. R. Cundari, and V. J. Gillet, Eds., Wiley, Hoboken, NJ, 2006, Vol. 22, pp. 169–228. Simulations of Protein Folding.

108. L. D. Landau and E. M. Lifshitz, *Mechanics*, Butterworth-Heinenann, Oxford, UK, 1976.

109. R. Elber, in *Computer Simulations in Condensed Matter Systems: From Materials to Chemical Biology*, Springer, Berlin, 2006, Vol. 1, pp. 435–451. Calculation of Classical Trajectories with Boundary Value Formulation.

110. A. Ulitsky and R. Elber, *J. Chem. Phys.*, **92**, 1510 (1990). A New Technique to Calculate Steepest Descent Paths in Flexible Polyatomic Systems.

111. R. Elber, A. Roitberg, C. Simmerling, R. Goldstein, H. Y. Li, G. Verkhivker, C. Keasar, J. Zhang, and A. Ulitsky, *Comput. Phys. Commun.*, **91**, 159 (1995). Moil—A Program for Simulations of Macromolecules.

112. R. Elber, *J. Chem. Phys.*, **93**, 4312 (1990). Calculation of the Potential of Mean Force Using Molecular Dynamics with Linear Constraints: An Application to a Conformational Transition in a Solvated Dipeptide.

113. R. Czerminsky and R. Elber, *J. Chem. Phys.*, **92**, 5580 (1990). Reaction Path Study of Conformational Transitions in Flexible Systems: Application to Peptides.

114. V. Zaloj and R. Elber, *Comput. Phys. Commun.*, **128**, 118 (2000). Parallel Computations of Molecular Dynamics Trajectories Using the Stochastic Path Approach.

115. A. F. Voter, F. Montalenti, and T. C. Germann, *Annu. Rev. Mat. Res.*, **32**, 321 (2002). Extending the Time Scale in Atomistic Simulation of Materials.

116. S. Izrailev, S. Stepaniants, B. Isralewitz, D. Kosztin, H. Lu, F. Molnar, W. Wriggers, and K. Schulten, in *Computational Molecular Dynamics: Challenges, Methods, Ideas*, P. Deuflhard, J. Hermans, B. Leimkuhler, A. E. Mark, S. Reich, and R. D. Skeel, Eds., Springer, Berlin, 1998, pp. 39–65. Steered Molecular Dynamics.

117. J. Schlitter, M. Engels, P. Kruger, E. Jacoby, and A. Wollmer, *Mol. Sim.*, **10**, 291 (1993). A Targeted Molecular Dynamics Simulation of Conformational Change: Application to the T $\leftrightarrow$ R Transition in Insulin.

118. A. E. Cardenas, unpublished work, 2007.

119. F. Pitici and R. Elber, in *Biophysical Society 50th Annual Meeting*, Biophysical Society, Salt Lake City, Utah, 2006, p. 51. Computer Simulations of Folding of Cytochrome C Variants.

120. W. H. Press, B. P. Flannery, S. A. Teukosky, and W. T. Vetterling, *Numerical Recipes*. Cambridge University Press, Cambridge, UK, 1986.

121. W. Humphrey, A. Dalke, and K. Schulten, *J. Mol. Graph.*, **14**, 33 (1996). VMD: Visual Molecular Dynamics.

122. V. Tsui and D. A. Case, *Biopolymers*, **56**, 275 (2000). Theory and Applications of the Generalized Born Solvation Model in Macromolecular Simulations.

123. G. D. Hawkins, C. J. Cramer, and D. G. Truhlar, *Chem. Phys. Lett.*, **246**, 122 (1995). Pairwise Solute Descreening of Solute Charges from a Dielectric Medium.

124. S. Sato, T. L. Religa, V. Daggett, and A. R. Fersht, *Proc. Natl. Acad. Sci. U.S.A.*, **101**, 6952 (2004). Testing Protein-Folding Simulations by Experiment: B Domain of Protein A.

125. P. G. Wolynes, *Proc. Natl. Acad. Sci. U.S.A.*, **101**, 6837 (2004). Latest Folding Game Results: Protein A Barely Frustrates Computationalists.

126. K. Arora and T. Schlick, *Chem. Phys. Lett.*, **378**, 1 (2003). Deoxyadenosine Sugar Puckering Pathway Simulated by the Stochastic Difference Equation Algorithm.

127. K. Arora and T. Schlick, *J. Phys. Chem. B*, **109**, 5358 (2005). Conformational Transition Pathway of Polymerase beta/DNA upon Binding Correct Incoming Substrate.

128. W. Lim and Y. P. Feng, *Biopolymers*, **78**, 107 (2005). Applying the Stochastic Difference Equation to DNA Conformational Transitions: A Study of B-Z and B-A DNA Transitions.

129. A. E. Cardenas and R. Elber, *Proteins: Struct., Funct., Genet.*, **51**, 245 (2003). Kinetics of Cytochrome c Folding: Atomically Detailed Simulations.

130. H. Roder, G. A. Elove, and S. W. Englander, *Nature*, **335**, 700 (1988). Structural Characterization of Folding Intermediates in Cytochrome c by H-Exchange Labeling and Proton NMR.

131. G. A. Elove, A. F. Chaffotte, H. Roder, and M. E. Goldberg, *Biochemistry*, **31**, 6876 (1992). Early Steps in Cytochrome-c Folding Probed by Time-Resolved Circular-Dichroism and Fluorescence Spectroscopy.

132. L. Pollack, M. W. Tate, N. C. Darnton, J. B. Knight, S. M. Gruner, W. A. Eaton, and R. H. Austin, *Proc. Natl. Acad. Sci. U.S.A.*, **96**, 10115 (1999). Compactness of the Denatured State of a Fast-Folding Protein Measured by Submillisecond Small-Angle X-Ray Scattering.

133. S. J. Hagen and W. A. Eaton, *J. Mol. Biol.*, **297**, 781 (2000). Two-State Expansion and Collapse of a Polypeptide.

134. S. Akiyama, S. Takahashi, T. Kimura, K. Ishimori, I. Morishima, Y. Nishikawa, and T. Fujisawa, *Proc. Natl. Acad. Sci. U.S.A.*, **99**, 1329 (2002). Conformational Landscape of Cytochrome c Folding Studied by Microsecond-Resolved Small-Angle X-Ray Scattering.

135. J. G. Lyubovitsky, H. B. Gray, and J. R. Winkler, *J. Am. Chem. Soc.*, **124**, 14840 (2002). Structural Features of the Cytochrome c Molten Globule Revealed by Fluorescence Energy Transfer Kinetics.

136. J. S. Valentine and P. J. Hart, *Proc. Natl. Acad. Sci. U.S.A.*, **100**, 3617 (2003). Misfolded Cuznsod and Amyotrophic Lateral Sclerosis.

137. R. W. Strange, S. V. Antonyuk, M. A. Hough, P. A. Doucette, J. S. Valentine, and S. S. Hasnain, *J. Mol. Biol.*, **356**, 1152 (2006). Variable Metallation of Human Superoxide Dismutase: Atomic Resolution Crystal Structures of Cu-Zn, Zn-Zn and as-Isolated Wild-Type Enzymes.

138. R. W. Strange, S. Antonyuk, M. A. Hough, P. A. Doucette, J. A. Rodriguez, P. J. Hart, L. J. Hayward, J. S. Valentine, and S. S. Hasnain, *J. Mol. Biol.*, **328**, 877 (2003). The Structure of Holo and Metal-Deficient Wild-Type Human Cu, Zn Superoxide Dismutase and Its Relevance to Familial Amyotrophic Lateral Sclerosis.

139. A. K. Faradjian and R. Elber, *J. Chem. Phys.*, **120**, 10880 (2004). Computing Time Scales from Reaction Coordinates by Milestoning.

140. R. Elber, *Biophys. J.*, **92**, L85 (2007). A Milestoning Study of the Kinetics of an Allosteric Transition: Atomically Detailed Simulations of Deoxy Scapharca Hemoglobin.

141. A. M. A. West, R. Elber, and D. Shalloway, *J. Chem. Phys.*, **126**, 145104 (2007). Extending Molecular Dynamics Timescales with Milestoning: Example of Complex Kinetics in a Solvated Peptide.

142. D. Moroni, P. G. Bolhuis, and T. S. van Erp, *J. Chem. Phys.*, **120**, 4055 (2004). Rate Constants for Diffusive Processes by Partial Path Sampling.

CHAPTER 8

Atomistic Simulation of Ionic Liquids

Edward J. Maginn

Department of Chemical and Biomolecular Engineering, University of Notre Dame, Notre Dame, Indiana 46556

INTRODUCTION

What exactly is an ionic liquid? The most straightforward and general definition is that an *ionic liquid* is a liquid composed completely of ions. By this admittedly tautological definition, NaCl is an ionic liquid if it is above 800°C. A eutectic mixture of LiCl and KCl above 355°C would also be an ionic liquid. However, these compounds are not what people mean when they talk about ionic liquids these days. "Normal" high-melting salts are generally referred to as *molten salts*, while the term *ionic liquid* has come to refer to salts with much lower melting points than NaCl or LiCl–KCl mixtures. A rather arbitrary definition that has been generally agreed upon in the research community is that an ionic liquid (IL) is a salt with a melting point below 100°C. Salts that melt below room temperature are referred to as *room temperature ionic liquids*, or RTILs. Measuring a melting point of an ionic liquid accurately is nontrivial, however, so the definition is used only as a guide. Many ILs form glasses and do not show an abrupt melting transition and can actually be induced to crystallize by heating the liquid. This *cold crystallization* phenomenon is typical of materials having sluggish dynamics and reflects the fact that supercooled liquids will crystallize if they are given enough thermal energy to reach their thermodynamically favored crystalline state from a supercooled metastable state.

Ionic liquids have gone from academic curiosity to a widely used (if not quite yet common) class of material in the span of about 15 years. In

Reviews in Computational Chemistry, Volume 26
edited by Kenny B. Lipkowitz and Thomas R. Cundari

John Wilkes' insightful review[1] of the history of ionic liquids up to 2002, he showed that these "neoteric" compounds are not so new after all. In fact, their history dates back to the nineteenth century, where probably the first documented case of an ionic liquid was recorded when a "red oil" was observed to form during a Friedel–Crafts reaction. Work in the early twentieth century demonstrated that simple ammonium salts could be liquids below room temperature. For example, ethylammonium nitrate has a melting point of 12°C. Even though ionic liquids have been known for many years, it took a long time for them to become popular in the research community. As shown in Figure 1, very little publication activity on ionic liquids existed prior to 2000. From 1980 to 1989, one finds from a Web of Science search that only 35 articles appeared that used the term "ionic liquid." Perhaps if we expand the search a bit and include those studies that used the term "molten salt" to mean "ionic liquid" as defined here, we may have retrieved a few more examples. Still, at one time in the recent past it was possible for a person to read every article published on the topic and still have time to eat, sleep, and carry out his or her own research. Everybody working in the field knew one another, and each of those researchers was familiar with the complete literature. What a difference a few years make!

The interest in ionic liquids has skyrocketed in the last 8–10 years, as demonstrated by the publication trend shown in Figure 1. Over 1000 studies a year are now published on ionic liquids, and it is no longer possible to read them all. Many conferences and symposia have been dedicated to ionic liquids

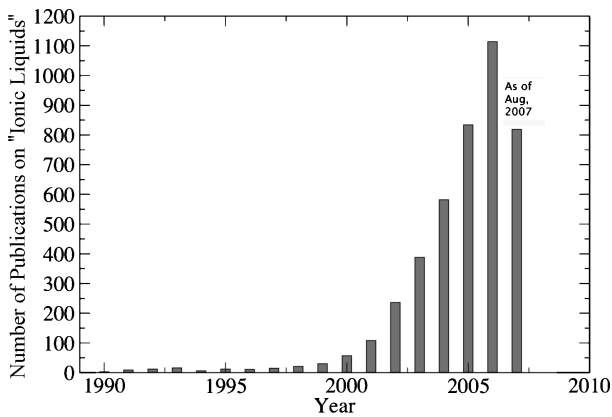

Figure 1 This plot demonstrates the phenomenal growth in the literature on ionic liquids. What is plotted is the number of studies that use the term *ionic liquid* as determined by a Web of Science search in August 2007. Less than 25 studies were published per year on the topic up until 1999. Since then, the number of studies has increased dramatically, such that now well over 1000 a year are published on ionic liquids. The patent literature on ionic liquids has experienced similar growth.

over the past few years, with perhaps the highlight being the first international Congress on Ionic Liquids (COIL), held in Salzburg, Austria, in 2005, in which more than 400 participants came together to discuss ionic liquid research topics. This was followed by COIL-2 in Yokohama, Japan, in 2007, in which over 600 people attended. A new congress will be held every 2 years, with the venues for 2009, 2011, and 2013 already set. As a research topic, ionic liquids have arrived.

Why has the interest in ionic liquids been growing at such a fast pace? Certainly, part of the growth is the result of the fact that ionic liquids are just plain interesting substances, and, as such, scientists want to study them. Figure 2 shows a photo of a sample of the ionic liquid 1-*n*-hexyl-3-methylimidazolium bis(trifluoromethylsulfonyl)imide (or $[C_6mim][Tf_2N]$, for short). It *is* amazing to see a pure salt that looks just like water. Actually, this ionic liquid is a bit more viscous than water, so it looks more like glycerol or a mineral oil than water. Nevertheless, liquid salts that can be poured at room temperature are curious substances and were bound to stimulate the imaginations of researchers. Ionic liquids are much more than lab curiosities, however, which is why commercial interest in them is so strong. Ionic liquids can possess a number of unique properties that enable them to be used in many applications where other materials are lacking.

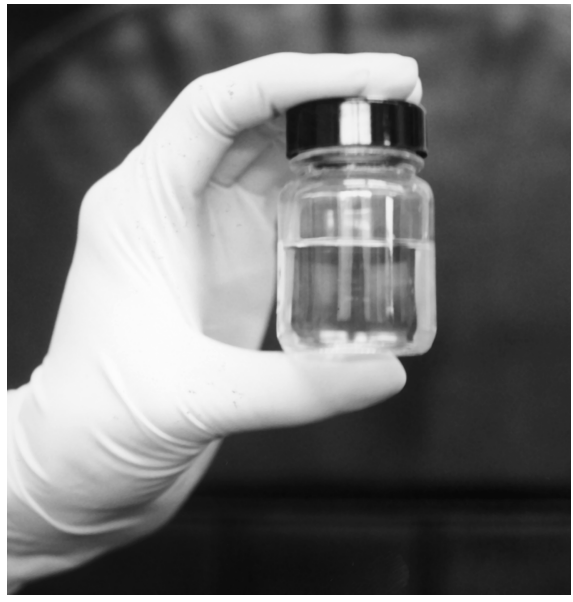

Figure 2 Sample of the ionic liquid 1-*n*-hexyl-3-methylimidazolium bis(trifluoromethylsulfonyl)imide made in the laboratory of Joan Brennecke at the University of Notre Dame. This ionic liquid is clear and stays liquid well below room temperature.

When discussing ionic liquid properties, it is important to realize that there is no such thing as a single ionic liquid because an extremely wide range of compounds can be categorized as ionic liquids. As such, one class may possess a particular property, while another class can have very different properties. Many people have been tripped up over the years by making broad general statements about ionic liquids and their properties, only to have counterexamples crop up. Given this caveat, however, we can list some general properties that many ionic liquids possess. First, ionic liquids have an exceedingly low volatility, to the point of being effectively nonvolatile. Of course, no substance is truly nonvolatile, and a recent article[2] has shown that some ionic liquids have a detectable vapor pressure and can actually be distilled! However, even these have *very low* vapor pressures, such that for all practical purposes they can be considered about as volatile as a solid. This is one of their major beneficial properties. Ionic liquids have a very broad liquidus range, on the order of several hundred degrees Celsius. Many tend to have thermal decomposition temperatures of around 300–400° C, making them quite stable. Second, ionic liquids can be made to dissolve a wide range of compounds, from polar molecules such as water and alcohols, to aromatic substances such as benzene, to polymeric substances such as cellulose, to gases such as carbon dioxide and sulfur dioxide.[3,4] This, combined with their low volatility, stimulated a great deal of research directed at their use as ''green'' solvents. The idea was that, unlike traditional organic solvents, ionic liquid solvents do not evaporate and thus cannot contribute to air pollution like conventional volatile organic compounds. The jury is still out, however, as to how truly green these substances are. Some have been shown to be highly toxic to aquatic organisms, while others have very low toxicity.[5] Third, ionic liquids are conductive, which opens up the possibility of using them in fuel cells, batteries, and other electrochemical devices. Ionic liquids can be made energetic, which suggests they could be used as low-volatility propellants.[6] Ionic liquids have also been shown to have highly desirable lubrication properties,[7] which when coupled with their thermal stability and low volatilty suggests great potential in high-performance applications. Ionic liquids have been used in sensing and other analytical devices, as catalysts, magnetic fluids, heat transfer fluids, and as heavy-metal extraction agents. The list could go on and on, which is really why these compounds are under such scrutiny today.

The other important factor to realize when talking about ionic liquids is that they have tremendous chemical diversity. An almost limitless number of compounds exist that can be made into an ionic liquid. Figure 3 shows a very small example of the types of cations and anions that can be combined to give ionic liquids. Estimates suggest that more than 10^8 different compounds can be made into an ionic liquid. This is due to the fact that different functional groups can be added to base cation or anion structures, which can have a profound effect on properties. For example, by pairing the same cation with a different anion, the melting point can be changed by over 100° C.[8] Similar

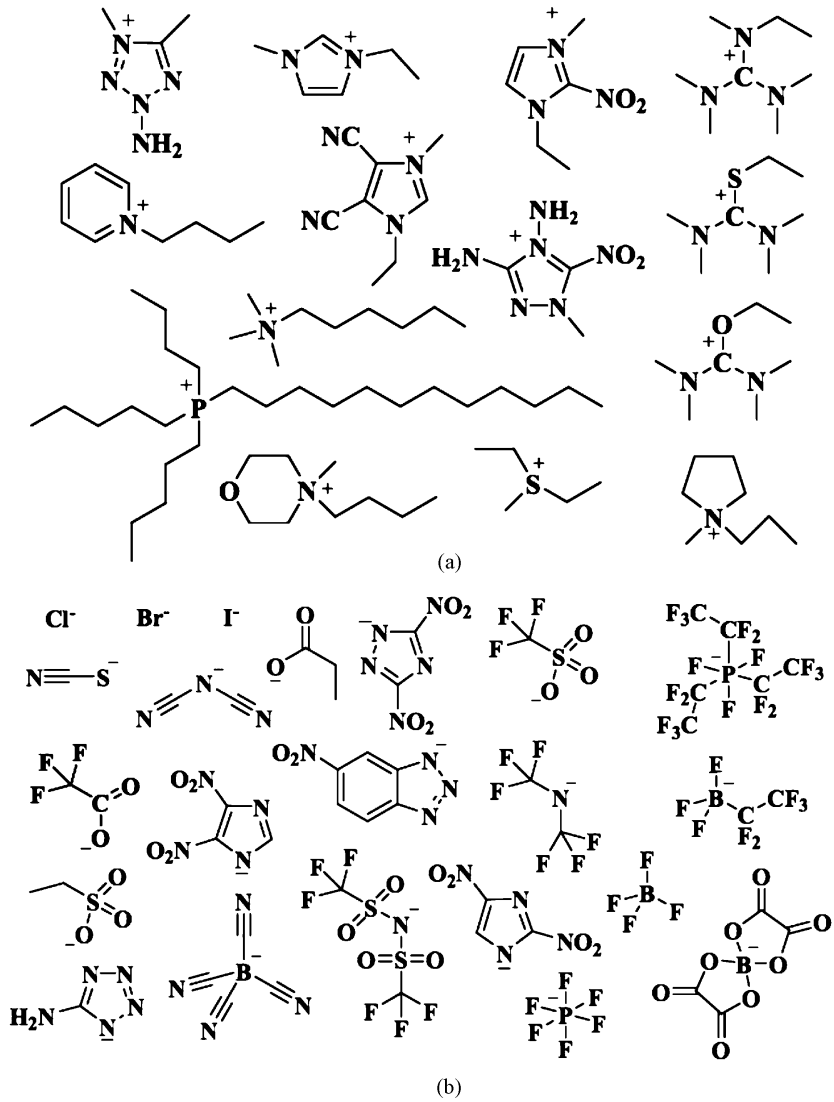

Figure 3 Small sample of the (a) cations and (b) anions that can be combined to make an ionic liquid. It has been estimated that there are well over 10^8 different compounds that could be made into ionic liquids. (Structures provided courtesy of Robin Rogers.)

dramatic changes in properties are observed when small changes are made to the functional groups on cations. For example, the solubility of ionic liquids with alcohols can be increased or decreased by varying the length of alkyl groups attached to the cation;[9] whether the solubility increases or decreases with increasing alkyl chain length, however, depends on the alcohol under

investigation. Many other examples can be given where seemingly small changes in structure result in qualitative changes in physical properties. This is because there is a subtle balance between van der Waals and electrostatic forces among the ions and any dissolved species, and this balance can be disrupted in unpredictable ways by small chemical or structural modifications. The ability to make such changes is exciting to synthetic chemists because it represents an opportunity to exploit the chemical diversity of ionic liquids to prepare materials having just the right properties for a particular application. It also presents them with a problem, however, because the very diversity that offers such opportunities also means that there is no way all possible ionic liquid compounds can be made and tested in the lab; there are simply too many choices, even if combinatorial methods are used.

Because reliable methods for predicting how properties depend on structure and composition are lacking, the search for new ionic liquids relies on chemical intuition or extrapolation of knowledge from related compounds. This limits progress severely and, indeed, only a relatively small number of ionic liquids have been made, characterized, and tested. The National Institutes of Standards and Technologies maintains a database of physical properties for ionic liquids,[10] and while the number of entries is growing every week, the actual number of different ionic liquids listed in the database is small. A few companies have begun selling ionic liquids, and the list of different ionic liquids in their catalogs is also growing. Still, the development of new ionic liquids has followed the same time-honored tradition of most of chemical research: Make a compound, test it, and use your instincts to tell you what to make next to get the properties you want. Granted this is an oversimplification, but not by much.

This is where atomistic simulation of ionic liquids enters the picture. Computational methods and force fields have advanced over the years, as has been well documented in the *Reviews in Computational Chemistry* series. This means our ability to predict how the properties of a particular material depend on the chemical constitution and structure of that material has increased substantially. Because experimental studies of conventional organic substances have had about a 100-year head start on computational studies, simulations have been often used in a "postpredictive" method for organic compounds. Comparisons are made between computed and known experimental properties, and some insight is gained into why the properties are the way they are. Of course, not all properties of all compounds are known experimentally at every state point, and so simulations are important in this regard. However, because the field of ionic liquids is so new, simulation methods are having a big impact on the direction of the field. Computations on new compounds are being carried out contemporaneously with experiments. Experimentalists are hungry for the insights simulations can provide. Properties are being predicted before they are measured, and indeed, simulations are helping drive the types of experiments that are being carried out. This happy coincidence, that a brand new class of

compounds has been discovered at the same time that computing power and molecular simulation methods have reached a sophistication and maturity level that permit them to be used to determine structure–property relationships quantitatively, is the focus of this chapter.

SHORT (PRE)HISTORY OF IONIC LIQUID SIMULATIONS

As a regular reader of this series is probably aware, the history of the computer and the history of molecular-level simulations are intimately connected. One of the earliest applications of the digital computer was a Monte Carlo simulation of a model fluid, carried out by Metropolis and co-workers[11] at Los Alamos National Laboratory in 1953. Soon after, Alder and Wainwright at Livermore,[12,13] Rahman at Argonne,[14] and Verlet at Yeshiva University[15] used a deterministic method called *molecular dynamics* to compute the properties of simple liquids. Whereas the early simulations focused on calculating properties of idealized "hard" fluids or slightly more realistic but still simple liquids such as argon, ionic liquid systems are much more complex and require more sophisticated treatment to get accurate results. Nevertheless, the tools these pioneering researchers used—Monte Carlo and molecular dynamics—are still the workhorses of the field today.

The idea behind a molecular simulation is in principle simple. Given an accurate description of the energetic interactions between a collection of atoms and a set of initial atomic coordinates (and in some cases, velocities), the positions (and again, if desired, velocities) of these atoms are advanced subject to a set of thermodynamic constraints. If the atoms are advanced stochastically, the method is called *Monte Carlo*, or *MC*. The term Monte Carlo encompasses a wide range of numerical analysis methods, but here we refer to Metropolis-style MC in which atoms are moved about randomly in such a way so as to satisfy a limiting probability distribution. There will be more on this later. (As an aside, the name Monte Carlo comes from the fact that random numbers are used, and, hence, there is a sense of the simulations being like a game of chance. When this technique was developed, the place to gamble was Monte Carlo, and hence the name stuck. Perhaps if the method had been developed today it would be called "Las Vegas"?)

Note that velocities are not required for MC because atomic positions are changed randomly. If the positions and velocities of the atoms are advanced deterministically, we call the method *molecular dynamics*, or *MD*. MD relies upon numerical integration of the classical equations of motion and, hence, requires that forces (gradients of the potential energy) be known. Since any numerical procedure is approximate, the trajectories that result from an MD simulation are technically only pseudodeterministic. This is a detail that we

need not concern ourselves with; we will call MD a deterministic method, but we know this is only approximately true. Other simulation methods exist that are part stochastic and part deterministic, and these are becoming increasingly useful to compute properties of complex systems.

The trajectories generated using MD or MC will be consistent with the energetic model imposed on the system. If the methods have been implemented correctly, the trajectories will also be consistent with the limiting probability distribution of the particular statistical mechanical ensemble under which the simulations were run. Atomic positions are all that is needed to, at least in principle, compute all the thermodynamic properties of the model system. If the velocities are also available (i.e., if an MD simulation was run), then time-dependent properties may also be computed. Assuming the simulations have been carried out properly, the resulting trajectories provide an *exact* solution for the model system. Therefore, the degree to which the simulation results agree with experimental data for the "real" system tells us how good the model is at representing the real system. This is how simulations are often used, and one can think of them as a "theoretical" result. Alternatively, if we use simulation methods to model a theoretical system for which an approximate analytical solution exists, the level of agreement between the simulation and theory tells us how accurate the theoretical approximation is. Used in this manner, simulations are like a computational "experiment" against which theory can be tested. Both approaches have been used for ionic liquids, though the former method is far more common and will be the focus of this review.

The above comments emphasize the fact that a great deal of attention must be paid to the model used to represent the atomic species and their energetic interactions if quantitative property predictions are desired. Much of the early work on ionic liquid simulations has focused on this, and so we will need to discuss this in some detail if we are to understand how simulations are used for these systems. The place to start discussing potential models for ionic liquids is with the early work on molten alkali halides. Even though these materials do not fall under our definition of ionic liquids, almost all the current simulation approaches to ionic liquids have their roots in these early studies. In what follows, the shorthand term *force field* will be used to represent a set of analytic equations that approximate the energetic interactions among atoms in a system. We know that these interactions take many forms, from strong forces characteristic of covalent bonds to weaker forces representative of van der Waals interactions, and long-range electrostatic interactions.

One of the earliest functional forms used to model alkali halides is due to Huggins and Mayer.[16] They modeled the electrostatic interactions between ions by placing formal charges q_i on each atom center. Short-range repulsive interactions were modeled with an exponential function, and long-range attractive interactions with two terms representing dipole–dipole and dipole–

quadrupole interactions. The Huggins and Mayer force field thus has the following form:

$$U_{ij}(r_{ij}) = \frac{q_i q_j}{r_{ij}} + B_{ij}\,\exp(-\alpha_{ij} r_{ij}) - \frac{C_{ij}}{r_{ij}^6} - \frac{D_{ij}}{r_{ij}^8} \qquad [1]$$

where i and j can be either a cation or anion, and U_{ij} is the potential energy of species i due to species j, which are separated from each other by a distance r_{ij}. The van der Waals terms were parameterized by Mayer.[17] Tosi and Fumi[18] developed parameters for the repulsive part of this function to reproduce the solid-phase properties of alkali halides having the rock salt structure. Many authors subsequently used this parameterization (or variations of it) to simulate a wide range of alkali halides in both the solid and molten states. Sangster and Dixon[19] have reviewed much of the early work in this field, and their study is an excellent starting point for those interested in these systems. The Tosi–Fumi potential still enjoys wide use today.[20,21] It is generally thought that static properties are captured fairly well with this model, but its ability to model dynamic properties accurately has been questioned recently due to its neglect of ion-induced polarization. Work by Galamba and co- workers[22–24] suggests that shear viscosities and thermal conductivities of molten NaCl and KCl are over predicted by 10–20% with this force field. There are also questions as to how well this model reproduces static properties away from the state point at which it was parameterized. For example, a comparison of the pressure dependence of the melting point for NaCl computed with the Tosi–Fumi force field[25] and experimental data[26] is given in Figure 4. Although the Tosi–Fumi force field

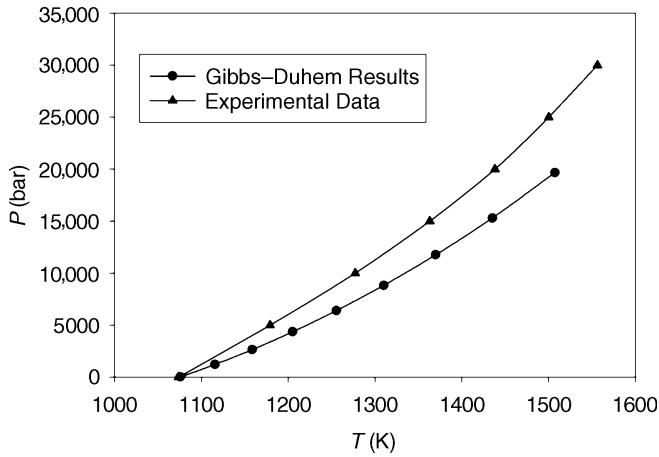

Figure 4 Computed (circles)[25] solid–liquid coexistence curve for NaCl versus experimental data (triangles).[26] Although agreement is good at atmospheric pressure, the slope of the coexistence curve is off and thus the melting point is overestimated severely at high pressure.

reproduces the atmospheric pressure melting point quantitatively, it predicts a significantly higher melting temperature as pressure (and hence density) increases.

The results for alkali halides demonstrate that a simple force field like that given in Eq. [1] can reproduce many of the experimental properties of a molten salt. It appears to capture much of the physics of these systems correctly, which is cause for optimism. Contrarily, it is difficult to obtain both thermodynamic *and* transport properties correctly with the same model; differences of 10–20% between computed and experimental transport properties are typical for alkali halide force fields that nominally get thermodynamic properties correct. Therefore, we should expect similar or even larger differences between experimental properties of ionic liquids and those obtained from simulations if this same general class of force field is used. Additionally, even if a particular property is modeled accurately at a given state point, one should not expect that property will be modeled accurately at another state point. That is, *transferability* of the force field to other conditions can be problematic and is a concern. Finally, note that the ionic liquids shown in Figure 3 are much more complicated than simple alkali halides. The alkali halide force fields were parameterized against known crystal data. Such data are often lacking for ionic liquids, and there exist many more kinds of ionic liquids than alkali halides. Moreover, people have been simulating alkali halides for over 30 years, and they still cannot predict everything about them with simulations. We should therefore expect it will be *much harder* to develop force fields for ionic liquids, and our expectations of their accuracy should be modest.

EARLIEST IONIC LIQUID SIMULATIONS

As should be apparent by now, simulating ionic liquids raises many new challenges that are not present with molten alkali halides. First, the cations and anions are no longer spheres but are instead multiatom molecular species. This means that the functional form of Eq. [1] is inadequate for treating these systems; additional intramolecular terms need to be developed to model bonded interactions accurately. Second, the ions are large and contain many intramolecular degrees of freedom; great care is needed to ensure proper sampling is obtained, making it likely that the computational costs will be high. Third, part of the inaccuracy of the alkali halide force fields is due to the primitive "fixed-charge" method for handling electrostatic interactions; a more sophisticated polarizable force field may be necessary to model these systems. Finally, unlike alkali halides, there is a dearth of experimental data with which to parameterize the force field (especially when the earliest ionic liquid simulation studies were conducted). As suggested in the introductory remarks, however, that is one of the main reasons for wanting to model ionic liquids in

the first place. If all the necessary experimental data were in hand, there would be little practical need to carry out simulations. This means *predictive methods* will be needed to estimate parameters, and fitting to experimental data is not likely to be a viable strategy (at least for awhile).

Faced with these challenges, a handful of research groups forged ahead anyway and began simulating ionic liquids. All used a classical force field with the same basic features as the Huggins and Mayer force field of Eq. [1], although intramolecular terms were treated in different manners. It is a bit difficult to say in a historical context what the first simulation of an ionic liquid was, given the ambiguity with which an ionic liquid is defined. Hawlicka and Dlugoborski[27] conducted a molecular dynamics study of tetramethylammonium chloride dissolved in water in 1997 with the intent of studying hydrophobic phenonema in aqueous solutions, certainly a relevant topic for ionic liquids. In early 2000, Oberbrodhage[28] conducted a molecular dynamics simulation study of tetrabutylammonium iodide dissolved in formamide as well as at the interface between formamide and hexane. Oberbrodhage was interested in the use of tetrabutylammonium iodide as a phase-transfer catalyst. The melting points of tetramethylammonium chloride and tetrabutylammonium iodide are too high to fall under our definition of an ionic liquid, but the quaternary ammonium cation, when paired with other anions, is used extensively as an ionic liquid.[29] These two groups were probably unaware of the then growing interest in ionic liquids when they published their studies.

In 2001, Hanke, Price and Lynden-Bell[30] were the first to conduct an atomistic simulation of compounds that can be called ionic liquids under our definition. They used molecular dynamics to model the crystalline state of 1,3-dimethylimidazolium chloride ($[C_1mim][Cl]$), 1,3-dimethylimidazolium hexafluorophosphate ($[C_1mim][PF_6]$), 1-ethyl-3-methylimidazolium chloride ($[C_2mim][Cl]$), and 1-ethyl-3-methylimidazolium hexafluorophosphate ($[C_2mim][PF_6]$). They also modeled the liquid state of $[C_1mim][Cl]$ and $[C_1mim][PF_6]$, both of which are relatively high melting substances. Because of this (and the need to speed dynamics and thus limit computation times), the liquid simulations were carried out at temperatures between 400 and 500 K. The form of the potential function they used was

$$U_{ij}(r_{ij}) = \frac{q_i q_j}{r_{ij}} + (A_{ii}A_{jj})^{1/2} \exp\left[-\frac{(B_{ii}+B_{jj})r_{ij}}{2}\right] - \frac{(C_{ii}C_{jj})^{1/2}}{r_{ij}^6} \qquad [2]$$

which has the same form as Eq. [1], except the dipole–quadrupole term is omitted. This is also the functional form used by Williams and Cox to model azohydrocarbons.[31] Bond lengths were kept fixed, as were all bond angles except those between the N–C–H atoms in the methyl groups. Partial charges q_i were located at each atomic center, with values determined from the atomic multipole moments derived from a distributed multipole analysis[32] of the

second-order Møller–Plesset (MP2) correlated charge density of each ion, calculated using a 6-31G** basis set. The repulsion–dispersion parameters (*A*, *B*, and C) were taken from the work of Williams for C, H, and N,[31] Cl,[33] and F.[34]

Hanke, Price and Lynden-Bell[30] used the widely available DL_POLY simulation package[35] to conduct the simulations. By current standards their simulation times were short (100 ps) and their system sizes were small (192 ion pairs). Even so, they were able to compute a number of useful properties, including molar volumes, average energies, liquid structure in the form of radial distribution functions, and mean-square displacements as a function of time. As we now know, the simulations were too short to obtain reliable self-diffusivities, but the liquid structure they observed was important in helping us begin to understand how these ions organize in a liquid. The computed distribution of the chloride anion about the cation agreed well with subsequent experimental neutron diffraction studies.[36] Hanke and co-workers[30] were unable to compare any of the other computed properties against experiment, in large part because of the paucity of experimental data for the ionic liquids they studied.

A common approximation used in liquid-phase simulations involves coarse graining where carbon atoms and the hydrogen atoms bonded to them are lumped into a single "united-atom" interaction site. This greatly reduces the number of pairwise interactions that must be computed but does so by sacrificing some chemical reality. Hanke and co-workers[30] investigated the effect of this approximation by carrying out some simulations using a united-atom representation of the methyl and methylene units, while in other simulations they used explicit "all-atom" representations. The united-atom models tended to yield denser systems than did the explicit atom versions, and the dynamics of the ions appeared to be faster for the less dense all-atom systems.

In early 2002, the journal *Green Chemistry* published a special issue dedicated to ionic liquids in which two simulation studies appeared. Hanke, Atamas and Lynden-Bell[37] reported results of a study in which the solvation behavior of water, methanol, dimethyl ether, and propane in [C_1mim][Cl] was computed. They used the same force field as given in Eq. [2], with a united-atom treatment of the cation and solute methyl and methylene units. DL_POLY MD simulations were run on 192 ion pairs for up to 200 ps, and the local structure of the solutes about the two ions as well as the energetic interactions were computed. They found that the solute hydroxyl groups associated mainly with the chloride anion and that each water molecule associated with two chloride ions via hydrogen-bonding interactions. The ether and alkane did not associate as strongly with the anion; cation arrangement about the solutes was diffuse. The authors speculated that solutes with dipole moments would associate mainly with the imidazolium ring because of its positive charge. This same group published another study[38] in which the same system was studied, but the excess chemical potential of each solute

was computed using thermodynamic integration. By comparing the signs and magnitudes of the excess chemical potentials, the relative solubility of the solutes in this ionic liquid could be determined. This was the first example of a free energy calculation within an ionic liquid system, and it confirmed the importance of hydrogen bonding and charge–charge interactions for the solvation behavior of ionic liquids.

In that same *Green Chemistry* issue, Shah, Brennecke, and Maginn[39] reported the results of an isothermal-isobaric MC study on the ionic liquid 1-*n*-butyl-3-methylimidazolium hexafluorophosphate ([C_4mim][PF_6]). This was the first (and still one of the few) MC studies of an ionic liquid. Nearly all computational researchers study ionic liquids with MD, perhaps because of the widespread availability of MD codes and the relative scarcity of similar MC codes. As discussed later, this situation is changing and there are good reasons for choosing to use MC methods to study these materials. Maginn's group computed the molar volume, cohesive energy density (and thus enthalpy of vaporization), isothermal compressibility, and volumetric expansion coefficient. They also computed the liquid structure of this system in the form of radial distribution functions and found that the order was very long range—much longer than what is observed in ordinary liquids, a phenomenon that was explained as being due to the long-range nature of the Coulombic interactions between the ions. Several new developments were introduced in that work. First, [C_4mim][PF_6] was the most widely studied ionic liquid at the time from an experimental standpoint, and a fair amount of experimental property data was available against which to compare the results, thereby providing the first direct test of the ability of simulations to match experimental properties. It was also the first simulation of a low-melting ''room temperature'' ionic liquid. Since then, we have learned that the PF_6^- anion hydrolyzes in the presence of water, giving off hydrofluoric acid, so this ionic liquid will probably find limited practical use, although many experimental and simulation studies are still being conducted on this compound. Second, this study introduced a force field having the following functional form:

$$U_{\text{tot}} = \sum_{i,j<i} \left\{ 4\epsilon_{ij} \left[\left(\frac{\sigma_{ij}}{r_{ij}} \right)^{12} - \left(\frac{\sigma_{ij}}{r_{ij}} \right)^{6} \right] + \frac{q_i q_j}{r_{ij}} \right\} + U(\phi) \qquad [3]$$

where the repulsion–dispersion interactions were modeled with a 12-6 Mie (or Lennard-Jones) potential. Because the cation contains a flexible butyl side chain, a dihedral potential of the following form was used:

$$U(\phi) = \nu_0 + \frac{\nu_1}{2}[1 + \cos(\phi)] + \frac{\nu_2}{2}[1 - \cos(2\phi)] + \frac{\nu_3}{2}[1 + \cos(3\phi)] \qquad [4]$$

The partial charges used in Eq. [3] were derived from ab initio calculations of a single gas-phase ion pair at the restricted Hartree–Fock (RHF)/6-31G* level of theory followed by fitting to the electrostatic potential of the minimized structure using the CHarges from ELectrostatic Potential Grid (CHELPG) method.[40] A united-atom model was adopted, with all hydrogens subsumed into their neighboring carbon atoms, and the PF_6^- anion was treated as a sphere. The Lennard-Jones and dihedral parameters for the cation were taken directly from the OPLS force field,[41] using similar compounds as surrogates. The anion Lennard-Jones potential was scaled using SF_6 as a model. Most researchers now use the OPLS or CHARMM[42] force field functional form in ionic liquid simulations.

The calculations done by Shah, Brennecke and Maginn[39] demonstrated that, by using a simple force field like that in Eq. [3] along with parameters obtained from a mix of quantum calculations and literature sources, properties such as liquid densities could be reproduced to within 3–5% over a very wide temperature range, and that derivative properties such as expansivities and compressibilities could also be obtained to reasonable accuracy. This study[39] was also the first to estimate an enthalpy of vaporization for an ionic liquid. Although many researchers had stated previously that ionic liquids were "non-volatile" and had "no detectable vapor pressure,"[43] this work predicted that the enthalpy of vaporization was large but not infinite, suggesting that ionic liquids should indeed have a vapor pressure. It has now been shown conclusively that ionic liquids *do* have a measurable vapor pressure, and it is most encouraging that recent measurements of the enthalpy of vaporization[44–46] agree very well with these early modeling predictions.

Later that same year, several other studies appeared in which force fields having the basic functional form as that in Eq. [3] were developed for imidazolium-based ionic liquids. Margulis, Stern and Berne[47] conducted MD simulations of $[C_4mim][PF_6]$ using an explicit atom model that included fully flexible bond lengths and bond angles, in addition to a dihedral potential. Partial charges were fit to the electrostatic potential obtained from Hartree–Fock calculations, while all other cation parameters were taken from the all-atom OPLS potential.[41] The parameters for PF_6^- were taken from previous work of Kaminsky and Jorgensen.[48] Margulis, Stern and Berne[47] conducted a number of MD simulations in which they used 200 ps of equilibration time and 50 ps of production time. Computed liquid-phase densities were in very good agreement with experimental values. They also examined the nature of the dynamics of the system and were the first group to note anomalous and complex dynamical behavior, indicative of a supercooled liquid. This anomalous dynamical behavior turns out to have been an extremely important finding as related to our ability to compute dynamical properties of ionic liquids, as we shall see later. They also made the first estimate of the conductivity of an ionic liquid from a simulation, using the apparent self-diffisivities and the Nernst–Einstein model.

Morrow and Maginn[49] also carried out a molecular dynamics study of $[C_4mim][PF_6]$, using an explicit-atom and fully flexible model with a force field having the following functional form:

$$U = \sum_{\text{bonds}} k_b(r - r_0)^2 + \sum_{\text{angles}} k_\theta(\theta - \theta_0)^2 + \sum_{\text{dihedrals}} k_\chi[1 + \cos(n\chi - \delta)] + \sum_{\text{impropers}} k_\psi(\psi - \psi_0)^2 + \sum_{i=1}^{N-1}\sum_{j>1}^{N}\left\{4\epsilon_{ij}\left[\left(\frac{\sigma_{ij}}{r_{ij}}\right)^{12} - \left(\frac{\sigma_{ij}}{r_{ij}}\right)^{6}\right] + \frac{q_i q_j}{4\epsilon_0 r_{ij}}\right\} \quad [5]$$

This force field function contains not only dihedral, Lennard-Jones, and Coulombic terms, but it also includes bond stretching, angle bending, and improper ring bending contributions modeled with harmonic potentials. This is the same form used by Margulis, Stern, and Berne, except they did not consider improper bending terms. Morrow and Maginn[49] used a somewhat more sophisticated quantum method than previous studies for obtaining partial charges on each atom. They also utilized Lennard-Jones and dihedral angle parameters for similar compounds that were available in the CHARMM database.[42] The force field yielded excellent liquid densities and derivative properties. In fact, the explicit-atom model did significantly better at matching the experimental density than did this group's earlier united-atom model.[39] Figure 5 compares the performance of these two models. The united-atom model underpredicted the molar volume (overpredicted the density) by almost 5%, while the explicit-atom model was accurate to within 1%. This is consistent

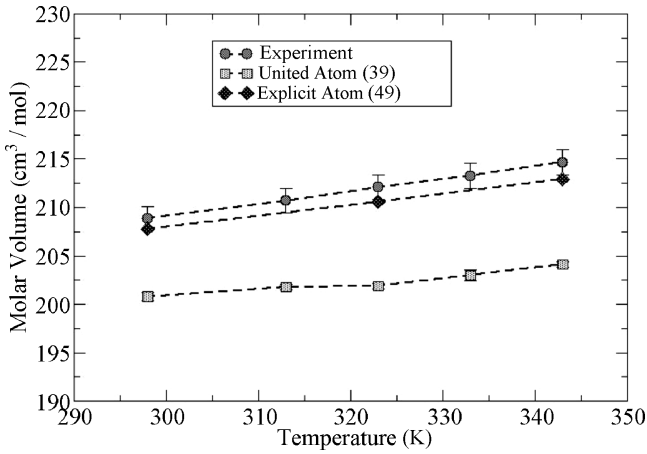

Figure 5 Comparison of the experimental density for $[C_4mim][PF_6]$ as a function of temperature[50] and results obtained using a united-atom model[39] and a more detailed explicit-atom model.[49]

with the results of Hanke, Prince and Lynden-Bell,[30] who also observed that their united-atom models tended to give denser systems than their explicit-atom counterparts. These findings suggest that explicit-atom models are more accurate than united-atom models possibly because of their greater realism, although one could tune the united-atom parameters to get as accurate a result as wanted. Nearly all subsequent simulation studies of ionic liquids have relied on explicit-atom models.

The simulation times in the Morrow and Maginn[49] study were significantly longer than that used in any simulation of an ionic liquid up to that point. Equilibration times ranged from 700 to 1000 ps, and production runs of 4 ns were carried out. As foreshadowed by the work of Margulis and coworkers,[47] long simulations are required if reasonable dynamical properties are to be obtained with these fluids. This is because ionic liquids tend to exhibit very sluggish dynamical behavior at room temperature, reminiscent of supercooled liquids. While densities and other static properties appear to converge within 50–100 ps, rotational time constants were calculated to be much longer than even the 4-ns simulation run time. The picture that began to emerge from this and the work of others[47] is that reasonably short simulations suffice for computing static properties (although proper equilibration is required), but very long simulations might be required if dynamic properties are being probed.

The group of de Andrade, Boes and Stassen published two studies during 2002 in which MD was used to examine imidazolium-based ionic liquids. The first[51] was a study of 1-ethyl-3-methylimidaziolium tetrachloroaluminate, and the second[52] was a follow-up study in which a force field was proposed for the 1-ethyl-3-methylimidaziolium and 1-butyl-3-methylimidaziolium cations paired with the tetrachloroaluminate and tetrafluoroborate anions. Their force field was based on the AMBER functional form,[53] which is similar to that used in the previous works. Derivation of the force field followed the same procedure outlined earlier, including gas-phase calculation of the ions followed by partial charge assignment for each atom by fitting to reproduce the quantum electrostatic potential. The RESP method within the package GAMESS[54] was used, but other methods give similar (though not identical) results. Intramolecular terms as well as nonbond Lennard-Jones parameters were taken from literature sources for similar compounds. Their liquid densities were in near perfect agreement with experiment and computed enthalpies of vaporization, once again, suggested that ionic liquids should have some volatility (3 years later experimentalists made such measurements). Finally, they estimated self-diffusion coefficients, but the short (200-ps) simulation times lead one to believe that these systems are not yet in the diffusive regime. One of the most interesting results from their study is that they were able to compare their computed liquid structure with neutron diffraction data that had just become available;[55] remarkably good agreement between the computed liquid structure and the neutron diffraction

results indicate that the model captures well the underlying liquid structure. This latter result echoes the point made earlier in this chapter: Our understanding of the physical chemistry of ionic liquids is being advanced by the simultaneous and synergistic application of modeling and experiment. This is possible because molecular modeling has "come of age" just in time to play a key role in understanding these new materials.

At the conclusion of 2002, four groups had published studies in which the properties of different imidazolium-based ionic liquids had been computed using five different force fields. Several things became clear as a result of these studies. First, *relatively simple fixed charge force fields of the kind shown in Eq. [5] do a remarkably good job of reproducing liquid densities and liquid structure*. This statement has to be tempered somewhat by the fact that only in a few of the cases were comparisons with experiment made, and then only for a limited number of properties. Moreover, different force fields gave similar liquid densities, although explicit-atom models performed better than united-atom models. The fact that different parameter sets give similar densities means that density is not a particularly stringent test of a force field. Second, information on liquid structure was being obtained, and it appeared that *ionic liquids had longer range order than ordinary molecular liquids*. Third, simulations of mixtures demonstrated the *importance of hydrogen bonding on solvation* and suggested that solute polarity is important in determining its solubility. Fourth, the simulations indicated that *ionic liquids should have some detectable vapor pressure and enthalpy of vaporization*, even though that aspect of ionic liquids had not yet been confirmed experimentally. Fifth, and perhaps most important, these studies demonstrated that *carrying out simulations of ionic liquids is only slightly more difficult than for ordinary liquids*. In essence, these early studies paved the way for the broader research community to use simulations to compute properties for ionic liquids. People took notice, and the number of modeling studies on ionic liquids grew very rapidly.

MORE SYSTEMS AND REFINED MODELS

Once it became apparent that standard modeling tools such as MD and MC could be used with conventional force fields to simulate ionic liquids, a number of other groups began making significant contributions to the field. In fact, dozens of studies have appeared in the last few years on the topic. In this section, we review some of the significant works and discuss some of the different properties that have been computed while emphasizing their successes and shortcomings. Because there exist so many works on this topic in the literature, it is not possible to discuss every one; those reviewed here represent a cross section of the kinds of systems being examined by scientists and properties that are being computed.

Force Fields and Properties of Ionic Liquids Having Dialkylimidazolium Cations

Given that almost all of the initial experimental work focused on ionic liquids having a dialkylimidazolium cation, it is perhaps not surprising that most simulation studies have likewise focused on this cation. After all, if this was what experimental researchers thought to be the most useful system, modelers certainly wanted to make sure that they studied the most relevant systems. In hindsight, following that trajectory was unfortunate because there are *many* other cations that are both useful from a technological perspective and of interest to scientists from a fundamental perspective. Nonetheless, for several years almost all of those other cations were ignored by modelers in favor of ionic liquids containing the imidazolium cation. As discussed earlier, already five different imidazolium force fields had been proposed and used to model ionic liquids. Over the next few years, several more force fields, all having the same basic functional form as Eq. [5], were proposed for the imidazolium cation. Each new force field was derived in a more rigorous manner, using higher accuracy quantum methods and relying more on first-principles calculations than on literature parameters from similar organic compounds.

Urahata and Riberio[56] proposed an imidazolium force field in which the methyl and methylene units of the alkyl chain were treated as united-atom segments. They varied the length of the chain from methyl to octyl, and also studied F^-, Cl^-, Br^-, and PF_6^- anions. Importantly, their calculations matched experimental structure factors. Their work was interesting because they were the first to show that the detailed structure of the liquid changes depending on the length of the alkyl chain. Later studies would demonstrate that long alkyl chains lead to the formation of nanoscale polar and nonpolar domains in these systems, but the work by Urahata and Riberio gave the first inkling of this concept.

Canongia Lopes, Deschamps and Padua[57] introduced what they termed a ''systematic'' explicit-atom force field for imidazolium-based ionic liquids. Their force field is based on the OPLS-AA/AMBER functional form, and the authors sought to make it as transferable as possible. That is, components of a molecule already contained in the OPLS-AA database should be compatible with this force field, and, in fact, many of the terms from the OPLS force field were used for the ionic liquid. To perform the parameterization, they first minimized the energy of a gas-phase ion at the HF/6-31G(d) level. Single-point energy calculations were then conducted at the more accurate MP2/cc-pVTZ(f) level. Bond and angle terms were reparameterized if the minimized structure value deviated significantly from the OPLS value. Otherwise, the OPLS value was used. Key dihedral angle energy profiles were computed from quantum calculations, and customized dihedral potential parameters were fit to this energy profile. This was the first time dihedral angle parameters were specifically fit to a quantum calculation of an ionic liquid. As

with other force fields, partial charges were fit to the electrostatic potential obtained from the quantum calculations. The level of quantum theory used by these authors was superior to that used in previous calculations. The authors were careful to summarize previously developed force fields and highlight the differences between their new force field and the others. To validate their force field, the authors ran 200-ps flexible isothermal-isobaric MD simulations using the DL_POLY package on five crystal structures for which lattice constants were known. They then compared their computed lattice constants with those obtained experimentally. They also conducted liquid-phase simulations (300 ps under isothermal-isobaric conditions) on nine different compounds, combining the [C_2mim], [C_4mim], and [C_6mim] cations with the PF_6^-, NO_3^-, and Cl^- anions. Of the nine liquids and five solids, they were able to compare their results to six liquid densities and five crystal densities. Densities deviated from experiment within the range of 1–5% for all substances, which is about the level of accuracy obtained in previous works. This was the first time, however, that comparison was made to crystalline densities. In doing this, the ionic liquid modeling effort came full circle, using the same criterion Tosi and Fumi[18] used to develop alkali halide potentials. The force field developed by Canongia Lopes and co-workers[57] is important because it has become one of the most widely used force fields for this class of ionic liquids. This is mainly due to the rigor with which it was developed, its wide applicability, and the generality and popularity of the OPLS-type force field. The list of force field parameters in the original study contained some typographical errors, some of which were corrected in an corrigendum.[58] The updated and correct set of parameters are now located on the authors' website,[59] and it is recommended that parameters be obtained from that source. This group has extended its force field to include many more cations and anions, and those parameters can also be found on the website.[59]

Liu, Huang and Wang[60] proposed a "refined" force field for imidazolium-based ionic liquids, shortly after the work of Canongia Lopes and co-workers[57] appeared. Their force field consists of explicit atoms and is based on the AMBER functional form. Unlike previous studies in which some bond and angle force constants came from literature sources, these authors determined all of these intramolecular terms from a quantum mechanical frequency analysis of an energy-minimized structure. Vibrational wavenumbers for a large number of modes in the cation were computed and compared to values given by their force field as well as from the standard AMBER force field and from infrared (IR) data. The same protocol was used for PF_6^- and BF_4^- anions. As was done by Canongia Lopes et al.,[57] some of the dihedral angle parameters were fit to the energy profiles obtained from quantum calculations. Finally, the Lennard-Jones parameter for the hydrogen bonded to the C2 carbon in the imidazolium ring was adjusted to enable the force field to match ab initio energies calculated for several conformations.

This group then used their force field to carry out MD simulations with the program MDynaMix.[61] They simulated five different pure ionic liquids: $[C_1mim][Cl]$ (the same system examined by the Lynden-Bell group), $[C_1mim][PF_6]$, $[C_2mim][BF_4]$, $[C_4mim][BF_4]$, and $[C_4mim][PF_6]$. For each liquid, a total of 192 ion pairs were simulated for 100 ps. Liquid densities generally agreed with experiment and with previous simulations. Although this force field appears to be the most advanced of all the imidazolium force fields, the liquid densities computed with it are not significantly different from those obtained with the earlier, more ad hoc force fields. This is a recurring theme for many systems that have been studied to date. While liquid densities are an attractive experimental property with which to compare simulation results, it is a property that is remarkably insensitive to the force field and consequently is not a particularly useful measure for discriminating between "good" and "bad" force fields. Liu, Huang, and Wang[60] point this out, stating that liquid densities are fairly insensitive to charge distributions. This force field did achieve slightly better agreement with experimental densities than previous studies, however, and the authors attribute this to the fitting they did on the C2 hydrogen van der Waals parameters. They also computed enthalpies of vaporization and the various components of the intermolecular energy showing that, as the alkyl chain length increases, the van der Waals interactions become more dominant and more negative in energy. This points to the fact that the "nonpolar" regions of the ionic liquid are interacting in a favorable, stabilizing manner, a finding similar to that of Urahata and Riberio.[56]

It was noted that the anions tend to localize near the C2 carbon on the imidazlium ring in many of the previous simulation studies.[37,39,49] The corresponding ab initio calculations show this region of the ring to have the greatest concentration of positive charge, and that the hydrogen attached to the C2 carbon has a high Bronsted acidity, validating the tendency for the negatively charged anion to localize near this region. Liu, Huang and Wang[60] showed this in a graphical way, plotting the relative probability distribution of different anions about the cations, an example of which is shown in Figure 6. The different colors in the original publication correspond to different probabilities of observing the center of a PF_6^- anion about a $[C_4mim]$ cation. The anion resides in several different places during the course of the simulation, but the most populated regions are near C2. Interestingly, the region near the butyl chain is devoid of anion density; apparently, the nonpolar alkyl group "sweeps out" a region around the cation, such that the anion resides, on average, at other locations that are more polar and less sterically congested.

We finish the discussion of force fields developed for imidazolium-based systems by describing the work of Voth and co-workers who simulated $[C_2mim][NO_3]$ first with traditional fixed-charge models[62] and then with a model that included electronic polarizability.[63] For the fixed-charge system, Del Popolo and Voth[62] used a force field having the AMBER function form, with parameters for the cation and anion taken from existing sources. They

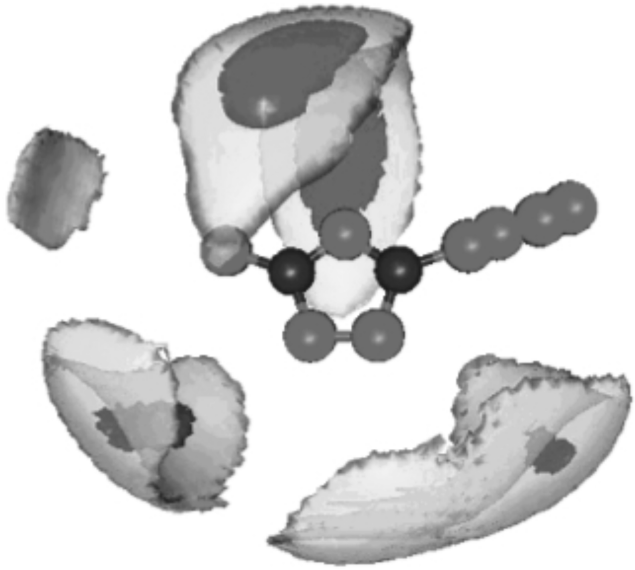

Figure 6 Three-dimensional probability distributions of PF_6^- around C_4mim cation. The dark and light bounded contour surfaces are drawn at 20 and 6 times the average density, respectively. (Image from the work of Liu and co-workers.[60] Used with permission.)

performed MD simulations with the code DL_POLY, with 500-ps production runs to obtain averages, and they found similar ordering of the cations and anions as observed in previous studies.

Del Popolo and Voth[62] computed dynamical properties at 400 K and observed very long overall rotational relaxation times, consistent with the slow dynamics observed by Margulis, Stern, and Berne[47] as well as by Morrow and Maginn.[49] They showed the clearest evidence up to that point that the dynamic motion of ionic liquids bears a resemblance to that of supercooled or glassy systems, an issue that will be described more fully later in this chapter.

This group later examined the same $[C_2mim][NO_3]$ system but used a force field that accounts for electronic polarizability instead of treating partial charges as fixed entities.[63] This was the first time a polarizable model was used to study an ionic liquid, and the authors found that the dynamics became faster when polarizability was included compared to the results from a fixed-charge model. The Newtonian shear viscosity at 400 K was estimated to be 6.84 cP with the fixed-charge model but 4.72 cP with the polarizable model as an example. Interestingly, static properties, e.g., liquid structure, are essentially unchanged when the two models are compared. The authors attribute the dynamical differences to the fact that charge neutrality among ion clusters

can only be achieved via translational motion with fixed charges. Ion clusters form "cages" that are long lived and slow the dynamics. When charge fluctuations are allowed as with a polarizable model, however, an additional charge screening mechanism is operative that allows the system's dynamics to increase somewhat.

Force Fields and Properties of Other Ionic Liquids

There exist several other cation types that can be made into ionic liquids, although, as mentioned previously, most experimental and simulation studies have been limited to the imidazolium cation. A small number of computational studies have been conducted on systems containing other cations, including pyridinium, phosphonium, guanidinium, and triazolium, and, there has also been work on developing force fields and computing properties for ionic liquids containing anions beyond the standard set of halides, PF_6^-, BF_4^-, and NO_3^-. Here we review some of those studies.

Cadena and co-workers[64] developed a force field for the alkyl-pyridinium cation, and simulated 1-*n*-hexyl-3-methylpyridinium bis(trifluoromethylsulfonyl)imide ([C_6mpy][Tf_2N]), 1-*n*-octyl-3-methylpyridinium bis(trifluoromethylsulfonyl)imide ([C_8mpy][Tf_2N]), and 1-*n*-hexyl-3,5-dimethylpyridinium bis (trifluoromethylsulfonyl)imide ([C_6dmpy][Tf_2N]). They used a mix of quantum calculations and parameters available in the CHARMM database[42] to parameterize the pyridinium force field, which has the functional form of Eq. [5]. For the [Tf_2N] anion the parameters developed by Canongia Lopes and Padua were used.[65]

Molecular dynamics simulations were conducted at a series of temperatures for 5 ns, each using NAMD.[66] Liquid densities, compressibilities, and expansivities were computed between 298 and 348 K and compared to experimental data. They observed that there exists a significant history dependence of the liquid densities. That is, computed densities depended on the equilibration history, even though 5-ns production runs were carried out. As Del Popolo and Voth[62] observed for [C_2mim][NO_3] at 400 K, significant non-Gaussian dynamics are in effect, suggesting that, at least for these ionic liquids, calculating even static properties such as densities can be problematic due to the sluggish dynamics of the system and that great care must be taken to ensure proper equilibration. The authors also conducted experimental nuclear magnetic resonance (NMR) investigations to measure self-diffusion coefficients of the cations and anions. They showed that the MD simulations had not yet achieved diffusive behavior, even after 5 ns, so direct comparison of experimental and calculated self-diffusivities was not possible. Their computed rotational relaxation times for the cations and anions showed that the cations with the longest alkyl groups had rotational relaxation times greater than 10 ns at 298 K, and greater than 2 ns even at 348 K. The [Tf_2N] anion had faster rotational relaxation times, but they still ranged from 4 ns at 298 K to 0.8 ns at

348 K. This was an important finding because many groups had begun to compute dynamic properties of ionic liquids from relatively short simulations. As shown in detail below, care should be taken when computing dynamical properties in ionic liquids; due to their sluggish dynamics, much longer simulation times may be required than are commonly used for ordinary liquids.

Canongia Lopes and Padua extended their previously developed imidazolium force field to include *N*-alkylpyridinium and tetraalkylphosphonium cations.[67] They also developed parameters for the Cl^-, Br^-, and the dicyanamide [$N(CN)_2^-$] anions using the same basic procedure in their previous study.[57] When reasonable, extant parameters were available in the OPLS database, these were used, but missing parameters, or parameters in disagreement with ab initio structures, were fit. Because their main concern was with what they term ''molecular simulation'' rather than ''molecular mechanics,'' they did not attempt to get each vibrational mode perfectly correct. Rather, they focused more on dihedral angle parameters and partial charges, as these have the biggest effect on bulk properties. To test the force field, isothermal-isobaric MD simulations were run using DL_POLY, with 200-ps equilibration runs and production runs of at least 400 ps. Densities of crystals and the liquid phase were computed and, when possible, compared with experiment. Computed crystal densities were all within 3.4% of experiment, while no computed liquid density differed from experiment by more than 2.5%. No comparison was made between this pyridinium force field and that proposed by Cadena and co-workers.[64]

Triazolium-based ionic liquids are being examined as possible energetic materials, and determining the physical properties of such substances is difficult to do experimentally. Modeling studies are therefore of considerable practical interest. Cadena and Maginn[68] developed parameters for a series of triazolium-based ionic liquids, following the procedure this group had used previously. The cations considered include 1,2,4-triazolium, 1,2,3-triazolium, 4-amino-1,2,4-triazolium, and 1-methyl-4-amino-1,2,4-triazolium. Each cation was paired with a nitrate or perchlorate anion. They used MD to compute liquid-phase heat capacities, cohesive energy densities/enthalpies of vaporization, gravimetric densities/molar volumes (as a function of temperature and pressure), self-diffusivities, rotational time constants, and various pair correlation functions. They computed heat capacities and crystal lattice parameters in the solid phase. Of all of these properties, only lattice parameters have been measured experimentally (and only for four of the triazolium compounds). The agreement with the experimental crystal structures was good, with overall computed densities deviating from experiment by anywhere from 0.6 to 3.2%. When properties were compared with that of the imidazolium-based ionic liquid, the triazolium-based materials were found to have much smaller molar volumes, higher cohesive energy densities, and larger specific heat capacities. They also tended to be less compressible, have a higher gravimetric density and faster rotational dynamics, but to have similar translational dynamics as their imidazolium counterparts.

Zhou and co-workers[69] developed a force field for ionic liquids containing a tetrabutylphosphonium cation ([$P(C_4)_4$]) paired with the following amino acid-derived anions: glycine ([Gly]-), alanine ([Ala]-), serine ([Ser]-), lysine ([Lys]-), leucine ([Leu]-), isoleucine ([Ile]-), phenylalanine ([Phe]-), proline ([Pro]-), methionine ([Met]-), aspartic acid ([Asp]-), glutamic acid ([Glu]-), glutamine ([Gln]-), and taurine ([Tau]-). These ionic liquids had been synthesized by their group and evaluated for potential use in CO_2 capture applications. The force field parameters were developed using the same basic techniques as used by other groups for different ionic liquids. Isothermal-isobaric MD simulations were then conducted using the MDynaMix code. Each pure liquid simulation was on 192 ion pairs with 1-ns production runs. Liquid densities, heat capacities, and liquid microstructure were computed and compared to experiment. Liquid densities were generally accurate to within a few percent. Heat capacities were computed by difference from simulations at adjacent temperatures using the following expression:

$$C_p(T,P) \approx \left[\frac{H(T+\Delta T) - H(t)}{\Delta T}\right]_P \qquad [6]$$

where H is the enthalpy and ΔT is some small temperature differential over which the heat capacity is assumed constant. The computed heat capacities agreed less well with experiment than did the densities, differing anywhere from 1 to 43% with no identifiable trend. We suspect this may not necessarily be an indication of a poor force field, but rather that Eq. [6] should not be used to compute heat capacities. Each harmonic bonded term in the classical potential (Eq. [5]) will add Nk_B to the heat capacity, which is generally a gross overestimation. This is a widely known limitation of classical force fields having the form of Eq. [5].

Our group has computed heat capacities from simulations using a different approach.[64] Instead of using Eq. [6], one can split the heat capacity into ideal gas and excess terms:

$$C_p = C_p^{\mathrm{ig}}(T,P) + C_p^{\mathrm{ex}} = \left(\frac{\partial\langle H^{\mathrm{ig}}\rangle}{\partial T}\right)_P + \left(\frac{\partial\langle H^{\mathrm{ex}}\rangle}{\partial T}\right)_P \qquad [7]$$

where H^{ig} contains intramolecular contributions to the heat capacity and H^{ex} contains all intermolecular nonbonded terms. The angle brackets indicate an ensemble average. The ideal gas contribution to the heat capacity can be computed accurately from a quantum calculation of the ions in the gas phase. The excess portion can be computed via finite difference (Eq. [6]) from classical condensed-phase simulations, with H^{ex} replacing the total enthalpy. We found this method typically yields more consistent and more accurate heat capacities; we suspect that if the heat capacities for the [$P(C_4)_4$] amino acid liquids were

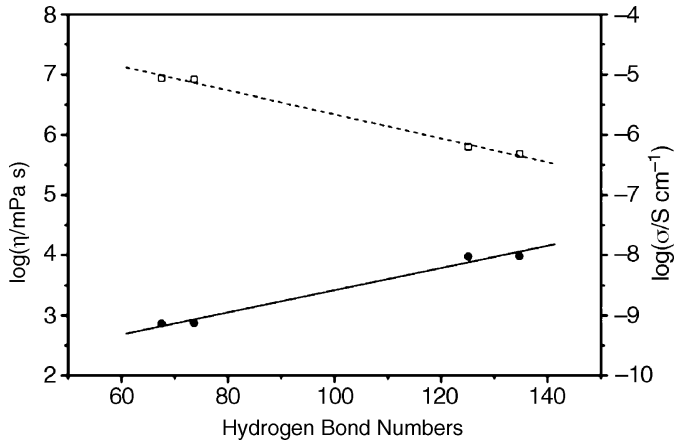

Figure 7 Experimental conductivities (open squares) and viscosities (filled circles) plotted against the calculated number of hydrogen bonds among anions in $[P(C_4)_4]$ amino acid ionic liquids.[69] The mobility of the liquid decreases as hydrogen bonding among anions increases. (Used with permission.)

computed in this manner, they may have agreed better with experiment. It would be interesting to investigate this issue further.

A hydrogen-bonding analysis was also performed by Zhou and coworkers[69] in which the number of hydrogen bonds between an oxygen and a hydroxyl hydrogen on an anion were counted. Figure 7 shows a plot of the experimental viscosity and conductivity versus the number of hydrogen bonds calculated for that particular ionic liquid. The correlation is clear—the greater the number of hydrogen bonds, the slower the dynamics (i.e., higher the viscosity and lower the thermal conductivity). The authors conclude that the relatively high viscosity of this class of material is due to the ease with which these materials form hydrogen bonds. If this trend can be shown to hold for other ionic liquids, it might be an effective screening method in molecular design for identifying ionic liquids with high and low viscosities.

Liu et al. developed force field parameters for *N*,*N*,*N*′,*N*′-tetramethylguanidinium (TMG) ionic liquids paired with formate, lactate, perchlorate, trifluoroacetate, and trifluoromethylsulfonate anions.[70] The force field has the typical AMBER form, and parameterization was done in much the same way that other force fields have been developed, with harmonic bond and angle terms fit to quantum-derived vibrational frequencies, and where dihedral angle parameters were fit to ab initio energy profiles computed for gas-phase ions. Liquid densities were computed from 100-ps MD runs at temperatures ranging from 298 to 373 K. The computed densities agree well with experiment for all but the system containing the trifluoromethylsulfonate anion, in which case the density was overpredicted by a fair amount. The authors attribute this to possible problems with the charge distribution and Lennard-Jones

parameters used for the anion. Enthalpies of vaporization were computed and found to range from 50 to 185 kJ/mol, depending on the compound and temperature. The lower value is small for ionic liquids and suggests significant volatility; it would be interesting to see if experimental vapor pressure measurements confirm this. Finally, by analyzing distribution functions, it was found that the amino group on the cation formed hydrogen bonds with all five anions studied.

The same group then proposed a force field for 11 different cyclic guanidinium cations paired with the nitrate anion.[71] Their approach to force field development followed the same methods used before. Production runs were carried out for 1 ns at temperatures between 320 and 450 K. Because most of the compounds studied have glass transition temperatures or melting points above room temperature, only a small number of experimental densities exist for comparison. In general, it was found that the simulations systematically underpredict the liquid density by about 5%, which the authors speculate is due to problems in the parameterization of the Lennard-Jones parameters in the force field. Self-diffusion coefficients were computed from the Einstein relation over the trajectories from 200 to 600 ps. As discussed below, the authors were careful to test that their systems were in the diffusive regime. It is surprising that true diffusive motion was observed, however, given that a total mean-squared displacement of only about 0.06 nm^2 was observed over the time in which the self-diffusivity was computed. This length is much shorter than the axis of either ion. Nevertheless, estimates of the self-diffusivity were on the order of 1×10^{-11} m^2/s, and from this and the Stokes–Einstein model, estimates of the viscosity and conductivity were made.

SOLUTES IN IONIC LIQUIDS

Although pure ionic liquid properties are important, many applications envision the use of ionic liquids as solvents or separation agents, where properties of ionic liquids mixed with other species are paramount. Relatively few simulations have been carried out to study the properties of ionic liquids with dissolved solutes, but the number of studies on this topic has increased recently. Here we review several of these studies.

As mentioned earlier, Hanke, Atamas and Lynden-Bell[37] conducted the first simulation study of solvation in ionic liquids by investigating the behavior of water, methanol, dimethyl ether, and propane in [C_1mim][Cl]. Using thermodynamic integration,[38] they computed the difference in excess chemical potential of those same solutes in [C_1mim][Cl] and ranked the solubilities on the basis of relative excess chemical potentials. In 2003, they examined[72] benzene and a hypothetical uncharged "benzene" in [C_1mim][Cl] and [C_1mim][PF_6] by using the same thermodynamic integration technique and showed that the charged "aromatic" benzene is much more favorably

solvated by the ionic liquids than is the uncharged "aliphatic" benzene, although they were unable to compute absolute free energies and hence actual solubilities. They found significant differences in the organization of the ions about the two different benzene molecules. As shown in Figures 8(a) and 8(b), the cations of the ionic liquid organize very strongly above and below the plane of the charged benzene, while the anions organize around the equator of benzene. This is driven by the charge distribution in benzene itself; it is more positive around its equator and more negative above and below its plane. In contrast, the cation and anion distribution is much more uniform about the uncharged aliphatic benzene.

Hanke and Lynden-Bell[73] carried out another study of water dissolved in hydrophilic [C_1mim][Cl] and hydrophobic [C_1mim][PF_6] in which isochoric-isothermal MD simulations were run at 127°C on mixtures containing water mole fractions of 0.05, 25, 50, 75, and 99.5%. They computed excess volumes, enthalpies, and internal energies of mixing and compared the results between the two ionic liquids and found that the excess properties between the two systems differed qualitatively, as might be expected. Unfortunately, no experimental data was available for these systems against which to compare their results. The authors pointed out, however, that the magnitude of computed quantities such as excess molar volumes were consistent with those for other ionic liquid systems for which data was available.

Cadena and co-workers[74] published a joint experimental and molecular modeling study directed at explaining the high solubility of CO_2 in imiadzolium-based ionic liquids. The simulations involved the liquid properties of pure [C_4mim][PF_6] and 1-*n*-butyl-2,3-dimethylimidazolium hexafluorophosphate ([C_4mmim][PF_6]). The latter material was studied to examine the role played by the acidic proton at the C2 position of the cation; by blocking this site with an additional methyl group, its effect on liquid structure and CO_2 solubility could be assessed. MD runs were done at 25, 50, and 70°C for the pure ionic liquids and for mixtures containing 10 mol% CO_2. Simulated densities are roughly 2% lower than experimental values for [C_4mim][PF_6] and 4–6% higher than the experimental values for [C_4mmim][PF_6]. The simulations found that the partial molar volume for CO_2 at the mixture concentration is 33 cm^3/mol in [C_4mim][PF_6] and 28 cm^3/mol in [C_4mmim][PF_6]. The experimental value for [C_4mim][PF_6] is about 29 cm^3/mol but no experimental data exist for [C_4mmim][PF_6]. The relatively small partial molar volumes reflect the fact that the liquid volume expands very little upon dissolution of CO_2 into an ionic liquid, indicating that the underlying liquid network is not greatly perturbed by the presence of CO_2 at these concentrations. The simulations show that CO_2 does not associate to any great extent with the C2 position of the cation, regardless of whether there is a methyl group present or not. This is due to the fact that the anion associates preferentially with this part of the cation, thereby "blocking" most direct interactions with CO_2. It was found that CO_2 associates preferentially with the [PF_6] anion, and adopts a "tangent"

conformation in which it lays flat against the nearly spherical PF_6 anion. The simulations are consistent with the overall findings of the experiments presented in the work in which the anion was found to have a much more profound effect on CO_2 solubility than does the cation.

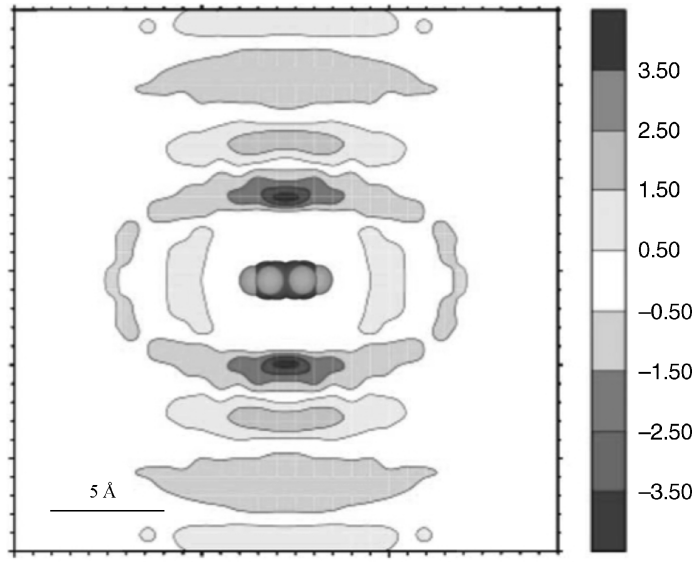

(a)

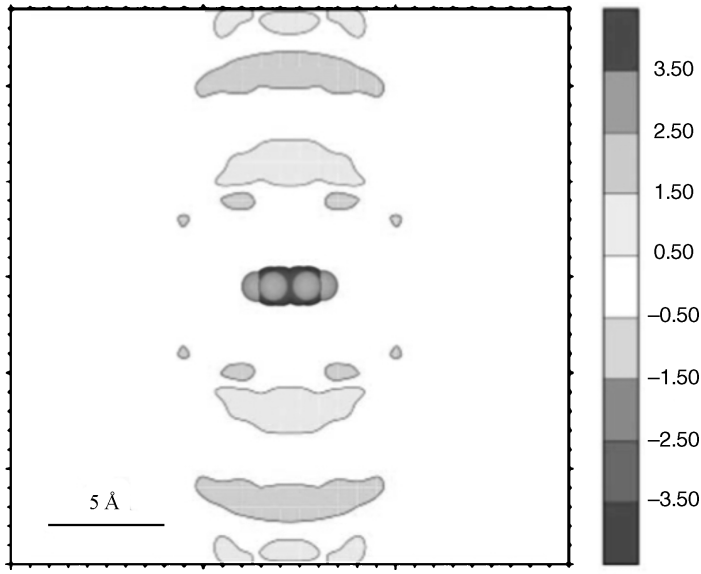

(b)

Deschamps, Costa Gomes and Padua[75] computed the relative solubility of argon, methane, oxygen, nitrogen, and carbon dioxide in $[C_4mim][PF_6]$ and $[C_4mim][BF_4]$ at 1 bar and temperatures of 303, 323, and 343 K using the free-energy perturbation algorithm in DL_POLY. The simulations gave the correct relative order of solubility in $[C_4mim][PF_6]$, but the temperature dependence of the solubility for the nonpolar gases was exactly opposite that observed experimentally. It has been found experimentally that the partial molar enthalpy of solution for many nonpolar gases such as nitrogen and oxygen is zero or slightly positive. In contrast, the simulations predicted that they were slightly negative, thus giving the wrong temperature dependence. For CO_2, however, the simulations predict correctly that solvation is exothermic. The radial distributions for the CO_2 / $[C_4mim][PF_6]$ system showed that CO_2 does not localize near the C2 carbon of the cation, but rather prefers the C4 and C5 carbons. The authors also found that the CO_2 molecules lay flat against the PF_6 anion. Both of these results are consistent with the findings of Cadena and co-workers.[74]

Computing the solvation of gases in liquids involves two processes: creation of a cavity within the solvent capable of hosting the solute (often termed a "free volume" process), and activation of the solute–solvent interactions. Deschamps, Costa Gomes and Padua[75] computed the free volume in ionic liquids by performing hard sphere insertions into the pure ionic liquid and determining the probability of finding a cavity of a particular size. They found the probability of cavity formation in an ionic liquid to be lower than what is observed in either water or *n*-hexane at the same temperature, and thus the work of cavity formation in an ionic liquid is greater than for conventional solvents. They also saw little difference in the free volumes between the two ionic liquids they studied. To evaluate the interactions between solute and solvent, the authors computed the solubility of CO_2 and N_2 in both ionic liquids in which electrostatic terms were used to model the quadrupole moment of the gases. They then repeated the calculations with CO_2 and N_2 models having no

Figure 8 (a) Cross section of the three-dimensional probability distributions around benzene in $[C_1mim][Cl]$. The sixfold axis of the benzene molecule lies in the vertical direction, and the twofold axis of the molecule lies in the horizontal direction, perpendicular to the field of view. The difference in distributions of the cations and anions is shown; regions in the lightest shades are more likely to contain anions, while dark shades correspond to regions containing cations (see original publication for color plots). The scale is in multiples of the average concentration of cations (or anions) in the solution. (Taken from Ref. 72. Used with permission.) (b) Cross section of the three-dimensional probability distributions around uncharged "benzene" in $[C_1mim][Cl]$. The difference in distributions of the cations and anions is shown; regions in the lightest shades are more likely to contain anions, while dark shades correspond to regions containing cations (see original publication for color plots). Note that the differences are much less than in the simulations of the "real" benzene (a). (Taken from Ref. 72. Used with permission.)

quadrupole moment and found that the solubility was significantly lower for CO_2 and slightly lower for N_2 when compared to the results with a quadrupole moment. Finally, the authors computed the solubility of water in the ionic liquid. Because water is a liquid under the conditions they studied, a thermodynamic integration process was used. They determined that the infinite dilution activity coefficient of water in $[C_4mim][PF_6]$ is 4.7 ± 3.6, which agrees well with the experimental value of 5.36.[76]

Shah and Maginn[77] carried out a Monte Carlo study of CO_2 solubility in $[C_4mim][PF_6]$ to compute the Henry's law constant of CO_2 using the test particle insertion free energy perturbation method. The Henry's law constant for solute 2 dissolved in solvent 1, $H_{2,1}$, is defined as

$$H_{2,1} = \lim_{x_2 \to 0} \frac{f_2}{x_2} \qquad [8]$$

where f_2 is the fugacity of the solute in the gas phase, and x_2 is the mole fraction of the solute in the liquid phase. The fugacity is related to the excess chemical potential according to the following expression:

$$H_{2,1} = k_B T \rho_1 \ \exp\left(\frac{\mu_2^{ex}}{k_B T}\right) \qquad [9]$$

where k_B is the Boltzmann constant and ρ_1 is the liquid-phase density. The excess chemical potential is obtained from the test particle insertion method by inserting many noninteracting CO_2 molecules into the liquid over the course of a constant temperature and pressure simulation and computing the ratio

$$\mu_2^{ex} = -k_B T \ \ln \frac{\langle V \exp(-U_{test}/k_B T) \rangle}{\langle V \rangle} \qquad [10]$$

where U_{test} is the energy of the test molecule inserted into the system and the angled brackets signify ensemble averages. Their simulations predicted that CO_2 solubility in this ionic liquid is 2–3 times higher than what is observed experimentally; the computed partial molar enthalpy of absorption is about 7 kJ/mol more negative than experiment as well.

Part of the inaccuracy of these results can be attributed to the force field used, which included a united-atom model for the cation and an explicit-atom model for the anion. This model,[77] unlike Shah and Maginn's previous united-atom model,[39] underestimated the pure liquid density by about 5%, which should lead to higher gas solubilities on the basis of free volume arguments. The other source of error rests with the simulation method itself. Kofke and Cummings[78] have shown that single-stage free energy perturbation methods

like that used by Shah and Maginn[77] suffer from convergence problems, especially for systems that are dense and have specific interactions such as ionic liquids. More sophisticated simulation methods are required to overcome these limitations, and Shah and Maginn subsequently implemented an expanded ensemble Monte Carlo method[79] that improves the test particle insertion approach significantly. This method involves a series of Monte Carlo moves that change the strength with which the solute molecule couples with the solvent, ranging from no coupling (an ideal gas) to full coupling (a dissolved solute molecule). By collecting the frequency with which the system visits the ideal-gas state and fully coupled state, the excess chemical potential of the solute (and hence, Henry's law constant) can be computed. Additional self-adapting bias factors were used to further improve sampling. The authors used the method to compute the Henry's law constants of water, carbon dioxide, ethane, ethene, methane, oxygen, and nitrogen in $[C_4mim][PF_6]$. Their results were in good qualitative agreement with experiment, and in many cases, quantitative agreement was achieved. For example, the computed Henry's law constant for water at 298 K is 0.07 ± 0.02 bar, while the experimental result is 0.17 ± 0.02 bar. For CO_2 the computed value is 46 ± 16 bar, while the experimental value is 53.4 bar. These results suggest that earlier inaccuracies are due more to sampling problems than to inherent inaccuracies in the force field used.

Complete isotherms for CO_2, CO, and H_2 in $[C_4mim][PF_6]$ were computed by Urukova, Vorholz, and Maurer[80] using the isothermal-isobaric Gibbs ensemble Monte Carlo method. In Gibbs ensemble Monte Carlo studies, separate gas-phase and liquid-phase systems are coupled virtually so that exchanges of molecules take place between the two phases to satisfy the phase equilibrium condition. Temperatures ranging from 293 to 393 K and pressures up to 9 MPa were simulated, using a rigid model for the ionic liquid and parameters taken from Shah and Maginn.[39] They found that the simulations agree remarkably well with available experimental data. The original study[80] contained a small conversion factor error, however, which, when corrected,[81] gives results that are not as close to experiment as indicated in the original study.

Shi and Maginn[82] proposed a new type of Monte Carlo method they call continuous fractional component Monte Carlo, or CFC MC. This is a simulation procedure that enables isotherms to be computed accurately for gases and vapors in ionic liquids by inserting and deleting molecules gradually, instead of performing the moves all in one step. They used CFC MC to compute isotherms of water and carbon dioxide in 1-*n*-hexyl-3-methylimidazolium bis(trifluoromethylsulfonyl)imide ($[C_6mim][Tf_2N]$).[83] Figure 9 shows an example of the accuracy that can be obtained with the method; the computed isotherm is in quantitative agreement with three independent sets of experimental data up to about 70 bar.[84–86] At the very highest pressure of 200 bar, it appears that the simulations underpredict slightly the CO_2 concentration, which may reflect

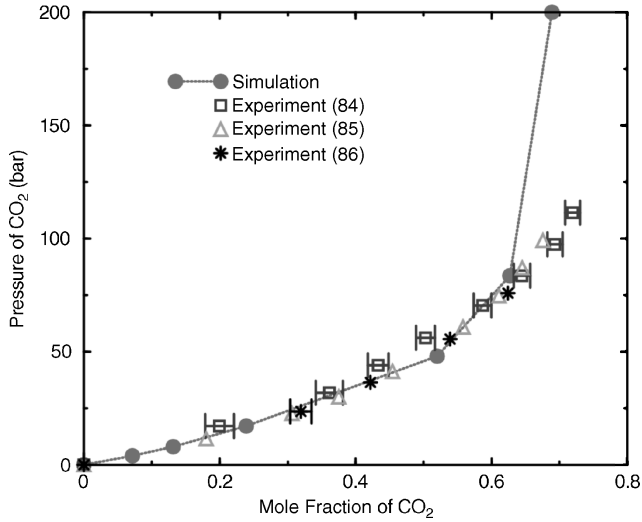

Figure 9 Comparison of simulated and experimental isotherms for CO_2 in $[C_6mim][Tf_2N]$ at 333 K. The experimental data come from Brennecke and co-workers,[84] Maurer and co-workers,[85] and Scurto.[86]

the fact that the repulsive part of the force field is inadequate or that three-body interactions (neglected in this force field) are important at these high densities. The authors also computed the solubility of water in this ionic liquid, and the agreement with the lone experimental data point (at saturation) was quantitative.

Chaumont and Wipff[87] have carried out a number of computational studies investigating the solvation of metal ions in ionic liquids. This is an important topic because ionic liquids have the potential to be effective, environmentally benign, metal extractants for aqueous metallic ions. In 2003 Wipff's group used MD simulations to study the solvation of La^{3+}, Eu^{3+}, and Yb^{3+} in $[C_4mim][PF_6]$ and in $[C_2mim][AlCl_4]$.[87] They used force fields previously developed to model the ionic liquid, while metal ion parameters were fit to hydration free energy data. Pure ionic liquid phases were simulated first using MD, and then one M^{3+} (M = La, Eu, or Yb) and three NO_3^- ions were immersed into the system. After a relaxation schedule, 1.2-ns MD simulations were run and the resulting trajectories analyzed. The authors also computed the free energy differences for solvated cations by using thermodynamic integration to find that the M^{3+} ions become surrounded rapidly by six PF_6^- anions in the case of $[C_4mim][PF_6]$ and eight $AlCl_4^-$ anions in the case of $[C_2mim][AlCl_4]$. As the metal cation size was increased, the distance between the metal ion center and the anion F^- or Cl^- atoms also increased, as expected. They find that the PF_6^- anions solvating the metal ions are much more mobile than are the $AlCl_4^-$ anions. In each case, the neutralizing

NO_3^- anions are surrounded by four to five imidazolium cations. Chaumont, Engler and Wipff employed the same technique to examine the solvation of uranyl and strontium nitrates as well as uranyl chlorides in the same ionic liquids.[88] As was observed in the previous study, the anions of the ionic liquids solvate the strontium and uranyl ions preferentially. Detailed radial distribution functions and coordination numbers were computed. This group has extended this work by making comparisons of computed solvation ordering with data from experimental spectroscopic studies.[89]

A study investigating the interface of water–ionic liquid binary systems was done by Sieffert and Wipff,[90] who carried out MD simulations in which simulation boxes of water and the ''hydrophobic'' ionic liquid [C_4mim][Tf_2N] were joined. They also premixed water and the ionic liquid and studied the demixing process. They varied the type of water model used as well as the overall charge on the ionic liquid ions to see how these variables can affect the results. Long simulations (20–40 ns) were run to enable the boxes to ''mix'' (for initial conditions in which water and the ionic liquid were separated) and ''demix'' (for initial conditions in which water and the ionic liquid were initially mixed at high temperature). Their calculations provide a detailed dynamic picture of phase separation as shown in Figure 10 for one such

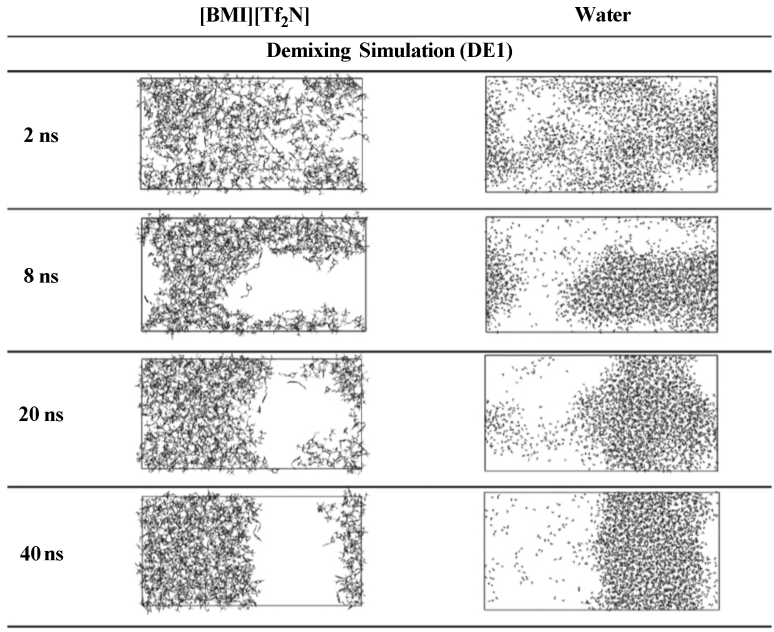

Figure 10 Time evolution of the demixing of [C_4mim][Tf_2N] (designated in the figure as [BMI][Tf_2N]) and TIP3P water, starting from completely mixed liquids. Snaphots are shown at different times, with the liquid components shown side by side for clarity. (Image from Ref. 90 and used with permission.)

simulation, where a nearly planar water–ionic liquid interface forms after about 40 ns. Sieffert and Wipfff computed the total amount of water that dissolves in the ionic liquid phase to find that the quantity varies depending on whether the simulation starts from an initially homogeneous "mixed" state or from a heterogeneous "unmixed" state. For example, on the order of 60 water molecules are present in the ionic liquid phase when a homogeneous system demixes, but only 25 water molecules infiltrate the ionic liquid phase from an initially heterogeneous system. This is clear evidence that the simulations have not reached thermodynamic equilibrium and are instead exhibiting "hysteresis." The authors recognize this, stating that full convergence is not obtained even with the long 20–40 ns simulations. This study demonstrates nicely the problem with MD when it comes to computing phase equilibrium; the time-scale limitations hinder significantly the ability of systems to come to equilibrium, particularly when an interface is present, and this is why we believe MC methods, like the CFC MC approach discussed above, are far superior for computing phase equilibrium. Unfortunately, fewer choices exist when it comes to general and easy-to-use MC codes than for MD codes, and so, MC simulations have seen less use.

Molecular dynamics simulations focused on the solvation dynamics of a hypothetical dimer probe molecule in $[C_2mim][PF_6]$ and $[C_2mim][Cl]$ have been done by Kim and co-workers.[91] The solvation dynamics were characterized by the time correlation function of the vertical energy difference of two solute states relevant to a charge shift. The vertical energy difference between an initial state i and a final state f, $\Delta E_{i\to f}$, is assumed to be comprised of only Coulombic terms. The time correlation function is computed as

$$C_{i\to f}(t) = \frac{\langle \delta\Delta E_{i\to j}(t)\delta\ \Delta E_{i\to j}(0)\rangle}{\langle (\delta\Delta E_{i\to j})^2\rangle} \qquad [11]$$

where the angle brackets refer to ensemble averages and

$$\Delta E_{i\to j} = \Delta E_{i\to j} - \langle \Delta E_{i\to j}\rangle \qquad [12]$$

These authors find that there is a very fast mode that causes the correlation function to decay by about 70% in the first 0.2–0.3 ps at 400 K. Rapid oscillations of the correlation function exist in this regime, with a frequency of roughly 26 ps^{-1}. This mode is attributed to the vibration of the anions in their first solvation shell. A very slowly decaying multiexponential portion of the correlation function also exists. The authors find that the short time dynamics are dominated by the anion motion, which is mostly translational in nature.

There is a huge disparity between the cation and anion dynamics, a feature first observed for $[C_4mim][PF_6]$ by Morrow and Maginn.[49]

To assess the polarity of the ionic liquids, Kim's group[91] computed the average energy difference between a nonpolar probe solute and an ion-pair solute in which formal charges of +1 and −1 were placed on the dimer atom centers. This energy difference is expected to give qualitatively similar results as those obtained using spectroscopic probes of polarity. The calculations result in large blue shifts that are qualitatively similar to experimental observations and are consistent with the known solvation power of ionic liquids. The reorganization free energy for transitions between a nonpolar and an ion-pair solute were computed to be 45–40 kcal/mol, indicating that considerable solvent reorganization is required for these systems.

At about the same time as this work was published, Znamenskiy and Kobrak[92] simulated the absorption spectrum of betaine-30, a commonly used solvatochromic probe molecule, in $[C_4mim][PF_6]$. They investigated the interactions responsible for the solvatochromic shift. Because this shift is used experimentally to assess solvent polarity, the calculations can thus provide a direct window into the nature of polarity in ionic liquid systems. To conduct the study, a single molecule of betaine-30 was immersed in a liquid containing 200 ion pairs. Twelve independent 1-ns runs were then carried out, and from that the absorption spectrum was computed. They observe two distinct time scales: one on subpicosecond time scales and one that is on the order of 100 ps. This result is consistent with previous simulation studies as well as time-resolved fluorescence spectroscopy experiments.[93] Although the actual absorption spectra computed do not agree quantitatively with experimental results, the qualitative features do.

IMPLICATIONS OF SLOW DYNAMICS WHEN COMPUTING TRANSPORT PROPERTIES

As mentioned earlier when discussing some of the work by Margulis and Berne,[47] Del Popolo and Voth,[62] and Morrow and Maginn,[49] the dynamical behavior of ionic liquid systems is complex and its behavior is characterized as akin to that of a supercooled liquid.[47] A large number of experimental and simulation studies have been carried out recently that investigated the dynamics of ionic liquid systems. It is not an exaggeration to say that an entire review article could be written on this topic alone, so a comprehensive review of that literature is not possible. Instead, we summarize briefly a few of those results and point out some of the things to be aware of when computing dynamic properties of ionic liquids, while referring the interested reader to the original studies for more details.

Recall that Del Popolo and Voth[62] computed the dynamics of [C_2mim][NO_3] and saw evidence of what they termed dynamic heterogeneity. This can be quantified using a so-called non-Gaussian parameter,[94] $\alpha(t)$, given by

$$\alpha(t) = \frac{3}{5}\frac{\langle|\Delta r(t)|^4\rangle}{\langle|\Delta r(t)|^2\rangle^2} - 1 \qquad [13]$$

where $\Delta r(t)$ is the displacement of an ion center of mass over some time t, and the angle brackets refer to an ensemble average. For a Gaussian distribution of displacements, characteristic of normal liquid diffusive motion, $\alpha(t) = 0$. The extent to which this parameter is nonzero is indicative of dynamic heterogeneity characteristic of subdiffusive motion. They also characterized the dynamics by computing the van Hove correlation function, defined as

$$G_s(r,t) = \frac{1}{N}\left\langle \sum_{i=1}^{N} \delta[r_i^c(t) - r_i^c(0) - r] \right\rangle \qquad [14]$$

This correlation function measures the probability that the center of mass of a molecule is at position r^c at time t given that it was at the origin, $r^c(0)$, at time 0. $G_s(r,t)$ exhibits Gaussian behavior at very short times due to free particle behavior, and in the long time, hydrodynamic limit it will also be Gaussian. Most liquids have Gaussian behavior at intermediate time scales, but supercooled liquids display non-Gaussian behavior at intermediate time scales due to dynamic heterogeneity. Figure 11 shows the van Hove correlation function and the non-Gaussian parameter for [C_2mim][NO_3]. At intermediate times the non-Gaussian parameter (inset) for both the cation and anion are nonzero, and the van Hove correlation function deviates significantly from Gaussian behavior.

Hu and Margulis[95,96] studied the dynamics of [C_4mim][PF_6] by carrying out MD simulations on the neat liquid for 3 ns at 400 and 500 K, and for 9 ns at 300 K. At 300 K, the non-Gaussian parameter $\alpha(t)$ reached a maximum at about 2.5 ns, while the maximum occurred at just over 100 ps at 400 K, in agreement with Del Popolo and Voth's findings.[62] From their computed van Hove correlation function, they found that most ions diffuse more slowly than what would be expected for Gaussian dynamics. However, a small group of ions diffuse much faster than what is expected. Interestingly, a small number of highly mobile ions move further in 200 ps than the less mobile ions do over 2000–3000 ps. Hu and Margulis also found that translational mobility is totally decoupled from rotational mobility for the [PF_6] anion, but the two are coupled tightly for the [C_4mim] cation. They then went on to simulate the absorption and emission spectra of the organic probe molecule 2-amino-7-nitrofluorene (ANF) by immersing a single ANF molecule, in both the

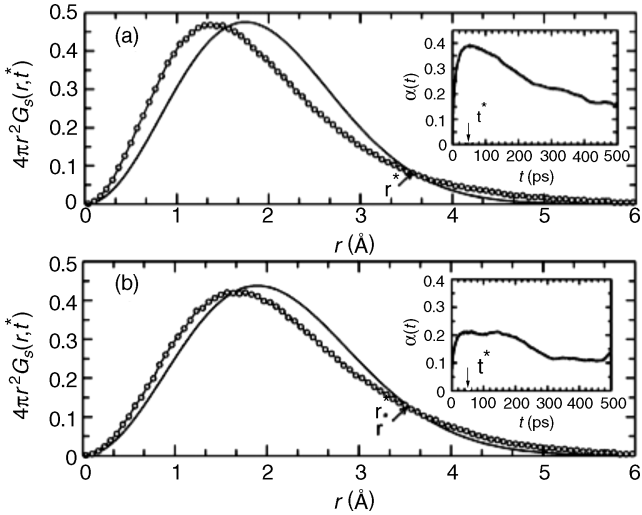

Figure 11 van Hove correlation function $G_s(r,t)$ (line with circles) and Gaussian approximation $G_s^0(r,t)$ (solid line), for (a) $[C_2mim]^+$ and (b) $[NO_3]^-$, evaluated at the delay time t^* in which the non-Gaussian parameter, $\alpha(t)$, reaches its maximum. $r*$ marks the crossing point of $G_s(r,t^*)$ with $G_s^0(r,t^*)$. Insets: non-Gaussian parameters $\alpha(t)$, as a function of time, for (a) $[C_2mim]^+$ and (b) NO_3^-. (Figure taken from Ref. 62 and used with permission.)

ground state and excited-state, into a liquid consisting of 125 ion pairs. The ground- and excited-state charge distributions, which were computed quantum mechanically, had dipole moments of 7.73 and 18.73 debye (D), respectively. All other force field terms were assumed to be the same for the ground and excited states, thus, the method is similar to that used by Znamenskiy and Kobrak.[92] Hu and Margulis[95,96] found that the emission of the probe molecule depends strongly on the absorption wavelength, an observation that is not found in ordinary liquids but often seen in gels. The genesis of this so-called red-edge effect is that the solvent relaxation is much slower than the fluorescence time scale, and consequently relaxation takes place only in the local environment of the solute (and not from the "average" solvent environment). The solute molecules are "trapped" in long-lived solvent "cages" and so do not relax on the time scale of excitation relaxation. When the same calculations were performed for ANF in methanol (a solvent with fast dynamics), no absorption wavelength dependence on the emission was found. The simulations confirmed the interpretations of experimental observations by Samanta and co-workers[97,98] and confirmed the presence of dynamic heterogeneities in these systems, which have a profound influence on the system's dynamics. Hu and Margulis[95,96] find that the dynamic heterogeneity giving rise to the red-edge effect is nearly gone at 500 K.

What are the implications of these studies on the calculation of macroscopic dynamical properties of ionic liquids? At the very least, they suggest that one should be careful when applying standard computational techniques used for simple liquids to ionic liquids. Most of these techniques assume ergodic behavior, but the work described above shows this may not always be the case. Due to the sluggish dynamics of ionic liquid systems, one should carry out very long simulations to ensure adequate sampling.

Consider the simplest dynamic property one can compute, the self-diffusivity, D_s. The standard approach for computing D_s is to conduct an equilibrium MD simulation and accumulate the mean-square displacement as a function of time. The self-diffusivity is then computed using the Einstein equation:

$$D_s = \frac{1}{6}\lim_{t\to\infty}\frac{d}{dt}\langle|r(t) - r(0)|^2\rangle \qquad [15]$$

where the term in angle brackets is the mean-square displacement (MSD). By plotting the MSD as a function of time and taking the slope, one gets an estimate of the self-diffusivity. The problem with Eq. [15] is that it is valid only in the limit of "infinite" time, where "infinite" implies times much longer than the longest relevant relaxation times. How long is this for an ionic liquid? As the results above suggest, even at temperatures as high as 400 K, these times can be longer than 10 ns, which makes for an expensive and time-consuming simulation. There are at least three tests one can apply to check if a system exhibits diffusive behavior. First, one can compute the non-Gaussian parameter for the system using Eq. [13], making sure that the MSD is tracked for times long enough for this parameter to reach zero. The other approaches involve observing the MSD itself.

Figure 12 is a plot of MSD of the $[C_8mpy]$ cation at 298 K, obtained from a simulation of the neat ionic liquid $[C_8mpy][Tf_2N]$.[64] The dashed lines are the individual x, y, and z components of the MSD, while the solid line is the overall displacement. For a homogeneous system, the x, y, and z components should all be equal, and they appear to be so for this system. A slope of this plot can be calculated, and a self-diffusivity estimated using Eq. [15], but the question is, does applying Eq. [15] to the data in Figure 12 give a reliable self-diffusivity? This can be determined simply by testing whether the mean-square displacement versus time has a slope of unity, as it must for a diffusive system. In general the mean-square displacement will have a power law dependence on time, according to

$$\langle|r(t) - r(0)|^2\rangle \propto t^{\beta} \qquad [16]$$

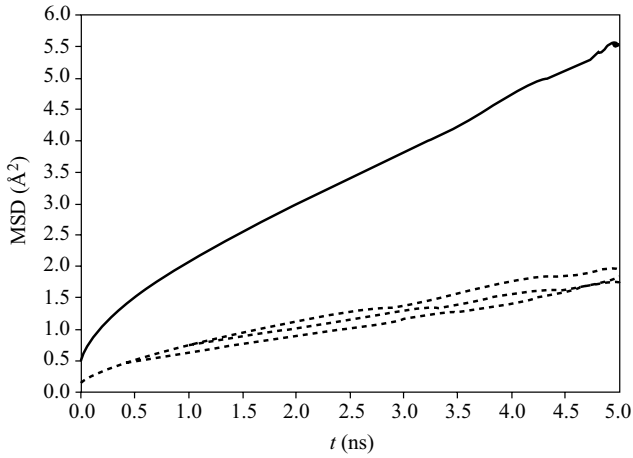

Figure 12 The MSD for the [C_8mpy] cation in [C_8mpy][Tf_2N] at 298 K. The solid line is the overall MSD, while the dashed lines are the individual Cartesian components. (Taken with permission from Ref. 64.)

The parameter β can be computed as a function of time using the following expression:

$$\beta(t) = \frac{d\ \log(\Delta r^2)}{d\ \log(t)} \qquad [17]$$

When β approaches unity, the system is in the diffusive regime and a reliable self-diffusivity can be computed. When β is less than unity, the system is in the subdiffusive regime. Figure 13 shows how β varies as a function of time for the [C_8mpy] cation. β has only reached a value of 0.6 after 3 ns, which clearly indicates subdiffusive motion. The statistics become noisy after 4 ns, and it appears that the system is starting to achieve diffusive behavior after 5 ns. Figure 14 shows how the "apparent" self-diffusivity varies depending upon which time interval of the MSD Eq. [15] is used. At the shortest times, the "self-diffusivity" appears to be about five times larger than it is when the longest time period of the MSD is used; this is simply a reflection of the fact that the cations exhibit ballistic motion at short times. Interestingly, if one (erroneously) reported the self-diffusivity from a very short simulation of this system, the resulting value would be in better agreement with experiment[64] than would the long-time result, again pointing out the danger of blindly applying conventional techniques used with normal liquid systems to ionic liquids. While no "normal" liquid system could be expected to show subdiffusive behavior over the course of a 5-ns simulation, one would expect subdiffusive dynamics on this time scale for polymeric and glass-forming liquids, so be forewarned to anticipate this behavior with ionic liquids. For

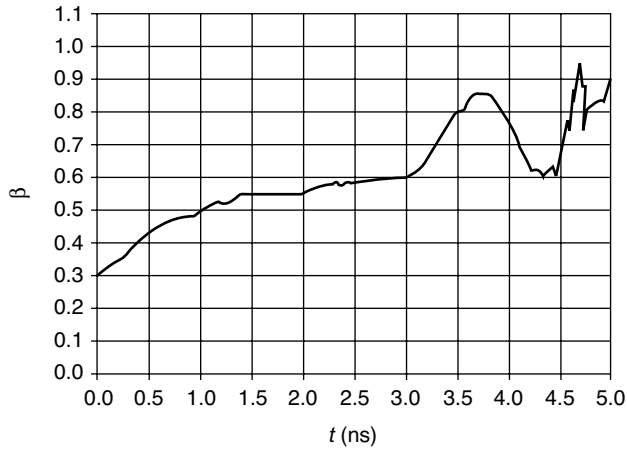

Figure 13 Plot of the diffusive parameter β for $[C_8mpy][Tf_2N]$ at 298 K, computed from the mean-square displacement. For diffusive behavior to be observed, $\beta = 1$. The system is clearly in the subdiffusive regime. (Taken from Ref. 64 and used with permission.)

this reason it may be more appropriate to adopt simulation techniques developed in the polymer community when simulating ionic liquids, rather than applying methods commonly used for simple molecular liquids.

Finally, we note a third and rather simple test to apply to the MSD to determine if diffusive behavior has been achieved. Diffusive behavior implies

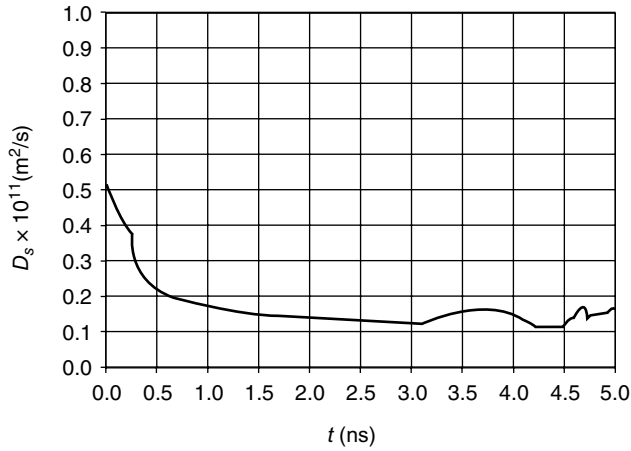

Figure 14 Apparent self-diffusivity for the $[C_8mpy]$ cation in $[C_8mpy][Tf_2N]$ at 298 K, obtained from taking slopes along various time domains of the MSDs. (Taken from Ref. 64 and used with permission.)

that the molecules in question undergo a random walk. One empirical criterion for determining if a random walk takes place is that a molecule must move over some distance longer than a nominal length scale associated with that particular molecule. One measure of this length scale is the maximum distance between two atoms in the molecule, given as

$$R_{\max} = \sqrt{(r_i - r_j)^2} \qquad [18]$$

where r_i and r_j are the positions of atoms furthest apart in the molecule. For most ionic liquids, this value is on the order of 5–10 Å. To observe diffusive motion, a simulation should be run long enough for the MSD to reach at least 25–100 Å.[2] Figure 12 shows that for [C_8mpy[Tf_2N] at 298 K the MSD has not reached 6 Å^2 even after 5 ns. This means that, on average, most of the ions have not even moved the length of two carbon–carbon bonds, making it highly unlikely that diffusive motion is operative.

COMPUTING SELF-DIFFUSIVITIES, VISCOSITIES, ELECTRICAL CONDUCTIVITIES, AND THERMAL CONDUCTIVITIES FOR IONIC LIQUIDS

There have been several studies undertaken to compute macroscopic transport properties of ionic liquids, despite the difficulties mentioned above. These properties include the self-diffusivity, viscosity, electrical conductivity, and thermal conductivity. In this section we review some of these works, but first some background is given on how these transport properties are computed.

The most common method for computing a transport property is to carry out an equilibrium molecular dynamics simulation and compute the integral of the appropriate time correlation function. The general formula is given as

$$\gamma = \int_0^\infty dt \langle \dot{\xi}(t) \dot{\xi}(0) \rangle \qquad [19]$$

where γ is the transport coefficient and ξ is the perturbation in the Hamiltonian associated with the particular transport property under consideration and $\dot{\xi}$ signifies a time derivative. Integrals of the form given by Eq. [19] are known as *Green–Kubo integrals*.[99] Detailed discussions of the theory behind this approach may be found in standard references.[94,99]

It is easy to show that an integrated form of Eq. [19] results in an "Einstein" formula similar to Eq. [15]. Thus an equivalent expression for γ is

$$2t\gamma = \langle (\xi(t) - \xi(0))^2 \rangle \qquad [20]$$

For self-diffusivity, ξ is the Cartesian atom position, and the time correlation function in Eq. [19] is of the molecular velocities. For the shear viscosity, the integral in Eq. [19] is of the time correlation of the off-diagonal elements of the stress tensor. For the thermal conductivity the integral is over the energy current, and for the electrical conductivity the integral is over the electric current.[99]

An important implicit assumption in Eqs. [19] and [20] is that *the time over which these expressions are evaluated is much larger than the correlation time of the variable* ξ. This assumption is often satisfied easily for simple liquids, where relaxation times are fast. For ionic liquids, however, we have seen that correlation times can be very long—on the order of 10 ns or more. Moreover, a very large separation of time scales exists for different motions of the ions. Application of Eqs. [19] and [20] to systems with such long correlation times can be problematic. Equation [19] is particularly suspect. If it is assumed that $\xi(t)$ obeys Gaussian statistics, the standard error in the time correlation function is approximated as[99]

$$\text{Error} \approx \sqrt{\frac{2\tau}{t_{\text{run}}}\langle \xi^2 \rangle} \qquad [21]$$

where τ is the characteristic correlation time and t_{run} is the length of the simulation. The problem with ionic liquids is that, even though the relevant correlation functions decay rather quickly, it is not clear that all the relevant dynamical processes contributing to a particular transport coefficient are being probed on this time scale. An example of this was demonstrated clearly by Urahata and Ribeiro[100] who computed various single-particle time correlation functions for $[C_1mim][Cl]$ (see Figure 15) and showed that a vast separation of time scales exist in this system. The correlation functions associated with the ring center of mass and the alkyl chain dihedral angles decorrelate quickly. However, reorientational motion of the ring takes place on time scales that are orders of magnitude slower. Not surprisingly, the mean-square displacement over these time scales also shows distinct regions.

Computing a transport coefficient to within 1% accuracy requires a simulation that is several orders of magnitude longer than the relaxation time, assuming Eq. [21] is valid. With ionic liquids, this is challenging for properties such as the viscosity because the high viscosity is the result of a low modulus and a long relaxation time. Thus the stress correlation function is low amplitude but long ranged in time and easily overwhelmed by the noise associated with rapid intramolecular modes that have nothing to do with the long-time relaxation processes.

The first attempt to compute the self-diffusivity of an ionic liquid was by Hanke and co-workers,[30] who determined the mean-square displacement of $[C_1mim][Cl]$ over 15 ps and extracted a self-diffusivity using Eq. [15]. As we now know, this time frame is almost certainly too short a simulation to

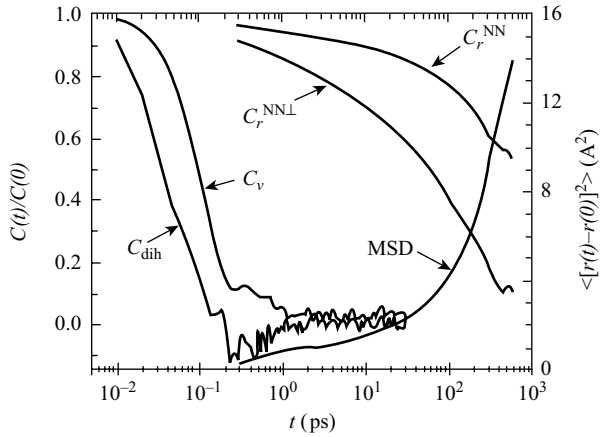

Figure 15 Single-particle time correlation functions of imidazolium cations. Correlation functions include: velocity of geometric center of the imidazolium ring, $C_v(t)$, dihedral angle of the alkyl chain, $C_{\text{dih}}(t)$, reorientation projected along the NN direction, $C_{r\text{NN}}(t)$, and NN direction, $C_{r\text{NN}}(t)$, and MSD of geometric center of the imidazolium ring. The scale for MSD is on the right of the figure. (From Ref. 100 and used with permission.)

observe diffusive motion (the mean-square displacement over this time interval was about 0.5 Å^2). Margulis and co-workers[47] computed the self-diffusivity for $[C_4\text{mim}][PF_6]$ over a similar time scale of about 40 ps. What is interesting is that these (and other calculations from that time period) give estimated self-diffusivities that are of the same order of magnitude as what has been determined experimentally using NMR;[101] such agreement can be taken as being fortuitous. As mentioned in the last section, Cadena and co-workers[64] showed in a combined experimental and molecular modeling study that for alkylpyridinium ionic liquids with the $[Tf_2N]$ anion, simulations longer than 5 ns are required to obtain reliable self-diffusivites near room temperature conditions. As a result, much of the recent work has focused on computing transport properties at elevated temperatures where the simulations are much faster.

Earlier we mentioned that Voth and co-workers[63] conducted equilibrium MD simulations on $[C_2\text{mim}][NO_3]$ at 400 K and computed the self-diffusivity and shear viscosity using both a fixed charge and polarizable force field. They computed the viscosity not from integrating the stress–stress autocorrelation function as is normally done, but rather from integrating the so-called transverse current correlation function, details of which are found in a work by Hess.[102] They used the standard Einstein formula (Eq. [15]) for the self-diffusivity and were careful to ensure that diffusive behavior was achieved when computing the self-diffusivity. Their calculated values of ca. $1 \times 10^{-11}\ \text{m}^2/\text{s}$ for the polarizable model and ca. $5 \times 10^{-12}\ \text{m}^2/\text{s}$ are reasonable. The finding that the polarizable model yielded faster dynamics than with the nonpolarizable model

was a critical and somewhat surprising result, leading the authors to suggest that including polarizability in the model effectively results in more screening taking place between ions, thereby enabling the ions to move past each other with greater ease than when polarizability is absent. This is a reasonable conclusion but has not been investigated further by any other groups. It is an issue that is certain to be investigated in the near future.

The transverse current correlation function was integrated by Voth and co-workers[63] to compute the shear viscosity. Viscosities of 4.74 cP were calculated for the polarizable model, while the fixed-charge model gave a value of 6.84 cP. Both results are consistent with the experimental value of 4.42 cP. Again, the fixed-charge model results in slower dynamics than does the polarizable model, and the polarizable model agrees better with the experiments than does the fixed-charge model. This study provides convincing evidence that the inclusion of polarizability will yield faster dynamics in a particular model, and many authors have since commented on this. The problem is that polarizable models are much more demanding computationally than are fixed-charge models. It is desirable to determine if polarizable force fields are absolutely necessary for such simulations, especially given that the transport properties for other liquids can be computed adequately without resorting to polarizable models.

At this point, a comment is warranted on how Voth and co-workers[63] computed the viscosity because it has relevance to the other studies described below. As discussed earlier, there is an implicit assumption in the use of equilibrium fluctuation formulas when computing transport coefficients. It is assumed that the time scale over which the transport coefficient is evaluated is longer than the correlation times of the quantity being evaluated. In the case of the work by Voth and co-workers, this was verified for the self-diffusivity, where the slope of the mean-square displacement was taken over 1 ns. For the shear viscosity, however, integrals of the transverse current correlation function were taken over time scales ranging from 1 to 10 ps. The reason such short times were used is that the correlation function decays to zero very rapidly, and so long-time integration was numerically impossible. This does not mean, however, that the time scale relevant for viscosity is only 1–10 ps. We know that the viscosity of a liquid depends on many orientational and rotational relaxation processes, all of which occur on time scales orders of magnitude longer than 10 ps, calling into question exactly what is being computed from integrals over such a short time. Is it the "global" shear viscosity? Or, might it instead reflect some type of "local" apparent shear viscosity for molecules? This is not to criticize the work of Voth and co-workers; indeed, as shown below, several other studies have computed the viscosity in the same way. Rather, this issue is raised for the novice modeler because it needs further exploration by the modeling community.

Bhargava and Balasubramanian[103] used equilibrium MD to compute the self-diffusivity, shear viscosity, and electrical conductivity for $[C_1mim][Cl]$ at

425 K. They used a large system (864 ion pairs) and carried out impressively long runs, equilibrating their system for 5 ns and performing a 16-ns production run. To compute the shear viscosity, they took the average of 10 separate Green–Kubo integrations, each of which was over a 1-ns time period. Likewise, the electrical conductivity was evaluated from 11 independent 90-ps Green–Kubo integrations. The self-diffusivity was not evaluated from a Green–Kubo integral, but rather from the integrated Einstein formula (Eq. [15]). Figure 16 depicts the short- and long-time behavior of the cation and anion mean-square displacement, obtained from a single 6-ns trajectory. Both ions appear (by the heuristics defined earlier) to be in the diffusive regime; the computed self-diffusivities for the anion and cation are 1.33×10^{-10} and $1.88 \times 10^{-10}\,m^2/s$, respectively. It is interesting to see that the larger cation actually has a greater self-diffusivity than the smaller chloride anion. This curious behavior has been observed repeatedly for imidazolium-based ionic liquids in simulations[49,60,104] as well as in experiments.[105,106] It is not a universal phenomenon for ionic liquids, however, as Cadena and co-workers showed with simulation and NMR experiments of alkylpyridinium [Tf_2N] ionic liquids.[64] Urahata and Ribeiro[100] were the first to explain why imidazolium cations have larger self-diffusivities than the anions to which

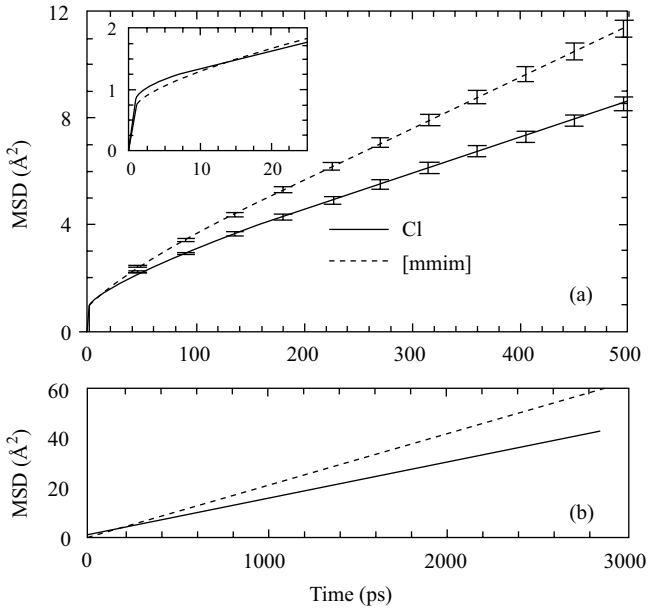

Figure 16 (a) Mean-squared displacement data of [C_1mim] and [Cl] at 425 K. The inset shows the same data at short times. Note the larger inertial motion of chloride ions, as expected. (b) Mean-squared displacement data from a single long trajectory of 6 ns. (Taken from Ref. 103 and used with permission.)

they are paired. Using MD simulations, they explained this behavior as being due to less hindered dynamics for the cation ring translational motion along the direction of the carbon at the 3 position in the ring. This is the same direction that exhibits the lowest frequency contribution to vibrational density of states obtained by Fourier transforming velocity–time correlation functions.

The top plot in Figure 17 contains the stress–stress autocorrelation function for [C_1mim][Cl] at 425 K calculated by Bhargava and Balasubramanian.[103] The rapid oscillations are due to high-frequency intramolecular motions of the cation. The correlation function shows a rapid short-time decay but a very slow long-time decay, as can be seen in the bottom graph in

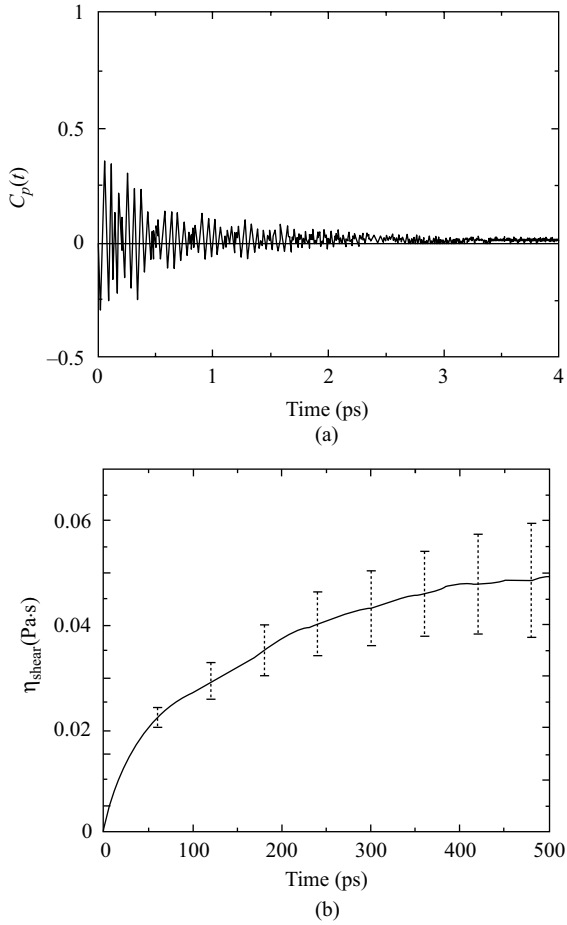

Figure 17 (a) Stress–stress correlation function for [C_1mim][Cl] at 425 K. (b) Estimated viscosity from integrating the stress–stress correlation function. Notice the difference in time scales. (From Ref. 103 and used with permission.)

Figure 17 where the convergence of the Green–Kubo integral is plotted. Despite the fact that the actual stress–stress correlation function has essentially reached zero after about 3 ps, the integral itself is still increasing after 500 ps. This behavior is entirely consistent with the results of Urahata and Ribeiro (shown in Figure 15), and the other dynamical studies discussed earlier. There is a large separation of time scales for different motions, so computing a transport coefficient that depends on these different modes requires time scales longer than the longest relevant relaxation time. A similar observation was made by Rey-Castro and Vega for $[C_2mim][Cl]$,[107] who computed the self-diffusivity, shear viscosity, and electrical conductivity using equilibrium MD over a temperature range of 380–486 K. These authors improved their estimates by fitting their time correlation function results to empirical analytic expressions and then integrating those expressions.

Before leaving the topic of Green–Kubo integrals for transport properties, we mention briefly the characteristics of the electric current correlation functions that are used to compute the electrical conductivity. Figure 18 shows the electric current and velocity autocorrelation functions for $[C_2mim][Cl]$ at 486 K and 1 bar. The current fluctuations decay rapidly and appear to vanish

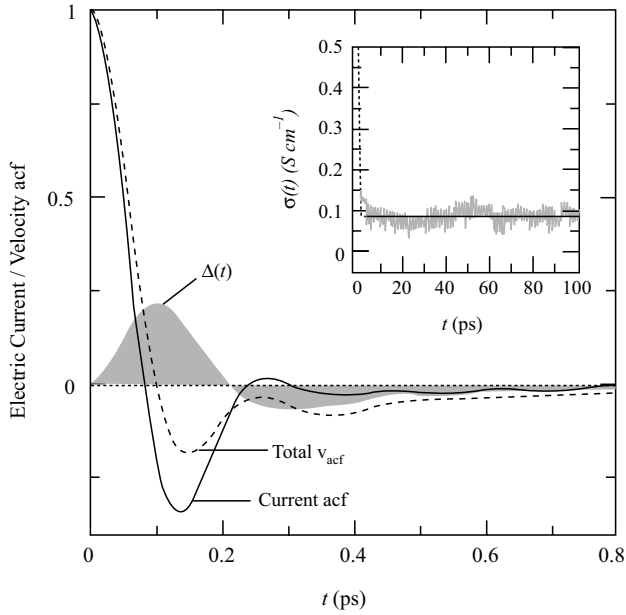

Figure 18 Normalized electric current autocorrelation function of $[C_2mim][Cl]$ at 486 K and 1 bar (bold solid line); total velocity autocorrelation function (dashed line); and difference between them (gray). The inset shows the running integral of the electrical conductivity (gray line), together with the best-fit exponential decay function (black line). (From Ref. 107 and used with permission.)

within 1 ps. The resulting time integral of the correlation function is affected by the large statistical noise (see inset of the figure), and, therefore, the accuracy in the estimated values of the electrical conductivity is poor; at the two lowest temperatures the uncertainties are of the same order of magnitude as the conductivity.[107] Estimated conductivities for this system are about 0.1 S/cm, which is within an order of magnitude or so of the expected value.

The point we make here is that it is unclear whether a transport property can be computed from a time integral over less than 100 ps in a liquid having widely varying dynamical time scales, some of which are in the nanosecond time scale. In general, it has been found that viscosities and conductivities computed using Green–Kubo integrals tend to result in slower dynamics (higher viscosities, lower conductivities) than what is observed experimentally, an effect that is often attributed to the neglect of polarizability. Another overlooked factor, however, could be with the methods themselves; because short-time integrals are incapable of capturing the contribution that long-time relaxation processes have on a transport property, it may be that these methods are only probing a ''local'' transport characteristic of the system. Such behavior is well known in the polymer melt literature, where relaxation times are quite long.[108] It is not that the methods themselves are ''incorrect,'' it is just that numerically evaluating the integrals accurately is difficult and can lead to incorrect results.

An alternative to using Green–Kubo integrals is to use either the (formally equivalent) integrated Einstein formula (Eq. [20]) or to implement a nonequilibrium method. In both cases, the appropriate response function can be averaged over an arbitrarily long time, thereby avoiding the numerical problems associated with Green–Kubo integrals. Use of these methods will not necessarily reduce computation time, but they may overcome the numerical problems associated with ionic liquid systems.

Borodin and Smith[109] used equilibrium MD to compute the self-diffusivity, viscosity, and electrical conductivity of *N*-methyl-*N*-propylpyrrolidinium bis (trifluoromethylsulfonyl)imide ($[C_3mpyro][Tf_2N]$) at temperatures between 303 and 393 K. Importantly, in all cases they used an Einstein-type equation to compute the transport coefficients. They were extremely careful in the way they equilibrated the system; production runs varied from 8 ns at the highest temperature to 16 ns at the lowest temperature. They also developed and utilized a many-body polarizable force field for this system. Figure 19 shows the computed self-diffusivites compared against NMR values from Nicotera and co-workers.[110] The agreement is outstanding. Figure 20 shows that the electrical conductivity also matches unpublished experimental data collected by Henderson of the U.S. Naval Academy quite well. Borodin and Smith were not able to make direct comparisons between their computed viscosities and experimental results, however, due to a lack of experimental data at which temperatures the simulations were run, though extrapolated values appeared reasonable. The results of this study demonstrate that transport coefficients

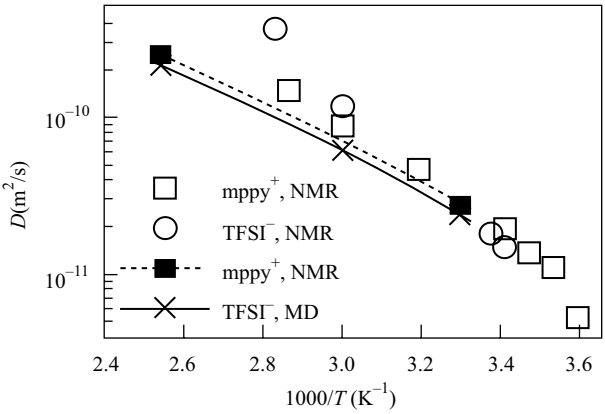

Figure 19 Computed self-diffusivity of *N*-methyl-*N*-propylpyrrolidinium bis(trifluoromethylsulfonyl)imide as a function of temperature, with comparison to experiment. (From Ref. 109 and used with permission.)

can be computed with quantitative accuracy. The distinguishing features of this work are that *long simulations* were used, as was a *polarizable* model and transport coefficients were computed with *Einstein-type transport equations*, in which averages were collected over long times. How important are each of these factors in determining the value of the transport coefficient? There has been no systematic study to answer this question to date, but it is obviously an important question that needs to be addressed.

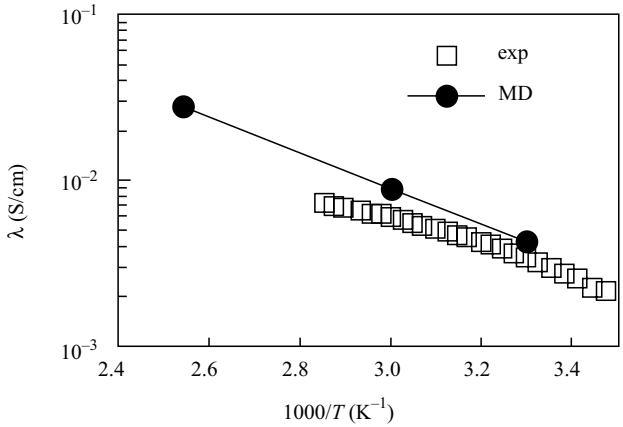

Figure 20 Computed electrical conductivity of *N*-methyl-*N*-propylpyrrolidinium bis (trifluoromethylsulfonyl)imide compared with experimental results from the unpublished work of Henderson. (From Ref. 109 and used with permission.)

More recently, Bhargava and Balasubramanian[111] proposed a refined force field for [C_4mim][PF_6]. The main modification they made is to treat the total charge on the cation and anion as an adjustable parameter. They found that by scaling the total charge to +0.8 e and −0.8 e, they were able to achieve better agreement between computed liquid structure and that obtained with ab initio MD simulations results (see below). They also obtained better agreement between computed and experimental surface tensions. Importantly, the self-diffusivities they computed from the Einstein relation were roughly a factor of 10 *higher* than what was obtained with a force field in which charges on the cations and anions were formally +1 e and −1 e. The agreement between calculated and experimental self-diffusivities is excellent. They attribute this to the fact that the reduced total charge is a better model for the actual charge distribution in the condensed phase, thereby approximating the screening that exists in the liquid. This suggests (though does not yet prove) that a combination of long simulation times over which the transport property is computed and some sort of polarizable model (whether it be an actual polarizable model or one with effective charges) will provide the best dynamical properties for ionic liquids.

Nonequilibrium Methods for Computing Transport Properties

An alternative to using equilibrium MD for computing transport coefficients is to use nonequilibrium molecular dynamics (NEMD) in which a modified Hamiltonian is used to drive the system away from equilibrium. By monitoring the response of the system in the limit of a small perturbation, the transport coefficient associated with the perturbation can be calculated. There is a rich literature on the use of NEMD to calculate transport coefficients; the interested reader is referred to the excellent monograph by Evans and Morriss[112] and the review article by Cummings and Evans.[113] The basic idea behind the technique is that a system will respond in a linear fashion to a small perturbation. The following linear response theory equation is applicable in this limit:

$$J = -L\nabla X \qquad [22]$$

where J is the response, X is the perturbation, and L is the transport coefficient. For example, Eq. [22] takes the following form for the viscosity:

$$j_y(p_x) = -\eta \frac{\partial v_x}{\partial y} \qquad [23]$$

where $j_y(p_x)$ is the momentum flux, $\partial v_x/\partial y$ is the velocity gradient or shear rate, and η is the shear viscosity. The most widely used NEMD approach for viscosity calculations is the so-called SLLOD algorithm[113] in which a shear rate is imposed on the system and the resulting stress is computed. The shear viscosity is found at a given shear rate from the following expression:

$$\eta = -\frac{P_{xy}}{\dot{\gamma}} \qquad [24]$$

where P_{xy} is the xy component of the stress tensor and $\dot{\gamma}$ is the shear rate.

There are several major advantages of using NEMD. Unlike equilibrium MD methods that rely on small natural fluctuations in quantities such as the stress, the ''signal'' in a NEMD simulation is often strong due to the external perturbation: the stronger the perturbation, the stronger the signal. In addition, the computed quantity is determined by averaging the relevant response variable for as long as required. This means that simulations much longer than any correlation time can (in principle) be carried out. Finally, equilibrium MD only gives a linear response value. For example, only the Newtonian (zero shear rate) viscosity is obtained from equilibrium MD. In contrast, NEMD enables one to compute the shear-dependent viscosity so that shear thinning/non-Newtonian behavior can be studied. There are downsides to the NEMD methods, however. Application of the SLLOD method for viscosity requires special ''sliding brick'' boundary conditions and a modification to the Ewald sum (if it is used to compute long-range Coulombic interactions), for example. Aside from these minor technical difficulties, a bigger problem with the SLLOD method is that it requires the calculation of the stress, a quantity that is difficult to converge in a simulation. Finally, because applied shear rates in simulations are typically much larger than experimental shear rates (due to the need to obtain an adequate signal), some method of extrapolating results to the zero shear rate limit is required if the linear response transport coefficients are to be calculated.

An alternative NEMD method has been developed that is much simpler to implement than is the SLLOD method, particularly for charged systems such as ionic liquids. The method is called reverse nonequilibrium molecular dynamics (RNEMD) and was first developed as a means for computing thermal conductivity[114] but has also been applied to viscosity.[115] It differs from conventional equilibrium and nonequilibrium methods where the ''cause'' is an imposed shear rate and the measured ''effect'' is a momentum flux/stress. RNEMD does the opposite; it imposes the difficult to compute quantity (the momentum flux or stress) and measures the easy to compute property (the shear rate or velocity profile). The method is very simple to implement because it only requires periodic swapping of momenta between atoms at different positions in the box. These swaps set up a velocity profile in the system (i.e., a shear rate). By tracking the frequency and amount of momentum

exchanged during the swap moves, the momentum flux is known. It is a simple matter to combine this with the measured shear rate to compute the shear viscosity via Eq. [23]. The method requires no modification to boundary conditions or the Ewald sum.

We have confirmed that the RNEMD method gives identical results to equilibrium MD and SLLOD calculations for the Lennard-Jones fluid, molten NaCl, water, alcohols, and alkanes[116] and have applied it to compute the viscosity of $[C_2mim][Tf_2N]$ as a function of temperature and water content.[117] Figure 21 shows the computed viscosity as a function of temperature. The solid line is a Vogel–Fulcher–Tamman fit to a large number of experimental data points. The agreement with experiment is excellent. Note that these results were obtained with a fixed-charge model in which the cation and anion were forced to have a formal charge of unity. The viscosity was also calculated for mixtures of $[C_2mim][Tf_2N]$ and water; it is known that water tends to lower the viscosity of ionic liquids dramatically, and the simulations captured this trend well (although the drop in calculated viscosity was not as great as what is observed experimentally). Most interesting is that the drop in viscosity observed experimentally and in the simulations is *less* than what would be predicted from simple empirical correlations. The conventional wisdom that small amounts of water dissolved in ionic liquids causes some inordinately large drop in the viscosity is not true; water does not decrease the viscosity as much as would be expected from "ideal" mixture viscosity models. The calculations show that water forms hydrogen-bonded clusters in the ionic liquid. As a result, the molar volume of the mixture remains somewhat lower than what would occur if the water had been mixed ideally (uniformly) with the

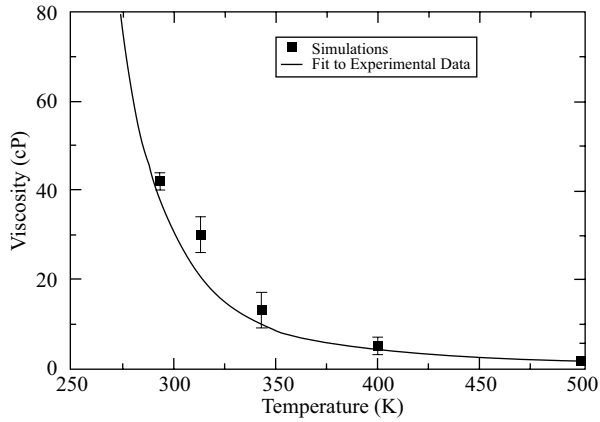

Figure 21 Computed viscosity as a function of temperature (symbols) compared to a correlation of a large number of data points (solid line) for $[C_2mim][Tf_2N]$. (Results are from Ref. 117.)

ionic liquid. As a consequence, the viscosity, which is sensitive to the liquid's density, does not drop as much. The calculations predict that mixtures of ionic liquids and nonpolar species, which would not cluster as easily as water, will actually decrease the viscosity of the mixture more than does water.

The RNEMD method has also been used to compute the thermal conductivity of 1-ethyl-3-methylimidazolium ethylsulfate ([C_2mim] [$EtSO_4$]) as a function of water content[118] using the simple point charge (SPC) model for water.[119] We are unaware of any experimental thermal conductivity data for this system, and we have not seen any previous thermal conductivity simulations for any other ionic liquids. Table 1 shows the computed values at 348 K. Note that the experimental thermal conductivity of pure water at this temperature is 0.66 W/(m K). Thus the SPC model overpredicts the thermal conductivity of pure water by nearly 30%.

Only a few experimental measurements of ionic liquid thermal conductivity exist. For example, [C_2mim][BF_4] has a value of 0.193 ± 0.006 W/(m K) at 350 K,[120] while [C_4mim][PF_6] has a thermal conductivity of 0.147 ± 0.007 W/(m K) at 335 K.[121] The computed values for [C_2mim] [$EtSO_4$] thus appear to be reasonable. Note that the thermal conductivity of the pure ionic liquid is much lower than that of water, and, it remains low even at a water mole fraction of 0.75.

To summarize, less work has been done on modeling transport properties of ionic liquids than on modeling properties such as liquid structure and density, but this area of research is undergoing rapid developments. We have emphasized here that one must be very careful when computing transport coefficients about the underlying assumptions being made. First, simulations must be run for times longer than the relevant dynamical relaxation processes in the liquid; at lower temperatures, these times can exceed 10 ns. Second, we argued against using the Green–Kubo integration methods because of the numerical inaccuracy associated with conducting lengthy integrations of time correlation functions that fluctuate near zero. Either integrated Einstein-like formulas or NEMD techniques should be used. Third, polarizability in a force field tends to increase the dynamics of the system, but it has not been shown that inclusion of polarizability is necessary to obtain

Table 1 Computed Thermal Conductivities for [C_2mim][$EtSO_4$] as a Function of Water Content at 348 K

Mole Fraction Water	Thermal Conductivity (W/m K)
0.00	0.167 ± 0.002
0.26	0.176 ± 0.003
0.50	0.187 ± 0.003
0.75	0.242 ± 0.005
1.00	0.85 ± 0.01

Source: From Ref. 118.

accurate transport properties; more work needs to be done to test the accuracy obtained with fixed-charge versus polarizable models. Finally, when care is taken, transport properties can be modeled accurately using atomistic simulations. This is encouraging because it suggests that ionic liquids may not be so "special" after all and that the simulation techniques developed and applied to the study of conventional liquids can be used successfully to study ionic liquids as well.

COARSE-GRAINED MODELS

Fully atomistic simulation of an ionic liquid is computationally demanding. Using state-of-the-art computing clusters and advanced codes, a reasonable MD simulation at a single liquid-state point may take several days. Multiple-state points can of course be run in parallel if processors are available. Moreover, highly parallelized MD codes such as NAMD,[66] LAMMPS,[122] and DL_POLY[35] can speed up these calculations significantly. MC calculations are embarrassingly parallel and can also be conducted using a "job farm" approach.[123] Running long enough simulations to derive reliable thermodynamic and transport properties, especially at lower temperatures, is still quite challenging, Although simulations of systems containing more than 10 million atoms have been carried out, "ordinary" calculations usually involve no more than tens of thousands of atoms and length scales of a few nanometers. If one is interested in computing properties that emerge only over very long length scales (say micron scale) are greater, performing a detailed atomistic simulation quickly becomes intractable. If having absolute accuracy is less important than deriving a qualitative insight, then performing detailed simulations may not be the best selection.

One approach that can be used to speed up calculations and enable larger systems to be examined is to develop a *coarse-grained* model of the ionic liquid. A classical atomistic simulation can already be thought of as a *coarse-grained* quantum calculation in which the detailed treatment of electronic degrees of freedom are replaced by semiempirical analytic functions. The type of coarse graining referred to in this section goes even further, by coarse graining the classical atomistic model. In essence, coarse graining seeks to eliminate nonessential degrees of freedom to arrive at a simplified representation of the system. Because there are fewer degrees of freedom when using a coarse-grained model and, often, the interactions between degrees of freedom are simple, calculations can be fast and very large systems can be studied for long periods.

The literature on coarse graining is vast and cannot be treated in any detail here. There are many examples of coarse-graining strategies for biomolecules[124] and polymers,[125] but there have not been as many studies for ionic liquids. A tutorial on coarse graining has been published in this book

series.[126] The united-atom ionic liquid force fields[30,39,56,127] are examples of coarse-grained models. The basic idea behind this approach is to group atoms together into single interaction sites. Usually, methyl and methylene groups are each treated as a single site. The accuracy of a coarse-grained model depends critically on how the model is developed. Typically, the functional form of the model is preselected, and parameters are fit to match some property of the fully atomistic model. If a poor choice is made for the preselected analytical function form, then the model will fail to give accurate results.

Wang, Izekov, Yan and Voth[128] recently proposed *multiscale coarse graining* (MSCG) for modeling of an ionic liquid. Their method is based on the concept that the forces on coarse-grained sites should "match" as closely as possible the forces in the atomistic sites that make up the coarse-grained sites. To do this, an atomistic force field of the type described by Eq. [5] is set up for an ionic liquid, and individual atoms are then "lumped" into coarse-grained sites, as shown in Figure 22. An atomistic simulation is performed and the forces on all the atoms associated with each coarse-grained site are recorded. The parameters in an empirical potential function representing the coarse-grained model are then adjusted until the forces present in the coarse-grained sites match, in a least-squares sense, the forces on the atoms constituting the coarse-grained sites. The authors show that structural properties such as radial distribution functions agree well with the fully atomistic calculations. Densities and compressibilities are also captured well, although the

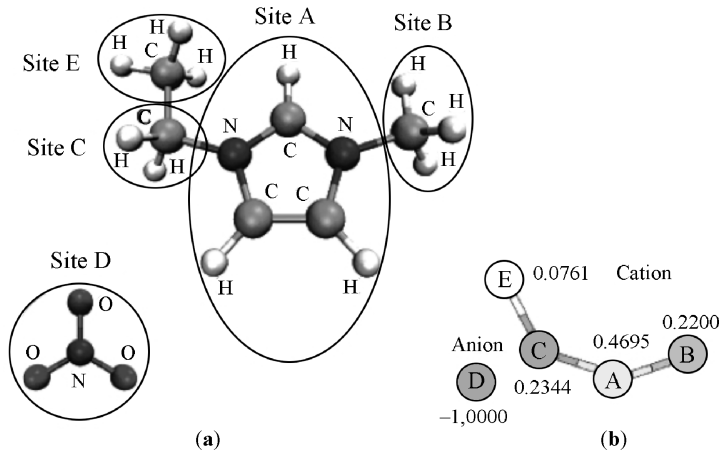

Figure 22 Coarse-graining strategy used to reduce the number of interaction sites required to model an ionic liquid. In (a) the cation is represented with four sites A, B, C, and E, while the anion is represented with a single site D. In (b) the simplified coarse-grained model is depicted with associated site charges. (From Ref. 128 and used with permission.)

dynamics of the system are overestimated significantly with the model, as is to be expected.

Wang and Voth[129] studied the local structure of the $[C_4mim][NO_3]$ system using this coarse-grained model and found that the tail groups formed relatively stable domains at a suitable temperature and when enough attractive interactions exist between the nonpolar groups on the cationic side chain. These domains are depicted in Figure 23. At the same time, Canongia Lopes and Padua[130] reported results using a fully atomistic model in which they also observed "nanodomains" of order among polar and nonpolar parts of the ionic liquid $[C_nmim][PF_6]$, where n is a variable length alkyl chain. They color-coded different regions of the ionic liquid (shown in gray tones in Figure 24) and observed segregation among the "polar" and "nonpolar" groups. In particular, they found that as the alkyl chain length increased, the nonpolar regions percolated the entire simulation box. This finding caused a great deal of excitement in the experimental ionic liquids community, and since then many experimental[131] and theoretical[132] studies have been carried out to confirm and explain that ordering. Coarse-grained models can thus provide qualitative insight into the behavior of ionic liquids and can stimulate and guide new experimental investigations while informing us of the details of liquid-phase organization in ways that are difficult to see experimentally.

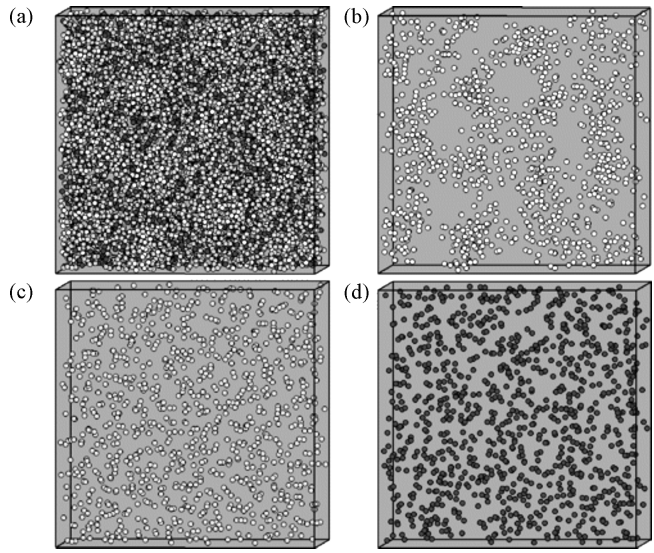

Figure 23 One snapshot of a coarse-grained representation of $[C_4mim][NO_3]$ with 1000 ion pairs at $T = 700$ K with (a) all atoms, (b) tail groups only, (c) head groups only, and (d) anions only. Notice the tail groups organize into domains. (From Ref. 129 and used with permission.)

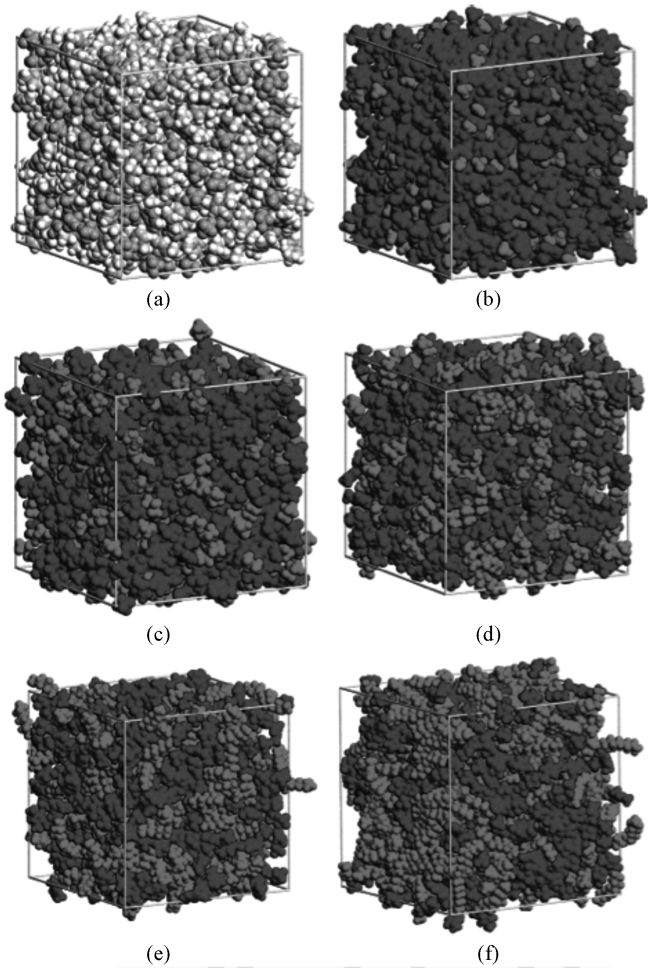

Figure 24 Snapshots of simulation boxes containing 700 ions of $[C_n\text{mim}][PF_6]$. The charged and nonpolar domains that form in ionic liquids are represented by dark and light gray spheres, respectively, in boxes (b)–(f). Box (a) shows CPK coloring for the same configuration shown in box (b) (see original publication for color). The ionic liquids in each box are: (a) $[C_2\text{mim}][PF_6]$; (b) $[C_2\text{mim}][PF_6]$; (c) $[C_4\text{mim}][PF_6]$; (d) $[C_6\text{mim}][PF_6]$; (e) $[C_8\text{mim}][PF_6]$; (f) $[C_{12}\text{mim}][PF_6]$. (From Ref. 130 and used with permission.)

AB INITIO MOLECULAR DYNAMICS

On the other end of the modeling spectrum are quantum-based methods one can use to carry out simulations that treat the energetics of the system even

more fully than is done with atomistic classical simulations. Whereas quantum calculations are implemented regularly to develop the classical force fields used in condensed-phase simulations, one can also conduct simulations in which a quantum calculation is used to compute the energy and forces on each atom present in the system. Such methods go by various names including ab initio molecular dynamics or first-principles molecular dynamics and have become popular since the release of easy-to-use software. Two of the more commonly used programs are CPMD[133] and SIESTA,[134] both of which use density functional theory with pseudopotentials. Because ab inito MD is significantly more demanding of computational resources than is classical MD, only very small system sizes can be examined and only for very short periods of time. This limits its usefulness significantly when it comes to computing properties of ionic liquids. Moreover, although ab initio methods are in principle "exact," in practice various approximations go into the methods used in ab initio MD, and the treatment of attractive dispersion interactions in density functional theory is questionable. Nevertheless, the calculations can provide some insight about local interactions present in these systems that could be useful in understanding solvation and reaction.

Del Popolo, Lynden-Bell and Kohanoff[135] conducted the first ab initio MD calculation of a condensed-phase ionic liquid in 2005. They modeled [C_1mim][Cl] using the SIESTA code. Although they state that this is a room temperature ionic liquid, it is actually a solid at room temperature, but it does melt below 100°C and so fits our definition of an ionic liquid. The bulk of their calculations were on eight ion pairs, with six trajectories, each run for up to 7 ps. It is impossible to equilibrate a system in only 7 ps due to the slow dynamics of ionic liquids. Therefore, classical simulations were first run to generate equilibrated systems, and then these configurations were used as initial conformations for the SIESTA runs. The authors simulated the crystalline phase and liquid phase and examined overall structure and orientation of the phases. Later, Bhargava and Balasubramanian[136] carried out CPMD simulations on 32 ion pairs of [C_1mim][Cl]. They computed the liquid structure and found good agreement between quantum-derived radial distribution functions and those obtained from classical MD. They also computed the vibrational density of states from the Fourier transform of the velocity autocorrelation function and made frequency assignments for each of the modes. As was the case with the work by Del Popolo, Lynden-Bell and Kohanoff,[135] however, deuterium was substituted for hydrogen to enable larger time steps to be taken, and so the calculated frequencies are shifted.

Ab initio MD methods are certain to gain popularity as computational power grows, but they are presently too expensive to use to obtain quantitative estimates of properties. Quantum MD is most useful for computing spectra, for helping validate and improve classical force fields, and for studying reactivity in ionic liquids, something classical simulations cannot do.

HOW TO CARRY OUT YOUR OWN IONIC LIQUID SIMULATIONS

Can anybody perform an atomistic simulation of an ionic liquid? The answer to this question is a qualified "yes," but it calls to mind the old joke that just because you can buy a knife, it does not mean you can be a surgeon. Likewise, just because someone can install a MD or MC software program does not mean that they will be able to obtain meaningful results by running the code. Like any aspect of science, be it experimental or computational, there is a learning curve that must be overcome before you get to the point where you can obtain meaningful results. In the "old days" when this author began molecular modeling research, there were only a few books available and most of the "tricks of the trade" were passed on by word of mouth. The *Reviews in Computational Chemistry* series had just begun in response to this situation, and the Internet consisted of ARCHIE and Gopher searches. Therefore, if you wanted to do molecular modeling you bought a book such as *Computer Simulation of Liquids* by Allen and Tildesley[99] and wrote your own code on an expensive (and therefore, usually shared) Unix workstation. In other words, the activation barrier for modeling was high, and those who paid the energy penalty were usually pretty sophisticated programmers and modelers by the time they had completed a simulation. Thanks to the prevalence of commercial and open-source software, graphical user interfaces, and instant downloads, a novice can set up and start running a simulation in an afternoon, while 15 years ago it might have taken several months just to get started. This development is a good thing, but it brings forth the warning that care must be taken so that the results being generated are meaningful and interpreted correctly. In this section, some guidelines and tips are provided for those new to modeling and who want to conduct classical simulations of ionic liquids.

The first question a new user needs to answer is: What do I want to get out of a simulation? The answer to this question really dictates the type and level of sophistication needed for the simulation. If you are interested in liquid structure or basic volumetric properties, either MD or MC methods will do just fine. If you need information on dynamics, then only MD will do. If you are more interested in thermodynamic phase behavior, however, MC is the best tool to use. These statements seem benign, but if you are new to modeling you should also be aware that many modeling researchers are passionate advocates of either MD or MC, but not both. They tend to use only one of these methods and reject the other method, probably because they are so heavily invested in the one method they use. The arguments about which method is "best" brings to mind (to this author at least) the fervor with which people argue over whether "Windows" or "Mac" is better. Our group is agnostic about which simulation method is better, and so we choose the right tool for the problem at hand. We think you should do the same.

What Code?

As is apparent from the discussion of previous work, the most popular simulation method in use right now to study ionic liquids is by far MD. Consequently, very little phase behavior work has been done on ionic liquids but much has been done on computing volumetric properties, liquid structure, and dynamics. Part of the reason for this state of affairs is that there are a large number of MD codes available for free or at very low cost. Some of the more popular ones that have been used for ionic liquid simulations include DL_POLY,[35] NAMD,[66] CHARMM,[137] LAMMPS,[122] GROMACS,[138] AMBER,[139] and MDynaMix.[61] Each has a different input and output format, and loading the correct force field parameters and other input commands can be tricky. Fortunately, each program has reasonably good documentation and a large user base that is good about answering questions. Each of the aforementioned programs has strengths and weaknesses, so your choice of software will depend, to some extent, on what properties you want to compute. We note in passing that commercial vendors market software that can be used to run simulations of ionic liquids. The advantage of using commercial software is that they come with easy-to-use interfaces and more support; in our experience, however, these codes tend to lag behind their open-source and academic rivals in terms of speed and innovative features. Those companies all have sufficient promotional materials available so there is no need to discuss their products here, and we focus only on noncommercial codes. For full disclosure, our group uses our own software developed in-house over many years. For large-scale MD calculations, we also use NAMD and LAMMPS.

NAMD is a very fast parallel MD code that scales to hundreds of processors on the right architecture machine. On commodity clusters it scales nicely to 32–128 processors. It is the recipient of the 2002 Gordon Bell award and is well supported and documented by the Theoretical and Computational Biophysics group at the University of Illinois. It may be downloaded from that group's website (http://www.ks.uiuc.edu/Research/namd/). NAMD has as its focus biophysics, so is not necessarily designed with ionic liquids in mind. It mainly uses the protein data bank molecular structure format for input and output of coordinates, which can become a bit unwieldy for ionic liquids. It is helpful to construct molecules with standard molecular drawing software and generate the requisite pdb files this way. NAMD is free and the source code (written in C++) is distributed with the binaries, though we find modification of the source code to be a daunting task. It is compatible with the popular molecular rendering package VMD[140] developed by the same group at Illinois. Our group has used NAMD for several years whenever we needed to run long MD simulations, and we find it to be efficient and relatively easy to use.

LAMMPS is also a well-parallelized and fast MD code. It was designed more for materials modeling and so in many ways is better suited than NAMD

for ionic liquids simulations. It is capable of modeling the liquid, solid, or gaseous state. It can model atomic, polymeric, biological, metallic, granular, and coarse-grained systems using a variety of force fields and boundary conditions, thus making it more flexible (in our view) than NAMD. LAMMPS is distributed as an open-source code under the terms of the GNU general public license. Current versions (last major release, or upgraded with all subsequent bug fixes and new features, or older FORTRAN90/FORTRAN77 versions) can be downloaded directly from the LAMMPS website (http://lammps.sandia.gov/). The last major release is also available on SourceForge. The primary developers of LAMMPS are Steve Plimpton, Paul Crozier, and Aidan Thompson at the Computer Science Research Institute, Sandia National Laboratory, although many others have contributed to the code. LAMMPS is written in C++ and is relatively easy to add to or modify, at least compared to NAMD. Becasue it is an open-source code, the authors encourage others to add features to LAMMPS, and in fact there are dozens of people around the world who have added features to LAMMPS and are listed now as ''co-authors'' of the code. LAMMPS has many nice features, including methods for computing the viscosity with nonequilibrium MD and the ability to use parallel tempering and hybrid Monte Carlo.

DL_POLY is a parallel molecular dynamics simulation package developed at Daresbury Laboratory by William Smith, T. R. Forester, and Ilian Todorov. Two versions of the code exist. DL_POLY2 uses replicated data parallelism and is best suited for systems containing up to 30,000 atoms and machines with 100 processors or less. DL_POLY3 uses domain decomposition (as does NAMD and LAMMPS) and so can handle larger systems of up to a million atoms or more and 1000 processors. Academic institutions may obtain a license to the code free of charge by visiting http://www.cse.scitech.ac.uk/ccg/software/DL_POLY/. Commercial users must contact the authors regarding use terms. DL_POLY is written in FORTRAN90 and can be modified by its users. It is designed as a very general MD code, capable of simulating a wide variety of molecule types and of using a range of different force field functions. Right now it is probably the most widely used MD package for ionic liquid simulations.

GROMACS (http://www.gromacs.org/) is another freely available MD code designed primarily for biomolecules but capable of being used for ionic liquid simulations. GROMACS was first developed in Herman Berendsen's group, in the Department of Biophysical Chemistry at Groningen University. Like LAMMPS, there are now several developers from all over the world adding to this code. The developers have started a wiki (http://wiki.gromacs.org/index.php/Main_Page) to help both old and new users with step-by-step instructions for setting up and running a simulation. GROMACS is written primarily in C, with some pieces written in FORTRAN and assembly language.

CHARMM, which stands for Chemistry at HARvard Molecular Mechanics, is one of the oldest and most widely used MD codes. It originated

in Martin Karplus' group at Harvard and is used mainly for simulating biomolecules, but it is flexible enough to simulate any molecular system including ionic liquids. It utilizes the CHARMM force field, which contains parameters for a large number of molecules. To use CHARMM for ionic liquids, the force field file must be edited to add parameters and atom types. CHARMM has an extensive user base with online forums to help answer almost any question. Academic users can acquire the software from the development team. Commercial users may obtain the software from Accelrys. Additional information on CHARMM is at http://www.charmm.org/.

AMBER (Assisted Model Building with Energy Refinement)[139] consists of a package of about 50 different programs and a set of public domain force fields. AMBER was originally developed under the direction of the late Peter Kollman and also has a large user base, mainly in the biological simulation area. AMBER has MD capabilities, as well as other techniques such as free energy calculation methods, replica exchange (parallel tempering) methods, and normal mode calculation procedures. AMBER is available to academicians for a nominal fee and to commercial users for a somewhat more significant fee. Information on AMBER is available at http://amber.scripps.edu/.

Finally, we mention the MD code MDynaMix, which has also been used to model ionic liquids. This program is based on the MOLDYN program created by Aatto Laaksonen, available from the CCP5 program library, Daresbury Lab, UK. However, starting in 1993 Alexander Lyubartsev has been making extensive changes to the code. This code is written in FORTRAN77 and performs all the standard calculations. It uses standard AMBER/CHARMM-type force fields and can be freely downloaded at http://www.fos.su.se/~sasha/md_prog.html.

What if you want to carry out MC simulations? Here, your options are much more limited. Some commercial modeling packages that have Monte Carlo features in them exist, including software sold by Hyperchem, Accelrys, and Schrodinger. In our opinion, none of these codes are adequate for computing phase behavior in ionic liquids. As far as we are concerned, the best open-source Monte Carlo code for ionic liquid simulations is Towhee,[123] available on SourceForge. Towhee was originally designed for the prediction of fluid-phase equilibria using atom-based force fields and the Gibbs ensemble, with particular attention paid to algorithms addressing molecule conformation sampling. The code has subsequently been extended to include several ensembles and many different force fields. The program contains several built-in ionic liquid force fields, and adding a new force field from published data is a relatively straightforward task. Towhee is maintained by Marcus Martin, who heads a small consulting company called Useful Bias. Although Towhee is free, Useful Bias will provide fee-based consulting on its use and extension. Towhee is currently undergoing extensive upgrades that will make it useful for phase equilibrium simulations of ionic liquids.

Some of the MD codes mentioned above (such as DL_POLY, AMBER, and NAMD) can perform thermodynamic integration and various free energy perturbation calculations. These techniques can be used to compute excess chemical potentials of solutes in ionic liquids and thereby obtain information on solvation. We believe MC methods are better suited for these types of calculations, however.

Force Fields

We have already reviewed many of the force fields used to model ionic liquids, and there are many more we could have listed. Almost all have the basic AMBER/CHARMM/OPLS style, which makes them compatible with all the MD and MC codes listed above. If accounting for polarizability is desired, only certain programs will be capable of carrying out these simulations (e.g., AMBER). From a user standpoint, a common question is: How do you know which force field to choose and how do you implement it? This is a difficult question to answer because, as demonstrated earlier, many different force fields and their associated parameter sets give similar properties such as liquid density. However, as was also shown, small variations in parameter sets can make a huge difference in both thermodynamic and transport properties. There is no easy way to tell which of the many published force fields is the right one to use; depending on the property of interest, the safest approach is to carry out benchmark calculations on systems for which experimental data is available and then extend the force field to other related systems. The best advice for now is to choose a force field from one of the studies reviewed in this chapter in which extensive validation has been performed. Parameters can then be added for new ionic liquids by following the recipes outlined in the studies. Fortunately, there are a number of current research efforts directed at developing more robust and automated ways of generating reliable force fields for ionic liquids, and beginning users will be able to draw on this work in the near future.

Data Analysis

Analyzing the output of a simulation can be one of the most difficult aspects of molecular modeling research. At the end of an MD simulation you are left with a huge collection of energies, forces, atomic positions, and velocities. How do you extract from this the information you want? One way is to write utility programs to do the analysis. There are many examples available to help with this, and standard textbooks provide good example codes.[99,141] If you do not want to do this, then some of the codes listed above have analysis utility tools that can help. LAMMPS, for example, has a collection of python-based pre- and postprocessing tools associated with it called Pizza.py. It can perform animations, extract thermodynamic data, read and

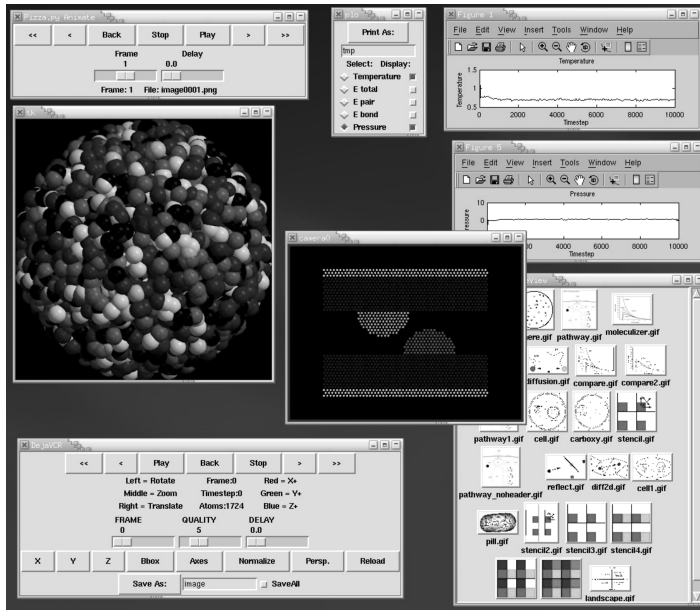

Figure 25 Screenshot of some of the features available in the analysis code pizza.py.

write LAMMPS input/output, and convert to other formats, among other things. Figure 25 shows a screenshot of several of these tools in action. DL_POLY writes output to a series of files from which the user can extract essential data fairly easily. It also has a Java-based graphical user interface that helps with job submission and analysis. NAMD also writes out a summary of properties, and it has a seamless interface with VMD that enables easy visualization and animation of trajectories. Calculation of other properties such as radial distribution functions, transport properties, or most thermodynamic properties, however, generally requires that the user write his or her own analysis software.

Operating Systems and Parallel Computing

Most large-scale atomistic simulations take place these days in a *cluster computing* environment in which a large number of commodity processors running Linux are hooked together to make a parallel computer. Of course, there are also specialized high-performance supercomputers that are run at scientific data centers. For the commodity clusters, parallelization is handled with various implementations of the message passing interface (MPI). If you work in a university or national lab environment, then there are most certainly experts all around you who know all about this and can help with installing

and running the software. If you prefer to "do it yourself," most of the codes provide detailed enough instructions to install the software on your own if you have a little patience. If you obtain the source code, you can in principle compile and run standalone versions of the software on a desktop machine. The Mac OS X operating system runs native Unix, so installation on this architecture is just like that on a Linux machine as long as you have installed the appropriate compilers. For Windows machines, a compiler (or programming environment like Visual C++) will be required to carry out the installation if the code does not come with precompiled binaries. Alternatively, the Linux emulation package Cygwin (http://www.cygwin.com/) can be installed to trick your Windows machine into thinking it is a Linux box, and then regular Linux installation instructions can be followed. A tutorial on high-performance computing in computational chemistry was published in Volume 6 of this book series[142] and provides much useful information for the beginner.

SUMMARY AND OUTLOOK

Seven years ago, there were no examples of classical simulations being used to study ionic liquids. Currently, a new publication on this topic appears about every week. The tremendous growth in ionic liquids simulation is due in part to the current popularity of ionic liquids, but the main driver for such studies is the fact that these calculations are generating useful results that are helping us understand the physical chemistry of ionic liquids. Simulations have given us the first detailed pictures of ionic liquid structure; they have shown how the ions organize in the liquid phase, how solutes interact with the ions, and that nanoscale segregation among polar and nonpolar groups occurs. All of these predictions have been subsequently confirmed experimentally. Simulations first predicted the enthalpies of vaporization of ionic liquids, and subsequent experimental work confirmed these predictions. Simulations have been used to study solvation dynamics and the agreement with experimental spectroscopic studies has been excellent. Simulations have been used to predict a wide range of ionic liquid properties including densities, heat capacities, self-diffusivities, viscosities, electrical and thermal conductivities, and solubilities. Many of these latter calculations were postpredictive, meaning that they were carried out on systems for which the experimental results were known. In general, there has been good agreement with the experiment results, thereby establishing confidence in the simulation methods. There have also been property calculations of ionic liquids that have not yet been made; these predictions are still awaiting experimental confirmation. Used in this mode, simulations are helping drive the discovery process for new ionic liquids having properties tuned for particular applications. It is imperative that atomistic simulations and experimental studies become complementary tools in the search for both fundamental understanding and practical application of

ionic liquids. This tutorial is intended to encourage and facilitate the adoption of simulation techniques and protocols by additional ionic liquid researchers to further our understanding of these fascinating substances.

ACKNOWLEDGMENTS

I thank my colleagues who have worked with me over the years on simulations of ionic liquids: Timothy Morrow, Jindal Shah, Cesar Cadena, David Eike, David Couling, David Tagler, Nate Stober, Wei Shi, Sai Jayaraman, Manish Kelkar, Keith Gutowski, and Burcu Eksioglu. This work has been funded by the Air Force Office of Scientific Research, the National Science Foundation, the U.S. Department of Energy, and the Indiana 21st Century Technology Fund. I especially thank Dr. Steve Plimpton and the Computer Science Research Institute at Sandia National Laboratory, Albuquerque, New Mexico, for hosting me on a sabbatical visit, during which time this chapter was written.

REFERENCES

1. J. S. Wilkes, *Green Chem.*, **4**, 73 (2002). A Short History of Ionic Liquids—From Molten Salts to Neoteric Solvents.
2. M. J. Earle, J. M. S. S. Esperanca, M. A. Gilea, J. N. C. Lopes, L. P. N. Rebelo, J. W. Magee, K. R. Seddon, and J. A. Widegren, *Nature*, **439**, 831 (2006). The Distillation and Volatility of Ionic Liquids.
3. J. L. Anthony, E. J. Maginn, and J. F. Brennecke, *J. Phys. Chem. B*, **106**, 7315 (2002). Solubilities and Thermodynamic Properties of Gases in the Ionic Liquid 1-*n*-butyl-3-methylimidazolium Hexafluorophosphate.
4. J. L. Anderson, J. K. Dixon, E. J. Maginn, and J. F. Brennecke, *J. Phys. Chem. B*, **110**, 15059 (2006). Measurement of SO_2 Solubility in Ionic Liquids.
5. P. Nockemann, B. Thijs, K. Driesen, C. R. Janssen, K. Van Hecke, L. Van Meervelt, S. Kossmann, B. Kircher, and K. Binnemans, *J. Phys. Chem. B*, **111**, 5254 (2007). Choline Saccharinate and Choline Acesulfamate: Ionic Liquids with Low Toxicities.
6. C. B. Jones, R. Haiges, T. Schroer, and K. O. Christe, *Angw. Chem.—Int. Ed.*, **45**, 4981 (2006). Oxygen-Balanced Energetic Ionic Liquid.
7. B. S. Phillipsa and J. S. Zabinskib, *Trib. Lett.*, **17**, 555 (2004). Ionic Liquid Lubrication Effects on Ceramics in a Water Environment.
8. J. G. Huddleston, A. E. Visser, W. M. Reichert, H. D. Willauer, G. A. Broker, and R. D. Rogers, *Green Chem.*, **3**, 156 (2001). Characterization and Comparison of Hydrophillic and Hydrophobic Room Temperature Ionic Liquids Incorporating the Imidazolium Cation.
9. J. M. Crosthwaite, S. N. V. K. Aki, E. J. Maginn, and J. F. Brennecke, *Fluid Phase Equil.*, **228**, 303 (2005). Liquid Phase Behavior of Imidazolium-Based Ionic Liquids with Alcohols: Effect of Hydrogen Bonding and Non-Polar Interactions.
10. NIST Ionic Liquids Database (IL Thermo), http://ilthermo.boulder.nist.gov/ILThermo/mainmenu.uix.
11. N. Metropolis, A. W. Rosenbluth, M. N. Rosenbluth, A. N. Teller, and E. Teller, *J. Chem. Phys.*, **21**, 1087 (1953). Equation of State Calculations by Fast Computing Machines.

12. B. J. Alder and T. E. Wainwright, *J. Chem. Phys.*, **31**, 459 (1959). Studies in Molecular Dynamics. I. General Method.

13. B. J. Alder and T. E. Wainwright, *Phys. Rev.*, **127**, 359 (1962). Phase Transition in Elastic Disks.

14. A. Rahman, *Phys. Rev.*, **136**, A405 (1964). Correlations in the Motion of Atoms in Liquid Argon.

15. L. Verlet, *Phys. Rev.*, **159**, 98 (1967). Computer "Experiments" on Classical Fluids. I. Thermodynamical Properties of Lennard-Jones Molecules.

16. M. L. Huggins and J. E. Mayer, *J. Chem. Phys.*, **1**, 643 (1933). Interatomic Distances in Crystals of the Alkali Halides.

17. J. E. Mayer, *J. Chem. Phys.*, **1**, 270 (1933). Dispersion and Polarizability and the van der Waals Potential in the Alkali Halides.

18. M. P. Tosi and F. G. Fumi, *J. Phys. Chem. Solids*, **25**, 31 (1964). Ionic Sizes and Born Repulsive Parameters in the NaCl-Type Alkali Halides. I.

19. M. J. Sangster and M. Dixon, *Adv. Phys.*, **25**, 247 (1976). Interionic Potentials in Alkali Halides and Their Use in Simulations of the Molten Salts.

20. C. Valeriani, E. Sanz, and D. Frenkel, *J. Chem. Phys.*, **122**, 194501 (2005). Rate of Homogenous Crystal Nucleation in Molten NaCl.

21. E. Sanz and C. Vega, *J. Chem. Phys.*, **126**, 014507 (2007). Solubility of KF and NaCl in Water by Molecular Simulation.

22. N. Galamba, C. A. Nieto de Castro, and J. F. Ely, *J. Phys. Chem. B.*, **108**, 3658 (2004). Molecular Dynamics Simulation of the Shear Viscosity of Molten Alkali Halides.

23. N. Galamba, C. A. Nieto de Castro, and J. F. Ely, *J. Chem. Phys.*, **120**, 8676 (2004). Thermal Conductivity of Molten Alkali Halides from Equilibrium Molecular Dynamics Simulations.

24. N. Galamba, C. A. Nieto de Castro, and J. F. Ely, *J. Chem. Phys.*, **122**, 22450, (2005). Shear Viscosity of Molten Alkali Halides from Equilibrium and Nonequilibrium Molecular-Dynamics Simulations.

25. D. M. Eike, J. F. Brennecke, and E. J. Maginn, *J. Chem. Phys.*, **122**, 014115 (2005). Toward a Robust and General Molecular Simulation Method for Computing Solid-Liquid Coexistence.

26. J. Akella, S. N. Vaidya, and G. C. Kennedy, *Phys. Rev.*, **185**, 1135 (1969). Melting of Sodium Chloride at Pressures to 65 kbar.

27. E. Hawlicka and T. Dlugoborski, *Chem. Phys. Lett.*, **268**, 325 (1997). Molecular Dynamics Simulations of the Aqueous Solution of Tetramethylammonium Chloride.

28. J. Oberbrodhage, *Phys. Chem. Chem. Phys.*, **2**, 129 (2000). Phase Transfer Catalysts Between Polar and Non-Polar Media: A Molecular Dynamics Simulation of Tetrabutylammonium Iodide at the Formamide / Hexane Interface.

29. J. Sun, M. Forsyth, and D. R. MacFarlane, *J. Phys. Chem. B*, **102**, 8858 (1998). Room Temperature Molten Salts Based on the Quaternary Ammonium Ion.

30. C. G. Hanke, S. L. Price, and R. M. Lynden-Bell, *Mol. Phys.*, **99**, 801 (2001). Intermolecular Potentials for Simulations of Liquid Imidazolium Salts.

31. D. E. Williams and S. R. Cox, *Acta Crystallogr. B*, **40**, 404 (1984). Nonbonded Potentials for Azahydrocarbons—The Importance of the Coulombic Interaction.

32. A. J. Stone and M. Alderton, *Mol. Phys.*, **56**, 1047 (1985). Distributed Multipole Analysis—Methods and Applications.

33. L. –Y. Hsu and D. E. Williams, *Acta Crystallogr. A*, **36**, 277 (1980). Intermolecular Potential Function Models for Crystalline Perchlorohydrocarbons.

34. D. E. Williams and D. J. Houpt, *Acta Crystallogr. B*, **42**, 286 (1986). Fluorine Nonbound Potential Parameters Derived from Crystalline Perfluorocarbons.

35. W. Smith and T. R. Forester, *J. Mol. Graphics*, **14**, 136 (1996). DL_POLY 2.0. A General-Purpose Parallel Molecular Dynamics Simulation Package.

36. C. Hardacre, S. E. J. McMath, M. Nieuwenhuyzen, D. T. Bowron, and A. K. Soper, *J. Phys.: Condens. Matt.*, **15**, S159 (2003). Liquid Structure of 1,3-Dimethylimidazolium Salts.

37. C. G. Hanke, N. A. Atamas, and R. M. Lynden-Bell, *Green Chem.*, **4**, 107 (2002). Solvation of Small Molecules in Imidazolium Ionic Liquids. A Simulation Study.

38. R. M. Lynden-Bell, N. A. Atamas, A. Vasilyuk, and C. G. Hanke, *Mol. Phys.*, **100**, 3225 (2002). Chemical Potentials of Water and Organic Solutes in Imidazolium Ionic Liquids: A Simulation Study.

39. J. K. Shah, J. F. Brennecke, and E. J. Maginn, *Green Chem.*, **4**, 112 (2002). Thermodynamic Properties of the Ionic Liquid 1-*n*-Butyl-3-methylimidazolium Hexafluorophosphate from Monte Carlo Simulations.

40. C. M. Breneman and K. B. Wiberg, *J. Comput. Chem.*, **11**, 361 (1990). Determining Atom-Centered Monopoles from Molecular Electrostatic Potentials. The Need for High Sampling Density in Formamide Conformational Analysis.

41. W. L. Jorgensen, D. S. Maxwell, and J. Tirado-Rives, *J. Am. Chem. Soc.*, **118**, 11225 (1996). Development and Testing of the OPLS All-Atom Force Field on Conformational Energetics and Properties of Organic Liquids.

42. A. D. MacKerell, D. Bashford, M. Bellott, R. L. Dunbrack, J. D. Evanseck, M. J. Field, S. Fisher, J. Gao, H. Guo, S. Ha, D. Joseph-McCarthy, L. Kuchnir, K. Kuczera, F. T. K. Lau, C. Mattos, S. Michnick, T. Ngo, D. T. Nguyen, B. Prodhom, W. E. Reiher III, B. Roux, M. Schlenkrich, J. C. Smith, R. Stote, J. Straub, M. Watanabe, J. Wiorkiewicz-Kuczera, D. Yin, and M. Karplus, *J. Phys. Chem. B*, **102**, 3586 (1998). All-Atom Empirical Potential for Molecular Modeling and Dynamics Studies of Proteins.

43. K. R. Seddon as quoted by M. Freemantle, in *C&E News*, **78**, 37 (2000). Eyes on Ionic Liquids.

44. Y. U. Paulechka, D. H. Zaitsau, G. J. Kabo, and A. A. Strechan, *Thermochim. Acta*, **439**, 158 (2005). Vapor Pressure and Thermal Stability of Ionic Liquid 1-Butyl-3-methylimidazolium bis(trifluoromethylsulfonyl)amide.

45. D. H. Zaitsau, G. J. Kabo, A. A. Strechan, Y. U. Paulechka, A. Tschersich, S. P. Verevkin, and A. Heintz, *J. Phys. Chem. A*, **110**, 7303 (2006). Experimental Vapor Pressures of 1-Alkyl-3-methylmidazolium bis(trifluoromethylsulfonyl) Imides and a Correlation Scheme for Estimation of Vaporization Enthalpies of Ionic Liquids.

46. L. M. N. B. F. Santos, J. N. Canongia Lopes, J. A. P. Coutinho, J. M. S. S. Esperanca, L. R. Gomes, I. M. Marrucho, and L. P. N. Rebelo, *J. Am. Chem. Soc.*, **129**, 284 (2007). Ionic Liquids: First Direct Determination of Their Cohesive Energy.

47. C. J. Margulis, H. A. Stern, and B. J. Berne, *J. Phys. Chem. B*, **106**, 12017 (2002). Computer Simulation of a "Green Chemistry" Room-Temperature Ionic Solvent.

48. G. A. Kaminsky and W. L. Jorgensen, *J. Chem. Soc., Perkin Trans.*, **2**, 2365 (1999). Host-Guest Chemistry of Rotaxanes and Catenanes: Application of a Polarizable All-Atom Force Field to Cyclobis(paraquat-*p*-phenylene) Complexes with Disubstituted Benzenes and Biphenyls.

49. T. I. Morrow and E. J. Maginn, *J. Phys. Chem. B*, **106**, 12807 (2002). Molecular Dynamics Study of the Ionic Liquid 1-*n*-Butyl-3-methylimidazolium Hexafluorophosphate. Corrigendum: T. I. Morrow, and E. J. Maginn, *J. Phys. Chem. B*, **107**, 9160 (2003).

50. Z. Gu and J. F. Brennecke, *J. Chem. Eng. Data*, **27**, 339 (2002). Volume Expansivities and Isothermal Compressibilities of Imidazolium and Pyridinium-Based Ionic Liquids.

51. J. de Andrade, E. S. Boes, and H. Stassen, *J. Phys. Chem. B*, **106**, 3546 (2002). A Force Field for Liquid State Simulations on Room Temperature Molten Salts: 1-Ethyl-3-methylimidazolium Tetrachloroaluminate.

52. J. de Andrade, E. S. Boes, and H. Stassen *J. Phys. Chem. B*, **106**, 13344 (2002). Computational Study of Room Temperature Molten Salts Composed by 1-Alkyl-3-methylimidazolium Cations—Force Field Proposal and Validation.

53. W. D. Cornell, P. Cieplak, C. I. Bayly, I. R. Gould, K. M. Merz, Jr., D. M. Ferguson, D. C. Spellmeyer, T. Fox, J. W. Caldwell, and P. A. Kollman, *J. Am. Chem. Soc.*, **117**, 5179 (1995).

A Second Generation Force Field for the Simulation of Proteins, Nucleic Acids, and Organic Molecules.

54. M. W. Schmidt, K. K. Baldridge, J. A. Boatz, S. T. Elbert, M. S. Gordon, J. J. Jensen, S. Koseki, N. Matsunaga, K. A. Nguyen, S. Su, T. L. Windus, M. Dupuis, and J. A. Montgomery, *J. Comput. Chem.*, **14**, 1347 (1993). General Atomic and Molecular Electronic Structure System.
55. S. Takahashi, K. Suzuya, S. Kohara, N. Koura, L. A. Curtiss, and M. L. Saboungi, *Z. Phys. Chem.*, **209**, 209 (1999). Structure of 1-Ethyl-3-methylimidazolium Chloroaluminates: Neuron Diffraction Measurements and Ab Initio Calculations.
56. S. M. Urahata and M. C. C. Ribeiro, *J. Chem. Phys.*, **120**, 1855 (2004). Structure of Ionic Liquids of 1-Alkyl-3-methylimidazolium Cations: A Systematic Computer Simulation Study.
57. J. N. Canongia Lopes, J. Deschamps, and A. A. H. Padua, *J. Phys. Chem. B*, **108**, 2038 (2004). Modeling Ionic Liquids Using a Systematic All-Atom Force Field.
58. J. N. Canongia Lopes, J. Deschamps, and A. A. H. Padua, *J. Phys. Chem. B*, **104**, 2038 (2004). Modeling Ionic Liquids Using a Systematic All-Atom Force Field.
59. Ionic Liquid Force Field Parameters Developed by Canongia Lopes and Padua: http://therm10.univ-bpclermont.fr/~apadua/.
60. Z. Liu, S. Huang, and W. Wang, *J. Phys. Chem. B*, **108**, 12978 (2004). A Refined Force Field for Molecular Simulation of Imidazolium-Based Ionic Liquids.
61. A. P. Lyubartsev and A. Laaksonen, *Comput. Phys. Commun.*, **128**, 565 (2000). M.Dyna-Mix—A Scalable Portable Parallel MD Simulation Package for Arbitrary Molecular Mixtures.
62. M. G. Del Popolo and G. A. Voth, *J. Phys. Chem. B*, **108**, 1744 (2004). On the Structure and Dynamics of Ionic Liquids.
63. T. Yan, C. J. Burnham, M. G. Del Popolo, and G. A. Voth, *J. Phys. Chem. B*, **108**, 11877 (2004). Molecular Dynamics Simulation of Ionic Liquids: The Effect of Electronic Polarizability.
64. C. Cadena, Q. Zhao, R. Q. Snurr, and E. J. Maginn, *J. Phys. Chem. B*, **110**, 2821 (2006). Molecular Modeling and Experimental Studies of the Thermodynamic and Transport Properties of Pyridinium-Based Ionic Liquids.
65. J. N. Canongia Lopes and A. A. H. Padua, *J. Phys. Chem. B*, **108**, 16893 (2004). Molecular Force Field for Ionic Liquids Composed of Triflate or Bistriflylimide Anions.
66. J. C. Philips, R. Braun, W. Wang, J. Gumbart, E. Tajkhorshid, E. Villa, C. Chipot, R. D. Skeel, L. Kale, and K. Schulten, *J. Comput. Chem.*, **26**, 1781 (2005). Scaleable Molecular Dynamics with NAMD.
67. J. N. Canongia Lopes and A. A. H. Padua, *J. Phys. Chem. B*, **110**, 19586 (2006). Molecular Force Field for Ionic Liquids III: Imidazolium, Pyridinium, and Phosphonium Cations; Chloride, Bromide, and Dicyanamide Anions.
68. C. Cadena and E. J. Maginn, *J. Phys. Chem. B*, **110**, 18026 (2006). Molecular Simulation Study of Some Thermophysical and Transport Properties of Triazolium-Based Ionic Liquids.
69. G. Zhou, X. Liu, S. Zhang, G. Yu, and H. He, *J. Phys. Chem. B*, **111**, 7078 (2007). A Force Field for Molecular Simulation of Tetrabutylphosphonium Amino Acid Ionic Liquids.
70. X. M. Liu, S. J. Zhang, G. H. Zhou, G. W. Wu, X. L. Yuan, and X. Q. Yao, *J. Phys. Chem. B*, **110**, 12062 (2006). New Force Field for Molecular Simulation of Guanidinium-Based Ionic Liquids.
71. X. Liu, G. Zhou, S. Zhang, G. Wu, and G. Yu, *J. Phys. Chem. B*, **111**, 5658 (2007). Molecular Simulation of Guanidinium-Based Ionic Liquids.
72. C. G. Hanke, A. Johansson, J. B. Harper, and R. M. Lynden-Bell, *Chem. Phys. Lett.*, **374**, 85 (2003). Why Are Aromatic Compounds More Soluble Than Aliphatic Compounds in Dimethylimidazolium Liquids?
73. C. G. Hanke and R. M. Lynden-Bell, *J. Phys. Chem. B*, **107**, 10873 (2003). A Simulation Study of Water-Dialkylimidazolium Ionic Liquid Water Mixtures.

74. C. Cadena, J. L. Anthony, J. K. Shah, T. I. Morrow, J. F. Brennecke, and E. J. Maginn, *J. Am. Chem. Soc.*, **126**, 5300 (2004). Why Is CO_2 So Soluble in Imidazolium-Based Ionic Liquids?

75. J. Deschamps, M. Costa Gomes, and A. A. H. Padua, *Chem. Phys. Chem.*, **5**, 1049 (2004). Molecular Simulation Study of Interactions of Carbon Dioxide and Water with Ionic Liquids.

76. J. L. Anthony, E. J. Maginn, and J. F. Brennecke, *J. Phys. Chem. B*, **105**, 10942 (2001). Solution Thermodynamics of Imidazolium-Based Ionic Liquids in Water.

77. J. K. Shah and E. J. Maginn, *Fluid Phase Equil.*, **222–223**, 195 (2004). A Monte Carlo Simulation Study of the Ionic Liquid 1-*n*-Butyl-3-methylimidazlium Hexafluorophosphate: Liquid Structure, Volumetric Properties and Infinite Dilution Solution Thermodynamics with CO_2.

78. D. A. Kofke and P. T. Cummings, *Fluid Phase Equil.*, **150–151**, 41 (1998). Precision and Accuracy of Staged Free Energy Perturbation Methods for Computing the Chemical Potential by Molecular Simulation.

79. J. K. Shah and E. J. Maginn, *J. Phys. Chem. B*, **109**, 10395 (2005). Monte Carlo Simulations of Gas Solubility in the Ionic Liquid 1-*n*-Butyl-3-methylimidazolium Hexaflurophosphate.

80. I. Urukova, J. Vorholz, and G. Maurer, *J. Phys. Chem. B*, **109**, 12154 (2005). Solubility of CO_2, CO and H_2 in the Ionic Liquid [bmim][PF_6] from Monte Carlo Simulations.

81. I. Urukova, J. Vorholz, and G. Maurer, *J. Phys. Chem. B*, **110**, 18072 (2006). Correction to "Solubility of CO_2, CO and H_2 in the Ionic Liquid [bmim][PF_6] from Monte Carlo Simulations."

82. W. Shi and E. J. Maginn, *J. Chem. Theory Comput.*, **3**, 1451 (2007). Continuous Fractional Component Monte Carlo: An Adaptive Biasing Method for Open System Atomistic Simulations.

83. W. Shi and E. J. Maginn, *J. Phys. Chem. B* **112**, 2045 (2008). Atomistic Simulation of the Absorption of Water in the Ionic Liquid 1-*n*-Hexyl-3-methylimidazolium bis(trifluoromethylsulfonyl)imide ([hmim][Tf_2N].

84. S. N. V. K. Aki, B. R. Mellein, E. M. Saurer, and J. F. Brennecke, *J. Phys. Chem. B*, **108**, 20355 (2004). High Pressure Phase Behavior of Carbon Dioxide with Imidazolium-Based Ionic Liquids.

85. J. Kumelan, A. P. S. Kamps, D. Tuma, and G. Maurer, *J. Chem. Thermodyn.*, **38**, 1396 (2006). Solubility of CO_2 in the Ionic Liquid [hmim][Tf_2N].

86. A. M Scurto, personal communication, University of Kansas, 2007.

87. A. Chaumont and G. Wipff, *Phys. Chem. Chem. Phys.*, **5**, 3481 (2003). Solvation of M^{3+} Lanthanide Cations in Room-Temperature Ionic Liquids. A Molecular Dynamics Investigation.

88. A. Chaumont, E. Engler, and G. Wipff, *Inorg. Chem.*, **42**, 5348 (2003). Uranyl and Strontium Salt Solvation in Room-Temperature Ionic Liquids. A Molecular Dynamics Investigation.

89. C. Gaillard, A. Chaumont, I. Billard, C. Hennig, A. Ouadi, and G. Wipff, *Inorg. Chem.*, **46**, 4815 (2007). Uranyl Coordination in Ionic Liquids: The Competition Between Ionic Liquid Anions, Uranyl Counterions, and Cl^- Anions Investigated by Extended X-ray Absorption Fine Structure and UV-Visible Spectroscopies and Molecular Dynamics Simulations.

90. N. Sieffert and G. Wipff, *J. Phys. Chem. B*, **110**, 13076 (2006). The [BMI][Tf_2N] Ionic Liquid/Water Binary System: A Molecular Dynamics Study of Phase Separation and of the Liquid-Liquid Interface.

91. Y. Shim, J. Duan, M. Y. Choi, and H. J. Kim, *J. Chem. Phys.*, **119**, 6411 (2003). Solvation in Molecular Ionic Liquids.

92. V. Znamenskiy and M. N. Kobrak, *J. Phys. Chem. B*, **108**, 1072 (2004). Molecular Dynamics Study of Polarity in Room-Temperature Ionic Liquids.

93. R. Karmakar and A. Samanta, *J. Phys. Chem. A*, **106**, 4447 (2002). Solvation Dynamics of Coumarin-153 in a Room Temperature Ionic Liquid.

94. D. A. McQuarrie, *Statistical Mechanics*, University Science Books, Sausalito, CA, 2000.
95. Z. H. Hu and C. J. Margulis, *Proc. Nat. Acad. Sci., U.S.A.*, **103**, 831 (2006). Heterogeneity in a Room Temperature Ionic Liquid: Persistent Local Environments and the Red-Edge Effect.
96. Z. H. Hu and C. J. Margulis, *Proc. Nat. Acad. Sci., U.S.A.*, **104**, 9546 (2007). Heterogeneity in a Room Temperature Ionic Liquid: Persistent Local Environments and the Red-Edge Effect. Corrigendum: [**103**, 831 (2006)].
97. P. Mandal, M. Sarkar, and A. Samanta, *J. Phys. Chem. A*, **108**, 9048 (2004). Excitation-Wavelength-Dependent Fluorescence Behavior of Some Dipolar Molecules in Room Temperature Ionic Liquids.
98. A. Paul, P. K. Mandal, and A. Samanta, *J. Phys. Chem. B*, **109**, 9148 (2005). On the Optical Properties of the Imidazolium Ionic Liquids.
99. M. P. Allen and D. J. Tildesley, *Computer Simulation of Liquids*, Oxford University Press Oxford, 1987.
100. S. M. Urahata and M. C. C. Ribeiro, *J. Chem. Phys.*, **122**, 024511 (2005). Single Particle Dynamics in Ionic Liquids of 1-Alkyl-3-methylimidazolium Cations.
101. H. A. Every, A. G. Bishop, D. R. MacFarlane, G. Oradd, and M. Forsyth, *Phys. Chem. Chem. Phys.*, **6**, 1758 (2004). Transport Properties in a Family of Dialklyimidazolium Ionic Liquids.
102. B. Hess, *J. Chem. Phys.*, **116**, 209 (2002). Determining the Shear Viscosity of Model Liquids from Molecular Dynamics Simulations.
103. B. L. Bhargava and S. Balasubramanian, *J. Chem. Phys.*, **123**, 144505 (2005). Dynamics in a Room Temperature Ionic Liquid: A Computer Simulation Study.
104. S. U. Lee, J. Jung, and Y.-K. Han, *Chem. Phys. Lett.*, **406**, 332 (2005). Molecular Dynamics Study of the Ionic Conductivity of 1-*n*-Butyl-3-methylimidazolium Salts as Ionic Liquids.
105. T. Umecky, M. Kanakubo, and Y. Ikushima, *Fluid. Phase Equil.*, **228–229**, 329 (2005). Self-Diffusion Coefficients of 1-Butyl-3-methylimidazolium Hexafluorophosphate with Pulsed-Field Gradient Spin-Echo NMR Technique.
106. M. Kanakubo, K. R. Harris, N. Tsuchihashi, K. Ibuki, and M. Ueno, *J. Phys. Chem. B*, **111**, 2062 (2007). Effect of Pressure on Transport Properties of the Ionic Liquid 1-Butyl-3-methylimidazolium Hexafluorophosphate.
107. C. Rey-Castro and L. F. Vega, *J. Phys. Chem. B*, **110**, 14426 (2006). Transport Properties of the Ionic Liquid 1-Ethyl-3-methylimidazolium Chloride from Equilibrium Molecular Dynamics Simulation. The Effect of Temperature.
108. M. Vladkov and J. L. Barrat, *Macromol. Theory Simulat.*, **15**, 252 (2006). Linear and Nonlinear Viscoelasticity of a Model Unentangled Polymer Melt.
109. O. Borodin and G. D. Smith, *J. Phys. Chem. B*, **110**, 11481 (2006). Structure and Dynamics of *N*-Methyl-*N*-propylpyrrolidinium Bis(trifluoromethanesulfonyl)imide Ionic Liquid from Molecular Dynamics Simulations.
110. I. Nicotera, C. Oliviero, W. A. Henderson, G. B. Appetecchi, and S. Passerini, *J. Phys. Chem. B*, **109**, 22814 (2005). NMR Investigation of Ionic Liquid–LiX Mixtures: Pyrrolidinium Cations and $TFSI^-$ Anions.
111. B. L. Bhargava and S. Balasubramanian, *J. Chem. Phys.*, **127**, 114510 (2007). Refined Potential Model for Atomistic Simulations of Ionic Liquid [bmim][PF_6].
112. D. J. Evans and G. P. Morriss, *Statistical Mechanics of Nonequilibrium Liquids*, Academic, London, 1990.
113. P. T. Cummings and D. J. Evans, *Ind. Eng. Chem. Res.*, **31**, 1237 (1992). Nonequilibrium Molecular Dynamics Approaches to Transport Properties and Non-Newtonian Fluid Rheology.
114. M. M. Zhang, E. Lussetti, L. E. S. de Souza, and F. Müller-Plathe, *J. Phys. Chem. B*, **109**, 15060 (2005). Thermal Conductivities of Molecular Liquids by Reverse Nonequilibrium Molecular Dynamics.

115. F. Müller-Plathe, *Phys. Rev. E*, **59**, 4894 (1999). Reversing the Perturbation in Nonequilibrium Molecular Dynamics: An Easy Way to Calculate the Shear Viscosity of Fluids.

116. M. S. Kelkar, J. L. Rafferty, E. J. Maginn, and J. I. Siepmann, *Fluid. Phase Equil.*, **260**, 218 (2006). Prediction of Viscosities and Vapor-Liquid Equilibria for Five Polyhydric Alcohols by Molecular Simulation.

117. M. S. Kelkar and E. J. Maginn, *J. Phys. Chem. B*, **111**, 4867 (2007). Effect of Temperature and Water Content on the Shear Viscosity of the Ionic Liquid 1-Ethyl-3-methylimidazolium bis (trifluoromethylsulfonyl)imide As Studied by Atomistic Simulations.

118. M. S. Kelkar, W. Shi, and E. J. Maginn, University of Notre Dame, unpublished work, 2007.

119. H. J. C. Berendsen, J. P. M. Postma, W. F. van Gunsteren, and J. Hermans, *Intermolecular Forces*, Reidel, Dordrecht, 1981.

120. M. E. Van Valkenberg, R. L. Vaughn, M. Williams, and J. S. Wilkes, *Thermochim. Acta*, **425**, 181 (2005). Thermochemistry of Ionic Liquid Heat-Transfer Fluids.

121. D. Tomida, S. Kenmochi, T. Tsukada, K. Qiao, and C. Yokoyama, *Int. J. Thermophys.*, **28**, 1147 (2007). Thermal Conductivities of [bmim][PF_6], [hmim][PF_6], and [omim][PF_6] from 294 to 335 K at Pressures up to 20 MPa.

122. LAMMPS—Large-scale Atomic/Molecular Massively Parallel Simulator, Sandia National Laboratory, http://lammps.sandia.gov/.

123. MCCCS Towhee, http://towhee.sourceforge.net.

124. B. S. Khatri and T. C. B. McLeish, *Macromolecules*, **40**, 6770 (2007). Rouse Model with Internal Friction: A Coarse Grained Framework for Single Biopolymer Dynamics.

125. J. Baschnagel, K. Binder, W. Paul, M. Laso, U. W. Suter, I. Batoulis, W. Jilge, and T. Burger, *J. Chem. Phys.*, **95**, 6014 (1991). On the Construction of Coarse-Grained Models for Linear Flexible Polymer Chains—Distribution Functions for Groups of Consecutive Monomers.

126. R. Faller in *Reviews in Computational Chemistry*, K. B. Lipkowitz and T. R. Cundari, Eds., Wiley-VCH, Hoboken, NJ, 2007, Vol. 23, pp. 233–262. Coarse Grain Modeling of Polymers.

127. Z. P. Liu, X. P. Wu, and W. C. Wang, *Phys. Chem. Chem. Phys.*, **8**, 1096 (2006). A Novel United Atom Force Field for Imidazolium-Based Ionic Liquids.

128. Y. Wang, S. Izvekov, T. Yan, and G. A. Voth, *J. Phys. Chem. B*, **110**, 3564 (2006). Multiscale Coarse-Graining of Ionic Liquids.

129. Y. Wang and G. A. Voth, *J. Phys. Chem. B*, **110**, 18601 (2006). Tail Aggregation and Domain Diffusion in Ionic Liquids.

130. J. N. A. Canongia Lopes and A. A. H. Padua, *J. Phys. Chem. B*, **110**, 3330 (2006). Nanostructural Organization in Ionic Liquids.

131. A. Triolo, O. Russina, H. J. Bleif, and E. Di Cola, *J. Phys. Chem. B*, **111**, 4641 (2007). Nanoscale Segregation in Room Temperature Ionic Liquids.

132. A. A. Aerov, A. R. Khokhlov, and I. I. Potemkin, *J. Phys. Chem. B*, **111**, 10189 (2007). Microphase Separation in a Mixture of Ionic and Nonionic Liquids.

133. R. Car and M. Parrinello, *Phys. Rev. Lett.*, **55**, 2471 (1985). Unified Approach for Molecular Dynamics and Density Functional Theory.

134. J. M. Soler, E. Artacho, J. D. Gale, A. Garcia, J. Junquera, P. Ordejon, and D. Sanchez-Portal, *J. Phys.: Condens. Matt.*, **14**, 2745 (2002). The Siesta Method for Ab Initio Order-N Materials Simulation.

135. M. G. Del Popolo, R. M. Lynden-Bell, and J. Kohanoff, *J. Phys. Chem. B*, **109**, 5895 (2005). Ab Initio Molecular Dynamics Simulation of a Room Temperature Ionic Liquid.

136. B. L. Bhargava and S. Balasubramanian, *J. Phys. Chem. B*, **111**, 4477 (2007). Insights into the Structure and Dynamics of a Room Temperature Ionic Liquid: Ab Initio Molecular Dynamics Simulation Studies of 1-*n*-Butyl-3-methylimidazolium Hexafluorophosphate ([bmim][PF_6]) and the [bmim][PF_6]-CO_2 Mixture.

137. B. R. Brooks, R. E. Bruccoleri, B. D. Olafson, D. J. States, S. Swaminathan, and M. Karplus, *J. Comput. Chem.*, **4**, 187 (1983). CHARMM: A Program for Macromolecular Energy, Minimization, and Dynamics Calculations. See also: http://www.charmm.org/.

138. H. J. C. Berendsen, D. van der Spoel, and R. van Drunen, *Computer Phys. Comm.*, **91**, 43 (1995). GROMACS—A Message Passing Parallel Molecular Dynamics Implementation.

139. D. A. Case, T. E. Cheatham, III, T. Darden, H. Gohlke, R. Luo, K. M. Merz, Jr., A. Onufriev, C. Simmerling, B. Wang, and R. Woods. *J. Comput. Chem.* **26**, 1668 (2005). The AMBER Biomolecular Simulation Programs.

140. VMD—Visual Molecular Dynamics. http://www.ks.uiuc.edu/Research/vmd/.

141. D. Frenkel and B. Smit, *Understanding Molecular Simulation*, Academic San Diego, 2002.

142. R. A. Kendall, R. J. Harrison, R. J. Littlefield, and M. F. Guest, in *Reviews in Computational Chemistry*, K. B. Lipkowitz and D. B. Boyd, Eds., VCH, Weinheim, 1995, Vol. 6, pp. 209–316. High Performance Computing in Computational Chemistry: Methods and Machines.

Author Index

Reviews in Computational Chemistry, Volume 26
edited by Kenny B. Lipkowitz and Thomas R. Cundari

Subject Index

Computer programs are denoted in boldface, databases and journals are in italic

Reviews in Computational Chemistry, Volume 26
edited by Kenny B. Lipkowitz and Thomas R. Cundari